Physics of the Solid State, Vol. 43, No. 1, 2001, pp. 1–8. Translated from Fizika Tverdogo Tela, Vol. 43, No. 1, 2001, pp. 3–10.

METALS AND SUPERCONDUCTORS

On the Velocity of a 4π Kink Moving under the Action of Current

A. S. Malishevskiĭ, V. P. Silin, and S. A. Uryupin

Lebedev Institute of Physics, Russian Academy of Sciences, Leninskiĭ pr. 53, Moscow, 117924 Russia
e-mail: malish@sci.lebedev.ru

Received May 3, 2000

Abstract—The dependence of bias current density through a junction on the velocity of a uniformly moving vortex carrying two magnetic flux quanta is established in the approximation of weakly nonlocal Josephson electrodynamics. It is shown that the velocity quantization of free motion of the vortex, which is induced by the Cherenkov interaction with Swihart waves, leads to the emergence of a discrete family of curves on the velocity–current plane. © *2001 MAIK "Nauka/Interperiodica".*

The experimental work by Dueholm *et al.* [1] necessitated the formulation of an approach in Josephson vortex electrodynamics to construct a description of coherent structures in long Josephson junctions, which could move uniformly in the absence of dissipation, carrying several magnetic flux quanta. Such coherent vortex structures were called $2\pi n$ kinks, since an ordinary Josephson vortex carrying only one magnetic flux quantum corresponds to a 2π change in the phase difference $\varphi(z, t)$ upon a change in the coordinate z from $-\infty$ to $+\infty$. The first analytic solution describing such a coherent structure in a nondissipative Josephson junction between two bulk superconductors was obtained in 1993 [2, 3] and corresponded to a 4π kink. This solution was obtained in the framework of nonlocal electrodynamics corresponding to very high critical densities of the Josephson current, for which the Josephson length λ_j is smaller than the London length λ. An analytic description of a 4π kink was obtained in [4] under similar conditions, but for a junction with sandwich geometry. This solution finally made it possible to construct a description of a 4π kink [5], corresponding to junctions with a low Josephson critical current density, for which

$$\lambda \ll \lambda_j. \tag{1}$$

Along with analytic approaches [2–5], a numerical approach to the study of nonlocal generalizations of the sine–Gordon equation was also developed. This generalization corresponding to nonlocal electrodynamics was used to construct a numerical description of a 4π kink [6, 7]. An important step made in [6] was the application of the weakly nonlocal approximation in which fourth-order derivatives, along with second-order derivatives, were also taken into account in an equation generalizing the sine–Gordon equation. It is clear now that such an approximation is realized when inequality (1) is satisfied and when the velocity of a vortex is close to the Swihart velocity v_s, which is the maximum possible for the free motion of an ordinary 2π kink in the sine–Gordon equation. This approximation was used for obtaining an analytic description of a 4π kink [5]. All numerical and analytic descriptions of 4π kinks obtained in this approximation moved freely with a velocity characteristic for a given model. An important numerical result was obtained by Alfimov *et al.* [7], who observed a 4π kink with a nonmonotonic dependence on the coordinate in addition to a 4π kink with a monotonic spatial dependence. It was found that the monotonic and nonmonotonic 4π kinks move at different velocities. It should be emphasized that this is similar to a certain extent to the known numerical results obtained by Peyrard and Kruskal [8] using a discrete model of Josephson junctions.

The results of the description of 4π kinks mentioned above were obtained for an ordinary sine nonlinear dependence of the superconducting current through the junction on the phase difference φ of the wave functions of Cooper pairs. There exists another model proposed by Aubry and Le Daeron [9, 10] for describing dislocations and by Volkov [11, 12] for describing Josephson junctions. The Aubry–Volkov model [9–12] envisages a periodic saw-tooth dependence of the superconducting current density on the phase difference φ, which leads to a large number of analytical results for nonlinear running waves. This model was used in [13] to obtain a countable set of 4π kinks. It was proved that owing to the resonant Cherenkov interaction with Swihart waves, 4π kinks trap waves in the gaps between 2π kinks. In the coherent structures formed as a result, the waves play the role of an adhesive which glues vortices together [14]. As a result of Cherenkov trapping of waves by vortices, the coherent structures of 4π kinks are characterized by discrete numbers corresponding to the number of waves accommodated in the region of vortex gluing. The velocities of free motion of different vortices in this case are discrete (quantized).

It should be noted that apart from the Aubry–Volkov model, there is one more exactly solvable model [15],

in which the sine is simulated by a sequence of isosceles triangles. Dissipation is taken into account in this model conventionally by supplementing D'Alembert's differential operator with two differential terms. The term with the first-order time derivative describes the ohmic losses in the material separating the superconductor, while the term with a mixed third-order derivative of the phase difference for wave functions of Cooper pairs (the first-order derivative is with respect to time and the second-order derivative is with respect to the coordinates) describes the so-called surface losses associated with normal electrons in the superconductors. Sakai [15] proved that, in the case of considerable surface losses, a 4π kink driven by a bias current may exist in such a model. It should be emphasized that the free motion of such a 4π kink, which exists owing to strong dissipation, is ruled out. This distinguishes qualitatively the 4π kinks considered in [15] from those in [13, 14].

In the present paper, the Aubry–Volkov model is used to analyze the induced motion of a 4π kink under the action of a bias current density j. The dependence of j on the velocity v of a 4π kink derived by us is an analog of the current–voltage characteristic (IVC). It is proved that each eigenvalue v_n of the velocity of free motion of a 4π kink is the origin for a pair of $j(v)$ curves. This leads to the formation of the IVC band on the (v, j) plane.

1. BASIC EQUATIONS

As the starting equation in our analysis, we will use [6, 16]

$$\frac{1}{\omega_j^2}\frac{\partial^2\varphi}{\partial t^2} - \lambda_j^2\frac{\partial^2\varphi}{\partial z^2} - \frac{\lambda^2\lambda_j^2}{2}\frac{\partial^4\varphi}{\partial z^4} + F[\varphi] = -\pi J - \frac{\beta}{\omega_j^2}\frac{\partial\varphi}{\partial t} + \frac{\eta\lambda_j^2}{\pi\omega_j^2}\frac{\partial^3\varphi}{\partial t\partial z^2}. \quad (2)$$

Here, ω_j is the Josephson frequency, j_c is the critical density of the Josephson current, $J \equiv j/j_c$, β characterizes the dissipation in the junction separating the superconductors, and η characterizes the so-called surface dissipation determined by the normal electrons in the superconductors. The operator on the left-hand side of Eq. (2) differs from the operator used usually, in the so-called local theory, in the third term containing a fourth-order derivative with respect to the coordinates. Such an approximation of the equation is associated with the approximation of weak spatial nonlocality. It is productive, for example, when the velocity of vortices is close to Swihart velocity $v_s \equiv \lambda_j\omega_j$. The last term on the left-hand side of Eq. (2) in the Aubry–Volkov model is given by

$$F[\varphi] = \varphi - 2\pi I\left[\frac{\varphi}{2\pi} + \frac{1}{2}\right], \quad (3)$$

where $I[x]$ is the integral part of the number x. In accordance with Eq. (3) and following [4], we will use the following notation:

$$\omega_j \equiv 4\sqrt{|e|j_c d/\hbar\epsilon}, \quad \lambda_j \equiv c(\sqrt{\hbar/\lambda|e|j_c})/4,$$

where e is the electron charge, c is the velocity of light, $2d$ is the thickness of the layer separating the superconductors, and ϵ is the dielectric constant of this layer.

Subsequent analysis is devoted to vortices moving at a constant velocity v, for which

$$\varphi = \varphi(\zeta), \quad \zeta \equiv z - vt,$$

and Eq. (2) assumes the following form:

$$\left(1 - \frac{v^2}{v_s^2}\right)\lambda_j^2\frac{d^2\varphi}{d\zeta^2} + \frac{\lambda^2\lambda_j^2}{2}\frac{d^4\varphi}{d\zeta^4} - F[\varphi] = \pi J - \frac{\beta v}{\omega_j^2}\frac{d\varphi}{d\zeta} + \frac{\eta\lambda_j^2 v}{\pi\omega_j^2}\frac{d^3\varphi}{d\zeta^3}. \quad (4)$$

In the range of the parameters under investigation, the characteristic scale of the spatial variation of a 4π kink is

$$\lambda_j' \equiv \lambda_j\sqrt{1 - (v/v_s)^2}. \quad (5)$$

Accordingly, using the dimensionless variable $\xi \equiv \zeta/\lambda_j'$ for the function $\psi(\xi) = \varphi(\lambda_j'\xi)$, we can write, in accordance with Eq. (4),

$$\varepsilon^2\frac{d^4\psi}{d\xi^4} + \frac{d^2\psi}{d\xi^2} - F[\psi] = \pi J - \bar{\beta}\frac{d\psi}{d\xi} + \bar{\eta}\frac{d^3\psi}{d\xi^3}. \quad (6)$$

Here and below, we use the following notation:

$$\varepsilon^2 = \varepsilon^2(v) \equiv \frac{\lambda^2}{2\lambda_j^2[1 - (v/v_s)^2]^2},$$

$$\bar{\beta} = \bar{\beta} \equiv \frac{\beta}{\omega_j}\frac{v/v_s}{\sqrt{1 - (v/v_s)^2}}, \quad (7)$$

$$\bar{\eta} = \bar{\eta}(v) \equiv \frac{\eta}{\pi\omega_j}\frac{v/v_s}{[1 - (v/v_s)^2]^{3/2}}.$$

In order to make our calculations less cumbersome, we will henceforth confine our analysis to the case when

$$\lambda^2/2\lambda_j^2 \ll \varepsilon^2 \ll 1. \quad (8)$$

In this case, Eq. (6) is a differential equation in which the coefficient of the highest order derivative is a small parameter.

2. PHASE DIFFERENCE IN A JUNCTION WITHOUT OHMIC LOSSES

In this section, we consider the limiting case of Eq. (6), in which ordinary dissipative effects are neglected, $\beta = \eta = 0$, and the only dissipative effect is associated with losses associated with Cherenkov radiation. In this case, we have

$$\varepsilon^2\frac{d^4\psi}{d\xi^4} + \frac{d^2\psi}{d\xi^2} - F[\psi] = \pi J. \tag{9}$$

We construct a continuous solution of this equation, satisfying the conditions $-\pi < \psi < \pi$ for $\xi < -\xi_j$; $\psi(-\xi_j) = \pi$; $\pi < \psi < 3\pi$ for $-\xi_j < \xi < \xi_j$; $\psi(\xi_j) = 3\pi$; and $3\pi < \psi < 5\pi$ for $\xi > \xi_j$.

The process of solving the equation begins at the leading edge of a vortex, where $\xi > \xi_j$. Considering that there are no waves in front of the vortex, we assume that all the derivatives of the function ψ are equal to zero for $\xi \longrightarrow +\infty$. In accordance with Eq. (9) and under the assumption that

$$J < 1, \tag{10}$$

we obtain the following expression for the phase difference of a 4π kink for $\xi \longrightarrow +\infty$:

$$\psi(+\infty) = 4\pi - \pi J.$$

For the leading edge of the vortex, we obtain from Eqs. (3) and (9)

$$\varepsilon^2\frac{d^4\psi}{d\xi^4} + \frac{d^2\psi}{d\xi^2} - \psi = -4\pi + \pi J, \quad \xi > \xi_j. \tag{11}$$

Since $\psi(\xi_j) = 3\pi$, the solution of Eq. (11) is given by

$$\begin{aligned}\psi(\xi) = \psi_h(\xi) &= 4\pi - \pi J - \pi(1-J)\exp[-k_1(\xi-\xi_j)] \\ &\equiv 3\pi + \pi(1-J)\{1-\exp[-k_1(\xi-\xi_j)]\},\end{aligned} \tag{12}$$

where the size of the region where the solution attains the constant value $4\pi - \pi J$ is determined, in units of the quantity defined in Eq. (5), by the number

$$k_1 = \frac{1}{\sqrt{2}\varepsilon}\sqrt{\sqrt{1+4\varepsilon^2}-1} \simeq 1 - \frac{\varepsilon^2}{2}. \tag{13}$$

For the central region of the vortex, where $\pi < \psi < 3\pi$, we obtain the following equation from Eqs. (3) and (9):

$$\varepsilon^2\frac{d^4\psi}{d\xi^4} + \frac{d^2\psi}{d\xi^2} - \psi = -2\pi + \pi J, \quad -\xi_j < \xi < \xi_j.$$

A solution to this equation satisfying the joining condition for the solution itself and its first three derivatives with the solution in Eq. (12) and its derivatives, respectively, is given by

$$\begin{aligned}\psi(\xi) = \psi_b(\xi) &= 2\pi - \pi J[1 - e^{-k_1(\xi-\xi_j)}] \\ &+ \frac{\pi}{k_0^2 + k_1^2}\{2k_1^2\cos[k_0(\xi-\xi_j)] \\ &+ k_0^2 e^{k_1(\xi-\xi_j)} - k_1^2 e^{-k_1(\xi-\xi_j)}\},\end{aligned} \tag{14}$$

where the wave number

$$k_0\frac{1}{\sqrt{2}\varepsilon}\sqrt{\sqrt{1+4\varepsilon^2}+1} \simeq \frac{1}{\varepsilon} + \frac{\varepsilon}{2} \tag{15}$$

defines the wavelength $\lambda_0 = 2\pi/k_0$ of Swihart waves emitted by a moving vortex. Equating the function in Eq. (14) to π at the point $\xi = -\xi_j$, we obtain the condition

$$\begin{aligned}1 - J(1 - e^{2k_1\xi_j}) + (k_0^2 + k_1^2)^{-1}\{2k_1^2\cos(2k_0\xi_j) \\ + k_0^2\exp(-2k_1\xi_j) - k_1^2\exp(2k_1\xi_j)\} = 0,\end{aligned} \tag{16}$$

which connects the quantities J, ξ_j, and v. This condition will be subsequently used for deriving the dependence $J(v)$.

Let us now describe the tail part of the vortex, for which $\psi < \pi$. Equation (9) assumes the form

$$\varepsilon^2\frac{d^4\psi}{d\xi^4} + \frac{d^2\psi}{d\xi^2} - \psi = \pi J, \quad \xi < -\xi_j. \tag{17}$$

A solution to this equation can be presented in the form

$$\begin{aligned}\psi(\xi) = \psi_t(\xi) &= -\pi J + A_t\cos k_0\xi \\ &+ B_t\sin k_0\xi + C_t\exp[k_1(\xi+\xi_j)].\end{aligned} \tag{18}$$

Here, C_t describes the spatially monotonic dependence of the vortex, while A_t and B_t characterize the field of the Cherenkov radiation of Swihart waves in the tail of the vortex, which is associated with the accelerating action of the current on the vortex. The joining of solutions in Eqs. (14) and (18) and their first three derivatives gives

$$A_t = \frac{4\pi k_1^2}{k_0^2 + k_1^2}\cos k_0\xi_j, \qquad B_t = 0,$$

$$C_t = \frac{\pi}{k_0^2 + k_1^2}(k_0^2 e^{-2k_1\xi_j} + k_1^2 e^{2k_1\xi_j}) - \pi J e^{2k_1\xi_j}$$

and another relation between the quantities J, ξ_j, and v, which supplements condition (16):

$$J = (k_0^2 + k_1^2)^{-1}(k_1^2 - k_0^2 e^{-2k_1\xi_j}). \tag{19}$$

Thus, the distribution of the phase difference of a 4π kink in the entire space is described by the functions

$\psi_h(\xi)$ in Eq. (12), $\psi_b(\xi)$ in Eq. (14), and $\psi_t(\xi)$ in Eq. (18). The phase difference in the leading edge of the vortex decreases exponentially from $4\pi - \pi J$ to 3π. At the middle of the vortex, there appear periodic trigonometric functions corresponding to Swihart waves in addition to the terms describing the monotonic dependence of ψ. The tail part of the vortex is described by a trigonometric function corresponding to Swihart waves emitted by the vortex and contains a monotonic term decreasing to $-\pi J$, $J < 1$.

The description of the vortex structure becomes even more clear if we present the solutions in Eqs. (12), (14), and (18) in a form which appears naturally when we construct a solution with the help of the Fourier transformation on the entire ξ axis. Indeed, using relation (19) and introducing the notation

$$\begin{aligned} C &\equiv k_1^2/(k_0^2 + k_1^2), \\ f(\xi) &\equiv k_0^2(k_0^2 + k_1^2)^{-1}\exp(-k_1|\xi|), \\ \psi_{2\pi,\omega}(\xi) &\equiv \pi + \pi[1 - f(\xi)]\,\mathrm{sgn}\,\xi, \\ \psi_{2\pi,\omega}(\xi) &\equiv 2\pi C\theta(-\xi)\cos(k_0\xi), \end{aligned} \tag{20}$$

where $\theta(\xi)$ is a Heaviside step function and $\mathrm{sgn}\,\xi \equiv 2\theta(\xi) - 1$ is the signum function, we obtain the following expression for the phase difference of a 4π kink:

$$\begin{aligned} \psi(\xi) &= -\pi J + \psi_{2n,m}(\xi + \xi_j) + \psi_{2\pi,m}(\xi - \xi_j) \\ &\quad + \psi_{2\pi,m}(\xi + \xi_j) + \psi_{2\pi,\omega}(\xi - \xi_j). \end{aligned} \tag{21}$$

In accordance with Eq. (21), in the limit of small currents defined by Eq. (10), a 4π kink is the sum of two 2π kinks localized near the points $-\xi_j$ and ξ_j. Each of the 2π kinks emits Swihart waves [see Eq. (20)] which interfere with one another for $\xi < -\xi_j$. In the absence of current ($J = 0$), the waves emitted by the 2π kinks are absent in the tail part of the vortex. We are left only with oscillations localized in the interior region of the vortex and ensuring the gluing of two 2π kinks into a single 4π kink. If, however, the current differs from zero, the field of Cherenkov radiation is induced in the tail of the vortex. In other words, when a 4π kink is accelerated by the current, Swihart waves are not trapped in the region confined between two kinks and form an oscillating trace in the tail part of the vortex. Thus, the tail of the 4π kink is periodically modulated by the Swihart waves emitted by the vortex.

3. RELATION BETWEEN THE CURRENT AND THE VORTEX VELOCITY

Relations (16) and (19) connecting the current J, the coordinate ξ_j, and the vortex velocity v allow us to establish the form of the function $J(v)$. We write these relations in the form

$$(1 + \delta^2)J = 2\delta^2\cos^2(k_0\xi_j), \tag{22}$$

$$(1 + \delta^2)J = \delta^2 - \exp(-2k_1\xi_j), \tag{23}$$

where we denote $\delta \equiv k_1/k_0$ and the numbers k_0 in Eq. (15) and k_1 in Eq. (13) depend on the vortex velocity through the small parameter ε in Eq. (7). Since $\varepsilon \ll 1$, we have

$$\delta \simeq \varepsilon - \varepsilon^3 \ll 1. \tag{24}$$

Taking into account the smallness of the parameter ε, we obtain the size of the interior part of the vortex from Eqs. (23) and (24):

$$2\xi_j = \ln\left(\frac{1}{\varepsilon^2 - J}\right). \tag{25}$$

A solution to Eq. (25) has meaning only if the current density for a given vortex velocity does not exceed the quantity

$$J_0(v) \equiv \varepsilon^2(v). \tag{26}$$

Taking into account relation (25), we obtain from Eqs. (22) and (24) the following equation for $J(v)$:

$$J = 2\varepsilon^2\cos^2\left[\frac{1}{2\varepsilon}\ln\left(\frac{1}{\varepsilon^2 - J}\right)\right]. \tag{27}$$

In order to determine the function $J(v)$, we write Eq. (27) in the form

$$\begin{aligned} &\left(1 - \frac{J}{J_0}\right)\exp\left[\mp\varepsilon\arccos\left(1 - \frac{J}{J_0}\right)\right] \\ &\quad = \exp\left[2\ln\frac{1}{\varepsilon} - \pi\varepsilon(2n + 1)\right]. \end{aligned} \tag{28}$$

In this equation, the integer quantity n numbers the discrete set of the functions $J(v)$ connecting the vortex velocity with the current. The functions $J(v)$ corresponding to different values of n describe the current-induced motion of vortices with different internal structures characterized by the number of Swihart wavelengths fitting into them.

In the absence of current, we find from Eq. (28) that the parameter ε, and hence the velocity of a freely moving 4π kink, assumes discrete values labeled by the number n:

$$\frac{1}{\varepsilon_n}\ln\frac{1}{\varepsilon_n} = \pi\left(n + \frac{1}{2}\right). \tag{29}$$

Taking into account inequalities (8), we find that the number n must lie in the interval

$$1 \ll n \ll \frac{2\sqrt{2}}{\pi}\frac{\lambda_j}{\lambda}\ln\left(\frac{\lambda_j}{\lambda}\right). \tag{30}$$

For such values of n, we find from Eq. (29)

$$\varepsilon_n \simeq \left[\pi\left(n + \frac{1}{2}\right)\right]^{-1}\ln\left[\pi\left(n + \frac{1}{2}\right)\right] \simeq \frac{\ln(\pi n)}{\pi n} \ll 1. \tag{31}$$

In the presence of a bias current, the situation becomes different. Now, Eq. (28) describes the relation between

the current J and the vortex velocity v for each number n from the interval defined in Eq. (30). Each number n corresponds to two $J(v)$ curves in view of the presence of two signs of arccos in the exponential on the left-hand side of Eq. (28). On the current–velocity plane, such curves originate at the point $v = v_n$, $J = 0$, where

$$\frac{v_n}{v_s} \simeq 1 - \frac{\lambda}{2\sqrt{2}\lambda_j \varepsilon_n} \simeq 1 - \frac{\pi n \lambda}{2\sqrt{2}\lambda_j \ln(\pi n)}$$

corresponds to solution (31) of Eq. (29).

When the vortex velocity v is close to v_n to such an extent that

$$\frac{1}{\varepsilon_n^2} \simeq \left(\frac{\pi n}{\ln \pi n}\right)^2 \gg 4\sqrt{2}\pi n \frac{\lambda_j}{\lambda}\frac{v - v_n}{v_s} \geq -\frac{1}{2}, \qquad (32)$$

the solution of Eq. (28) has the form

$$J_\pm \simeq \varepsilon_n^4 \left\{1 + 4\sqrt{2}\pi n \frac{\lambda_j}{\lambda}\frac{v - v_n}{v_s} \pm \sqrt{1 + 8\sqrt{2}\pi n \frac{\lambda_j}{\lambda}\frac{v - v_n}{v_s}}\right\} \ll \varepsilon_n^2. \qquad (33)$$

For an insignificant difference between v and v_n, when

$$\frac{|v - v_n|}{v_s} \ll \frac{1}{8\sqrt{2}\pi n}\frac{\lambda_j}{\lambda}, \qquad (34)$$

we obtain from Eq. (33)

$$J_+ \simeq 2\varepsilon_n^4, \quad J_- \simeq \left(4\pi n \frac{\lambda_j}{\lambda}\right)^2 \left(\frac{v - v_n}{v_s}\right)^2 \varepsilon_n^4.$$

The function J_- vanishes for $v = v_n$. In the interval defined in Eq. (34), the function J_- increases monotonically with the difference between v and v_n both for increasing and decreasing velocities. The velocity range in which $dJ_-/dv < 0$ is an analog of an unstable IVC characterized by a negative differential resistance.

At the point

$$v = v_i(n) \simeq v_n - \frac{\lambda}{8\sqrt{2}\pi n \lambda_j} v_s \simeq v_s\left[1 - \frac{\lambda}{2\sqrt{2}\lambda}\left(\frac{\pi n}{\ln \pi n} + \frac{1}{4\pi n}\right)\right],$$

the functions J_- and J_+ have equal values and their derivatives have infinitely large values. For $v < v_l(n)$, Eq. (28) has no solution for a given n.

As the value of v increases so that the difference between v and v_n satisfies the condition

$$\frac{1}{\varepsilon_n^2} \gg 4\sqrt{2}\pi n \frac{\lambda_j}{\lambda}\frac{v - v_n}{v_s} \gg 1,$$

we obtain from Eq. (33)

$$J_\pm \simeq 4\sqrt{2}\pi n \varepsilon_n^4 \frac{\lambda_j}{\lambda}\frac{v - v_n}{v_s}\left\{1 \pm \sqrt{\frac{1}{2\sqrt{2}\pi n}\frac{\lambda}{\lambda_j}\frac{v_s}{v - v_n}}\right\}. \qquad (35)$$

In accordance with relations (30) and (35), the difference between the functions J_- and J_+ is relatively small.

Finally, we will write the solution of Eq. (28) for $v > v_n$ lying outside the interval in Eq. (32) when the values of $J_\pm$ are exponentially close to the limiting value $J_0(v)$:

$$J_\pm \simeq \varepsilon^2 - \exp\{-\pi\varepsilon[4n + 2 \pm 1]/2\} \simeq J_0(v) = (\lambda^2/2\lambda_j^2)[1 - (v/v_s)^2]^{-2}. \qquad (36)$$

Consequently, the curves $J_-(v)$ and $J_+(v)$ asymptotically approach each other according to an exponential law as we move away from the point v_n.

The $J(v)$ curves corresponding to different values of n begin at points v_n separated from one another by the interval

$$v_n - v_{n+1} \simeq \left|\frac{dv_n}{dn}\right| \simeq \frac{\pi\lambda}{2\sqrt{2}\lambda_j \ln \pi n} v_s.$$

Under the conditions in question, this difference is smaller than the interval

$$v - v_n \simeq \frac{\lambda}{4\sqrt{2}\lambda_j \varepsilon_n \ln \pi n} v_s \simeq \frac{1}{2\pi\varepsilon_n}\left|\frac{dv_n}{dn}\right| > \left|\frac{dv_n}{dn}\right|, \qquad (37)$$

on which the curves $J_-(v)$ and $J_+(v)$ corresponding to a given n approach each other. Thus, the curves corresponding to smaller numbers n are generated prior to the convergence of the curves $J_-(v)$ and $J_+(v)$ corresponding to a number n on a scale of the order of the value given by Eq. (37). In the region of convergence of the curves with different values of n, all these curves are exponentially close to the limiting curve $J_0(v)$ in Eq. (36). A set of curves with numbers $n = 3, 4, \ldots, 10$, illustrating these regularities, is presented in Fig. 1. The existence of a discrete set of closely spaced $J(v)$ curves corresponding to a certain value v_n of the velocity of a freely moving vortex allows us to speak of the linewidth of a certain unified dependence $J(v)$. It follows from what has been said above that the physical reason behind this linewidth is the possible existence of different states of a 4π kink with different structures of the field of Swihart waves both in the interior region of width $2\xi_j$ and in the tail region $\xi < -\xi_j$ of the vortex. The number of such vortex structures increases with the velocity of a 4π kink.

The inset to Fig. 1 shows the dependence of J on v in the vicinity of $v = v_5$. This dependence resembles, to a considerable extent, the one describing the so-called stringent conditions of excitation of a new steady state when the main state of a hydrodynamic flow loses its

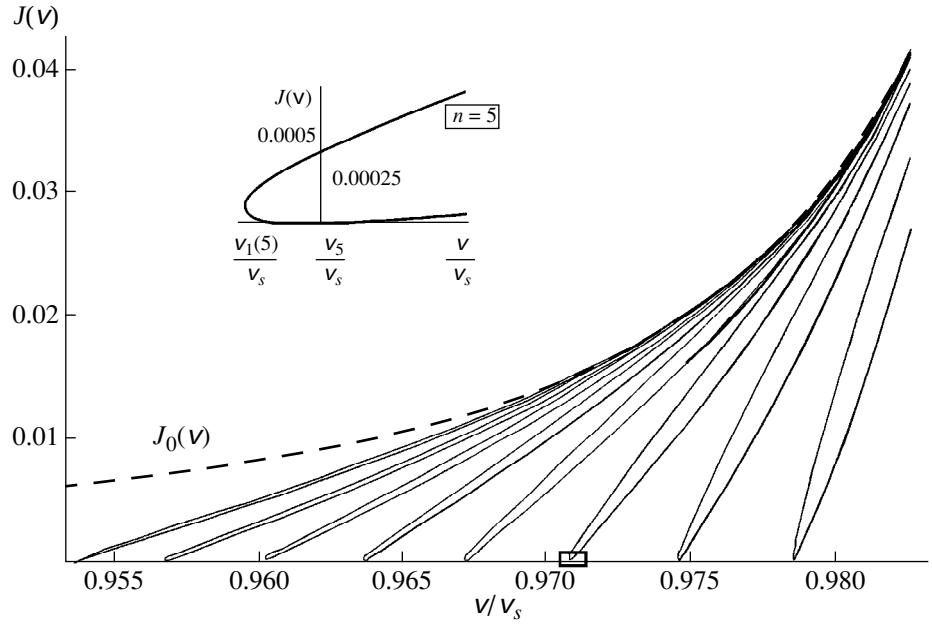

Fig. 1. Relation between the current and the velocity of a 4π kink for $\lambda/\lambda_j = 10^{-2}$. Pairs of curves emerging on the abscissa axis correspond to $n = 3, 4, \ldots, 10$. The dashed curve corresponds to the limiting dependence $J_0(V)$. The inset shows the segment of the $J(V)$ curve in the vicinity of $V = V_5$.

stability [17]. A similar dependence is also typical of hard excitation of a radio-frequency generator. As usual, the segment on the curve in the inset to Fig. 1, on which $dJ/dV < 0$, turns out to be unstable. On the other hand, such a curve corresponds to a hysteresis dependence for which a transition from the lower branch of the curve to the upper branch can occur jumpwise for various values of V.

4. RELATION BETWEEN THE CURRENT AND THE VORTEX VELOCITY WHEN OHMIC LOSSES ARE TAKEN INTO CONSIDERATION

In this section, we describe the results of an analysis based on Eq. (6), taking into account not only the Cherenkov interaction of a Josephson vortex with Swihart waves but also ordinary ohmic loses occurring in the substance separating the superconductors and in the superconductors, owing to the presence of normal electrons in them. For the motion of 4π kinks we are interested in, we confine our analysis to the case when the bias current density j is not high. We assume that ohmic dissipation is comparatively weak so that

$$\Delta k_0 \equiv \frac{1}{2\sqrt{1+4\varepsilon^2}}(\bar{\beta} + k_0^2\bar{\eta}) \ll k_0,$$

$$\Delta k_1 \equiv \frac{1}{2\sqrt{1+4\varepsilon^2}}(\bar{\beta} - k_1^2\bar{\eta}) \ll k_1.$$

In this case, in analogy with Section 2, we can write the following expressions characterizing the coordinate dependence $\psi(\xi)$ for a uniformly moving 4π kink:

$$\psi_h(\xi) = 3\pi + \pi(1-J)$$

$$\times\{1 - \exp[-(k_1 + \Delta k_1)(\xi - \xi_j)]\}, \quad \xi > \xi_j,$$

$$\psi_b(\xi) = 2\pi - \pi J - \pi(1-\Delta_1)(1+\delta^2)^{-1}$$

$$\times \exp[-(k_1 + \Delta k_1)(\xi + \xi_j)]$$

$$+ \pi(1+\Delta_1)(1+\delta^2)^{-1}\exp[(k_1 - \Delta k_1)(\xi - \xi_j)]$$

$$+ 2\pi\delta^2(1+\delta^2)^{-1}\exp[\Delta k_0(\xi - \xi_j)]\{\cos k_0(\xi - \xi_j)$$

$$- \Delta_0 \sin k_0(\xi - \xi_j)\}, \quad -\xi_j < \xi < \xi_j,$$

$$\psi_t(\xi) = -\pi J + 2\pi(1+\Delta_1)(1+\delta^2)^{-1}$$

$$\times \cosh[(k_1 - \Delta k_1)\xi_j]\exp[(k_1 - \Delta k_1)\xi]$$

$$+ 2\pi\delta^2(1+\delta^2)^{-1}[\cos k_0(\xi - \xi_j) - \Delta_0 \sin k_0(\xi - \xi_j)]$$

$$\times \exp[\Delta k_0(\xi - \xi_j)] + 2\pi\delta^2(1+\delta^2)^{-1}[\cos k_0(\xi + \xi_j)$$

$$- \Delta_0 \sin k_0(\xi + \xi_j)]\exp[\Delta k_0(\xi + \xi_j)], \quad \xi < -\xi_j.$$

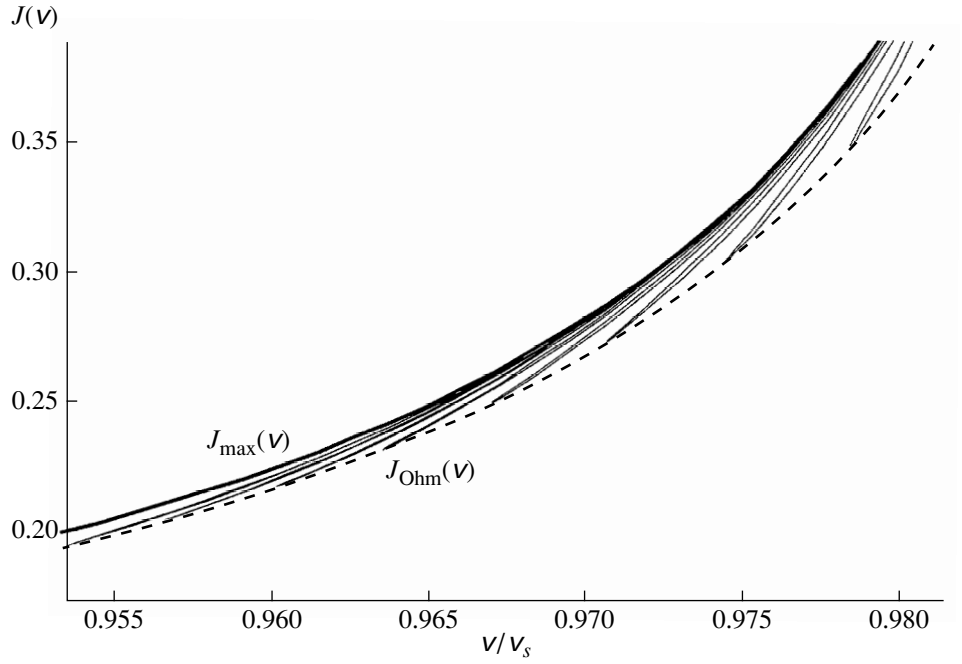

Fig. 2. Dependence of the current on the vortex velocity in a junction with ohmic losses for $\beta/\omega_j = 0.1$, $\eta/\pi\omega_j = 0.002$, and $\lambda/\lambda_j = 0.01$. The band contains pairs of curves corresponding to $n = 3, 4, \ldots, 10$.

Here, we have used the following notation:

$$\Delta_0 \equiv \frac{1}{2k_0\sqrt{1+4\varepsilon^2}}[(3\sqrt{1+4\varepsilon^2}+2)\bar{\beta} + (\sqrt{1+4\varepsilon^2}+2)k_0^2\bar{\eta}] \ll 1,$$

$$\Delta_1 \equiv \frac{1}{2k_1\sqrt{1+4\varepsilon^2}}[(3\sqrt{1+4\varepsilon^2}-2)\bar{\beta} + (2-\sqrt{1+4\varepsilon^2})k_1^2\bar{\eta}] \ll 1.$$

Finally, the relations generalizing Eqs. (22) and (23) to the case when ohmic dissipation is taken into account have the form

$$(1+\delta^2)J = \delta^2 + \Delta_1 + (1+\Delta_1)\exp[-2(k_1-\Delta k_1)\xi_i] + 2\delta^2[\cos 2k_0\xi_j + \Delta_0 \sin 2k_0\xi_j]\exp[-2\Delta k_0\xi_j], \quad (38)$$

$$(1+\delta^2)J = \delta^2 + \Delta_1 - (1-\Delta_1)\exp[-2(k_1+\Delta k_1)\xi_j]. \quad (39)$$

In the limit defined by Eq. (8) and under the assumption that the damping of Swihart waves in the interior region of the vortex is small, i.e.,

$$2\xi_j\Delta k_0 \simeq \left(\bar{\beta} + \frac{1}{\varepsilon^2}\bar{\eta}\right)\xi_j \ll 1,$$

Eqs. (38) and (39) give, first, the relation

$$2\xi_j \simeq \ln\frac{1}{\varepsilon^2 - J + (\bar{\beta}+\bar{\eta})/2} \simeq 2\pi n\varepsilon,$$

characterizing the size of the interior region of the vortex filled with Swihart waves, and, second, the equation

$$J - \frac{\bar{\beta}+\bar{\eta}}{2} = 2\varepsilon^2\cos^2\left[\frac{1}{2\varepsilon}\ln\left(\frac{1}{\varepsilon^2 - J + (\bar{\beta}+\bar{\eta})/2}\right)\right], \quad (40)$$

relating the current to the vortex velocity. It obviously follows from Eq. (40) that in the approximation applied here, we have

$$J = J_{\mathrm{Ohm}}(v) + J_{\mathrm{Ch}}(v), \quad (41)$$

where the ohmic current J_{Ohm} is given by the relation

$$J_{\mathrm{Ohm}} \equiv \frac{1}{2}(\bar{\beta}+\bar{\eta}) = \frac{v/v_s}{2\sqrt{1-(v/v_s)^2}}\left\{\frac{\beta}{\omega_j} + \frac{\eta}{\pi\omega_j}\frac{1}{1-(v/v_s)^2}\right\} \quad (42)$$

and the Cherenkov current J_{Ch} is defined by the solution of Eq. (27). Figure 2 illustrates relation (41). The curves in this figure correspond to the following relations characterizing the Josephson junction from [18]: $\beta/\omega_j = 0.1$, $\eta/\pi\omega_j = 0.002$, and $\lambda/\lambda_j = 0.01$. The dashed curve corresponds to the dependence in Eq. (42), while the upper solid curve corresponds to the relation

$$J_{\max}(v) = J_{\mathrm{Ohm}}(v) + J_0(v),$$

in which, in accordance with Eqs. (7) and (26), we have

$$J_0(v) = \frac{\lambda^2}{2\lambda_j^2[1-(v/v_s)^2]^2}.$$

The above analysis, which is a description of the motion of a 4π kink (coherent pair of 2π kinks) induced by the bias current, allows us to derive a simple analytical relation between the velocity of uniform motion of such a vortex and the current inducing this motion. Simple analytic formulas have been obtained in the limit defined by Eq. (8), when

$$\lambda^2/2\lambda_j^2 \ll J_0(v) \ll 1.$$

The set of $J(v)$ dependences emerging in our analysis due to the Cherenkov rearrangement of the vortex structure can be distinguished experimentally for comparatively low ohmic losses in the region

$$J_{\mathrm{Ohm}}(v) \le J(v) \le J_{\max}(v) = J_{\mathrm{Ohm}}(v) + J_0(v).$$

This manifestation is simplified considerably at low temperatures, when we can neglect ohmic losses at the surface owing to freezing out of normal electrons. In this case, Cherenkov losses become comparable to ohmic losses or even exceed them for

$$\frac{\lambda^2}{\lambda_j^2} > \frac{\beta}{\omega_j}\left(1-\frac{v^2}{v_s^2}\right)^{3/2} \gg \frac{\beta}{\omega_j}\left(\frac{\lambda}{\lambda_j}\right)^{3/2}.$$

The last inequality can be satisfied in junctions with small ohmic losses for which $\beta^2/\omega_j^2 \ll \lambda/\lambda_j$.

ACKNOWLEDGMENTS

This research was supported by the Russian Foundation for Basic Research, project no. 00-02-16076, the Scientific Council on Superconductivity (assignment "Abrikosov–Josephson Vortices"), and the State program supporting leading science schools, project no. 00-15-96720.

REFERENCES

1. B. Dueholm, O. A. Levring, J. Mygind, *et al.*, Phys. Rev. Lett. **46** (19), 1299 (1981).
2. Yu. M. Aliev and V. P. Silin, Phys. Lett. A **177**, 259 (1993).
3. Yu. M. Aliev and V. P. Silin, Zh. Éksp. Teor. Fiz. **104** (1), 2526 (1993) [JETP **77**, 142 (1993)].
4. V. P. Silin and S. A. Uryupin, Zh. Éksp. Teor. Fiz. **108** (6), 2163 (1995) [JETP **81**, 1179 (1995)].
5. V. P. Silin and A. V. Studenov, Phys. Lett. A **264**, 324 (1999).
6. G. L. Alfimov, V. M. Eleonsky, N. E. Kulagin, and N. V. Mitzkevich, Chaos **3**, 405 (1993).
7. G. L. Alfimov, V. M. Eleonsky, and L. M. Lerman, Chaos **8**, 257 (1998).
8. M. Peyrard and M. D. Kruskal, Physica D (Amsterdam) **14**, 88 (1984).
9. S. Aubry and P. J. Le Daeron, Physica D (Amsterdam) **7**, 240 (1983).
10. S. Aubry, J. Phys. C **16** (13), 2497 (1983).
11. A. F. Volkov, Physica C (Amsterdam) **183**, 177 (1991).
12. A. F. Volkov, Physica C (Amsterdam) **192**, 306 (1992).
13. A. S. Malishevskii, V. P. Silin, and S. A. Uryupin, Phys. Lett. A **253**, 333 (1999).
14. A. S. Malishevskiĭ, V. P. Silin, and S. A. Uryupin, Zh. Éksp. Teor. Fiz. **117** (4), 771 (2000) [JETP **90**, 671 (2000)].
15. S. Sakai, Phys. Rev. B **36** (1), 812 (1987).
16. V. P. Silin and A. V. Studenov, Zh. Éksp. Teor. Fiz. **117**, 1230 (2000) [JETP **90**, 1071 (2000)].
17. L. D. Landau and E. M. Lifshitz, *Course of Theoretical Physics*, Vol. 6: *Fluid Mechanics* (Pergamon, New York, 1987; Nauka, Moscow, 1988).
18. N. Martucciello, J. Mygind, V. P. Koshelets, *et al.*, Phys. Rev. B **57** (9), 5444 (1998).

Translated by N. Wadhwa

Physics of the Solid State, Vol. 43, No. 1, 2001, pp. 110–112. Translated from Fizika Tverdogo Tela, Vol. 43, No. 1, 2001, pp. 108–110.

MAGNETISM AND FERROELECTRICITY

Self-Synchronization Dynamics in the Process of the Generation of a Second Harmonic in $BaTiO_3$

É. V. Bursian and V. V. Rychgorskiĭ

St. Petersburg Pedagogical Institute, St. Petersburg, 191186 Russia

e-mail: bursian@AB3841.spb.edu

Received May 12, 2000

Abstract—A model of self-synchronization in the process of second-harmonic generation in a quadratic medium with a small coherence length is verified by investigations of the dependences of the output intensity on the intensity and the repetition frequency of excitative pulses. © *2001 MAIK "Nauka/Interperiodica".*

In the process of second-harmonic generation, the phase difference of secondary waves with a frequency of 2ω generated at the 0 and x points equals $x(k_{2\omega} - 2k_\omega)$. The phase difference of π is reached at the distance of the coherence length, $l_c = \pi/(k_{2\omega} - 2k_\omega)$. Back pumping of the energy from $I_{2\omega}$ to I_ω begins at distances $x > l_c$. Commonly, due to dispersion, the inequality $k_{2\omega} > 2k_\omega$ takes place and l_c is small. However, accounting for birefringence ($n_{e,2\omega} < n_{0,\omega}$), we can obtain $k_{2\omega} = 2k_\omega$ and $l_c \longrightarrow \infty$ in some crystals. This phenomenon is known as ordinary wave synchronism. It is absent in barium titanate, and l_c does not exceed 10 μm. Miller [1] explained the appreciable generation of the 2ω harmonic in thick $BaTiO_3$ crystals by the presence of a regular structure with the wave vector $\mathbf{q} = \mathbf{k}_{2\omega} - 2\mathbf{k}_\omega$ providing the momentum conservation (quasi-synchronism, or quasi phase matching). Such a structure could also be created artificially using external effects [2]. This finds wide use now mainly in devices based on $LiNbO_3$ crystals in which the appropriate micro domain structure is created.

Investigations of the angular distribution of the generated 2ω wave (the maxima are observed at angles of ±7°) [3] suggest that the quasi-regular 90° domain structure in $BaTiO_3$ at room temperature could be such a structure.

However, this scattering of the 2ω waves is observed not in all crystals and completely disappears close to the phase transition. Nevertheless, the intensity $I_{2\omega}$ of the wave going out of the crystal is not decreased, but can even be increased by several times. It was shown in [4] that in the process of the propagation of an intense light wave of the ω frequency and the generation of a wave of the 2ω frequency in a quadratic medium with no ordinary wave synchronism (due to birefringence) and no quasi-synchronism (due to the appropriate structure), the following three-step process can occur and result in the energy accumulation of the 2ω wave despite the small coherence length.

(1) The $I_{2\omega}$ intensity maxima occur at the distances that are multiples of $\Lambda = 2l_c = 2\pi/(k_{2\omega} - 2k_\omega)$. The quantity $I_{2\omega}$ falls down to zero between these points in the absence of synchronism. A layered structure is created [4] in the medium, $I_{2\omega}(x) \sim (4/q^2)\sin^2(qx/2)$, where $q = 2\pi/\Lambda$.

(2) The field of the 2ω wave changes the properties of the medium at each x point, changing not only the refractive index, or the first-order electric susceptibility $\chi^{(1)}$ (photo refractive effect), but also the second-order susceptibility $\chi^{(2)}$ (second-order photo refractive effect). An induced structure $\chi(x)$ is formed with the same period of $\Lambda = 2l_c$.

(3) The induced structure has turned out to be exactly that required for quasi-synchronism: $\mathbf{q} = \mathbf{k}_{2\omega} - 2\mathbf{k}_\omega$. That is, it provides the second-harmonic accumulation despite the absence of synchronism in the original crystal. Thus, the appearing 2ω wave creates the $\chi(x)$ relief in a quadratic medium which is necessary for its generation. This process was called self-synchronism (auto quasi-phase matching, or AQPM).

We verify the AQPM model in this work by the measurement of the $I_{2\omega}$ intensity of the second harmonic as a function of the I_ω intensity of the pumping wave and the repetition frequency of the pumping pulses. The installation consisted of a pulse IR-laser ($\lambda = 1.06$ μm, pulse duration 18 ns), a stepped calibrated beam splitter, a beam coupler, a heated cell with a crystal, a green optical filter, a flexible optical guide, and a monochromator with a photo multiplier at the output registering the intensity $I_{2\omega}$. The I_ω intensity was recorded by a high-frequency photodiode installed for measuring the light reflected from the beam splitter. Scattering of the signal was used to provide photodiode operation in a linear regime. The signals from the recorders were displayed on storage oscillographs and measured with an accuracy of about 5%.

The laser instability caused some difficulties, especially at the beginning of its operation before the estab-

lishment of the stationary regime, in particular when using single pulses. At the same time, we should avoid illumination of the crystal by a large number of pulses to prevent the crystal from heating. Therefore, we used a special gate, selecting one or several pulses from a series with the required relative pulse duration given by the laser switched on ahead. The overall operation consisting of the laser switching on with a required pulse frequency, the gate operation, synchronization of the oscillographs, and processing of the data obtained was provided by a computer in accordance with the assigned program.

A specified irradiation exposure is necessary for the $\chi(x)$ structure to be created. Consequently, the dependence of $I_{2\omega}$ on I_ω squared must not be linear, as it used to be for the mechanisms of second-harmonic generation involving stationary structures or ordinary synchronism. The experimental dependence of the $I_{2\omega}(I_\omega^2)$ dependence is presented in Fig. 1 by dots. It can be seen that there is no resulting outward 2ω intensity at small pumping intensities. There is an increase in the $I_{2\omega}$ intensity at some threshold value of I_ω (and, consequently, the $I_{2\omega}$ threshold value), following which the dots fit the straight line passing through the origin of the coordinates. In our opinion, this is evidence in favor of the proposal about the structure induced by the 2ω wave itself.

On the other hand, when the pumping pulses follow each other rather rarely, the induced structure can relax to zero each time. If the pulse-repetition period T is small, the following pulse will utilize the $\chi(x)$ structure induced by the preceding pulse. This is supported by the experimental dependence presented by the points in Fig. 2.

At a frequency higher than 10 Hz, the S-shaped region disappears in the $I_{2\omega}(I_\omega^2)$ dependence and the dots fall on a straight line (line *2* in Fig. 1).

The variation of χ produced by a strong field is very small in a perfect crystal. The proposed mechanism can be realized in a ferroelectric crystal with impurities, as the variation of χ associated with a change of the valence state of impurity atoms or with processes of nonlinear ferroelectric polarization (domain-wall displacements) should be adequate. In this case, it can be suggested that, first, the creation of the $\chi(x)$ profile due to the photorefractive effect, as well as its disappearing, needs time (Fig. 3). Second, the saturation associated with a limited value of χ_{lim} should occur. Then, the χ value at the point x corresponding to a maximum increases in time during the pulse in accordance with the law

$$\frac{d\chi}{dt} = pI_{2\omega}\Delta t(\chi_{lim} - \chi),$$
$$\frac{\chi_{lim} - \chi_2}{\chi_{lim} - \chi_1} = \exp(-pI_{2\omega}\Delta t), \quad (1)$$

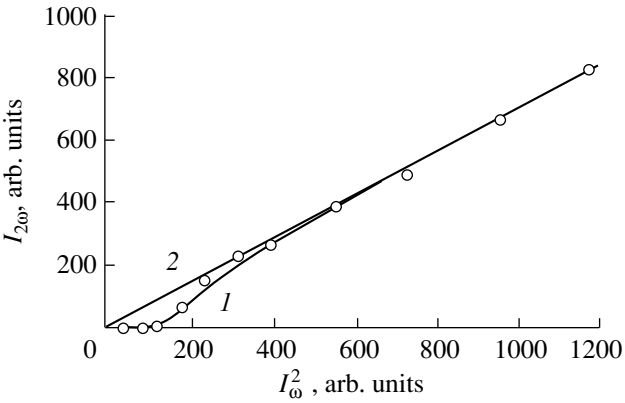

Fig. 1. Dependence of the intensity of the generated wave going out of the crystal on the squared intensity of the exciting wave calculated for (*1*) $\tau = 0.5$ s and $\nu = 1$ Hz and (*2*) $\tau = 0.5$ s and $\nu = 80$ Hz.

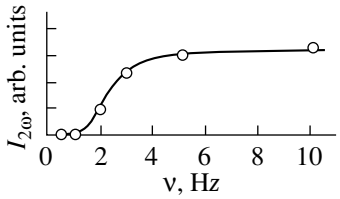

Fig. 2. Dependence of the intensity of the generated wave on the repetition frequency of the exciting pulses.

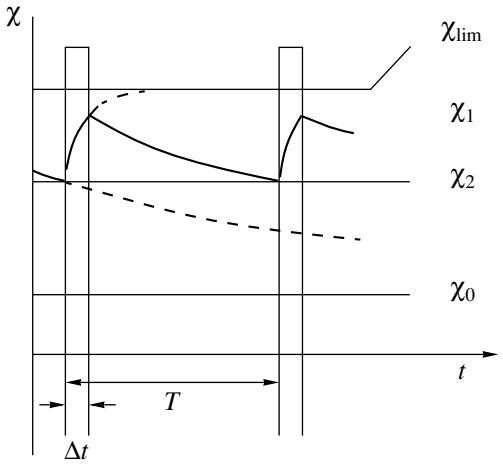

Fig. 3. The creation and relaxation of the χ relief.

where χ_2 and χ_1 are the electric susceptibility values at the end of the illumination and at the end of the time lapse between the pulses, respectively; Δt is the pulse duration (Fig. 3); and p is a parameter characterizing

the illumination efficiency. The χ value relaxes between the pulses, tending to a value χ_0

$$\frac{\chi_1 - \chi_0}{\chi_2 - \chi_0} = \exp(-1/(\nu\tau)), \quad (2)$$

where ν is the pulse-repetition frequency and τ is the relaxation time. If we put

$$I_{2\omega} \approx \chi_2(I_{2\omega}, \nu)I_\omega^2, \quad (3)$$

then a solution of these two equations by numerical methods leads to the $I_{2\omega}(I_\omega^2)$ dependences presented in Fig. 1 by solid curves. These curves can be in reasonable agreement with the experimental data at a successful choice of the parameters. The agreement will be better if the avalanche-like increase of $I_{2\omega}(I_\omega^2)$ is accounted for, but the equations will be more complicated.

Drawing a family of such curves for the different ν and a given I_ω we can plot the graph of $I_{2\omega}(\nu)$, which reproduces the experimental S-shaped curve (solid line in Fig. 2) for a successful choice of the parameters.

Thus, the analysis undertaken confirms at least the qualitative validity of the model considering the induced and relaxed structure that provides the AQPM effect.

ACKNOWLEDGMENTS

This work was supported by the Russian Foundation for Basic Research, project no. 00-02-16735, and the Ministry of Education of the Russian Federation.

REFERENCES

1. R. C. A. Miller, Phys. Rev. **134** (5A), A1313 (1964).
2. S. K. Esayan, V. V. Lemanov, and A. M. Arutunyan, Ferroelectr. Lett. Sect. **1**, 13 (1983).
3. É. V. Bursian and V. G. Zalesskiĭ, Fiz. Tverd. Tela (St. Petersburg) **41** (6), 1076 (1999) [Phys. Solid State **41**, 980 (1999)].
4. É. V. Bursian and V. V. Rychgorskiĭ, Izv. Akad. Nauk, Ser. Fiz. **64** (6), 1129 (2000).

Translated by N. Kovaleva

Physics of the Solid State, Vol. 43, No. 1, 2001, pp. 113–116. Translated from Fizika Tverdogo Tela, Vol. 43, No. 1, 2001, pp. 111–114.

MAGNETISM AND FERROELECTRICITY

Manifestation of a Structural Disorder in the Polarization Kinetics of a KD_2PO_4 Ferroelectric

V. V. Gladkiĭ and V. A. Kirikov

Shubnikov Institute of Crystallography, Russian Academy of Sciences, Leninskiĭ pr. 59, Moscow, 117333 Russia

e-mail: el_mech@ns.crys.ras.ru

Received May 30, 2000

Abstract—Crystalline potassium dideuterophosphate subjected to a slowly varying or a dc electric field has been found to exhibit polarization features which indicate the presence of a structural disorder characteristic of inhomogeneous systems. Continuous distribution spectra of the relaxation time are drawn from the experimental data and a phenomenological analysis of the depolarization of the crystal. It is shown that the spectra have an anomalous width and vary with temperature in a way suggesting the transformation of domain-wall potential barriers. © *2001 MAIK "Nauka/Interperiodica".*

1. INTRODUCTION

KD_2PO_4 (DKDP) has been attracting considerable interest for many decades due to its clearly pronounced anomalous physical properties and application potential [1]. This crystal undergoes a first-order phase transition whose T_C increases with an increase in the deuterium concentration. In the vicinity of T_C, its physical properties are described by the Landau–Ginzburg–Devonshire theory, so that the experimental data on polarization are even in a satisfactory quantitative agreement with calculations. It is essential that all the polarization features characteristic of ferroelectrics, in which the polarization is an order parameter, are clearly pronounced only in slowly varying (quasi-static) electric fields [2].

This paper reports experimental data indicating that the polar phase of DKDP crystals is characterized by a structural disorder which manifests itself in specific features of the polarization and depolarization kinetics and that, at a temperature far from the phase transition, the infralow-frequency spectra of the relaxation time distribution exhibit an anomaly.

2. EXPERIMENTAL TECHNIQUE

A DKDP crystal of good optical quality was obtained by the high-growth-rate method [3]. X-ray topography of such crystals indicates a fairly good structural homogeneity [4]. The deuterium content is 96.5%, and the phase transition temperature T_C is 218.5 K.

The polarization P of the crystal was measured automatically by the electrometric compensation method on a setup described in considerable detail elsewhere [5]. The dielectric hysteresis loop of the dependence of P on the electric field E was obtained by varying E in steps of 12 V with a duration of 40 s and a period of ~1 h. The relaxation of P was measured by rapidly turning E on and off for 190 min. The permittivity was measured by the standard technique on a capacitance bridge at a frequency of 1 kHz.

The crystal sample was a rectangular platelet ($3 \times 4 \times 0.3$ mm in size) cut perpendicularly to the polar axis. The major faces of the platelet were ground and coated with a conductive silver paste. The error in stabilizing the cryostat temperature did not exceed 0.03 K.

3. RESULTS AND DISCUSSION

Figure 1a shows quasi-static dielectric hysteresis loops $P(E)$ for three complete cycles of variations in the E field, Fig. 1b shows the permittivity ε as a function of E, and Fig. 1c shows the relaxation of the polarization P in the E field whose magnitude is less than the hysteresis loop halfwidth. The loops are not rectangular in shape, the saturation of P (and ε) in the field range covered is weakly pronounced, and only a slight deviation is observed in the P traces between the first two cycles, which reproduce themselves subsequently with a satisfactory accuracy. The relaxation of P in an arbitrarily low field E passes through two stages, namely, a jump of P followed by its smooth variation. The first stage reflects the fast over-barrier motion of domain walls. The second stage is a slow, thermally activated process. A similar evolution of P with time is observed in the polar phase for any E and for all temperatures, down to 150 K. The latter observation suggests that in the DKDP crystal under study, unlike the TGS crystal [6], the coercive field E_c has a continuous distribution, rather than a discrete value. As a result, when E is turned on, only the part of the crystal whose volume increases with an increase in E becomes involved in the process of fast polarization. A similar situation was observed earlier in the Rb_2ZnCl_4 crystal, whose inho-

1063-7834/01/4301-0113$21.00

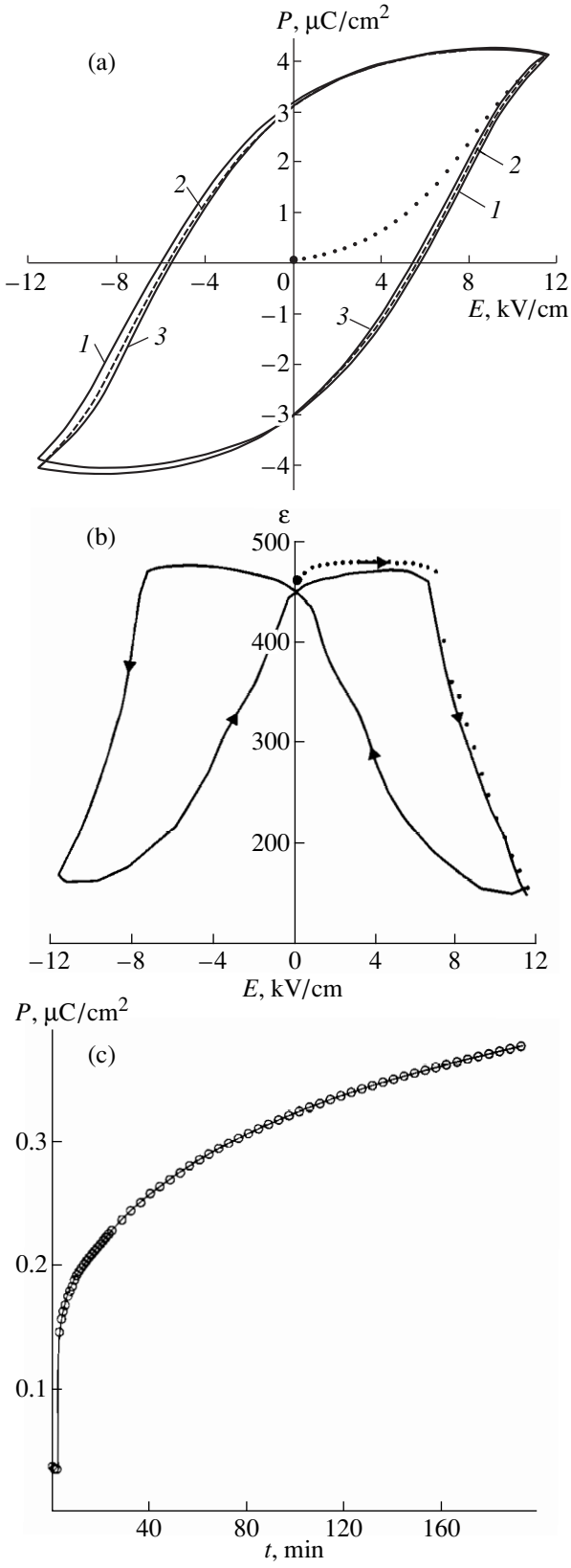

Fig. 1. Dielectric hysteresis loops for (a) polarization P and (b) permittivity ε as functions of the electric field E and (c) P relaxation in field E = 0.8 kV/cm for a DKDP crystal. T = 217.9 K. The numerals *1*, *2*, and *3* specify the order of the successive cycles of variations in P.

mogeneous structure is apparently due to a random internal electric field distorting the local symmetric two-minimum functions of the free energy of P [6]. Note also that the absence of a definite E_c in the crystal affects the shape of the hysteresis loops in the dependences of P and ε on E. Indeed, the former loop has a rising and a decaying P branch with a noticeable slope (with a finite dP/dE derivative) instead of a jump in P, and the latter loop exhibits broad plateaus instead of sharp maxima of ε within the same range of the field E (Figs. 1a, 1b). In other words, the region of the relatively fast crystal polarization switching is fairly diffuse within a rather wide range of the quasi-static field E.

The slow, thermally activated stage in the DKDP polarization relaxation follows a universal power law

$$p = (P_e - P(t))/(P_e - P_0) = 1/(1 + t/a)^n, \qquad (1)$$

where P_e and P_0 are the equilibrium and initial polarizations, respectively; $P(t)$ is the polarization at the instant of time t; and a and n are the fitting parameters. Relationship (1) corresponds to the normalized distribution function of the relaxation time τ

$$f(\tau) = [1/a\Gamma(n)](a/\tau)^{1+n}\exp(-a/\tau), \qquad (2)$$

where $\Gamma(n)$ is the gamma function and $\int_0^\infty f(\tau)d\tau = 1$. Function (2) passes through a maximum $f_{\max}(\tau)$ at $\tau_m = a/(1 + n)$ [6].

The function $f(\tau)$ can, in principle, provide information on the distribution of potential barriers for the relaxation centers (domain walls). We present below the results of measurements of the depolarization and recovery kinetics of the $f(\tau)$ functions derived from these experimental data in the range of the temperature T_0 of the polar phase of the crystal in which ε has a weakly pronounced anomaly, more specifically, an inflection point. Figure 2 displays the temperature dependence of ε, in which the maximum corresponds to the phase transition point T_C = 218.5 K, the region of interest is confined within a box, and the anomalous point T_0 is identified by an arrow. The open circles refer to the ε data obtained in a cooling run, and the filled ones, to those measured under heating. The procedure used in polarization and subsequent depolarization is explained in the inset showing the variation in P with time. At points *1* and *3*, voltages of 100 and 200 V are switched on, respectively. Between points *2*, *3* and *4*, *5*, the polarization builds up slowly. At point *5*, the voltage (E = 3.3 kV/cm) applied to the crystal is switched off and depolarization starts stepwise to point *6* and then slowly proceeds by the thermal activation mechanism, which is analyzed using relationships (1) and (2). The P jumps in the plot are one more illustration of the aforementioned absence of a definite coercive field in the crystal under study.

Figure 3 exemplifies the process of slow depolarization at three temperatures. The initial points (filled cir-

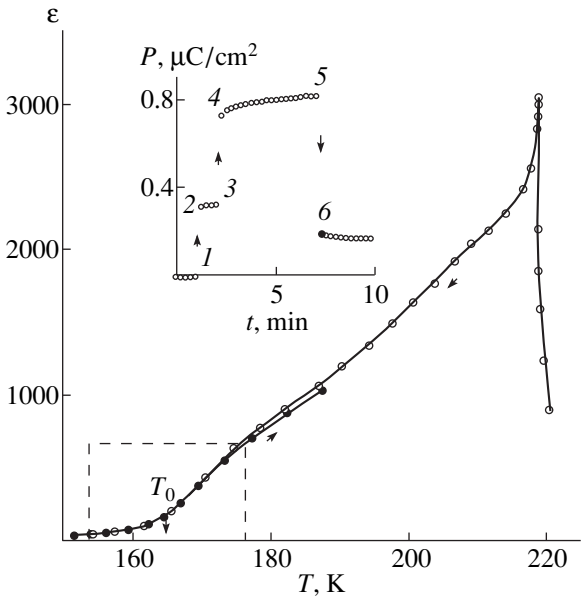

Fig. 2. Temperature dependence of the permittivity ε of a DKDP crystal. Open and filled circles refer to the cooling and heating runs, respectively. The inset shows variations in polarization P with time t upon switching on (points *1*, *3*) and off (point *5*) the electric field E = 3.3 kV/cm before the depolarization measurement.

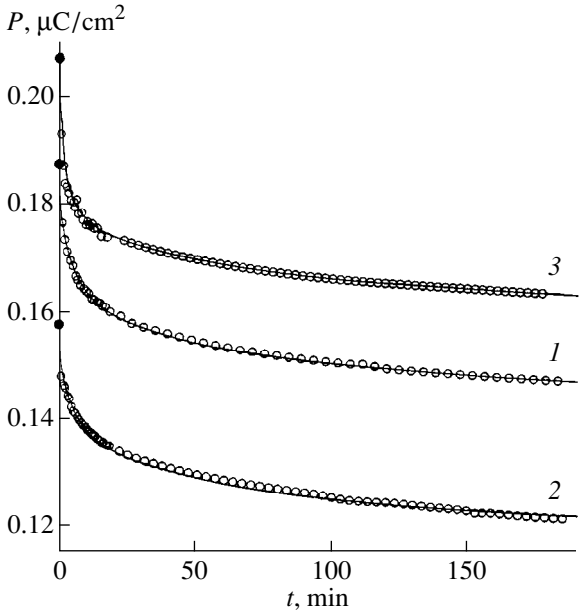

Fig. 3. Depolarization of a DKDP crystal at various temperatures T (K): (*1*) 153.25, (*2*) 164.91, and (*3*) 167.58. Circles are experimental data, and solid lines correspond to calculations.

cles) correspond to point *6* in the inset to Fig. 2. The open circles refer to experimental data. The solid lines correspond to the calculations according to formula (1). The jumps preceding the slow process are $\Delta P \simeq 0.6\ \mu C/cm^2$ for all curves, and the equilibrium values of the polarization are $P_e \simeq 0$. Figure 4 displays the $f(\tau)$ spectra, which are plotted using formula (2) with the a and n parameters obtained by fitting the experimental data with the power function (1). The values of a, n, the most probable time $\tau_m = a/(1 + n)$, and the area $S = \int_{\tau_1}^{\tau_2} f(\tau)d\tau$, where τ_1 and τ_2 are the minimum and maximum relaxation times corresponding to $f(\tau) = 0.1 f_{max}(\tau)$, are given in the table.

The errors of the parameters, which were determined in the same way as in [6], are $|\delta a/a| = |\delta P/P_0|(1 + t_m/a)/n(t_m/a) \simeq (1/n)|\delta P/P_0| \simeq 0.05$, $|\delta n/n| = [1/n\ln(t_m/a)]|\delta P/P_0| \simeq 0.01$, and $|\delta\tau_m/\tau_m| = |\delta a/a| + |\delta(1 + n)/(1 + n)| \simeq 0.06$. Here, $t_m \simeq 190$ min is the maximum time of the $P(t)$ measurement, $\delta P = 3.2 \times 10^{-4}\ \mu C/cm^2$, $P_0 \simeq 0.16\ \mu C/cm^2$, and $|\delta P/P_0| = 0.002$. The low values $S \simeq 0.1$ given in the table indicate that the greater part (≃0.9) of the relaxing regions should have very short and long times τ. The long times τ are not measured directly in the experiment and are obtained by extrapolating the experimental data.

It can readily be shown that the small magnitude of the exponent n in expression (1) (see table) permits a satisfactory fit of the experimental data within a fairly large time interval with a logarithmic dependence as well. Indeed, for $n \ll 1$, the dimensionless polarization $p(t)$ in expression (1) can be approximately represented as $p(t) \simeq 1 - n\ln(1 + t/a)$ and the $f(\tau)$ distribution can be represented in the form of a function which differs from zero only within a region bounded by finite values of τ.

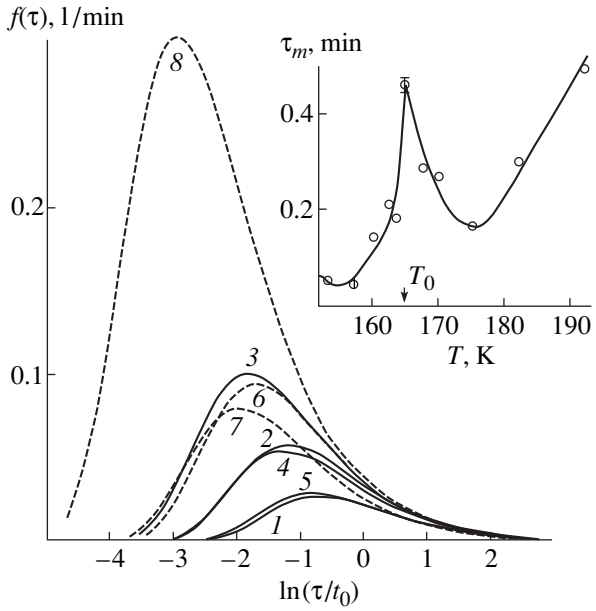

Fig. 4. Distribution spectra $f(\tau)$ of the relaxation time τ upon depolarization of a DKDP crystal at various temperatures T (K): (*1*) 192.09, (*2*) 182.07, (*3*) 175.07, (*4*) 167.58, (*5*) 164.91, (*6*) 163.56, (*7*) 160.24, and (*8*) 153.25. The inset shows the temperature dependence of the most probable time τ_m at a maximum of the $f(\tau)$ function, $t_0 = 1$ min.

Parameters of the depolarization time distribution spectra of the DKDP crystal

T, K	192.1	182.1	175.1	167.6	164.9	163.6	160.2	153.2
a, min	0.52	0.32	0.17	0.3	0.48	0.19	0.15	0.06
n	0.038	0.049	0.046	0.043	0.037	0.048	0.032	0.044
τ_m, min	0.5	0.303	0.165	0.287	0.46	0.183	0.144	0.053
S	0.09	0.12	0.12	0.07	0.09	0.12	0.08	0.11

The possibility of approximating $p(t)$ by a logarithmic dependence is apparently characteristic of many inhomogeneous systems with slow relaxation (see, e.g., [7]).

The $f(\tau)$ distribution in the vicinity of the T_0 point varies nonmonotonically with the temperature. As a crystal is cooled, the distribution shifts first toward small τ, then in the opposite direction, and, finally, again to small values of τ. The temperature dependence of the most probable relaxation time τ_m (the inset to Fig. 4) provides an insight into the anomalous variation in $f(\tau)$. It is seen that τ_m has a distinct maximum at the same point T_0 where the temperature dependence of ε undergoes an inflection. The bar shows the maximum error in the determination of τ_m at $T = T_0$. At other temperatures, the error is several times smaller. Obviously, the $f(\tau)$ distribution is related, in accordance with the Arrhenius law [5], to the potential barrier distribution for the relaxation centers (specifically for domain walls). However, the mechanism underlying the anomalous temperature behavior of such a distribution remains unclear.

Thus, the study of polarization kinetics over a broad temperature range, unlike the methods based on measurements at relatively high frequencies, allowed us to reveal specific features in the properties of the macroscopic structure of a polar material with long-lived metastable states. For the DKDP crystals studied, the most essential features are the lack of reproducibility of the dielectric hysteresis loops obtained in the first cycles, the absence of a distinct coercive field, and a very broad spectrum of polarization relaxation times. Similar (but more clearly pronounced) indications of a structural disorder were observed earlier in the SBN relaxor, a substantially more inhomogeneous material [8]. This feature of the structure is possibly common for many real crystals.

ACKNOWLEDGMENTS

We are grateful to A.E. Voloshin for providing the crystals for the study.

This work was supported by the Russian Foundation for Basic Research, project no. 99-02-17303.

REFERENCES

1. M. E. Lines and A. M. Glass, *Principles and Applications of Ferroelectrics and Related Materials* (Oxford Univ. Press, Oxford, 1977; Mir, Moscow, 1981).
2. E. V. Sidnenko and V. V. Gladkiĭ, Kristallografiya **17** (5), 978 (1972) [Sov. Phys. Crystallogr. **17**, 861 (1972)].
3. N. P. Zaitseva, L. N. Rashkovich, and S. N. Bogatyreva, J. Cryst. Growth **148**, 272 (1995).
4. I. L. Smolsky, A. E. Voloshin, N. P. Zaitseva, *et al.*, Philos. Trans. R. Soc. London, Ser. A **357**, 2631 (1999).
5. V. V. Gladkiĭ, V. A. Kirikov, S. V. Nekhlyudov, and E. S. Ivanova, Fiz. Tverd. Tela (St. Petersburg) **39** (11), 2046 (1997) [Phys. Solid State **39**, 1829 (1997)].
6. V. V. Gladkiĭ, V. A. Kirikov, E. S. Ivanova, and S. V. Nekhlyudov, Fiz. Tverd. Tela (St. Petersburg) **41** (3), 499 (1999) [Phys. Solid State **41**, 447 (1999)].
7. S. Krupicka, *Physik der Ferrite und der verwandten magnetischen Oxide* (Academia, Praha, 1973; Mir, Moscow, 1976), Vol. 2.
8. V. V. Gladkiĭ, V. A. Kirikov, S. V. Nekhlyudov, *et al.*, Pis'ma Zh. Éksp. Teor. Fiz. **71** (1), 38 (2000) [JETP Lett. **71**, 24 (2000)].

Translated by G. Skrebtsov

Physics of the Solid State, Vol. 43, No. 1, 2001, pp. 117–126. Translated from Fizika Tverdogo Tela, Vol. 43, No. 1, 2001, pp. 115–123.

LATTICE DYNAMICS AND PHASE TRANSITIONS

Low-Temperature Phase Transitions and Dynamics of Ammonium in $(NH_4)_3H(SO_4)_2$ and $[(NH_4)_{1-x}Rb_x]_3H(SO_4)_2$ Crystals

L. S. Smirnov[1], A. I. Baranov[2], L. A. Shuvalov[2], L. Bobrowicz-Sarga[3, 4], I. Natkaniec[3, 5], and S. Waplak[6]

[1] *SSC RF Institute of Theoretical and Experimental Physics, Bol'shaya Cheremushkinskaya ul. 25, Moscow, 117259 Russia*

[2] *Shubnikov Institute of Crystallography, Russian Academy of Sciences, Leninskiĭ pr. 59, Moscow, 117333 Russia*

[3] *Frank Laboratory of Neutron Physics, Joint Institute for Nuclear Research, Dubna, Moscow oblast, 141980 Russia*

[4] *Institute of Physics, Mickiewicz University, Poznan, 61-614 Poland*

[5] *Niewodniczanski Institute of Nuclear Physics, Poznan, 61-614 Poland*

[6] *Institute of Molecular Physics, Poznan, 61-614 Poland*

e-mail: lsmirnov@nf.jinr.ru; baranov@ns.crys.ras.ru

Received May 26, 2000

Abstract—The $(NH_4)_3H(SO_4)_2$ and $[(NH_4)_{0.82}Rb_{0.18}]_3H(SO_4)_2$ crystals are investigated by dielectric spectroscopy, inelastic incoherent neutron scattering (IINS), and neutron powder diffraction. A comparative analysis of the data obtained is given. It is shown that the phase transitions *II* ⟷ *III*, *III* ⟷ *IV*, *IV* ⟷ *V*, and *V* ⟷ *VII* in the $(NH_4)_3H(SO_4)_2$ crystal are accompanied by changes in the orientation ordering of the NH_4^+ ions. In the $[(NH_4)_{0.82}Rb_{0.18}]_3H(SO_4)_2$ crystal, these phase transitions are completely suppressed and the long-range order inherent in the *II* phase is retained over the entire temperature range covered (6–300 K). It is revealed that this crystal at the temperature $T_g \approx 70$ K undergoes a transition to the dipole glass phase, which is attended by "freezing" the orientation disordering of the ammonium ions. © *2001 MAIK "Nauka/Interperiodica".*

1. INTRODUCTION

Crystals of triammonium hydrogen disulfate $(NH_4)_3H(SO_4)_2$ (TAHS) belong to a large family of $M_3H(AO_4)_2$ (M = Na, K, Rb, and Sc; A = S and Se) crystals with ferroelectric, ferroelastic, and superionic properties. These crystals are of special interest, because they can undergo a diversity of phase transitions [1–10]

I ⟷	413 K ⟷	*II* ⟷	265 K ⟷	*III* ⟷	139 K ⟷	*IV* ⟷	133 K ⟷	*V* ⟷	63 K ⟷	*VII*
$R\bar{3}m$ [4]	*A*2/*a* [6, 7]	*P*2/*b* [7]	?	?	?					
$R\bar{3}$ [3]		*P*2/*n* [8]	incommensurate [9].							

The high-temperature paraelastic phase *I* has a trigonal structure (space group $R\bar{3}m$, $Z = 1$ [4] or $R\bar{3}$ [5]). The monoclinic ferroelastic phase *II* (space group *A*2/*a*, $Z = 4$ [6, 7]) has been studied most extensively. In the crystal structure of this phase, there are two nonequivalent ammonium groups. One of them, $NH_4(I)$, occupies the special positions on a twofold axis, and the other group, $NH_4(II)$, occupies the general positions. This structure is characterized by three types of hydrogen bonds [6]: (i) the N(*I*)–H···O bonds in which the hydrogen atom links the N(*I*) atom to an oxygen atom of the SO_4^{-2} ion, (ii) bifurcational bonds of the N(*II*)–H···2O type in which the hydrogen atom links the N(*II*) atom to two oxygen atoms, and (iii) the short symmetric bonds O–H···O ($R_{O\cdots O} = 2.54$ Å) in which each two neighboring SO_4^{-2} ions are linked via the acid proton to form individual dimers $(SO_4HSO_4)^{-3}$.

The $NH_4(I)$ tetrahedron is slightly distorted and, hence, has a dipole moment. Suzuki and Makita [6] assumed that, in the *II* phase at room temperature, the $NH_4(I)$ groups both can be ordered and can execute slow reorientations, whereas the $NH_4(II)$ ammonium ions are most probably ordered. The SO_4^{-2} tetrahedron is also somewhat distorted, which manifests itself in the fact that the length of the S–O(2) bond (1.518 Å) directed toward the acid proton is larger than that of the other three bonds (1.450 Å). This distortion of the SO_4^{-2} ion results in the formation of the dipole moment parallel to the S–O(2) bond.

As follows from x-ray structure analysis, the *III* phase also has a monoclinic symmetry (space group

*P*2/*b* [7] or *P*2/*n* [8]). It should be noted that crystal structures of the *IV, V,* and *VII* phases have not been determined to date.

According to Baranov *et al.* [10], crystals of trirubidium hydrogen disulfate $Rb_3H(SO_4)_2$ (TRHS) undergo only one high-temperature structural phase transition at $T_{II-I'} = 476$ K from the monoclinic phase *II* (space group *C*2/*c* [11]) to the cubic phase *I'* with a high protonic conductivity. It should be remarked that the occurrence of two irreversible transitions revealed in TRHS at temperatures of 329 and 399 K in the earlier works [11, 12] was not confirmed in [10]. A deuterated analog of TRHS, namely, TRDS, also undergoes a low-temperature antiferroelectric transition at $T = 71$ K, which is due to the ordering of deuterons in the double-well potential of the acid deuterium bond [11]. The ionic radius of rubidium is virtually identical to that of ammonium, and, at room temperature, $Rb_3H(SO_4)_2$ (hereafter, TRHS) and TAHS have identical crystal structures (with insignificantly different unit cell parameters) [13]. It is important that the length of the acid hydrogen bond in TRHS ($R_{O\cdots O} = 2.484$ Å [13]) is only slightly less than that in TAHS.

It is clear that the radical difference between the sequences of phase transitions in TAHS and TRHS, in which the unit cell parameters of crystals at room temperature differ insignificantly, can be associated with the ammonium ion, because it has the orientational degrees of freedom and forms the aforementioned hydrogen bonds. However, the role of acid protons responsible for the $I \longleftrightarrow II$ phase transition in TRDS remains unclear. In our opinion, investigations into the phase transitions and lattice dynamics in mixed $[(NH_4)_{1-x}Rb_x]_3H(SO_4)_2$ crystals can provide answers to this problem.

In the present work, we studied the TAHS and $[(NH_4)_{0.82}Rb_{0.18}]_3H(SO_4)_2$ (TARHS) crystals by dielectric spectroscopy, neutron powder diffraction, and inelastic incoherent neutron scattering (IINS) over a wide range of temperatures with the aim of elucidating the behavior of ammonium ions and acid protons in different phases of TAHS and TARHS.

2. EXPERIMENTAL TECHNIQUE

Single crystals of the $(NH_4)_3H(SO_4)_2$ and $[(NH_4)_{0.82}Rb_{0.18}]_3H(SO_4)_2$ compounds were grown from aqueous solutions by slow cooling. The dielectric spectra of these crystals were recorded in the temperature range 6–300 K at frequencies from 10 Hz to 1 MHz.

The inelastic incoherent neutron scattering (IINS) spectra and neutron powder diffraction were measured on a NERA-PR inverted-geometry neutron spectrometer installed on an IBR-2 pulsed neutron source (Frank Laboratory of Neutron Physics, Joint Institute for Nuclear Research, Dubna) by using the time-of-flight technique in the temperature range 10–300 K. The IINS spectra were measured with a beryllium filter and crystal analyzers from pyrolytic graphite (the elastic line of the spectra was observed at $E_0 = 4.65$ meV or $\lambda_0 = 4.15$ Å [14]) with a resolution from 2 to 4% in the transfer energy range 5–2000 cm^{-1}. The total densities of phonon states $G(E)$ were calculated from the experimental IINS intensities within the single-phonon incoherent approximation according to the program described in [15]. The neutron powder diffraction spectra measured on the NERA-PR spectrometer made it possible to determine a set of experimental interplanar distances *d*, which were used in calculations of the unit cell parameters with the AUTOX autoindexing program [16].

3. RESULTS

3.1. Dielectric properties. For the most part, the results obtained in the investigation into the dielectric properties of TAHS are in good agreement with the data available in the literature [1–3, 17, 18]. It is worth noting that the energies of the *II*, *III*, *IV,* and *V* phases are close to the energy of the state with a parallel ordering of dipoles. As can be seen from Fig. 1, the temperature dependences of the permittivity ε_c along the pseudotrigonal axis *c* in these phases are described by the Curie–Weiss law

$$\varepsilon = \varepsilon_\infty + \frac{C}{T - T_0}, \qquad (1)$$

where ε_∞ is chosen to be 5.7 in all the phases. It should be emphasized that the Curie constants in the *II*, *III*, *IV,* and *V* phases (2800, 1350, 750, and 550 K, respectively) are characteristic of intrinsic ferroelectrics and antiferroelectrics with phase transitions of the order–disorder type [19]. On the other hand, according to [1, 3, 17, 18], these phases exhibit no ferroelectric properties and a smeared maximum in the dependences $\varepsilon_c(T)$ at $T_{\varepsilon_{max}} \approx 240$ K disagrees with the aforementioned phase transition. Therefore, the large Curie constants indicate only that the free energies of the *II*, *III*, *IV,* and *V* phases in TAHS are close to the energy of the ferroelectric state. This inference is also supported by the evolution of the above maximum of ε_c in the mixed $[(NH_4)_3H(SO_4)_2]_{1-y}$–$[(ND_4)_3D(SO_4)_2]_y$ crystals with an increase in the concentration, which finally results in its splitting into two peaks at $y \geq 0.8$ and the appearance of the intermediate ferroelectric phase *VI* [17, 18].

The phase transitions $II \longleftrightarrow III$ and $III \longleftrightarrow IV$ are second-order phase transformations, whereas the phase transitions $IV \longleftrightarrow V$ and $V \longleftrightarrow VII$ are first-order phase transformations. The above features of the dielectric properties and the second-order phase transition $III \longleftrightarrow IV$ in the absence of macroscopic spontaneous polarization allow us to assume that the *III* and *IV* phases are antiferroelectric. Then, the $V \longleftrightarrow VII$ transition should be the transition between the ordered

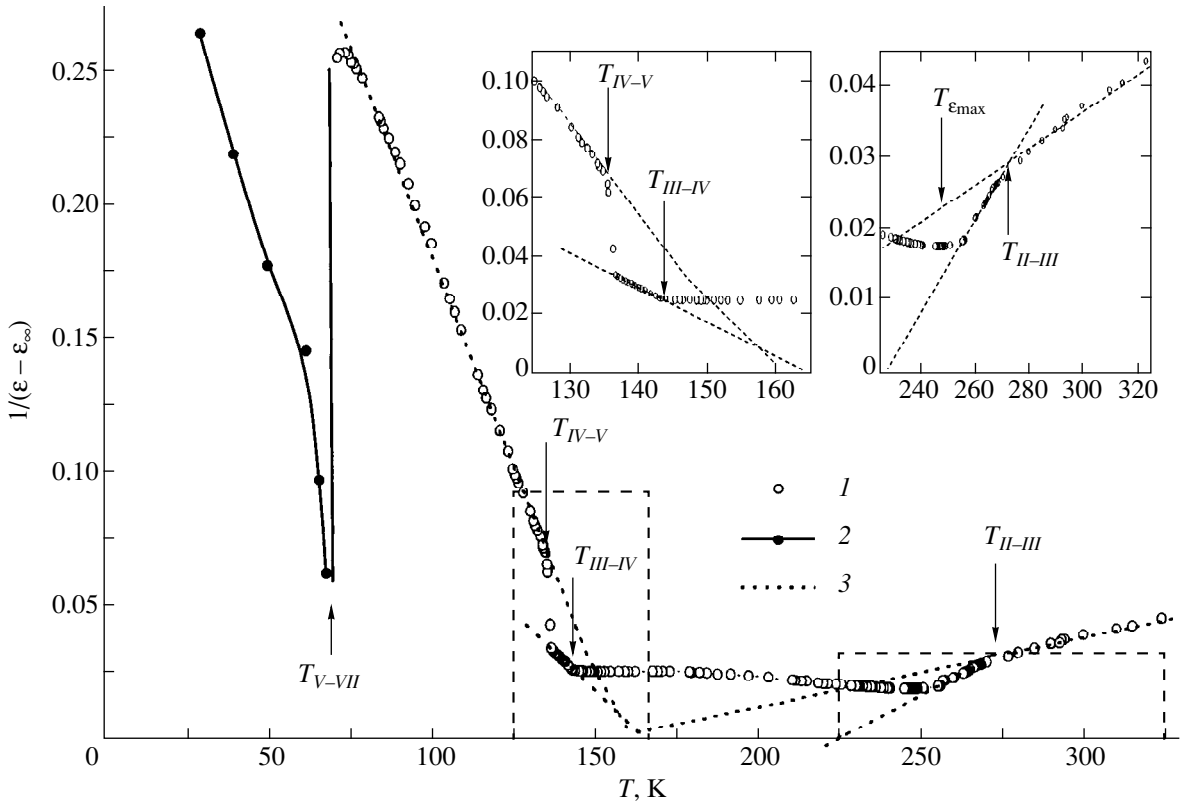

Fig. 1. Temperature dependences of the reciprocal of the permittivity $1/\varepsilon_c$ for the $(NH_4)_3H(SO_4)_2$ crystal: (*1*) the experimental data obtained at a frequency of 1 MHz, (*2*) the $1/\varepsilon_0$ values obtained by the extrapolation of the frequency dependences of $1/\varepsilon_c$ to zero frequency, and (*3*) approximation by the Curie–Weiss law [relationship (1)].

antiferroelectric and ferroelectric phases. Since the symmetry groups of both phases in this case are not related by the group–subgroup relationship, the phase transition must necessarily be the first-order phase transition [19]. Actually, as the *V* ⟷ *VII* phase transition point is approached from high temperatures, the permittivity falls short of large values, which are characteristic of the proper ferroelectric second-order transition or the first-order transition close to the second-order transition. Upon transition to the ferroelectric phase *VII*, the permittivity ε_∞ of a single-domain sample jumpwise decreases and remains constant with a further decrease in the temperature [10]. Moreover, the *V* ⟷ *VII* phase transition exhibits a considerable temperature hysteresis ($\Delta T \approx 10$ K) and is often attended by cracking of samples. Despite a pronounced first-order character and the low temperature of the *V* ⟷ *VII* phase transition, the domain structure formed in the ferroelectric phase is very labile, which manifests itself in a strong low-frequency dispersion of the quasi-Debye type. It should also be noted that the temperature dependence of the static permittivity ε_0 (which was calculated from the frequency dependences of ε_c) in the *VII* phase radically differs from the dependence $\varepsilon_\infty(T)$ and jumpwise increases upon the transition to the ferroelectric phase. With allowance made for the fact that the dielectric dispersion associated with the domain structure is observed only in the directions lying in the *m* symmetry plane, it can be concluded that the polar axis lies in this plane, its direction is close to that of the pseudotrigonal axis *c*, and the point symmetry group of the ferroelectric phase *VII* is *m*.

The substitution of the rubidium ion for the ammonium ion leads to a substantial change in the temperature dependences of the permittivity, specifically in the low-temperature range. As was shown in [10], even at small concentrations ($x \approx 0.03$) of rubidium in the $[(NH_4)_{1-x}Rb_x]_3H(SO_4)_2$ crystals, the structural phase transitions *II* ⟷ *III* and *IV* ⟷ *V* and also the ferroelectric transition *V* ⟷ *VII* are virtually suppressed, and the *III* ⟷ *IV* phase transition becomes smeared. It can be seen from Fig. 2 that, for the TARHS composition studied in the present work, with the rubidium concentration $x = 0.18$, the Curie–Weiss law [relationship (1)] is fulfilled only in the temperature range that corresponds to the *II* phase in TAHS, and the values of the Curie constant and ε_∞ are identical to those in the *II* phase of TAHS. However, the Curie–Weiss temperature T_0 in a mixed TARHS crystal is 90 K lower than that in TAHS (Fig. 1). Furthermore, the dependence $1/\varepsilon_c(T)$ for TARHS has neither a kink typical of the *II* ⟷ *III* phase transition nor jumps at the *IV* ⟷ *V*

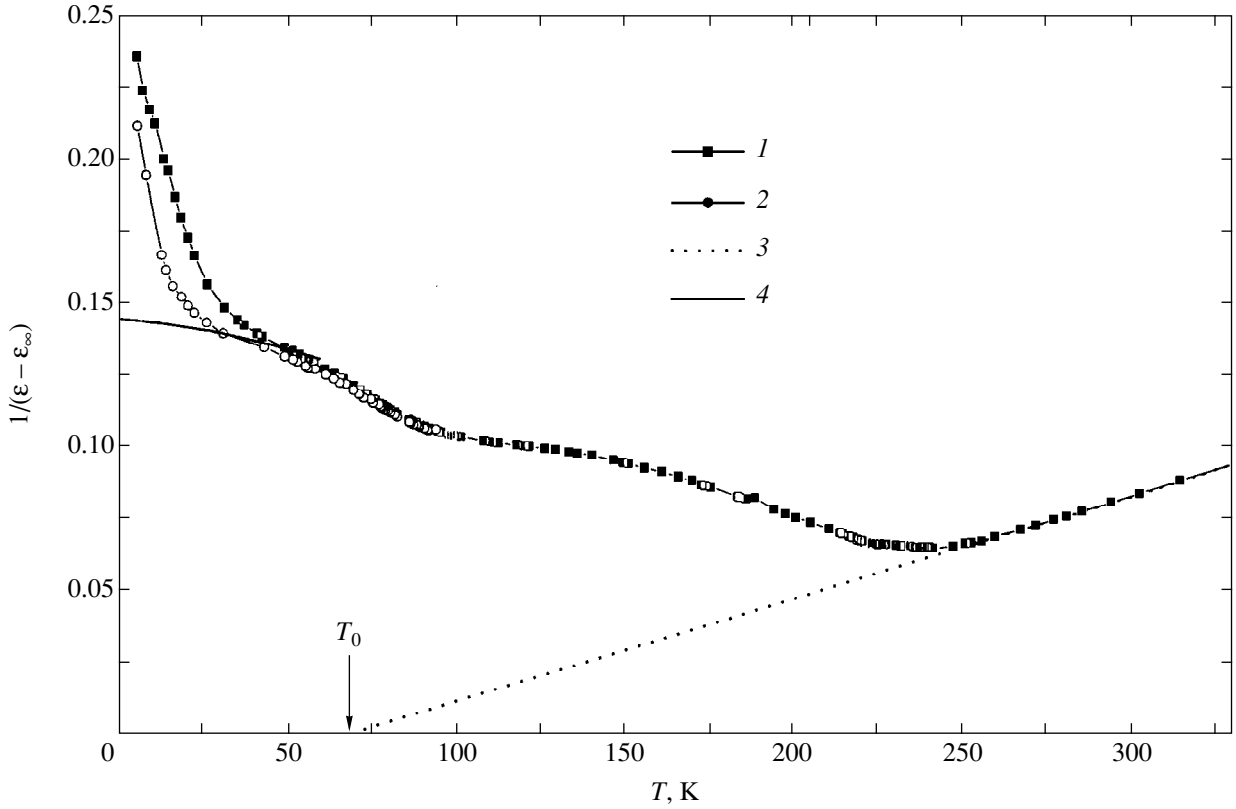

Fig. 2. Temperature dependences of the reciprocal of the permittivity $1/\varepsilon_c$ for the $[(NH_4)_{0.82}Rb_{0.18}]_3H(SO_4)_2$ crystal, measured at frequencies of (*1*) 1 MHz and (*2*) 1 kHz, (*3*) approximated by the Curie–Weiss law [relationship (1)], and (*4*) the $1/\varepsilon_0$ values calculated from the frequency dependences of ε_c.

and *V* ⟷ *VII* transition points, which suggests the suppression of these phase transformations. A strongly smeared anomaly is only retained in the range of the *III* ⟷ *IV* phase transition. At the same time, a frequency-dependent dielectric anomaly, which is typical of transitions to a dipole glass phase, is observed in this dependence in the vicinity of $T \approx 20$ K. A detailed analysis of the dielectric dispersion in this crystal is beyond the scope of this work and will be presented in a separate paper.

3.2. Neutron diffraction. The neutron powder diffraction spectra of TAHS at different temperatures are displayed in Fig. 3a. A visual examination of these spectra revealed that they differ from each other and can be identified as the spectra of the *VII* phase at 10 K, the *V* phase at 80 K, the *III* phase at 241 K, and the *II* phase at 290 K. The unit cell parameters of TAHS at room temperature (phase *II*) are determined from the experimental interplanar distances *d* and are as follows: a = 10.167 Å, b = 5.863 Å, c = 15.421 Å, and β = 101.8°. These values are in reasonable agreement with the data available in the literature [6].

The neutron powder diffraction spectra of TARHS at different temperatures are depicted in Fig. 3b. It is seen that a variation in the temperature virtually does not affect the set of reflections located in the range of interplanar distances *d* from 2.8 to 3.7 Å, except for the change in the reflection location due to the thermal expansion of the crystal. At each temperature, the measured interplanar distances are adequately described by a monoclinic unit cell. The temperature dependences of the monoclinic unit cell parameters for TARHS are shown in Fig. 4. A monotonic behavior of these dependences indicates that the crystal symmetry of TARHS remains unchanged in the studied temperature range 10 K < T < 290 K.

This is in good agreement with the inference made from the dielectric data for TARHS (Fig. 2) that the structural phase transitions are absent in this temperature range.

The neutron powder diffraction data obtained in this work for TARHS also agree with the data of x-ray single-crystal diffraction of the $[(NH_4)_{1-x}Rb_x]_3H(SO_4)_2$ crystal with x = 0.57 [20], according to which no phase transitions occur in the temperature range 180 K < T < 290 K, and the *II* phase is retained, at least, down to 180 K.

3.3. Inelastic incoherent neutron scattering. The differences between the IINS spectra [the scattering intensity $I(\lambda)$ as a function of the wavelength of incident neutrons] of the TAHS and TARHS crystals at dif-

ferent temperatures are no less radical (Fig. 5). These spectra involve three components: the elastic line at $\lambda_0 = 4.15$ Å, the temperature-dependent wings of this elastic line [which are determined by the quasi-elastic incoherent neutron scattering (QINS)], and regions of inelastic incoherent neutron scattering from internal and external lattice modes of the TAHS and TARHS crystals in the wavelength range $0.5 < \lambda < 3.9$ Å.

The changes observed in the IINS spectra of TAHS with an increase in temperature reflect the changes in neutron scattering due to structural phase transitions. In particular, at temperatures of 10 (phase *VII*), 80 (phase *V*), and 120 K (phase *V*), the QINS does not contribute to the total IINS intensity. This suggests that the ammonium ions in these phases are orientationally ordered. It should be noted that the fine structures of the IINS spectra in the range of lattice modes at 10 and 80 K differ considerably, which indicates a change in the vibrational spectrum of TAHS upon the *VII* ⟷ *V* phase transition. Therefore, the *VII* ⟷ *V* ferroelectric phase transition at 68 K can be considered a transition between two phases with the ordered ammonium ions at which the phonon spectrum substantially changes owing to the transformation of the crystal structure. This conclusion agrees with the above results of dielectric measurements.

For the *IV* phase, the IINS spectrum was not measured for technical reasons associated with the narrow temperature range of this phase $\Delta T \approx 6$ K. However, already at $T = 152$ K, i.e., somewhat above the *IV* ⟷ *III* phase transition temperature, the IINS spectrum includes a contribution of QINS, which indicates the dynamic orientation disordering of ammonium ions in the *III* phase. Therefore, it can be assumed that the *IV* ⟷ *III* phase transition (characterized as antiferroelectric according to the dielectric data) can be due to a disordering of the ammonium ions. The dynamic orientation disordering of ammonium ions, which arises with an increase in the temperature as a result of the transitions from the *V* phase (at $T = 120$ K) to the *III* phase (at $T = 152$ K), leads to a noticeable smearing in the fine structure of the IINS spectrum in the range of lattice modes. A further increase in the temperature is accompanied by an increase in the QINS contribution and a rise in the anharmonicity of ammonium ions,

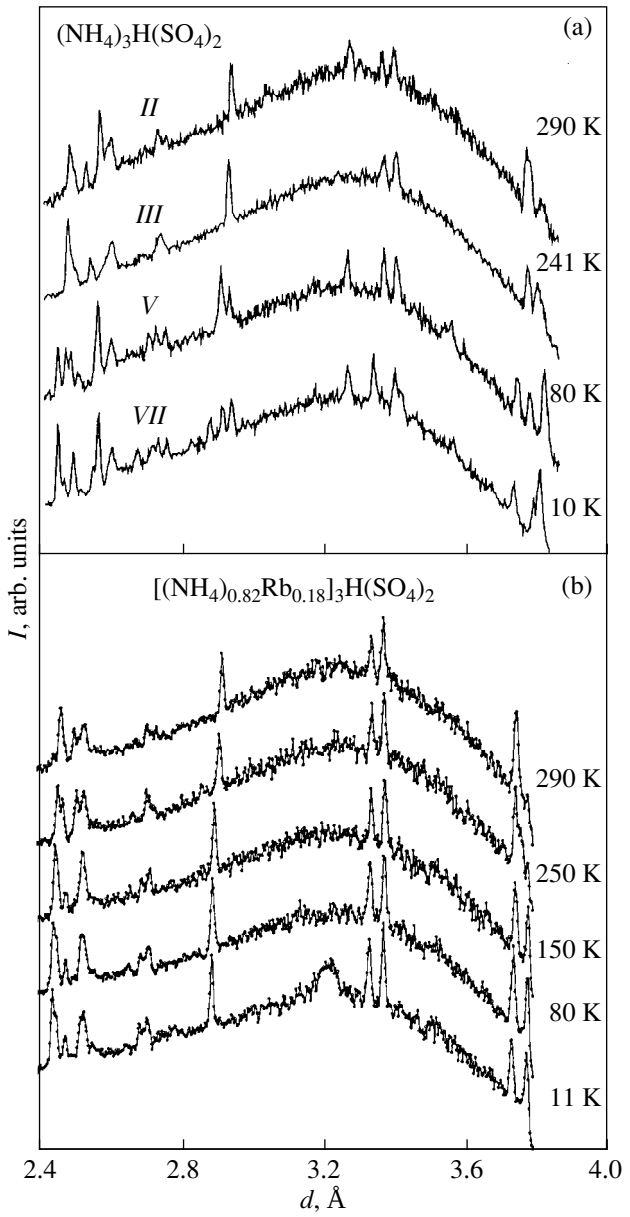

Fig. 3. Dependences of the neutron powder diffraction spectra on *d* at different temperatures: (a) $(NH_4)_3H(SO_4)_2$ and (b) $[(NH_4)_{0.82}Rb_{0.18}]_3H(SO_4)_2$.

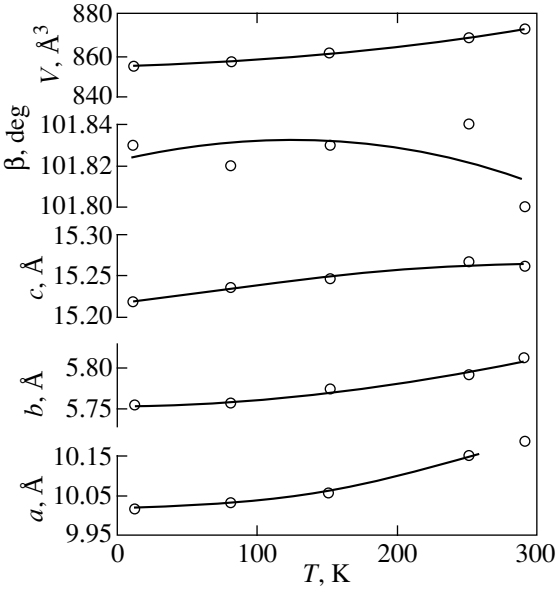

Fig. 4. Temperature dependences of the unit cell parameters for the monoclinic *II* phase of $[(NH_4)_{0.82}Rb_{0.18}]_3H(SO_4)_2$ crystals.

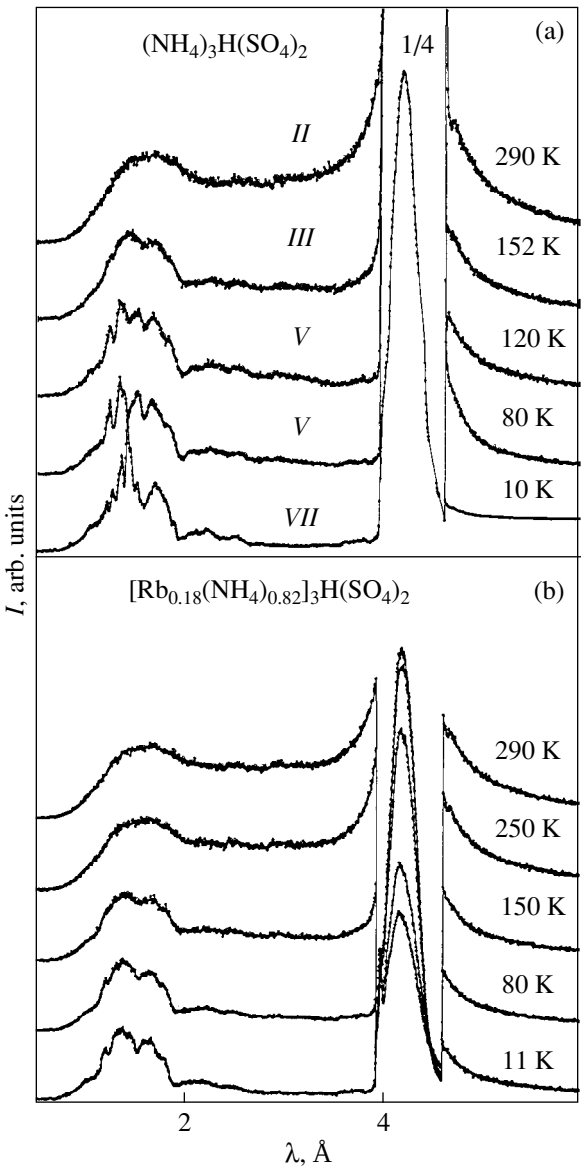

Fig. 5. Dependences of the inelastic incoherent neutron scattering spectra on λ at different temperatures: (a) $(NH_4)_3H(SO_4)_2$ and (b) $[(NH_4)_{0.82}Rb_{0.18}]_3H(SO_4)_2$.

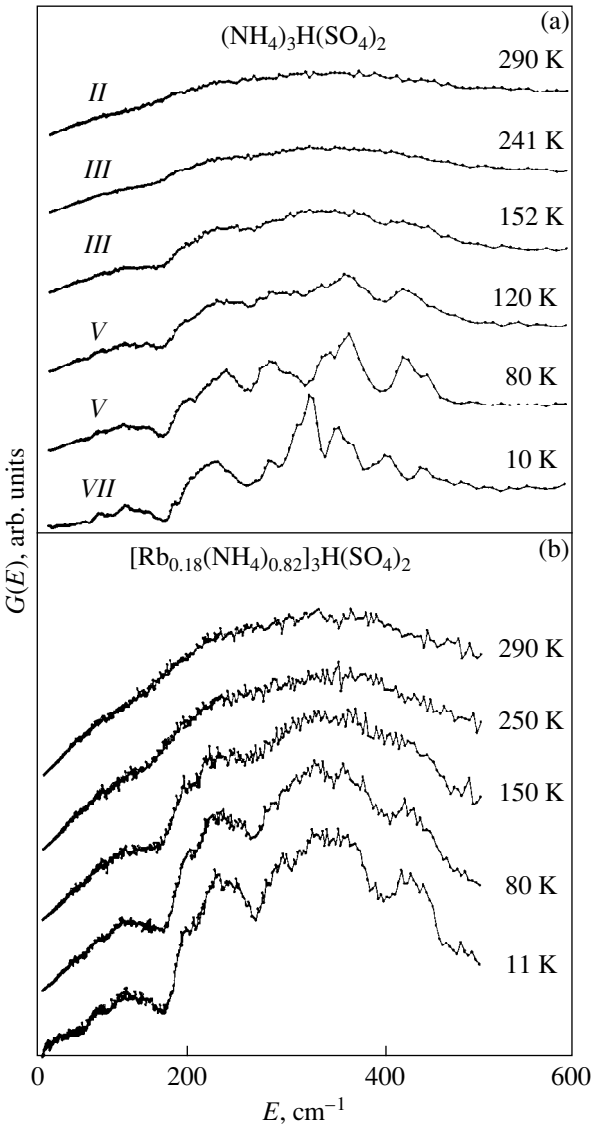

Fig. 6. Total densities of phonon states $G(E)$ for (a) $(NH_4)_3H(SO_4)_2$ and (b) $[(NH_4)_{0.82}Rb_{0.18}]_3H(SO_4)_2$ crystals at different temperatures.

which manifests itself in a line broadening of the $G(E)$ spectrum. The IINS spectrum of the *II* phase at 290 K contains one broad maximum that characterizes the contributions from both neutron scattering by lattice modes and the strong QINS (on the wings of the elastic scattering line) by dynamically orientationally disordered ammonium ions (Fig. 5a).

Therefore, the IINS spectra of TAHS demonstrate that the dynamic disordering of ammonium ions occurs in the sequence of phase transitions $V \longleftrightarrow IV \longleftrightarrow III$. However, judging only from these spectra, we cannot reveal the specific role of the $NH_4(I)$ and $NH_4(II)$ ammonium ions in the observed sequence of phase transitions.

The temperature variation in the IINS spectra of TARHS considerably differs from that observed for TAHS. At $T = 10$ K, the main difference in the IINS spectra of TARHS and TAHS is observed in the wavelength range $0.5\ \text{Å} < \lambda < 2\ \text{Å}$, which corresponds to the neutron scattering by lattice modes. As follows from Fig. 5b, at 10 K, the line width in the IINS spectrum of TARHS is larger than that in the spectrum of TAHS. An increase in the temperature up to 80 K is attended by the broadening of spectral lines for TARHS without their noticeable transformation. At 150 K, the IINS spectrum in the range of lattice modes consists of two overlapping broad maxima, which arise as the result of a further broadening of spectral lines and the appear-

ance of the QINS contribution (at about 150 K) on the wings of the elastic scattering line. A further increase in the temperature to 250 and 290 K leads to the appearance of one broad maximum in the IINS spectrum in the range of lattice modes and an increase in the QINS contribution.

The IINS spectra obtained substantiate the above conclusion (reasoning from the data of dielectric measurements and neutron powder diffraction) that TARHS does not undergo structural phase transitions in the temperature range 10–290 K. The QINS contribution to the IINS spectra measured at temperatures of 150 K and above indicates that the transition to the orientational glass state most likely occurs in the temperature range between 80 and 150 K.

Figures 6a and 6b show the generalized phonon densities of states $G(E)$ for TAHS and TARHS crystals, respectively. It is seen that the $G(E)$ spectra of TAHS in the *VII* (T = 10 K) and *V* (T = 80 K) phases differ substantially. This means that an increase in the temperature leads to a substantial transformation of the crystal structure in the course of the *VII* ⟷ *V* phase transition. A comparison between the $G(E)$ spectrum of the *V* phase at a temperature of 120 K and the spectrum of the *III* phase at a temperature of 152 K shows that the sequence of phase transitions *V* ⟷ *IV* and *IV* ⟷ *III* results in changes in the vibrational spectra of the crystal lattice. This is reflected in the difference between the $G(E)$ spectra of the *V* and *III* phases in the energy range from 240 to 380 cm^{-1}. Moreover, an increase in the temperature leads to a smearing in the fine structure of the $G(E)$ spectra of the *V* and *III* phases due to a broadening of peaks of the lattice modes as a consequence of an increase in the anharmonicity of ammonium ions.

Analysis of the $G(E)$ spectra of the TARHS crystal shows that their main characteristics remain unchanged in the temperature range 10–290 K. This once more supports the inference that no phase transitions in this compound occur below room temperature. Note that the $G(E)$ spectrum of the TAHS crystal in the *II* phase is smeared owing to the anharmonicity of the ammonium ions. Hence, by comparing this spectrum with the $G(E)$ spectrum of the mixed TARHS crystal, we cannot elucidate how the replacement of ammonium ions by rubidium ions affects the vibrational spectrum. By virtue of the anharmonicity, the $G(E)$ spectra of both crystals at 150 K are virtually identical, even though the phases at this temperature are different (the *III* phase in TAHS and the *II* phase in TARHS). This gives grounds to assume that the *II* ⟷ *III* phase transition is not accompanied by a considerable change in the orientational dynamics of ammonium ions, and the replacement of ammonium by rubidium up to the concentrations $x \leq 0.18$ insignificantly affects the librational modes of ammonium. Since the IINS intensity is predominantly determined by neutron scattering from hydrogen atoms, our attempts to reveal the contribution of the other atoms of the studied compounds to the change in the $G(E)$ spectra have failed.

4. DISCUSSION

Reasoning from the IINS results and the available data on infrared and Raman light scattering [21–24], the lattice part of the $G(E)$ spectra of the TAHS and TARHS crystals can be divided into three regions: translational and librational modes of the SO_4^{2-} ion in the energy range $0 < E < 150$ cm^{-1}, translational modes of the NH_4^+ ion in the energy range $150 < E < 250$ cm^{-1}, and librational modes of the NH_4^+ ion in the energy range $250 < E < 400$ cm^{-1} [21]. The spectra of the *V* and *VII* phases in the region of librational modes are characterized by a finer structure compared to the spectra of these phases in the region of translational modes and can be deconvoluted into individual modes by approximating the contribution of each mode in the form of a Gaussian line. The librational modes separated in the $G(E)$ spectra of the TAHS crystal in the *V* and *VII* phases and their energies determined in such a manner are listed in Table 1.

A comparison of the librational modes determined by the IINS technique for the NH_4^+ ion in the TAHS crystal with the infrared and Raman data taken from

Table 1. Comparison between the excitation energies determined by the IINS technique for TAHS and the Raman data taken from [23] (energies are given in cm^{-1})

Phase *V*		Phase *VII*		Assignment
IINS 80 K	Raman scattering [23] 120 K	IINS 10 K	Raman scattering [23] 50 K	
	243		243	ν_6^+
255	255	260	257	ν_6^+
281	275	288	286	ν_6^+
316	310	305	308	ν_6^+
345		332	331	ν_6^+
		351	351	ν_6^+
		371		ν_6^+
		390		ν_6^+
410				ν_6^+
436		432		$\nu_2^-(SO_4^{2-})$

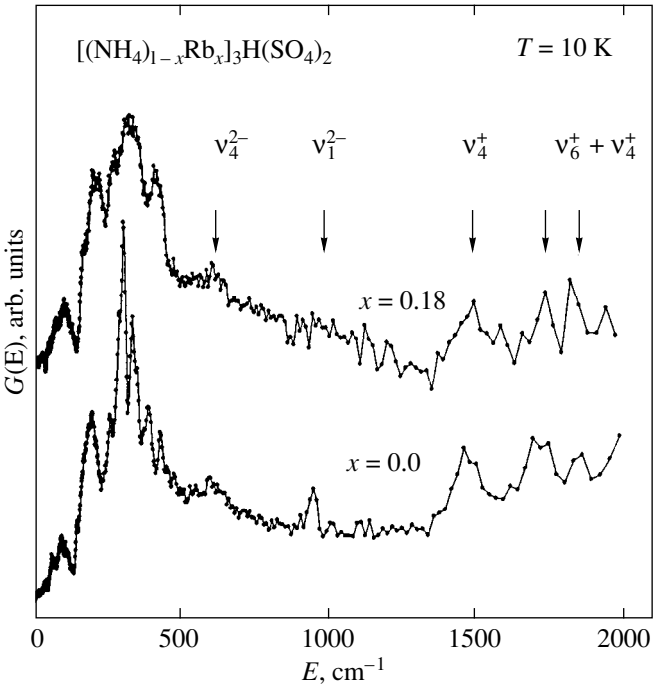

Fig. 7. Spectra $G(E)$ of the $(NH_4)_3H(SO_4)_2$ and $[(NH_4)_{0.82}Rb_{0.18}]_3H(SO_4)_2$ crystals at 10 K with locations of the internal modes for NH_4^+ and SO_4^{2-} ions.

[21–24] shows their reasonable agreement. The exception is provided by the librational modes with energies of 345 and 410 cm^{-1} for the *V* phase and 371 and 390 cm^{-1} for the *VII* phase. As follows from comparison between the librational modes of the NH_4^+ ions in the *V* and *VII* phases, the energies of certain modes in both phases coincide to within the error of their determination or the shift due to the crystal lattice transformation. At the same time, there are modes observed only in one of these phases. For example, the librational mode with an energy of 410 cm^{-1} manifests itself only in the *V* phase and the librational modes with energies of 351, 371, and 390 cm^{-1} are observed only in the *VII* phase. A simple correlation between the librational modes of the NH_4^+ ions in the *VII* and *V* phases can present difficulties in the case when the possible splitting of particular librational modes of the *V* phase upon phase transition to the *VII* phase is disregarded, because this phase transition is accompanied by a lowering in the symmetry. Since the energies of the librational modes are most sensitive to the nearest environment, the change observed in the librational spectrum upon the $V \longleftrightarrow VII$ phase transition reflects the changes in the interatomic distances and the site symmetry of ammonium ions.

Of special note is the mode whose energy remains virtually unchanged upon the $VII \longleftrightarrow V$ phase transition (288 and 281 cm^{-1}, respectively). This mode clearly manifests itself in the Raman spectra of both phases (see Table 1) and is close in energy to the O···O mode (279 cm^{-1}) in $K_3H(SO_4)_2$ [25].

The main difference between the $G(E)$ spectra of the TARHS and TAHS crystals is observed in the region of librational modes in which the $G(E)$ spectrum of TARHS at 11 K has no fine structure and involves a broad band (Fig. 6b). This shape of the $G(E)$ spectrum can be explained by the fact that the TARHS crystal at low temperatures is in the state of the orientational glass. In the earlier work [26], we observed a similar effect for the mixed $Rb_{2-x}(NH_4)_xSO_4$ crystals in the concentration range $0.4 < x < 1.2$, which corresponds to the state of orientational glass. The changes in the spectrum with an increase in temperature are caused by the transition from the state of orientational glass with a "frozen" local structural disordering to the state with a dynamic disordering of structural units, specifically ammonium ions. In this respect, we should note that the temperature of this transition was not specially determined by the neutron scattering technique in our experiments.

The $G(E)$ spectra of the $[(NH_4)_{1-x}Rb_x]_3H(SO_4)_2$ (x = 0.0 and 0.18) samples in the energy range 0–2000 cm^{-1}

Table 2. Comparison between the energies of internal modes in tetrahedral structural units and acid hydrogen bonds (energies are given in cm^{-1})

Complex	ν_4^{2-}	ν_1^{2-}	ν_{OH-out}	ν_4^+	ν_{OH-out}	$\nu_6^+ + \nu_4^+$
$Na_3H(SO_4)_2$ [25]			947		947	
$K_3H(SO_4)_2$ [25]			1140		1550	
$Rb_3H(SO_4)_2$ [25]			1140		1550	
$(NH_4)_3H(SO_4)_2$	610	952			1478	1725, 1857
$[(NH_4)_{0.82}Rb_{0.18}]_3H(SO_4)_2$	612				1485	1739, 1826
SO_4^{2-} [27, 28]	613	981				
NH_4^+ [28]				1397		1685

are displayed in Fig. 7. The results obtained in analysis of the observed modes are presented in Table 2. The ν_4^{2-} and ν_1^{2-} modes of the SO_4^{2-} ion and the ν_4^+ mode of the ammonium ion can be separated in the above energy range. The energies determined for the ν_4^{2-} and ν_1^{2-} modes are close to those reported in [27] for the SO_4^{2-} ion. The energy of the ν_4^+ mode is close to the experimental and calculated energies given in [27, 28]. By analogy with the interpretation of optical spectra, the mode at energies of 1725 and 1857 cm^{-1} for the crystal with $x = 0.0$ and at energies of 1739 and 1826 cm^{-1} for the crystal with $x = 0.18$ can be treated as the $\nu_6^+ + \nu_4^+$ Raman mode. By using the observed energies of the ν_4^+ mode, it is possible to determine the energies of the librational modes and to verify the validity of the mode assignment given in Table 1. These results lend support to the view that the ammonium ion in the studied systems can be considered a rigid rotator.

Thus, the characteristic features of the low-temperature phase transitions in the $[(NH_4)_{1-x}Rb_x]_3H(SO_4)_2$ ($x = 0.0$ and 0.18) crystals were determined by a combined method (dielectric and neutron spectroscopy). It was demonstrated that the phase transitions *II* ⟷ *III*, *III* ⟷ *IV*, *IV* ⟷ *V*, and *V* ⟷ *VII* in TAHS are governed by the behavior of ammonium ions, because the substitution of rubidium ions for ammonium ions even at small Rb^+ concentrations brings about the stabilization of the *II* phase in TARHS. This phase transforms to the phase of orientational glass with a decrease in the temperature. It can be assumed that the NH_4–NH_4 interaction between ammonium ions provides a way of realizing the sequence of phase transitions in TAHS, because no phase transitions occur in TRHS. However, even an insignificant amount of rubidium ions replacing ammonium ions in TAHS considerably affects the internal energy of the TARHS crystal and brings it closer to the internal energy of TRHS. The cooperative interaction between ammonium ions ceases to play the decisive role but continues to make its contribution, since a decrease in the temperature of the mixed TARHS crystal leads to the transition to the state of orientational glass.

5. CONCLUSION

The results obtained in this work demonstrated that the orientational dynamics of ammonium ions is of fundamental importance in cooperative phenomena observed in $(NH_4)_3H(SO_4)_2$ and mixed $[(NH_4)_{1-x}Rb_x]_3H(SO_4)_2$ crystals. The combination of dielectric and neutron spectroscopy made it possible to reveal the specific features of the phase transitions in TAHS. It was shown that the *II* ⟷ *III*, *III* ⟷ *IV*, and *IV* ⟷ *V* phase transitions are accompanied by the orientation ordering of ammonium ions and can be described as the order–disorder transitions, whereas the *V* ⟷ *VII* phase transition can be treated as the displacive first-order transition between crystal structures with orientationally ordered ammonium ions. However, the particular role of the $NH_4(I)$ and $NH_4(II)$ ammonium groups in the sequence of phase transitions *II* ⟷ *III*, *III* ⟷ *IV*, and *IV* ⟷ *V* can be determined only with the use of single-crystal neutron diffraction. At present, this problem remains unsolved.

The decisive role of ammonium ions in the sequence of phase transitions *II* ⟷ *III* ⟷ *IV* ⟷ *V* ⟷ *VII* was clearly demonstrated using the substitution of rubidium ions for ammonium ions. Upon doping the TAHS crystal by rubidium even in a small amount, the internal energy of the mixed TARHS crystal radically changes and approaches the internal energy of the TRHS crystal in which the *II* phase is observed down to liquid-helium temperatures. However, the cooperative interaction between ammonium ions is retained in the TARHS crystal, which manifests itself in the transition from the *II* phase to the state of orientational glass with a decrease in temperature.

ACKNOWLEDGMENTS

This work was supported in part by the Russian Foundation for Basic Research, project nos. 98-02-16944, 00-15-96797, and 99-02-17443.

REFERENCES

1. K. Gesi, Phys. Status Solidi A **33**, 479 (1976).
2. L. Schwalowsky, V. Vinnichenko, A. Baranov, *et al.*, J. Phys.: Condens. Matter **10**, 3019 (1998).
3. K. Gesi, J. Phys. Soc. Jpn. **42**, 1785 (1977).
4. K. Sooryanarayana and T. N. Guru Row, Phase Transitions **58**, 263 (1996).
5. T. Fukami, K. Horiuchi, K. Nakasone, and K. Furukawa, Jpn. J. Appl. Phys. **35**, 2253 (1996).
6. S. Suzuki and Y. Makita, Acta Crystallogr. B **B34**, 732 (1978).
7. M. Kamoun, M. H. Ben Ghozlen, and A. Daoud, Phase Transitions **9**, 247 (1987).
8. R. H. Chen, Li-Ming Wang, and S. C. Yang, Phase Transitions **37**, 141 (1992).
9. M. Fujimoto and B. V. Sinha, Ferroelectrics **46**, 227 (1983).
10. A. I. Baranov, V. V. Dolbinina, E. D. Yakushkin, *et al.*, Ferroelectrics **217**, 285 (1998).
11. S. Fortier, M. E. Frazer, and R. D. Heyding, Acta Crystallogr. C **C41**, 1139 (1985).
12. M. Ichikawa, J. Phys. Soc. Jpn. **45**, 355 (1978).
13. K. Gesi, J. Phys. Soc. Jpn. **48**, 886 (1980).
14. I. Natkaniec, S. I. Bragin, J. Brankowski, and J. Mayer, Proc. ICANS XII Abingdon RAL Report No. 94-025 (1993), Vol. 1, p. 89.

15. E. F. Sheka, I. V. Markichev, I. Natkaniec, and V. D. Khavryuchenko, Fiz. Élem. Chastits At. Yadra **27**, 493 (1996) [Phys. Part. Nucl. **27**, 204 (1996)].
16. V. B. Zlokazov, Comput. Phys. Commun. **85**, 415 (1995).
17. T. Osaka, J. Makita, and K. Gesi, J. Phys. Soc. Jpn. **49**, 593 (1980).
18. K. Gesi, K. Ozawa, T. Osaka, and J. Makita, J. Phys. Soc. Jpn. **49**, 1083 (1980).
19. V. G. Vaks, *Introduction to the Microscopic Theory of Ferroelectrics* (Nauka, Moscow, 1973).
20. W. Bronowska, V. Videnova-Adrabinska, and A. Pietraszko, Ferroelectrics **172**, 411 (1995).
21. P. Kumura Acharya and P. S. Narayanan, Indian J. Pure Appl. Phys. **11**, 514 (1973).
22. M. Kamoun, A. Lautie, F. Romain, A. Daoud, and A. Novak, in *Dynamics of Molecular Crystals*, Ed. by J. Lascombe (Elsevier, Amsterdam, 1987), p. 219.
23. M. Kamoun, A. Lautie, F. Romain, and A. Novak, J. Raman Spectrosc. **19**, 329 (1988).
24. P. Rajagopal, G. Aruldhas, and V. Ramakrishnan, J. Phys. Chem. Solids **50**, 675 (1989).
25. F. Fillaux, A. Lautie, J. Tomkinson, and G. J. Kearley, Chem. Phys. **154**, 135 (1991).
26. I. Natkaniec, M. L. Martínez-Sarrión, L. Mestres, *et al.*, Physica B (Amsterdam) **241–243**, 487 (1997).
27. K. Nakamoto, *Infrared Spectra of Inorganic and Coordination Compounds* (Wiley, New York, 1963; Mir, Moscow, 1966).
28. M. L. Martínez-Sarrión, L. Mestres, I. Natkaniec, A. Pawlukojc, L. S. Smirnov, and L. A. Shuvalov, Kristallografiya, 2001 (in press).

Translated by O. Borovik-Romanova

Physics of the Solid State, Vol. 43, No. 1, 2001, pp. 127–136. Translated from Fizika Tverdogo Tela, Vol. 43, No. 1, 2001, pp. 124–131.

LATTICE DYNAMICS AND PHASE TRANSITIONS

Entropy and the Mechanism of Phase Transitions in Elpasolites

I. N. Flerov and M. V. Gorev

Kirenskiĭ Institute of Physics, Siberian Division, Russian Academy of Sciences, Akademgorodok, Krasnoyarsk, 660036 Russia
e-mail: flerov@iph.krasnoyarsk.su

Received April 10, 2000; in final form, May 29, 2000

Abstract—The phase transitions in series of crystals with the general formulas $A_2BB'X_6$ (X = F, Cl, Br, or CN) and $Pb_2BB'O_6$ that belong to the elpasolite family (space group $Fm\bar{3}m$) are analyzed. The influence of the size and the shape of cations and anions on the entropy and the mechanism of structural distortions is discussed.

1. INTRODUCTION

Among perovskite-like compounds, the elpasolite family is the most representative owing to the great diversity of possible substitutions for atoms in crystals of the general formula $A_2BB'X_6$. According to [1], more than 350 compounds with a similar structure were known until recently, and, as follows from crystal chemical analysis, more than 1500 new elpasolites can be obtained based on halides alone. In the initial phase, crystals of this family have a cubic symmetry with the space group $Fm\bar{3}m$–O_h^5 ($z = 4$). Unlike the simple perovskites ABX_3 in which all octahedra are equivalent, elpasolites (also referred to as ordered perovskites) contain two types of ionic groups (BX_6 and $B'X_6$) alternating along three fourfold axes. Therefore, an elpasolite cubic cell can be treated as a perovskite cell with twice the unit cell parameter. The crystal structure of the cryolite $A_3B'X_6$ in which the A and B atoms are chemically equivalent is a special case of the elpasolite structure.

As was noted in [2], the most pronounced feature of the perovskite structure is that its topology (i.e., an ideal atomic arrangement) is thermodynamically extremely stable, whereas a real crystal structure (i.e., an actual atomic arrangement) appears very unstable. This statement is likely true for all perovskite-like crystals or, at least, for those with a three-dimensional crystal framework. It is because of the instability of real crystal structures that these crystals can undergo structural phase transitions.

Crystal lattice distortions caused by structural phase transitions are often considered in the framework of two limiting mechanisms, namely, the displacive-type and order–disorder mechanisms. These mechanisms can be most adequately defined as follows. In the case of displacements, the instability arises from long-range cooperative interactions and brings about local distortions, and, in the case of order–disorder, the local distortions stem from local instabilities [3]. As a rule, the features characteristic of both mechanisms can manifest themselves in one form or another in the behavior of different physical properties of the same crystal. In this respect, the question as to which mechanism plays a leading part in each special case is of particular importance.

Before proceeding to phase transitions in elpasolites (cryolites), we discuss the results obtained for ferroelectrics [3] and ferroelastics [4, 5] with a perovskite structure ($Pm\bar{3}m$). The interpretation of phase transitions in these groups of crystals as the displacive-type transitions was supported by the following experimental results. Compounds of the first group were characterized by the soft modes in the initial and distorted phases and large Curie constants. Compounds of the second group, apart from the soft modes, exhibited insignificant changes in the entropy. At the same time, the experimental data obtained for many compounds of both groups were interpreted as the evidence for the existence of local structural distortions above the phase transition temperature: diffuse x-ray scattering, the central peak in the light scattering spectra, the birefringence, and the excess heat capacity. These findings gave impetus to the development of different theoretical models. For example, according to [6], the cooperative motion of ions in the structure is associated with the possible transition ("crossover") from the displacive-type mechanism to the order–disorder mechanism at a certain temperature above the phase transition point T_0. This is caused by a critical increase in the correlation length as the T_0 temperature is approached, resulting in the formation and growth of dynamic clusters—small groups of bound atoms, which are displaced from high-symmetry equilibrium positions in the same direction.

The results of structure refinement within the cluster and (or) anharmonic phonon models were compared for a number of ferroelastic perovskites $SrTiO_3$, $KMnF_3$, $RbCaF_3$, $CsPbCl_3$, and $CsPbBr_3$. Hutton *et al.*

[4, 5] analyzed the precision structural data in the framework of different models and made the following conclusions.

(1) A simple model with a multiple-well potential for X atoms inadequately describes the initial structure: the *R* factor (15%) is very large even as compared to the harmonic model ($R = 7\%$).

(2) Allowance made for the anharmonicity of atomic vibrations leads to a substantial decrease in the *R* factor (4%).

(3) It is difficult to decide between two models, namely, the cluster and anharmonic phonon models, when the predicted cluster distribution function does not exhibit a pronounced behavior inherent in the order–disorder systems.

Armstrong [7] analyzed the NMR and NQR data obtained for certain of the aforementioned perovskites and arrived at rather contradictory results. On the one hand, the author believed that these data confirm the crossover above T_0 from the behavior that corresponds to the displacive-type mechanism to the behavior associated with the formation of dynamic clusters in the structure. On the other hand, it was noted that the experimental response of the system is very complex due to the presence of defects in the crystals, so that the experimental data cannot provide a sufficiently reliable corroboration of the crossover phenomenon theory.

Unfortunately, the data on changes in the entropy upon phase transitions were not used in analyzing the results obtained in [4, 5, 7]. It should be mentioned that this change in the entropy is rather small for many perovskite-like crystals studied in these works.

In the present work, we analyzed the data on the structure, phonon spectra, and physical properties of elpasolites (cryolites) and discussed the possible mechanisms of structural phase transitions. Consideration was given to several series of compounds whose composition involves different X atoms (F, Cl, Br, O, and CN). The change in the entropy upon phase transition was used as a major characteristic. Since the entropy is a fundamental quantity and can be determined experimentally, the study of the interrelation between the entropy and specific disordering phenomena is of crucial importance.

2. HALOID ELPASOLITES WITH ATOMIC IONS

According to crystal chemical analysis [1], the elpasolite structure can be realized in halides containing fluorine, chlorine, and bromine.

As a rule, the refinement of the initial cubic structure of halogen-containing crystals is performed within one or, in the best case, two approximations without consideration of alternative models and, rather frequently, under the assumption that halogen atoms occupy the 24*e* position (on the edge of a cubic cell). As can be seen from Table 1, the thermal parameters substantially differ for different elpasolites and the same crystal studied by different authors. Of special interest are the results obtained in the theoretical treatment of structural models that account for the anisotropy and the anharmonicity of vibrations of halogen atoms and their possible arrangement in other crystallographic positions. The inclusion of anisotropic thermal vibrations led to a decrease in the *R* factor in K_2NaCrF_6 and K_2NaFeF_6 crystals [12]. The anisotropy parameter B_{33}/B_{11} for the Rb_2KFeF_6 crystal, which undergoes a phase transition at $T_0 \approx 170$ K, appears to be two or three times larger than that for the Rb_2NaFeF_6 crystal [10, 11], in which, according to the analysis of interatomic bond strengths [8], no phase transition occurs down to 0 K.

Makarova *et al.* [9] thoroughly examined the temperature dependence of the thermal vibration amplitudes for the $Cs_2NaNdCl_6$ elpasolite. It was shown that the thermal ellipsoids for Cs, Na, and Nd atoms are spherical, and only the vibrations of chlorine atoms are characterized by an appreciable anisotropy and anharmonicity. Note that both the anisotropy and the anharmonicity for elpasolite structures turned out to be more pronounced than those for perovskites [8]. These results indicate that only halogen ions are crucial; i.e., they are responsible for the lattice instability which leads to the phase transition.

Attempts were made to refine the structure of the Rb_2KScF_6 elpasolite in the isotropic approximation when fluorine atoms occupy one of the crystallographic positions 24*e*, 96*j*, and 192*l* [8]. It follows from Table 1 that the disordering of fluorine atoms over four (96*j*) or eight (192*l*) positions results in a substantial decrease in the thermal parameter B_{iso} compared to that for the 24*e* position. Since the thermal parameters and the reliability factors are very close for both variants of disordering, it is rather difficult to choose a particular variant. In our opinion, these findings suggest that a considerable anharmonicity of vibrations is more likely to be characteristic of fluorine atoms than the disordering over several positions.

A substantial number of haloid elpasolites either undergo structural phase transitions (whose nature is usually ferroelastic) or exist in a distorted phase up to the melting temperature. According to the group-theoretic analysis [14], diverse distortions of the $Fm\bar{3}m$ structure become possible due to octahedron rotations and (or) polar displacements of atoms.

Among chlorides and bromides, series of crystals with the general formula $Cs_2NaM^{3+}Cl(Br)_6$ that undergo one phase transition to the tetragonal phase $I4/m$ have been studied most extensively [8]. In terms of the model proposed in [14], the corresponding structural distortions can be attributed to the (00φ) rotations of octahedra about one of the fourfold axes of the cubic cell.

Fluoro-elpasolites exhibit a greater diversity of the A_2B combinations of atoms. As a result, these com-

Table 1. Thermal parameters for halogen atoms in different crystallographic positions of the cubic phase in the isotropic (B_{iso}) and anisotropic (B_{11}/B_{33}) approximations

Compound	24*e*			96*j*	192*l*	T_1, K	Reference
	B_{iso}, Å^2	$(B_{11}/B_{33})_h$	$(B_{11}/B_{33})_{anh}$	B_{iso}, Å^2	B_{iso}, Å^2		
$Cs_2NaPrCl_6$	2.2 (R = 4.4%)					153	[8]
$Cs_2NaNdCl_6$		4.3 (2.9%)	6.5 (2.8%)			132	[9]
Rb_2NaHoF_6	1.2 (5.8%)					172	[8]
Rb_2NaFeF_6		2.6 (4%)				<0	[10]
		1.3 (1.3%)				<0	[11]
Rb_2KFeF_6		5.3 (4%)				170	[10]
		4.4 (1.9%)				170	[11]
K_2NaCrF_6		3.2 (2.1%)				?	[11]
	1.95 (13%)	5.6 (12.5%)				?	[12]
K_2NaFeF_6	1.84 (5.9%)	16 (4.6%)				?	[12]
Rb_2KScF_6	6.2 (6.4%)			1.8 (5.0%)	1.8 (5.5%)	252	[8]
$(Nb_4)_3GaF_6$					1.8 (12%)	250	[13]

Note: The reliability factors R are given in parentheses. T_1 is the temperature of the phase transition from the cubic phase. The subscripts "h" and "anh" refer to the harmonic and anharmonic models, respectively.

pounds can undergo the single $Fm\bar{3}m$–$I4/m$ (Rb_2Na and Cs_2K), successive $Fm\bar{3}m$–$I4/m$–$P2_1/n$ (Rb_2K) and $Fm\bar{3}m$–$I4/m$–$C2/m$–$P2_1/n$ (Cs_2Rb), and flip–flop $Fm\bar{3}m$–$P2_1/n$ (Rb_2K) phase transitions [8].

As follows from the group-theoretic analysis of possible distortions of the elpasolite structure [14], the $Fm\bar{3}m$–$I4/m$ phase transition is associated with the soft mode at the center of the Brillouin zone. Actually, the soft mode belonging to the Γ point was found in studies of inelastic neutron scattering in the cubic phase of $Cs_2NaBiCl_6$ [15] and $Cs_2NaTmBr_6$ [16] crystals. Let us now dwell on the characteristic features of the cubic phase in the aforementioned elpasolites. First, we note the quasi-two-dimensional motion of octahedra, which can be explained by the fact that a rotation of one octahedron about a particular cubic axis results in the distortion of the whole octahedron layer orthogonal to this axis. Second, a substantial damping of phonons was revealed at temperatures 10–20 K below the T_0 temperature, which made unambiguous determination of the soft mode frequency impossible in this temperature range. The temperature determined by the extrapolation of the linear dependence $\omega^2(T)$ to $\omega^2 = 0$ turned out to be considerably below the phase transition temperature obtained in other experiments. According to Bührer and Güdel [16], this discrepancy is caused by the deviation of the $\omega^2(T)$ function from the linear behavior in the vicinity of T_0 due to the interaction between acoustic and optical modes with the same symmetry. However, it should be noted that the afore-

Table 2. Thermodynamic characteristics of phase transitions in haloid elpasolites with atomic cations [8]

$A_2B^+B^{3+}X_6$	Type of distorted structure	SR	T_i, K	$T^{-1}dT/dp$, GPa^{-1}	$\Delta S/R$
$Cs_2NaBiCl_6$	$I4/m$	00φ	100	0.28	0.20
$Cs_2NaNdCl_6$	$I4/m$	00φ	132	0.33	0.23
$Cs_2NaPrCl_6$	$I4/m$	00φ	153	0.32	0.21
$Cs_2NaLaCl_6$	$I4/m$	00φ	210	0.26	0.26
$Cs_2NaTmBr_6$	$I4/m$	00φ	102	0.32	0.21
Cs_2NaYBr_6	$I4/m$	00φ	139	0.31	0.18
Rb_2NaDyF_6	$I4/m$	00φ	166		0.20
Cs_2KDyF_6	$I4/m$	00φ	160		0.20
Cs_2RbDyF_6	$I4/m$	00φ	251	0.06	0.20
	$C2/m$	0φφ	205	−0.05	0.47
	$P2_1/n$	ψφφ	196	−0.09	
Rb_2KFeF_6	?	?	170	0.78	1.88
Rb_2KGaF_6	?	?	123	0.90	1.73
Rb_2KScF_6	$I4/m$	00φ	252	0.07	0.20
	$P2_1/n$	ψφφ	223	0.01	0.51
Rb_2KInF_6	$I4/m$	00φ	283	0.07	0.18
	$P2_1/n$	ψφφ	264	0.03	0.59
Rb_2KLuF_6	$I4/m$	00φ	370	0.06	1.05
	$P2_1/n$	ψφφ	366	0.05	
Rb_2KErF_6	$P2_1/n$	ψφφ	395	0.06	0.95
Rb_2KHoF_6	$P2_1/n$	ψφφ	400	0.05	1.13
Rb_2KTbF_6	$P2_1/n$	ψφφ	412	0.06	

Note: SR denotes the system of octahedron rotations, and R is the gas constant.

mentioned elpasolites undergo the first-order phase transition, and this is primarily the reason why the T_c temperature (at which $\omega^2(T) = 0$) does not coincide with the phase transition temperature T_0. At the same time, the $T_0 - T_c$ values determined from the neutron scattering [16] and calorimetric [17, 18] data differ significantly and, hence, the assumption that the $\omega^2(T)$ function deviates from the linearity near the T_0 temperature holds some validity.

The phonon spectra of fluoro-elpasolites were studied in the tetragonal phase of Rb_2KScF_6 by Raman spectroscopy and in the cubic phase of Rb_2KHoF_6 by neutron scattering [8]. However, the soft vibrational modes were found in none of the crystals. Furthermore, a diffuse scattering peak was observed for the cubic phase of Rb_2KHoF_6. These data, together with the above results of the structural investigations of Rb_2KScF_6 (in which the best results were obtained in the case when fluorine atoms in the cubic phase were disordered over four or eight positions), allowed us to assume that the mechanism of phase transitions in fluorine-containing crystals has specific features as compared to chloride and bromide crystals.

Now, we consider how the phase transitions in haloid elpasolites can be characterized according to the calorimetric data. As follows from the heat capacity measurements in bromides (M^{3+} = Y and Tm) [18] and chlorides (M^{3+} = Bi, Nd, Pr, and La) [17], the $Fm\bar{3}m$–$I4/m$ transition is the first-order phase transformation close to the tricritical point. An increase in the size of the M^{3+} ion from crystal to crystal leads to an increase in the temperature of the phase transition and the degree of its closeness to the tricritical point. It was also found that the entropy change upon the phase transition does not depend on the size of M^{3+} and X^- ions and has a relatively small value: $\Delta S = (0.18–0.26)R$ (Table 2).

Unlike chlorides and bromides, the $Fm\bar{3}m$–$I4/m$ transition in all the fluorides studied is the second-order phase transformation close to the tricritical point. One of the possible reasons for the difference in the type of phase transitions in these groups of elpasolites is the

different scale of effects caused by the coupling between the order parameter and the deformation, which is determined by the reduced shift in the phase transition temperature under the hydrostatic pressure $(dT_0/dp)T_0^{-1}$ [8]. This quantity in crystals with X = Cl and Br is almost five times larger than that in fluoride crystals (Table 2). It should be mentioned that the reduced shift in the temperature of the $I4/m$–$P2_1/n$ phase transition increases with an increase in the size of the M^{3+} ion and, for the compound with $M^{3+} = Lu^{3+}$, becomes as large as the shift typical of the $Fm\bar{3}m$–$P2_1/n$ flip–flop transition. At the same time, the entropy changes upon the $Fm\bar{3}m$–$I4m$ phase transition in fluorides fall in the range of entropy changes that are characteristic of chlorides and bromides (Table 2). Consequently, the entropy $\Delta S = (0.22 \pm 0.04)R$ (which can more likely be treated as typical of the displacive phase transition) could be considered as corresponding to one vibrational degree of freedom due to rotations of octahedral ionic groups in the elpasolite structure. Indeed, even in the case when three phase transitions associated with the successive rotations of octahedra about three axes of the cubic phase occur in Cs_2RbDyF_6 (Table 2), the total entropy change is equal to the sum of the entropies corresponding to the simple rotations $\Sigma\Delta S_i \approx 0.67R \approx 3 \times 0.22R$ [8].

However, the "universality" of the entropy change is not necessarily observed in haloid elpasolites. Examples are provided by a number of $Rb_2KM^{3+}F_6$ crystals (Table 2) [8]. Unfortunately, the space group of the distorted phase is unknown, and, hence, it is difficult to assign the considerable entropy change $\Delta S = R\ln 6 = 1.79R$ to particular critical ions in compounds with M^{3+} = Ga and Fe (Table 2). It can only be stated that this value with a high probability corresponds to ordering processes in the structure. This assumption is supported by the data obtained by Massa *et al.* [11], who did not rule out that fluorine ions in the $Fm\bar{3}m$ phase can occupy four positions. An increase in the size of M^{3+} ions (and, correspondingly, the unit cell parameter a_0) leads to the successive (000)–(00φ)–(ψφφ) (M^{3+} = Sc, In, and Lu) and, then, flip–flop (000)–(ψφφ) (M^{3+} = Er, Ho, and Tb) phase transitions with the resulting monoclinic distortion owing to a superposition of octahedra rotations. An increase in the a_0 parameter in a series of $Rb_2KM^{3+}F_6$ crystals is accompanied by a change in the bond strength which causes an increase in the anisotropy (and anharmonicity) of atomic vibrations of fluorine [8]. In turn, this should bring about an increase in the entropy of the corresponding phase transitions [19]. Actually, the quantity $\Sigma\Delta S = \Delta S_1 + \Delta S_2$ increases from crystal to crystal according to the increase in the anharmonicity parameter $\langle x\rangle^2/a_0^2$ of atomic vibrations of fluorine, where $\langle x\rangle$ is the mean displacement of critical atoms [8]. However, even the maximum experimental value $\Sigma\Delta S = 1.13R$ (for Rb_2KHoF_6) appeared to be less than the entropy $\Sigma\Delta S = 1.39R = R\ln 4$ which would be observed for the phase transition associated with a partial ordering of fluorine ions occupying eight and two positions in the $Fm\bar{3}m$ and $P12_1/n1$ phases, respectively [8]. At the same time, it is not improbable that the last phase transition can take place in $Rb_2KM^{3+}F_6$ elpasolites with a further increase in the size of M^{3+} ions and, correspondingly, in the anharmonicity parameter (for example, at $M^{3+} = La^{3+}$). Thus, the series of crystals under consideration can likely provide an example of the possible change in the mechanism of the phase transition from the displacive type to the order–disorder type due to an increase in the anharmonicity of the vibrations of critical ions.

3. HALOID ELPASOLITES AND CRYOLITES WITH MOLECULAR CATIONS

There is another way to affect the vibrations of critical fluorine ions and (or) their position in the structure of the initial cubic phase and, hence, the phase transition mechanism. The elpasolite (cryolite) structure is retained when the spherical atomic cations of potassium and (or) rubidium in $Rb_2KM^{3+}F_6$ crystals are replaced by the tetrahedral ammonium ions [8]. A number of substituted compounds, such as $(NH_4)_3M^{3+}F_6$ (M^{3+} = Al, Ga, Cr, V, Fe, Sc, and In), $(NH_4)_3KM^{3+}F_6$ (M^{3+} = Al and Fe), and $Cs_2(NH_4)FeF_6$, undergo phase transitions (Table 3) [20–22]. Unfortunately, the data on ammonium elpasolites are insufficient for detailed

Table 3. Thermodynamic characteristics of phase transitions in fluorine-containing cryolites and elpasolites with ammonium cations [8, 20–23]

Compound	Type of distorted structure	T_i, K	$\Delta S/R$
$(NH_4)_2KAlF_6$	?	250	
	?	186	
$(NH_4)_2KFeF_6$	?	290	
$Cs_2(NH_4)FeF_6$	?	190	
$(NH_4)_3AlF_6$	?	220	2.23
	?	190	0.51
$(NH_4)_3CrF_6$	*Tr*	270	2.33
$(NH_4)_3GaF_6$	*Tr*	250	2.77
$(NH_4)_3VF_6$	*Tr*	280	2.99
$(NH_4)_3FeF_6$	*Tr*	267	2.98
$(NH_4)_3ScF_6$	$P2_1/n1$	330	1.61
	$I12/m1$	290	0.81
	$P\bar{1}$	243	0.08

Note: *Tr* denotes the triclinic symmetry, and *R* is the gas constant.

consideration. In the $(NH_4)_3M^{3+}F_6$ cryolites, as in fluoro-elpasolites with atomic cations, an increase in the M^{3+} ion size (the a_0 parameter) leads to an increase in the temperature of the stable initial cubic phase. However, there are considerable differences in the properties of these compounds. First, the triclinic symmetry of the low-temperature phase and the absence of the intermediate tetragonal phase $I4/m$ upon successive phase transitions are characteristic of ammonium cryolites [23]. Second, the total entropy change upon transition from the cubic phase to the triclinic phase varies in the narrow range $\Sigma\Delta S = (2.33–2.99)R$ from crystal to crystal and does not depend on the sequence of phase transitions (Table 3). A large entropy clearly indicates that certain processes of structural ordering proceed in ammonium cryolites as a result of successive (M^{3+} = Al, Sc, and In) or single (M^{3+} = Cr, Ga, V, and Fe) phase transitions. The model proposed by Tressaud *et al.* [21] for the possible ordering of ions upon the $Fm\bar{3}m$–$P\bar{1}$ phase transition was also successfully applied to the description of the successive phase transitions [22]. The orientational disordering of $(M^{3+}F_6)^{3-}$ octahedra in the cubic phase is due to the distribution of fluorine atoms over eight positions (192*l*) [13] [see the data for $(NH_4)_3GaF_6$ in Table 1]. In the triclinic low-temperature phase, the octahedra (fluorine atoms) are completely ordered and occupy one position. To put it differently, the contribution of octahedron ordering to the entropy change is equal to $R\ln 8 = 2.08R$. Out of two ammonium ions that occupy different crystallographic positions (8*c* and 4*b*), only the latter ion in the cubic phase is disordered over two orientations according to the symmetry of its position. Consequently, the entropy change that corresponds to the ordering of ammonium ions is equal to $R\ln 2 = 0.69R$. Thus, the ordering processes in ammonium cryolites cannot be attended by an entropy change of larger than $\Sigma\Delta S = R(\ln 8 + \ln 2) = 2.77R$. This value is in reasonable agreement with the experimental data (Table 3). In the crystals characterized by successive phase transitions, the ordering processes occur in two steps [22]. The phase transition from the cubic phase is associated with a partial ordering of octahedra ($\Delta S = R\ln 4$), which results in a forced ordering of ammonium tetrahedra ($\Delta S = R\ln 2$). The octahedra are completely ordered upon transition between two monoclinic modifications ($\Delta S_2 \approx R\ln 2$). The third phase transition ($\Delta S_3 = 0.08R$) is unrelated to the order–disorder processes. The model under consideration is consistent with the NMR data obtained by Sasaki *et al.* [24]. For cryolites with successive phase transitions, an anomalous behavior is observed at the temperature T_1 for the spin-lattice relaxation times of protons (T_{1H}) and fluorine nuclei (T_{1F}). At the temperature T_2, considerable changes are observed only for T_{1F}.

It was found that the structure of ammonium cryolites strongly depends on the external pressure [22]. The investigation of the pressure–temperature phase diagram for a cryolite with M^{3+} = Sc that underwent three phase transitions demonstrated that both intermediate monoclinic phases disappear with a decrease in the volume of the unit cell under the pressure. At $p \geq 1.2$ GPa, the direct $Fm\bar{3}m$–$P\bar{1}$ phase transition is observed, as is the case in compounds with a smaller size of the M^{3+} ion (Cr, Ga, V, and Fe) at atmospheric pressure. This is the reason why the total entropy change upon successive phase transitions in $(NH_4)_3ScF_6$ corresponds to the entropy of the phase transition in $(NH_4)_3GaF_6$. In turn, at relatively low pressures $p \geq 0.045$ GPa, the $(NH_4)_3GaF_6$ cryolite undergoes two phase transitions, as is the case in $(NH_4)_3AlF_6$ which has the least volume of the $Fm\bar{3}m$ unit cell among ammonium cryolites. Three phase transitions are observed in the gallium compound at $p \geq 0.25$ GPa. Therefore, it is not improbable that the third transition can occur in aluminum cryolite under the pressure.

In order to elucidate in greater detail the role played by particular ionic groups in the phase transition within the above model, it is desirable to perform the following investigations.

(i) It is expedient to refine the positions of atoms and their thermal parameters in the cubic and distorted phases not only for cryolites, but also for elpasolites with ammonium ions, because spherical and tetrahedral cations can occupy different crystallographic positions in the latter compounds. In this case, several alternative structural models should be taken into consideration.

(ii) Reliable information on the entropy of phase transitions in ammonium elpasolites should be obtained by calorimetric techniques.

(iii) The effect of the pressure on the phase transitions in $(NH_4)_3AlF_6$ and ammonium elpasolites should be studied with the aim of constructing the generalized p–T phase diagram.

4. ELPASOLITES WITH MOLECULAR ANIONS

Let us analyze how the elpasolite structure in crystals with atomic cations is affected by replacing spherical halogen ions with molecular ions $(CN)^-$. The space group $Fm\bar{3}m$ is retained in $Cs_2LiM^{3+}(CN)_6$ compounds. The structure of these compounds was investigated by Swanson and Lucas [25]. In their work, the authors considered a model in which Cs, Li, and M atoms occupy special positions (with the coordinates 1/4, 1/4, 1/4; 1/2, 1/2, 1/2; and 0, 0, 0, respectively), and the C and N atoms are located on the cell edge (24*e*). A pronounced anisotropy of vibrations is characteristic of the $(CN)^-$ molecular anion. The vibration amplitudes of the C and N atoms along the z axis (cell edge) are virtually identical. The displacements in the direction perpendicular to the cell edge are substantially larger, especially for the nitrogen atom. The motion of the Cs atom is also characterized by an anomalously large

root-mean-square amplitude of vibrations. For all the studied $Cs_2LiM^{3+}(CN)_6$ compounds, the Cs–N interatomic distances are appreciably larger than the sum of their ionic radii. On the other hand, the Li–N bond length is comparable to this sum. According to [25], these are the reasons for the weak interaction between Cs^+ and $(CN)^-$ ions and the considerable thermal displacements of cesium and nitrogen atoms.

A large volume of holes occupied by cesium atoms between octahedra plays a decisive role in the instability of the cubic phase: as the unit cell parameter increases, the cubic lattice becomes increasingly unstable with respect to the displacements of Cs atoms and the rotations of $M^{3+}(CN)^{3-}$ octahedra. In this respect, it is interesting to note the correlation between a monotonic increase in the vibration amplitudes of Cs, N, and C atoms and an increase in the cell size. Since the bond lengths remain unchanged to within the error of their determination in all the $Cs_2LiM^{3+}(CN)_6$ compounds, the changes in the unit cell parameter a_0 and the size of the hole occupied by cesium atoms between octahedra are determined by the change in the M^{3+}–C bond length. Some characteristics of the phase transitions in $Cs_2LiM^{3+}(CN)_6$ elpasolites are listed in Table 4. It is seen that the stability loss temperature of the cubic phase increases with an increase in the unit cell parameter a_0. The sole exception is provided by the elpasolite with M^{3+} = Ir. As was shown in [25], the phase transition to the tetragonal phase $P4/nmc$ belongs to the first-order transformations and is associated with the condensation of the X_2^+ soft mode at a point of the Brillouin zone boundary. The structural distortions can be explained by the antiferrodistorsion rotations of $M^{3+}(CN)_6$ octahedra. Note that this type of tetragonal distortion of the elpasolite structure differs from that observed in the haloid crystals (see Section 2). The next phase transition (to the monoclinic phase $P2_1/n$) is the second-order transformation associated with the condensation of the X_5^+ mode that corresponds to the octahedron rotations and the displacements of Cs atoms. It is worth noting that investigations of the monoclinic phase structure and the Raman spectra did not reveal noticeable distortion of the octahedra in $Cs_2LiCr(CN)_6$ [25] and $Cs_2KFe(CN)_6$ [26] crystals.

Thus, on the one hand, the sequence of phases (cubic–tetragonal–monoclinic), which is realized upon replacement of the atomic cation by the molecular cation in the elpasolite structure, is similar to that observed in fluoro-elpasolites. On the other hand, the phase transition between the cubic and tetragonal phases in cyanides is associated with the soft mode at the point of the Brillouin zone boundary.

Unfortunately, since the data on the entropy of phase transitions in the $Cs_2LiM^{3+}(CN)_6$ crystals are unavailable, it is impossible to trace the effect of a considerable anisotropy of atomic vibrations of nitrogen and cesium on the entropy change.

Table 4. Characteristics of successive phase transitions in $Cs_2LiM^{3+}(CN)_6$ elpasolites [25]

M^{3+}	a_0, Å	T_1, K	Space group	T_2, K	Space group
Co	10.495	183	$P4/nmc$	168	$P2_1/n$
Fe	10.571	221		170	
Mn	10.677	273			
Cr	10.780	348	$P4/nmc$	310	$P2_1/n$
Ir	10.720	418	$P4/nmc$	335	$P2_1/n$

5. OXYGEN-CONTAINING ELPASOLITES (ORDERED PEROVSKITES)

Many oxides $A_2B'B''O_6$ crystallize in a perovskite-like structure and can undergo phase transitions of different types. The ratios between the ionic radii of B' and B'' cations and also between their charges affect the character of ordering and, correspondingly, the structural characteristics and physical properties. Partly or completely disordered compounds exhibit diffuse phase transitions and relaxor phenomena. The ordered compounds (elpasolites) undergo "sharp" (nonsmeared) transformations whose sequence considerably depends on the cation type. Among these compounds are lead-containing elpasolites such as Pb_2MgWO_6, Pb_2CoWO_6, and Pb_2MgTeO_6.

Baldinozzi *et al.* [27–29] carried out the precision structural investigation of the cubic phase $Fm\bar{3}m$ in these compounds. The composition disorder in the arrangement of the B' and B'' cations was found in none of the elpasolites. At the same time, it turned out that the thermal parameters (or the root-mean-square displacements u^2) and the reliability factors R have the least values for the structural model according to which the oxygen atoms occupy the positions 24*e* and execute pronounced anisotropic vibrations in the plane perpendicular to the B'–O–B'' bond and the lead atoms are disordered over 6, 12, or 4 local positions in accord with the possible displacements along the [100], [110], and [111] directions. As follows from [27, 28], the model in which the lead atoms occupy 12 equivalent positions is most preferential. The u^2 displacements and the R factors for the isotropic and disordering models are presented in Table 5. Thus, the structure of oxide compounds, unlike haloid elpasolites (cryolites), involves two types of critical ions, which, in principle, are responsible for the displacive phase transitions (rotations of oxygen octahedra) and the order–disorder phase transitions (the ordering of lead atoms).

Different sequences of phase transitions are observed in Pb_2MgWO_6, Pb_2CoWO_6, and Pb_2MgTeO_6 elpasolites (Table 6). Incommensurate phases with the

Table 5. Root-mean-square displacements $\bar{u}^2$ of oxygen and lead atoms for the isotropic model (O and Pb atoms occupy the 24*e* and 8*c* positions, respectively) and disordering model

Compound	$\bar{u}^2$, Å^2				T_1, K	Reference
	O	Pb	O	Pb		
	24*e*	8*c*	Displaced	Model [110]		
Pb_2MgWO_6	0.018	0.036	0.005	0.011	313	[27]
	(5.6%)		(4.5%)			
Pb_2CoWO_6	0.034	0.045	0.005	0.005	303	[28]
	(5.9%)		(5.3%)			
Pb_2MgTeO_6	0.016	0.020			190	[29]
	4.5%					

Note: T_1 is the stability loss temperature of the cubic phase. The reliability factor *R* is given in parentheses.

same symmetry were found in the last two compounds. The incommensurate structure in Pb_2MgTeO_6 is retained, at least, down to 6 K. The existence of the intermediate phase in Pb_2MgWO_6 was not established unambiguously. The structure of the low-temperature phases was refined only for Pb_2MgWO_6 and Pb_2MgTeO_6 [27, 29]. It was demonstrated that, in the orthorhombic phase of Pb_2MgWO_6, the lead atoms are displaced along the $[010]_p$ direction of the pseudocubic cell and the octahedra are slightly rotated and distorted. The modulated displacements of oxygen and lead atoms are observed in the rhombohedral phase of Pb_2MgTeO_6. Moreover, the lead atoms remain disordered. The space group of the orthorhombic phase in Pb_2CoWO_6 was determined ambiguously: *Pmcn* or $P2_1cn$ [28].

Analysis of the Raman spectra of the low-temperature phases in Pb_2MgWO_6 [31] and Pb_2MgTeO_6 [32] revealed soft modes in the low-frequency range. It was assumed that the phase transition in Pb_2MgWO_6 is associated with the condensation of two modes X_{10} and Σ_3 at the boundary and within the Brillouin zone, respectively. In Pb_2MgTeO_6, the soft mode is condensed at an incommensurate point of the Brillouin zone.

The study of inelastic neutron scattering in the cubic phase of Pb_2CoWO_6 also revealed the soft mode that belongs to the *X* point of the Brillouin zone and corresponds to rotations of the oxygen octahedra [33]. The condensation of this mode leads to a lowering in the crystal symmetry to tetragonal [14]. However, the low-temperature phase in Pb_2CoWO_6 has a lower symmetry. This seeming contradiction can be explained by the fact that the phase transitions in this compound, as in other oxygen-containing elpasolites, are governed by two mechanisms and two order parameters. Apparently, the primary parameter corresponds to displacements of oxygen atoms (octahedron rotations) that lead to a distortion of holes between octahedra and a lowering of their symmetry, which gives rise to the secondary order parameter associated with the ordering of lead atoms.

Therefore, in oxygen-containing elpasolites, the structural distortions upon phase transitions can be caused by the simultaneously occurring processes of ordering and displacement of different ions (Pb_2MgWO_6 and Pb_2CoWO_6) and only by the displacement processes (Pb_2MgTeO_6).

The question arises: How do these models of structural distortions correlate with the data of calorimetric measurements?

Although ordered oxygen-containing perovskites have been thoroughly investigated for many years, the data on the heat capacity of Pb_2MgWO_6 and Pb_2CoWO_6 have been obtained by adiabatic calorimetry only recently. This made it possible to determine

Table 6. Characteristics of phase transitions in oxygen-containing elpasolites

Compound	Type of distorted structure	T_i, K	$\Delta S/R$	Reference
Pb_2MgWO_6	*Pmcn*	313	1.7	[27, 30]
Pb_2CoWO_6	*IM*	303	1.15	[28, 30]
	Pmcn / $P2_1cn$?	256	0.18	
Pb_2MgTeO_6	$R\bar{3}m$	188		[29]
	($\delta\delta\delta$)			
	$R\bar{3}$	142		
	($\delta\delta\delta$)			

Note: *IM* denotes the incommensurate monoclinic phase, and *R* is the gas constant.

reliably the entropy changes upon phase transitions (Table 6) [30]. In order to separate the contributions from the displacement and ordering processes to the entropy, it would be expedient to obtain the data on the excess entropy of Pb_2MgTeO_6 in which the phase transitions result only in the displacement of oxygen ions. Unfortunately, at present, detailed information on the heat capacity of Pb_2MgTeO_6 is unavailable. We intend to perform these investigations in the immediate future. However, it is known (see Section 2) that, in haloid elpasolites, the displacive phase transitions associated with small rotations of octahedra are usually accompanied by relatively small entropy changes $\Delta S/R \approx 0.2$. By assuming that this quantity for oxide compounds differs insignificantly, the main contribution to the entropy of structural transformations in Pb_2MgWO_6 and Pb_2CoWO_6 should be determined by the secondary order parameter of phase transitions, i.e., by the ordering of lead atoms. On the other hand, the experimental entropies for these elpasolites fall in the range $R\ln 4$–$R\ln 6$. In the framework of the model considered above, this means that lead atoms in the orthorhombic phase are incompletely ordered, because, otherwise, the entropy change should be equal to $R\ln 12$. This assumption is in good agreement with the structural data, according to which lead atoms that occupy 12 local disordered positions in the cubic phase are displaced along the $[010]_p$ direction of the pseudocubic cell in the orthorhombic phase [27]. This implies that lead atoms in the partly ordered low-temperature phase occupy two or four disordered positions, which results in the entropy changes $R\ln 12/2 = R\ln 6$ and $R\ln 12/4 = R\ln 3$, respectively.

6. CONCLUSION

The main results obtained in the above analysis of the phase transitions in the crystals with an elpasolite (cryolite) structure can be summarized as follows.

(1) For the most part, the structural and calorimetric data are in agreement, provided that they are considered within the model concepts of phase transitions.

(2) The mechanism of structural transformations essentially depends on the size and the shape of cations and anions. Changes in the size and the shape of ions can lead to substantial changes in the anharmonicity of vibrations of atomic ions and (or) the appearance of an orientational ordering of nonspherical (molecular) ions. In turn, this affects the magnitude and the behavior of the excess entropy.

(3) In haloid crystals, the entropy of the cubic-to-tetragonal phase transition is constant.

(4) In oxygen-containing compounds, there occur phase transitions associated with two order parameters which arise from the displacement of atoms of one type and the ordering of atoms of another type in the structure. In order to separate the contributions from different mechanisms of transformations to the entropy, it is advisable to carry out the calorimetric investigations of crystals in which the phase transitions are associated only with displacements of oxygen atoms (for example, Pb_2MgTeO_6).

ACKNOWLEDGMENTS

This work was supported by the International Association of Assistance for the promotion of co-operation with scientists from the New Independent States of the former Soviet Union (project INTAS no. 97-10177) and the Russian Foundation for Basic Research (project no. 00-02-16034).

REFERENCES

1. B. V. Beznosikov and K. S. Aleksandrov, Preprint No. 753.F, IF SO RAN (Kirenskiĭ Institute of Physics, Siberian Division, Russian Academy of Sciences, Krasnoyarsk, 1994).
2. E. Salje, Philos. Trans. R. Soc. London, Ser. A **328**, 409 (1989).
3. N. Sicron, B. Ravel, Y. Yacoby, *et al.*, Phys. Rev. B **50** (18), 13168 (1994).
4. J. Hutton and R. J. Nelmes, J. Phys. C: Solid State Phys. **14** (12), 1713 (1981).
5. J. Hutton, R. J. Nelmes, G. M. Meyer, and V. R. Eiriksson, J. Phys. C: Solid State Phys. **12** (24), 5393 (1979).
6. A. D. Brause and R. A. Cowley, *Structural Phase Transitions* (Taylor and Francis, Philadelphia, 1981; Mir, Moscow, 1984).
7. R. L. Armstrong, Prog. Nucl. Magn. Reson. Spectrosc. **21**, 151 (1989).
8. I. N. Flerov, M. V. Gorev, K. S. Aleksandrov, *et al.*, Mater. Sci. Eng. R **24** (3), 81 (1998).
9. I. P. Makarova, S. V. Misjul, L. A. Muradyan, *et al.*, Phys. Status Solidi B **121** (2), 481 (1984).
10. R. Haegele, W. Verscharen, and D. Babel, Z. Naturforsch. B **30** (3), 462 (1975).
11. W. Massa, D. Babel, M. Epple, and W. Rüdorff, Rev. Chim. Miner. **23** (4–5), 508 (1986).
12. K. Knox and D. W. Mitchell, J. Inorg. Nucl. Chem. **21** (1/2), 253 (1961).
13. S. Schwarzmann, Z. Kristallogr. **120**, 286 (1964).
14. K. S. Aleksandrov and S. V. Misyul', Kristallografiya **26** (8), 1074 (1981) [Sov. Phys. Crystallogr. **26**, 612 (1981)].
15. F. Prokert and K. S. Aleksandrov, Phys. Status Solidi B **124** (2), 503 (1984).
16. W. Bührer and H. U. Güdel, J. Phys. C: Solid State Phys. **20** (25), 3809 (1987).
17. I. N. Flerov, M. V. Gorev, and A. E. Usachev, Fiz. Tverd. Tela (St. Petersburg) **36** (1), 106 (1994) [Phys. Solid State **36**, 57 (1994)].
18. I. N. Flerov, W. Bührer, M. V. Gorev, *et al.*, J. Phys.: Condens. Matter **2** (46), 9019 (1990).
19. V. G. Vaks, *Introduction to the Microscopic Theory of Ferroelectrics* (Nauka, Moscow, 1973).
20. W. Massa, Z. Anorg. Allg. Chem. **427**, 235 (1976).

21. A. Tressaud, S. Khairoun, L. Rabardel, *et al.*, Phys. Status Solidi A **96** (1), 407 (1986).
22. M. V. Gorev, I. N. Flerov, and A. Tressaud, J. Phys.: Condens. Matter **11** (39), 7493 (1999).
23. M. V. Gorev, I. N. Flerov, S. V. Mel'nikova, *et al.*, Izv. Akad. Nauk, Ser. Fiz. **64** (6), 1104 (2000).
24. A. Sasaki, Y. Furukawa, and D. Nakamuda, Ber. Bunsenges. Phys. Chem. **93**, 1142 (1989).
25. B. I. Swanson and B. C. Lucas, Inorg. Chem. **17** (10), 2717 (1978).
26. F. Herren, A. Ludi, and P. Fischer, Acta Crystallogr. B **B35**, 3129 (1979).
27. G. Baldinozzi, Ph. Sciau, M. Pinot, and D. Grebille, Acta. Crystallogr. B **B51**, 668 (1995).
28. G. Baldinozzi, Ph. Sciau, and J. Lapasset, Phys. Status Solidi A **133** (1), 17 (1992).
29. G. Baldinozzi, D. Grebille, Ph. Sciau, *et al.*, J. Phys.: Condens. Matter **10**, 6461 (1998).
30. I. N. Flerov, M. V. Gorev, and Ph. Sciau, J. Phys.: Condens. Matter **12** (5), 559 (2000).
31. G. Baldinozzi, Ph. Sciau, and A. Bulou, J. Phys.: Condens. Matter **7**, 8109 (1995).
32. G. Baldinozzi, Ph. Sciau, and A. Bulou, J. Phys.: Condens. Matter **9**, 10531 (1997).
33. W. Bührer, W. Brixel, and H. Schmid, *Phonons 85* (World Scientific, Singapore, 1985), p. 325.

Translated by O. Borovik-Romanova

Physics of the Solid State, Vol. 43, No. 1, 2001, pp. 137–144. Translated from Fizika Tverdogo Tela, Vol. 43, No. 1, 2001, pp. 132–139.

LOW-DIMENSIONAL SYSTEMS AND SURFACE PHYSICS

Raman Light Scattering in Nanoporous Carbon Obtained from Silicon and Titanium Carbides

A. M. Danishevskiĭ*, É. A. Smorgonskaya*, S. K. Gordeev, and A. V. Grechinskaya****

**Ioffe Physicotechnical Institute, Russian Academy of Sciences, Politekhnicheskaya ul. 26, St. Petersburg, 194021 Russia*

***Central Research Institute of Materials, St. Petersburg, Russia*

Received March 24, 2000; in final form, May 12, 2000

Abstract—A study is reported on the Raman spectra of nanoporous carbon prepared in a chemical reaction from polycrystalline α-SiC and TiC. The spectra are shown to be of a multicomponent nature, which distinguishes this group of materials from graphites and disordered carbon structures. A series of low-frequency modes are detected. Anisotropy and dispersion effects are revealed. The results obtained argue in favor of a cluster structure of nanoporous carbon and size quantization of the electronic and vibrational spectra in carbon nanoclusters. The main structural elements of the nanoclusters in the porous framework are small fragments of bent or broken graphene sheets. The presence of fragments close in structure to strained cubic or hexagonal diamond is observed in a number of cases. © *2001 MAIK "Nauka/Interperiodica".*

Raman scattering (RS) spectroscopy of light produces a wealth of information on the vibrational properties and short-range order of carbon materials [1–4]. RS spectroscopy has been used to study a rich variety of forms of solid carbon, from the various crystalline modifications and nanocluster systems (fullerenes, nanotubes, nanocapsules, etc.) to amorphous, glassy, or fiber structures. By comparing the vibrational modes observed in RS spectra of the nanoporous carbon (npor-C) studied in this work with data available for other carbon forms, one can draw conclusions on the character of the valence bonds and structure of the material.

The RS spectrum of ordered graphite consists of narrow bands near 1581 (the so-called *G* band) and 42 cm^{-1}, which correspond to two types of lattice vibrations of E_{2g} symmetry in graphene sheets with sp^2-hybridized valence bonds [1]. Slight disordering of the graphite lattice is capable of slightly shifting the *G* band to either side.

The RS spectrum of microcrystalline or disordered graphites exhibits one more peak usually called the *D* band. The *D*-band Raman shift in samples excited by argon laser radiation with λ_{exc} = 488 nm is 1355 cm^{-1} [1]. The *D* band is usually associated with the small size of the ordered regions and the existence of distinct boundaries of crystallites, which result in a violation of the RS wave-vector selection rules. The ratio of integrated intensities of the *D* and *G* bands (I_D/I_G) in graphite powders grows linearly with decreasing grain size [1], while in disordered graphite structures, it decreases with increasing anneal temperature as the degree of ordering (graphitization) increases [3]; this can be used to estimate the linear dimensions of crystallites in graphene sheets [1, 2]. The *G* band in graphite grains crushed to ~25 Å in size broadens and shifts to higher frequencies, up to 1590 cm^{-1} [1]. The shift is accompanied by the splitting off of a 1620 cm^{-1} band.

It has recently been shown [5] that the *D* band in polycrystalline graphite shifts linearly in frequency as the exciting photon energy $\hbar\omega_{exc}$ changes (the shift coefficient is 50 cm^{-1}/eV). Note that the *G* band at 1581 cm^{-1} does not shift significantly; however, at low $\hbar\omega_{exc}$, an additional band appears nearby, at ~1620 cm^{-1}.

The Raman spectra of hollow nanocluster carbon systems, such as nanotubes of various modifications, are considerably more complex. As follows from theoretical calculations [6] and experiments [7], these systems can exhibit a large number of Raman bands in the low- (below 300 cm^{-1}), medium-, and high-frequency (1200–1800 cm^{-1}) spectral ranges. The last range includes the regions of the *G* and *D* bands observed in graphites. In particular, in spectra of nanotubes, one may expect several discrete modes near the *G* band (1571, 1585, 1586, 1587, 1591 cm^{-1}). Nanotubes, as well as microcrystalline graphite, exhibit a dependence of the *D*-band position and of the I_D/I_G ratio on the exciting photon energy [8]. The low-frequency (including the so-called breathing) and medium-frequency modes observed on single-wall [7] and, in still larger numbers, on multiwall nanotubes, raw graphite rods, and single graphene sheets [9] are typical of carbon nanoclusters.

This paper reports the first results of a Raman spectroscopy study of nanoporous carbon (npor-C), which is prepared from polycrystalline carbides of silicon (SiC) and titanium (TiC) by reacting away the carbide-forming elements (Si, Ti) with chlorine. The npor-C obtained in this way represents a poorly studied group of nanocluster carbon materials, which have neverthe-

less already found application in technology (electrodes in superhigh-capacity capacitors, high-efficiency molecular filters, cold emitters). Extending the application areas of npor-C farther requires a comprehensive investigation of its structure and properties. As shown by the first results obtained in x-ray diffraction studies [10, 11], as well as by x-ray photoelectron spectroscopy (XPS) [12], while the materials prepared from different starting carbides exhibit certain similarities, they also reveal noticeable differences, which relate, in particular, to the character of carbon atom stacking, valence-electron hybridization, and nanocluster size and morphology. The comparative studies of the Raman spectra of different kinds of npor-C performed in this work provide additional information on the nanocluster structure.

1. SAMPLE PREPARATION

Bulk samples of npor-C in the form of plane wafers about 1 mm thick were prepared from powdered silicon (α-SiC) or titanium (TiC) carbides subjected to a preliminary heat treatment in a methane environment. The starting carbides are known to have different crystallographic symmetry; indeed, α-SiC crystallites have a hexagonal structure with alternating Si and C atomic planes, whereas TiC is characterized by a NaCl-type cubic structure. Compact carbide stocks were placed in a reactor, where they reacted with chlorine at a temperature of ~900°C. In this process, the carbide-forming elements, i.e., Si or Ti, which form volatile compounds with chlorine, were removed. The residues of possible adsorbates were eliminated by placing the samples in an argon flow. The final product was high-porosity npor-C samples with a carbon framework and a total porosity of ~70 vol %. It should be noted that the npor-C samples thus prepared contained a small amount (7–8 wt %) of pyrocarbon produced in the course of the heat treatment of the carbides in methane. The pyrocarbon plays the part of a binder, conferring the desired mechanical strength to the samples.

Part of the npor-C samples obtained from α-SiC were prepared without pyrocarbon. In this case, before chlorination, the starting carbide material with pyrocarbon inclusions was subjected to high-temperature silicidation to transform the pyrocarbon to inclusions of the β-SiC cubic phase. The subsequent chlorination removed silicon from both the starting and newly formed carbide, so that the nanoporous carbon framework extended throughout the bulk of the sample. The material of this type will be referred to in what follows as npor-C⟨SiC⟩*A*. The npor-C⟨SiC⟩*B* and npor-C⟨TiC⟩*B* notation with symbol B will identify the samples containing pyrocarbon.

According to XPS data, the carbon content in samples of all types was in excess of 98 at. %. As is shown by adsorption measurements, the materials of this group are characterized by highly uniform nanopore sizes, an extremely developed surface of the carbon framework, and a high adsorption capacity [13, 14]. Estimates made by the crack-pore model yield ~8 Å for the pore size in npor-C⟨SiC⟩.

2. MEASUREMENT TECHNIQUE

The Raman intensity from the npor-C samples was measured with a DFS-52 double-grating spectrometer under excitation with linearly polarized radiation of an argon (λ_{exc} = 488.0 or 514.5 nm) and a krypton (λ_{exc} = 647.1 nm) laser operating at a power density of (5–10) × 10^2 W/cm^2. The measurements were made in a 90° scattering geometry under oblique exciting-light incidence (the angle of incidence ~55°). As a rule, the light was polarized in the plane of incidence. Scattered radiation with polarization parallel and perpendicular to the plane of incidence was detected. Thus, the Raman spectra obtained corresponded to two polarization configurations denoted usually by *HH* and *HV*, where the first symbols relate to the incident; the second, to the scattered light. The type-*A* material was subjected to additional measurements in the *VV* configuration, where both the incident and the scattered light were polarized perpendicular to the plane of incidence. All measurements were carried out at room temperature. For convenience of comparison, the spectra are presented in arbitrary units for the scattered intensity, without taking into account the background components.

3. RESULTS AND DISCUSSION

Figures 1 and 2 display Raman spectra of the npor-C samples studied in the *HH* and *HV* polarization configurations at the pump wavelength λ_{exc} = 488.0 nm (npor-C⟨SiC⟩*B* and npor-C⟨TiC⟩*B*) or 514.5 nm (npor-C⟨SiC⟩*A*). While the spectra observed differ noticeably from one another, they can be divided in all cases into two main, fairly broad regions. By analogy with microcrystalline graphite, it appears natural to refer to the higher-energy region as the *G** band and the lower-energy region as the *D** band. Note that in the spectra of npor-C samples, both bands, *G** and *D**, were very weak. Therefore, in what follows, we are going to discuss only the spectral components that were found to be the strongest (reproducible) and/or coinciding or similar in the magnitude of the Raman shift in different spectra.

One can readily see that, irrespective of the type of material, none of the *G** and *D** bands can be described by a single Lorentzian in either polarization configuration and, moreover, these bands are strongly asymmetric with respect to the maximum, which implies that their broadening is inhomogeneous. Against the background of the *G** and *D** bands, one clearly sees more narrow peaks or shoulders. In some spectra, one actually observes a split of the *G** and *D** bands into components. When the polarization configuration changes, these features generally shift in frequency, which also

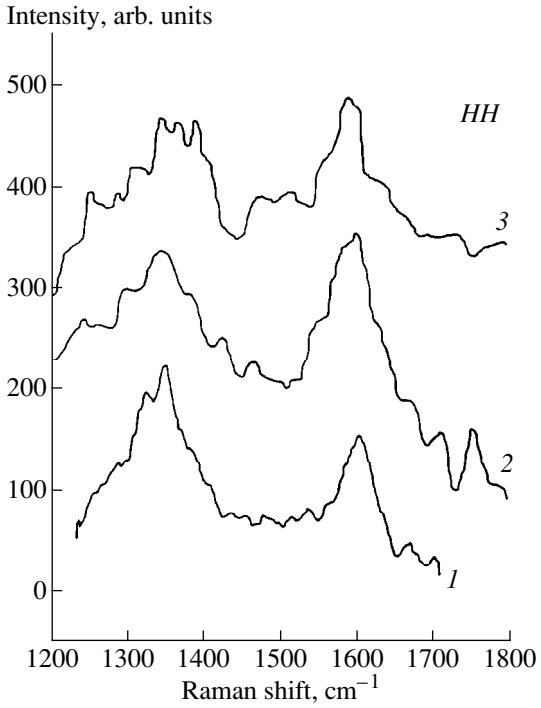

Fig. 1. *HH* Raman spectra of npor-C: (*1*) npor-C⟨SiC⟩*A*, (*2*) npor-C⟨SiC⟩*B*, and (*3*) npor-C⟨TiC⟩*B*; λ_{exc}(nm): (*1*) 514.5 and (*2*, *3*) 488.0.

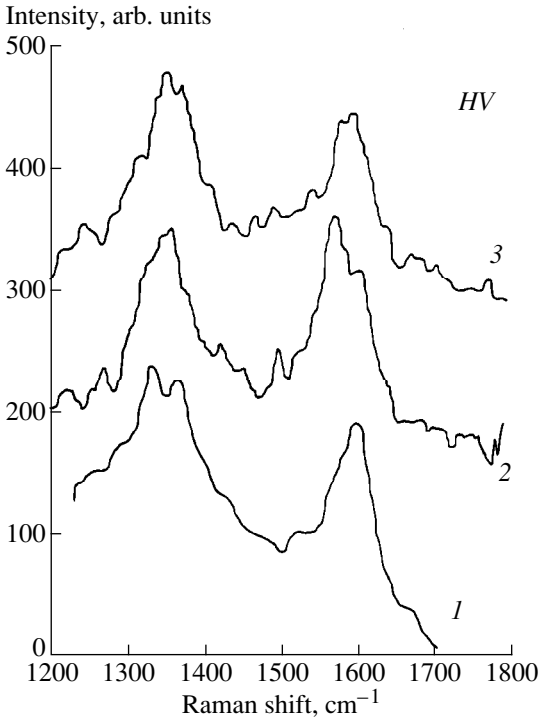

Fig. 2. *HV* Raman spectra of npor-C: (*1*) npor-C⟨SiC⟩*A*, (*2*) npor-C⟨SiC⟩*B*, and (*3*) npor-C⟨TiC⟩*B*; λ_{exc}(nm): (*1*) 514.5 and (*2*, *3*) 488.0.

occurs in the absence of distinct splitting. This is accompanied by a change in the intensity ratio in the region of the features, which makes the shape of the broad *G** and *D** bands substantially dependent on the scattered polarization. These observations argue for a multicomponent character of the vibrational spectrum of the materials under study and anisotropy of the corresponding vibrational modes.

Consider the specific features of the *HH* spectra of the npor-C samples prepared from different carbides in more detail (Fig. 1). One sees immediately that the absolute maximum of the broad *G** band is shifted relative to the above-mentioned narrow *G* band of graphite at 1581 cm^{-1} toward higher frequencies and lies at 1588, 1600, and 1602 cm^{-1} for the npor-C⟨TiC⟩*B*, npor-C⟨SiC⟩*B*, and npor-C⟨SiC⟩*A*, respectively. At the same time, the spectra of both type-*B* samples also exhibit noticeable features near 1581 cm^{-1}, while the spectrum of the type-*A* sample does not have the 1581 cm^{-1} feature at all. The samples of type *B* reveal a shoulder in the interval from 1620 to 1625 cm^{-1}. All the samples also have weak features in the vicinity of 1670 cm^{-1}.

On the low-frequency side of the *G** band, near 1550–1560 cm^{-1}, the spectra of both type-*B* samples exhibit clearly pronounced features, which are practically indistinguishable in the spectrum of the npor-C⟨SiC⟩*A* sample. In the samples of types *A* and *B* prepared from SiC, one also observes a feature near 1534 cm^{-1}.

The broad *D** band seen in the *HH* spectra of all the three samples studied splits into several components. For the npor-C⟨SiC⟩*A* sample, these are the main peak at 1351 cm^{-1} and an additional one at 1326 cm^{-1}. There are also two shoulders with inflections near 1301 and 1380 cm^{-1}. In the case of npor-C⟨SiC⟩*B*, the main peak is located near 1348 cm^{-1}, but it is also, most likely, a superposition of several components. In particular, one can clearly see a shoulder at 1333 cm^{-1}, a frequency close to the well-known Raman mode at 1331 cm^{-1} for a tetrahedrally coordinated carbon of diamond structure. In addition, one observes a low-frequency asymmetric peak near 1300 cm^{-1} and a high-frequency peak in the vicinity of 1382 cm^{-1}, which are very close in frequency to the already mentioned inflections in the *HH* spectrum of npor-C⟨SiC⟩*A*. The splitting of the *D** band manifests itself most clearly in the *HH* spectrum of npor-C⟨TiC⟩*B*. Near the maximum, one observes three peaks of nearly the same intensity, with two of them (at 1348 and 1382 cm^{-1}) coinciding in position with the features in the npor-C⟨SiC⟩*B* spectrum.

The broad *G** band in the Raman spectra of npor-C⟨SiC⟩*A* obtained in the *HV* polarization configuration (Fig. 2) reaches an absolute maximum at 1602 cm^{-1}, as in the *HH* spectrum of this sample. The same Raman shift corresponds to the side maximum of the *G** band

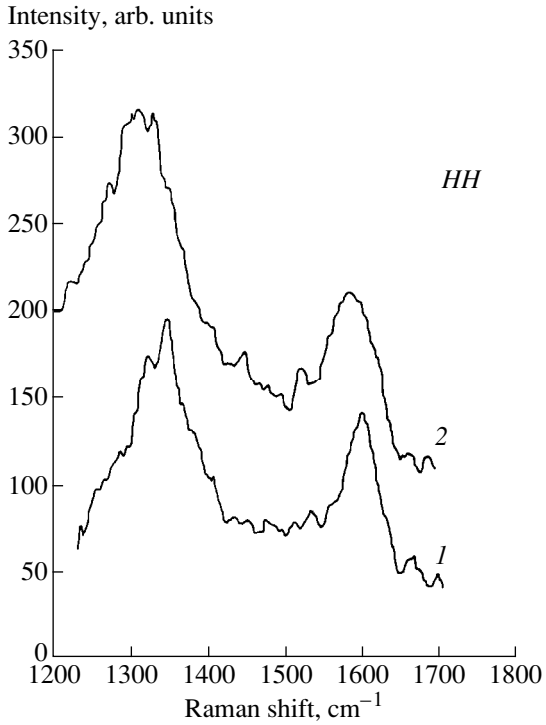

Fig. 3. Raman spectra of an npor-C⟨SiC⟩*A* sample excited by different laser radiation lines (nm): (*1*) 514.5 and (*2*) 647.1.

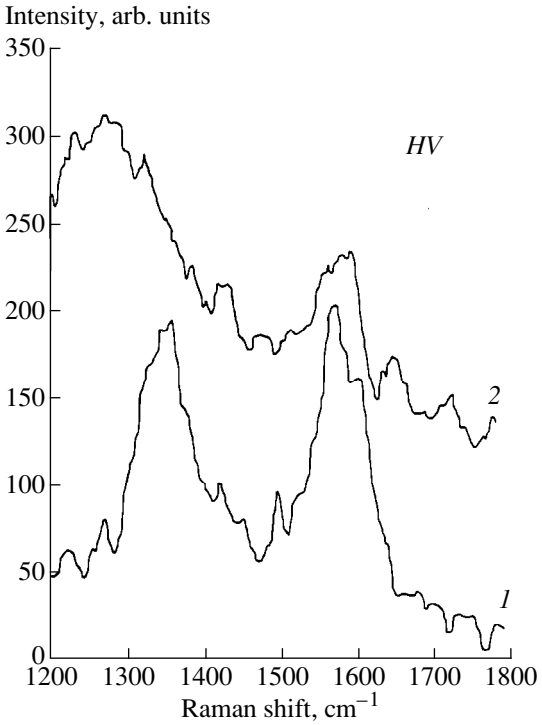

Fig. 4. Raman spectra of an npor-C⟨SiC⟩*B* sample excited by different laser radiation lines (nm): (*1*) 488.0 and (*2*) 647.1.

in the *HV* spectrum of npor-C⟨SiC⟩*B*. The main peak of the *G** band of npor-C⟨TiC⟩*B* (1599 cm^{-1}) also lies close to this frequency. At the same time, in npor-C⟨SiC⟩*B*, the absolute maximum of the *G** band is shifted relative to the 1581-cm^{-1} graphite line toward lower frequencies and lies at 1576 cm^{-1}. The spectra of npor-C⟨SiC⟩*A* and npor-C⟨TiC⟩*B* also have features near 1583 cm^{-1}.

The *D** band in the *HV* spectrum of npor-C⟨SiC⟩*A* is split into two main components lying at 1333 and 1369 cm^{-1}. The first, which is close to the Raman line of diamond at 1331 cm^{-1}, was already mentioned as a shoulder in the *D** band of the *HH* spectrum of npor-C⟨SiC⟩*B*, and the second line is located close to one of the three strong components (1367 cm^{-1}) in the *HH* spectrum of npor-C⟨TiC⟩*B* (Fig. 1). Splitting is also seen in the *HV* spectrum of npor-C⟨TiC⟩*B*, but the peak positions here are different, 1356 and 1377 cm^{-1}. A feature near 1379 cm^{-1}, a frequency close to the latter frequency, is also observed in the spectrum of npor-C⟨SiC⟩*B*. Recall that features near 1380–1382 cm^{-1} were also detected in the HH spectra of both types of samples prepared from SiC (Fig. 1). In npor-C⟨SiC⟩*B*, one likewise observes a splitting of the *D** band in the *HV* spectrum into two components, 1348 and 1362 cm^{-1}, with the first of them coinciding in position with the absolute maximum of the *D** band in the *HH* spectra of both type-*B* samples. At a frequency near 1333 cm^{-1}, corresponding to the peak in the npor-C⟨SiC⟩*A* spectrum, one can also see a shoulder in the spectrum of npor-C⟨TiC⟩*B*. Note that in all the npor-C samples, the *D** band also reveals several features on its low-frequency side.

The variation of Raman spectra with exciting wavelength λ_{exc} is a characteristic feature of all the npor-C samples studied. Figures 3 and 4 compare the spectra of npor-C⟨SiC⟩*A* and npor-C⟨SiC⟩*B* obtained at λ_{exc} = 647.1 nm with those measured at λ_{exc} = 514.5 and 488.0 nm discussed above. One readily sees that the whole *D**-band region in both spectra obtained at the longer wavelength excitation is shifted toward lower frequencies, as observed in the case of polycrystalline graphite [5] and nanotubes [8]. Note that here, as in [5, 8], the *D** band is higher in intensity than the *G** band.

A comparison of the shapes of the *D** band in the *HH* spectra of npor-C⟨SiC⟩*A* (Fig. 3) reveals that some spectral features are retained under variation of λ_{exc}, but the intensity ratio of the individual components changes. For instance, the 1351 cm^{-1} component, which is strongest at λ_{exc} = 514.5 nm, is seen only as a shoulder at λ_{exc} = 647.1 nm, but, in the latter case, a distinct peak appears at 1331 cm^{-1}, which matches exactly the diamond Raman peak. In addition, at lower frequencies, new features become noticeable near 1292 and 1311 cm^{-1}.

In npor-C⟨SiC⟩*B* (Fig. 4), the low-frequency shift and the relative growth of the *D**-band intensity in the HV spectra observed to occur with increasing λ_{exc} are pronounced even more clearly. At λ_{exc} = 647.1 nm, the absolute maximum of the *D** band lies at 1276 cm^{-1}. A number of features, at 1222, 1236, 1297, and 1329 cm^{-1}, were detected on both sides of this maximum. It should be pointed out that, while identical or similar features are also seen at λ_{exc} = 488.0 nm, they are considerably weaker than the strong components at 1348 and 1362 cm^{-1}. It is significant that these components are practically unobservable at λ_{exc} = 647.1 nm. Note also that the 1276-cm^{-1} mode detected in the *HV* spectrum of npor-C⟨SiC⟩*B* is seen in the *HH* spectra of npor-C⟨SiC⟩*A* (Fig. 3).

As λ_{exc} increases, the *G** band also undergoes a change in the relative scattered intensities of its various modes. In particular, the *HH* spectrum of npor-C⟨SiC⟩*A* (Fig. 3) exhibits, in addition to the 1602-cm^{-1} component, a stronger 1582-cm^{-1} mode close to the graphite mode, which determines the absolute maximum of the *G** band at λ_{exc} = 647.1 nm. By contrast, the intensity redistribution in the *G** band of the *HV* spectrum of the npor-C⟨SiC⟩*B* sample (Fig. 4) occurs in favor of the higher-frequency components; indeed, the 1576-cm^{-1} mode becomes relatively weaker in order to transform into a shoulder, a spike appears near 1586 cm^{-1}, and the main maximum in this spectral region is displaced to a position near 1598 cm^{-1}.

The changes in the Raman spectra of npor-C observed to occur under variation of the exciting photon energy $\hbar\omega_{exc}$ argue for a strong frequency dispersion of the Raman susceptibility tensor in the $\hbar\omega_{exc}$ region under study and for the resonant nature of scattering, which involves practically all the observed vibrational modes. An explanation of the shift of the *D* band with variation of $\hbar\omega_{exc}$ in microcrystalline graphite was proposed in [5]. It was assumed that the *D* band originates from resonant scattering with the emission of a phonon whose (nonzero) momentum corresponds to the resonant excitation of an indirect virtual electron–hole pair in the Brillouin zone, which becomes possible because of the interaction of this pair with a structural defect. The *D** band of npor-C consists of several spectral components, and the above interpretation requires invoking additional assumptions, for instance, on the splitting of the electronic spectrum in carbon nanoclusters into size quantization subbands or sublevels. Size quantization effects in nanoclusters are apparently also responsible for the observed change in the relative intensity of the spectral components in the *G** band induced by the variation of $\hbar\omega_{exc}$. The quantity $\hbar\omega_{exc}$ actually selects the electronic states in the cluster spectrum that satisfy the resonance condition and provide the largest contribution to the Raman susceptibility for a given $\hbar\omega_{exc}$. However, the intensity of a Raman component depends on the probability of the corresponding virtual electronic and vibrational transitions and, hence, on the symmetry of the states involved. As a result, different modes can be excited by different electronic states and the relation between the intensities of individual components in a Raman spectrum can vary with varying energy $\hbar\omega_{exc}$ and polarization of the exciting and scattered radiation. Note that such dispersion effects in Raman spectroscopy are characteristic of discrete molecular spectra [15]. Resonant scattering associated with splitting of the electronic spectrum was observed to occur on single-wall nanotubes [7].

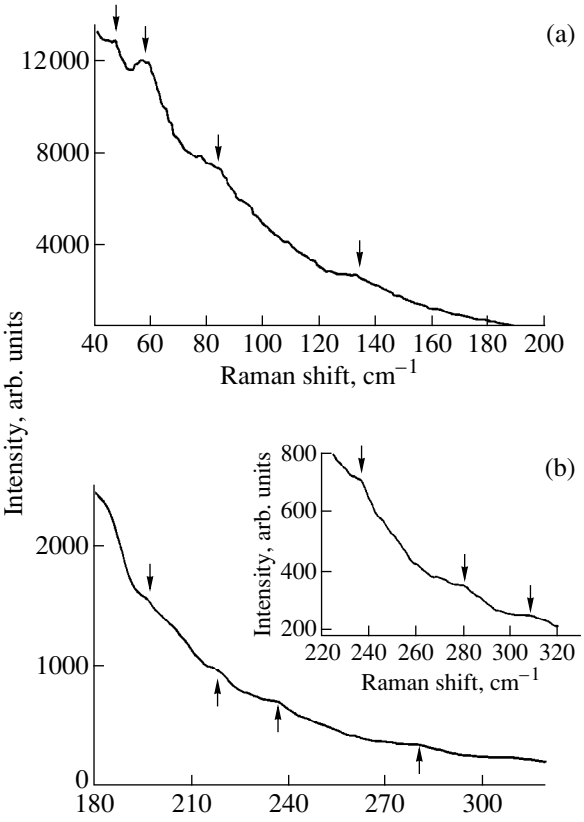

Fig. 5. Low-frequency *HV* Raman spectra of an npor-C⟨SiC⟩*A* sample obtained at λ_{exc} = 647.1 nm. The curves corresponding to different frequency intervals are shown in different scales (a, b). The arrows identify the spectral features observed against the background of Rayleigh scattering.

The vibrational properties of the npor-C and carbon nanoclusters of other types, including nanotubes [7], raw graphite rods, and single graphene sheets [9], allow for a certain qualitative analogy in the low-frequency range. Figure 5 presents a scattering spectrum of the npor-C⟨SiC⟩*A* sample excited in the 40–320-cm^{-1} interval by radiation with λ_{exc} = 647.1 nm. Because the sample surface was fairly rough, the Raman spectrum was observed against a background of intense Rayleigh scattering. As can be seen from Fig. 5, one can isolate a number of features in the Raman spectrum: at 46.7,

56.4, 84, and 133 cm^{-1}, as well as at 198, 218, 237, 280, and 309 cm^{-1}. Note that this range includes the Raman molecular rotational spectra of water, nitrogen, and oxygen (see, e.g., [16]), which could be adsorbed by npor-C from air and, generally speaking, contribute to the observed scattering. However, only one of these modes (133 cm^{-1}) coincides with one of the weak modes in the Raman rotational spectrum of water, whereas the strongest water lines are not seen in the spectrum observed. In addition, the spectra of the npor-C samples do not exhibit any known relations characteristic of the Raman rotational spectra of the above molecules. The series of low-frequency modes found for npor-C⟨SiC⟩*A* do not coincide with similar modes observed in the spectra of other types of npor-C studied by us. One of the modes observed, namely, that at 56.4 cm^{-1}, coincides with a band found in carbon nanoclusters [9]. This permits one to assign the above-mentioned modes to vibrations in the carbon clusters.

As follows from an analysis of the Raman spectra in Figs. 1 and 2, many features observed in the same (and, sometimes, even different) polarization configurations are very similar or coincide in the npor-C samples of different types studied here, although the amplitudes of the corresponding modes differ substantially in some cases. For instance, the spectra revealing a distinct peak in one case may exhibit only a relatively weak shoulder in another and vice versa. It should be taken into account that a porous system can always have considerable stresses, which are certainly different in materials prepared of carbide polycrystals of different symmetry and composition. Therefore, there is nothing strange in the slight frequency shifts and Raman-mode amplitude redistribution observed in different samples. Of real significance is the close similarities between many features in the spectra considered. These similarities imply that the carbon framework in npor-C consists primarily of fragments of the same type (although, possibly, not of them only) with a complex structure of the valence bonds, as well as of the electronic and vibrational spectra. It is the presence in the density of electronic and vibrational states of clearly pronounced features, which is characteristic of small clusters with a discrete spectrum of localized states, that accounts for the resonant excitation of Raman modes discussed above.

In addition to the similarity, the Raman spectra exhibit differences in the cluster structure between the various types of npor-C samples. Type-*B* materials contain, in addition to a system of nanoclusters forming from the grains of the starting carbides, the pyrocarbon binder. Pyrocarbon does not have nanopores and represents a strongly disordered graphitelike material characterized by Raman modes in the interval from 1565 to 1585 cm^{-1} [17]. Such features are indeed observed in the spectra presented here: the main peak of the *G** band at 1576 and the 1583-cm^{-1} peak in the HV spectra of npor-C⟨SiC⟩*B* and npor-C⟨TiC⟩*B*, respectively (Fig. 2), as well as a number of features on the low-frequency side of the *G** band in the *HH* spectra of these samples (Fig. 1).

The main component of the *G** band in the npor-C⟨SiC⟩*A* samples (without pyrocarbon) is shifted strongly to higher frequencies (1602 cm^{-1}) compared with graphite, so that the Raman shift turns out to be substantially larger than that for the finest graphite powder in [1]. Assuming the trend to a *G* band shift with decreasing grain size [1] to persist at such large shifts, one may conclude that the carbon clusters in the type-*A* material are so small as to make the idea of them as graphitelike fragments no more than a matter of convention. Graphitelike clusters in npor-C⟨SiC⟩*A* can be revealed only under resonant excitation with a wavelength λ_{exc} = 647.1 nm, i.e., in conditions where the main peak of the *G** band shifts to 1582 cm^{-1}. It is possible that carbon nanoclusters in npor-C⟨SiC⟩*A* are primarily small fragments of strongly bent or "broken" graphene layers, as is assumed in the case of the so-called "rigid" carbon, i.e., carbon that does not transform to graphite under high-temperature carbon annealing [18].

The spectra of type-*B* materials also exhibit similar high-frequency maxima, namely at 1600 cm^{-1} in the *HH* spectrum of npor-C⟨SiC⟩*B* and at 1599 cm^{-1} in the *HV* spectrum of npor-C⟨TiC⟩*B*. We believe that they are produced by very small carbon particles, identical or similar in structure, which are created when the carbide-forming elements in the grains of the starting carbides are removed. The stronger polarization of the above spectral modes in type-*B* materials compared with npor-C⟨SiC⟩*A* is possibly due to the internal stresses being of a different nature.

The above-mentioned presence in the *HV D** band of npor-C⟨SiC⟩*A* of the 1333-cm^{-1} peak and of features at the same frequency in the *HH* spectrum of npor-C⟨SiC⟩*B* and in the *HV* spectrum of npor-C⟨TiC⟩*B* (Figs. 1, 2) suggests that the npor-C structure contains small diamond-like fragments. Because the *HH* spectrum of npor-C⟨SiC⟩*A* excited at λ_{exc} = 514.5 nm clearly does not have this mode (i.e., the scattered radiation is polarized), one might conjecture that this mode is associated with clusters of a hexagonal or strongly distorted (strained) cubic diamond. The *VV* spectrum of the *D** band of npor-C⟨SiC⟩*A*, which was obtained at λ_{exc} = 514.5 nm specifically in this connection (Fig. 6), provides support for this conjecture. In this case, the narrow peak at 1331 cm^{-1} can be identified with the main maximum of the *D** band and can be reliably assigned to the diamond component of the Raman spectrum. We may recall that the 1331-cm^{-1} diamond mode is also seen in the HH spectrum of npor-C⟨SiC⟩*A* at λ_{exc} = 647.1 nm (Fig. 3).

The above results are in good accord with earlier data obtained in x-ray diffraction and XPS studies of these samples [10–12]. The diffraction patterns mea-

sured on the samples of type B exhibited fairly broad reflections of a complex shape in the region of reflection (0002) of graphite (at diffraction angles $2\theta = 20°$–$26.5°$) and reflections (100) and (101) of graphite or (111) of diamond ($2\theta = 41°$–$48°$). The strong inhomogeneous broadening of the reflections suggests that the carbon framework is made up of a set of clusters of different types, which apparently includes graphitelike fragments containing turbostratically disordered graphite and defected or bent graphene layers. The (0002) reflection observed in npor-C⟨SiC⟩A samples is still more diffuse and is barely seen against the background in the $2\theta = 16°$–$27°$ interval [19]. These x-ray diffraction data also suggest that the graphitelike fragments are so small or so strongly distorted that there is hardly any sense in considering them as distinct structural elements. At the same time, the reflection at $2\theta = 41°$–$48°$ remains practically as distinct as the one seen in type-B samples. This may mean that the structure of the material of type A (and, possibly, of type B as well) likewise has distorted diamond-like fragments, which is in agreement with the above results obtained by Raman spectroscopy.

The conclusion that the graphene layers are bent was also drawn from the XPS measurement of 1*s* and valence electrons in type-B npor-C samples [12]. The binding energy of the 1*s* electron in npor-C, E_b = 284.6–284.7 eV (for graphite, E_b = 284.3 eV), as well as the shape of the valence-band spectrum, argue convincingly for the hybridization having an intermediate character between sp^2 (graphite) and sp^3 (diamond) for most (>60%) of the valence C–C bonds. Moreover, XPS data have established the curvature of the graphene layers in npor-C⟨SiC⟩B to be larger than in npor-C⟨TiC⟩B. As for Raman spectra, they have thus far only revealed the fact that these materials have different structures. It is also worthwhile to note that the XPS data [12] are not inconsistent with the conclusion that diamond-like fragments exist in type-B materials, while not providing unambiguous evidence for its support.

Thus an analysis of Raman spectra of npor-C samples showed that the microstructure of the porous carbon framework in materials of this class consists mostly of fragments of the same type, which, nevertheless, does not rule out the possibility of their structural parameters (the character of the valence bonding, size, and shape) depending on the starting carbide and the preparation technology. All the materials considered are not amorphous. The substantially larger number of the first-order Raman modes compared with graphites argues for npor-C having a cluster structure with the internal organization of the nanoclusters differing strongly from that of graphite. In this connection, the observation of a series of low-frequency modes, which are characteristic of nanotubes and some other nanocarbon modifications, appears particularly significant [6]. The strong polarization dependence of the Raman susceptibility is connected with the anisotropy in the nanocluster sizes and structure. The electronic and vibrational spectra of npor-C are apparently determined by the superposition of discrete levels of the anisotropic states localized in the nanoclusters. In this case, the quasi-momentum selection rules are no longer valid for electronic and vibrational transitions within a cluster, as a result of which multicomponent Raman spectra should exhibit, in addition to anisotropy, clearly pronounced dispersion and resonance effects as the exciting photon energy is varied.

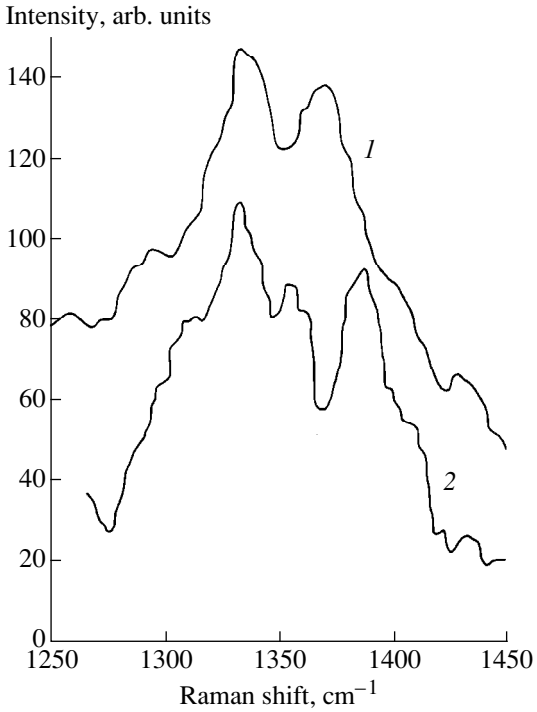

Fig. 6. The D^* region in the Raman spectra of an npor-C⟨SiC⟩A sample obtained in different polarization configurations: (*1*) HV and (*2*) VV.

ACKNOWLEDGMENTS

This work was supported by the Skeleton Technology Group (Sweden), the Russian Foundation for Basic Research (grant no. 99-02-17984), and the Ministry of Science of the Russian Federation (the "Fullerenes and Atomic Clusters" program, grant no. 98-059).

REFERENCES

1. R. J. Nemanich and S. A. Solin, Phys. Rev. B **20** (2), 392 (1979).
2. D. S. Knight and W. B. White, J. Mater. Res. **4**, 385 (1989).
3. T. C. Chieu, M. S. Dresselhaus, and M. Endo, Phys. Rev. B **26**, 5867 (1982).
4. H. Hiura, T. W. Ebbesen, K. Tanigaki, and H. Takahashi, Chem. Phys. Lett. **202**, 509 (1993).

5. I. Pocsik, M. Hundhausen, M. Koos, and L. Ley, in *Proceedings of the International Symposium of Carbon, Tokyo, 1998*, P11–08, p. 652; J. Non-Cryst. Solids **227–230**, 1083 (1998).
6. J. Yu, R. K. Kalia, and P. Vashishta, Europhys. Lett. **32** (1), 43 (1995).
7. A. M. Rao, E. Richter, Shunji Bandow, *et al.*, Science **275**, 187 (1997).
8. J. Kastner, T. Pichler, H. Kuzmany, *et al.*, Chem. Phys. Lett. **221**, 53 (1994).
9. Y. Ando, X. Zhao, H. Shimoyama, *et al.*, Int. J. Inorg. Mater. **1**, 77 (1999).
10. A. M. Danishevskii, R. N. Kyutt, E. A. Smorgonskaya, *et al.*, in *Proceedings of the 24th International Conference on Physics of Semiconductors, Jerusalem, 1998*, P–Tu 197.
11. R. N. Kyutt, É. A. Smorgonskaya, S. K. Gordeev, *et al.*, Fiz. Tverd. Tela (St. Petersburg) **41** (5), 891 (1999) [Phys. Solid State **41**, 808 (1999)]; Fiz. Tverd. Tela (St. Petersburg) **41** (8), 1484 (1999) [Phys. Solid State **41**, 1359 (1999)].
12. S. K. Gordeev, A. V. Grechinskaya, A. M. Danishevskii, *et al.*, in *Proceedings of the 4th Biennial International Workshop "Fullerenes and Atomic Clusters" (IWFACT99), St. Petersburg, 1999*, p. 133; Mol. Mater. **13**, 355 (2000).
13. S. K. Gordeev and A. V. Vartanova, Zh. Prikl. Khim. (St. Petersburg) **66** (7), 1080 (1994); **66** (9), 375 (1994).
14. S. K. Gordeev, A. V. Vartanova, S. G. Zhukov, I. N. Gran', V. V. Sokolov, T. I. Mazaeva, and R. G. Avarbe, RF Patent No.2026735, MKlb B 01 J 20/20, Byull., No. 2 (1995).
15. M. M. Sushchinsky, *Raman Spectra of Molecules and Crystals* (Nauka, Moscow, 1969; Israel Program for Scientific Translations, Jerusalem, 1973).
16. A. Weber, in *Raman Spectroscopy of Gases and Liquids*, Ed. by A. Weber (Springer-Verlag, Berlin, 1979; Mir, Moscow, 1982).
17. Pham V. Huong, Diamond Related Mater. **1**, 33 (1990).
18. E. Buiel and J. R. Dahn, Electrochim. Acta **45**, 121 (1999).
19. A. M. Danishevskiĭ, R. N. Kyutt, É. A. Smorgonskaya, *et al.*, in *Proceedings of the II International Conference on Amorphous and Microcrystalline Semiconductors, St. Petersburg, 2000*, p. 95.

Translated by G. Skrebtsov

Physics of the Solid State, Vol. 43, No. 1, 2001, pp. 145–150. Translated from Fizika Tverdogo Tela, Vol. 43, No. 1, 2001, pp. 140–145.

LOW-DIMENSIONAL SYSTEMS AND SURFACE PHYSICS

Optical Properties of Nanodiamond Layers

A. E. Aleksenskiĭ*, V. Yu. Osipov*, A. Ya. Vul'*, B. Ya. Ber*, A. B. Smirnov*, V. G. Melekhin*, G. J. Adriaenssens, and K. Iakoubovskii****

** Ioffe Physicotechnical Institute, Russian Academy of Sciences, Politekhnicheskaya ul. 26, St. Petersburg, 194021 Russia*

*** Catholic University of Leuven, B-3001, Heverlee-Leuven, Belgium*

Received May 18, 2000

Abstract—Thin ultradisperse diamond (UDD) layers deposited from a water suspension are studied by optical and x-ray photoelectron spectroscopy (XPS). The effective band gap determined by the 10^4-cm^{-1} criterion for ozone-cleaned UDD is 3.5 eV. The broad structureless photoluminescence band (380–520 nm) is associated with radiative recombination through a system of continuously distributed energy levels in the band gap of diamond nanoclusters. The optical absorption of the material at 250–1000 nm originates from absorption on the disordered nanocluster surface containing threefold-coordinated carbon. The surface of UDD clusters subjected to acid cleaning contains nitrogen–oxygen complexes adsorbed in the form of NO_3^- nitrate ions. Annealing in a hydrogen atmosphere results in desorption of the nitrate ions from the cluster surface. The evolution of the oxygen (O1*s*) and nitrogen (N1*s*) lines in the XPS spectra under annealing of a UDD layer is studied comprehensively. *© 2001 MAIK "Nauka/Interperiodica".*

1. INTRODUCTION

The structure and phase transitions in ultradisperse diamond (UDD) clusters have been intensively studied during the past three to four years [1–4]. However, very little attention was paid to the investigation of complexes adsorbed on the surface of such clusters. At the same time, the large specific surface area in UDDs, as in other ultradisperse materials (measured in hundreds of square meters per gram), stresses the importance of this issue. The first attempts at analyzing atomic complexes on the surface of UDD clusters were apparently an investigation into the adsorption and desorption of water molecules on the UDD cluster surface upon annealing in various atmospheres, which was performed by IR spectroscopy [5], and detection by x-ray photoelectron spectroscopy (XPS) of nitrogen and oxygen in UDD layers deposited onto silicon substrates by electrophoresis [6].

This work was intended to expand our knowledge of the optical properties of UDD layers as a model object with a characteristic cluster size of about 50 Å, in which various quantum-confinement effects may manifest themselves [7].

In this work, we used visible and IR spectroscopy, photoluminescence, Raman scattering spectroscopy, and XPS. The XPS method, except in the already mentioned work [6], is widely employed in investigating the evolution and reconstruction of the surface of single-crystal diamonds and CVD-prepared diamond films, as well as the adsorption and desorption of atoms from these surfaces [8, 9].

2. SAMPLES AND EXPERIMENTAL TECHNIQUE

We studied UDD layers deposited from water suspensions. The starting product for the suspension was carbon prepared by detonation synthesis from a 60 : 40 mixture of trinitrotoluene with hexagen [10]. The UDD suspensions used to prepare the UDD layers were of two types: in the first, the ultradisperse diamond was isolated by removing non-diamond phases with nitric acid at an elevated temperature (200–230°C) and, in the second, ozone treatment was used [11]. It is known that ozone treatment ensures a better cleaning of amorphous carbon (the *sp*2 phase) from the diamond nanocluster surface [11]. The material obtained after acid cleaning was a suspension of ultradisperse diamond in a 30–40% water solution of nitric acid with an UDD concentration of about 3 wt %. Suspension sedimentation lasted a few hours, with a boundary appearing between the clarified and thickened layers. The further process of obtaining the water suspension used in subsequent studies consisted in multiple dilution with distilled water, mixing, and removal of the thickened layer. In both cases, when the diamond fraction was isolated with nitric acid or by ozone cleaning, the UDD concentration in water at the final stage of dilution was 0.04 wt % and the suspension sedimentation time was no less than 20 days.

As is known, clusters of UDD, like those of other ultradisperse materials, coalesce to form aggregates. In the UDD used to prepare the suspension, the clusters were about 45 Å in size. The average diameter of the aggregates in the suspension was determined from the sedimentation characteristics in the Stokes approximation and was approximately equal to 410 Å.

The layers were prepared by the deposition of UDD aggregates from the water suspension onto substrates

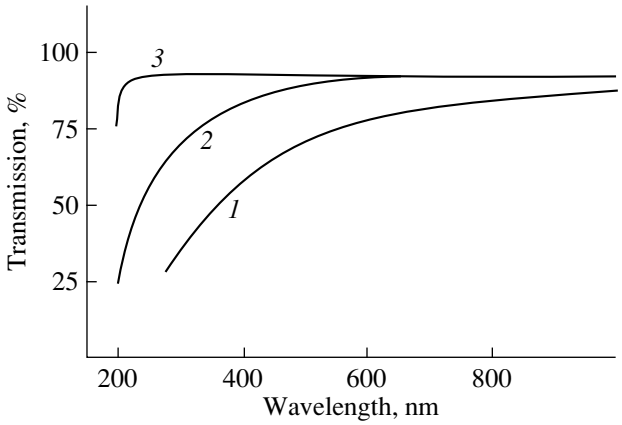

Fig. 1. Transmission spectra of two UDD layers differing in cleaning method: (*1*) acid cleaning with a layer thickness of 1870 ± 60 Å; (*2*) ozone cleaning with a layer thickness of 1890 ± 100 Å; and (*3*) transmission spectrum of the quartz substrate. T = 300 K.

of quartz, silicon, CaF_2, or BaF_2 via water evaporation [12]. The layer thicknesses measured by the ellipsometric technique at the wavelength λ = 632.8 nm ranged from 1200 to 3500 Å.

To remove clusters of volatile adsorbed components from the surface and to passivate the surface electronic states, the layers were annealed in a hydrogen atmosphere at 450–820°C.

The chemical composition of the samples was studied by x-ray photoelectron spectroscopy on a PHI 5500 electron spectrometer equipped with a hemispherical energy analyzer. The photoemission spectra were excited by monochromatized AlK_α (1486.5 eV) radiation. We studied the regions of the photoelectron peaks of carbon (C1*s*), nitrogen (N1*s*), and oxygen (O1*s*). The sample charging was suppressed by irradiation with a low-energy electron beam. The photoelectron peaks were deconvolved into components after background subtraction by the Shearley algorithm, with subsequent approximation of the peak shape by Gaussians. The elemental composition of the samples was estimated from the relative peak areas after background subtraction by means of the element sensitivity factors given in [13].

3. RESULTS AND DISCUSSION

Figure 1 shows transmission spectra of two UDD layers, which were practically equal in thickness but were prepared from differently cleaned suspensions. It is seen that, unlike the acid-treated UDD layer, the layer prepared by ozone cleaning is practically transparent in the range from 600 to 1000 nm. The effective band gap, derived from the energy at which the absorption coefficient takes on the value of 10^4 cm^{-1} [12, 14], is 3.5 eV for the ozone-cleaned UDD, which is substantially less than that for a single-crystal diamond (E_g = 5.5 eV). This does not appear strange, because the presence of sp^2-hybridized carbon even in small amounts can appreciably reduce E_g. For instance, it was reported that the fourfold-coordinated amorphous carbon (*ta*-C), in which 85% of the atoms form sp^3 bonds and 15% form sp^2 bonds, has a band gap $E_g \sim 2.4$ eV and that a decrease in the fraction of sp^2 bonds results in an increase in E_g [14]. At the same time, the E_g value we

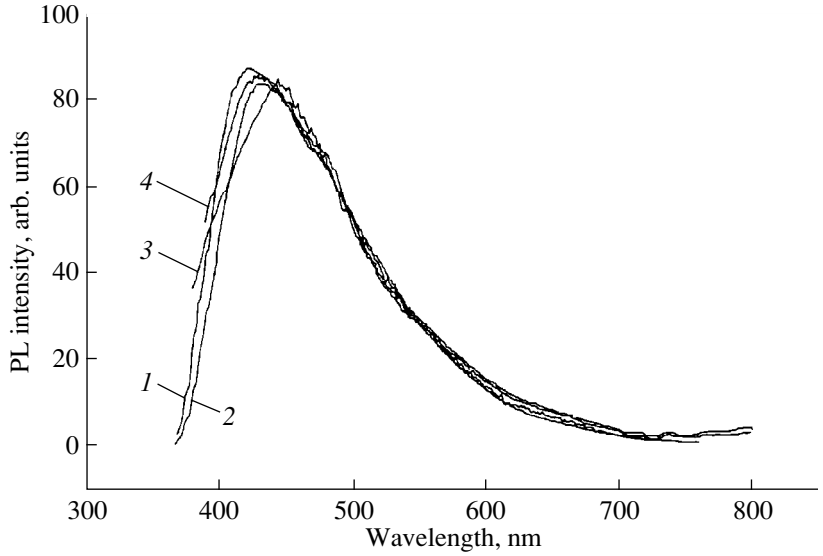

Fig. 2. Luminescence spectra of UDD layers on quartz at T = 300 K: (*1*, *2*) ozone cleaning and (*3*, *4*) acid cleaning. Excitation wavelength (nm): (*1*, *2*) 210 and (*3*, *4*) 254.

found is in good agreement with the data obtained in [15], where the value E_g = 3.3 eV for a nanocrystalline diamond was determined by electron energy loss spectroscopy (EELS).

According to our model proposed earlier, the UDD cluster consists of an sp^3-hybridized crystalline diamond core 45 Å in diameter, which is surrounded by a layer of amorphous carbon with sp^2-hybridized bonds [3, 11, 16]. The optical absorption spectra of UDD layers are not at variance with this model. It can be assumed that the optical absorption of the material in the range 250–1000 nm is due to the presence of the sp^2 phase [12]. The smaller fraction of sp^2-hybridized bonds in the ozone-cleaned UDD accounts for the larger optical transparency of the layers.

Figure 2 displays photoluminescence (PL) spectra of the UDD layers. The exciting-photon wavelength was 210–254 nm. The spectra of both types of layers are practically identical and actually represent a broad "blue" luminescence band with a maximum near 450 nm and a full width at a half-maximum (FWHM) of about 130 nm. It can be conjectured that this structureless PL band is associated with radiative recombination via a system of continuously distributed energy levels in the band gap of the diamond nanoclusters. The validity of this assumption is borne out by the findings of [17, 18], according to which the structural disorder on the nanodiamond surface and the presence of carbon in the threefold-coordinated state and of dangling bonds on the surface of the nanoclusters are responsible for the high density of surface states in the diamond band gap. Some features of the density of states in the band gap of nanocrystalline diamond, which are connected with the disordered carbon layer surrounding the crystalline core of the diamond nanocluster, were pointed out in [15]. Note that a broad band with a weakly pronounced structure was observed earlier in the PL spectrum of nanodiamonds within the wavelength range 380–550 nm [19]. However, Kompan *et al.* [19] interpreted the nature of the observed PL band by identifying it with the corresponding intrinsic defects of a single-crystal diamond, which contribute to the structureless PL in the same spectral range.

As is seen from Fig. 3, the Raman spectrum of the UDD layer exhibits, besides the narrow band at 1324 cm^{-1} associated with the crystalline diamond phase, broad bands at 1240 and 1600 cm^{-1} due to the maxima in the phonon density of states of the *sp*2-coordinated carbon [20]. It is known that the shift of the maximum in the Raman spectrum is due to phonon confinement effects in nanosized samples [2, 3, 21]. In this case, the shift δ is 6 cm^{-1}, whereas in the UDD powders used in the preparation of the suspension, it reached 10 cm^{-1} [3].

The data [3] calculated within the phonon-confinement model under the assumption that the UDD cluster has a spherical shape can be used to estimate the mean

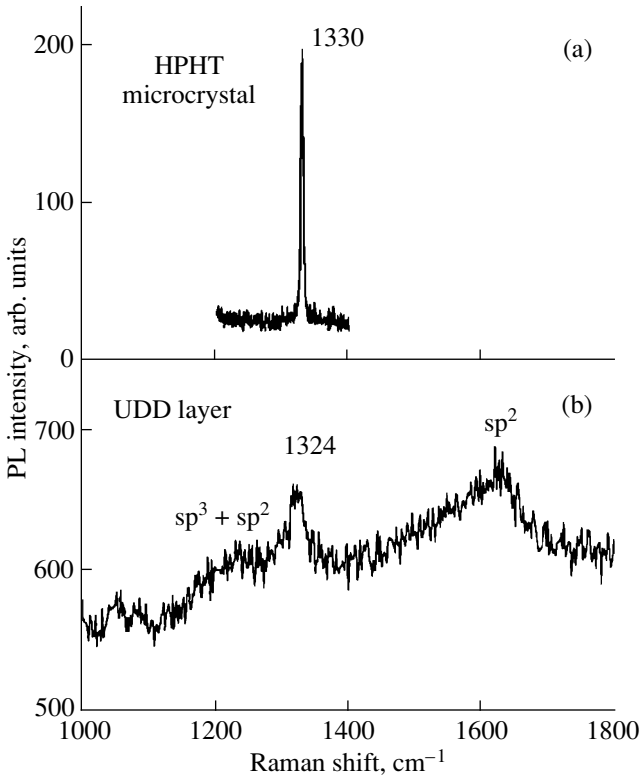

Fig. 3. Raman spectra of (b) an UDD layer (acid cleaning) 3000 Å thick on silicon and (a) a microcrystalline HPHT diamond. The spectra are excited by the 488-nm argon laser line. The radiation power is 25 mW. Top panel (a) shows for comparison the δ-shaped Raman line of microcrystalline HPHT diamond at 1330 cm^{-1}. The mean size of the HPHT diamond grains is approximately 200 μm.

size of diamond nanocrystals. For δ = 6 cm^{-1}, the nanocrystal size is 50 Å. As is seen from Fig. 3b, the Raman line corresponding to the diamond phase is corrupted by noise interference and is about 30 cm^{-1} wide. The latter two factors account for the error of ±1 cm^{-1} in the determination of the shift δ and, correspondingly, the error of ±4 Å in the determination of the nanocrystal size.

The XPS results show that the unannealed samples contain 70 at. % C, 8 at. % N, and 22 at. % O. Since the samples have a disperse structure and the chemical composition of a grain is nonuniform over the grain thickness, quantitative analysis cannot provide anything but an estimate. Carbon in these samples resides in two chemically different states, namely, the sp^2-hybridized state with a binding energy of 284.4 eV and the sp^3-hybridized state with a binding energy of 285.8 eV (Fig. 4a). The relatively high intensity of the C1*s* peak that corresponds to the sp^2-hybridized carbon can be associated with the aforementioned structure of the carbon cluster containing an outer shell of sp^2-hybridized carbon. The complex shape of the nitrogen N1*s* peak (Fig. 4b) also implies the existence of

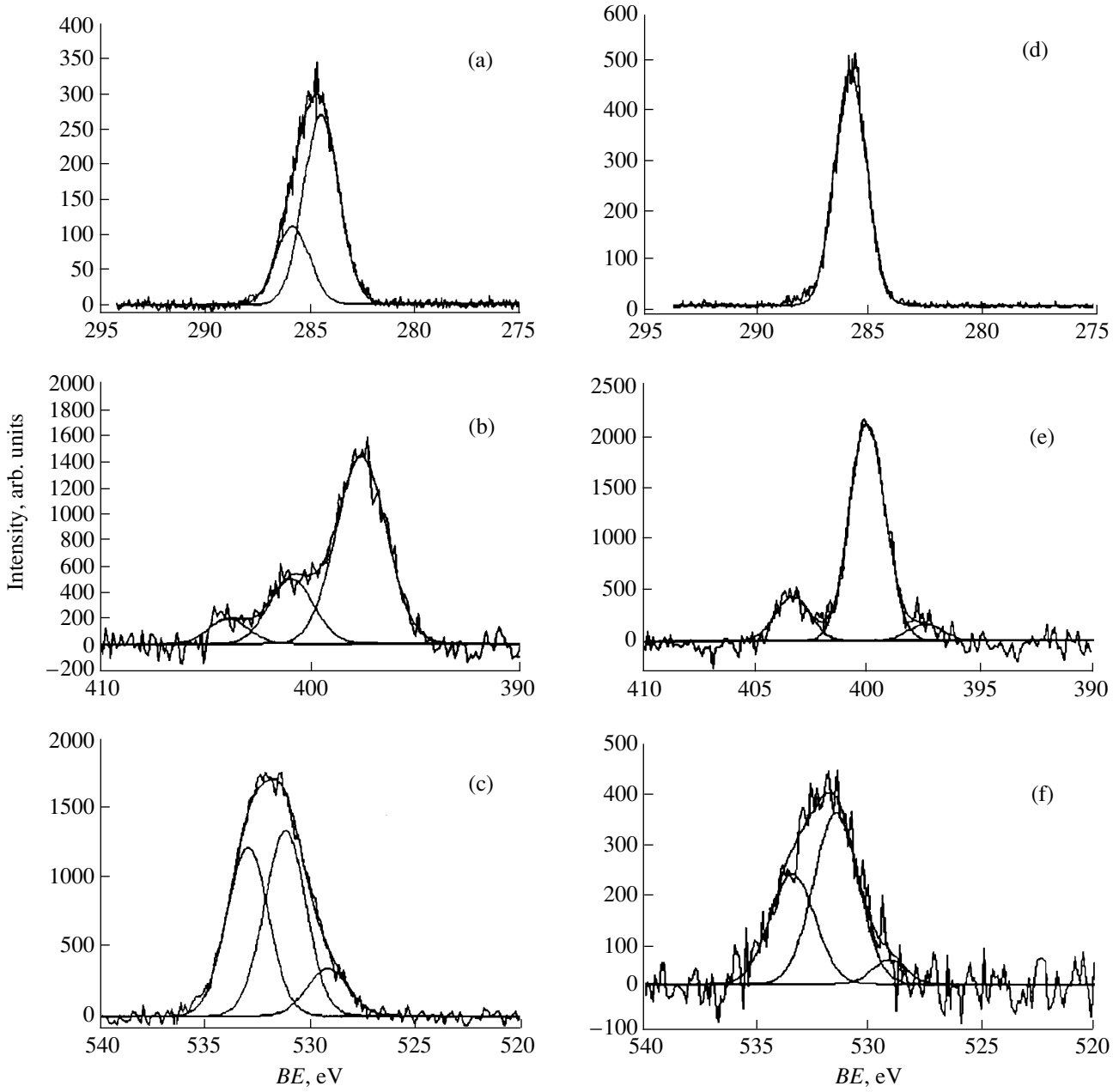

Fig. 4. XPS spectra of UDD layers (acid cleaning, thickness $d \cong 3000$ Å) on silicon (a–c) before and (d–f) after annealing in a hydrogen atmosphere at 810°C. XPS spectra: (a, d) C1*s* carbon, (b, e) N1*s* nitrogen, and (c, f) O1*s* oxygen.

nitrogen atoms with different chemical environments in the sample. The available data on the binding energies of the N1*s* level in carbon and oxygen compounds with different chemical bonds are fairly contradictory (see, e.g., [22, 23]). However, it can be assumed that a sample contains the N–C(sp^3) (397.6 eV), N–C(sp^2) (400.1 eV), and N–O (404.0 eV) bonds. The photoemission peak O1*s* represents a triplet (Fig. 4c) whose strongest components with binding energies of 531.7 and 533.4 eV correspond to different oxygen–carbon bonding types.

The elemental composition of the samples subjected to annealing in a hydrogen atmosphere at 810°C for 1 h can be estimated as 87 at. % C, 7 at. % N, and 6 at. % O. Note that practically all carbon atoms are in the sp^3-hybridized state with a C1*s*-level binding energy of 285.8 eV (Fig. 4d). The triplet structure of the N1*s* peak (Fig. 4e) again suggests that the sample contains nitrogen atoms with N–C(sp^3) (397.6 eV), N–C(sp^2) (400.1 eV), and N–O (403.4 eV) bonds. It is worth noting that, compared to the unannealed samples, the intensity of the N–C(sp^3) (397.6 eV) peak decreased

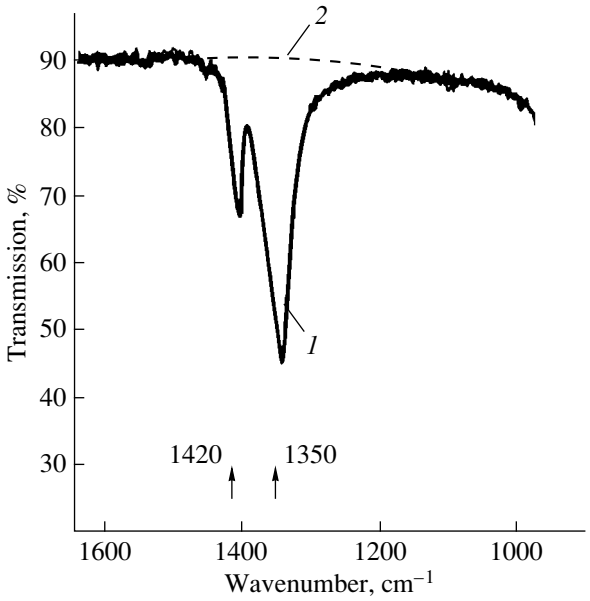

Fig. 5. A fragment of an IR transmission spectrum of a UDD layer on a BaF_2 substrate in the range 1600–1000 cm^{-1} (curve *1*). Acid cleaning. Layer thickness is 2200 Å. Curve *2* represents the transmission spectrum of the BaF_2 substrate in the same spectral range. T = 300 K.

and the intensity of the N–C(sp^2) (400.1 eV) peak increased. The O1*s* triplet (Fig. 4f) is similar to that observed in the sample before annealing and contains peaks with binding energies of 531.5 and 533.4 eV.

Note that before the annealing, the amounts of oxygen and nitrogen were in the ratio of about O/N = $22/8 \approx 3$, whereas after the annealing, this ratio decreased (O/N = $6/7 \approx 1$). The total amount of nitrogen and oxygen in the material of a layer decreased from 30 to 13 at. %. This implies that the annealing resulted in desorption of the nitrogen–oxygen groups from the surface of the diamond nanoclusters. The XPS data should be analyzed with due regard for the fact that nitrogen is one of the components of detonating explosives and, therefore, the nitrogen content in the interior of the forming UDD particles can be high [6].

The above data can be explained by assuming that the surface of unannealed UDD clusters contains nitrogen–oxygen complexes adsorbed in the form of NO_3^- nitrate ions. This is argued for by the following consideration. The UDD water suspension contains, in some cases, a small amount of NO_3^- nitrate ions, which remains after cleaning of the detonation products in aqueous nitric acid and subsequent washing with distilled water. Part of the nitrate ions present in the suspension is already adsorbed on the surface of the UDD aggregates.

In some cases, the IR transmission spectra of the unannealed samples of acid-cleaned UDD layers, which were deposited onto BaF_2 substrates, exhibited a strong absorption band with two maxima at 1350 and 1420 cm^{-1} (Fig. 5). The absolute magnitude of the absorption coefficient in this range was in excess of 5×10^3 cm^{-1}. In our opinion, this strong absorption could be explained as follows. In the course of deposition of an UDD layer, the interaction of the nitric acid remaining in the suspension with the substrate material produces $Ba(NO_3)_2$, because the features observed in the IR transmission spectrum at 1300–1470 cm^{-1} coincide precisely with those of the transmission spectrum of the $Ba(NO_3)_2$ salt in the same spectral range [24]. After annealing for 1 h in a hydrogen atmosphere at 600°C, the specific absorption in this range disappeared completely, which is easily explained by the decomposition of the barium nitrate and the desorption of the volatiles.

Thus, the data obtained from IR spectroscopy and XPS measurements confirm the presence of UDD aggregates with adsorbed nitrate ions in the UDD suspension which was used to prepare the nanodiamond layers.

ACKNOWLEDGMENTS

We are grateful to S.G. Yastrebov and M.V. Baĭdakova for their participation in discussions of the results.

This work was supported by the Russian Research Program “Fullerenes and Atomic Clusters” (“Film-2” project), the NATO HTECH Linkage Grant (LG no. 973290), and, in part, by the State Program “The Physics of Solid-State Nanostructures” (project no. 99-3014).

REFERENCES

1. V. L. Kuznetsov, I. L. Zilberberg, Yu. V. Butenko, *et al.*, J. Appl. Phys. **86** (2), 863 (1999).
2. Jian Chen, S. Z. Deng, Jun Chen, *et al.*, Appl. Phys. Lett. **74** (24), 3651 (1999).
3. A. E. Aleksenskiĭ, M. V. Baĭdakova, A. Ya. Vul’, *et al.*, Fiz. Tverd. Tela (St. Petersburg) **39** (6), 1125 (1997) [Phys. Solid State **39**, 1007 (1997)].
4. A. E. Aleksenskii, M. V. Baidakova, V. Yu. Davydov, *et al.*, in *Proceedings of the Fifth International Symposium on Diamond Materials, Paris, 1997*, Ed. by J. L. Davidson, W. D. Brown, A. Gicquuel, B. V. Spitsyn, and J. C. Angus (Electrochemical Society, Pennington, 1998); Proc.—Electrochem. Soc. **97-32**, 58 (1998).
5. Shengfu Ji, Tianlai Jiang, Kang Xu, and Shuben Li, Appl. Surf. Sci. **133**, 231 (1998).
6. E. Maillard-Schaller, O. M. Kuettel, L. Diederich, *et al.*, Diamond Related Mater. **8**, 805 (1999).
7. Y. K. Chang, H. H. Hsieh, W. P. Pong, *et al.*, Phys. Rev. Lett. **82** (26), 5377 (1999).
8. Tzu-Chi Kuo, R. L. McCreery, and G. M. Swain, Electrochem. Solid-State Lett. **2** (6), 288 (1999).
9. G. Francz, P. Kania, G. Gantner, *et al.*, Phys. Status Solidi A **154**, 91 (1996).
10. A. I. Lyamkin, E. A. Petrov, A. P. Ershov, *et al.*, Dokl. Akad. Nauk SSSR **302**, 611 (1988).

11. A. E. Aleksenskiĭ, M. V. Baĭdakova, A. Ya. Vul', and V. I. Siklitskiĭ, Fiz. Tverd. Tela (St. Petersburg) **41** (4), 740 (1999) [Phys. Solid State **41**, 668 (1999)].
12. A. E. Aleksenskiĭ, V. Yu. Osipov, N. A. Kryukov, *et al.*, Pis'ma Zh. Tekh. Fiz. **23** (22), 39 (1997) [Tech. Phys. Lett. **23**, 874 (1997)].
13. J. E. Moulder, W. F. Stickle, P. E. Sobol, and K. D. Bomben, *Handbook of X-ray Photoelectron Spectroscopy: A Reference Book of Standard Spectra for Identification and Interpretation of XPS Data* (Eden Prairie, Physical Electronics, 1992).
14. Y. Lifshitz, Diamond Related Mater. **8**, 1659 (1999).
15. H. Hirai, M. Terauchi, M. Tanaka, and K. Kondo, Diamond Related Mater. **8**, 1703 (1999).
16. M. V. Baĭdakova, A. Ya. Vul', V. I. Siklitskiĭ, and N. N. Faleev, Fiz. Tverd. Tela (St. Petersburg) **40** (4), 776 (1998) [Phys. Solid State **40**, 715 (1998)].
17. P. Keblinski, D. Wolf, S. R. Phillpot, and H. Gleiter, J. Mater. Res. **13** (8), 2077 (1998).
18. P. Keblinski, D. Wolf, S. R. Phillpot, and H. Gleiter, MRS Bull., No. 9, 36 (1998).
19. M. E. Kompan, E. I. Terukov, S. K. Gordeev, *et al.*, Fiz. Tverd. Tela (St. Petersburg) **39** (12), 2156 (1997) [Phys. Solid State **39**, 1928 (1997)].
20. R. Al-Jishi and G. Dresselhaus, Phys. Rev. B **26**, 4514 (1982).
21. M. J. Lipp, V. G. Baonza, W. J. Evans, and H. E. Lorenzana, Phys. Rev. B **56** (10), 5978 (1997).
22. T. Thorigen, G. Lippold, V. Riede, *et al.*, Thin Solid Films **348**, 103 (1999).
23. E. D'Anna, M. L. de Giorgi, A. Luches, *et al.*, Thin Solid Films **347**, 72 (1999).
24. K. Nakamoto, *Infrared Spectra of Inorganic and Coordination Compounds* (Wiley, New York, 1963; Mir, Moscow, 1966), p. 94.

Translated by G. Skrebtsov

Physics of the Solid State, Vol. 43, No. 1, 2001, pp. 151–156. Translated from Fizika Tverdogo Tela, Vol. 43, No. 1, 2001, pp. 146–151.

LOW-DIMENSIONAL SYSTEMS AND SURFACE PHYSICS

Transmission Electron Microscopy of GaN Columnar Nanostructures Grown by Molecular Beam Epitaxy

V. V. Mamutin, N. A. Cherkashin, V. A. Vekshin, V. N. Zhmerik, and S. V. Ivanov

Ioffe Physicotechnical Institute, Russian Academy of Sciences, Politekhnicheskaya ul. 26, St. Petersburg, 194021 Russia

e-mail: mam@beam.ioffe.rssi.ru

Received May 26, 2000

Abstract—The GaN columnar crystals of nanometric sizes have been grown by molecular beam epitaxy with high-frequency plasma initiation of nitrogen discharge. The types and distribution of defects in these nanostructures on the (0001) sapphire substrates are studied by transmission electron microscopy (TEM). It is revealed that inversion domains begin to form almost at the interface irrespective of the presence of an initial low-temperature buffer layer. The critical diameter of dislocation-free columns, their density, and mean sizes are determined. It is shown that the low-temperature buffer layer affects the density of dislocations, their spatial distribution, and the mean sizes of columns. The nanosizes of grown crystals suggest a further use of these crystals and the growth method for producing molecular-beam epitaxial quantum-size objects (quantum dots and wires) in a promising AlGaInN system. © *2001 MAIK "Nauka/Interperiodica".*

1. INTRODUCTION

In recent years, wide-band-gap semiconductors in the AlGaInN system have been the most extensively investigated and promising materials for the creation of emitters operating in the visible (from green to ultraviolet) wavelength range and power high-temperature electronic devices [1–3]. The low-dimensional quantum confinement effects in quantum wires, disks, and dots are considered the most promising for improving the quality of optical devices (light-emitting diodes, lasers, and light-sensitive detectors) and nanostructures [4]. Different-type low-dimensional structures are produced by various methods such as etching, growth on profile-etched substrates, over-growth of lithographically formed nanostructures, and growth on substrates misoriented at small angles. All these methods are rather complicated and require multistage technological operations. Moreover, nitrides (GaN) possess a high chemical durability to liquid etchants, whereas dry (plasma) etching has a tendency toward the introduction of defects and distortion of the surface. On the other hand, selective epitaxy presents difficulties associated with the preparation of nanostructures with a high density. However, the possibility exists of growing low-dimensional structures with the use of self-organization effects without pregrowth and postgrowth treatment [5, 6]. Many works dealt with self-organization processes in the AlGaInN system used for producing quantum-size objects. For example, Yoshizawa *et al.* [7] obtained GaN nanocolumns with a mean diameter of ~53 nm on an Al_2O_3(0001) substrate.

It should be noted that self-organization processes in various systems have been investigated in many recent works [5–7]. However, the studies concerned with the oriented growth of low-dimensional crystals (for example, whiskers) "remained somewhat in the shade" after the elucidation of its mechanism [8], even though the characteristic sizes (nanometers) of the objects under investigation were close to those obtained in recent years (for example, quantum dots) by different methods, for example, by molecular beam epitaxy. Up to now, there have been only a few works dealing with the growth of low-dimensional crystals under conditions of molecular beam epitaxy (see, for example, [9, 10]). Their growth proceeds through the so-called vapor–liquid–solid (VLS) mechanism, which was proposed and experimentally confirmed by Wagner and Ellis [8]. This process should be carried out in the ranges of temperatures and saturations in which the thermodynamically possible reaction is hindered by kinetic limitations. In practice, this means that the temperature can be 100–200 K below the temperature usually used in the epitaxial growth [9], which offers new possibilities for growing compounds with a high volatility of the components involved (specifically, indium) and for forming solid solutions (GaInN and AlInN) with these components. In early works on the growth of A^3B^5 compounds from vapor, whiskers and dendritic crystals were obtained by accident and treated as a curious phenomenon or an undesirable crystallization product. After the discovery of the vapor–liquid–solid mechanism, there appeared a number of publications devoted to the purposeful growth of A^3B^5 whiskers [11, 12]. However, information on the oriented growth of these crystals is very limited. It is these data that can provide a better insight into the growth mechanism and open up the way for practical use of whisker structures. Furthermore, the data on the growth of quantum-size objects by the vapor–liquid–solid mechanism are virtu-

ally unavailable in the literature on self-organization processes.

The main defects in GaN are threading dislocations, stacking faults, and, to a smaller extent, dislocation loops. The majority of the threading dislocations are generated at the substrate–growing layer interface and grow along the **c** axis. The threading dislocations with opposite Burgers vectors do not meet with each other and cannot annihilate. Therefore, the problem of decreasing the defect density should be solved beginning with the initial stages of the growth. By decreasing the defect density in GaN buffer layers, it is possible to avoid many difficulties associated with the application of the so-called epitaxial lateral over-growth method [13], which involves the over-growth of a streaky structure preliminarily formed on the substrate in order to decrease the dislocation density. In this respect, it was of interest to investigate and elucidate the mechanism of defect formation at the earliest stages of growth at the heteroboundary with a substrate and to decrease the defect density by using low-temperature buffer layers or other techniques.

In this work, we demonstrated that self-organizing nanometer-sized objects—the GaN columns oriented along the *c* axis—can be obtained *in situ* on Al_2O_3(0001) substrates by molecular beam epitaxy with high-frequency initiation of plasma nitrogen discharge [14] without postgrowth treatment. Moreover, we studied their structural properties. It was shown that these objects can be grown with the use of a compact coaxial magnetron source with high-frequency-capacitance initiation of the discharge. The structure of GaN columnar (whisker) nanocrystals, the formation of defects in transition layers below nanocrystals at the heteroboundary between GaN and the (0001) sapphire substrate, and the propagation of defects and dislocations from the interface deep into the GaN columns were investigated for the first time by transmission electron microscopy (TEM).

2. EXPERIMENTAL TECHNIQUE

The GaN layers were grown on (0001) sapphire substrates with the use of an ÉP-1203 molecular epitaxy apparatus (devised at the Research Institute of Analytical Instrument Making, Chernogolovka, Russia) under a vacuum of ~10^{-10} Torr. A chamber was equipped with a Turbovac-560 thurbomolecular pump (Leybold–Heraeus) with an effective evacuation rate of ~350 l/s. A coaxial magnetron source of activated nitrogen had an original design with high-frequency-capacitance initiation of the discharge (13.56 MHz), which provided a growth rate as high as 2 μm/h at a high-frequency power of ~150 W [9, 14]. As far as we know, until recently, there was no information (except for [14]) on the use of activated nitrogen sources with such a discharge in molecular beam epitaxial processes with plasma activation. In a series of experiments, metallic gallium was fed from a standard effusion cell at temperatures from 1100 to 1300°C, and the flow rate of nitrogen was equal to 1–5 sccm/min (standard cubic centimeter per minute). The reverse sides of substrates were coated with titanium. The substrates were secured on a molybdenum clamping holder with a window for direct radiation heating from the reverse side. In the course of growth, the surface of a growing layer was monitored using a high-energy electron diffraction (HEED) system. The substrate temperature was calibrated against the known melting points of metals (indium, tin, aluminum, and silver) and InSb and was checked against the dependence of the temperature on the heater power. The temperature was determined accurate to within ~10 K. Gallium nitride was grown at the temperature T_s = 750–800°C. The sapphire substrates were not chemically etched. They were only degreased prior to the growth and then were annealed under vacuum at 1000°C for 30 min until the appearance of the characteristic HEED pattern (fringes), which corresponded to a clean atomically smooth surface. Thereafter, the nitridation was carried out at the substrate temperature T_s = 900–1000°C for 20–30 min.

The grown samples to be studied were of two types: (1) samples with a ~20- to 30-nm-thick low-temperature GaN buffer layer grown at a temperature of ~300°C and (2) samples without low-temperature buffer layer. The growth of the GaN base layer was carried out at temperature T_s ~ 770°C for 1.5–2 h at a rate of 0.8 μm/h for samples of the first type (with a low-temperature buffer layer) and 1.0 μm/h for samples of the second type (without a low-temperature buffer layer). The growth rates were determined from the column heights in images obtained with a CamScan S4-90 FE, field emission scanning electron microscope (SEM). The column height was equal to 1–2 μm (Figs. 1a, 1b). The column diameter determined from the SEM micrographs varied in the ranges 20–70 nm for structures with a buffer layer and 40–80 nm for structures without buffer layer. The growth was performed in a gallium-enriched medium. This was evidenced from the appearance of gallium drops at considerably lower temperatures of the gallium cell and lower temperatures of the substrate at the same flow rates of nitrogen and the same high-frequency power, and also from the characteristic HEED pattern that corresponded to these conditions (narrow thin lines without dashes and broadenings which are typical of nitrogen-rich conditions). Upon the growth of columnar structures, no gallium drops were observed owing to high growth temperatures (above ~700°C) at which excess gallium actively reevaporated from the substrate surface [15]. Under these conditions, the growth most likely proceeds through the vapor–liquid–solid mechanism, because the absence of drops is not an argument against this mechanism [9]. In the earlier experiments with a high-frequency discharge on sapphire and GaAs substrates [10], we obtained regularly arranged GaN and InN nanocolumns with somewhat larger mean

diameters ranging from 100 to 300 nm. Moreover, we studied the growth mechanism, compared the results with the theory [16], and showed that the growth proceeded through the vapor–liquid–solid mechanism [9].

In addition to the control over geometric sizes of nanometer-sized objects, the TEM technique was used to visualize defects typical of GaN, such as dislocations, extended domain boundaries, and stacking faults [17–20]. In the present work, the samples were examined using a Philips EM-420 electron microscope operating at an accelerating voltage of 100 kV. The standard technique was applied to the sample preparation, which involved the mechanical treatment (grinding and polishing) and sputtering of the material by Ar^+ ions with an energy of 4 keV at an angle of 14° with respect to the sample surface. The samples were obtained in a cross-sectional $(2\bar{1}\,\bar{1}\,0)$ geometry.

3. RESULTS AND DISCUSSION

Analysis of the SEM images demonstrated that the growth of a GaN layer in the first-type (with a low-temperature buffer layer) and second-type (without buffer layer) samples was accompanied by the formation of columnar structures (Figs. 1a, 1b). The main types of defects observed in these structures were threading dislocations, stacking faults in the (0001) basal plane, and inversion domains. It turned out that the growth of the GaN base layer on a low-temperature thin GaN buffer and without it (only with nitridation of the substrate) resulted in almost the same interface—a 20- to 30-nm-thick thin defect transition layer (seen in the TEM image) at the heteroboundary with the substrate. These data are in agreement with the results obtained by Byun *et al.* [17], according to which a thin amorphous buffer layer is directly formed by plasma treatment of sapphire, which is similar to our conditions of the substrate nitridation with nitrogen plasma prior to the growth. In our structures, the mean thicknesses of the transition layer in the first- and second-type samples were estimated at 28 and 23 nm, respectively. The column lengths in these samples were equal to 1 and 2 μm, respectively.

As can be seen from the TEM images of samples of both types, the formation of a GaN columnar structure does not imply that columns necessarily grow starting from the buffer layer (Figs. 2, 4). In addition to columns emanating from the interface, there are inversion domains adjacent to these columns, which, taken together, form a unity. During the growth of a GaN layer, broad columns with diameters of the order of 100–300 nm are separated into narrower columns. This separation is observed on the surface of a particular column beginning with a height of approximately 200 nm. The mean column diameters measured at the surface and the mean distances between columns are listed in the table. We failed to achieve a clear visualization of the distance between the columns in the second-type

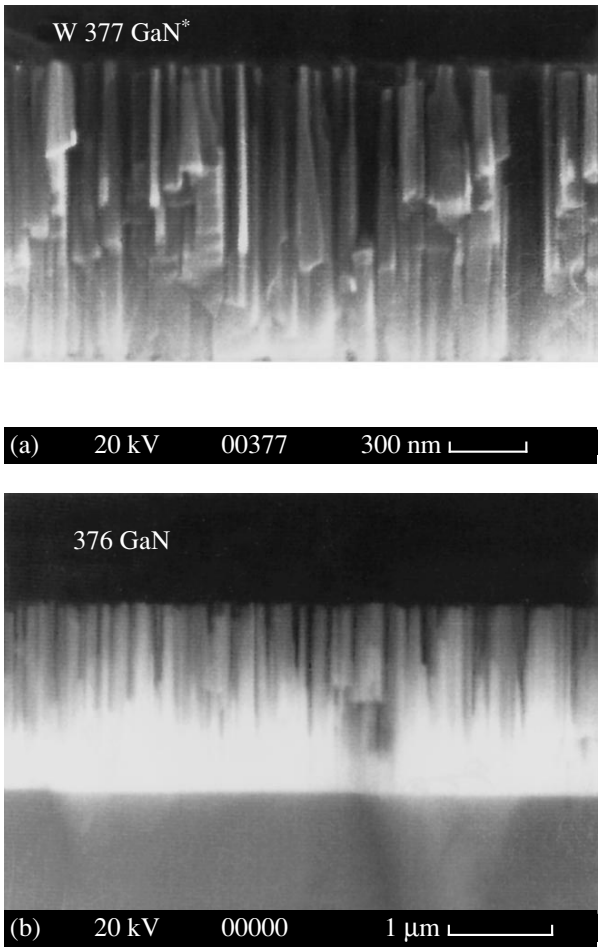

Fig. 1. SEM micrographs of columnar structures on cleavages of (a) the first-type sample grown with a low-temperature buffer layer and (b) the second-type sample without buffer layer.

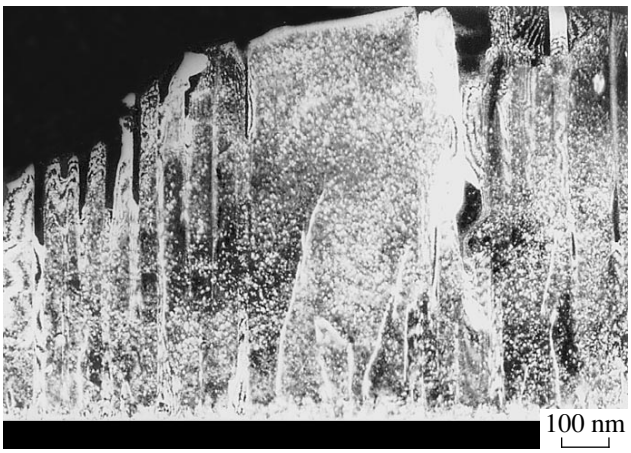

Fig. 2. A cross-section $(2\bar{1}\,\bar{1}\,0)$ TEM weak-beam (g, $3g$) image of the first-type sample with a 28-nm-thick buffer layer for the operating reflection (0002).

Results of analyzing the electron microscope images for $GaN/Al_2O_3(0001)$ samples of two types

Sample no.	Dislocation density, 10^9 cm^{-2}			Column density, 10^9 cm^{-2}	Mean distance between columns, nm	Mean column thickness, nm
	screw	edge	mixed			
377(I)	5.7 ± 0.5	6.4 ± 0.6	6.4 ± 0.6	12 ± 3	14 ± 3	50 ± 18
376(II)	14 ± 3	6 ± 2	6 ± 2	10 ± 1		60 ± 4

samples with a thinner transition layer because of the certain locality of the TEM technique. It is worth noting that the first-type samples with a low-temperature buffer and a 28-nm-thick transition layer exhibit a substantial scatter in column diameters, whereas the distribution of distances between columns remains uniform throughout the film (see table).

In order to elucidate the origin of the inversion domain formation, we examined the interface between the Al_2O_3 substrate, the GaN transition layer, and the GaN base layer. As is seen from the $(2\bar{1}\,\bar{1}\,0)$ cross-section dark-field images obtained with the operating reflections (0002) and $(01\bar{1}0)$ for the first- and second-type samples (Figs. 3a, 3b and 5a, 5b, respectively), the transition layer is not uniformly crystallized and homogeneous throughout the thickness. In the transition layer, there exist regions (about 50 nm thick) displaced with respect to each other in the $[01\bar{1}1]$ direction, which form the initial portions of inversion domain boundaries. Note that these displacements arise from the stepped substrate surface (Figs. 3, 5). The transition layer, as a whole, consists of the (0001) stacking faults, which is confirmed by the presence of dark and bright alternating lines parallel to the interface in the $(01\bar{1}0)$ image (Figs. 3b, 5b). As is known [18], the polarity of this plane can be judged from a specific contrast (bright or dark) of the last line, which bounds the stacking fault. It is seen that the contrasts of these lines for buffer regions that correspond to columns and inversion domains are opposite, which supports different polarities of the matrix columns and the inversion domains (Figs. 3, 5). Xin *et al.* [19] showed that, depending on the operating reflection (0002) or $(01\bar{1}0)$, the contour contrast perpendicular to the interface at the inversion domain boundary makes it possible to determine the type of this boundary. With this technique, we found that the inversion domains have the $(01\bar{1}0)$ and $(11\bar{2}0)$ boundaries (Figs. 3, 5).

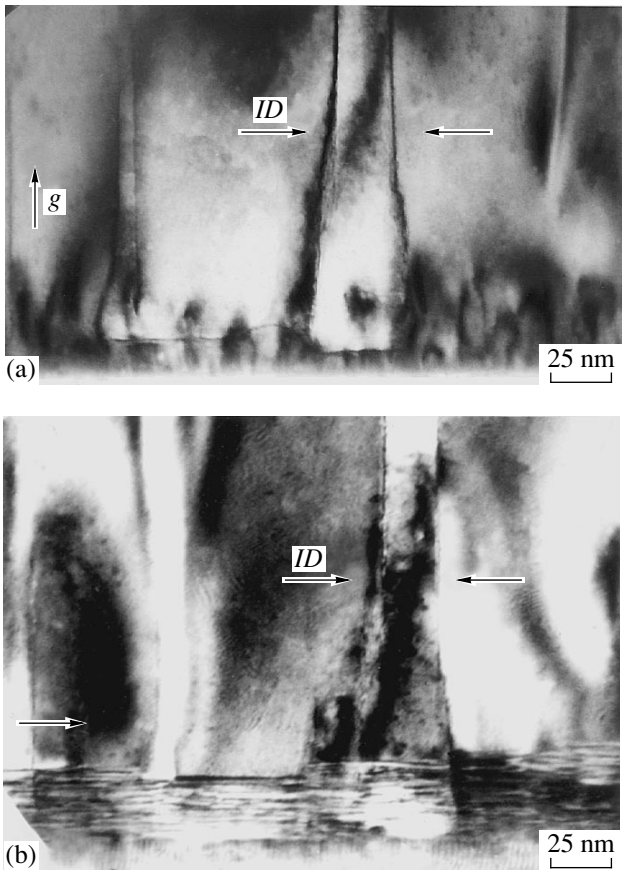

Fig. 3. Cross-section $(2\bar{1}\,\bar{1}\,0)$ TEM dark-field images of the first-type sample with a 28-nm-thick buffer layer for the operating reflections (a) (0002) and (b) $(01\bar{1}0)$.

Threading dislocations of different types were investigated using a method based on the extinction of dislocation contrast when the direction of the operating reflection was perpendicular to the Burgers vector **b**. In this case, the images were obtained under weak-beam (g, $3g$) conditions at which a strong contrast of strain fields induced by dislocations was suppressed. A clear contrast observed for threading dislocations under weak-beam (g, $3g$) conditions for the operating reflection $(01\bar{1}0)$ and its extinction for the operating reflection (0002) allowed us to conclude that these are edge dislocations with the Burgers vector $\mathbf{b} = \langle hk10\rangle$. Wu *et al.* [20] revealed that dislocations of this type are partial edge dislocations with the Burgers vectors $\mathbf{b} = 1/3\langle 11\bar{2}0\rangle$ and $\mathbf{b} = 1/3\langle 2\bar{1}\,\bar{1}0\rangle$.

The screw dislocations with the Burgers vector $\mathbf{b} = \langle 0002\rangle$ were identified reasoning from the contrast in the $(2\bar{1}\,\bar{1}\,0)$ cross-section for the operating reflection (0002) and the extinction of the contrast for the operat-

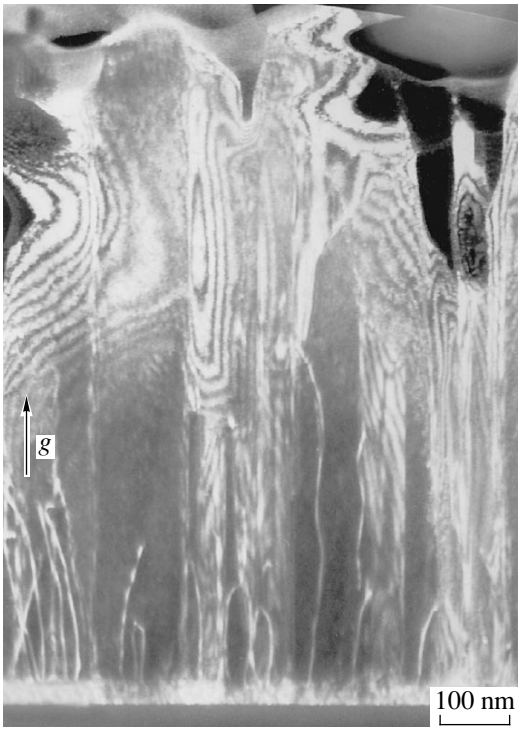

Fig. 4. A cross-section $(2\bar{1}\,\bar{1}\,0)$ TEM weak-beam (g, $3g$) image of the second-type sample with a 23-nm-thick buffer layer for the operating reflection (0002).

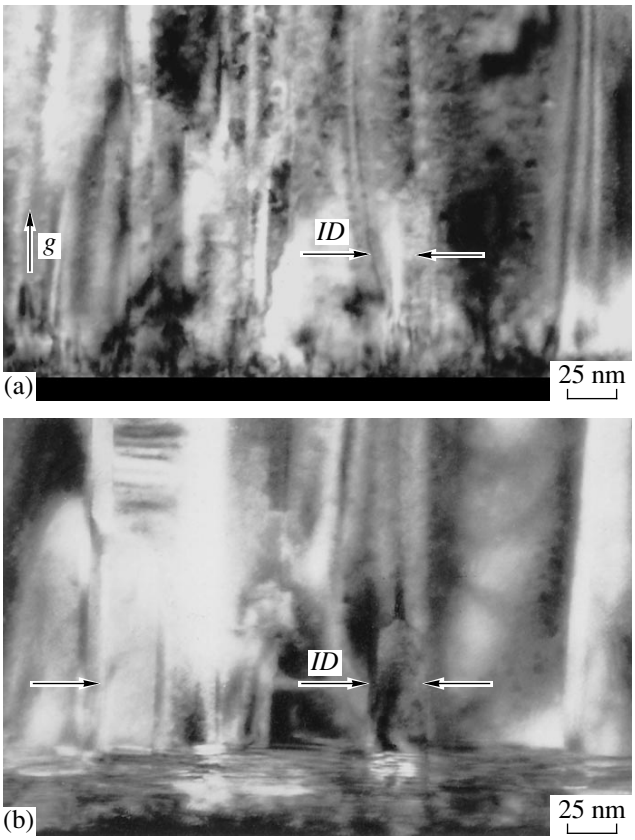

Fig. 5. Cross-section $(2\bar{1}\,\bar{1}\,0)$ TEM dark-field images of the second-type sample with a 23-nm-thick buffer layer for the operating reflections (a) (0002) and (b) $(01\bar{1}\,0)$.

ing reflection $(01\bar{1}\,0)$. Dislocations that exhibit a contrast (or its partial extinction) under all the above conditions have the Burgers vector $\mathbf{b} = \langle hk1m\rangle$. According to [20], dislocations with a similar contrast are the mixed dislocations with the Burgers vector $\mathbf{b} = 1/3[11\bar{2}\,\bar{3}]$. The densities of the screw, edge, and mixed threading dislocations were determined from analysis of the TEM images of samples of two types (see table). The data on the mean column sizes obtained by the TEM method are somewhat different from those obtained by the SEM method because of the locality of the former method.

It is of interest that the dislocations in the first-type sample with a 28-nm-thick transition layer (the growth with a low-temperature GaN buffer) exhibit an inhomogeneous spatial distribution over the film. In particular, the highest dislocation density is observed either in the region of inversion domains or in the GaN columns whose thickness exceeds a critical size of ~50 nm. It should be noted that this critical size coincides with the mean thickness of the GaN columns (see table). The diameter of an inversion domain decreases to 13 nm with distance away from the interface, but the domain with the $\{01\bar{1}\,0\}$ and $\{11\bar{2}\,0\}$ boundaries intergrows up to the surface. In the second-type sample with a 23-nm-thick transition layer (the growth without buffer layer), the mean column size increases and the distance between the columns decreases considerably. No dependence of the dislocation density on the spatial arrangement and the size of columns was found for this sample.

All the foregoing allow us to draw the following inferences. The GaN nanocolumns with a mean diameter of 50 nm were grown on the (0001) sapphire substrates by using self-organization processes upon molecular beam epitaxy with a high-frequency plasma activation without postgrowth treatment (for example, plasma etching). In the sample with a low-temperature buffer layer, the minimum diameter of columns was equal to ~20 nm and their mean density was $\sim 10^{10}$ cm^{-2}. Most likely, the higher density of columns and their smaller mean diameter in the sample with a low-temperature buffer layer can be explained by the higher density of steps at the low-temperature buffer and (or) the larger diffusion length of atoms along the surface at lower rates of growth (lower flow rates of gallium). The mean dislocation density was equal to $\sim 2 \times 10^{10}$ cm^{-2}, and no dislocations were observed in columns whose diameter was less than 50 nm. In the GaN layer without the low-temperature buffer, the minimum column size was equal to ~50 nm. Reasoning from the gallium-rich

growth conditions and the earlier investigations into the growth mechanism under similar conditions [9], we can conclude that, in our case, the growth most probably proceeds through the vapor–liquid–solid mechanism; however, a detailed elucidation calls for further investigations.

Summing up the results obtained in TEM observations, we can note the following. The GaN columnar structure is formed under the growth conditions described above. In addition to single columns, there are regions containing both GaN column and inversion domains adjacent to this column. The columns can originate both at the interface and on the surface of initially wide columns beginning with a certain height. The examination of the interface showed that the stepped surface of the substrate leads to displacements of the buffer regions along the $(01\bar{1}1)$ direction, which initiates the formation of inversion domain boundaries. A further deposition of the material is accompanied by a decrease in the diameter of inversion domains to 13 nm and their intergrowth with the $\{01\bar{1}0\}$ and $\{11\bar{2}0\}$ boundaries up to the surface. In the first-type sample with a 28-nm-thick transition layer, there exist dislocation-free columns with diameters less than 50 nm (which coincides with the mean column diameter in this sample), even though the total dislocation density is rather high (1.9×10^{10} cm^{-2}). For the second-type sample with a 23-nm-thick transition layer, the mean column diameter increases and the distance between the columns decreases substantially. Moreover, the dislocation density increases to 2.6×10^{10} cm^{-2}. Therefore, it can be concluded that the growth of GaN columnar structures is governed to a large extent by the initial growth conditions (with a low-temperature buffer layer and without it). This is likely explained by an increase in the step density at the surface of the buffer layer, even though the defect transition layers with almost identical thicknesses are formed upon growth in both cases.

The mechanism of the growth of columnar nanostructures, the role of low-temperature buffer layers in the further improvement of the nitride crystal quality (which is an urgent problem [21]), and the controlled growth of dislocation-free whiskers with a mean diameter of less than the critical value (~50 nm) and their use in practice invite further investigation.

ACKNOWLEDGMENTS

This work was supported by the Russian Foundation for Basic Research (project no. 99-02-17103) and the "Physics of Solid-State Nanostructures" Program of the Ministry of Science and Technology of the Russian Federation.

REFERENCES

1. S. Strite and H. Morkos, J. Vac. Sci. Technol. B **10**, 1237 (1992).
2. S. Nakamura, M. Senoh, and S. Nagahama, Jpn. J. Appl. Phys. **35**, L74 (1996).
3. I. Akasaki, S. Sota, and H. Sakai, Electron. Lett. **32**, 1105 (1996).
4. Y. Arakawa and H. Sakai, Appl. Phys. Lett. **40**, 939 (1982).
5. R. Notzel, J. Temmyo, and T. Tamamura, Nature **369**, 131 (1994).
6. K. Y. Cheng, K. C. Hsieh, and J. N. Baillargen, Appl. Phys. Lett. **60**, 2892 (1992).
7. M. Yoshizawa, A. Kikuchi, M. Mori, *et al.*, Jpn. J. Appl. Phys. **36** (43), L459 (1997).
8. R. S. Wagner and W. C. Ellis, Appl. Phys. Lett. **5** (4), 89 (1964).
9. V. V. Mamutin, Pis'ma Zh. Tekh. Fiz. **25** (18), 55 (1999) [Tech. Phys. Lett. **25**, 741 (1999)].
10. G. Pozina, J. P. Bergman, B. Monemar, *et al.*, Phys. Status Solidi B **216**, 445 (1999).
11. S. M. Polyakov, E. N. Laverko, and V. M. Marakhonov, Kristallografiya **15** (3), 598 (1970) [Sov. Phys. Crystallogr. **15**, 519 (1970)].
12. M. Koguchi, H. Kakibyashi, and M. Yazawa, Jpn. J. Appl. Phys. **31** (7), 2061 (1992).
13. A. Sakai, H. Sunakawa, and A. Usui, Appl. Phys. Lett. **71**, 2259 (1997).
14. V. V. Mamutin, V. N. Zhmerik, T. V. Shubina, *et al.*, Pis'ma Zh. Tekh. Fiz. **24** (12), 30 (1998) [Tech. Phys. Lett. **24**, 467 (1998)].
15. A. R. Smith, V. Ramachandran, R. M. Feenstra, *et al.*, MRS Internet J. Nitride Semicond. Res. **3**, 12 (1998).
16. E. I. Givargizov and A. A. Chernov, Kristallografiya **18** (1), 147 (1973) [Sov. Phys. Crystallogr. **18**, 89 (1973)].
17. D. Byun, H.-J. Kim, C. H. Hong, *et al.*, Phys. Status Solidi A **176**, 643 (1999).
18. V. M. Kosevich and L. S. Palatnik, *Electron Microscope Image of Dislocations and Stacking Faults: A Reference Manual* (Nauka, Moscow, 1976).
19. Y. Xin, P. D. Brown, T. S. Cheng, *et al.*, in *Proceedings of the Royal Microscopical Society Conference on Microscopy of Semiconducting Materials, Oxford, 1997* (Inst. of Physics Publ., Bristol, 1997), p. 217.
20. X. H. Wu, L. M. Brown, D. Kapolnek, *et al.*, J. Appl. Phys. **80** (6), 3228 (1996).
21. S.-H. Cho, X.-Q. Shen, and H. Okumura, Phys. Status Solidi A (2000) (in press).

Translated by O. Borovik-Romanova

Physics of the Solid State, Vol. 43, No. 1, 2001, pp. 157–165. Translated from Fizika Tverdogo Tela, Vol. 43, No. 1, 2001, pp. 152–158.

LOW-DIMENSIONAL SYSTEMS AND SURFACE PHYSICS

Electrostatic Model of Band-Gap Renormalization and the Photoluminescence Line Shape in a GaAs/AlGaAs Two-Dimensional Layer at a High Excitation Level

N. A. Poklonski and A. I. Siaglo

Belarussian State University, F. Skoriny pr. 4, Minsk, 220050 Belarus

e-mail: poklonski@phys.bsu.unibel.by

Received February 28, 2000; in final form, May 30, 2000

Abstract—An electrostatic model for calculating the band-gap renormalization in a two-dimensional (2D) semiconductor layer (quantum well) due to the Coulomb interaction between nonequilibrium charge carriers has been proposed. Consideration is given only to the first quantum-well energy levels for electrons and heavy holes. The exchange and correlation energies are calculated for the first time taking into account the charge-carrier potential energy fluctuations created by electrons and holes along the 2D layer. A relationship for the screened Coulomb potential along the 2D layer is derived, which, within the extremely narrow quantum-well approximation, transforms into the known expression. The band-gap renormalization and the photoluminescence line shape for the GaAs 2D layer in an $Al_xGa_{1-x}As$ matrix are computed depending on the concentration of nonequilibrium electrons and holes. The calculated band-gap renormalization is in agreement with the available experimental data at a high photoexcitation of the quantum well when the electrons and holes form the 2D plasma. © *2001 MAIK "Nauka/Interperiodica".*

1. INTRODUCTION

The exchange and correlation interactions between free charge carriers lead to a reduction in the band gap E_g in both three-dimensional (3D) crystalline semiconductors and two-dimensional (2D) layers [1–5]. For example, as the concentrations of nonequilibrium electrons n and holes p increase from zero to $n = p \approx 3 \times 10^{12}$ cm^{-2}, the band gap in a GaAs 2D layer (with the thickness $L \approx 10$ nm in an $Al_{0.3}Ga_{0.7}As$ matrix) at $T \approx 4.2$ K decreases by approximately 60 meV [4, 5]. According to Volkov *et al.* [6], electrons and holes at concentrations $n = p \approx 5 \times 10^{10}$ cm^{-2} and more in the GaAs layer with a thickness of 30 nm form an electron–hole plasma and are not bound into excitons.

Schmitt-Rink *et al.* [1] explained the band-gap renormalization $\Delta E_g > 0$ in a quantum-well 2D layer only by the convergence of the conduction (c) and valence (v) band edges as a result of the exchange interaction between charge carriers. In the framework of the model proposed by Das Sarma *et al.* [2], ΔE_g in a 2D layer was calculated within the random-phase approximation for the wave functions of electrons and holes with due regard for their interaction with phonons (in the Fröhlich approximation for 3D crystals). Fluctuations in the potential energy of electrons and holes along the 2D layer due to their Coulomb interaction with each other and with impurity ions were ignored in [1, 2]. This complicated the analysis of changes in the band gap E_g and the spectral distribution of photoluminescence in a 2D layer at different parameters of the layer and matrix materials and photoexcitation levels.

The aim of the present work was to calculate the band-gap renormalization in a photoexcited 2D layer (quantum well) with the inclusion of electrostatic potential fluctuations (created by the electron–hole plasma along the layer) on the basis of the model proposed earlier in [7, 8] for a doped 3D crystal.

2. BASIC RELATIONSHIPS

The GaAs quantum wells in an $Al_xGa_{1-x}As$ matrix are usually produced on the crystallographic plane (100). Let us define the 2D layer (quantum well) by the $X0Y$ plane and the perpendicular $0Z$ axis. The layer area is S, and the layer thickness is L.

The energy of an electron (a hole) E_{jn} (E_{jp}) at the jth quantum-well level can be estimated within the infinitely deep quantum-well approximation [1, 9]: $E_{jn(p)} = (\pi j\hbar)^2/2m^{(z)}_{n(p)}L^2$, where $m^{(z)}_{n(p)}$ is the effective electron (hole) mass responsible for the energy quantization across the 2D layer (the subscripts n and p refer to electrons and holes, respectively).

As in the GaAs 3D crystal, the E_{jn} energy and the density of states for electrons are calculated using the mass $m^{(z)}_n = m^{(xy)}_n = 0.0665m_0$ (where m_0 is the mass of a free electron). The $E_{jph(l)}$ energies for holes are determined using the effective masses [1, 9–11]: $m^{(z)}_{ph} =$

$m_0/(\gamma_1 - 2\gamma_2) = 0.4m_0$ for a heavy hole and $m_{pl}^{(z)} = m_0/(\gamma_1 + 2\gamma_2) = 0.087m_0$ for a light hole (where $\gamma_1 = 6.98$ and $\gamma_2 = 2.25$ are the Luttinger parameters [10]). The density of states for holes in the 2D layer in the (100) plane is computed with $m_{ph}^{(xy)} = m_0/(\gamma_1 + \gamma_2) = 0.11m_0$ and $m_{pl}^{(xy)} = m_0/(\gamma_1 - \gamma_2) = 0.21m_0$.

Since $m_{pl}^{(z)} < m_{ph}^{(z)}$, the quantum energy level of a light hole E_{1pl} is located in the v band at a greater depth compared to the level of a heavy hole E_{1ph}. Therefore, E_g is equal to the energy gap between the first quantum levels of electrons and heavy holes $E_g = E_{g0} + E_{1n} + E_{1ph}$, where E_{g0} is the band gap in the 3D crystal. The dependences of $E_{1n(ph)}$ on the thickness of the GaAs 2D layer in an AlAs matrix were obtained by Franceschetti and Zunger [12].

For simplicity of calculations, hereafter, we will consider only the first quantum levels ($j = 1$) of electrons and heavy holes that form a two-dimensional plasma. Since only heavy holes will be included in further calculations, the subscript *ph* will be replaced by *p*.

According to the model proposed earlier [7, 8], the one-particle energies of the correlation $E^{(cor)}$ and exchange ($E_n^{(exc)}$ and $E_p^{(exc)}$) interactions between electrons (*n*) and heavy holes (*ph*) additively enter into the relationship for the band-gap renormalization ΔE_g in the quantum well, that is,

$$\Delta E_g = E_g - E_g' = E^{(cor)} + E_n^{(exc)} + E_p^{(exc)} > 0, \quad (1)$$

where E_g' is the band gap in the 2D layer upon excitation of an electron–hole gas and E_g is the energy gap in the 2D layer at $n = p = 0$.

Let us now consider a high level of the photoexcitation of the 2D layer, i.e., the case when the concentration of impurity ions in this layer is negligibly small compared to the concentration of nonequilibrium electrons and holes and can be ignored. Then, the electroneutrality equation has the form $n = p$. We take into account that the potential energy U of both an electron and a hole fluctuates along the 2D layer due to the interaction of charge carriers with each other. By generalizing the results obtained in [1, 4] to the case of electrostatic potential fluctuations [7, 8], the mean two-dimensional concentration of delocalized electrons *n* (holes *p*) at a finite temperature can be written as

$$\begin{aligned} n &= \frac{m_n^{(xy)}}{\pi\hbar^2}\int_{-\infty}^{+\infty} G_n dU \int_U^{+\infty} f_n dE, \\ p &= \frac{m_p^{(xy)}}{\pi\hbar^2}\int_{-\infty}^{+\infty} G_p dU \int_U^{+\infty} f_p dE, \end{aligned} \quad (2)$$

where $f_{n(p)}(E) = (1 + \exp((E - F_{n(p)}/k_BT))^{-1}$ is the Fermi–Dirac function for electrons (holes), $E = (\hbar k)^2/2m_n^{(xy)} + U$ is the energy of the electron (heavy hole) with the quasi-wave vector $\mathbf{k}$ along the quantum well, $F_{n(p)}$ is the Fermi quasi-level in the $c(v)$ band, k_BT is the thermal energy, and $G_{n(p)}(U)$ is the density of potential energy distribution of electrons (holes).

The energy and the Fermi level $F_{n(p)}$ of the electron (hole) are reckoned from the first quantum level of the electron $E_{1n} = (\pi\hbar)^2/2m_n^{(z)}L^2$ [for the heavy hole, $E_{1p} = (\pi\hbar)^2/2m_p^{(z)}L^2$] deep into the allowed energy band without photoexcitation of the 2D layer.

We assume that the density of distribution of the potential energy U of the electron (hole) over the 2D layer is Gaussian

$$G_{n(p)}(U) = \frac{1}{\sqrt{2\pi}W}\exp\left(-\frac{U^2}{2W^2}\right), \quad (3)$$

where $W = W_n = W_p$ is the root-mean-square fluctuation of the energy.

At $W \gg k_BT$ (formally, at temperature $T \longrightarrow 0$), from relationships (2) with due regard for expression (3) within the approximation of the complete degeneracy of electrons at the first quantum level in the *c* band (heavy holes in the v band), we have [13–15]

$$\begin{aligned} n = p &= \frac{m_{n(p)}^{(xy)}}{2\pi\hbar^2}\int_{-\infty}^{F_{n(p)}}(F_{n(p)} - U)G_{n(p)}dU = \frac{m_{n(p)}^{(xy)}}{2\pi\hbar^2} \\ &\times\left\{F_{n(p)}\left[1 + \mathrm{erf}\left(\frac{F_n(p)}{W\sqrt{2}}\right)\right] + \frac{2W}{\sqrt{2\pi}}\exp\left(-\frac{F_n^{2(p)}}{2W^2}\right)\right\}. \end{aligned} \quad (4)$$

At $W \ll k_BT$ [formally, in the absence of fluctuations, $G_{n(p)} \longrightarrow \delta(U)$], from relationships (2), it follows that [16]

$$\begin{aligned} n = p &= \frac{m_{n(p)}^{(xy)}}{\pi\hbar^2}\int_0^{+\infty} f_{n(p)}dE \\ &= \frac{m_{n(p)}^{(xy)}k_BT}{\pi\hbar^2}\ln\left[1 + \exp\left(\frac{F_{n(p)}}{k_BT}\right)\right]. \end{aligned} \quad (5)$$

Note that, at $T \longrightarrow 0$, the concentration of electrons (heavy holes) at the first quantum level is approximately equal to the total concentration $n = p$, provided that the averaged (over the 2D layer) maximum kinetic energy of the electron (hole) $\overline{E_{n(p)}^{(kin)}}$ satisfies the condition

$$\overline{E_{n(p)}^{(\mathrm{kin})}} = \int_{-\infty}^{F_{n(p)}} (F_{n(p)} - U) G_{n(p)} dU = \frac{\pi\hbar^2 n}{m_{n(p)}^{(xy)}} < \overline{E_{2n(p)}} - \overline{E_{1n(p)}}. \quad (6)$$

As was shown in [1, 9], the difference between the energies of the second and first quantum levels can be estimated as $\overline{E_{2n(p)}} - \overline{E_{1n(p)}} \approx 3(\pi\hbar)^2/2m_{n(p)}^{(z)}L^2$. Then, from relationship (6), it follows that our analysis can be restricted only to the first quantum levels in the c and v bands of the 2D layer: $n < 3\pi/2L^2$ and $p < 3\pi m_p^{(xy)}/2L^2 m_p^{(z)}$.

2.1. Let us consider models for the charge density distribution over the two-dimensional electron–hole plasma. The root-mean-square fluctuation W of the electrostatic potential energy of an electron and a hole can be calculated with due regard for the fact that they are not bound into the excitons; i.e., they should be spaced apart from each other along the 2D layer. According to the quasi-classical estimates [17], the distance between the electron (hole) and the nearest electron or hole is approximately equal to the diameter of the 2D region per electron (hole): $2r_c = 2(\pi(n + p))^{-1/2}$. The charge density distribution for each electron (hole) in the calculation of W can be expressed in the form

$$\rho_{n(p)} = \rho_1 = \frac{\mp e}{\pi r_c^2 L}\theta(r_c - r), \quad (7)$$

where $\theta(r_c - r)$ is the Heaviside function [$\theta(r_c - r) = 0$ at $r > r_c$ and $\theta(r_c - r) = 1$ at $r \le r_c$].

In the Debye–Hückel calculations of the screening length and the correlation energy $E^{(\mathrm{cor})}$, each electron (hole) can be represented in the form of a "wire" whose charge density is uniformly distributed across the 2D layer. At a high concentration of photoexcited charge carriers ($r_c \ll L$), it follows from Eq. (7) that

$$\rho_{n(p)} = \rho_2 = \begin{cases} \mp(e/L)\delta(\mathbf{r}) & \text{at } -L/2 \le z \le l/2 \\ 0 & \text{at } z < -L/2;\ z > L/2, \end{cases} \quad (8)$$

where $\delta(\mathbf{r})$ is the two-dimensional Dirac function.

The exchange interaction $\overline{E_{n(p)}^{(\mathrm{exc})}}$ of electrons (holes) in the 2D layer cannot be calculated by specifying only the charge density. It is necessary to use the wave function of the electron (hole) with the quasi-wave vector $\mathbf{k}$ at the first quantum level ($j = 1$). Within the infinitely deep quantum-well approximation [9], we have

$$\Psi_{\mathbf{k}}(\mathbf{r}, z) = \left(\frac{2}{LS}\right)^{1/2} \cos\left(\frac{\pi z}{L}\right) \exp(i\mathbf{k}\mathbf{r}) \quad (9)$$

and the density of charge distribution is $\rho_{n(p)} = \rho_3 = \mp e|\Psi_{\mathbf{k}}(\mathbf{r}, z)|^2 = \mp(2e/LS)\cos^2(\pi z/L)$.

2.2. The root-mean-square fluctuation of the potential energy of an electron (hole) $W = W_n = W_p$ along the quantum well can be calculated using the pure Coulomb interaction only between the nearest delocalized charges [7, 8]. The charge density distribution for each electron (hole) is given by expression (7). The energy of the Coulomb interaction between two touching disks (each with radius r_c and thickness $L \le r_c$), whose charge $\pm e$ is uniformly distributed over the volume, virtually does not differ from the energy of interaction between the same point charges separated by the distance $2r_c = 2(\pi(n + p))^{-1/2} = 2(2\pi n)^{-1/2}$. Hence, the magnitude of the interaction energy $|U_i|$ for the two nearest electrons (holes) in the 2D layer is taken to be $|U_i| \approx e^2/(8\pi\varepsilon r_c)$. For the closest packing of charged particles along the 2D layer, each particle has the six nearest neighbors in the first coordination sphere. In this case, in the absence of correlation between the location and the charge sign of a particle, at $n = p$, we have

$$W = \left(\sum_{i=1}^{6} P_i U_i^2\right)^{1/2} \approx \sqrt{6}\frac{e^2}{8\pi\varepsilon r_c} = \frac{e^2}{4\pi\varepsilon_r\varepsilon_0}(3\pi n)^{1/2}, \quad (10)$$

where $P_i = 1$ is the probability that the nearest neighbor of a particular electron is the electron or hole and $\sum_{i=1}^{6} P_i U_i = 0$.

Note that the ratio $\gamma_{n(p)}$ between the magnitude of the mean potential energy of the Coulomb interaction for two particles and the mean kinetic energy of a particle [relationship (6)] in the two-dimensional electron–hole plasma is $\gamma_{n(p)} = |U_t|/\overline{E_{n(p)}^{(\mathrm{kin})}} = (e^2 m_{n(p)}^{(xy)}/4\pi\varepsilon\hbar^2)(2\pi n)^{-1/2}$. In the GaAs 2D layer at $10^{11}\ \mathrm{cm}^{-2} < n = p < 3 \times 10^{13}\ \mathrm{cm}^{-2}$, the energy parameter of plasma imperfection [18, 19] varies in the ranges $\gamma_n = 1.3$–0.07 for electrons and $\gamma_p = 2.1$–0.12 for heavy holes. Consequently, the electron–hole plasma becomes more perfect with an increase in the level of photoexcitation of the 2D layer.

2.3. Now, we dwell on the screening of the Coulomb potential of an electron (hole) in the photoexcited plasma of the 2D layer. The total electrostatic potential $\varphi(\mathbf{r}, z)$ of the charge $\mp e$ with the density $\rho_{n(p)} = \rho_2$ according to relationship (8) and its screening cloud with the density $\rho_s = e(p(\varphi) - n(\varphi))$ can be found from the linearized Poisson equation (in the cylindrical coordinate system)

$$\frac{1}{r}\frac{\partial}{\partial r}\left(r\frac{\partial\varphi}{\partial r}\right) + \frac{\partial^2\varphi}{\partial\varphi^2} = -\frac{(\rho_{n(p)} + \rho_s)}{\varepsilon} \approx \begin{cases} \pm\frac{e}{\varepsilon L}\delta(\mathbf{r}) + \frac{2\boldsymbol{\varphi}(\mathbf{r}, z)}{L, \lambda} & \text{at } -\frac{L}{2} \le z \le \frac{L}{2} \\ 0 & \text{at } z < -\frac{L}{2}, z > \frac{L}{2}, \end{cases} \quad (11)$$

where $\varepsilon = \varepsilon_r\varepsilon_0$ is the static permittivity of the 2D layer crystal lattice, ε_0 is the permittivity of free space, $\rho_s(\mathbf{r}, z) = -2\varepsilon\varphi(\mathbf{r}, z)/L\lambda$ is the charge density of the screening cloud, and

$$\lambda^{-1} = \frac{e^2}{2\varepsilon}\left(\frac{\partial n}{\partial F_n} + \frac{\partial p}{\partial F_p}\right) \quad (12)$$

is the reciprocal of the screening length in the 2D layer [16, 20, 21].

At low temperatures ($k_BT \ll W$), from relationships (12) and (4), we obtain [13–15]

$$\lambda^{-1} = \frac{e^2}{4\pi\varepsilon\hbar^2}\left(m_n^{(xy)}\left(1 + \mathrm{erf}\left(\frac{F_n}{W\sqrt{2}}\right)\right) + m_p^{(xy)}\left(1 + \mathrm{erf}\left(\frac{F_p}{W\sqrt{2}}\right)\right)\right). \quad (13)$$

At high temperatures ($k_BT \gg W$), from relationships (12) and (5), we have [16, 20]

$$\lambda^{-1} = \frac{e^2}{2\pi\varepsilon\hbar^2}\left(\frac{m_n^{(xy)}}{1 + \exp(-F_n/k_BT)} + \frac{m_p^{(xy)}}{1 + \exp(-F_p/k_BT)}\right).$$

The potential $\varphi(\mathbf{r}, z)$ that obeys the Poisson equation (11) will be sought in the form

$$\varphi(\mathbf{r}, z) = \frac{\mp e}{2\varepsilon}\int \exp(i\mathbf{kr})\Phi(k, z)\frac{d^2\mathbf{k}}{(2\pi)^2} = \frac{\mp}{4\pi\varepsilon}\int_0^\infty kJ_0(kr)\Phi(k, z)dk, \quad (14)$$

where $J_0(kr) = (2\pi)^{-1}\int_0^{2\pi}\exp(ikr\cos\alpha)d\alpha$ is the zero-order Bessel function and $\Phi(k, z)$ is the Fourier transform of the $\varphi(\mathbf{k}, z)$ potential.

Substitution of Eq. (14) into expression (11) gives the equation for determination of $\Phi(k, z)$

$$\frac{\partial^2\Phi}{\partial z^2} - \left(k^2 + \frac{2}{L\lambda}\right)\Phi = -\frac{2}{L} \text{ at } -L/2 \le z \le L/2,$$
$$\frac{\partial^2\Phi}{\partial z^2} - k^2\Phi = 0 \text{ at } z < -L/2, z > L/2, \quad (15)$$

in which we took into account that $\delta(\mathbf{r}) = \int\exp(i\mathbf{kr})\frac{d^2\mathbf{k}}{(2\pi)^2} = \int_0^\infty\frac{kJ_0(kr)dk}{2\pi}$.

The combined equations (15) are solved taking into account that $\varphi(\mathbf{r}, z)$ becomes zero at $|z| \longrightarrow \infty$ and that the $\varphi(\mathbf{r}, z)$ potential and the electric induction are continuous at $r \neq 0$ and $z = \pm L/2$. Inside the 2D layer (at $-L/2 \le z \le L/2$), the projection of the electric induction onto the $0Z$ axis is equal to $-\varepsilon_r\varepsilon_0\partial\varphi(\mathbf{r}, z)/\partial z$. Outside the 2D layer (at $z < -L/2$ and $z > L/2$), the projection of the electric induction onto the $0Z$ axis is equal to $-\varepsilon_{rm}\varepsilon_0\partial\varphi(\mathbf{r}, z)/\partial z$, where $\varepsilon_{rm}\varepsilon_0$ is the static permittivity of the matrix. As a result, in the interval $-L/2 \le z \le L/2$, we have

$$\Phi(k, z) = \frac{2}{\tilde{k}^2 L} \times\left(1 - \frac{k\varepsilon_{rm}\cosh(\tilde{k}z)}{\tilde{k}\varepsilon_r\sinh(\tilde{k}L/2) + k\varepsilon_{rm}\cosh(\tilde{k}L/2)}\right), \quad (16)$$

where $\tilde{k}^2 = k^2 + 2/L\lambda$.

Let us average the density of the screening charge $\rho_s(\mathbf{r}, z)$ over the thickness of the 2D layer. From relationships (11), (14), and (16), it follows that

$$\rho_s(\mathbf{r}) = -\frac{2\varepsilon}{L\lambda}\frac{1}{L}\int_{-L/2}^{L/2}\varphi(\mathbf{r}, z)dz = \frac{\pm e}{4\pi\varepsilon}\frac{2\varepsilon}{L\lambda}\int_0^\infty kJ_0(kr)\Phi(k)dk, \quad (17)$$

where

$$\Phi(k) = \frac{1}{L}\int_{-L/2}^{L/2}\Phi(k, z)dz = \frac{2}{L\tilde{k}^2}\left(1 - \frac{2}{L\tilde{k}}\frac{k\varepsilon_{rm}\sinh(\tilde{k}L/2)}{\tilde{k}\varepsilon_r\sinh(\tilde{k}L/2) + k\varepsilon_{rm}\cosh(\tilde{k}L/2)}\right),$$

and the net charge screening the electron (hole) is equal to

$$2\pi L\int_0^\infty r\rho_s(r)dr = \pm e.$$

The averaged (over the thickness of the 2D layer) screened potential of the electron (hole) is given by

$$\varphi(\mathbf{r}) = \frac{1}{L}\int_{-L/2}^{L/2}\varphi(\mathbf{r}, z)dz = -\frac{L\lambda}{2\varepsilon}\rho_s(\mathbf{r}) = \frac{\mp e}{4\pi\varepsilon r}\chi\left(\frac{r}{\lambda}; \frac{L}{\lambda}; \frac{\varepsilon_r}{\varepsilon_{rm}}\right),$$

where $\chi(r/\lambda, L/\lambda, \varepsilon_r/\varepsilon_{rm})$ is the dimensionless screening function of the Coulomb potential in the plane of the layer (quantum well) [see Eq. (17)].

In the limit of a thin 2D layer ($L \ll \lambda$) when the permittivities of the layer and the matrix are equal to each

other ($\varepsilon_r = \varepsilon_{rm}$), the screening function takes the known form [16, 20]

$$\lim_{L \ll \lambda} \chi(r/\lambda, L/\lambda) = \chi(r/\lambda) = \int_0^\infty \frac{tJ_0(T)}{t + r/\lambda} dt.$$

2.4. As follows from [7, 8, 14], the Debye–Hückel energy of the correlation interaction between a hole and electrons screening the hole is defined as $E^{(cor)} = -(E_{pn} + E_{nn}) > 0$, where E_{pn} is the energy of the Coulomb interaction between the hole and the electron cloud screening the hole and E_{nn} is the interaction energy for electrons of the cloud (with the net charge equal to $-e$).

The magnitude of the energy of the pure Coulomb interaction between two electrons and (or) holes, which are separated by the distance r and whose distribution over the 2D layer is described by relationship (8), can be written as

$$|U(r)| = \frac{e^2}{4\pi\varepsilon L^2} \int_{-L/2}^{L/2} dz \int_{-L/2}^{L/2} \frac{dz'}{\sqrt{r^2 + (z - z')^2}} = \frac{e^2}{4\pi\varepsilon r} \xi(r, L), \quad (18)$$

where

$$\xi(r, L) = \frac{2r}{L}\left[\operatorname{arcsinh}\left(\frac{L}{r}\right) + \frac{r}{L}\left(1 - \sqrt{\left(\frac{L}{r}\right)^2 + 1}\right)\right], \quad \lim_{r \gg L} \xi(r, L) = 1.$$

Then, according to [7, 8, 14], with allowance made for the fact that the interaction of charge carriers is determined by relationship (18), we obtain

$$E_{pn} = E_{np} = -\frac{e}{4\pi\varepsilon} L \int \frac{|\rho_s(\mathbf{r})| \xi(r, L)}{r} d^2\mathbf{r} < 0,$$
$$E_{nn} = E_{pp} = \frac{1}{8\pi\varepsilon} L^2 \int \rho_s(\mathbf{r}) d^2\mathbf{r} \times \int \frac{\rho_s(\mathbf{r}') \xi(|\mathbf{r} - \mathbf{r}'|, L)}{|\mathbf{r} - \mathbf{r}'|} d^2\mathbf{r}' > 0, \quad (19)$$

in which the integration is performed over the entire area S of the quantum well (2D layer), $\rho_s(\mathbf{r}) = -2\varepsilon\varphi(\mathbf{r})/L\lambda$ is the density of the charge screening the "central" hole (electron) of the cloud [expression (17)], and $\xi(r, L)$ is defined by expression (18).

By using expressions (19), the correlation energy $E^{(cor)}$ at $0.03 < \lambda/L < 30$ (experimentally actual range) can be approximated by the following relationship:

$$E^{(cor)} = -(E_{pn} + E_{nn}) \approx 1.3 \ln\left(1 + 0.77\left(\frac{\lambda}{L}\right)^{0.74}\right) \frac{e^2}{4\pi\varepsilon_r\varepsilon_0\lambda}. \quad (20)$$

Since, the screening length λ, which is defined by relationship (12), does not depend on the thickness L of the 2D layer, it follows from expression (20) that the energy $E^{(cor)}$ increases with a decrease in L.

2.5. Now, we separately calculate the energies of exchange interactions between degenerate electrons and holes at temperature $T \longrightarrow 0$ with inclusion of the electrostatic potential fluctuations along the 2D layer.

According to [22, 23], the energy of the exchange interaction between an electron (hole) with the wave vector $\mathbf{k}$ and the other electrons (holes) of the 2D layer at the first quantum level can be represented in the form

$$E^{(exc)}_{n(p)}(\mathbf{k}) = \sum_{\mathbf{k}'} \int_{-L/2}^{L/2} dz' \int_{-L/2}^{L/2} dz \int d^2\mathbf{r} \int \frac{e^2}{4\pi\varepsilon|\mathbf{r} - \mathbf{r}'|} \times \Psi^*_{\mathbf{k}}(\mathbf{r}, z)\Psi^*_{\mathbf{k}'}(\mathbf{r}', z')\Psi_{\mathbf{k}}(\mathbf{r}', z')\Psi_{\mathbf{k}'}(\mathbf{r}', z) d^2\mathbf{r}'$$
$$= \frac{e^2}{2\varepsilon} \sum_{\mathbf{k}'} \frac{1}{|\mathbf{k} - \mathbf{k}'|} \longrightarrow \frac{e^2}{2\varepsilon} \frac{1}{(2\pi)^2} \int_{k' < k_{n(p)}} \frac{d^2\mathbf{k}'}{|\mathbf{k} - \mathbf{k}'|}.$$

Here, the wave function of the electron (hole) $\Psi_{\mathbf{k}}(\mathbf{r}, z)$ is defined by formula (9) and

$$k_{n(p)} = [2m^{(xy)}_{n(p)}(F_{n(p)} - U)/\hbar^2]^{1/2}$$

is the two-dimensional quasi-wave vector of the Fermi electron (hole) with the potential energy U and the maximum kinetic energy $F_{n(p)} - U$ in the 2D layer region.

As follows from [22, 23], the expression for the average [over the two-dimensional wave vector $\mathbf{k}$ of electron (hole)] energy of the exchange interaction per electron (hole) at $T \longrightarrow 0$ can be rearranged to the form (cf. [24])

$$E^{(exc)}_{n(p)} = \frac{1}{2} \frac{1}{\pi k^2_{n(p)}} \int_{k < k_{n(p)}} E^{(exc)}_{n(p)}(\mathbf{k}) d^2\mathbf{k} = \frac{e^2}{2(2\pi)^3\varepsilon k^2_{n(p)}} \times \int_{k < k_{n(p)}} d^2\mathbf{k} \int_{k' < k_{n(p)}} \frac{d^2\mathbf{k}'}{|\mathbf{k}' - \mathbf{k}|} \approx 0.42 \frac{e^2}{4\pi\varepsilon} k_{n(p)}. \quad (21)$$

The averaging of the energy defined by relationship (21) over the 2D layer at $W \gg k_B T$ gives the aver-

age energy of the electron–electron (hole–hole) exchange interaction per charge carrier, which is independent of the layer thickness L, that is,

$$\overline{E_{n(p)}^{(\mathrm{exc})}} = \int_{-\infty}^{+\infty} E_{n(p)}^{(\mathrm{exc})} G_{n(p)} dU \approx 0.42 \frac{e^2 \sqrt{2m_{n(p)}^{(xy)}}}{4\pi\varepsilon\hbar} \times \int_{-\infty}^{F_{n(p)}} (F_{n(p)} - U)^{1/2} G_{n(p)} dU > 0, \quad (22)$$

where the Fermi quasi-level $F_{n(p)}$ is determined from Eq. (4) taking into account Eq. (3).

Thus, relationships (1), (20), and (22) describe the energy-gap renormalization $\Delta E_g > 0$ in a 2D layer upon photoexcitation of the electron–hole plasma in the layer.

2.6. Let us now determine the luminescence line shape upon recombination of electrons and holes in a 2D layer as a function of their concentration and temperature.

Since the nonequilibrium charge carriers themselves produce the electrostatic potential relief along the 2D layer, the "vertical" and "nonvertical" events of recombination of an electron with a hole in the energy–coordinate space (the **r** space) can be considered equiprobable. This assumption distinguishes the proposed model from the model of band-to-band recombination, which accounts for the fluctuation potential of impurity ions in a 3D compensated semiconductor [25–27].

The probability of the recombination between the electron with the kinetic energy $E_c - U_c$ and the hole with the energy $E_v - U_v$ in the energy–quasi-momentum space (the **k** space) will be designated as P_{cv}. Let us consider two limiting cases: (i) the electron transitions from the c band to the v band are allowed without observance of the quasi-momentum selection rules when $P_{cv} = 1$ at all the energies $E_c - U_c$ and $E_v - U_v$, and (ii) only vertical transitions (the quasi-momenta of the electron and the hole are equal to each other) are allowed when

$$P_{cv} = \delta(m_n^{(xy)}(E_c - U_c) - m_p^{(xy)}(E_v - U_v)).$$

Without regard for the quasi-wave vector selection rules for electrons and holes, the spectral distribution of the photoluminescence intensity $I(\hbar\omega)$ with the photon energy $\hbar\omega$ is described by the relationship

$$I(\hbar\omega) \propto \int_{-\infty}^{+\infty} f_n(E_c) f_p(\hbar\omega - E_g' - E_c) dE_c \times \int_{-\infty}^{E_c} G_n(U_c) dU_c \int_{-\infty}^{\hbar\omega - E_g' - E_c} G_p(U_v) dU_v, \quad (23)$$

where $E_g' = E_{g0} + E_{1n} + E_{1p} - \Delta E_g$ is the band gap in the photoexcited 2D layer. The Fermi quasi-level $F_{n(p)}$ in the function $f_{n(p)}$ is determined by relationships (2).

Note that expression (23) specifies the known relationship for the intensity $I(\hbar\omega)$ of the band-to-band recombination radiation [4, 5] for the case of Gaussian fluctuations in the potential energy of an electron (hole) along the 2D layer. The photoluminescence without observance of the quasi-wave vector selection rules and in the absence of fluctuations in the potential energy of electrons and holes along the 2D layer [at $G_{n(p)} \longrightarrow \delta(U)$] was considered by Afonenko *et al.* [28].

In the case when only vertical electron transitions from the c band to the v band of the 2D layer in the **k** space are taken into account, formula (23) can be rearranged to the form

$$I(\hbar\omega) \propto \int_{-\infty}^{+\infty} G_n(U_c) dU_c \times \int_{-\infty}^{\hbar\omega - E_g' - U_v} G_p(U_v) f_n(E_{cc}) f_p(E_{vv}) dU_v, \quad (24)$$

where the total energies of the electron E_{cc} and the hole E_{vv} with the same quasi-wave vectors at the first quantum level in the c and v bands are as follows:

$$E_{cc} = \frac{m_p^{(xy)}(\hbar\omega - E_g' - U_v) + m_n^{(xy)} U_c}{m_n^{(xy)} + m_p^{(xy)}},$$

$$E_{vv} = \frac{m_n^{(xy)}(\hbar\omega - E_g' - U_c) + m_p^{(xy)} U_v}{m_p^{(xy)} + m_n^{(xy)}}.$$

3. COMPARISON BETWEEN RESULTS OF CALCULATIONS AND EXPERIMENTAL DATA

First, we evaluate the ratios between the energies W, $E^{(\mathrm{cor})}$, and $\overline{E_{n(p)}^{(\mathrm{exc})}}$, which, according to formulas (10), (20), and (22), characterize the electron–hole plasma in the GaAs 2D layer (L = 10 nm and ε_r = 12.4). For this quantum well, an increase in the concentration of nonequilibrium charge carriers from $n = p = 10^{11}$ to 3×10^{13} cm^{-2} leads to an increase in the ratio $(\overline{E_n^{(\mathrm{exc})}} + \overline{E_p^{(\mathrm{exc})}})/E^{(\mathrm{cor})}$ from 0.4 to 8 and the ratio $W/E^{(\mathrm{cor})}$ from 0.7 to 7.

Figure 1 displays the dependences of the band-gap renormalization $\Delta E_g = E^{(\mathrm{cor})} + \overline{E_n^{(\mathrm{exc})}} + \overline{E_p^{(\mathrm{exc})}} > 0$ on the concentration of nonequilibrium electrons (holes) for the GaAs quantum well in an $Al_xGa_{1-x}As$ matrix. The calculation of $\Delta E_g = E_g - E_g' > 0$ was performed

according to relationships (1), (20), and (22) at $L = 10$ (curve *1*) and 2 nm (curves *2*, *3*). The parameters used in the calculations were as follows: $m_n^{(xy)} = 0.0665m_0$, $m_{ph}^{(xy)} = m_p^{(xy)} = 0.11m_0$, and $\varepsilon_r = \varepsilon_{rm} = 12.4$. The experimental data shown by open triangles and circles (*a* and *b*) were taken from the review [4], and those designated by closed squares (*c*) were taken from [5]. The latter data for $L = 2.3$ nm correspond to the case when the bottom of the *c* band in an $Al_xGa_{1-x}As$ matrix which contains the GaAs 2D layer lies below the bottom of the *c* band in this layer [12]. The relative permittivity of the GaAs 2D layer at liquid-helium temperatures is $\varepsilon_r = 12.4$ (as in the 3D crystal [29]), and the relative permittivity of the matrix AlAs is $\varepsilon_{rm} = 10.1$.

As the concentration of nonequilibrium electrons and holes increases from $n = p = 10^{11}$ to 3×10^{13} cm^{-2}, the screening length λ calculated by formula (13) decreases from 5.4 to 2 nm, so that the condition for the applicability of approximation (20) for the correlation energy $E^{(cor)}$ is fulfilled for the data shown in Fig. 1.

At a weak photoexcitation of the GaAs 2D layers with thickness $L < 3$ nm, the indirect electron–hole radiative transitions are observed both in the coordinate and quasi-momentum spaces (*X* transitions). However, at a strong excitation, owing to the band-gap renormalization, the number of the direct Γ transitions typical of thicker 2D layers [12] becomes considerable and even predominant. Since the electrons are partly distributed outside the GaAs 2D layer, their contribution to the screening of the electron–hole interaction is smaller than the contribution of the heavy holes located inside the 2D layer. Consequently, the electrons distributed outside the 2D layer serve as the background which provides the electroneutrality of the system and affects the root-mean-square fluctuations $W_n = W_p$. In this respect, the calculations of ΔE_g were performed for two limiting cases: (i) the nonequilibrium electrons are distributed outside the 2D layer (Fig. 1, curve *2*), and (ii) the nonequilibrium electrons reside within the 2D layer (Fig. 1, curve *3*).

The ΔE_g values calculated under the assumption that the fluctuation potential is absent ($W \ll F_{n(p)}$) in the two-dimensional degenerate electron–hole plasma ($k_BT \ll F_{n(p)}$) are also shown in Fig. 1 (curves *4*, *5*). In this case, relationship (13) for the distance of the electrostatic field screening in the (100) plane of a "perfect" GaAs 2D layer at $n = p$ gives

$$\lambda = \frac{2\pi\varepsilon_r\varepsilon_0\hbar^2}{e^2(m_n^{(xy)} + m_p^{(xy)})} = 1.85 \text{ nm}. \quad (25)$$

Taking into account this result, the correlation energy $E^{(cor)}$ defined by expression (20) does not depend on the concentration of electrons and holes.

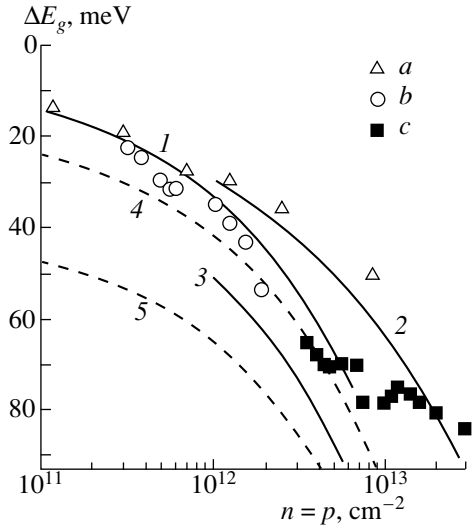

Fig. 1. Dependences of the band-gap renormalization ΔE_g on the concentration of nonequilibrium electrons (holes) for the GaAs quantum well in an $Al_xGa_{1-x}As$ matrix at $T = 4.2$ K. Points are the experimental data taken from (*a*, *b*) the review [4] at $L = 10$ nm and (*c*) [5] at $x = 1$ and $L = 2.3$ nm. Solid lines correspond to the calculations of ΔE_g from expressions (1), (19), and (22) at $L =$ (*1*) 10 and (*2*, *3*) 2 nm. The screening lengths are calculated taking into account (*1*, *3*) electrons and holes ($n = p$) and (*2*) only holes ($n \ll p$). Dashed lines represent the results of calculations without regard for the fluctuation potential ($W \ll F_{n(p)}$) at $L =$ (*4*) 10 and (*5*) 2 nm.

At $W \ll F_{n(p)}$, the Fermi level $F_{n(p)} = \pi\hbar^2 n/m_{n(p)}^{(xy)}$ is determined by the electroneutrality equation (4). Then, by using relationship (22) and taking into consideration that $G_{n(p)} \longrightarrow \delta(U)$, we obtain the exchange energy per electron (hole)

$$\overline{E_{n(p)}^{(exc)}} \approx 0.42\frac{e^2\sqrt{2m_{n(p)}^{(xy)}F_{n(p)}}}{4\pi\varepsilon\hbar} = 0.42\frac{e^2}{4\pi\varepsilon}\sqrt{2\pi n}, \quad (26)$$

which is identical for the degenerate electrons and holes.

Note that the experimental data on the band-gap renormalization $\Delta E_g > 0$ taken from different works (see review [4]) are not entirely consistent with each other. Most likely, such an inconsistency can be associated with different methods used in these works for estimating the concentration of nonequilibrium electrons and holes in the 2D layer. However, as was shown in [4, 5], ΔE_g increases with a decrease in the thickness *L* of the quantum well (2D layer). This is confirmed by our calculations (Fig. 1).

The photoluminescence spectra calculated from expression (24) for the GaAs quantum well with thickness $L = 10$ nm in an AlAs matrix at temperature $T = 4.2$ K and concentrations $n = p = 10^{11}$ and 3×10^{12} cm^{-2} are depicted in Fig. 2 (solid curves *1*, *3*). For this quan-

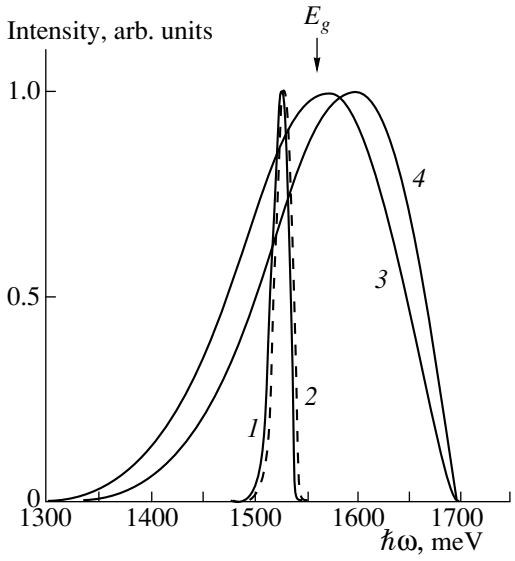

Fig. 2. Calculated photoluminescence spectra of the GaAs quantum well with the thickness $L = 10$ nm at $T = 4.2$ K for concentrations of nonequilibrium electrons and holes $n = p = (1, 2)\ 10^{11}$ and $(3, 4)\ 3 \times 10^{12}$ cm^{-2}. Curves *1* and *3* correspond to the calculations according to formula (24). Curves *2* and *4* represent the data calculated from expression (23).

tum well, according to [12], the energy gap in the absence of photoexcitation is $E_g = E_{g0} + E_{1n} + E_{1p} = 1564$ meV (where $E_{g0} = 1519$ meV, $E_{1n} = 38.2$ meV, and $E_{1p} = 6.6$ meV), $\Delta E_g = 18.7$ meV at $n = p = 10^{11}$ cm^{-2}, and $\Delta E_g = 43.1$ meV at $n = p = 3 \times 10^{12}$ cm^{-2}. The photoluminescence spectra computed by formula (23) without regard for the wave vector selection rules are displayed by dashed curves *2* and *4*. As can be seen, the difference between the photoluminescence spectra calculated in the framework of the proposed model with and without regard for the quasi-momentum selection rules is insignificant.

4. CONCLUSION

Thus, the electrostatic model for calculating the band-gap renormalization $\Delta E_g > 0$ upon strong photoexcitation of the 2D crystal layer was proposed. The fluctuation electrostatic potential produced by the photoexcited electron–hole plasma along the 2D layer was taken into consideration for the first time. The exchange and correlation energies of interactions between electrons and holes were calculated. The photoluminescence line shape for the GaAs 2D layer in an AlGaAs matrix was computed with due regard for only the first quantum levels in the *c* and *v* bands. The calculated values of the band-gap renormalization are in agreement with the available experimental data.

ACKNOWLEDGMENTS

We are grateful to F.N. Borovik and E.F. Kislyakov for their participation in discussions of the results.

This work was supported in part by the Belarussian Foundation for Basic Research, project no. F97-246.

REFERENCES

1. S. Schmitt-Rink, D. S. Chemla, and D. A. B. Miller, Adv. Phys. **38** (2), 89 (1989).
2. S. Das Sarma, R. Jalabert, and S.-R. Eric Yang, Phys. Rev. B **41** (12), 8288 (1990).
3. L. K. Kulik, A. I. Tartakovskiĭ, A. V. Larionov, *et al.*, Zh. Éksp. Teor. Fiz. **112** (1), 353 (1997) [JETP **85**, 195 (1997)].
4. R. Cingolani and K. Ploog, Adv. Phys. **40** (5), 535 (1991).
5. W. Langbein, S. Hallstein, H. Kalt, *et al.*, Phys. Rev. B **51** (3), 1946 (1995).
6. O. V. Volkov, E. V. Zhitomirskiĭ, I. V. Kukushkin, *et al.*, Pis'ma Zh. Éksp. Teor. Fiz. **66** (11), 730 (1997) [JETP Lett. **66**, 766 (1997)].
7. N. A. Poklonski, A. I. Siaglo, and F. N. Borovik, Fiz. Tekh. Poluprovodn. (St. Petersburg) **30** (10), 1767 (1996) [Semiconductors **30**, 924 (1996)].
8. N. A. Poklonski and A. I. Siaglo, Zh. Prikl. Spektrosk. **64** (3), 367 (1997).
9. P. Y. Yu and M. Cardona, *Fundamentals of Semiconductors: Physics and Materials Properties* (Springer-Verlag, Berlin, 1999), Chap. 9.
10. I. A. Merkulov and A. V. Rodina, Fiz. Tekh. Poluprovodn. (St. Petersburg) **28** (2), 321 (1994) [Semiconductors **28**, 195 (1994)].
11. J. M. Luttinger, Phys. Rev. **42** (4), 1030 (1956).
12. A. Franceschetti and A. Zunger, Phys. Rev. B **52** (20), 14664 (1995).
13. N. A. Poklonski and A. I. Siaglo, in *Proceedings of the Third Conference on Laser Physics and Spectroscopy, Grodno, 1997* (Minsk, 1997), Vol. 1, p. 354.
14. N. A. Poklonski and A. I. Siaglo, in *Physics, Chemistry, and Application of Nanostructures*, Ed. by V. E. Borisenko *et al.* (World Scientific, Singapore, 1997), p. 125.
15. V. K. Kononenko and D. V. Ushakov, Phys. Status Solidi B **211** (2), 743 (1999).
16. A. Ya. Shik, Fiz. Tekh. Poluprovodn. (St. Petersburg) **29** (8), 1345 (1995) [Semiconductors **29**, 697 (1995)].
17. V. F. Weisskopf, Usp. Fiz. Nauk **103** (1), 155 (1971); *Modern Physics from an Elementary Point of View*, Lectures given in the Summer Vacation Programme 1969 (CERN, Geneva, 1970).
18. A. B. Shmidt, *Statistical Thermodynamics of Classical Plasma* (Énergoatomizdat, Moscow, 1991).
19. A. Isihara, *Electron Liquids* (Springer-Verlag, Berlin, 1998).
20. N. S. Rytova, Vestn. Mosk. Univ., Ser. 3: Fiz., Astron., No. 3, 30 (1967).
21. T. Ando, A. Fowler, and F. Stern, *Electron Properties of Two-Dimensional Systems* (American Physical Society, New York, 1982; Mir, Moscow, 1985), p. 28; Rev. Mod. Phys. **54** (2), 437 (1982).

22. N. W. Ashcroft and N. D. Mermin, *Solid State Physics* (Holt, Rinehart, and Winston, New York, 1976; Mir, Moscow, 1979), Vol. 1.

23. O. V. Konstantinov, O. I. Obolenskiĭ, and B. V. Tsarenkov, Fiz. Tekh. Poluprovodn. (St. Petersburg) **31** (5), 571 (1997) [Semiconductors **31**, 480 (1997)].

24. A. V. Chaplik, Zh. Éksp. Teor. Fiz. **60** (5), 1845 (1971) [Sov. Phys. JETP **33**, 997 (1971)].

25. V. L. Bonch-Bruevich and S. G. Kalashnikov, *Physics of Semiconductors* (Nauka, Moscow, 1990), Chap. 19.

26. A. P. Levanyuk and V. V. Osipov, Usp. Fiz. Nauk **133** (3), 427 (1981) [Sov. Phys. Usp. **24**, 187 (1981)].

27. Yu. Ya. Tkach, Zh. Éksp. Teor. Fiz. **101**, 203 (1992) [Sov. Phys. JETP **74**, 109 (1992)].

28. A. Afonenko, V. K. Kononenko, I. S. Manak, and V. A. Shevtsov, Fiz. Tekh. Poluprovodn. (St. Petersburg) **31** (9), 1087 (1997) [Semiconductors **31**, 929 (1997)].

29. *Semiconductors—Basic Data*, Ed. by O. Madelung (Springer-Verlag, Berlin, 1996).

Translated by O. Borovik-Romanova

Physics of the Solid State, Vol. 43, No. 1, 2001, pp. 166–168. Translated from Fizika Tverdogo Tela, Vol. 43, No. 1, 2001, pp. 159–161.

LOW-DIMENSIONAL SYSTEMS AND SURFACE PHYSICS

Plasma Radiation from Sodium Films Induced by Slow Electrons

B. V. Stetsenko and A. I. Shchurenko

Institute of Physics, National Academy of Sciences of Ukraine, pr. Nauki 144, Kiev, 030339 Ukraine

e-mail: stetsen@iop.kiev.ua

Received March 23, 2000

Abstract—The radiation emitted by sodium films in the 2.5–5 eV photon energy range as a result of bombardment by 300-eV electrons is measured. It is shown that the feature observed in the region of 4 eV is associated with the radiative decay of surface plasmons, while the radiation emitted at 4.6 and 4.68 eV is due to the radiative decay of multipole plasmons. © *2001 MAIK "Nauka/Interperiodica".*

The advances made as a result of theoretical and experimental investigations of the dynamic screening of a field by a metal surface [1–6] provided additional information on the dispersion of surface plasmons and led to the prediction of a new branch of surface waves (multipole plasmons) interacting with the bulk optical waves at a frequency $\omega = 0.8\omega_p$, where ω_p is the plasma frequency.

We present below the results of investigations of multipole plasmons emerging in sodium films as a result of bombardment of the surface by low-energy electrons.

1. EXPERIMENTAL TECHNIQUE

The films studied by us were prepared by depositing 99.99% pure sodium metal on a tantalum ribbon by thermal vaporization at a rate of 10 nm/s. The residual gas pressure in the experimental tube was 10^{-10} Torr. A copper source was used for sputtering. The thickness of the film under investigation was measured by a quartz balance. The tantalum ribbon could be cooled to the nitrogen temperature and heated to the melting point of sodium or even higher temperatures. Photographs obtained in a scanning electron microscope showed that the ribbon had a statistically uneven surface with a predominant period of 100–200 nm. The choice of the materials used for vaporization and for the substrate made it possible to obtain high-purity sodium films on account of the mutual insolubility of metals. Films of thickness varying between 20 and 2000 nm were studied, each film being deposited on a substrate cleaned preliminarily by heating.

The emission of sodium radiation was stimulated by a 300-eV electron beam having a cross section of 1 mm^2 on the sample and a current 3×10^{-5} A. Such a choice of parameters rules out thermal heating of the film being studied or any other kind of variation under the action of the electron beam. The angle of incidence of electrons was 45°. The electron beam was extracted from the source through a sapphire window and was focused on the inlet slit of a monochromator. The emission spectra were registered by a photoelectric multiplier (PEM) counting single-electron pulses in the interval 2.5–5 eV. The spectral response of the PEM was measured by the technique described in [7]. The transmission band width of the quartz monochromator varied in the range of measurements from 0.04 eV (at a photon energy of 5 eV) to 0.09 eV (at a photon energy of 2.5 eV). The peak intensity of the monochromatic radiation emitted by sodium films was 200–300 photons/s.

We recorded the spectrum of radiation emitted at right angles to the sample surface in a solid angle 7°. Such an aperture minimized the intensity of the transient radiation. The observed radiation was associated with the radiative decay of surface plasmons with a wave vector equal to the reciprocal of the roughness period $\mathbf{q}$; i.e., $\mathbf{q} + \mathbf{k}_{sp} = 0$, where $\mathbf{k}_{sp}$ is the surface plasmon momentum [8, 9].

2. DISCUSSION OF RESULTS

The emission spectra measured in sodium films sputtered on a substrate at 77 K are shown in Fig. 1. The peak of the spectra was displaced towards lower quantum energies with increasing film thickness, while the intensity of the radiation at the peak decreased. A splitting of the spectra was observed for films with a thickness in the interval 40–200 nm.

As a film of thickness 1700 nm deposited on a substrate at 77 K (Fig. 1) was heated to 369 K (the melting point of sodium is 370.8 K under a pressure of 760 Torr), the emission spectrum recorded at this temperature revealed not only the principal peak associated with the radiative decay of surface plasmons, but also a peak at a quantum energy of 4.6 eV (curve *1* in Fig. 2). Upon a subsequent decrease in the temperature of the substrate to room temperature, the amplitude of the subsidiary high-frequency peak decreases, while the position of the peak corresponds to a higher energy of the quanta, viz., 4.68 eV (curve *2* in Fig. 2). This peak

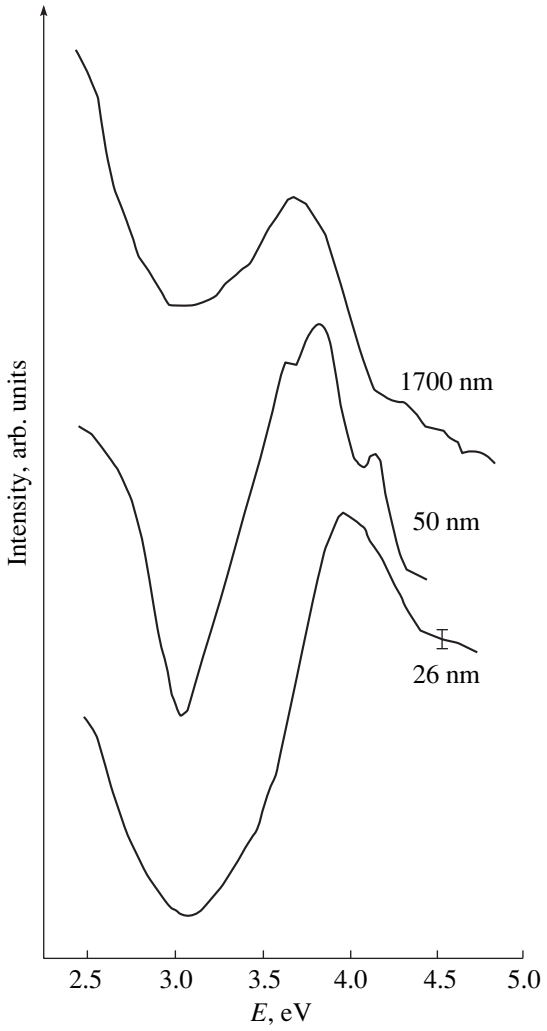

Fig. 1. Emission spectra of sodium films deposited on a substrate cooled to 77 K (the film thickness is indicated in the figure). Measurements were made at this temperature.

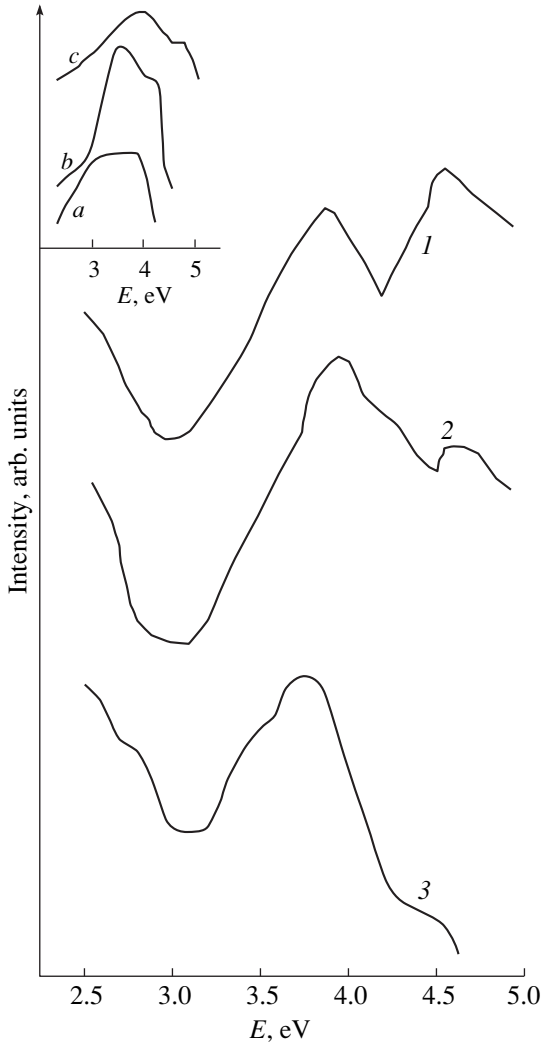

Fig. 2. Emission spectra of a sodium film of thickness 1700 nm deposited on a substrate cooled to 77 K. Spectra *1*, *2*, and *3* were recorded at a film temperature of 369 K, upon cooling to 293 K, and upon further cooling to 77 K, respectively. The inset shows the energy distribution of photoelectrons for different photon energies (eV): (*a*) 4.25, (*b*) 4.5, and (*c*) 5 [12].

disappears as the film is cooled further to 77 K (curve *3* in Fig. 2). The spectrum is reproduced upon a repetition of the heating–cooling cycle.

Among the emission spectra presented in this work, the high-frequency peaks at 4.6 and 4.68 eV formed as a result of heating of the sodium film are the most interesting ones. These peaks are in close proximity to the multipole plasmon frequency $0.8\omega_p = 4.58$ eV [5]. Such peaks, which are associated with multipole plasmons, were first detected in characteristic energy loss spectra for electrons in sodium films [4, 5]. The coincidence of frequencies in our case with the presented data unambiguously indicates that the radiative decay of multipole plasmons was observed in our experiment. Such a radiation was not detected in experiments on electron–phonon emission involving sodium films deposited on mirror surfaces of substrates [10], nor in the spectra presented in Fig. 1. This is even more astonishing in view of the fact that the effect of multipole phonons on the quantum yield has been proved convincingly in experiments on the photoelectric effect [2, 6, 11]. An increase in the quantum yield of the photoelectric effect for a photon energy close to the energy of a multipole plasmon was also observed in our experiment on the photoelectric effect in sodium films deposited on a highly polished mirror surface [12] (see inset to Fig. 2). The quantum yield of photoelectrons from sodium films of 1000 nm thickness increases at a frequency of 4.5 eV, i.e., at a frequency close to that of a multipole plasmon (see curve *b* in the inset to Fig. 2). The

increase in the quantum yield of the photoelectric effect at the multipole plasmon frequency is due to an increase in the optical wave field at the surface occurring as a result of the interaction of the bulk electromagnetic wave inducing the photoelectric effect with the surface. Such an interaction is possible if the law of conservation of the momentum component parallel to the surface is obeyed. This condition does not contradict the dispersion of multipole plasmons [5]. Hence, the radiation associated with the radiative decay of these plasmons must be observed. The fact that it has not been detected so far is probably because the phase volume occupied by a part of the dispersion curve $k_{mp} < \omega/c$ is small ($\mathbf{k}_{mp}$ is the multipole plasmon momentum). The electrons bombarding the surface mainly generate waves with a wave vector $k_{mp} = \dfrac{\omega}{c\sqrt{mc^2/2E}}$ [8]. Since we bombarded the surface with electrons having an energy of 300 eV, $k_{mp} \sim 30\omega/c$. This means that since $k_{mp} < \omega/c$, interaction with bulk waves is forbidden for most of the surface waves occupying a major part of the phase volume. Such an interaction can occur only if the surface contains inhomogeneities with a "period" $(k_{mp}/2\pi)^{-1}$ [8, 9]. Apparently, heating of the sodium film nearly to melting point in our case "roughens" the film surface to the scale $q^{-1} \sim 10$–100 Å. In this case, the law of momentum conservation is obeyed, i.e., $\mathbf{q} + \mathbf{k}_{mp} = 0$, leading to an interaction of the surface waves with the bulk waves. According to another possible mechanism, multipole plasmons are scattered at roughnesses and are transformed into plasmons with a small wave vector $k_{mp} < \omega/c$ [9]. If this is so, the mean free path of multipole plasmons must be of the order of the wavelength of light in a vacuum, i.e., 400 nm. The emergence of roughnesses upon heating of the film is due to the fact that its temperature is higher than the surface "roughening" temperature T_R at which the surface loses its smoothness and undergoes a phase transition (called the roughening transition) [13]. According to the experimental data presented in [13], $T_R = (0.6–0.7)T_m$ (T_m is the melting point). This gives the value 230 K for the T_R of sodium. Hence the "roughening" conditions are satisfied for the film under investigation at room temperature and above.

The roughness of the surface of sodium films of various thicknesses changes even at 77 K as can be seen from the spectra of surface plasmons (Fig. 1). For a small thickness (26 nm) of the deposited layer, the sodium film profile is almost identical to the profile of the substrate [9]. It can be seen from Fig. 1 that, as the film thickness increases, the principal peak is displaced towards lower quantum energies and splits into three peaks and the peak profile changes. All this qualitatively indicates a change in the spectrum of the surface roughnesses [14]. Thus, the displacement of the peak towards lower energies indicates that the roughnesses change the dispersion relation for surface plasmons, which leads to the emergence of roughnesses with a finer structure. It is quite possible that the displacement is mainly due to a broadening of the spectrum of the surface roughnesses toward shorter periods, since a frequency shift also entails a decrease in the intensity of the emitted radiation [14].

Thus, we have observed for the first time the radiation stimulated by the radiative decay of multipole plasmons in sodium films heated above the surface "roughening" temperature (roughening transition).

REFERENCES

1. P. J. Feibelman, Phys. Rev. B **9** (12), 5077 (1974).
2. L. Wallden, Phys. Rev. Lett. **54** (9), 943 (1985).
3. K. J. Song, D. Heskett, H. L. Dai, *et al.*, Phys. Rev. Lett. **61** (12), 1380 (1988).
4. K.-D. Tsuei and E. W. Plummer, Phys. Rev. Lett. **64** (1), 44 (1990).
5. K.-D. Tsuei, E. W. Plummer, A. Liebsch, *et al.*, Surf. Sci. **247**, 302 (1991).
6. G. A. Katrich, V. V. Klimov, N. V. Petrova, and I. N. Yakovkin, Izv. Akad. Nauk **58** (10), 7 (1994).
7. A. I. Shchurenko, B. V. Stetsenko, V. S. Lysenko, and I. P. Fesenko, Zh. Prikl. Spektrosk. **35** (2), 344 (1981).
8. E. Kretschmann, T. A. Callcott, and E. T. Arakawa, Surf. Sci. **91**, 237 (1980).
9. *Surface Polaritons*, Ed. by V. M. Agranovich and D. L. Mills (North-Holland, Amsterdam, 1982; Nauka, Moscow, 1985).
10. A. Shchurenko, Yu. Kulyupin, and B. Stetsenko, Solid State Commun. **33** (1), 141 (1980).
11. H. J. Levinson, E. W. Plummer, and P. J. Feibelman, Phys. Rev. Lett. **43** (13), 952 (1979).
12. I. I. Zelenskaya, Yu. A. Kulyupin, B. V. Stetsenko, *et al.*, Fiz. Tverd. Tela (Leningrad) **28** (4), 1208 (1986) [Sov. Phys. Solid State **28**, 677 (1986)].
13. J. Lapujoulade, Surf. Sci. Rep. **20**, 191 (1994).
14. M. S. Chang, T. A. Callcott, and E. Kretschmann, Surf. Sci. **91**, 245 (1980).

Translated by N. Wadhwa

Physics of the Solid State, Vol. 43, No. 1, 2001, pp. 169–175. Translated from Fizika Tverdogo Tela, Vol. 43, No. 1, 2001, pp. 162–168.

LOW-DIMENSIONAL SYSTEMS AND SURFACE PHYSICS

Kinetic Mechanism of Surface Instability Evolution during Etching, Corrosion, and Growth of Elastically Stressed Solids

Yu. G. Shreter*, Yu. T. Rebane*, D. V. Tarkhin*, B. K. Barakhtin, and V. V. Rybin****

** Ioffe Physicotechnical Institute, Russian Academy of Sciences, Politekhnicheskaya ul. 26, St. Petersburg, 194021 Russia*

*** Prometei Central Research Institute of Structural Materials, nab. Monastyrski 1, St. Petersburg, 193015 Russia*

Received April 10, 2000

Abstract—Corrosion precursors in the form of microgrooves appearing on the elastically compressed surface of a silicon plate under etching are investigated. No corrosion precursors are observed on the elastically stretched surface. This distinguishes the observed effect from corrosion cracking of metals, during which corrosion usually takes place on stretched surfaces. The general dynamic model proposed for the evolution of surface microgrooves during etching, corrosion, and growth of elastically stressed solids is based on the concept of two local etching (growth) rates which are linear functions of the local stress tensor. The model describes the kinetics of the process, and the asymmetry of corrosion evolution to the deformation sign. The role of stacking faults, dislocations, and artificially created surface steps in the evolution of corrosion in stressed silicon crystals is studied. © *2001 MAIK "Nauka/Interperiodica".*

Corrosion-induced cracking of metals and alloys is usually manifested in the formation of corrosion microgrooves on a stretched surface under the action of an aggressive medium [1]. The formation of corrosive microgrooves during the etching of the surface of silicon microcrystals under elastic compression of the surface was observed by us earlier [2]. The surface relief formed as a result of etching was analyzed by Asaro and Tiller [3], Grinfeld [4], and Srolovitz [5] on the basis of a thermodynamic equilibrium model of instability of a solid surface. The kinetics of relief evolution was not analyzed, and the role of the deformation (extension or compression) mode in this effect remained unclear.

This paper is devoted to the surface instability of a stressed solid subjected to etching, i.e., to an analysis of corrosion-induced cracking of the surface of a brittle body, e.g., monocrystalline silicon, under stress. Several experiments were made on polycrystalline ribbons of Fe–3 wt % Si alloy in the form of rolled and polished strips. It was found that deformation affects the efficiency of chemical reactions, but a detailed analysis of microscopic relief as a function of strain is hampered by the structural imperfection of the alloys under investigation.

We propose a general dynamic model of relief evolution and formation of microgrooves during etching, which is based on the concept of two (normal and tan-

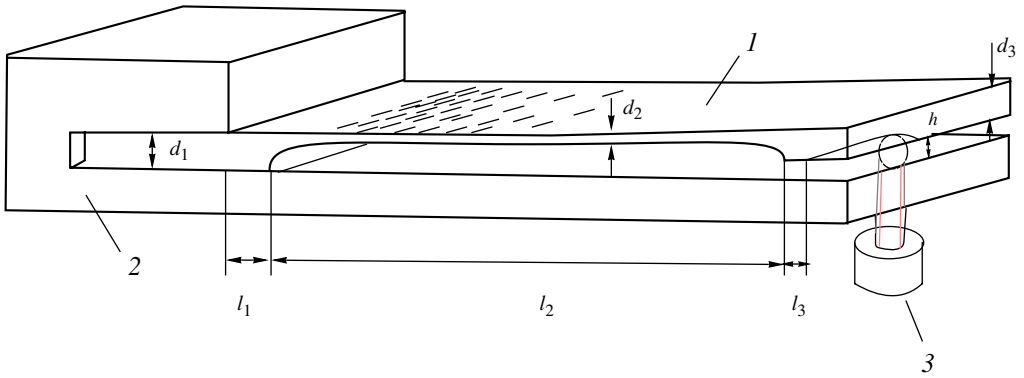

Fig. 1. (*2*, *3*) Setup for deforming the sample and (*1*) sample geometry. The sample thickness d_1 before etching is usually equal to d_3, d_2 is the thickness of the sample region under investigation, l_1 is the distance between the fixation point and the beginning of the region under investigation, l_2 is the length of the active region, l_3 is the distance from the point of application of the force through the screw *3* to the end of the region under investigation, and h is the sag of the sample being measured. The relation between the elastic strain ε varying along the investigated region and the sample parameters d, l, and h is presented in [2].

1063-7834/01/4301-0169$21.00 © 2001 MAIK "Nauka/Interperiodica"

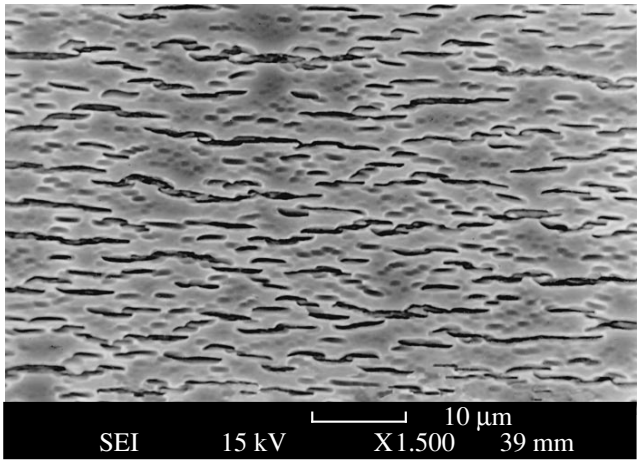

Fig. 2. Scanning electron micrograph of the surface of dislocation-free silicon after etching under elastic compression ($\varepsilon = 0.5\%$).

gential) local etching rates which are linear functions of the local stress tensor. This model explains the observed asymmetry of the effect to the deformation sign. In addition, we investigate the influence of structural defects (dislocations and oxidation-induced stacking faults), as well as inhomogeneities in the form of grooves, strips, and mesascopic structures, which are created artificially on the surface, on the form of the surface relief.

1. EXPERIMENTAL TECHNIQUE

The experiments on corrosion-induced cracking of silicon were made on a setup which was specially designed and made of teflon; this made it possible to bend a plate of the material under investigation elastically and to attain compressive and tensile strains up to 0.6% at room temperature (Fig. 1).

The sample size was $18 \times 3 \times 0.3$ mm, and the special shape of the samples is shown in Fig. 1. The central part of the samples under investigation had a thickness $d_2 = 0.1$–0.175 mm and a length $l_2 = 2$ or 8 mm and was etched by using the chemical etchant HNO_3 : CH_3COOH : HF in a ratio of 5 : 3 : 3.

The thicker part of the sample was fastened to the setup (see Fig. 1). The sample was loaded from below with the help of a gauged fluoroplastic screw (*3*) and could be controlled. The following two features of the setup used are worth noting:

(1) The proposed geometry of the sample, its fastening, and the point of application of the load made it possible to trace ("scan") the linear variation of stress over the length of the thinner part of the sample.

(2) Simultaneously, the effect of the strain sign could be verified, since one of the surfaces of the sample was subjected to compression and the other to extension.

The experiments were made at room temperature on Si samples in the elastic strain region. This allowed us to prevent the emergence of dislocations or any phase transformations which would complicate the interpretation of the effect [6, 7].

Main experiments were made on the samples of dislocation-free *p* type silicon with $\rho = 10\ \Omega$ cm, grown by the Czochralski technique. The samples were cut in the form of ribbons oriented along the $\langle 112 \rangle$ and $\langle 110 \rangle$ directions from a washer with a (111) orientation of the surface. The sample was mechanically polished and chemically etched in order to reduce the influence of surface defects. Dislocation-free silicon with a perfect structure was used to eliminate the influence of structural defects in the bulk on the phenomenon under investigation. We also studied dislocation-free Si samples with oxidation-induced stacking faults grown on the surface or with an artificially created surface relief. Some experiments were made on silicon samples containing grown-in dislocations. A number of experiments were carried out on rolled and polished ribbons made of Fe–3 wt % Si alloys and on samples of polycrystalline Si strips grown by the Stepanov method.

Corrosion effects on the surface of silicon under loading were studied using CP-4 as a polishing etchant and the Secco etching agent [8]. The choice of these etchants was dictated by their basically different response to structural defects. In contrast to CP-4, the etching rate in the Secco selective etchant increases abruptly in the region of structural defects, which is apparently associated with local deformations introduced by them. The entire construction (*2*) with the sample (*1*) (see Fig. 1) could be immersed directly in the etchant. The etching time was usually 15 s at 300 K.

2. DISCUSSION OF RESULTS

Etching of elastically stressed surfaces of silicon in the polishing etchant CP-4 left the surface smooth, while the Secco selective etchant revealed surface etching-induced defects on the compressed surface, which resembled microcracks. A typical pattern of a silicon surface obtained by using scanning electron microscopy after etching in Secco under elastic compression (strain $\varepsilon = 0.5\%$) is shown in Fig. 2. Etching-induced surface defects have a structure extended at right angles to the compression axis with a typical size of 1 μm along the compression axis and up to 10 μm at right angles to this axis if etching is carried out in Secco for 15 s. A typical cross-sectional profile of the defects obtained by atomic-force microscopy is shown in Fig. 3.

The distribution of etching-induced defects on surfaces with artificially created steps having a height of ~2 μm, obtained by using scanning electron microscopy, are presented in Figs. 4a and 4b. It can be seen that the step oriented along the compression axis does not affect the distribution of defects (see Fig. 4a), while

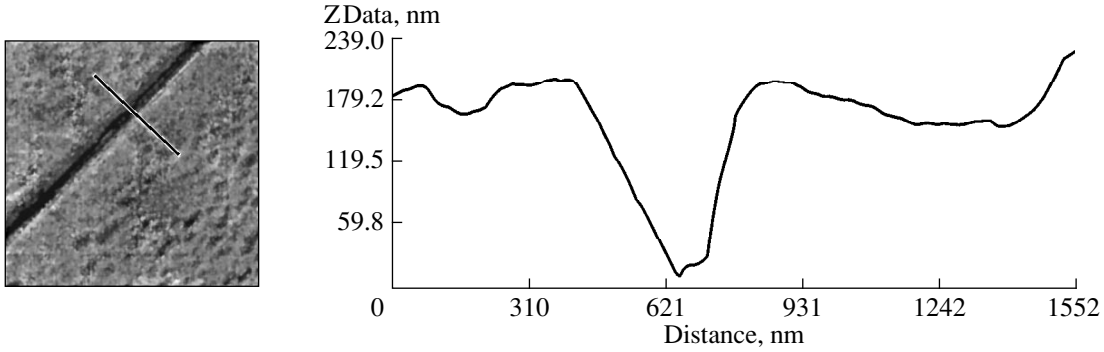

Fig. 3. Atomic-force micrograph of the surface etching-induced defect. The depth of the relief in nanometers is laid along the ordinate axis, and the distance on the sample surface across the surface defect is laid on the abscissa axis.

a defect-free zone is formed at the top of the step oriented at right angles or any other angle to the compression axis (see Fig. 4b). It should be noted that the size of the defect-free zone increases with the height of the artificially created step. Such a behavior reflects the redistribution of elastic stresses on profiled surfaces.

The patterns of distribution of etching-induced defects over a surface with specially created oxidation-induced stacking faults, which were obtained by using atomic-force microscopy, are presented in Figs. 5a and 5b. It can be seen that the point of emergence of a partial Frank dislocation bounding an oxidation-induced stacking fault at the surface is a source of nucleation of etching-induced surface defects. This effect can be explained by the concentration of elastic stresses in the regions where partial Frank dislocations emerge on the surface.

Figures 6a and 6b show patterns illustrating the etching of the compressed (111) surface of silicon with 60° grown-in dislocations, which were obtained by using scanning electron microscopy. It can be seen that the regions where 60° grown-in dislocations emerge on the surface serve as sources of nucleation of etching-induced surface defects. For low elastic stresses, a small fraction of dislocations initiates the growth of etching-induced surface defects. The number of such dislocations increases with the stress, attains saturation, and at still higher stresses defects can also be formed between dislocations. As in the case of oxidation-induced stacking faults and artificially created steps, the effect of grown-in dislocations on the formation of etching-induced defects can be explained by the concentration of elastic stresses in the regions of emergence of 60° dislocations at the surface.

All the above-mentioned defects do not affect the stress dependence of the density of etching-induced surface defects [2]; they only reflect the redistribution of elastic stresses. Analysis of etching-induced defects in elastically stressed polycrystalline silicon strips obtained by the Stepanov method revealed a pattern of etching-induced defect distribution on individual grains similar to that in monocrystalline silicon. Quantitative analysis of the defect density distribution as a function of strain is complicated by the ambiguity encountered in estimating this level due to the presence of grain boundaries, regions with a very high density of

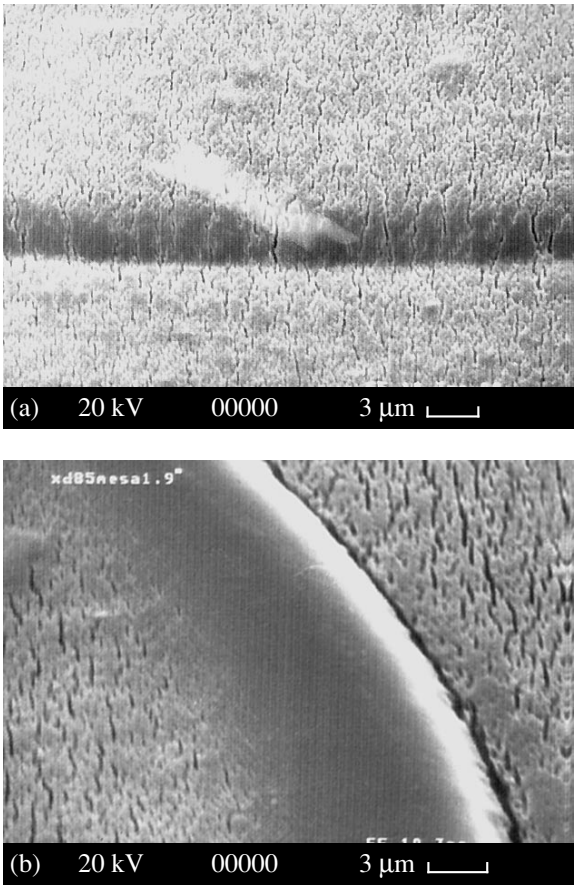

Fig. 4. Effect of surface relief and direction of compression on the distribution of etching-induced defects. Scanning electron micrograph of the surface with artificially created steps having a height of ~2 μm: (a) direct step oriented along the compression axis and (b) bent step oriented mainly at right angles to the direction of compression.

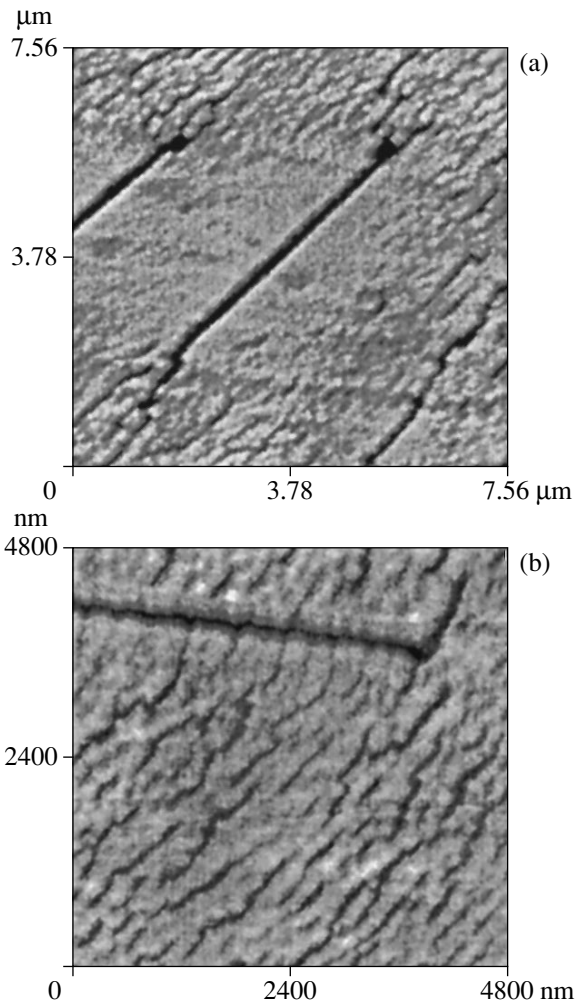

Fig. 5. Atomic-force micrograph of the etching-induced defect and specially created oxidation-induced stacking faults: (a) oxidation-induced stacking faults oriented at right angles to the compression axis and (b) oxidation-induced stacking faults oriented along the compression axis.

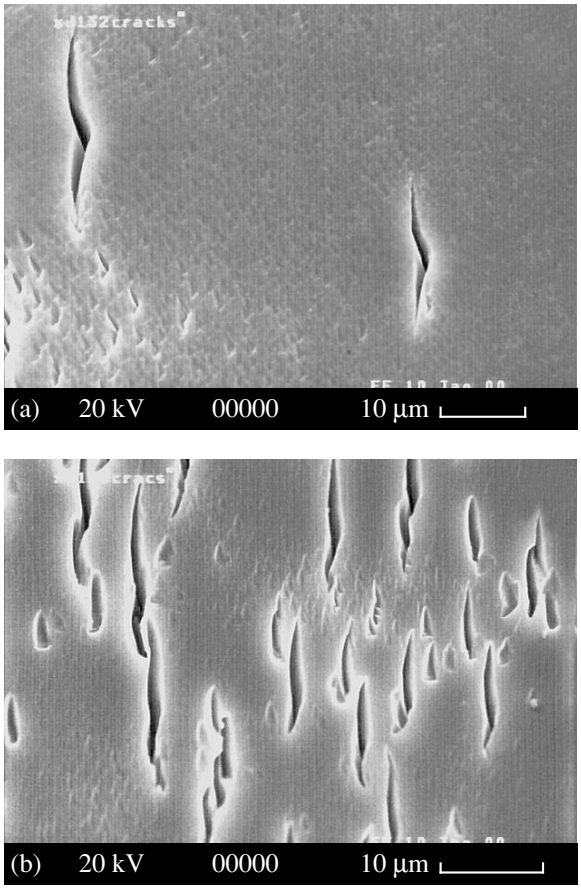

Fig. 6. Etching patterns of a compressed (111) surface of silicon with grown-in 60° dislocations obtained by scanning electron microscopy: (a) compression along ⟨112⟩ and (b) compression along ⟨110⟩.

dislocations, and built-in elastic stresses. Similar difficulties complicate the observation of etching-induced defects in more complex objects, such as alloys of iron with silicon.

The experiments aimed at the observation of etching-induced defects in silicon with a very high density of dislocations ($>10^8$ cm^{-2}) and a high boron doping level ($\rho = 0.005\ \Omega$ cm) revealed the absence of a characteristic relief of etching-induced defects even at strain levels up to 8×10^{-3}, which exceed the breakdown strain of $(5–6) \times 10^{-3}$ for ordinary monocrystalline silicon.

Study of etching kinetics on dislocation-free crystals under various stresses proved that the rate of etching out of surface defects is proportional to the elastic strain. The corresponding dependence of the reciprocal etching time to a depth of ~0.2 μm, which was determined from the instant at which the etched surface starts scattering white light, on the distance to the point of fixation of the cantilever is shown by dashed steps in Fig. 7. The solid curve shows the corresponding dependence of elastic strain ε on the distance x to the cantilever fixation point, which was calculated by formula (4) in [2]. The experimental dependence of the reciprocal etching time t^{-1} on the elastic strain ε can be described by the formula

$$t^{-1} = A(\varepsilon - \varepsilon_0), \qquad (1)$$

where $A = 10 \pm 2$ s^{-1} and $\varepsilon_0 = 0.0002 \pm 0.0002$.

We propose a general model of etching for theoretically describing the kinetics of surface relief evolution on the elastically compressed surface of a solid. The model is based on the concept of two local etching rates, i.e., the normal ν_n and tangential ν_t, which are linear functions of the isotropic part of the local stress tensor $\sigma(r) = \mathrm{Tr}(\sigma_{ik}(r))$. The advantage of this model is its applicability to all solids, including amorphous, microcrystalline, and crystalline materials. The correspond-

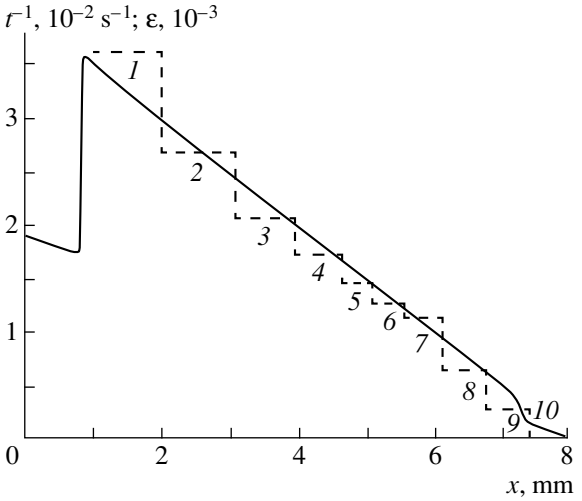

Fig. 7. Dependence of reciprocal etching time (to a depth of ~0.2 μm) on the distance to the cantilever fixation point (dashed steps). The etching depth was determined from the onset of scattering of white light by the etched surface. The solid line describes the theoretical dependence of elastic strain ε on the distance to the cantilever fixation point.

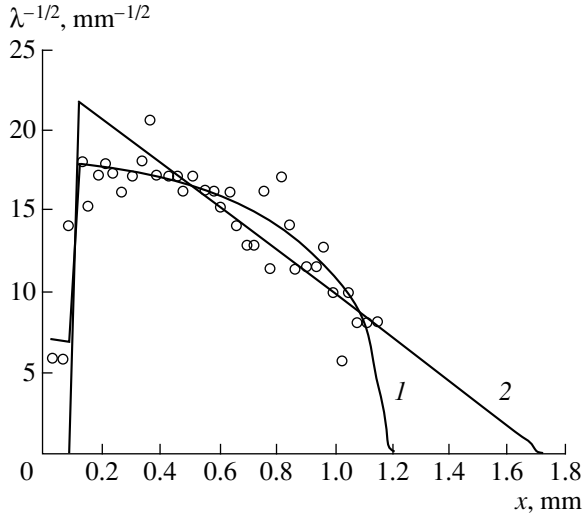

Fig. 8. Experimental dependence of the quantity $\lambda^{-1/2}$ as a function of the distance x to the fixation point, as well as the theoretical curves *1* and *2* calculated on the basis of formulas (8) and (9), respectively.

ing kinetic equation describing the time evolution of the surface relief profile $h(r, t)$ has the form

$$\begin{aligned} dh(r,t)/dt &= -[\nu_n + \sigma(r)(d\nu_n/d\sigma)] \\ &- [\nu_t + \sigma(r)(d\nu_t/d\sigma)]|\nabla h(r,t)|, \end{aligned} \tag{2}$$

where ν_n, ν_t, $d\nu_n/d\sigma$, and $d\nu_t/d\sigma$ are the experimentally determined empirical parameters. For $|\nabla h(r, t)| < 1$, the relation between $\sigma(r)$ and $h(r, t)$ is linear and the corresponding functional can be determined with the help of Green's function for the elastic isotropic half-space [9]:

$$\begin{aligned} \sigma(r) &= \sigma_{xx} + \sigma_{yy} = \sigma^0_{xx} + \sigma^0_{yy} + (\sigma^0_{yy} - \sigma^0_{xx}) \\ &\times \left[\frac{1+\nu}{2\pi^2} \int dq_x dq_y \frac{q_x^2}{\sqrt{q_x^2 + q_y^2}} e^{i(q_x r_x + q_y r_y)} \right. \\ &\left. \times \int dr'_x dr'_y e^{-i(q_x r'_x + q_y r'_y)} h(r') \right]. \end{aligned} \tag{3}$$

The exact solution of the integro-differential equations (2) and (3) cannot be presented analytically; consequently, analysis of the kinetics of evolution of the surface relief involves numerical simulation on a computer.

However, neglecting the off-diagonal component of functional (3) in quasi-momentum, we can obtain an approximate analytic solution of Eqs. (2) and (3), which has the following form for $\sigma_{yy} = 0$:

$$h(x, t) = \frac{1}{2\pi} \int dq e^{iqr_x} h_q(r), \tag{4}$$

where

$$\begin{aligned} h_q(t) &= \exp\{t/\tau_q(t)\} h_q(0), \\ 1/\tau_q(t) &= 2(\nu+1)\sigma^0 q \\ &\times (d\nu_n/d\sigma - q h_q(t) d\nu_t/d\sigma) - q\nu_t. \end{aligned} \tag{5}$$

Equation (5) implies that the reciprocal characteristic time $1/\tau_q(t)$ of evolution of a relief with a preset wave vector q is a linear function of the applied stress σ^0, which is in accord with the experimental data presented in Fig. 7.

Moreover, Eq. (5) shows that the evolution of a relief with a preset wave vector q terminates at a certain instant t_0 when it reaches the depth $h_q(t_0)$ defined as

$$\begin{aligned} h_q(t_0) &= \{(d\nu_n/d\sigma)/(d\nu_t/d\sigma) \\ &- \nu_t/[2(\nu+1)\sigma^0(d\nu_t/d\sigma)]\}/q. \end{aligned} \tag{6}$$

The approximate solution (5) implies the independent evolution of modes with different wave vectors q. However, the inclusion in Eq. (3) of the off-diagonal terms in q leads to suppression of modes with large values of q by modes with small values of q for comparable depths of the relief. Consequently, by transforming Eq. (6), we can derive a relation between the characteristic depth h_q of the relief obtained as a result of etching and its characteristic wave vector q:

$$\begin{aligned} q &= \{(d\nu_n/d\sigma)/(d\nu_t/d\sigma) \\ &- \nu_t/[2(\nu+1)\sigma^0(d\nu_t/d\sigma)]\}/h_q. \end{aligned} \tag{7}$$

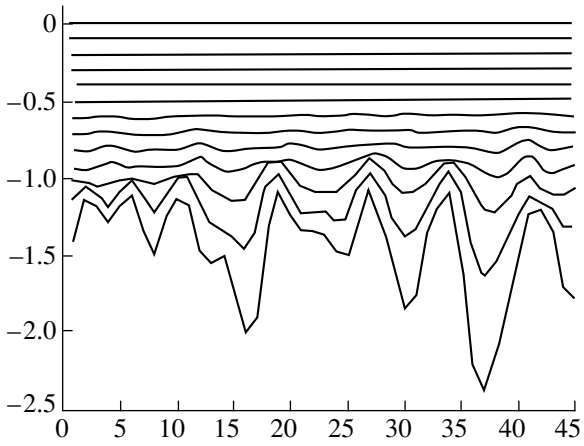

Fig. 9. Simulation of the kinetics of relief evolution on the basis of Eqs. (1) and (2). The depth of the etching profile in relative units is laid along the ordinate axis, and the distance along the direction of compression in relative units is laid along the abscissa axis. The sequence of curves (from top to bottom) reflects the variation of the relief in equal time intervals.

It can easily be seen that the characteristic wave vector q of the relief (which is inversely proportional to the characteristic wavelength $\lambda = 2\pi/q$), obtained as a result of etching, is inversely proportional to its depth h_q. For a given depth of the relief, its characteristic local wavelength λ is connected with the local deformation u_{ii} through the relation

$$\lambda \sim 1/(A - B/u_{ii}) \tag{8}$$

and not through the relation following from the theory developed by Asaro and Tiller [3] and Grinfeld [4]:

$$\lambda \sim 1/(u_{ii})^2. \tag{9}$$

Figure 8 shows the experimental dependence of the quantity $\lambda^{-1/2}$ as a function of the distance to the fixation point x, as well as the corresponding theoretical curves *1* and *2* calculated by formulas (8) and (9), respectively, taking into account the dependence $u_{ii}(x)$ presented in [2]. It can be seen that theoretical curve *1* describes the experimental data more accurately than curve *2*. Moreover, u_{ii} to the first power appears in Eq. (8) and, hence, the evolution of instability is sensitive to the sign of strain in accordance with the observed experimental data [2] and contradicts the theory developed by Asaro and Tiller [3] and Grinfeld [4].

Equation (5) shows that the instability of the etching front evolves under the condition

$$qh_q d\nu_t/d\sigma > d\nu_n/d\sigma \tag{10}$$

in the case of compression and

$$d\nu_n/d\sigma > qh_q d\nu_t/d\sigma \tag{11}$$

in the case of extension.

Inequalities (10) and (11) show that the instability evolves without a threshold (i.e., for $qh_q = 0$) for $d\nu_n/d\sigma < 0$ on a compressed surface and for $d\nu_n/d\sigma > 0$ on a stretched surface. Thus, the sign of the derivative $d\nu_n/d\sigma$ for a given combination of the material and the aggressive medium determines the surface (compressed or stretched) on which the etching relief will develop. The experimental data presented above prove that the sign of the derivative $d\nu_n/d\sigma$ is negative for a pair formed by silicon and the Secco etchant since the relief is observed on the compressed surface, while the magnitude of the derivative $d\nu_n/d\sigma$ is close to zero for the silicon–CP-4 pair since no relief is observed on either surface of the sample. For a pair formed by a metal and an aggressive medium, the sign of the derivative $d\nu_n/d\sigma$ must be positive since the corrosion-induced cracking is usually observed on a stretched surface of a metal [1].

Numerical simulation of the kinetics of relief evolution on the basis of Eqs. (2) and (3) is illustrated in Fig. 9. It can be seen that the characteristic of the relief obtained by numerical simulation correctly reflects the main features of the experimentally observed relief (see Fig. 3).

Thus, the facts presented above lead to the conclusion that the general model of etching based on the concepts of two local etching rates which are linear functions of the local stress tensor is in good agreement with the experimentally observed data.

It is interesting to note that for negative values of ν_t and ν_n, the model developed here describes the growth of anisotropically stressed crystalline films rather than of etching. Such a situation takes place, for example, for epitaxial films growing from the liquid or gaseous phase on asymmetric crystalline surfaces.

Equation (5) shows that the front instability of the surface evolves independently of the sign of the rates ν_t and ν_n under the conditions (10) or (11); i.e., the growth instability evolves without a threshold for $d\nu_n/d\sigma < 0$ in the case of an axially compressed surface and for $d\nu_n/d\sigma > 0$ in the case of an axially stretched surface.

Thus, the sign of the derivative $d\nu_n/d\sigma$, which is determined by the type of the surface, as well as by technological parameters such as temperature, pressure, and the chemical composition of the surrounding gaseous or liquid medium, determines the sample surface (compressed or stretched) on which growth instability will develop.

Thus, we have experimentally studied the kinetics of the formation of microgrooves during etching of elastically stressed surfaces of solids. It was found that stacking faults and dislocations can be centers of nucleation of microgrooves but do not affect the general form of their distribution as a function of surface stresses. The effect of the artificial surface relief is reduced exclusively to a redistribution of surface stresses and the change in the distribution of micro-

grooves associated with it. A general model of etching based on the concept of two local etching rates which are linear functions of the local stress tensor is proposed. The model provides a correct description of the dependence of the average separation between microgrooves on the magnitude and sign of the strain and makes it possible to simulate the kinetics of the formation of microgrooves. This model can also be applied for describing the instability of growth processes under uniaxial stresses.

ACKNOWLEDGMENT

This work was supported by the Russian Foundation for Basic Research, project no. 98-01-01084.

REFERENCES

1. *Chemical Encyclopedia*, Ed. by I. L. Knuyants (Sov. Éntsiklopediya, Moscow, 1983), p. 278.
2. Yu. G. Shreter, D. V. Tarkhin, S. A. Khorev, and Yu. T. Rebane, Fiz. Tverd. Tela (St. Petersburg) **41**, 1416 (1999) [Phys. Solid State **41**, 1295 (1999)].
3. J. Asaro and W. A. Tiller, Metall. Trans. **3**, 1789 (1972).
4. M. A. Grinfeld, Dokl. Akad. Nauk. SSSR **290**, 1358 (1986) [Sov. Phys. Dokl. **31**, 831 (1986)].
5. D. J. Srolovitz, Acta Metall. **37**, 621 (1989).
6. Y. G. Shreter, Y. T. Rebane, D. V. Tarkhin, S. A. Khorev, D. Cherns, and J. W. Steeds, in *Microscopy of Semiconducting Materials*, Ed. by A. G. Cullis and A. E. Staton-Bevan (Institute of Physics, Boston, 1995), p. 499; Inst. Phys. Conf. Ser. **146**, 499 (1995).
7. Y. G. Shreter, Y. T. Rebane, D. V. Tarkhin, *et al.*, Mater. Sci. Forum **196–201** (3), 1231 (1995).
8. F. Secco d'Aragona, J. Elecrochem. Soc. **119** (7), 948 (1972).
9. L. D. Landau and E. M. Lifshitz, *Course of Theoretical Physics*, Vol. 7: *Theory of Elasticity* (Nauka, Moscow, 1982; Pergamon Press, New York, 1986).

Translated by N. Wadhwa

Physics of the Solid State, Vol. 43, No. 1, 2001, pp. 17–18. Translated from Fizika Tverdogo Tela, Vol. 43, No. 1, 2001, pp. 19–20.

SEMICONDUCTORS AND DIELECTRICS

Nonlinear Magnetooptical Absorption in a Semiconductor

K. Yu. Zenkova, A. A. Zinchenko, and B. M. Nitsovich

Chernovtsy State University, ul. Kotsyubinskogo 2, Chernovtsy, 58012 Ukraine
e-mail: os-dpt@phys.chsu.cv.ua

Received June 1, 2000

Abstract—The influence of an external magnetic field on the optical characteristics of the exciton spectra of a semiconductor is studied. It is shown that the diamagnetic shift of the exciton level essentially changes the dynamics of the exciton absorption. The combination of the excitonic and magnetic properties of a crystal in the range of excitonic frequencies gives new opportunities to control the bistable behavior of the crystal. It is revealed that the magnetooptical response of the semiconductor to the laser field gives rise to bistable loops with respect to both the intensity of the incident light and the magnitude of the magnetic field. © *2001 MAIK "Nauka/Interperiodica".*

The most applicable possibilities of the creation of new optical information systems based on optical-bistability principles concern the way in which a laser field interacts with a nonlinear medium [1]. Optical studies of semiconductor materials in the visible and ultraviolet spectral ranges are particularly interesting. It is in the range of excitonic frequencies that the appearance of two and more stable optical states of a crystal provides new possibilities to record and store optical information and to control the evolution of nonlinear phenomena with the determination of their specific characteristic parameters when the external factors are changed [2]. Optical bistability can be realized by different mechanisms in which the appearance of a hysteresis loop in light transmission is associated either with a change in the laser-radiation parameters, such as frequency, intensity [3], and polarization [4], or with a change in external factors, such as pressure, temperature [5], the magnetic field, etc.

The aim of this paper is to investigate the dependence of the exciton absorption of the laser radiation on the magnetic field. If the external magnetic field is weak, the position of the excitonic level is determined by the squared magnitude of the magnetic field **H** [6]:

$$E(\mathbf{k}) = E_0 + \delta H^2 + L\left(\frac{ka}{\pi}\right)^2, \quad (1)$$

where $\delta = \dfrac{e^2 a_{ex}^2}{4\mu^*}$ and $L = \dfrac{\pi^2\hbar^2}{2m^* a^2}$ are the parameter of the diamagnetic shift and the width of the exciton band, respectively; E_0 is the bottom of the exciton band; a_{ex}, m^*, and μ^* are the radius and the effective and reduced exciton masses, respectively; e and m are the electron charge and mass, respectively; and a is the lattice constant of the crystal. A large number of articles have been devoted to the experimental investigations of the diamagnetic shift of exciton bands (see, e.g., [7]).

Investigation of the exciton spectral characteristics is connected with calculation of the system's mass operator $M = \Delta + i\Gamma$, which determines the coefficient of the excitonic absorption

$$K(\omega, H) = \frac{2\pi D_0^2}{L}\frac{\Gamma(x, h)}{[x - h - \Delta(x, h)]^2 + \Gamma^2(x, h)}. \quad (2)$$

Here, D_0 is the matrix element of the exciton–photon interaction; $x = (\hbar\omega - E_0)L^{-1}$ is the excitation frequency ω normalized to the width of the exciton band; and $h = \delta H^2 L^{-1}$ is the normalized magnitude of the magnetic field. The mass operator M is calculated by a standard method [8].

According to Eqs. (1) and (2), a shift of the exciton band to higher energies occurs as the magnetic field is increased. If the frequency of the incident light is fixed, for example, at the maximum of the absorption band x_{max}, then the crystal can be switched into the transparent regime by changing the magnitude of the magnetic field. Obviously, the extent of the crystal blooming depends on the ratio between the magnitude of the diamagnetic shift and the half-width of the band of exciton absorption. The larger their ratio, the broader the switching range.

The interaction between the crystal and the laser field leads to the generation of exciton gas of controlled density in the crystal. In this case, the coefficient of the excitonic absorption also depends on the filling numbers of the exciton states N, which are determined by the intensity of the external radiation I and (according to Eq. (1)) the magnitude of the magnetic field [8]:

$$N = IK(\omega, H). \quad (3)$$

At zero magnetic field ($H = 0$), the solution of Eq. (3) describes the standard optical bistability $I_B(I)$, since it accounts for the hysteresis loop in the dependence $N(I)$ at the fixed frequency of the input signal [3]. The

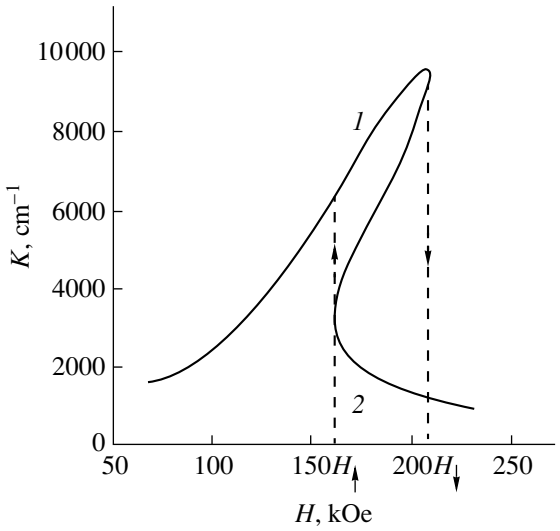

Dependence of the absorption coefficient on the magnitude of the magnetic field for the frequency of the input signal $x_S = -0.0021$.

switching-on of the magnetic field results in a shift of the exciton band and, hence, in a change in the frequency at which the optical bistability occurs. In this case, the condition

$$x_S^h = x_S + h \tag{4}$$

should be fulfilled.

There is no optical bistability at any other frequency of the input signal. This means that the frequency $x_S = x_L - h$, at which the bistable states $I_B(I)$ occur at the output in the crystal, can be achieved by varying the magnetic field H and using a laser with a given frequency $x_L > x_{\max}$.

On the other hand, the density of the exciton gas in the semiconductor is a complicated function of the magnetic field $N(H)$. The form of this dependence is determined by the balance equation (3). If the laser frequency ω_0 and intensity I_0 are fixed, the number of excitons can be calculated from the formula $K(N) = N/I_0$ for different magnitudes of the magnetic field and the dependence $N(h)$ can be determined. The calculations carried out reveal that the number of excitons in the crystal is a nonmonotonic function of the field and, in a certain range of magnetic fields, $N(h)$ exhibits an S-shaped dependence on the magnetic field. This indicates that the appearance of magnetooptical bistability is possible in these semiconductors. The calculated absorption coefficient $K(H)$ leading to the magnetooptical bistability is shown in the figure. The calculation was performed for a CdS-type semiconductor with the parameters taken from [3] and for a fixed frequency $x_S = -0.0021$. As is seen from the figure, there are two stable values of the absorption coefficient (portions *1* and *2* of the curve) in a certain range of values of the magnetic field $\Delta H = H_\downarrow - H_\uparrow$. The calculations indicate that the width of the range of the magnetooptical bistability does not depend on the frequency of the input signal. Increasing the frequency, for example, by Δx_L, we obtain an identical magnetooptical bistability but for another value of the magnetic field $H' = H + \Delta x_L$. Thus, the shift from the absorption maximum to higher energies of the spectrum requires larger fields to realize the magnetooptical bistability.

REFERENCES

1. H. Gibbs, *Optical Bistability: Controlling Light with Light* (Academic, New York, 1985; Mir, Moscow, 1988).
2. D. A. B. Miller, J. Opt. Soc. Am. B **1** (6), 857 (1984).
3. B. M. Nitsovich and C. Yu. Zenkova, Opt. Eng. **34** (4), 1072 (1995).
4. B. M. Nitsovich and K. Yu. Zenkova, Fiz. Tverd. Tela (St. Petersburg) **38** (5), 1626 (1996) [Phys. Solid State **38**, 897 (1996)].
5. G. Zartov, K. Panajotov, T. Tenev, and R. Peyeva, Proc. SPIE **3573**, 516 (1998).
6. R. P. Seĭsyan, *Spectroscopy of Diamagnetic Excitons* (Nauka, Moscow, 1984).
7. B. Evans and P. Young, Proc. Phys. Soc. London **91** (572), 475 (1967).
8. A. S. Davydov, *Theory of the Solid State* (Nauka, Moscow, 1976).

Translated by A. Poushnov

Physics of the Solid State, Vol. 43, No. 1, 2001, pp. 176–184. Translated from Fizika Tverdogo Tela, Vol. 43, No. 1, 2001, pp. 169–176.

LOW-DIMENSIONAL SYSTEMS AND SURFACE PHYSICS

Fluctuation-Induced Electromagnetic Interaction of a Moving Particle with a Plane Surface

G. V. Dedkov and A. A. Kyasov

Kabardino-Balkar State University, ul. Chernyshevskogo 173, Nalchik, 360004 Russia

e-mail: gv_dedkov@rekt.kbsu.ru

Received April 21, 2000

Abstract—The most general (nonrelativistic) formulas for the force of attraction to the surface and for the drag of a nonrelativistic atom moving parallel to it, as well as for the lateral and normal forces acting on a moving dipole molecule and on a charged particle (in the case of parallel and perpendicular motion), are derived for the first time in the framework of the fluctuational electromagnetic theory. The dependences of these forces on the velocity, temperature, separation, and dielectric properties of the atom and the surface are derived. The effect of the nondissipative resonance interaction between a moving neutral atom and the field of surface plasmons, as well as the possible emergence of a positive (accelerating) force acting on the atom (nanoprobe), is substantiated theoretically. The role of dynamic fluctuational forces and their possible experimental measurement when using the quartz microbalance technique and an atomic-force microscope (in the dynamic mode), as well as during deceleration of atomic beams in open nanotubes, are considered. The correctness of the obtained results is confirmed by their agreement with most of the available theoretical relations derived by other authors. *© 2001 MAIK "Nauka/Interperiodica".*

The study of the dynamic fluctuation-induced electromagnetic interaction of atoms and molecules with flat or bent surfaces is interesting for an analysis of the results of experiments involving various operational conditions of scanning electron probe microscopes [1, 2], as well as of the quartz microbalance technique [3–5], and in connection with the possible control of particle beams with the help of nanotubes [6].

To our knowledge, the first publications in this field appeared at the beginning of the 1980s [7–9]. It was proved that, along with the Van der Waals force of attraction to the surface, which is generally also a function of the particle velocity **V**, a drag force of the type defined in Eq. (1) also appears. In view of the apparent analogy with hydrodynamics, this force was called the "frictional force" and the proportionality factor η was called the "friction coefficient":

$$\mathbf{F} = -\eta\mathbf{V}. \tag{1}$$

Schaich and Harris [7] obtained the dependence $\eta(z) \sim z^{-10}$ for the interaction of neutral particles with a metal surface, where z is the distance to the surface. A completely different dependence ($\eta(z) \sim z^{-5}$) was derived by Mahanti [8], in our earlier publications [2, 10], and by Tomassone and Widom [11]. In particular, the following expression was obtained in [11] for the interaction of a dipole molecule with a metal surface for the dipole axis d oriented along the normal to the surface

$$\eta(z) = \frac{3d^2}{8\pi\sigma z^5} \tag{2a}$$

(σ is the electrical conductivity of the metal), while the corresponding expression for the interaction of a spherical atom with the surface has the form

$$\eta(z) = -\frac{3\hbar}{4\pi z^5}\int_0^\infty \alpha''(\omega)\Delta''(\omega)\frac{d}{d\omega} \times \frac{1}{(\exp(\omega\hbar/k_BT)-1)}d\omega, \tag{2b}$$

where $\alpha''(\omega)$ is the imaginary part of the dynamic polarizability of the atom, $\Delta(\omega) = \dfrac{\varepsilon_2(\omega)-1}{\varepsilon_2(\omega)+1}\Delta''(\omega)$ is the imaginary component of this quantity, $\varepsilon_2(\omega)$ is the dielectric constant of the medium, $\hbar$ is Planck's constant, T is the temperature, and k_B is Boltzmann's constant.

It should be noted that, in accordance with Eq. (2b), $\eta = 0$ for $T = 0$. In our opinion, this conclusion is basically incorrect. On the contrary, according to Mahanti [8] and the results obtained by us earlier [2, 10], the coefficient η does not vanish at zero temperature either. It should be noted that the authors of the above-mentioned publications used different computational methods: the methods of quantum perturbation theory [7, 8],

the formalism of Green's and Kubo's functions [11], and the fluctuational electromagnetic theory [2, 10].

A similar problem was studied recently by Pendry [12] and later by Volokitin and Persson [13], who considered the fluctuation-induced friction between two half-spaces separated by a plane gap of width z. These authors also found that the friction coefficient is equal to zero for $T = 0$ and the nonzero component of the frictional force was found to be proportional to the third power of the velocity.

Such a serious discrepancy in the obtained results necessitates a more detailed analysis of the scope of a related problem in the consistent theory of electromagnetic fluctuations [14]. The corresponding (nonrelativistic) analysis at $T = 0$ was carried out by us [10, 15] for a plane [10] and a cylindrical [15] surface. We derived general formulas for the dynamic attraction potential and the drag force acting on an atom moving parallel to the surface. The present work aims at a generalization of the results obtained in [2, 10] to the case of arbitrary temperatures and velocities for moving neutral atoms, polar molecules, and ions (in the case of a plane surface). We failed to derive final formulas for an atom moving along the normal to the surface since we could not separate the space and time variables while solving Poisson's equations.

1. AN ATOM MOVING PARALLEL TO A PLANE SURFACE: GENERAL RELATIONS

We consider a spherically symmetric atomic particle having a polarizability $\alpha(\omega)$ and moving at a nonrelativistic velocity $V \ll c$ parallel to a plane surface with a given dielectric constant $\varepsilon(\omega)$ (see figure). We assume that the distance h between the particle and the surface is much larger than the characteristic size r_0 of atoms: $h \gg r_0$. The time lag can be neglected if the following condition is observed: $\omega_0 h/c \ll 1$, where ω_0 is the characteristic frequency of the motion of electrons in the atoms. This condition implies that the time it takes for light to propagate from an atom to the surface is much shorter than the characteristic period of oscillations of atomic electrons. Spatial dispersion is disregarded here. In this case, in the range of distances $r_0 \ll h \ll c/\omega_0$, the particle can be regarded as a pointlike fluctuating dipole with zero average value of the dipole moment $\mathbf{d}^{sp}$ and a nonzero average value of the square of this quantity.

In order to calculate the dynamic potential of attraction of the atom to the surface and the frictional force in Eq. (1), we use the general equations of the nonrelativistic electromagnetic theory for a medium, as well as fluctuation–dissipation relations. We write the following expression for the polarization vector created in the medium by spontaneous fluctuations of the dipole moment $\mathbf{d}^{sp}$:

$$\mathbf{P}^{sp}(r, t) = \delta(x - Vt)\delta(y)\delta(z - h)\mathbf{d}^{sp}. \quad (3)$$

It should be noted that all the vector quantities in the theory of electromagnetic fluctuations are considered as quantum-mechanical operators in the Heisenberg representation. In order to calculate the electric field created by the polarization given by Eq. (3), we write the Poisson equation for the scalar potential [16]

$$\Delta\Phi = 4\pi \mathrm{div}\mathbf{P}^{sp} \quad (4)$$

and represent the quantities appearing in Eq. (4) in the form of Fourier integrals as functions of the variables x, y, and t:

$$\Phi(\mathbf{r}, t) = \iiint \frac{dk_x dk_y d\omega}{(2\pi)^3} \Phi_{\omega k}(z) \exp[i(k_x x + k_y y - \omega t)],$$

$$\mathbf{P}^{sp}(\mathbf{r}, t) = \iiint \frac{dk_x dk_y d\omega}{(2\pi)^3} \mathbf{P}^{sp}_{\omega k}(z) \exp[i(k_x x + k_y y - \omega t)].$$

In this case, Eq. (4) for the Fourier components assumes the form

$$\left(\frac{d^2}{dz^2} - k_x^2 - k_y^2\right)\Phi_{\omega k}(z) = 4\pi\delta(z - h)\{ik_x d_y^{sp}(\omega - k_x V) + ik_y d_x^{sp}(\omega - k_x V)\} + 4\pi\delta'(z - h)d_z^{sp}(\omega - k_x V). \quad (5)$$

A solution of this equation that satisfies the boundary conditions of continuity for the potential and the normal component of the electric induction on the surface $z = 0$ has the form [10]

$$\Phi_{\omega k}(z) = \frac{2\pi}{k} e^{-k(z+h)} \Delta(\omega)\{ik_x d_x^{sp}(\omega - k_x V) + ik_y d_y^{sp}(\omega - k_x V) + kd_z^{sp}(\omega - k_x V)\} + \frac{2\pi}{k} e^{-k|z-h|}\{-ik_x d_x^{sp}(\omega - k_x V) - ik_y d_y^{sp}(\omega - k_x V) + \mathrm{sgn}(z - h)kd_z^{sp}(\omega - k_x V)\}, \quad (6)$$

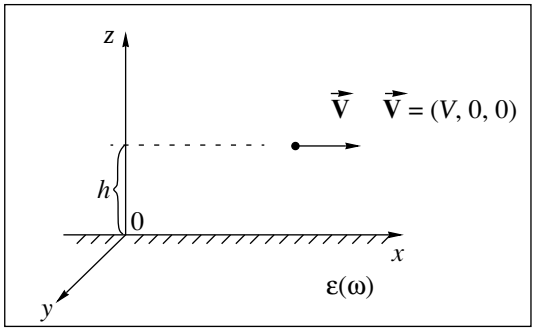

Geometry of the interaction of a particle with a plane surface.

where $k = \sqrt{k_x^2 + k_y^2}$ and $\Delta(\omega)$ has the same meaning as in Eq. (3). The first term in Eq. (6) describes the polarization potential of the medium that is associated with the fluctuation-induced electromagnetic field of the atom (this follows from the fact that $\Delta(\omega) = 0$ for $\varepsilon(\omega) = 1$), while the second term is the field produced by the fluctuating dipole.

For $T \neq 0$, the free energy (interaction potential) of a particle with the surface in the dipole approximation is defined as [17]

$$U_{\text{int}} = -\frac{1}{2}\langle \mathbf{dE}\rangle = \\ = -\frac{1}{2}\langle \mathbf{d}^{sp}\mathbf{E}^{in}\rangle = -\frac{1}{2}\langle \mathbf{d}^{in}\mathbf{E}^{sp}\rangle = U_1 + U_2, \tag{7}$$

where the angle brackets denote complete quantum-mechanical and statistical averaging, the first term being determined by spontaneous fluctuations of the dipole moment $\mathbf{d}^{sp}(t)$ of the atom, while the second is determined by fluctuations of the electromagnetic field $\mathbf{E}^{sp}(\mathbf{r}, t)$ of the surface at the point $(\mathbf{r}, t)$ where the particle is located.

In order to find U_1, we write the operators $\mathbf{d}^{sp}(t)$ and $\mathbf{E}^{in}(\mathbf{r}, t)$ in the form of Fourier integrals taking into account that the particle position vector is $\mathbf{r} = (Vt, 0, h)$ and express the Fourier component $\mathbf{E}^{in}_{\omega k}(h)$ through the induced potential $\Phi^{in}_{\omega k}(h)$ with the help of Eq. (6). Then we substitute the Fourier component of the operators $\mathbf{d}^{sp}(t)$ and $\mathbf{E}^{in}(\mathbf{r}, t)$ into Eq. (7) and expand the emerging correlators of the dipole moment by using the fluctuation–dissipation theorem [18]

$$\langle d_i^{sp}(\omega) d_k^{sp}(\omega')\rangle \\ = 2\pi\delta_{ik}\delta(\omega + \omega')\hbar\alpha''(\omega)\coth(\omega\hbar/2k_{\text{B}}T). \tag{8}$$

Finally, taking into account the analytic properties of the functions $\alpha(\omega)$ and $\varepsilon(\omega)$ associated with the evenness of the real parts and the oddness of the imaginary parts [16] and carrying out simplifying algebraic transformations, we reduce the expressions for U_1 to the form

$$U_1(h, V) \\ = -\frac{\hbar}{\pi^2}\iiint d\omega dk_x dk_y k\exp(-2kh)\coth\frac{\omega\hbar}{2k_{\text{B}}T} \tag{9}$$
$$\times\alpha''(\omega)[\Delta'(\omega - k_x V) + \Delta'(\omega + k_x V)].$$

The quantities with one or two primes correspond to the real and imaginary parts of the relevant functions. Here and below, we assume that integration is carried out over positive frequencies and wave vector components.

Similarly, in order to calculate U_2, we write $\mathbf{d}^{in}$ and $\mathbf{E}^{sp}$ in the form of Fourier integrals and substitute them into Eq. (7). Taking into account the linear relation between the induced dipole moment $\mathbf{d}^{in}$ of the particle and the fluctuational electromagnetic field $\mathbf{E}^{sp}$ of a surface atom, we obtain an expression for U_2 in the form of a multiple integral of the spectral density of the electric field fluctuations $\mathbf{E}^{sp}$. In accordance with the general results of the theory of electromagnetic fluctuations, this spectral density can be expressed in terms of the imaginary part of the retarded Green function for a photon in the medium that satisfies the equation [14]

$$\left(\text{curl}_{ik}\text{curl}_{kl} - \frac{\omega^2}{c^2}\delta_{il}\varepsilon(\omega, \mathbf{r})\right)D^R_{lm}(\omega, \mathbf{r} - \mathbf{r}') \\ = -4\pi\hbar\delta_{im}(\mathbf{r} - \mathbf{r}'). \tag{10}$$

In the nonrelativistic limit ($c \longrightarrow \infty$), the solution of Eq. (10) leads to the following expression for the spectral density of the fluctuational electromagnetic field of the surface at the point of the location of the particle ($z = h$):

$$\langle \mathbf{E}^{sp}_{\omega k}(h)\mathbf{E}^{sp}_{\omega' k'}(h)\rangle \\ = 2(2\pi)^4 k\exp(-2kh)\hbar\coth\frac{\omega\hbar}{2k_{\text{B}}T}\Delta''(\omega) \tag{11}$$
$$\times\delta(\omega + \omega')\delta(k_x + k_x')\delta(k_y + k_y').$$

Using this expression, integrating with respect to the variables ω', k_x', and k_y' and taking into account the analytical properties of the functions $\alpha(\omega)$ and $\varepsilon(\omega)$, we obtain the potential U_2:

$$U_2(h, V) = -\frac{\hbar}{\pi^2}\iiint d\omega dk_x dk_y k\exp(-2kh)\coth\frac{\omega\hbar}{2k_{\text{B}}T} \\ \times\Delta''(\omega)[\alpha'(\omega - k_x V) + \alpha'(\omega + k_x V)]. \tag{12}$$

Summing up Eqs. (9) and (12), we obtain the final formula for the potential of the interaction between a moving atom and a plane surface [2]:

$$U_{\text{int}}(h, V) = -\frac{\hbar}{\pi^2}\iiint d\omega dk_x dk_y k\exp(-2kh)\coth\frac{\omega\hbar}{2k_{\text{B}}T} \\ \times\{\alpha''(\omega)[\Delta'(\omega - k_x V) + \Delta'(\omega + k_x V)] \\ + \Delta''(\omega)[\alpha'(\omega - k_x V) + \alpha'(\omega + k_x V)]\}. \tag{13}$$

This formula is a generalization of a well-known expression for the energy of the Van der Waals interaction of a neutral spherically symmetric particle with a plane surface to the case of a finite velocity and a finite temperature of the surface. In order to prove this, we put $V = 0$ and $T = 0$ in Eq. (13). This gives

$$U_{\text{int}}(h) = -\frac{2\hbar}{\pi^2}\iiint d\omega dk_x dk_y k\exp(-2kh) \\ \times[\alpha''(\omega)\Delta'(\omega) + \alpha'(\omega)\Delta''(\omega)] \tag{14}$$

$$= -\frac{2\hbar}{\pi^2}\int\int\int d\omega dk_x dk_y k\exp(-2kh)\mathrm{Im}\int_0^\infty d\omega\alpha(\omega)\Delta(\omega).$$

Then the integral over the wave vectors k_x and k_y can be evaluated through an elementary transition to polar coordinates (the result is $\pi/8h^3$), while the integral over frequencies can be transformed by rotating the integration contour through 90° to make it coincide with the upper imaginary half-axis. This gives

$$\mathrm{Im}\int_0^\infty d\omega\alpha(\omega)\Delta(\omega) = \int_0^\infty d\omega\alpha(i\omega)\Delta(i\omega). \quad (15)$$

Ultimately, we obtain the well-known result for the static attractive potential of the atom to the surface [17]:

$$U_{\mathrm{int}}(h) = -\frac{\hbar}{4\pi h^3}\int_0^\infty d\omega\alpha(i\omega)\Delta(i\omega). \quad (16)$$

In Eq. (14), we can additionally carry out integration with respect to the variable k_y using the Sommerfeld integral representation for the MacDonald function [19]

$$K_\nu(z) = \int_0^\infty \exp(-z\cosh u)\cosh(\nu u)du, \ \mathrm{Re}z > 0, \quad (17)$$

which leads to a simpler expression for the potential:

$$U_{\mathrm{int}}(h, V) = -\frac{\hbar}{\pi^2}\int_0^\infty d\omega\int_0^\infty dk_x k_x^2(K_0(2k_x h) + K_2(2k_x h))$$

$$\times \coth\frac{\omega\hbar}{2k_{\mathrm{B}}T}\{\alpha''(\omega)[\Delta'(\omega - k_x V) + \Delta'(\omega + k_x V)] \quad (18)$$

$$+ \Delta''(\omega)[\alpha'(\omega - k_x V) + \alpha'(\omega + k_x V)]\}.$$

Let us now calculate the frictional force F. For a steady motion of the particle, this force is connected with the energy dissipation of the fluctuational electromagnetic field per unit time through the well-known relation

$$-\frac{dW}{dt} = FV = \int\langle\mathbf{jE}\rangle d^3\mathbf{r}. \quad (19)$$

The energy dissipation rate, as well as the interaction potential, can also be presented as a sum of two independent components

$$-\frac{dW}{dt} = FV = \int\langle\mathbf{j}^{sp}\mathbf{E}^{in}\rangle d^3\mathbf{r} + \int\langle\mathbf{j}^{in}\mathbf{E}^{sp}\rangle d^3\mathbf{r} \quad (20)$$

which are associated with the contributions from the fluctuating dipole moment of the atom and the fluctuational electromagnetic field of the surface, respectively, where $\mathbf{j}^{sp} = \dfrac{\partial\mathbf{P}^{sp}}{\partial t}$, $\mathbf{P}^{sp}$ is defined by formula (3), and $\mathbf{j}^{in}$ can be expressed in terms of $\mathbf{E}^{sp}$ through a linear integral relation. Carrying out calculations similar to those made above and taking into account the fluctuation–dissipation relations (8) and (11), we find [2]

$$F(h, V) = \frac{2\hbar}{\pi^2 V}\int d\omega\int\int dk_x dk_y k\exp(-2kh)\coth\left(\frac{\omega\hbar}{2kT}\right)$$

$$\times\{(\omega + k_x V)[\Delta''(\omega)\alpha''(\omega + k_x V)$$

$$-\Delta''(\omega + k_x V)\alpha''(\omega)] + (\omega - k_x V) \quad (21)$$

$$\times[\Delta''(\omega)\alpha''(\omega - k_x V) - \Delta''(\omega - k_x V)\alpha''(\omega)]\}.$$

After evaluation of the integral over k_y, formula (21) can be reduced to the double integral

$$F(h, V) = \frac{\hbar}{\pi^2 V}\int_0^\infty d\omega\int_0^\infty dk_x k_x^2[K_0(2k_x h) + K_2(2k_x h)]$$

$$\times\coth\frac{\omega\hbar}{2k_{\mathrm{B}}T}\{(\omega + k_x V)[\alpha''(\omega + k_x V)\Delta''(\omega)$$

$$-\Delta''(\omega + k_x V)\alpha''(\omega)] + (\omega - k_x V) \quad (22)$$

$$\times[\Delta''(\omega)\alpha''(\omega - k_x V) - \alpha''(\omega)\Delta''(\omega - k_x V)]\}.$$

Formulas (21) and (22) generalize the results obtained by us earlier [10] to the case of finite temperatures and make it possible to determine the frictional force for any nonrelativistic velocities without confining the analysis to the linear approximation. In the limit $V \longrightarrow 0$, Eq. (22) can be simplified even further. After integrating over the wave vectors, we can write the contribution to the frictional force, which is linear in velocity, in the form [2]

$$F = -\eta(h)V = -\frac{3\hbar V}{8\pi h^5}\int_0^\infty d\omega\left\{2\left[\alpha''(\omega)\frac{d\Delta''(\omega)}{d\omega}\right.\right.$$

$$\left.-\Delta''(\omega)\frac{d\alpha''(\omega)}{d\omega}\right] + \omega\left[\alpha''(\omega)\frac{d^2\Delta''(\omega)}{d\omega^2}\right. \quad (23)$$

$$\left.\left.-\Delta''(\omega)\frac{d^2\alpha''(\omega)}{d\omega^2}\right]\right\}\coth\left(\frac{\omega\hbar}{2kT}\right).$$

In spite of the obvious similarity to formula (2b), this relation differs basically from it. The main difference is that the integrand in Eq. (23) contains the derivatives of the dielectric component instead of Planck's distribution, and hence the friction coefficient differs from zero for $T = 0$. In the latter case, after simplifications connected with the integration by parts, formula (23) can be written in a still more compact form [2]

$$F = -\eta(h)V = -\frac{3\hbar V}{4\pi h^5}\int_0^\infty d\omega\alpha''(\omega)\frac{d\Delta''(\omega)}{d\omega}. \quad (24)$$

2. NONDISSIPATIVE (RESONANCE) INTERACTION OF A MOVING ATOM WITH A SURFACE WAVE

In contrast to the potential (and force) of attraction to the surface, which contain cross products of the real and imaginary parts of the functions $\alpha(\omega)$ and $\Delta(\omega)$, the drag force defined by formulas (22)–(24) contains products of only the imaginary parts of these functions and is ultimately determined by the overlap integral of the absorption spectra of the atom and the surface, which are shifted relative to each other by $\Delta\omega = \pm k_x V$ due to the Doppler effect. Thus, the structure of the expression for the frictional force clearly demonstrates its dissipative nature. However, the obtained results also permit the existence of nondissipative lateral forces. We will carry out the analysis using the well-known formula for the polarizability of an atom in the ground state [20]:

$$\alpha(\omega) = \sum_n \frac{e^2 f_{0n}}{m[\omega_{0n}^2 - \omega^2 - i\omega\gamma_{0n}]}, \qquad (25)$$

where f_{0n} is the oscillator strength for a transition from the ground state (0) of the atom to a state (n) of the discrete spectrum and ω_{0n} and γ_{0n} are the transition frequency and the absorption line width, respectively. We assume that, for $V = 0$, the atom and the surface are characterized by two narrow absorption lines with frequencies ω_{0n} and ω_s (the latter is equal to the frequency of a surface plasmon, which satisfies the dispersion equation $\varepsilon(\omega_s) + 1 = 0$, [21]) and the conditions $\gamma_{0n} \ll \omega_{0n}$, $\gamma_s \ll \omega_s$, and $\max(\gamma_{0n}, \gamma_s) \ll |\omega_{0n} - \omega_s|$ are satisfied. The last inequality indicates that the overlap integral for the absorption lines is negligibly small. In this case, the imaginary parts of the functions $\alpha(\omega)$ and $\Delta(\omega)$ can be written in the form

$$\alpha''(\omega) = \frac{\pi e^2 f_{0n}}{2m\omega_{0n}}\delta(\omega - \omega_{0n}), \qquad (26)$$

$$\Delta''(\omega) = \frac{2\pi}{\left|\frac{\partial\varepsilon}{\partial\omega}\right|_{\omega=\omega_s}}\delta(\omega - \omega_s). \qquad (27)$$

Substituting Eqs. (25)–(27) into Eq. (24) and integrating with respect to the frequencies, we obtain [11]

$$F(h, V) = -\frac{\hbar e^2 f_{0n}}{Vm\omega_{0n}\left|\frac{\partial\varepsilon}{\partial\omega}\right|_{\omega=\omega_s}} \times \int_0^\infty dk_x k_x^3 (K_0(2k_x h) + K_2(2k_x h)) \times \left\{\delta\left(k_x - \frac{\omega_s - \omega_{0n}}{V}\right) - \delta\left(k_x + \frac{\omega_s - \omega_{0n}}{V}\right)\right\}. \qquad (28)$$

According to this equation, the contribution to the lateral force for $\omega_s > \omega_{0n}$ comes only from the first delta function in the braces; hence, $F < 0$ and the particle is decelerated, its kinetic energy being spent for exciting a surface wave. In the opposite case, when $\omega_s < \omega_{0n}$, the contribution to the integral in Eq. (28) comes from the second delta function and the particle is accelerated, receiving energy from the surface wave, while the lateral force becomes nondissipative. Subsequent integration of Eq. (28) with respect to the wave vector leads to a formula taking into account both cases, i.e.,

$$F(h, V) = -\frac{\hbar e^2 f_{0n}\,\mathrm{sgn}(\omega_s - \omega_{0n})}{Vm\omega_{0n}\left|\frac{\partial\varepsilon}{\partial\omega}\right|_{\omega=\omega_s}}\left(\frac{\Delta\omega}{V}\right)^3 \times \left[K_0\left(\frac{2\Delta\omega h}{V}\right) + K_2\left(\frac{2\Delta\omega h}{V}\right)\right], \qquad (29)$$

where $\Delta\omega = |\omega_s - \omega_{0n}|$. An analysis of formula (29) proves that the force $F(h, V)$ as a function of the velocity has a peak which is the sharper, the smaller the difference $\Delta\omega$. For low velocities, when $\frac{2\Delta\omega h}{V} \gg 1$, we can use the asymptotic expression for the MacDonald functions for large values of the argument [19]: $K_n(x) \longrightarrow \sqrt{\frac{\pi}{2x}}\exp(-x)$. In this case, it follows from Eq. (29) that the frictional force is exponentially small for $\frac{2\Delta\omega h}{V} \gg 1$. As the velocity increases, the quantity $F(h, V)$ increases rapidly, attaining its maximum value for $V = 0.95\Delta\omega h$. Upon a further increase in the velocity, the function $F(h, V)$ tends asymptotically to zero, but this transition occurs more smoothly. Thus, the nondissipative interaction of a moving atom with a surface wave, which is described by Eq. (29), is of a resonance nature and the equality $V = 0.95\Delta\omega h$ can be regarded as the resonance condition. In this case, we must require that the condition $2\Delta\omega h \ll c$ under which a nonrelativistic analysis is possible be satisfied. Consequently, the difference in the frequencies must satisfy the relation $\gamma_{0,s} \ll \Delta\omega \ll c/2h$.

It is interesting to note that the effect considered above is similar to a certain extent to the Landau collisionless damping in a plasma, but in our case the role of spatial dispersion and the velocity distribution of particles are insignificant. In addition, as was proved in [2], the effect of the accelerating force (in the approximation linear in velocity) may also be observed in the case when the dielectric functions have a more general form. This aspect will be considered in Section 4.

3. INTERACTION OF POLAR MOLECULES AND IONS WITH THE SURFACE

The generality of the method used by us here makes it possible to calculate easily the attractive potentials and frictional forces for polar molecules and ions. Moreover, this can also be done for a motion along the normal to the surface. Some of the results presented here were obtained by other authors who used alternative methods [6, 11, 22–25], which provides another opportunity to verify our theory.

In the case of a neutral particle (polar molecule), we assume that it possesses a permanent time-independent dipole moment $\mathbf{d} = (d_x, d_y, d_z)$. Irrespective of the direction of motion of the dipole, it is convenient to calculate the force acting on it by using the formula $\mathbf{F} = (\mathbf{d}\nabla)\mathbf{E}^{ind}$, where the Fourier component of the induced field can be expressed in terms of the Fourier component of the potential in Eq. (6). Calculations give the following expressions for the normal and lateral components of the force:

(1) lateral motion:

$$F_z(h, V) = -\frac{2}{\pi}\int\int dk_x dk_y \Delta'(k_x V)\exp(-2kh) \times (k_x^2 d_x^2 + k_y^2 d_y^2 + k^2 d_z^2), \quad (30a)$$

$$F_x(h, V) = -\frac{2}{\pi}\int\int dk_x dk_y \frac{k_x}{k}\Delta''(k_x V)\exp(-2kh) \times (k_x^2 d_x^2 + k_y^2 d_y^2 + k^2 d_z^2). \quad (30b)$$

(2) Normal motion (in this case, both conservative and nonconservative interaction forces are perpendicular to the surface):

$$F_z(z, t) = -\frac{d_x^2 + d_y^2 + 2d_z^2}{2}\int_0^\infty dk k^3 \Delta(-ikV)\exp(-2kz), \quad (30c)$$
$$z = Vt.$$

Formula (30a) describes the interaction of a moving dipole with its image. For $V = 0$, after the integration over the wave vectors, this formula leads to an expression well known in electrostatics for the force of attraction of a stationary dipole to its image [16]:

$$F_z(h) = -\frac{3(d_x^2 + d_y^2 + 2d_z^2)}{16h^4}\left(\frac{\varepsilon - 1}{\varepsilon + 1}\right), \quad (31)$$

where ε is the static dielectric constant of the medium.

The integration of Eq. (30b) in the linear approximation in velocity gives the frictional force in the form

$$F = -\frac{3(3d_x^2 + d_y^2 + 4d_z^2)V}{32h^5}\frac{d\Delta''(\omega)}{d\omega}\bigg|_{\omega = 0}, \quad (32)$$

which has the same dependence on distance as in Eq. (24). In the case of a conducting surface, we can use the low-frequency approximation for the dielectric constant [16]

$$\varepsilon(\omega) = 1 + i\frac{4\pi\sigma}{\omega} \quad (33)$$

(σ is the static electrical conductivity) to easily transform Eq. (32) to

$$F = -\frac{3(3d_x^2 + d_y^2 + 4d_z^2)V}{64\pi\sigma h^5}. \quad (34)$$

In this case, we have $F = -\frac{3d^2 V}{16\pi\sigma h^5}$ for the orientation of the dipole moment at right angles to the surface, which agrees completely with the result obtained by Tomassone and Widom [11] [see formula (2a)].

Similarly, taking into account Eq. (33) in the linear approximation in the velocity from Eq. (30c), we obtain

$$F_z(h, V) = -\frac{3(d_x^2 + d_y^2 + 2d_z^2)}{16h^4} - \frac{3(d_x^2 + d_y^2 + 2d_z^2)}{16\pi\sigma h^5}V. \quad (35)$$

Consequently, in analogy with the result obtained in [10], the friction coefficient for the motion along the normal to the surface is twice as large as for the lateral motion. The first term in Eq. (35) describes the conservative attraction of the dipole to the surface.

Formulas similar to Eqs. (30a), (30b), and (30c), which describe the interaction of particles having a charge $Z_1 e$ with a plane surface, have the following form [2]:

(1) Lateral motion:

$$F_z(z, V) = -\frac{2(Z_1 e)^2}{\pi}\int_0^{\pi/2} d\phi \int_0^\infty dk k \exp(-2kz)\Delta'(kV\cos\phi), \quad (36a)$$

$$F_x(z, V) = -\frac{2(Z_1 e)^2}{\pi}\int_0^{\pi/2} d\phi \cos\phi \times \int_0^\infty dk \exp(-2kz)\Delta''(kV\cos\phi). \quad (36b)$$

(2) Motion along the normal:

$$F_z(z, V) = -(Z_1 e)^2 \int_0^\infty dk k(-ikV)\exp(-2kz). \quad (36c)$$

Introducing the variable $\omega = kV\cos\phi$, we can easily reduce Eqs. (36a) and (36b) to a simpler form coincid-

ing with the result obtained in [23]:

$$F_z(z, V) = -\frac{2(Z_1e)^2}{\pi V^2}\int_0^\infty d\omega\omega K_1(2\omega z/V)\Delta'(\omega), \quad (37)$$

$$F_x(z, V) = -\frac{2(Z_1e)^2}{\pi V^2}\int_0^\infty d\omega\omega K_0(2\omega z/V)\Delta''(\omega). \quad (38)$$

In the plasma limit $\varepsilon(\omega) = 1 - \frac{\omega_p^2}{\omega(\omega + i0^+)}$ for the dielectric constant of the medium, formula (38) leads to another well-known result [22, 25]:

$$F_x(z, V) = -\frac{(Z_1e)^2\omega_s^2}{V^2}K_2\left(\frac{2\omega_s z}{V}\right), \quad (39)$$

where $\omega_s = \omega_p\sqrt{2}$ is the frequency of a surface plasmon. In the case of a conducting surface described by a dielectric constant of the form (33) in the linear approximation in velocity from (36b) we obtain

$$F_x(z, V) = -\frac{(Z_1e)^2}{16\pi\sigma z^3}V, \quad (40)$$

accordingly, for the motion along the normal, we have

$$F_z(z, V) = -\frac{(Z_1e)^2}{8\pi\sigma z^3}V. \quad (41)$$

Formulas (40) and (41) are in perfect accord with the results obtained in [11, 25]; in analogy with the drag of a dipole molecule [cf. Eqs. (34) and (35)], the friction coefficient for the motion along the normal to the surface is also twice as large as for the lateral motion.

Thus, the formulas obtained in this section agree with all analogous results obtained by other authors. To our knowledge, formulas (30) and (36) have not been presented before and are the most general relation in the given form since they can be used for calculations with dielectric functions of an arbitrary type.

4. ESTIMATION OF THE ROLE OF FLUCTUATION-INDUCED ELECTROMAGNETIC FORCES IN EXPERIMENTS

It would be interesting to estimate the drag forces acting on an adsorbate atom moving near a conducting surface in connection with the interpretation of the experiments carried out by using the quartz microbalance technique [3–5]. Let us suppose that the most intense line in the absorption spectrum of the atom has the frequency ω_{0n}. Assuming that the damping factor for the line is equal to zero, we can use Eq. (26) for the imaginary part of the atomic polarizability and write the dielectric function of the conducting medium in the Drude approximation (ω_p is the plasma frequency, τ is the relaxation time, and $\varepsilon(0) = 1$ for metals):

$$\varepsilon(\omega) = \varepsilon(0) - \frac{(\omega_p\tau)^2}{1 + (\omega\tau)^2} + \frac{i(\omega_p\tau)^2}{\omega\tau[1 + (\omega\tau)^2]}. \quad (42)$$

Substituting Eqs. (26) and (42) into Eq. (24) and carrying out elementary integration, we obtain

$$F = \frac{3\hbar e^2 f_0\tau^2 V}{4mz^5}\frac{y^2(12x^4 - 4x^2y^2 + 4x^2 - y^4)}{x(4x^4 - 4x^2y^2 + 4x^2 + y^4)^2}, \quad (43)$$

where $x = \omega_{0n}\tau$ and $y = \omega_p\tau$. An analysis of formula (43) shows that the sign of the force F depends on the relation between the absorption frequency of the atom and the plasma frequency. The force is decelerating for $\omega_p > \sqrt{2}\,\omega_{0n}$. This condition is satisfied for the parameters $\tau = 10^{-14}$–10^{-15} s and $\omega_p = 5$–15 eV, which are typical of metals, but the opposite situation is also possible for high-frequency absorption lines and the lateral force becomes accelerating. It should be noted, however, that the absolute values of the overlap integral for the spectra, which is determined by the factor in Eq. (43) depending on x and y, decrease rapidly with increasing ω_{0n}, and hence a detailed analysis of the absorption spectrum of the atom in the narrow frequency range in the vicinity of $\omega_p/\sqrt{2}$ is required to obtain a correct estimate of the resultant force F. According to calculations, the value of the overlap integral in typical experiments [3–5] involving the adsorption of a krypton atom on gold is close to –0.1 and the damping time of motion for $z = 0.4$ nm is equal to $\Delta t = MV/F = 0.6$ ns (M is the mass of the krypton atom), which is close to the experimentally observed value [26].

In the case when an atomic force microscope with a parabolic probe having a radius of curvature R and the equation of the surface $z = (x^2 + y^2)/2R$ is used, the friction coefficient in the case of lateral motion can be obtained by using formula (23) and the additive approximation, as well as the Clausius–Mossotti equation for expressing the polarizability in terms of the dielectric constant motion [2]:

$$\eta(h) = \frac{3}{64\pi}\frac{\hbar RJ}{h^3}, \quad (44)$$

where the frequency integral J is similar to the frequency integral in Eq. (23), in which $\alpha''(\omega)$ is replaced by $\mathrm{Im}\frac{\varepsilon_1(\omega) - 1}{\varepsilon_1(\omega) + 2}$, $\varepsilon_1(\omega)$ is the dielectric function of the probe material, and h is the distance from the probe apex and the surface. A more correct evaluation of the frictional force involves the determination of the spectrum of electromagnetic waves in the given geometry (a parabolic probe and a plane surface) and may lead to a change in the numerical factor in Eq. (44).

For typical scanning velocities of 10^{-4}–10^{-2} cm/s, the value of the fluctuational electromagnetic forces is from 3 to 6 orders of magnitude lower than the value of the static adhesive frictional forces [1, 2, 26] but these forces can make a significant contribution to the damping coefficients in the dynamic mode for vibrational frequencies of nanoprobes of the order of 1 to 10 MHz and for amplitudes from 1 to 10 nm. Hence, for diagnostics of the surface and for testing the theory of fluctuational forces, it would be interesting to make corresponding measurements for various combinations of materials of the probe and the sample, for various temperatures, and for other physical parameters. The first experimental results in this field have already been obtained [27, 28].

It was proved in [6] that nanotubes with open ends can be effectively used as a micromanipulator for various types of radiation, including transporting and focusing of neutral atomic beams. When a beam enters a nanotube at a small angle to its axis, a channeling mode similar to that in a crystal can be realized. A considerable advantage of nanotubes is the existence of a radial symmetry of the continuous potential with a small range (0.1 to 0.2 nm) in the immediate vicinity of the walls. Consequently, the main part of the beam will move away from the walls of nanotubes with a radius of several nanometers without being scattered. If we take the above estimate of the drag time (1 ns) for an individual atom (due to fluctuational forces) as the starting point, 80 and 90% of the beam of atoms having an initial velocity of 1000 m/s and trapped in a cylindrical channel are capable of traversing nanotubes of length 100 μm having radii of 5 and 10 nm, respectively. Thus, nanotubes can be used for modifying the surface of solids by low-energy (thermal) atomic beams. This can be done in the scanning mode of a probe microscope by attaching nanotubes to its cantilever [6].

Thus, the theory of dynamic fluctuational electromagnetic forces makes it possible to calculate the latter for a wide range of applied problems associated with the motion of neutral atomic, ionic, and molecular beams, as well as nanoprobes, near a flat surface. The obvious evidence of the correctness of the theory is the possible reproduction of its main results for the static and dynamic fluctuational interaction with the surface. However, the formulas obtained (for the drag forces acting on neutral atoms) differ considerably from the available formulas [11–13] since they predict the presence of finite frictional forces (that are linear in velocity) at zero temperature. This conclusion reflects the natural features of the electromagnetic forces of a fluctuational origin.

For the first time, we have substantiated the possible sign reversal for lateral forces acting on an atom (nanoprobe) moving near the surface which lead to its acceleration by the field of surface plasmons. The necessary conditions for such behavior are analyzed. In the case of a moving atom, this effect is of a resonance nature.

It has been proved that dynamic fluctuational electromagnetic forces can ensure the damping time for adsorbed particles, which is observed in experiments using a quartz microbalance. The measurement of such forces, as well as damping decrements for nanoprobes in the dynamic mode of scanning probe microscopes, may form the basis of diagnostic methods of studying the dielectric properties of thin surface layers and can also be used for verifying the dynamic mechanisms of friction. The experimental measurement of the dynamic frictional forces can also be used for studying the passage of atomic beams through open carbon nanotubes.

REFERENCES

1. G. V. Dedkov, Mater. Lett. **38**, 360 (1999); G. V. Dedkov, Wear **232** (2), 145 (1999).
2. G. V. Dedkov and A. A. Kyasov, Phys. Lett. A **259**, 38 (1999); Surf. Sci. **463**, 11 (2001); G. V. Dedkov and A. A. Kyasov, Pis'ma Zh. Tekh. Fiz. **25** (12), 10 (1999) [Tech. Phys. Lett. **25**, 466 (1999)].
3. M. Cieplak, E. Smith, and M. O. Robbins, Science **265**, 1209 (1994).
4. E. T. Watts, J. Krim, and A. Widom, Phys. Rev. B **41**, 3466 (1990).
5. J. Krim, D. H. Solina, and R. Chiarello, Phys. Rev. Lett. **66**, 181 (1991).
6. G. V. Dedkov, Nucl. Instrum. Methods Phys. Res. B **143**, 584 (1998).
7. W. L. Schaich and A. Harris, J. Phys. F: Met. Phys. **11**, 65 (1981).
8. J. Mahanti, J. Phys. B: At. Mol. Phys. **13**, 4396 (1980).
9. F. Sols and F. Flores, Solid State Commun. **42**, 687 (1982).
10. A. A. Kyasov, in *Collection of Scientific Works*, Ed. by V. E. Fortov and E. A. Kuz'menkov (Inst. Vys. Temp. Akad. Nauk SSSR, Moscow, 1991), p. 122.
11. M. S. Tomassone and A. Widom, Phys. Rev. B **56**, 4938 (1997).
12. J. B. Pendry, J. Phys. C **9**, 10301 (1997).
13. A. I. Volokitin and B. N. J. Persson, J. Phys.: Condens. Matter **11**, 345 (1999).
14. L. D. Landau and E. M. Lifshitz, *Statistical Physics* (Nauka, Moscow, 1978; Pergamon, Oxford, 1980), Part 2.
15. A. A. Kyasov, Available from VINITI No. 1407-B91 (1991).
16. L. D. Landau and E. M. Lifshitz, *Course of Theoretical Physics*, Vol. 8: *Electrodynamics of Continuous Media* (Nauka, Moscow, 1982; Pergamon, New York, 1984).
17. Yu. S. Barash, *Van der Waals Forces* (Nauka, Moscow, 1988).
18. L. D. Landau and E. M. Lifshitz, *Statistical Physics* (Nauka, Moscow, 1976; Pergamon, Oxford, 1980), Part 1.

19. A. F. Nikiforov and V. B. Uvarov, *Special Functions of Mathematical Physics: A Unified Introduction with Applications* (Nauka, Moscow, 1978; Birkhauser, Basel, 1987).
20. A. S. Davydov, *Quantum Mechanics* (Nauka, Moscow, 1973; Pergamon, Oxford, 1976).
21. R. H. Ritchie, Phys. Rev. **106**, 874 (1957).
22. F. Sols, P. Mirango, and F. Flores, Surf. Sci. **161**, 33 (1985).
23. R. García-Molina, A. Gras-Marti, A. Howie, and R. Ritchie, J. Phys. C: Solid State Phys. **18**, 5335 (1985).
24. D. L. Mills, Phys. Rev. B **15**, 763 (1977).
25. R. Núñez, P. M. Echenique, and R. H. Ritchie, J. Phys. C: Solid State Phys. **13**, 4229 (1980).
26. G. V. Dedkov, Usp. Fiz. Nauk **170** (6), 585 (2000).
27. B. Gotsmann, C. Seidel, B. Anczykowski, and H. Fuchs, Phys. Rev. B **60**, 11051 (1999).
28. I. Dorofeyev, H. Fuchs, G. Wenning, and B. Gotsmann, Phys. Rev. Lett. **83** (12), 2402 (1999).

Translated by N. Wadhwa

Physics of the Solid State, Vol. 43, No. 1, 2001, pp. 185–189. Translated from Fizika Tverdogo Tela, Vol. 43, No. 1, 2001, pp. 177–181.

FULLERENES AND ATOMIC CLUSTERS

Quantum Transitions and Magnetization of the Magnetic V_{15} Cluster in Strong Magnetic Fields

A. K. Zvezdin*, V. I. Plis*, A. I. Popov*, and B. Barbara**

**Moscow State Institute of Electronic Engineering (Technological University), Zelenograd, Moscow, 103498 Russia*

***Laboratoire de Magn. Lois Neel, CNRS, Grenoble, 38042 France*

Received December 28, 1999; in final form, May 23, 2000

Abstract—The process of rearrangement of the magnetic structure of the low-spin cluster V_{15} in superhigh magnetic fields is investigated. At low temperatures, this process is shown to manifest itself as three quantum jumps, each of which is a transition causing the spin of the complex to increase by two unities. The nature of these quantum jumps is discussed. The magnetization curve and the magnetic susceptibility are calculated.

INTRODUCTION

At the present time, magnetic mesoscopic systems attract considerable interest. These systems exhibit both specific quantum features characteristic of individual atoms and classical features typical of bulk single crystals. Among these systems are clusters containing *d* or *f* ions ($Mn_{12}Ac$, Fe_6, Fe_8, Fe_{10}, etc.) [1–11]. Advances in high-molecular chemistry have made possible the synthesis of magnetic clusters representing metal-organic molecules with a gigantic spin. Examples are $Mn_{12}Ac$, Fe_8, Fe_{17}, and V_{12} [1–11]. These clusters form molecular crystals, in which they keep their individuality because the bonds between the clusters are fairly weak. A unique property of such systems is molecular bistability [12]. This means that they behave as molecular magnets at sufficiently low temperatures and, in principle, can be used for information recording. It has recently been discovered that these clusters show macroscopic quantum magnetization tunneling [5, 8, 12], a property which is of great importance. A theoretical study of quantum coherence in magnetic clusters was also made [13]. These phenomena, undoubtedly, give some insight into the fundamental problems of magnetism and open up fresh interesting opportunities for quantum mechanical calculations. Until recently, only clusters with an integer spin, such as $Mn_{12}Ac$ ($S = 10$ in the ground state), Fe_8 ($S = 10$ in the ground state), and Mn_6R_6 ($S = 12$ in the ground state) were investigated. However, a study of clusters with a half-integer spin, such as the magnetic cluster V_{15}, is of prime interest for understanding the physics of magnetic nanoclusters, because, according to Kramers' theorem, the properties of systems with a half-integer spin may differ qualitatively from those of systems with an integer spin. This is why this cluster is of interest to investigators.

When studying mesoscopic properties, a cluster is usually considered in the ground-state multiplet approximation. However, in order to gain a better understanding of the physics of a cluster, one should investigate its internal structure, i.e., in our case, the exchange interactions between magnetic ions composing the cluster. The most direct method for studying these interactions is to investigate the complete magnetization curve in megagauss magnetic fields. This is the only objective of the present paper, which is devoted to a study of the behavior of crystals formed by V_{15}-polyoxyvanadate molecules ($K_6[V_{15}^{IV}As_6O_{42}(H_2O)] \cdot 8H_2O$). These crystals possess trigonal symmetry (space group $R3$) with $a = 14.029$ Å, $\alpha = 79.26°$, and $V = 2632$ Å^3 [11, 14]. The unit cell contains two V_{15} clusters. The V_{15} cluster comprises fifteen V^{IV} ions, each of which has a spin of $S = 1/2$. Ions V^{IV} are situated at the apexes of two planar hexagons and one triangle between them. The structure of the cluster is depicted schematically in Fig. 1. The exchange interaction between V^{IV} ions is antiferromagnetic in nature [14]. Because of this, in contrast to most organic clusters such as $Mn_{12}Ac$, which are high-spin systems, the V_{15} cluster has a low spin $S = 1/2$ in the ground state. The magnetic (dipole) interaction between the spins of neighboring clusters is negligible (several millikelvins). Each hexagon of the cluster (Fig. 1) has three pairs of strongly coupled spins ($J \approx -800$ K). The spin of each ion of the triangle is coupled with two pairs of spins, one of which belongs to the upper hexagon; the other, to the lower hexagon ($J' \approx J_1 \approx -150$, $J'' \approx J_2 \approx -300$ K). The exchange interaction between the spins situated at the apexes of the triangle is very weak ($J_0 \approx -2.5$ K [15]). The spin of the cluster in the ground state $S = 1/2$ is due to the antiferromagnetic interaction between V^{IV} ions; therefore, the cluster can be thought of as a multi-sublattice ferromagnet at the molecular level. The fundamental parameters of such a molecular ferrimagnet are exchange integrals which determine the

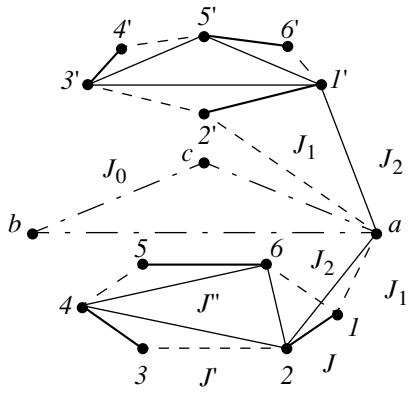

Fig. 1. Structure and exchange interactions of the V_{15} cluster (schematic).

magnetic structure of the cluster and its transformation under an external magnetic field. Using the magnetic $Mn_{12}Ac$ cluster as an example, it has been shown recently that the transition from the ferrimagnetic to a ferromagnetic state in magnetic clusters with antiferromagnetic exchange interaction between magnetic ions has a number of specific features qualitatively different from those in the case of a classical Néel ferrimagnet [9]. In this paper, we investigate this transformation of the spin structure of the V_{15} cluster, which comes to a close in ultrastrong magnetic fields. The magnetization and magnetic susceptibility of the cluster are calculated as a function of exchange constants, magnetic field, and temperature.

1. THE HAMILTONIAN, BASIC FUNCTIONS, AND ENERGY LEVELS

The Hamiltonian of the cluster is written in the form [1]

$$H = \sum_{n=1}^{7} H_n,$$

$$H_1 = -J(\mathbf{S}_1\mathbf{S}_2 + \mathbf{S}_3\mathbf{S}_4 + \mathbf{S}_5\mathbf{S}_6 + (\ldots)'), \quad (1)$$

$$H_2 = -J'(\mathbf{S}_2\mathbf{S}_3 + \mathbf{S}_4\mathbf{S}_5 + \mathbf{S}_6\mathbf{S}_1 + (\ldots)'), \quad (2)$$

$$H_3 = -J''(\mathbf{S}_2\mathbf{S}_4 + \mathbf{S}_4\mathbf{S}_6 + \mathbf{S}_6\mathbf{S}_2 + \mathbf{S}_1\mathbf{S}_3 + \mathbf{S}_3\mathbf{S}_5 + \mathbf{S}_5\mathbf{S}_1 + (\ldots)'). \quad (3)$$

$$H_4 = -J_1(\mathbf{S}_a\mathbf{S}_1 + \mathbf{S}_b\mathbf{S}_3 + \mathbf{S}_c\mathbf{S}_5 + \mathbf{S}_a\mathbf{S}_2' + \mathbf{S}_b\mathbf{S}_4' + \mathbf{S}_c\mathbf{S}_6'), \quad (4)$$

$$H_5 = -J_2(\mathbf{S}_a\mathbf{S}_2 + \mathbf{S}_b\mathbf{S}_4 + \mathbf{S}_c\mathbf{S}_6 + \mathbf{S}_a\mathbf{S}_1' + \mathbf{S}_b\mathbf{S}_3' + \mathbf{S}_c\mathbf{S}_5'), \quad (5)$$

$$H_6 = -J_0(\mathbf{S}_a\mathbf{S}_b + \mathbf{S}_b\mathbf{S}_c + \mathbf{S}_c\mathbf{S}_a), \quad (6)$$

$$H_7 = H_Z = 2\mu_B B\sum S_Z. \quad (7)$$

Here, summation is performed over all fifteen V^{IV} ions. The symbol (…)' designates an analogous expression involving the spins of the upper hexagon; and S_a, S_b, and S_c are the spins at the apexes of the triangle. According to [14], $J = -800$, $J' = J_1 = -150$, $J'' = J_2 = -300$, and $J_0 = -2.5$ K. However, it should be noted that these values of the exchange constants are rough estimates.

In [15], it was shown that at $B < 3$ T, the spin of the cluster in the ground state is $S = 1/2$. At $B = 3$ T, the magnetic structure of the cluster is changed with the result that the spin becomes equal to 3/2. In this case, $S_{az} = S_{bz} = S_{cz} = -1/2$ ($\langle S_{iz}\rangle = \langle S'_{iz}\rangle = 0$, $i = 1, \ldots, 6$). Further transformation of the magnetic cluster structure occurs in the range of ultrastrong magnetic fields, to a consideration of which we now proceed. Analysis shows that the orientation of spins S_a, S_b, and S_c remain unchanged in this case.

In the case of $S_{az} = S_{bz} = S_{cz} = -1/2$, we have

$$H_4 + H_5 = H_8 + H_9 \quad (8)$$

$$H_8 = \frac{1}{4}(J_1 + J_2)\sum_{i=1}^{6}(\hat{S}_{iz} - \hat{S}'_{iz}), \quad (9)$$

$$H_9 = \frac{1}{4}(J_2 - J_1)(\hat{S}_{2z} - \hat{S}_{1z} + \hat{S}_{4z} - \hat{S}_{3z} + \hat{S}_{6z} - \hat{S}_{5z} + (\ldots)'). \quad (10)$$

When studying the energy spectrum of the system, we take into account the hierarchy of the exchange interactions in the Hamiltonian H [see Eq. (8)]. We represent H in the form

$$H = H_0 + H',$$

where

$$H_0 = H_1 + H_Z, \quad (11)$$

while the Hamiltonian

$$H' = H - H_0$$

includes the remaining exchange interactions characterized by J_1, J', J_2, and J''. The energy levels corresponding to the Hamiltonian H_0 are

$$E_0(S) = -\frac{J}{2}\Big[S_{12}(S_{12}+1) + S_{34}(S_{34}+1) + S_{56}(S_{56}+1) - \frac{1}{2}\times\frac{3}{2}\times 3 + (\ldots)'\Big] + 2\mu_B B M_S = -JS + 2\mu_B B M_S + \text{const}, \quad (12)$$

where $S = \sum_{i=1}^{3}(\tau_i + \tau'_i)$, τ_i, $\tau'_i = 0, 1$; $S = 0, 1, \ldots, 6$; $\tau_1 = S_{12}$, $\tau_2 = S_{34}$, $\tau_3 = S_{56}$, $\tau'_1 = S'_{12}$, $\tau'_2 = S'_{34}$, $\tau'_3 = S'_{56}$; and $M_S = S, S-1, \ldots, -S$.

When studying the behavior of the magnetization and magnetic susceptibility of the cluster in strong magnetic fields and at low temperatures ($kT < 2\mu_B B$), it is sufficient to consider the states with $M_S = -S$. In this

case, Eq. (12) for the energy levels can be written as

$$E_0(S) = -JS - 2\mu_B BM_S. \quad (13)$$

The corresponding eigenfunctions are

$$\Psi_0(\tau_i, \tau_i') = \prod_{i=1}^{3} \sum_{m_1, m_2} \left(C^{\tau_i - \tau_i}_{\frac{1}{2}m_1(i)\frac{1}{2}m_2(i)} \left|\frac{1}{2}m_1(i)\right\rangle \left|\frac{1}{2}m_2(i)\right\rangle \right) \prod_{i=1}^{3} \sum_{m_1', m_2'} \left(C^{\tau_i' - \tau_i'}_{\frac{1}{2}m_1'(i)\frac{1}{2}m_2'(i)} \left|\frac{1}{2}m_1'(i)\right\rangle \left| \frac{1}{2}m_2'(i)\right\rangle \right). \quad (14)$$

It follows from Eq. (13) that all energy levels with $S = 0, 1, \ldots, 6$ cross simultaneously when $B = -J/(2\mu_B) \approx 560$ T. In this situation, it is quite important to take into account the corrections to the energy levels due to the perturbations described by the Hamiltonians H_2, H_3, H_8, and H_9. The effect of the perturbation H_8 reduces to renormalization of the exchange integral $J : J \longrightarrow \tilde{J} = J - \frac{1}{4}(J_1 + J_2)$. It is of prime importance that the perturbation $V(H_2, H_3, H_9)$ is additive and given by the sum of two independent contributions from the upper and lower hexagons.

Let us consider the contribution from the lower hexagon. In this case, naturally, the quantum number S corresponds only to the subsystem under consideration ($S = 0, 1, 2, 3$). Using the basis wave functions given by Eq. (14) and the perturbation Hamiltonian $V = H_2 + H_3 + H_9$ [see Eqs. (2), (3), (10)], we calculate the corrections δE to the energy levels defined in Eq. (13) for $S = 0, 1, 2, 3$.

In the case of $S = 0$, we have $\delta E(S = 0) = 0$. The $S = 1$ state is threefold degenerate and the corresponding basis wave functions $\Psi_0(\tau_1, \tau_2, \tau_3)$ given by Eq. (14) are $\Psi_1 = \Psi_0(1, 0, 0)$, $\Psi_2 = \Psi_0(0, 1, 0)$, and $\Psi_3 = \Psi_0(0, 0, 1)$. In this case, the perturbation Hamiltonian matrix has the form

$$\|V\| = \frac{1}{4}(J' + 2J'') \begin{Vmatrix} 0 & 1 & 1 \\ 1 & 0 & 1 \\ 1 & 1 & 0 \end{Vmatrix}. \quad (15)$$

The lowest energy is found from Eq. (15) to be

$$\delta E_{\min}(S = 1) = (J' + 2J'')/4. \quad (16)$$

The ground state with $S = 1$ is doubly degenerate. The excited state is separated from the ground state by $\Delta = -(J' + 2J'')/2$. For $J' = -150$ and $J'' = -300$ K, we have $\Delta \approx 400$ K. Therefore, the population of the excited state can be neglected up to room temperature.

Similarly, for the $S = 2$ state, we obtain

$$\delta E_{\min}(S = 2) = 0. \quad (17)$$

This level is also doubly degenerate, and the higher level is separated from it by $\Delta \approx 400$ K. In the case of $S = 3$, we have

$$\delta E_{\min}(S = 3) = -\frac{3}{4}(J' + 2J''). \quad (18)$$

It follows from Eqs. (13) and (16)–(18) that, as the magnetic field increases, the lowest energy levels corresponding to different values of S

$$E(S) = E_0(S) + \delta E_{\min}(S) \quad (19)$$

cross successively. The intersection of the energy levels $E(S = 0)$ and $E(S = 1)$ occurs at

$$B_1 = \frac{1}{2\mu_B}\left(-\tilde{J} + \frac{J' + 2J''}{4}\right). \quad (20)$$

The energy levels $E(S = 1)$ and $E(S = 2)$ cross at

$$B_2 = -\frac{1}{2\mu_B}\left(\tilde{J} + \frac{J' + 2J''}{4}\right). \quad (21)$$

Finally, the energy levels $E(S = 2)$ and $E(S = 3)$ intersect when the field is equal to

$$B_3 = -\frac{1}{2\mu_B}\left(\tilde{J} + \frac{3}{4}(J' + 2J'')\right). \quad (22)$$

Now, we determine the contributions from both hexagons:

$$\begin{aligned} &S_t = 0, \quad \delta E_{\min} = 0, \\ &S_t = 1, \quad \delta E_{\min} = (J' + 2J'')/4, \\ &S_t = 2, \quad \delta E_{\min} = (J' + 2J'')/2, \\ &S_t = 3, \quad \delta E_{\min} = 3(J' + 2J'')/4, \\ &S_t = 4, \quad \delta E_{\min} = 0, \\ &S_t = 5, \quad \delta E_{\min} = -3(J' + 2J'')/4, \\ &S_t = 6, \quad \delta E_{\min} = -3(J' + 2J'')/2. \end{aligned} \quad (23)$$

The behavior of the lowest energy levels of the V_{15} cluster $E(S_t) = E_0(S_t) + \delta E_{\min}(S_t)$ [see Eq. (23)] in superhigh magnetic fields is shown in Fig. 2.

2. MAGNETIZATION AND MAGNETIC SUSCEPTIBILITY OF THE V_{15} CLUSTER

The cluster magnetization in the approximation used is additive and given by the sum of the contributions from the two hexagons composed of V ions and from the triangle between them.

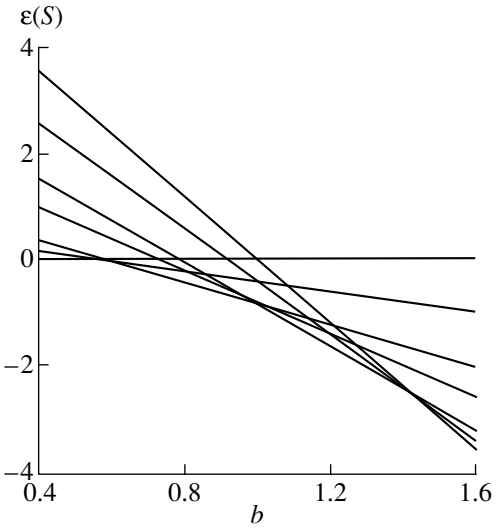

Fig. 2. Dependence of the lowest energy levels of the V_{15} cluster (in relative units, $\varepsilon(S) = E(S)/\tilde{\tilde{J}}$) on the magnetic field $b = 2\mu_B B/|\tilde{\tilde{J}}|$, where $\tilde{\tilde{J}} = \tilde{J} - (J' + 2J'' - J_1 - J_2)/4$.

The dependence of the cluster magnetization on the magnetic induction and the temperature is given by

$$M(B) = 4\mu_B \times \frac{\sum_{S=0}^{3} Sg(S)\exp[-(E(S) - 2\mu_B BS)/kT]}{\sum_{S=0}^{3} g(S)\exp[-(E(S) - 2\mu_B BS)/kT]} + 3\mu_B, \quad (24)$$

where $E(S)$ is determined by Eqs. (16)–(19), $g(0) = 1$, $g(1) = g(2)$, and $g(3) = 1$. In Eq. (24), the first term is the contribution from both hexagons, while the second is the contribution from the triangle. In order to analyze the magnetic properties of the V_{15} cluster, it is convenient to introduce dimensionless variables

$$b \approx 2\mu_B B/|\tilde{\tilde{J}}|,$$

$$\tau = T/|\tilde{\tilde{J}}|, \quad \varepsilon(S) = E(S)/|\tilde{\tilde{J}}|, \quad \mu = M/2\mu_B,$$

where

$$\tilde{\tilde{J}} = \tilde{J} + \frac{J' + 2J''}{4}.$$

Then, Eq. (24) takes the form

$$\mu(b, \tau) = 2\tilde{\mu}(b, \tau) + 3/2,$$
$$\tilde{\mu}(h, \tau) = Z^{-1}\sum_{S=0}^{3} Sg(S)\exp\left(-\frac{\varepsilon(S) - bS}{\tau}\right), \quad (25)$$
$$Z = \sum_{S=0}^{3} g(S)\exp\left(-\frac{\varepsilon(S) - bS}{\tau}\right).$$

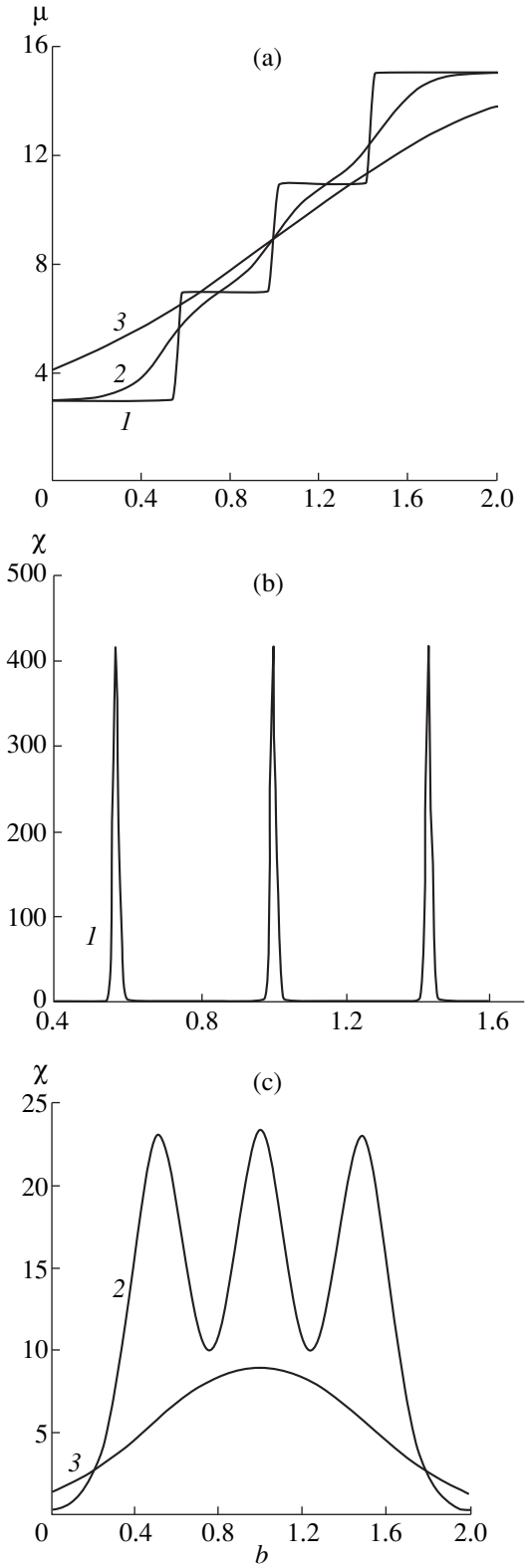

Fig. 3. Dependence of (a) the relative magnetization and (b, c) the magnetic susceptibility of the V_{15} cluster on the magnetic field $b = 2\mu_B B/|\tilde{\tilde{J}}|$, where $\tilde{\tilde{J}} = \tilde{J} - (J' + 2J'' - J_1 - J_2)/4$, $J = -800$ K, $J' \approx J_1 \approx -150$ K, and $J'' \approx J_2 \approx -300$ K [15] at various temperatures $\tau = kT/|\tilde{\tilde{J}}|$: (*1*) 0.005 ($T = 4.2$ K), (*2*) 0.089 ($T = 78$ K), and (*3*) 0.343 ($T = 300$ K).

With Eq. (25), the dimensionless magnetic susceptibility is easily found to be

$$\chi(b, \tau) = (\partial\mu(b, \tau)/\partial b)_\tau = 2\tau^{-1}\left\{Z^{-1}(b, \tau) \times \sum_{S=0}^{3} S^2 g(S) \exp\left(-\frac{\varepsilon(S) - bS}{\tau}\right) - \tilde{\mu}^2(b, \tau)\right\}. \quad (26)$$

Figure 3 shows the dependences of the magnetization (Fig. 3a) and magnetic susceptibility of the V_{15} cluster (Figs. 3b, 3c) on the external magnetic field calculated for $J = -800$, $J' = J_1 = -150$, and $J'' = J_2 = -300$ K in the cases of a low $T = 4.2$ K ($\tau = 0.005$), a high $T = 300$ K ($\tau = 0.343$), and the nitrogen boiling temperature $T = 78$ K ($\tau = 0.089$).

3. CONCLUSION

Thus, we theoretically investigated the rearrangement of the spin structure of the magnetic V_{15} cluster induced by an ultrastrong magnetic field. It is found that the changeover from the ferrimagnetic (spin $S = 3/2$) to a ferromagnetic ($S = 15/2$) magnetic structure occurs in three jumps equal to $2\mu_B$ each. All three jumps occur in the range of megagauss magnetic fields. For the values of the exchange integrals presented in [14], Eq. (8), we have, according to Eqs. (20)–(22), $B_1 = 350$, $B_2 = 612$, and $B_3 = 875$ T. All these jumps can be measured experimentally by a modern MK-1 oscillator [16], which is of great importance to the refinement of the exchange constants J, J_1, J', J_2, and J''.

ACKNOWLEDGMENTS

This work was supported by the Russian Foundation for Basic Research, grant no. 98-02-17440, the Ministry of Education of the RF (Fundamental-Science Program), grant no. 97-0-7.036, the Interdisciplinary Research and Development Program, project no. 97-1071, and the Federal Program "Integration," project no. K-0573.

REFERENCES

1. D. Gattecshi, A. Canecshi, L. Pardi, and R. Sessoli, Science **265**, 1054 (1994).
2. R. Sessoli, D. Gattecshi, A. Canecshi, and H. A. Novak, Nature **356**, 141 (1993).
3. J. R. Friedman, M. P. Sarachik, J. Tejada, and R. Ziolo, Phys. Rev. Lett. **76**, 3830 (1996).
4. L. Thomas, F. Lionti, R. Ballou, *et al.*, Nature **383**, 145 (1996).
5. V. V. Dobrovitski and A. K. Zvezdin, Europhys. Lett. **38**, 377 (1997).
6. R. Sessoli, Hin-Lien Tsai, A. R. Shake, *et al.*, J. Am. Chem. Soc. **115**, 1804 (1993).
7. A. Canecshi, D. Gattecshi, and R. Sessoli, J. Am. Chem. Soc. **113**, 5872 (1991).
8. L. Gunther, Europhys. Lett. **39**, 1 (1997).
9. A. K. Zvezdin and A. I. Popov, Zh. Éksp. Teor. Fiz. **109**, 2115 (1996) [JETP **82**, 1140 (1996)].
10. A. L. Barra, P. Debrunner, D. Gatteschi, *et al.*, Europhys. Lett. **35**, 133 (1996).
11. A. Muller and J. Doring, Angew. Chem., Int. Ed. Engl. **27**, 1721 (1991).
12. O. Kahn and C. Jay Martínez, Science **279**, 44 (1998).
13. A. K. Zvezdin, V. V. Dobrovitski, B. N. Harmon, and M. L. Katsnelson, Phys. Rev. B **58**, R14733 (1998).
14. D. Gattecshi, L. Pardi, A. L. Barra, and A. Muller, Mol. Eng. **3**, 157 (1993).
15. I. Chiourescu, W. Wernsdorfer, A. Muller, *et al.*, Phys. Rev. Lett. **84**, 3454 (2000).
16. A. D. Sakharov, Usp. Fiz. Nauk **88**, 725 (1966) [Sov. Phys. Usp. **9**, 294 (1966)].

Translated by Yu. Epifanov

Physics of the Solid State, Vol. 43, No. 1, 2001, pp. 19–22. Translated from Fizika Tverdogo Tela, Vol. 43, No. 1, 2001, pp. 21–24.

SEMICONDUCTORS AND DIELECTRICS

Electronic Structure of RbCl and Rb_2ZnCl_4 in the Solid and the Liquid State: Analysis of the Local Fine Structure of X-ray Absorption

A. V. Soldatov*, I. E. Shtekhin*, Ch. Li, K. Lu**, and H. Li****

** Rostov State University, pr. Stachki 194, Rostov-on-Don, 344090 Russia*
e-mail: stekhin@phys.rsu.ru

*** Condensed Matter Physics Department, Institute of Physics, Chinese Academy of Sciences, Beijing, 100080 China*

Received March 28, 2000

Abstract—Experimental absorption spectra were obtained near the absorption *K* edge of Rb in RbCl and Rb_2ZnCl_4 in the solid state and in a melt. Detailed analysis of the electronic structure of RbCl was conducted by means of the total multiple scattering method, and good agreement with the experimental spectrum was obtained. The fine structure of the unoccupied electronic states was determined in the conduction band of the compound studied. The unoccupied *p* states of rubidium were shown to be hybridized, for the most part, with the Cl *p* states in the conduction band. It was proved that the RbCl melts can be described in good approximation on the basis of the cluster model with the Debye–Waller parameter $\sigma^2 = 0.3$ Å^{-2}. © *2001 MAIK "Nauka/Interperiodica".*

Solid-state to liquid phase transitions are accompanied by considerable changes both in the local structure and in the electronic subsystem. Understanding the transition mechanism and the reasons for the induced changes serves to improve methods for growing ideal crystals. As a consequence, interest in the solid-state to liquid phase transitions is not only diminishing but is, actually, growing. Investigations of local structure changes are made by different methods, including neutron scattering [1, 2] and EXAFS spectroscopy [3–6]. The choice of these methods was determined by the fact that traditional x-ray diffraction methods for investigating crystal structure failed because of strong disordering of the crystals during the melting process.

To date, investigations of glasslike alloys [2], semiconducting Ga–Ge [7], $GaSe_2$ [1], and $GeSe_2$ alloys [3, 5] and ionic crystals [4, 6] have been completed. The last-named crystals are the objects most often used in studies due to their quite simple crystalline structure, which allows for the testing of new methods for investigating these substances. Moreover, ionic crystals are of independent interest themselves.

Rubidium tetrachlorzincanate Rb_2ZnCl_4 is an interesting object to study. This compound exhibits three phase transitions as the temperature is changed. At temperatures higher than 302 K, it has a structure of the β-K_2SO_4 type. Cooling to temperatures lower than 303 K leads to a transition into an incommensurate structure, which transforms at 189 K into a ferroelectric superstructure. On further cooling, rubidium tetrachlorzincanate is transformed into a monoclinic structure, whose symmetry has not yet been studied. The commensurate–incommensurate structural transition has been well investigated both theoretically and experimentally [8–11]. However, the transition into the liquid state has not yet attracted the attention of researchers it deserves. In order to study such a transition, we have experimentally measured the absorption spectra of rubidium in Rb_2ZnCl_4 and RbCl in the vicinity of the x-ray absorption edge (XANES spectra). The measured spectra have been analyzed theoretically by means of the total multiple scattering method.

The experiments were carried out as a joint project in the Japanese Photon Factory synchrotron center on the 10B lines [two-crystal monochromator with two flat Si(311) crystals] and on the 7C line (where a two-crystal monochromator with Si(111) crystals was also used). The electron flux energy inside the synchrotron ring attained 2.5 GeV, and the electron current was of the order of 150–300 mA. Some of the experiments were carried out in the Beijing synchrotron center (China) at the 4W1B line, where two flat Si(111) crystals were used as a monochromator. The current strength of the electron beam was 30 mA for an energy of 2.2 GeV. A detailed description of the experimental setup used for measuring XANES spectra for the liquid state was published earlier [3].

To obtain information from experimental x-ray absorption spectra of rubidium, one needs to carry out a theoretical analysis of the results [12]. It is possible to make such an analysis on the basis of different theoretical approaches: a tight-binding method [13], band calculations [14], etc. However, the multiple scattering method in the direct space [15, 16] has been applied with the most success. The use of the quasi-molecular approach [17] in similar cases (for interpretation of the

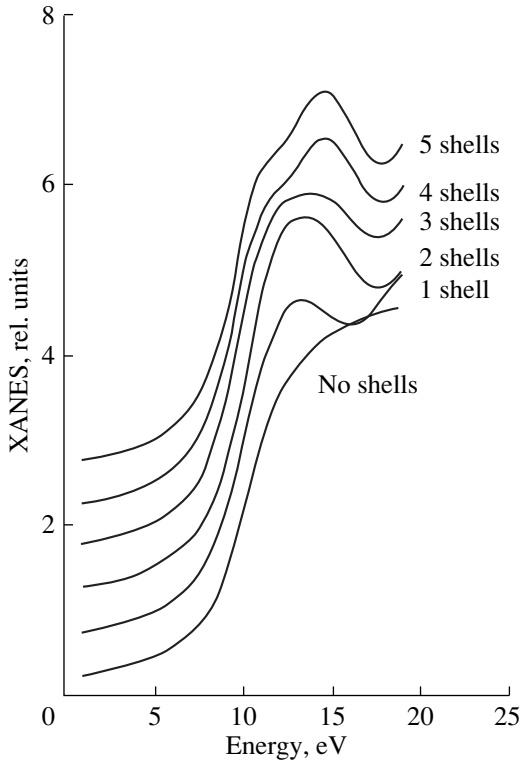

Fig. 1. Absorption spectrum of rubidium in RbCl in the solid state calculated for clusters of different size by the total multiple scattering method. Zero of the energetic scale corresponds to zero of the muffin-tin potential.

spectrum structure in the vicinity of the x-ray absorption *K* edge) does not give results as satisfactory as those given for the absorption *L* spectra associated with transitions between localized states.

An algorithm of the total multiple scattering method and the program complex G4XANES were described previously in [18]. The parameters and structure of the NaCl crystalline lattice with lattice constant 6.581 Å [19] were used in the calculations. To estimate phase shifts, we utilized the crystalline muffin-tin potential constructed by means of the Mattheiss scheme with mutually touching spheres. The exchange part of this potential was calculated in the Slater model with the exchange constant equal to 1.0. The atomic charge planes were found by the Dirac–Slater method. Phase shifts with the orbital angular momentum up to 3 were taken into account in our calculations. In order to compare the theoretical spectrum with an experimental one, we took into account some factors leading to the broadening of the spectrum (the finite lifetime of the core vacancy [20], the mean free path of the photoelectron [21], and the spectral resolution). All these factors contribute to the imaginary part of the complex potential used. We represent the theoretical spectra in a normalized form (i.e., the absorption coefficient in relative units of the atomic absorption coefficient at high energies) in all figures except Fig. 1. To obtain the absolute values of the absorption coefficient, these normalized values should be multiplied by the corresponding value of the atomic absorption coefficient.

Structure of a cluster describing the RbCl crystal

Coordination shell	Atom	Number of atoms in the shell	Shell radius, Å
1	Cl	6	3.29
2	Rb	12	4.65
3	Cl	8	5.7
4	Rb	6	6.58
5	Cl	24	7.36

In order to clarify the factors that influence the XANES Rb *K* spectra in Rb_2ZnCl_4 and to elaborate a method for studying the phase transition, analysis of the Rb spectrum was carried out on a relatively simple RbCl compound by using the total multiple scattering method. First, it was necessary to determine the minimum cluster size that would reproduce all the peculiarities of the experimental XANES spectrum. The results of the total multiple scattering calculation of the XANES Rb *K* spectra in the solid RbCl for clusters of different sizes are shown in Fig. 1. For simplicity, all spectra are shifted along the ordinate axis. The cluster parameters (their size and the number of atoms in each coordination shell) are shown in the table. The XANES spectrum consists of a single broad maximum and differs considerably from the experimental spectrum in the case of the cluster consisting of a single coordination shell, where the central rubidium atom is surrounded by six chlorine atoms. The calculated structure of the spectrum broadens when the next two coordination shells are added. The structure of the theoretical spectrum agrees with the experiment only when the number of coordination shells in the cluster reaches five. Further increase in the cluster size does not lead to any changes in the spectrum shape. Therefore, the XANES spectrum for the Rb *K* edge results from the multiple scattering of an excited photoelectron inside a cluster of large size (more than 33 atoms, including all types of atoms).

Figure 2 compares the experimental XANES data obtained for the first time for the *K* spectra of rubidium in the solid and liquid state. Zero of the scale used corresponds to 15189 eV in absolute energy units. This scale is utilized for convenience in comparing the experimental data with the calculated spectra, where the zero value of the muffin-tin energy is chosen as the origin of the coordinates [18]. In the obtained spectra, the same tendency is observed as in the earlier studied spectra [4]. After phase transition into the solid state takes place, all spectral peculiarities broaden considerably. As a result, the roll in the longwave region in the vicinity of 9 eV and the maximum in the region of 25 eV disappear, while the principle maximum in the

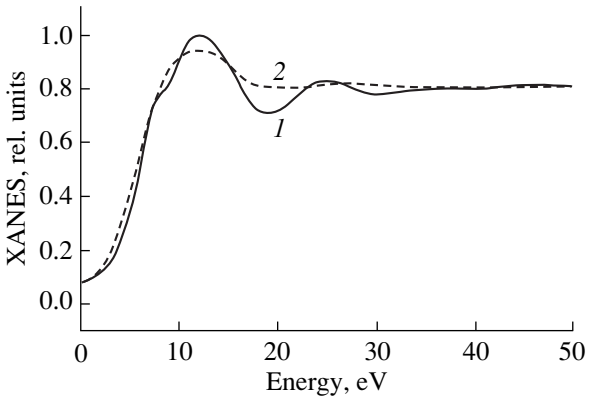

Fig. 2. Experimental XANES *K* spectra of rubidium in RbCl for (*1*) the solid state at 295 K and (*2*) a melt at 1023 K.

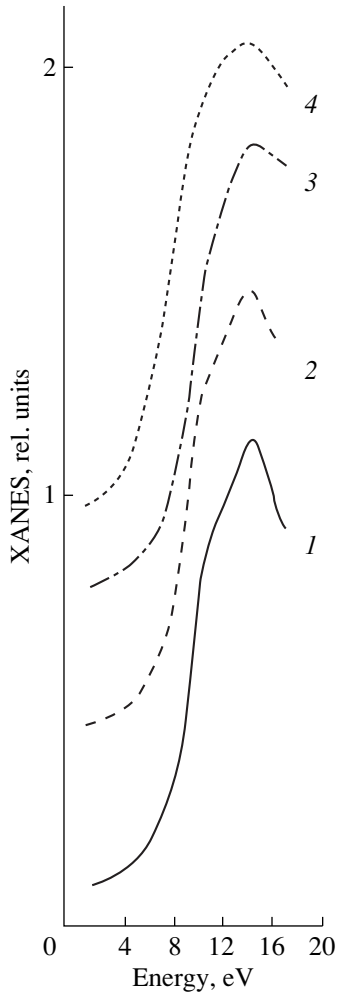

Fig. 3. Theoretically calculated rubidium spectrum in RbCl in a melt: (*1*) the Debye–Waller factor is not taken into account; theoretical approximation taking into account the Debye–Waller factor for (*2*) $\sigma^2 = 0.1$ and (*3*) 0.3 $Å^{-2}$; and (*4*) experimental spectrum of the compound considered.

vicinity of 13 eV decreases in intensity and increases in width.

Calculations for the RbCl melt were carried out in the Debye–Waller approximation [4]. The σ^2 parameter was chosen in such a way as to guarantee the best correspondence with the experiment. The consecutive changes in the spectrum structure that occur with increasing σ^2 are shown in Fig. 3. Good agreement with the experimental melt spectra is attained for $\sigma^2 = 0.3$ $Å^{-2}$ (Fig. 3). The same value of σ^2 for a melt was obtained in [4] by means of EXAFS analysis.

Comparing Figs. 1 and 2, one can conclude that the calculation method used gives results consistent with the experimental data. The square of the dipole matrix element of the transition probability is a monotonic smooth function. Taking into account that, in the dipole approximation, the absorption coefficient above the *K* edge is the product of the square of the matrix element of the transition probability and the partial density of *p* states of rubidium, one can conclude that the experimental spectrum gives precise information on the peculiarities of the amplitude energy distribution of the density of unoccupied *p* states of rubidium in the conduction band of the compound studied. The accuracy in this case is to within the matrix element. For this reason, we calculated the partial density of the *p* states of rubidium in the conduction band of RbCl in the ground state (Fig. 4). Analysis of the results obtained will be useful for investigating the peculiarities of the electron subsystems of the described compound and of the changes appearing in this compound in the course of the phase transition. The partial density of the unoccupied *p* states of Cl is shown in the same figure. A comparison of these two curves allows one to make a conclusion that the main peculiarities of the Rb and RbCl absorption spectra have a hybridized character.

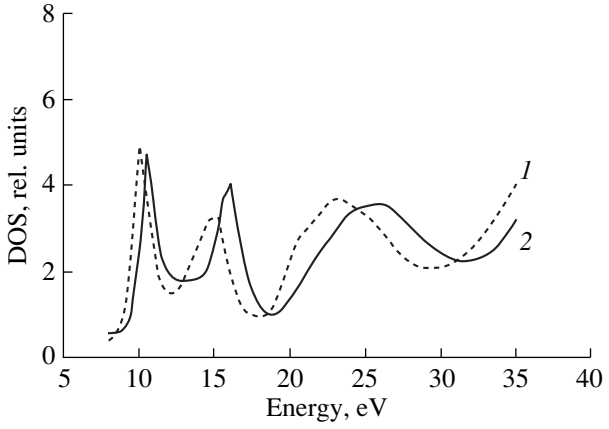

Fig. 4. Partial densities of states calculated for a cluster with five coordination shells, which approximates the RbCl crystal: (*1*) partial density of *p* states of Rb and (*2*) partial density of *p* states of Cl. Zero of the energetic scale corresponds to zero of the theoretical muffin-tin potential.

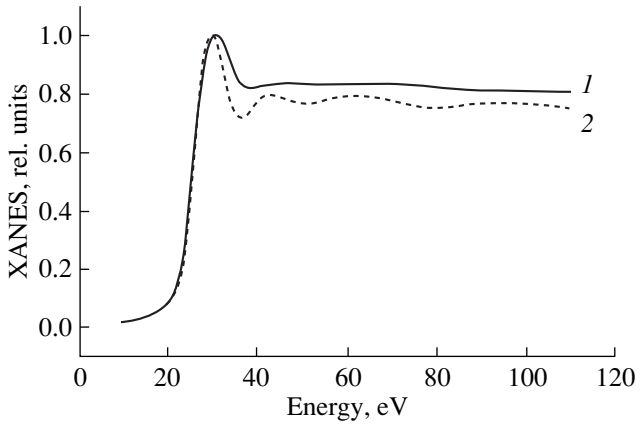

Fig. 5. Experimental XANES *K* spectra of rubidium in Rb_2ZnCl_4 for (*1*) the solid state at 300 K and (*2*) a melt at 823 K.

The experimental XANES *K* spectrum of rubidium in Rb_2ZnCl_4 in the solid and melted states, measured here for the first time, is represented in Fig. 5. Zero corresponds to an energy of 15171 eV. The peculiarities of the RbCl compound found above remain unchanged even for the more complex Rb_2ZnCl_4 compound. For the latter compound, similarly to RbCl, all the details of the spectrum broaden when the transition from the solid into the liquid state takes place. It is obvious that the σ^2 parameter will have the same order of magnitude both for this substance and for RbCl. Due to the complexity of the structure of the considered compound [8], theoretical calculations demand a large amount of computer time and will be presented elsewhere.

ACKNOWLEDGMENTS

This paper was supported by the Russian Foundation for Basic Research, grant no 96-02-10034, and the CNSF (China), grant no 19811121206.

REFERENCES

1. C. Massobrio, A. Pasquarello, and C. Roberto, Phys. Rev. Lett. **80**, 2342 (1998).
2. A. Meyer, J. Wuttke, W. Petry, *et al.*, Phys. Rev. Lett. **80**, 4454 (1998).
3. Y. Wang, K. Lu, and Ch. Li, Phys. Rev. Lett. **79**, 3664 (1997).
4. M. Minicucci and A. Di Cicco, Phys. Rev. B **56**, 11456 (1997).
5. A. V. Sapelkin, S. C. Bayliss, A. G. Lyapin, *et al.*, Phys. Rev. B **56**, 11531 (1997).
6. A. Di Cicco, M. J. Rosolen, R. Marassi, *et al.*, J. Phys.: Condens. Matter **8**, 10779 (1996).
7. R. V. Kulkarmi and D. Stroud, Phys. Rev. B **57**, 10476 (1998).
8. H. M. Lu and J. R. Hardy, Phys. Rev. B **45**, 7609 (1992).
9. V. Katkanant, P. J. Edwardson, J. R. Hardy, and L. L. Boyer, Phys. Rev. Lett. **57**, 2033 (1986).
10. P. J. Edwardson, V. Katkanant, P. J. Edwardson, *et al.*, Phys. Rev. B **35**, 8470 (1987).
11. P. J. Edwardson and J. R. Hardy, Phys. Rev. B **38**, 2250 (1988).
12. A. Bianconi, *X-ray Absorption: Principles, Applications, and Techniques of EXAFS, SEXAFS, and XANES* (Wiley, New York, 1983), p. 573.
13. L. A. Grunes, R. D. Leapman, C. N. Wilker, *et al.*, Phys. Rev. B **25**, 7157 (1982).
14. F. M. F. de Groot, J. Faber, J. M. Michiels, *et al.*, Phys. Rev. B **48**, 2074 (1993).
15. D. Norman, J. Stohr, R. Jaeger, *et al.*, Phys. Rev. Lett. **51**, 2052 (1983).
16. A. V. Soldatov, T. S. Ivanchenko, and A. Bianconi, Opt. Spektrosk. **77** (3), 421 (1994) [Opt. Spectrosc. **77**, 372 (1994)].
17. A. A. Pavlychev, A. S. Vinogradov, I. V. Kondrat'eva, and T. M. Zimkina, Fiz. Tverd. Tela (Leningrad) **27** (1), 209 (1985) [Sov. Phys. Solid State **27**, 123 (1985)].
18. S. Della Longa, A. V. Soldatov, M. Pompa, and A. Bianconi, Comput. Mater. Sci. **4**, 199 (1995).
19. R. W. G. Wyckoff, *Crystal Structure* (Interscience, New York, 1963).
20. *Unoccupied Electronic States: Fundamentals for XANES, EELS, IPS, and BIS*, Ed. by J. C. Fuggle and J. E. Inglesfield (Springer-Verlag, Berlin, 1992).
21. J. E. Muller, O. Jepsen, and J. W. Wilkins, Solid State Commun. **42**, 365 (1982).

Translated by A. Sonin

Physics of the Solid State, Vol. 43, No. 1, 2001, pp. 190–193. Translated from Fizika Tverdogo Tela, Vol. 43, No. 1, 2001, pp. 182–185.

FULLERENES AND ATOMIC CLUSTERS

Low-Temperature Heat Capacity and Heat Conductivity of Single-Crystal Synthetic Opals

V. N. Bogomolov*, L. S. Parfen'eva*, I. A. Smirnov*, H. Misiorek, A. Jezowski**, A. I. Krivchikov***, and B. I. Verkin*****

** Ioffe Physicotechnical Institute, Russian Academy of Sciences, Politekhnicheskaya ul. 26, St. Petersburg, 194021 Russia*
e-mail: Igor.Smirnov@shuvpop.ioffe.rssi.ru

*** Institute of Low-Temperature and Structural Research, Polish Academy of Sciences, 50-850 Wroclaw 2, Poland*

**** Institute for Low-Temperature Physics and Engineering, National Academy of Sciences of Ukraine, Kharkov, 310164 Ukraine*

Received May 26, 2000

Abstract—The heat capacity at constant pressure (in the range 3–50 K) and the lattice heat conductivity (from 5 to 75 K) of a single-crystal synthetic opal are measured. It is shown that the heat capacity of the opal behaves at these temperatures in a way similar to porous amorphous materials. The data on the heat conductivity suggest that single-crystal opals can be related to a class of semicrystalline (partially crystallized amorphous) materials. However, because of specific features of their crystal structure, the opals form a nonstandard type of semicrystalline material which we termed semiamorphous. © *2001 MAIK "Nauka/Interperiodica".*

Studies of the heat capacity κ of opals and related nanocomposites are dealt with in a large number of publications [1–6]. The opals studied were of varying degrees of perfection [1, 2]. The heat capacity (C) of opals has not been investigated before.

Opals are very interesting subjects for various physical experimentations. They exhibit a unique crystal structure of the fractal type [1, 7, 8]. Opals consist of closely packed spheres of amorphous SiO_2 ~2000–2500 Å in diameter (first-order spheres). These spheres contain an array of closely packed spheres of smaller sizes, ~300–400 Å (second-order spheres), which, in turn, are formed of closely packed particles ~100 Å in size (third-order spheres). The lattice of closely packed spheres has voids of the octahedral and tetrahedral types. Depending on the order of the spheres, the voids can also be divided into voids of the first, second, and third orders.

The octahedral and tetrahedral voids of the first, second, and third orders measure 800, 140, and 30 Å and 400, 70, and 15 Å, respectively. Their contributions to the total porosity of the opal are 26, 19, and 14%. Thus, the total porosity of the opal is ~59%. However, the actual total porosity, even of fairly perfect opal samples, is only 46–50% [2, 9]. This is due to a possible sintering of the second- and third-order SiO_2 spheres. The porosity of the first-order sphere array remains equal to the theoretical estimate, which is, as was mentioned above, 26% [1–6].

The voids in the opal are connected to one another through channels. The first-order amorphous SiO_2 spheres form a regular face-centered lattice with a lattice constant of ~3000–4000 Å. Thus, the opal can be considered an amorphous medium (the first-order amorphous SiO_2 spheres) with spatially modulated properties (the regular arrangement of the amorphous SiO_2 spheres making up a cubic lattice).

In this work, we measured the heat capacity at constant pressure (C_p) in the temperature range 3–50 K and the heat conductivity in the range 5–75 K for perfect synthetic opal single crystals.

The technique of sample preparation was described briefly in [1]. X-ray diffraction analysis showed that the opals are purely amorphous materials [2, 3, 5]. No trace of the crystalline SiO_2 phase was found in the samples studied. Optical structural analysis [2, 10] was used to determine the parameter of the cubic lattice formed by the first-order amorphous SiO_2 spheres. The SiO_2 sphere dimensions were comparable to the wavelength of visible light, which served in this case as an analog of x-rays in x-ray diffraction measurements. The SiO_2 amorphous spheres in the sample studied were ~2350 Å in size, and the crystal lattice constant was found to be ~3300 Å.

The heat capacity was determined by the adiabatic technique, and the heat conductivity was measured by a technique similar to that employed in [11].

The objective of this work was (i) to study the effect exerted on the heat capacity and heat conductivity of the opal by the spatial modulation of its properties (the regular arrangement of the first-order SiO_2 amorphous spheres) and by the corresponding "crystallinity" of the object under study and (ii) to determine the effect of the large opal porosity on $C(T)$.

1063-7834/01/4301-0190$21.00 © 2001 MAIK "Nauka/Interperiodica"

Figure 1 shows our data on the heat capacity $C_p(T)$ for the opal. For comparison, this figure also displays the available data on the heat capacity $C_v(T)$ for crystalline and amorphous SiO_2 [12] and on $C_p(T)$ for SiO_2 aerogels [13].

Figures 2 and 3 display our data for the opal sample in the C/T^3–T coordinates, to be compared with the corresponding data for amorphous and crystalline SiO_2 [12].

As is seen from Figs. 1–3, $C_p(T)$ of the opal sample behaves in a similar fashion to that of classical amorphous materials:

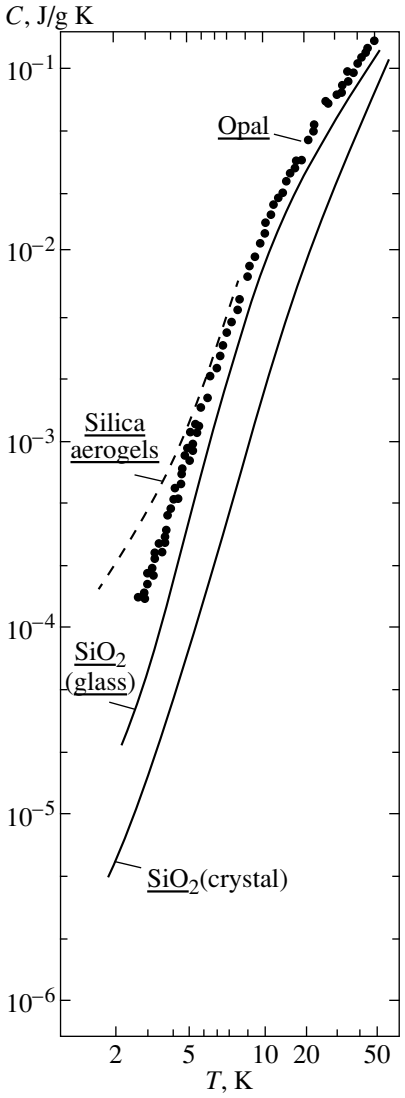

Fig. 1. Temperature dependences of the heat capacity for a number of amorphous and crystalline materials. Points are the results of our experiment for C_p of an opal sample (density is ~1.1–1.3 g/cm^3). The data for C_v of crystalline and amorphous SiO_2 (density of the amorphous material is ~2.2 g/cm^3) are taken from [12]; for C_p of two SiO_2 aerogel samples with densities of 0.275 and 0.145 g/cm^3, from [13].

(1) The heat capacity of the opal substantially exceeds that of crystalline SiO_2 and, insignificantly, that of amorphous SiO_2; however, starting from $T > 6$ K, it practically coincides with the heat capacity of highly porous SiO_2 aerogel (Fig. 1).

(2) The magnitude of C_p/T^3 increases with a decrease in temperature, passes through a bell-shaped maximum and a fairly sharp minimum, and rises again as the temperature decreases still more (Figs. 2, 3).

As follows from the classical model of the behavior of $C(T)$ in amorphous solids, at low temperatures ($T <$ 1 K) in glasses, $C \sim T$ (rather than $C \sim T^3$, as is the case in crystalline solids) and there is an excess of the heat capacity compared to crystals and to the Debye contribution to C, which can be calculated, for instance, from the sound velocity (Fig. 3) [12].

This behavior of $C(T)$ in amorphous solids is interpreted in terms of the phenomenological two-level-system tunneling model [14, 15]. As the temperature rises above 1 K, this model becomes progressively inapplicable. The heat capacity does not begin to increase as ~T, but in amorphous solids, it is still higher than in crystals up to approximately ~100 K [12]. Unfortunately, there is still no universally accepted explanation of the above effect. The heat capacities of amorphous and crystalline solids most frequently coincide at $T >$ 100 K [12].

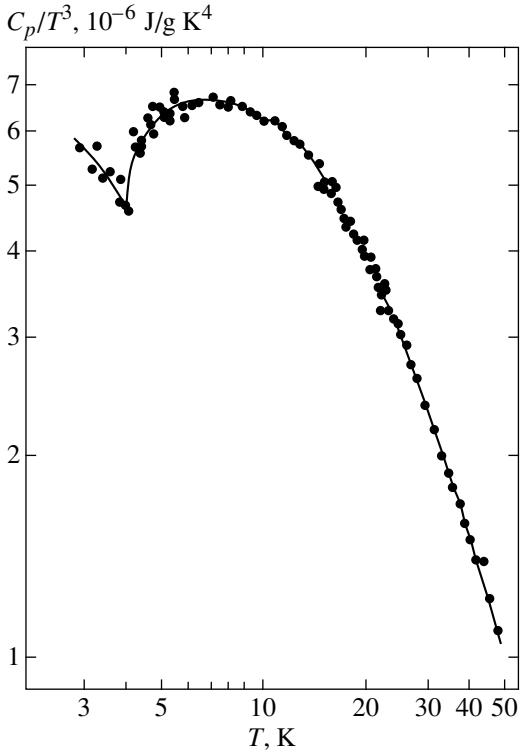

Fig. 2. Dependence of C_p/T^3 on T for the opal sample studied.

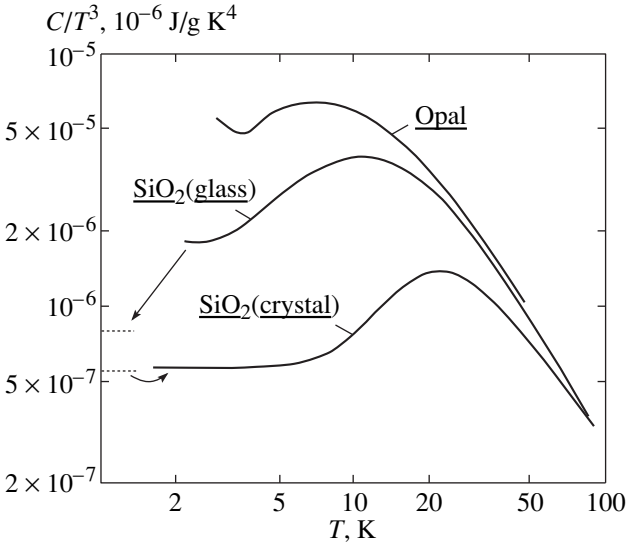

Fig. 3. Comparison of the behavior of $C/T^3 = f(T)$ for C_V of crystalline and amorphous SiO_2 [12] and for C_p of the opal sample studied. Dashed lines represent the heat capacity calculated from data on the elastic constants within the Debye model [12].

Thus, analysis of our data on the heat capacity of opals and comparison with the available data on the heat capacity of amorphous solids permit one to conclude that the behavior of $C(T)$ in opals does not exhibit any specific features associated with the regular arrangement of the first-order amorphous SiO_2 spheres (i.e., with the crystallinity). The heat capacity of opals behaves in a similar fashion to that of conventional porous amorphous materials.

Analysis of the data on the heat conductivity of the opal single crystal studied led us to the following new and interesting considerations.

The opal is an insulator, and, therefore, the experimentally measured heat conductivity is that of the crystal lattice κ_{ph}.

Earlier [1, 2], we studied the heat conductivity of synthetic opals with varying degrees of perfection. According to these measurements, the heat conductivity $\kappa_{ph}(T)$ of moderately perfect opal samples (not single crystals) showed a behavior typical of classical amorphous solids [1, 2]. At low temperatures (4–25 K), $\kappa_{ph} \sim T^2$, in the range 25–60 K, the heat conductivity exhibited a plateau, after which, at $T > 60$ K, it increased directly with $\sim T$. In more perfect samples (close in quality to single crystals), κ_{ph} behaved in a manner characteristic of a "semicrystalline" material [16, 17]. For these samples, $\kappa_{ph} \sim T$ throughout the temperature range covered (4–300 K). What is a classical "semicrystalline" material? It is an amorphous solid containing crystallized regions (i.e., the crystalline phase is embedded in an "amorphous sea" [16, 17]). These materials exhibit no plateau in $\kappa_{ph}(T)$, and the low-temperature heat conductivity can increase with temperature by a law from $\kappa_{ph} \sim T$ to $\kappa_{ph} \sim T^3$, depending on the actual amount of crystallized phase involved. The variations in κ_{ph} (a decrease in κ_{ph} at very low temperatures in semicrystalline materials compared to the amorphous matrix) and its temperature dependence are accounted for by the appearance of a thermal resistance at the amorphous-solid–crystal interfaces in semicrystalline materials [16, 17].

The experimental results on $\kappa_{ph}(T)$ obtained in this work for a perfect single-crystal opal sample are shown in Fig. 4a. We readily see that this graph has no plateau and that $\kappa_{ph} \sim T$ throughout the temperature range covered (Fig. 4b); i.e., in this experiment, too, the heat con-

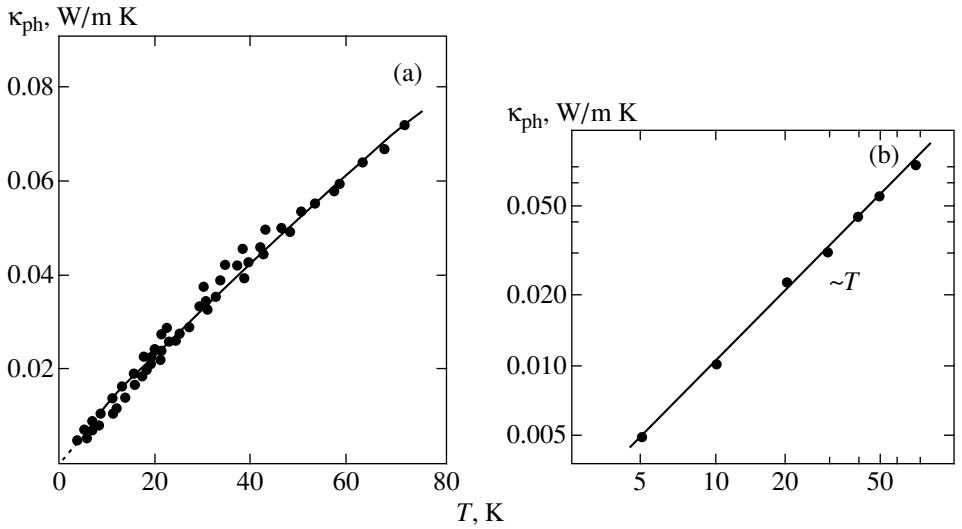

Fig. 4. Temperature dependence of κ_{ph} of the single-crystal synthetic opal: (a) in the κ_{ph}–T coordinates and (b) in the $\log \kappa_{ph} = f(\log T)$ coordinates. The points in Fig. 4b are the averaged data taken from Fig. 4a.

ductivity $\kappa_{ph}(T)$ exhibits properties characteristic of semicrystalline solids [1, 2, 16, 17].[1]

Let us try to find an explanation to the above results. Below, we consider several possible versions.

(1) The dependence of $\kappa_{ph} \sim T$ could correspond in our case to a temperature region above the plateau characteristic of amorphous solids, while the real plateau and the temperature dependence $\kappa_{ph} \sim T^2$ should be expected at lower temperatures ($T < 4$ K). This assumption is in conflict with

(i) our previous studies on the heat conductivity κ_{ph} of opals [1, 2], according to which the plateau is observed for amorphous opals in the range 25–60 K, whereas at 4–25 K, $\kappa_{ph} \sim T^2$; and

(ii) our present data on $C_p(T)$. The plateau in $\kappa_{ph}(T)$ and the bell-shaped hump in the dependence $C/T^3 = f(T)$ of amorphous solids approximately coincide in temperature (see, e.g., [12, 18]). For our opal, the hump in the graph $C/T^3 = f(T)$ lies near 10 K (rather than below 4 K).

(2) Amorphous opals contain regions of crystallized SiO_2, which account for the behavior of $\kappa_{ph}(T)$ characteristic of semicrystalline materials. This assumption should also be ruled out, because, as was already mentioned, x-ray diffraction measurements did not reveal any trace of crystalline SiO_2 in the sample under study.

(3) As was pointed out earlier, the opal possesses a unique crystal structure, which makes it simultaneously an amorphous solid and a crystal. The "amorphicity" is accounted for by the second- and third-order spheres, which do not form a regular substructure throughout the opal crystal. The regular cubic lattice formed by the first-order SiO_2 amorphous spheres is responsible for the crystallinity. Thus, in the case of the opal, we encountered a new type of semicrystalline material in which the amorphous phase (the first-order SiO_2 amorphous spheres) acts as "atomic masses" making up a cubic lattice with a giant lattice constant. Such a semicrystal, unlike the standard classical case [16, 17] (which we will call "a semicrystal of the 1st kind"), can be termed "a semicrystal of the 2nd kind." One can also introduce a new term by calling the latter a semiamorphous material.

The nature of the semicrystallinity (semiamorphicity), which manifests itself in the behavior of $\kappa_{ph}(T)$ in single-crystal opals, will be treated in a separate paper.

This study can be summed up as follows:

(1) The heat capacity of opals at low temperatures (3–50 K) behaves in a manner characteristic of porous amorphous materials.

(2) Analysis of experimental data on the lattice heat conductivity of single-crystal opals allowed us to relate them to a new unusual class of semicrystalline (semiamorphous) solids.

[1] The semicrystal model proposed for a single-crystal opal is not at variance with our data on the heat capacity of opals, because the heat capacity C of amorphous and partially crystallized amorphous materials at low temperatures always exceeds that calculated by the Debye model [17].

ACKNOWLEDGMENTS

We are grateful to N.F. Kartenko and N.V. Sharenkova for x-ray diffraction measurements and to A.V. Prokof'ev for an optical structural analysis of the opal samples studied.

The work was performed within the bilateral agreement between the Russian and Polish Academies of Sciences and was supported by the Russian Foundation for Basic Research (project no. 00-02-16883).

REFERENCES

1. V. N. Bogomolov, L. S. Parfen'eva, A. V. Prokof'ev, *et al.*, Fiz. Tverd. Tela (St. Petersburg) **37** (11), 3411 (1995) [Phys. Solid State **37**, 1874 (1995)].
2. V. N. Bogomolov, D. A. Kurdyukov, L. S. Parfen'eva, *et al.*, Fiz. Tverd. Tela (St. Petersburg) **39** (2), 392 (1997) [Phys. Solid State **39**, 341 (1997)].
3. L. I. Arutyunyan, V. N. Bogomolov, N. F. Kartenko, *et al.*, Fiz. Tverd. Tela (St. Petersburg) **39** (3), 586 (1997) [Phys. Solid State **39**, 510 (1997)].
4. L. I. Arutyunyan, V. N. Bogomolov, N. F. Kartenko, *et al.*, Fiz. Tverd. Tela (St. Petersburg) **40** (2), 379 (1998) [Phys. Solid State **40**, 348 (1998)].
5. V. N. Bogomolov, N. F. Kartenko, L. S. Parfen'eva, *et al.*, Fiz. Tverd. Tela (St. Petersburg) **40** (3), 573 (1998) [Phys. Solid State **40**, 528 (1998)].
6. V. N. Bogomolov, N. F. Kartenko, D. A. Kurdyukov, *et al.*, Fiz. Tverd. Tela (St. Petersburg) **41** (2), 348 (1999) [Phys. Solid State **41**, 313 (1999)].
7. V. N. Bogomolov and T. M. Pavlova, Fiz. Tekh. Poluprovodn. (St. Petersburg) **29** (5–6), 826 (1995) [Semiconductors **29**, 428 (1995)].
8. V. G. Balakirev, V. N. Bogomolov, V. V. Zhuravlev, *et al.*, Kristallografiya **38** (3), 111 (1993) [Crystallogr. Rep. **38**, 348 (1993)].
9. V. V. Ratnikov, Fiz. Tverd. Tela (St. Petersburg) **39** (5), 956 (1997) [Phys. Solid State **39**, 856 (1997)].
10. V. N. Bogomolov, A. V. Prokof'ev, and A. I. Shelykh, Fiz. Tverd. Tela (St. Petersburg) **40** (4), 648 (1998) [Phys. Solid State **40**, 594 (1998)].
11. A. Jezowski, J. Mucha, and G. Pompe, J. Phys. D: Appl. Phys. **20**, 1500 (1987).
12. R. C. Zeller and R. O. Pohl, Phys. Rev. B **4** (6), 2029 (1971).
13. T. Sleator, A. Bernasconi, D. Posselt, *et al.*, Phys. Rev. Lett. **66** (8), 1070 (1991).
14. P. W. Anderson, B. I. Halperin, and C. M. Varma, Philos. Mag. **25**, 1 (1972).
15. W. A. Phillips, J. Low. Temp. Phys. **7**, 351 (1972).
16. C. L. Choy and D. Greig, J. Phys. C: Solid State Phys. **8**, 3131 (1975).
17. A. Assfalg, J. Phys. Chem. Solids **36**, 1389 (1975).
18. D. A. Ackerman, D. Moy, R. C. Potter, *et al.*, Phys. Rev. B **23**, 3886 (1981).

Translated by G. Skrebtsov

Physics of the Solid State, Vol. 43, No. 1, 2001, pp. 194–196. Translated from Fizika Tverdogo Tela, Vol. 43, No. 1, 2001, pp. 186–188.

FULLERENES AND ATOMIC CLUSTERS

Sound Velocity in Single Crystals of Synthetic Opals

V. N. Bogomolov*, I. A. Smirnov*, N. V. Sharenkova*, and G. Bruls**

** Ioffe Physicotechnical Institute, Russian Academy of Sciences, Politekhnicheskaya ul. 26, St. Petersburg, 194021 Russia*

*** Goethe Universität, Frankfurt a. M., 60054 Germany*

e-mail: Igor.Smirnov@shuvpop.ioffe.rssi.ru

Received May 31, 2000

Abstract—The [111] longitudinal sound velocity (v_L) in a single-crystal synthetic opal has been measured at a frequency of 10 MHz in the temperature range 4.2–300 K. At 300 K, $v_L = 2.1 \times 10^5$ cm/s. The quantity $dv_L/v_{300\,K}(T)$ (where $dv_L = v_{T,\,K} - v_{300\,K}$) in the ranges 4.2–200 and 200–300 K behaves in the way typical of amorphous and crystalline solids, respectively. *© 2001 MAIK "Nauka/Interperiodica".*

Recent years have witnessed a considerable interest expressed by researchers in the properties of synthetic opals. Opals possess a very unusual crystal structure [1, 2], which accounts for a number of the unique physical properties they exhibit. Opals have turned out to be the only solid-state materials with a photonic band gap for visible light (photonic crystals). This has aroused the intense interest of experimenters and, accordingly, has stimulated an avalanche of papers dealing with this effect (see, e.g., the pioneering works [3–5]).

Opals represent a porous material with a regular arrangement of pores making up a regular lattice [1, 2]. This made it possible to construct a three-dimensional opal-based nanocomposite with a cubic lattice of a filler material ("matrix quasicrystals"), which is characterized by a giant lattice constant (~3000–4000 Å) and "heavy atomic masses" (see [6] and references therein).

Nanocomposites based on an opal with semiconductors introduced in its pores are promising materials for the development of large-density arrays of electronic devices (see, e.g., [7, 8]).

In what respect is the opal crystal structure unusual? Opals possess a fractal structure [9]. They consist of closely packed spheres of amorphous SiO_2, ~2000–2500 Å in diameter (first-order spheres). These spheres are made up of an array of SiO_2 spheres of a smaller diameter, ~300–400 Å (second-order spheres), which, in turn, are formed of SiO_2 particles about 100 Å in size (third-order spheres). The lattice of the closely packed spheres has octahedral and tetrahedral voids, which can also be subdivided into voids of the first, second, and third orders. In our analysis of the sound velocity data, we will be interested in the first-order structure of amorphous SiO_2 spheres and the total fraction of the opal porosity, which is 59% (the first-order pores add up to 26%). The voids in the opal are connected to one another through channels. The first-order amorphous SiO_2 spheres (and first-order octahedral, ~800 Å, and tetrahedral, ~400 Å, voids)[1] make up a regular face-centered cubic lattice with a giant spacing parameter of ~3000–4000 Å. The opal density is ~1.1–1.3 g/cm^3 [9].

Thus, opals can be considered an amorphous medium (first-order amorphous SiO_2 spheres) with spatially modulated properties (the regular arrangement of the amorphous SiO_2 spheres making up the cubic lattice).

Earlier, we studied the heat conductivity [1, 13, 14] and heat capacity [14] of single-crystal synthetic opals. It was shown that the heat capacity of these materials at constant pressure in the temperature range 3–50 K behaves similarly to porous amorphous solids. It could be expected that, at high temperatures, the heat capacity of opals would coincide with that of crystalline SiO_2. (At $T > 100$ K, the heat capacities of amorphous and crystalline solids, as a rule, coincide [15].)

The behavior of the lattice heat conductivity of single-crystal opals is similar to that of classical semicrystalline materials, which represent an amorphous solid with embedded crystallized regions. However, in the case of opals, we encountered a new kind of semicrystalline material, in which the amorphous phase (the first-order amorphous SiO_2 spheres) acts as "atomic masses" making up a cubic face-centered lattice. Such a "semicrystalline" material, unlike the classical case [16], was termed semiamorphous [14].

To gain a better understanding of the heat transport processes in opals, it was of interest to elucidate how the sound velocity would behave in these materials, specifically whether it would be affected by the spatial modulation of their properties (the regular arrangement of the first-order amorphous spheres and the ensuing

[1] In the course of the formation of opal-based nanocomposites, the first-order voids and channels are filled by various methods [6, 10–12] with metals, semiconductors, and insulators, which form, as already mentioned, matrix quasicrystals with a giant lattice constant and heavy atomic masses (i.e., voids ~800 Å in size filled with various materials).

Behavior of various physical parameters in a single-crystal opal at low and high temperatures

Parameter	Behavior	
	low temperatures	high temperatures
Sound velocity	Typical of amorphous materials, T = 4–200 K	Typical of crystalline materials, T = 200–300 K
Heat capacity	Typical of amorphous materials, T < 50 K	Typical of crystalline materials, T > 100 K
Lattice heat conductivity	Typical of semicrystalline (semiamorphous) solids, T = 4–300 K	

"crystallinity" of the medium) and how the "amorphicity" of the opal associated with the presence of embedded first-order amorphous SiO_2 spheres would manifest itself. Unfortunately, no studies of the sound velocity in opals have been carried out thus far.

In this work, the longitudinal sound velocity (v_L) in a single-crystal opal sample used in a previous work [14] was measured in the temperature range 4–300 K. The sample to be studied consisted of first-order amorphous SiO_2 spheres ~2350 Å in diameter, which made up a cubic face-centered lattice with the spacing parameter $\alpha \sim 3300$ Å [14].

The sound velocity v_L was measured at a frequency of 10 MHz along the [111] axis of the opal single crystal. The technique employed in the measurements was described in [17].

The sample measured $2.4 \times 2.5 \times 6$ mm (Fig. 1). The sound was launched along the 2.4-mm face, which coincided with the [111] crystallographic direction. The scheme of the v_L measurement is presented in Fig. 1. The quartz sensors were attached with Thiokol 32 cement. Special precautions were taken to prevent cement penetration into the bulk of the sample (the cement penetrated to a depth of no more than a few tenths of a millimeter, which did not introduce a significant error into the v_L measurement). The measurements were conducted under vacuum.[2] It was found that at 300 K, $v_L = 2.1 \times 10^5$ cm/s (the accuracy of determination was ~10%). The experimental results obtained for $dv_L/v_{300\,K} = f(T)$ ($dv_L = v_{T,K} - v_{300\,K}$) are shown in Fig. 1a. The quantity $dv_L/v_{300\,K}$ exhibits a nonstandard temperature dependence. Within the range 300–200 K, it increases with a decrease in temperature, as anticipated for crystalline solids, whereas in the range from 200 to 4 K, its temperature dependence is typical of amorphous materials (cf. Fig. 1b) [18–20]. The results obtained on $dv_L/v_{300\,K}(T)$ correlate well with the experimental data on the lattice heat capacity and the heat conductivity of single-crystal opals [14].

As with the heat capacity and heat conductivity, we encounter here the dual nature of opals in that they behave simultaneously as a crystal and as an amorphous solid.

As in the case of the heat capacity, the data obtained on $dv_L/v_{300\,K}(T)$ at low temperatures can be interpreted in terms of a two-level system tunneling model. As the

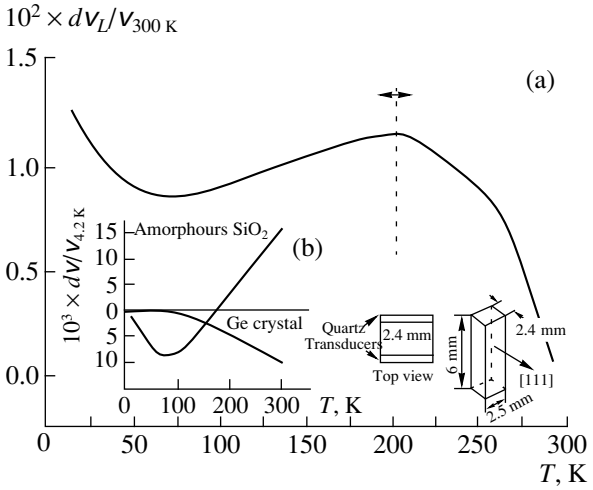

Fig. 1. Temperature dependences of (a) $dv_L/v_{300\,K}$ for a single-crystal synthetic opal and (b) $dv_L/v_{4.2\,K}$ for amorphous SiO_2 and crystalline Ge [18]. Shown in the lower right corner are the scheme of the measurements and the sample dimensions.

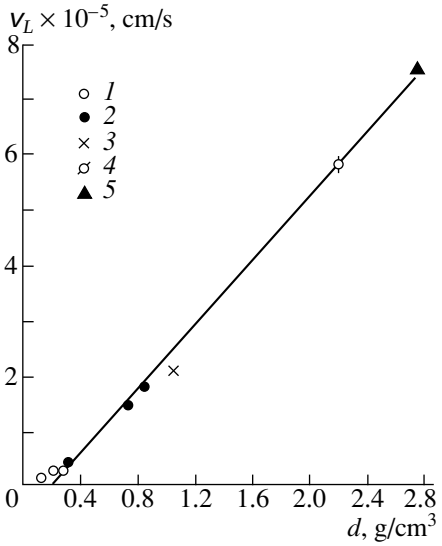

Fig. 2. The dependence of v_L on the density at 300 K for some materials based on amorphous SiO_2: (*1*) silica gels [21], (*2*) silica gels [22], (*3*) our data on the single-crystal synthetic opal, (*4*) amorphous SiO_2 [23, 24], and (*5*) amorphous SiO_2 after uniaxial compression up to 16 GPa at 300 K [25, 26].

[2] To speed up the onset of thermal equilibrium, ^{4}He was admitted into the chamber at a pressure of a few mbar. We believe that this should not affect the measured velocity v_L.

temperature increases, this model becomes gradually invalid, so that at high temperatures, the behavior of $dv_L/v_{300\,K}(T)$ is fully governed by the "crystalline" nature of the material.

The present experimental data and our earlier results obtained in a study of the heat capacity and heat conductivity of a single-crystal opal [14] are summarized in the table illustrating the behavior of v_L, κ_L, and C in various temperature ranges.

We note with interest the dependence of v_L on the density d of a number of materials based on amorphous quartz (amorphous quartz, amorphous SiO_2 subjected to uniaxial pressure, silica gels, and opals). This is shown in Fig. 2. One observes a linear dependence of v_L on d.

ACKNOWLEDGMENTS

We are grateful to A.V. Prokof'ev for crystallographic orientation of the opal sample for measurements.

This work was carried out within the bilateral agreement between the Russian Academy of Sciences and the German Scientific Society ("Advanced Materials with Collective Electronic Properties" project) and was supported by the Russian Foundation for Basic Research (project no. 00-02-16883).

REFERENCES

1. V. N. Bogomolov and T. M. Pavlova, Fiz. Tekh. Poluprovodn. (St. Petersburg) **29** (5–6), 826 (1995) [Semiconductors **29**, 428 (1995)].
2. V. G. Balakirev, V. N. Bogomolov, V. V. Zhuravlev, *et al.*, Kristallografiya **38** (3), 111 (1993) [Crystallogr. Rep. **38**, 348 (1993)].
3. V. N. Bogomolov, D. A. Kurdyukov, A. V. Prokof'ev, and S. M. Samoĭlovich, Pis'ma Zh. Éksp. Teor. Fiz. **63**, 56 (1996) [JETP Lett. **63**, 520 (1996)].
4. V. N. Bogomolov, A. V. Prokof'ev, and S. M. Samoĭlovich, Fiz. Tverd. Tela (St. Petersburg) **38** (9), 2722 (1996) [Phys. Solid State **38**, 1493 (1996)].
5. V. N. Bogomolov, S. V. Gaponenko, I. N. Germanenko, *et al.*, Phys. Rev. E **55** (6), 7619 (1997).
6. V. N. Bogomolov, N. F. Kartenko, D. A. Kurdyukov, *et al.*, Fiz. Tverd. Tela (St. Petersburg) **41** (2), 348 (1999) [Phys. Solid State **41**, 313 (1999)].
7. K. Kh. Babamuratov, V. V. Zhuravlev, Yu. A. Kumzerov, *et al.*, Fiz. Tverd. Tela (St. Petersburg) **35** (6), 1577 (1993) [Phys. Solid State **35**, 795 (1993)].
8. V. N. Bogomolov, Yu. A. Kumzerov, S. G. Romanov, and V. V. Zhuravlev, Physica C (Amsterdam) **208**, 371 (1993).
9. V. N. Bogomolov, L. S. Parfen'eva, A. V. Prokof'ev, *et al.*, Fiz. Tverd. Tela (St. Petersburg) **37** (11), 3411 (1995) [Phys. Solid State **37**, 1874 (1995)].
10. L. I. Arutyunyan, V. N. Bogomolov, N. F. Kartenko, *et al.*, Fiz. Tverd. Tela (St. Petersburg) **39** (3), 586 (1997) [Phys. Solid State **39**, 510 (1997)].
11. L. I. Arutyunyan, V. N. Bogomolov, N. F. Kartenko, *et al.*, Fiz. Tverd. Tela (St. Petersburg) **40** (2), 379 (1998) [Phys. Solid State **40**, 348 (1998)].
12. V. N. Bogomolov, N. F. Kartenko, L. S. Parfen'eva, *et al.*, Fiz. Tverd. Tela (St. Petersburg) **40** (3), 573 (1998) [Phys. Solid State **40**, 528 (1998)].
13. V. N. Bogomolov, D. A. Kurdyukov, L. S. Parfen'eva, *et al.*, Fiz. Tverd. Tela (St. Petersburg) **39** (2), 392 (1997) [Phys. Solid State **39**, 341 (1997)].
14. V. N. Bogomolov, L. S. Parfen'eva, I. A. Smirnov, *et al.*, Fiz. Tverd. Tela (St. Petersburg) **43** (1), 182 (2001) [Phys. Solid State **43**, 190 (2001)].
15. R. C. Zeller and R. O. Pohl, Phys. Rev. B **4** (6), 2029 (1971).
16. C. L. Choy and D. Greig, J. Phys. C: Solid State Phys. **8**, 3131 (1975).
17. B. Lüthi, G. Bruls, P. Thalmeier, *et al.*, J. Low. Temp. Phys. **95** (1/2), 257 (1994).
18. A. Jagannathan and R. Orbach, Phys. Rev. B **41** (5), 3153 (1990).
19. H. J. McSkimin, J. Appl. Phys. **24** (8), 988 (1953).
20. J. T. Krause and C. R. Kurkjian, J. Am. Ceram. Soc. **51** (4), 226 (1968).
21. T. Sleator, A. Bernasconi, D. Posselt, *et al.*, Phys. Rev. Lett. **66** (8), 1070 (1991).
22. R. Calemczuk, A. M. de Goer, B. Salce, and R. Maynard, in *Proceedings of the Fifth International Conference on Phonon Scattering in Condensed Matter, Urbana, Illinois, 1986*, Ed. by A. C. Anderson and J. P. Wolfe (Springer-Verlag, Berlin, 1986), p. 126.
23. W. F. Love, Phys. Rev. Lett. **31** (13), 822 (1973).
24. J. M. Grace, A. C. Grace, and A. C. Anderson, Phys. Rev. B **33** (10), 7186 (1986).
25. Da-Ming Zhu, Phys. Rev. B **50** (9), 6053 (1994).
26. A. Polian and M. Grimsditch, Phys. Rev. B **47** (21), 13979 (1993).

Translated by G. Skrebtsov

Physics of the Solid State, Vol. 43, No. 1, 2001, p. 197.

ERRATA

Erratum: "Grain Size, Stress, and Creep in Polycrystalline Solids" [*Phys. Solid State* 42 (8), 1456 (2000)]

F. R. M. Nabarro

The name of the author should read F.R.N. Nabarro.

1063-7834/01/4301-0197$21.00

Physics of the Solid State, Vol. 43, No. 1, 2001, pp. 23–28. Translated from Fizika Tverdogo Tela, Vol. 43, No. 1, 2001, pp. 25–29.

DEFECTS, DISLOCATIONS, AND PHYSICS OF STRENGTH

Radioluminescence of Ionized Electron Color Centers in LiF Crystals

L. A. Lisitsyna

Tomsk State Civil Engineering University, Solyanaya pl. 2, Tomsk, 634003 Russia
e-mail: lisitsyn@list.epd.tpu.edu.ru

Received March 20, 2000; in final form, May 19, 2000

Abstract—Photoluminescence (PL) and temporal variation of optical absorption and radioluminescence (RL) of LiF crystals after irradiation with an electron impulse are investigated by pulse spectrometry methods using different irradiation regimes and different degrees of initial radiation damage. The difference in the RL and PL characteristics of ionized F_2^+ and F_3^+ centers is revealed. Several mechanisms for inducing these centers by irradiation, which differ in energy and kinetic parameters and in temperature dependence, are proposed. It is established that the ionized centers in the radiation active state are created due to the interaction of the respective neutral centers with holes of different thermalization extent. A mechanism for the excitation of these radiation-active centers is proposed. © *2001 MAIK "Nauka/Interperiodica".*

Color-center accumulation with a gain in the integral absorbed radiation dose in a material influences the character and efficiency of the primary interaction of radiation with a substance. Application of pulsed measurement techniques allows one to investigate the interaction of electronic excitations with irradiation-induced defects by direct methods. For example, it was established that the energy yield of Frenkel pairs and self-trapped excitons in a regular lattice decreases with a gain of the absorbed radiation dose. At the same time, the efficiency of the radiative channel of dissipation of the absorbed energy increases [1]. The elucidation of the mechanisms of excitation of irradiation-induced radiation-active defects is of undoubted interest for a description of the processes of defect creation.

The present work is aimed at investigating the radioluminescence of F_2^+ and F_3^+ ionized electron color centers.

1. EXPERIMENTAL TECHNIQUE

Different types of electron centers (F, F_2, F_3, F_2^+, and F_3^+) were preliminarily created in a crystal. The required ratio between them was attained by variation of the temperature at which the crystal was irradiated, by the integral exposure dose, and by the temperature and duration of keeping the crystal after its irradiation. Then, the crystal was exposed to a single electron impulse (EI) with the following characteristics: an EI duration of 20 ns, an average electron energy of 200 keV, and a fluence of 10^{11} cm^{-2}.

The absorption relaxation kinetic curves were measured at the maxima of the absorption bands of color centers, and the radioluminescence (RL) decay kinetics of these centers was investigated in the time interval 10^{-8}–10^3 s after the termination of electron impulse exposure. The investigations were carried out for different temperatures, in the interval 80–300 K, at which the crystal was irradiated, and for various initial degrees of radiation damage of the material.

The change in the center concentration was estimated by the change in the absorption at the maxima of the absorption bands or by the change in the photoluminescence (PL) intensity of these centers. Since the centers are created not only during the EI exposure, but also after the irradiation, the absorption and PL of the irradiated crystal were measured in the specified time interval after the EI exposure.

Measurements of the absolute values of the F_3^+-center concentrations in LiF crystals are complicated due to the overlap of the absorption bands of these centers (460 and 420 nm [2]) and the band at 450 nm associated with F_2 centers. Therefore, only relative concentration changes were estimated from the PL intensity for these centers.

The dependences of the RL and PL intensities of color centers on the exposure dose at 300 K were investigated by the following method. The crystal was irradiated with an EI series having a repetition frequency of 1×10^{-2} Hz. The RL intensity of the centers was measured 10 ns after the termination of each EI of the series, while the PL intensity was measured just before the onset of the next EI. At a constant EI repetition frequency, the PL intensity is proportional to the number of centers created during the EI exposure and for the time interval between two sequential EIs.

The PL of the centers was investigated by exciting it in the corresponding absorption bands. The PL of F_2^+ centers was excited in a 650-nm band, that of F_2 centers, in a 450-nm band, and that of F_3^+ centers, in a 460-nm band.

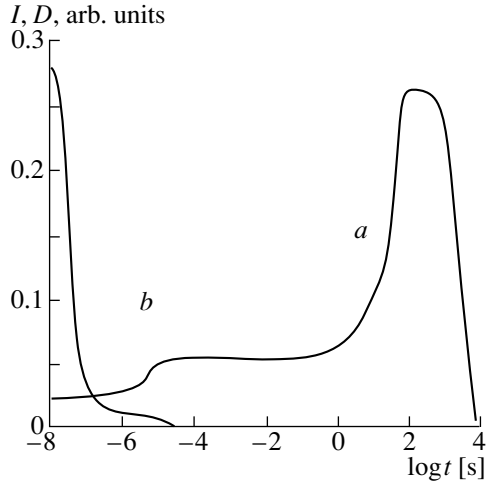

Fig. 1. Kinetics (*a*) of the absorption relaxation at the F_2^+-band maximum and (*b*) of the luminescence in the 910-nm band initiated by the exposure of the crystal to electron impulses at 300 K with F and F_2 centers present in the crystal prior to irradiation.

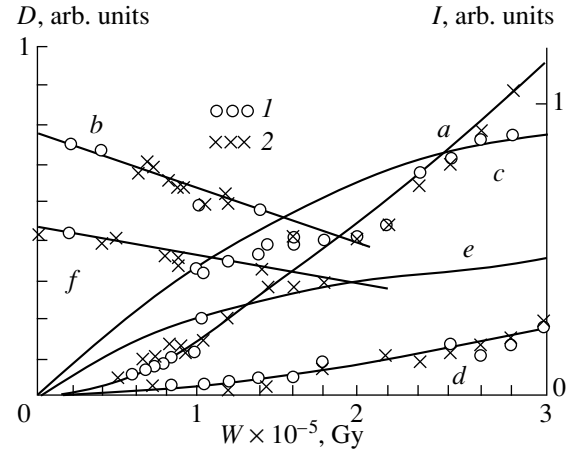

Fig. 2. Exposure-dose dependence of the absorption at the band maxima of (*1a*, *1b*) F_2, (*c*) F_2^+, and (*1d*, *1f*) F_3 centers; of the RL intensity at (*2a*, *2b*) 910 and (*2d*, *2f*) 530 nm; and (*e*) of the PL intensity of F_3^+ centers. The EI repetition frequency is $f = 1 \times 10^{-2}$ Hz and the temperature is (*a*, *c*–*e*) 300 and (*b*, *f*) 80 K.

2. EXPERIMENTAL RESULTS

2.1. Irradiation-Induced F_2^+ Centers

Three stages of the absorption increase at the maximum of the F_2^+ absorption band at 650 nm (Fig. 1) were shown earlier to be stimulated by electron impulse irradiation [3]. These stages can be recognized by their different characteristic times of response to EI duration. In the first of them, the response is inertialess, while the other two go on after irradiation. In the latter stages, the characteristic times of the absorption increase depend on the temperature at which the crystal was irradiated. These stages are associated with the corresponding mechanisms of center creation, which have different time and energy characteristics and lead to different temperature dependences of the processes.

It has been established that the first two stages of the absorption increase are due to the creation of the centers resulting from the interaction of F_2 centers with holes of different thermalization extent, whereas the third stage is due to the creation of F_2^+ centers resulting from the interaction of F centers and anion vacancies.

The RL appears as a result of EI irradiation of the crystal, and its spectrum consists of several bands. The spectral position of one band (910 nm) and its half-width and temperature dependence coincide with the corresponding characteristics of the PL of F_2^+ centers excited in the F_2^+ absorption band (650 nm).

The RL pulse at 910 nm reveals two components (Fig. 1). The short-term component is comparable in duration to the electron impulse and observable at any temperature in the interval 80–300 K. The long-term component appears at $T \geq T_a$, where T_a is the temperature of the delocalization of V_k centers in an LiF crystal (140 K).

Comparative analysis of the PL and RL characteristics of F_2^+ centers shows the following:

(1) The RL intensity of F_2^+ centers is proportional to the concentration of F_2 centers in the crystal at both 300 and 80 K (curves *a*, *b* in Fig. 2). At 300 K, the exposure-dose dependence of the number of F_2 centers accumulated in the crystal coincides with that of the RL intensity of F_2^+ centers excited in this case, as is seen from Fig. 2 (curve *a*). At 80 K, the experiment (curve *b* in Fig. 2) was carried out in the following way. The F, F_2, and F_2^+ centers were created in a crystal irradiated at 300 K. Then, the crystal was exposed to an EI series at 80 K. This extra radiation exposure led to the destruction of the accumulated centers, and luminescence at 910 nm was excited. In response to the exposure to the first EI of the series, all preliminarily accumulated F_2^+ centers were completely destroyed. However, the luminescence at 910 nm was observed not only after the exposure to the first EI of the series, but also after all subsequent EIs. In this case, the luminescence intensity was varied with the EI number (the extra exposure dose) and its change was proportional to the change in absorption at the F_2-band maximum.

In contrast to the RL, the PL intensity of F_2^+ centers does not depend on the concentration of F_2 centers in the crystal. This conclusion follows from the results of direct experiments on the excitation of the PL of F_2^+

centers in crystals with different concentrations of F_2 centers, but with the same concentration of F_2^+ centers.

(2) The RL intensity of F_2^+ centers excited by a single EI does not depend on the concentration of F_2^+ centers present in the crystal prior to irradiation. This can be concluded from the different exposure-dose dependences of the F_2^+-center RL excited after exposure to each successive EI and of the number of F_2^+ centers created for the time interval between two sequential EIs (curves *2a*, *c*, respectively, in Fig. 2).

In contrast to the RL, the PL intensity of F_2^+ centers is proportional to the concentration of F_2^+ centers in the concentration range investigated ($\leq 2 \times 10^{17}$ cm^{-3}).

(3) The temperature dependences of the short-duration component of the RL intensity and the PL intensity of F_2^+ centers are identical. Therefore, the activation energies for the processes of the RL and PL temperature quenching are coincident at $T \geq 130$ K (Fig. 3).

(4) The creation of F_2^+ centers is accompanied by the RL of these centers only at the first and the second stage (Fig. 1). At the third stage, F_2^+ centers are created in the ground state at 300 K, within a time interval of a second after the EI termination.

2.2. Irradiation-Induced F_3^+ Centers

In the RL spectrum of an LiF crystal excited by an EI, there is a band at 530 nm whose spectral position, half-width, and temperature dependence are coincident with the corresponding characteristics of the PL of F_3^+ centers.

The RL pulse at 530 nm, like the RL pulse at 910 nm described above, has a short-term component comparable with the EI in duration, and a long-term component appearing at the delocalization temperature of V_k centers in the crystal.

In contrast to the PL at 530 nm, the RL intensity in this spectral region does not depend on the concentration of F_3^+ centers present in the crystal prior to irradiation. This follows from the dissimilarity of the exposure-dose dependences of the F_3^+-center RL intensity excited under the EI exposure and of the F_3^+-center PL intensity proportional to the concentration of these centers created during the EI exposure and for the time interval between two sequential EIs (curves *2d*, *e* in Fig. 2).

The RL intensity at 530 nm is proportional to the concentration of neutral F_3 centers present in the crystal prior to irradiation. This is evident from a linear correlation, discovered by us, between the RL intensity and the optical absorption at the absorption band maximum (375 nm) of F_3 centers at 300 and 80 K (curves *f*, *d* in Fig. 2). The experiment, the results of which are presented in Fig. 2 by curve *f*, was carried out in the following way. The F, F_2, F_2^+, F_3^+, and F_3 centers were created in the crystal under irradiation at 300 K. Then, the crystal was exposed to an EI series at 80 K. The band at 530 nm in the RL spectrum appeared not only as a result of the exposure of the crystal, with F_3^+ centers having already been present in it, to the first EI, but also because of the action of all subsequent EIs of the series. As the extra EI exposure dose is increased, a correlation is observed between the decrease in the luminescence intensity in the 530-nm band and the optical absorption at the F_3-band maximum at 375 nm.

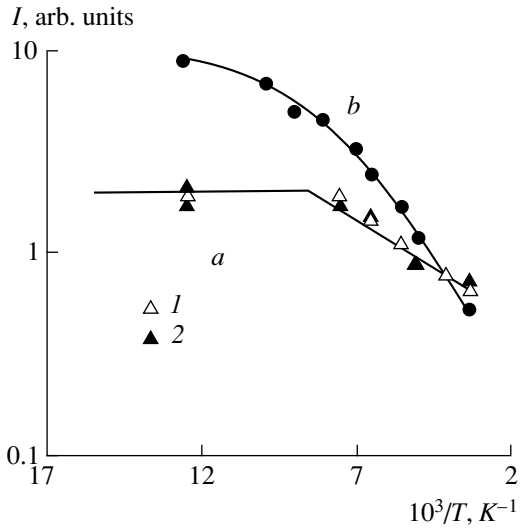

Fig. 3. Temperature dependence (*1a*) of the PL intensity at 910 nm excited in the 650-nm band and of the RL intensity at (*2a*) 910 and (*b*) 670 nm stimulated by a single EI exposure of an LiF crystal with F and F_2 centers.

The following conclusions can be drawn from the investigations into the irradiation-induced F_3^+ centers described above:

(1) The creation of F_3^+ centers in the radiation active state due to irradiation occurs in two time intervals: during EI exposure and after EI termination, with the delay time being determined by the V_k-center lifetime at a corresponding temperature. Only the long-term stages of the creation of these centers, observed after irradiation, were known previous to our investigations. The centers were created in the ground state as a result of two processes: the interaction of F_2 centers with anion vacancies and the interaction of F_2^+ centers with F centers [4–6].

(2) The number of F_3^+ centers in the radiation active state created under EI exposure correlates with the concentration of neutral F_3 centers preliminarily created in the crystal, but does not dependent on the concentration of F_3^+ centers preliminarily created in the crystal.

3. DISCUSSION

In the RL spectrum induced by the exposure of an LiF crystal to EIs, there are bands which coincide in spectral and kinetic parameters with the luminescence bands observed in the optically excited crystal. In particular, the RL at 910 and 530 nm can also be optically excited in the absorption bands of F_2^+ and F_3^+ centers, respectively.

The following general features were established through comparative analysis of the RL characteristics at 910 and 530 nm:

(1) The RL pulse at 910 nm, as well as at 530 nm, has a short-term and a long-term component, the latter appearing above the delocalization temperature of V_k centers.

(2) The RL intensities at 910 and 530 nm are independent of the concentrations of F_2^+ and F_3^+ centers, respectively, present in the crystal prior to irradiation.

(3) The RL intensities at 910 and 530 nm correlate with the concentrations of F_2^+ and F_3^+ centers, respectively, present in the crystal prior to irradiation.

The similarity between the features of F_2^+- and F_3^+-centers RL indicates the general mechanism of the luminescence excitation of these centers under EI exposure.

A set of experimental data on the irradiation-induced luminescence of color centers, obtained by us, indicates the identity of the PL and RL spectral and kinetic characteristics of the ionized centers. However, the presence of these ionized centers in the crystal prior to irradiation does not affect the EI-excited luminescence yield. To reconcile these, at first glance, contradictory results, we suggest that the ionized centers created during the EI exposure, but not those present in the crystal prior to irradiation, change to the radiation active state. Actually, direct quantitative measurements show that, in the crystal free of F_2^+ ionized centers prior to irradiation, their creation, as well as luminescence excitation at 910 nm in nanosecond and microsecond time intervals, takes place as a result of EI exposure (see, e.g., Fig. 1).

The ionized centers present in the crystal prior to irradiation are completely destroyed during a single EI at high excitation densities, such as those used in the present work. In this case, the capture of one electron by F_2^+ centers results in the creation of F_2 centers in the singlet and triplet radiation-active states [2], while the sequential capture of two electrons leads to the creation of F_2^- centers in the ground state [7]. The destruction of F_3^+ centers under EI exposure as a consequence of the capture of one or two electrons is followed by the creation of F_3 or F_3^- centers, respectively.

Thus, two alternative processes take place as a result of the exposure to each electron impulse: the destruction of all ionized centers present prior to irradiation and the creation of an additional number of ionized centers. The intensity of the arising RL, as well as the efficiency of the creation of ionized centers, is determined by the concentration of the corresponding neutral centers preliminary created. This indicates that only newly created F_2^+ and F_3^+ ionized centers are in the radiation-active state.

The following mechanisms of the luminescence excitation of the centers created are possible: (a) one due to the reabsorption of the radiation of the other centers and (b) one due to the transfer of the electronic excitation energy to the center created.

As is known, the absorptive transition in F_2^+ centers and the radiative transition in F_2 centers are coincident in position in the LiF spectrum [8]. The appearance of F_2^+-center luminescence during optical excitation in the F_2-center absorption band results from the reabsorption of F_2-center luminescence by F_2^+ centers:

$$F_2 \xrightarrow{h\vartheta} (F_2)^* \longrightarrow F_2 + h\vartheta(F_2),$$

$$F_2^+ + h\vartheta(F_2) \longrightarrow (F_2^+)^* \longrightarrow F_2^+ + h\vartheta(F_2^+).$$

The luminescence bands of both F_2 and F_2^+ centers are present simultaneously in the RL spectrum of a crystal exposed to EI irradiation. Therefore, there is no reason to exclude the reabsorption mechanism of F_2^+-center luminescence excitation. However, this mechanism cannot be considered as dominant in an irradiated crystal. Indeed, if the reabsorption mechanism were dominant, correlation between the RL intensities of F_2 and F_2^+ centers would be observed. However, there is no correlation observed either with a temperature variation during irradiation or with an additional creation of different F_2^+-center concentrations in the crystal at a constant F_2 concentration. For example, as has been established here, the F_2-center RL undergoes strong quenching at $T \geq 80$ K, whereas the F_2^+-center RL intensity remains unchanged until a temperature of 130 K is reached, above which quenching occurs (Fig. 3). It was shown in [9, 10] that the efficiency of the thermally activated intercombination transition within the F_2 center, which is the cause of F_2-center RL quenching, does not depend on the presence of F_2^+ centers in the crystal.

Thus, the following facts have been established: the coincidence of the kinetic parameters of the RL relaxation with the lifetime of band and self-trapped holes in the crystal; the correlation of the luminescence yield with the concentration of the corresponding charge neutral centers preliminary introduced into the crystal; and the independence of the luminescence yield from the corresponding ionized center present in the crystal.

All these facts together indicate, first, that the centers in the radiation-active state are created in the process of irradiation; second, that the corresponding neutral centers participate in the creation of the ionized centers; and, third, that the creation process involves both the band and self-trapped holes.

The following mechanism of creation of ionized centers in the radiation-active state is proposed. At the first stage, a band hole or a self-trapped hole is captured in the vicinity of the corresponding neutral center. At the second stage, tunneling of an electron from the neutral center to the hole results in the creation of an ionized center and a near-defect exciton. At the third stage, the energy transfer occurs from the near-defect exciton to the adjacent ionized center, followed by radiation from it. According to the mechanism proposed, the creation processes of F_2^+ centers, for example, can be represented by the following reactions: (a) the fast process

$$\begin{aligned} &F_2(S_0) + p \longrightarrow F_2^+ + e^0 \\ &\longrightarrow (F_2^+)^* \xrightarrow{\tau_0} (F_2^+) + h\vartheta(F_2^+) \end{aligned} \quad (1)$$

and (b) the slow process determined by the V_k-center mobility,

$$\begin{aligned} &F_2(S_0) + V_k \xrightarrow{\tau_v} F_2^+ + e^0 \\ &\longrightarrow (F_2^+)^* \xrightarrow{\tau_0} (F_2^+) + h\vartheta(F_2^+), \end{aligned} \quad (2)$$

where τ_0 is the radiative lifetime of the center; τ_v is the V_k-center lifetime; e^0 is a near-defect electron excitation; p and V_k are a band hole and a self-trapped hole, respectively; and $F_2(S_0)$ are F_2 centers in the ground singlet state.

The creation of F_3^+ centers in the radiation-active state is described by similar processes, starting with F_3 centers in both reactions.

If the center radiative lifetime and the EI duration are comparable, both products of the reaction in Eq. (1) can be detected after the termination of the EI exposure. One is detected by the absorption increase at the band maximum, while the other is determined from the appearance of the short-term component of the luminescence of the centers. Actually, in accordance with [11, 12], τ_0 of F_2^+ centers depends on temperature and equals 30 ns at 80 K and 15 ns at 300 K, while τ_0 of F_3^+ centers equals 8 ns and does not depend on temperature.

According to Eq. (2), the creation time of the ionized centers is determined by the V_k-center mobility, which is known to be dependent on the temperature at which the crystal is irradiated. The kinetic and energy parameters of this reaction coincide with the respective characteristics determined from the kinetic curves of absorption decrease in the V_k-absorption band.

In accordance with Eqs. (1) and (2), the relaxation kinetics of the absorption at the maximum of the absorption band of the ionized centers and the RL excitation kinetics for these centers must exhibit both a nanosecond and a slow component. This finds experimental evidence (see, e.g., Fig. 1).

The localization of a hole is suggested in the region of the neutral radiation defect, in accordance with Eqs. (1) and (2). One of the reasons for localization could be the lattice distortion in the defect region, which leads to a change in the migration conditions for electronic excitations in the crystal.

The lattice relaxation in the defect region results in potential profile distortion as compared to the perfect crystal. This distortion has an oscillatory character and spreads over a distance of several lattice constants. The occurrence of a barrier or a potential well very close to the defect depends on the relative size of the substitutional defect. Our estimates [1] suggest a potential well, appearing very close to the *F*-center region, for a positive charge in alkali halide crystals. A hole being separated from the defect by a certain distance can be trapped in the potential profile distortion region by one of its minima. It is likely that this situation occurs not only in the *F*-center region, for which estimates have been made, but also in the region of neutral defects, such as F_2 and F_3 centers.

Evidently, the localization of a charge of one sign in the lattice (holes in the case considered) initiates the attraction of a charge of the opposite sign to this region with the creation of a near-defect exciton (NDE). If a hole captures a band electron, an NDE is created near a neutral center. If an electron of a neighboring defect tunnels to the hole, an NDE is created near the ionized center as a result of this tunneling.

The fast creation of ionized centers (with respect to the EI exposure) with efficiency dependent on the concentration of the corresponding neutral centers and independent of temperature is evidence in favor of the tunneling creation process.

ACKNOWLEDGMENTS

This work was supported by the Ministry of Science (in the field “Laser Physics”).

REFERENCES

1. V. I. Korepanov, V. M. Lisitsyn, and L. A. Lisitsyna, Izv. Vyssh. Uchebn. Zaved., Fiz. **39** (11), 94 (1996).
2. L. A. Lisitsyna, Fiz. Tverd. Tela (St. Petersburg) **34** (9), 2694 (1992) [Sov. Phys. Solid State **34**, 1441 (1992)].
3. L. A. Lisitsyna, Fiz. Tverd. Tela (St. Petersburg) **34** (3), 961 (1992) [Sov. Phys. Solid State **34**, 513 (1992)].
4. J. Nahum and L. Wiegand, Phys. Rev. **158** (3), 814 (1967).

5. L. Zheng, Y. Ruan, S. Guo, *et al.*, Acta Phys. Sin. **35**, 1148 (1986).

6. H. Gu, L. Qi, L. Wan, and H. Guo, Opt. Commun. **70** (3), 141 (1989).

7. L. A. Lisitsyna, V. A. Kravchenko, and V. M. Reĭterov, Fiz. Tverd. Tela (Leningrad) **33** (3), 786 (1991) [Sov. Phys. Solid State **33**, 447 (1991)].

8. K. K. Shvarts, Ya. Zh. Kristapson, D. Yu. Lusis, and A. V. Podin', in *Radiation Physics* (Zinatne, Riga, 1967), Vol. V, p. 179.

9. L. A. Lisitsyna, V. A. Kravchenko, and V. M. Reĭterov, Fiz. Tverd. Tela (Leningrad) **33** (10), 2801 (1991) [Sov. Phys. Solid State **33**, 1583 (1991)].

10. L. A. Lisitsyna, I. V. Krasnousov, and V. M. Reĭterov, Fiz. Tverd. Tela (St. Petersburg) **34** (3), 823 (1992) [Sov. Phys. Solid State **34**, 440 (1992)].

11. L. Bosi, C. Bussolati, and G. Spinolo, Phys. Lett. A **32A** (3), 159 (1970).

12. T. Kurobori, T. Kanasaki, G. Imai, and N. Takeuchi, J. Phys. C **21**, L397 (1988).

Translated by N. Kovaleva

Physics of the Solid State, Vol. 43, No. 1, 2001, pp. 29–34. Translated from Fizika Tverdogo Tela, Vol. 43, No. 1, 2001, pp. 30–34.

DEFECTS, DISLOCATIONS, AND PHYSICS OF STRENGTH

Molecular Dynamics Simulation of Defect Formation in an Aluminum Crystal under Low-Energy Ion Bombardment

G. V. Kornich*, G. Betz, and A. I. Bazhin*****

** Zaporozhye State Technical University, Zaporozhye, 69063 Ukraine*
*** Institut für Allgemeine Physik, Technische Universität Wien, A-1040, Wien, Austria*
**** Donetsk State University, Universitetskaya ul. 24, Donetsk, 340055 Ukraine*
e-mail: gkornich@zstu.zaporizhzhe.ua

Received June 19, 2000

Abstract—Atomic collision cascades initiated by Ar and Xe ions (with energies of 25, 40, and 50 eV) normally incident on the Al(100) crystal surface at a crystal temperature of 300 K have been simulated by the molecular dynamics technique. The formation of vacancies and radiation-adsorbed and interstitial atoms in a cascade is discussed. It is demonstrated that the numbers of surface and bulk vacancies formed in cascades under bombardment of the Al(100) surface by Xe ions reach two maxima within 0.2–0.3 and 0.7–1.0 ps after the cascade initiation, whereas the number of vacancies generated under bombardment by Ar ions reaches one maximum within 0.2–0.3 ps after the cascade initiation. © *2001 MAIK "Nauka/Interperiodica".*

1. INTRODUCTION

The molecular dynamics technique [1, 2] with the use of many-body atom–atom potentials [3] makes it possible to describe correctly the formation of lattice defects at all stages, including the recombination of unstable defects in a low-energy atomic collision cascade under ion bombardment. Considerable interest is currently being expressed by researchers in the mechanisms of defect formation in the near-surface region of light crystalline targets upon their bombardment by heavy ions when nonlinear collisional effects (for example, the "clearing-the-way" effect [4]), which can be simulated using only the molecular dynamics technique, are accompanied by surface effects such as the formation of radiation-adsorbed atoms (adatoms) and surface vacancies [5–9]. In the present work, we discussed the elastic energy loss distribution of bombarding ions over the target depth, the formation of surface and bulk vacancies, as well as of radiation-adsorbed and interstitial atoms, and changes in the mean square displacements of atoms in the course of cascade evolution under normal bombardment of the Al(100) crystal surface by Ar and Xe ions with energies of 25, 40, and 50 eV at a crystal temperature of 300 K.

2. MOLECULAR DYNAMICS MODEL

Calculations were performed with a model Al crystal composed of 4032 atoms with a lattice constant of 4.05 Å. The periodic boundary conditions were imposed on the lateral faces [2]. All atoms were arranged in fourteen layers. The atom–atom interactions were described by the many-body potential, which, at high energies, was sewed together with the Ziegler–Biersack–Littmark potential [10]. The latter potential was also used to describe the ion–atom interactions. The equations of particle motion were solved by the Verlet method [2]. The integration was performed with a time step of no longer than 4.5 fs. The temperature was simulated by specifying a constant temperature in a layer on the lateral faces and the bottom of the crystal. This layer also dissipated the energy introduced by ions into the crystal [11]. Variations in the temperature in the crystal stabilized without interaction with ions were no more than 4% of the mean temperature. The interstitial atoms and vacancies were identified using an algorithm proposed by Karetta and Urbassek [6]. When the crystal defects were identified after the cascade evolution for 1 ps, the law of conservation of matter held good to better than 94%. The initial coordinates of ions incident on a given surface region [12] were calculated according to the law of random numbers. In all cases, we carried out 200 computations of collisional cascades and traced each cascade in the initial crystal for 4 ps.

3. RESULTS AND DISCUSSION

3.1. Elastic Energy Losses by Ions

The elastic energy loss distributions of ions over the depth of an Al crystal are shown in Fig. 1. In what follows, the data averaged over the number of simulated experiments for a particular quantity will be displayed in the figures. The reflected Ar and Xe ions carry away, on the average, an energy of 1–3 eV per bombarding ion from the crystal. As the initial energy increases, the

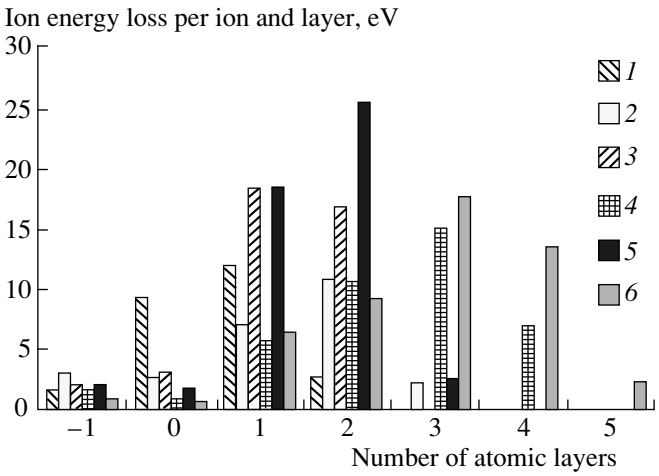

Fig. 1. Elastic energy loss distributions of (*1*, *3*, *5*) Ar and (*2*, *4*, *6*) Xe ions over the crystal depth at different energies *E* (eV): (*1*, *2*) 25, (*3*, *4*) 40, and (*5*, *6*) 50. Layers: –1 (energy carried away by reflected ions), 0 (adatom layer), and 1 (surface layer of the crystal).

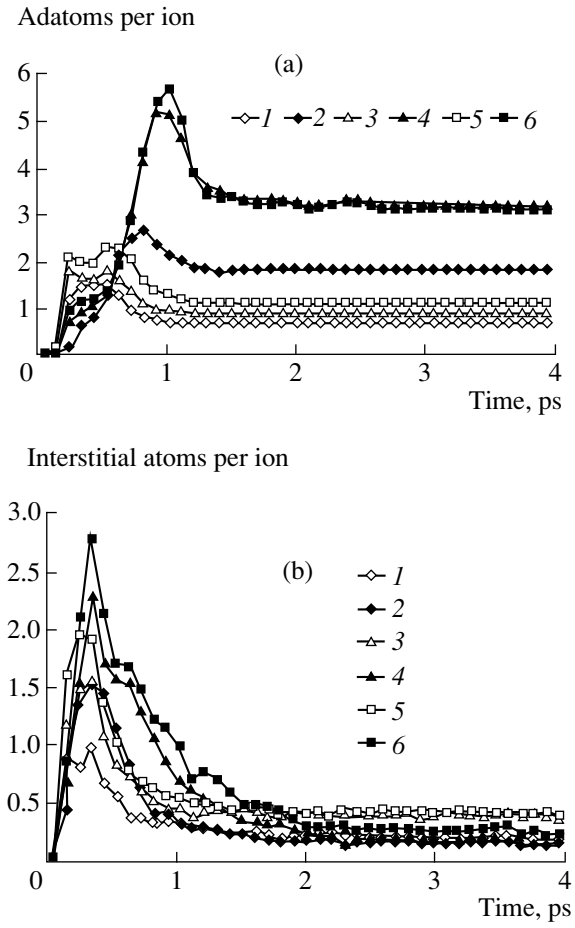

Fig. 2. Dependences of the number of (a) adatoms and (b) interstitial atoms on the cascade time upon bombardment by (*1*, *3*, *5*) Ar and (*2*, *4*, *6*) Xe ions with different energies *E* (eV): (*1*, *2*) 25, (*3*, *4*) 40, and (*5*, *6*) 50.

reflection coefficient of Ar ions remains equal to unity, whereas the reflection coefficient of Xe ions decreases from 0.96 at 25 eV to 0.73 at 40 eV and to 0.44 at 50 eV. This explains the small increase in the energy carried away by the reflected Ar ions and the opposite tendency observed for the Xe ions. Moreover, the energy losses of both ions in an adatom layer above the crystal surface also decrease. As can be seen from Fig. 1, the Xe ions penetrate deeper into the crystal as compared to the Ar ions, which, at initial energies of 40 and 50 eV, lose ~90% of the energy in the first and second atomic layers (including the adatom layer), whereas the Xe ions at the same energies lose ~60% of the initial energy in the third and fourth layers.

For Xe ions, the velocity component normal to the surface changes its sign within 0.2–0.4 ps after the initiation of the cascade as a result of simultaneous interaction between the Xe ion and two or three atoms knocked from equilibrium positions. Note that these atoms also interact with atoms of deeper layers. Cooperative retardation with subsequent simultaneous reflection of the heavy ion by a large number of light atoms of the lattice can be treated as the completion of processes in which light atoms of the target "clear the way" ahead of the moving heavy ion. These processes at higher energies were simulated by Shulga *et al.* [4]. The reflection of Ar ions proceeds through the same mechanism but is observed somewhat earlier, in the range 0.1–0.2 ps, and closer to the surface.

3.2. Radiation-Adsorbed and Interstitial Atoms

It is seen from Fig. 2a that, in all cases, the number of stable adatoms formed under bombardment by Xe ions (hereafter, the data for the Xe ions are shown by the curves with closed symbols) is larger than that produced under bombardment by Ar ions (the data for the Ar ions are displayed by the curves with open symbols). The number of adatoms (N_{ad}) produced under Xe ion bombardment reaches a maximum more slowly (~0.8–1.0 ps) compared to Ar ions (~0.2–0.6 ps). For both ions, an increase in the initial energy leads to a shift in the maximum toward longer times by 0.1–0.2 ps. In the case of Ar ions, the number of stable adatoms insignificantly increases with an increase in the ion energy. At the same time, the number of adatoms formed under Xe ion bombardment sharply increases as the ion energy increases from 25 to 40 eV. The number N_{ad} reaches a stationary value within 1.1 and 1.5 ps after the initiation of cascades by Ar and Xe ions, respectively.

In the case of Xe ions, the values of N_{ad} for all the initial energies increases more smoothly in the range 0.2–0.4 ps. This is caused by interactions of the incident ion and primary recoil atoms with the surface atoms and also, possibly, by the fact that curvilinear atomic collision sequences induced at the surface attain the same crystal surface [13]. Note that the atomic sub-

stitution collision sequences along the ⟨110⟩ directions can be induced in the Al crystal even at an ion energy of 25 eV, because, according to [14], the threshold generation energy for the atomic substitution collision sequences along these directions in the Al crystal with an interaction potential proposed in [10] is equal to 6 eV. In the same time range, these mechanisms of the adatom formation are also efficient in the case of Ar ions (see Fig. 2a), since Ar ion bombardment, as a rule, brings about the formation of the Al primary recoil atoms with higher energies and larger velocity components in the (100) plane as compared to their normal components. For example, after the 0.1-ps evolution of cascades at an initial energy of 25 eV for Ar and Xe ions, the ratio between the mean-square displacement components normal and parallel to the (100) plane was equal to 2.9 and 8.45 for Ar and Xe, respectively. It is seen from Fig. 2a that the formation of adatoms under Ar ion bombardment is limited by the above mechanisms.

The number N_{ad} of adatoms formed under bombardment by Xe ions reaches a maximum in the range 0.8–1.0 ps due to the interaction of the surface atoms with the ion reflected from deeper atomic layers and the recoil atoms. In this case, the momentum can be transferred to the surface atoms by generating two or three steps of the atomic substitution collision sequences in the range 0.4–0.6 ps, which are directed from the bulk of the crystal toward the surface and result in adatom formation. Note that the Xe ion can remain in the crystal. In turn, the mean energy of the Xe ions leaving the crystal is equal to 2.5–5.5 eV, whereas the mean energy of the Ar ions is 1.5–2.0 eV, depending on the initial energy. Therefore, the probability of the adatom formation by the Xe ion upon leaving the crystal is higher than that by the Ar ion. The mean residence time of Ar ions in the crystal is ~0.5 ps without regard to their initial energies. The mean residence time of Xe ions is equal to ~1.2 ps at ion energies of 40 and 50 eV and ~0.7 ps at an ion energy of 25 eV. This agrees with the times that correspond to the largest values of N_{ad}.

As can be seen from Fig. 2b, the number of interstitial atoms formed under ion bombardment reaches a stationary value within 1.0–1.6 ps after the cascade initiation for Ar ions and within 1.7–2.5 ps for Xe ions. The bombardment by Xe ions generates a larger number of interstitial atoms in the range ~0.2–1.5 ps. After cascade evolution for 2 ps, the number of interstitial atoms retained in the crystal in the case of Ar ions is somewhat larger than that in the case of Xe ions. This can be explained by the higher probability that the atomic substitution collision sequences along the ⟨110⟩ direction is formed by the Ar ions at the collisional stage of the cascade. Another mechanism of the formation of interstitial atoms in the Al crystal can consist in relocating the Al recoil atoms deep into the crystal by a distance equal to 1.5–2 lattice constants [15–17]. For Ar and Xe ions with an energy of 50 eV, the number of these relocations is equal to ~0.35 relocations per ion. The time it takes for the number of interstitial atoms N_{in} to reach the maximum value (~0.2–0.3 ps) does not depend on the energy and the type of ions and coincides with the characteristic time of the adatom formation at the collisional stage of the cascade. This suggests an identical mechanism of the formation of these defects in the range 0.2–0.5 ps.

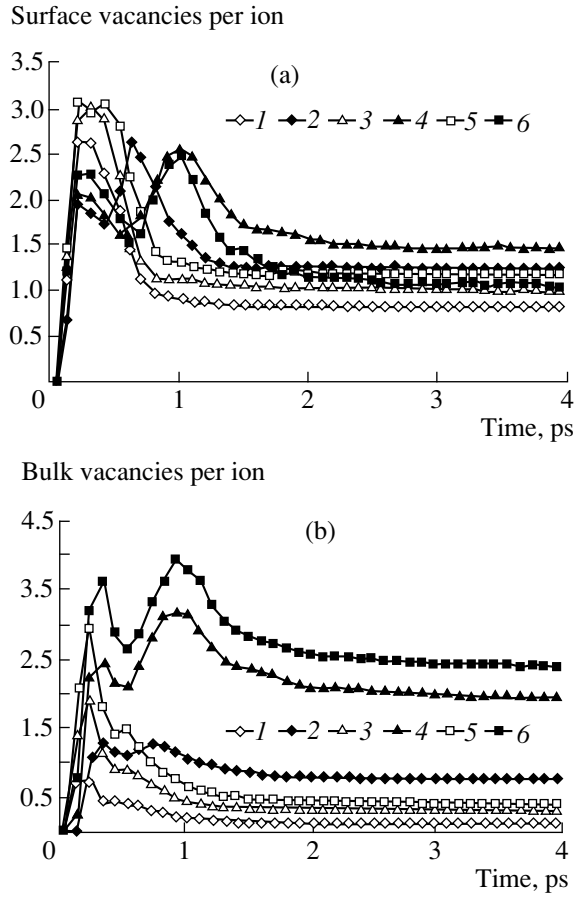

Fig. 3. Dependences of the number of (a) surface and (b) bulk vacancies on the cascade time upon bombardment by (*1*, *3*, *5*) Ar and (*2*, *4*, *6*) Xe ions with different energies *E* (eV): (*1*, *2*) 25, (*3*, *4*) 40, and (*5*, *6*) 50.

3.3. Surface and Bulk Vacancies

As is seen from Fig. 3a, the number of surface vacancies $N_{v,s}$ (vacancies in the first atomic layer) attains a maximum in the range 0.2–0.3 ps irrespective of the initial energy of Ar ions. The number $N_{v,s}$ reaches a stationary value within 1.2–1.6 ps after the cascade initiation. In the case of Xe ions, $N_{v,s}$ has two maxima. The first maximum is observed for all initial energies of the Xe ion in the same time range as for the Ar ions. The time that corresponds to the second maximum depends on the initial ion energy: its value is

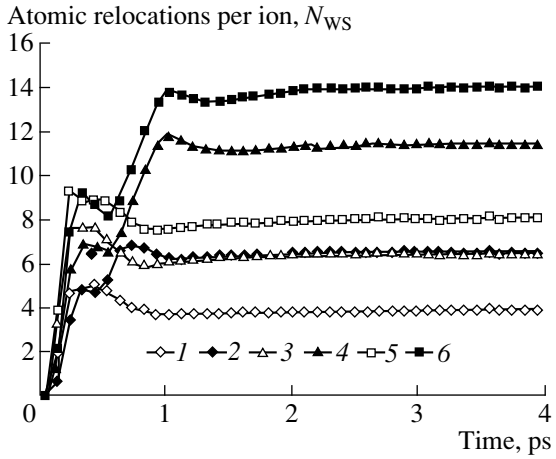

Fig. 4. Dependences of the number of atoms leaving their Wigner–Seitz cells (N_{WS}) on the cascade time upon bombardment by (*1*, *3*, *5*) Ar and (*2*, *4*, *6*) Xe ions with different energies *E* (eV): (*1*, *2*) 25, (*3*, *4*) 40, and (*5*, *6*) 50.

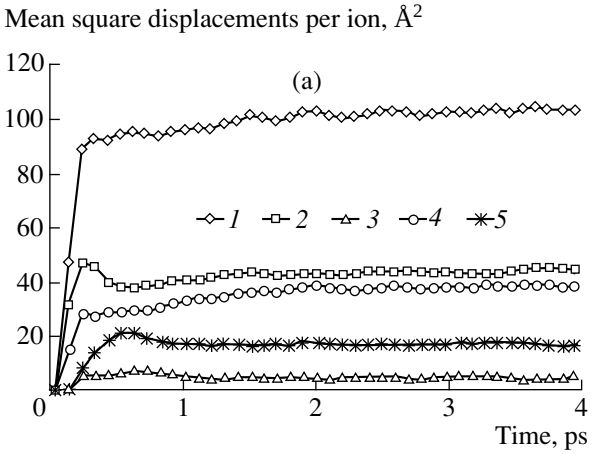

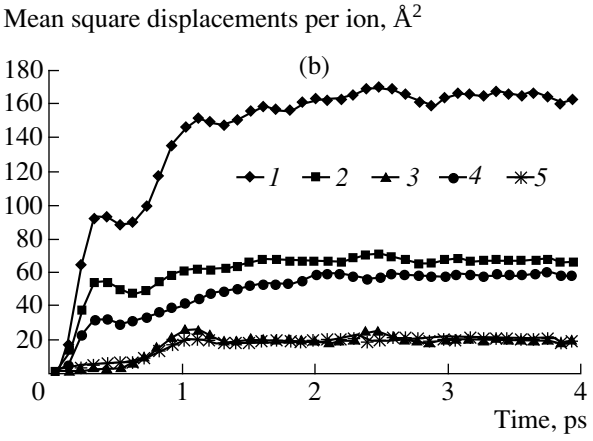

Fig. 5. Dependences of the components of mean square displacements on the cascade time upon bombardment by (a) Ar and (b) Xe ions with an energy of 50 eV: (*1*) R^2, (*2*) R_x^2, (*3*) $R_{x,\,ad}^2$, (*4*) R_{yz}^2, and (*5*) $R_{yz,\,ad}^2$.

equal to 0.6–0.7 ps at an energy of 25 eV and 1.0–1.1 ps at energies of 40 and 50 eV. As a rule, the second maximum of $N_{v,\,s}$ is attained upon bombardment by the Xe ions which penetrate into the crystal at a rather small depth (1–3 atomic layers) and have a sufficiently high energy to form the adatom and the surface vacancy upon leaving the target. For Xe ions, the number of surface vacancies reaches a stationary value within 1.7–2.5 ps after the cascade initiation. The number of stable surface vacancies at ion energies of 25 and 40 eV is larger in the case of Xe ions, whereas at an ion energy of 50 eV after 2.3 ps, this number for Ar ions only slightly exceeds that for Xe ions.

It can be seen from Fig. 3b that the number of bulk vacancies $N_{v,\,b}$ (the vacancies are located deeper in the first atomic layer) at different energies of Ar and Xe ions attains maxima in the same time ranges as the number of surface vacancies $N_{v,\,s}$, because vacancies of both types are generated through the same mechanism. The bombardment by Xe ions generates a considerably larger number of stable bulk vacancies due to a deeper penetration of heavy ions into the crystal and the attendant relocations of atoms from the bulk toward the surface. As for surface vacancies, the number of stable bulk vacancies drastically increases with an increase in the ion energy from 25 to 40 eV. At an initial energy of 25 eV, the cascade evolution for 4 ps results in a spatial separation of vacancies (located in the first three atomic layers) and interstitial atoms (located in the fourth to twelve atomic layers). At initial energies of 40 and 50 eV, the profiles of vacancies and interstitial atoms overlap in the fourth to sixth layers.

3.4. Cascade Relocations of Atoms

The dependences of the number of atoms leaving their Wigner–Seitz cells N_{WS} on the cascade time are depicted in Fig. 4. The number of atomic relocations at the relaxation stage of the cascade is larger for Xe ions at all bombarding ion energies. The number of atoms N_{WS} attains a stationary value within 0.9–1.3 and 1.5–2.0 ps after the cascade initiation for Ar and Xe ions, respectively. The time dependence of N_{WS} exhibits two maxima for the cascades initiated by Xe ions and one maximum for the cascades induced by Ar ions. Note that the largest values of N_{WS} are observed at the same times as those of $N_{v,\,s}$ and $N_{v,\,b}$ in Fig. 3. The first maximum of N_{WS} is determined by atomic relocations at the collisional stage of the cascade when the ion penetrates into the crystal. The second maximum is associated with the backward motion of the Xe ion and its related collective movement of atoms toward the surface. For Ar ions, both stages of the ion motion in the crystal differ in time by ~0.1 ps, which leads to the appearance of one maximum in the dependence of N_{WS}. In this case, the probability of atomic relocations associated with the motion of the Ar ion from the crystal is less than that

of a similar process with the participation of the Xe ion for the energy reasons considered in Section 3.2 and also because the Ar ions virtually do not penetrate deep into the crystal. In particular, at an ion energy of 50 eV, the number of atomic relocations from layer to layer in the [100] direction deep into the Al crystal is equal to ~3.2 relocations per ion for ions of both types, whereas the number of relocations toward the surface is 5.85 and 1.82 relocations per ion for Xe and Ar ions, respectively.

The mean square atomic displacements per cascade (R^2) were calculated from the relationship

$$R^2 = \sum_{i=1}^{N_{\mathrm{WS}}} [(x_i - x_{0i})^2 + (y_i - y_{0i})^2 + (z_i - z_{0i})^2],$$

where x_{0i}, y_{0i}, and z_{0i} and x_i, y_i, and z_i are the initial and current coordinates ($i = 1, \ldots, N_{\mathrm{WS}}$) of atoms leaving their Wigner–Seitz cells. The above inferences concerning the atomic relocations are illustrated by the dependences of the components of mean square displacements on the cascade time upon bombardment by Ar and Xe ions with an energy of 50 eV (Figs. 5a, 5b). In the case of Ar ions, the mean square displacement components R_x^2 in the [100] direction (the initial direction of the ions) and R_{yz}^2 in the (100) plane within the crystal drastically increase for the first 0.2 ps. The displacements of adatoms $R_{yz,\,\mathrm{ad}}^2$ on the (100) surface increase within 0.1 ps after the cascade initiation and attain a maximum for ~0.5 ps. At the same time, the adatom displacements $R_{x,\,\mathrm{ad}}^2$ normal to the surface insignificantly affect R^2. For the Xe ions, weak maxima in the dependences of R_x^2 and R_{yz}^2 in the range 0.3–0.4 ps in Fig. 5b correspond in time to the first maxima of $N_{v,\,s}$ and $N_{v,\,b}$ (Figs. 3a, 3b) and the maximum of N_{in} (Fig. 2b). The contribution of adatoms to R^2 for the first 0.5 ps of the cascade evolution is insignificant, even though it increases beginning with 0.1 ps. The second sharp increase in R^2 (Fig. 5b) in the range 0.5–1.0 ps is primarily due to an increase in $R_{x,\,\mathrm{ad}}^2$ and $R_{yz,\,\mathrm{ad}}^2$, even though R_x^2 and R_{yz}^2 also increase in this range.

Upon bombardment by Xe ions with an energy of 25 eV, the mean square displacement components R_x^2 and R_{yz}^2 predominantly contribute to R^2 for the first 0.3 ps, whereas the contribution from atoms is small. In the range 0.5–1.0 ps, the main contribution to R^2 is made by the adatoms ($R_{x,\,\mathrm{ad}}^2 + R_{yz,\,\mathrm{ad}}^2 \sim 17$ Å^2), whereas R_x^2 and R_{yz}^2 are equal to 2 and 4 Å^2, respectively. In the case of Ar ions with an energy of 25 eV, the mean square displacement attains a sole maximum for ~0.5 ps. For Ar and Xe ions with an energy of 40 eV, the dependences of the mean square displacement components are in qualitative agreement with those obtained at an initial energy of 50 eV.

4. CONCLUSION

Therefore, upon bombardment of the Al crystal by Xe ions with energies of 25, 40, and 50 eV, the time dependences of $N_{v,\,s}$ and $N_{v,\,b}$ exhibit two maxima in the ranges 0.2–0.3 and 0.8–1.0 ps. It was demonstrated that the first maximum appears upon penetration of the Xe ion into the crystal and stems from the atom–atom and ion–atom interactions which bring about the formation of adatoms and interstitial atoms. The second maximum is associated with the motion of the reflected ion and the accompanying atoms away from the bulk of the crystal toward the surface. In turn, this process is attended by the formation of adatoms, even though the maximum in the time dependence of N_{ad} is not resolved into two separate peaks. In the case of Ar ions, only one maximum at 0.2–0.3 ps is observed in the time dependences of $N_{v,\,s}$ and $N_{v,\,b}$, irrespective of the ion energy. In the simulation of collision cascades in Cu and Ni crystals under the same bombardment conditions and with the potentials proposed in [18] and [10], one maximum of the number $N_{v,\,s}$ and one or two maxima of N_{ad} are usually observed in the course of the cascade evolution.

ACKNOWLEDGMENTS

This work was supported by the Vienna Technical University, grant no. GZ 41002 / 8-19 / 91.

G.V. Kornich acknowledges the support of the Austrian Foundation for Research in the course of his work at the Institut für Allgemeine Physik, Technische Universität Wien, Wien, Austria.

REFERENCES

1. D. E. Harrison, Jr., Radiat. Eff. **70**, 1 (1983).
2. M. J. Haile, *Molecular Dynamics Simulation—Elementary Methods* (Wiley, New York, 1992).
3. S. Erkos, Phys. Rep. **278**, 79 (1997).
4. V. I. Shulga, M. Vicanek, and P. Sigmund, Phys. Rev. A **39**, 3360 (1989).
5. R. P. Webb and D. E. Harrison, Radiat. Eff. Lett. Sect. **86**, 15 (1983).
6. F. Karetta and H. M. Urbassek, J. Appl. Phys. **71**, 5410 (1992).
7. H. Gades and H. M. Urbassek, Phys. Rev. B **50**, 11167 (1994).
8. G. V. Kornich, G. Betz, and B. V. King, Nucl. Instrum. Methods Phys. Res., Sect. B **115**, 461 (1996).

9. G. V. Kornich and G. Betz, Nucl. Instrum. Methods Phys. Res., Sect. B **117**, 81 (1996).

10. F. Gao, D. J. Bacon, and G. J. Ackland, Philos. Mag. A **67**, 275 (1993).

11. H. J. Berendsen, J. P. M. Postma, W. F. V. Gunsteren, *et al.*, J. Chem. Phys. **81**, 3684 (1984).

12. G. Betz, M. J. Pellin, J. W. Burnett, and D. M. Gruen, Nucl. Instrum. Methods Phys. Res., Sect. B **58**, 429 (1991).

13. A. M. Mazzone, Philos. Mag. Lett. **70**, 93 (1994).

14. D. J. Bacon, H. F. Deng, and F. Gao, J. Nucl. Mater. **205**, 84 (1993).

15. S. Valkealahti and R. M. Nieminen, Nucl. Instrum. Methods Phys. Res., Sect. B **18**, 356 (1987).

16. G. V. Kornich and G. Betz, Nucl. Instrum. Methods Phys. Res., Sect. B **143**, 455 (1998).

17. G. V. Kornich, G. Betz, and A. I. Bazhin, Nucl. Instrum. Methods Phys. Res., Sect. B **153**, 383 (1999).

18. H. Gades and H. M. Urbassek, Nucl. Instrum. Methods Phys. Res., Sect. B **69**, 232 (1992).

Translated by O. Borovik-Romanova

Physics of the Solid State, Vol. 43, No. 1, 2001, pp. 35–38. Translated from Fizika Tverdogo Tela, Vol. 43, No. 1, 2001, pp. 35–38.

DEFECTS, DISLOCATIONS, AND PHYSICS OF STRENGTH

Grain-Boundary Dislocation Climb and Diffusion in Nanocrystalline Solids

I. A. Ovid'ko and A. B. Reĭzis

Institute of Problems in Machine Science, Russian Academy of Sciences, Vasil'evskiĭ ostrov, Bol'shoĭ pr. 61, St. Petersburg, 199178 Russia

e-mail: ovidko@def.ipme.ru

Received May 12, 2000

Abstract—The effect of grain-boundary dislocation transformations on diffusion in nanocrystalline solids is discussed. A theoretical model describing the enhancement of diffusion processes associated with the climb of grain-boundary dislocations in nanocrystalline solids is developed. © *2001 MAIK "Nauka/Interperiodica".*

The physical properties of nanocrystalline solids differ substantially from those of polycrystals of the same chemical composition (see, e.g., [1–10]). In particular, the nanocrystalline solids synthesized in strongly nonequilibrium conditions exhibit anomalously enhanced diffusion for at least a certain time after preparation [2, 9, 10]. For instance, the self-diffusion coefficient in nanocrystalline fcc materials exceeds by two to four orders of magnitude the grain-boundary diffusion coefficient in polycrystalline fcc materials of the same chemical composition [2, 9, 10].

According to [2], there are three factors that account for the enhanced diffusion in nanocrystalline solids: (1) Relaxation of grain-boundary structures, which occurs through relative grain displacements and reduces the free volume of grain-boundary structures, is impeded in nanocrystalline solids (this is due to the fact that the geometric conditions of relaxation of adjacent grain boundaries are usually poorly compatible because of the small nanocrystallite size). (2) In nanocrystalline solids, the volume fraction of triple grain-boundary junctions, where diffusion proceeds faster than in the "usual" grain boundaries, is extremely large. (3) The concentration of impurities which interfere frequently with grain-boundary diffusion is lower in nanocrystalline solids than in polycrystals.

However, the explanation put forward in [2] for the enhanced-diffusion phenomenon in nanocrystalline solids does not take into account the part played by grain-boundary dislocations in diffusion processes. At the same time, ensembles of grain-boundary dislocations are characterized by an extremely high density in nanocrystalline materials and strongly affect many physical properties of these materials (see, e.g., [11, 12]). The main objective of this work was to develop a theoretical model that would describe the effect of grain-boundary dislocation climb on diffusion processes in nanocrystalline solids.

1. GRAIN-BOUNDARY DISLOCATION TRANSFORMATIONS IN NANOCRYSTALLINE SOLIDS

Nanocrystalline solids are usually prepared under strongly nonequilibrium conditions (see, e.g., [1–5]). A nonequilibrium defect structure forms in the grain-boundary phase. In particular, the grain boundaries contain "excess" grain-boundary dislocations and, in addition, the geometrically necessary conditioned grain-boundary dislocations (i.e., dislocations that account for the misorientation of boundaries and which are associated with the structural geometry of the boundaries) are randomly displaced relative to their equilibrium spatial positions [11–13] (Fig. 1a). During a certain relaxation period after the synthesis of a nanocrystalline sample, the ensemble of grain-boundary dislocations undergoes transformations, which are accompanied by a decrease in its energy. The excess dislocations annihilate, and the geometrically neces-

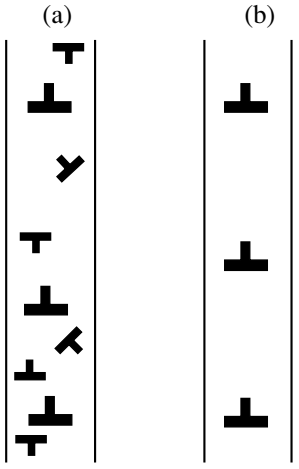

Fig. 1. Dislocation structure of (a) nonequilibrium and (b) equilibrium grain boundaries.

1063-7834/01/4301-0035$21.00 © 2001 MAIK "Nauka/Interperiodica"

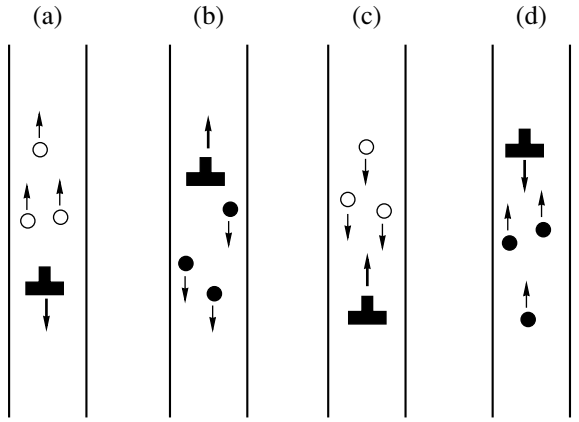

Fig. 2. Grain-boundary dislocation climb.

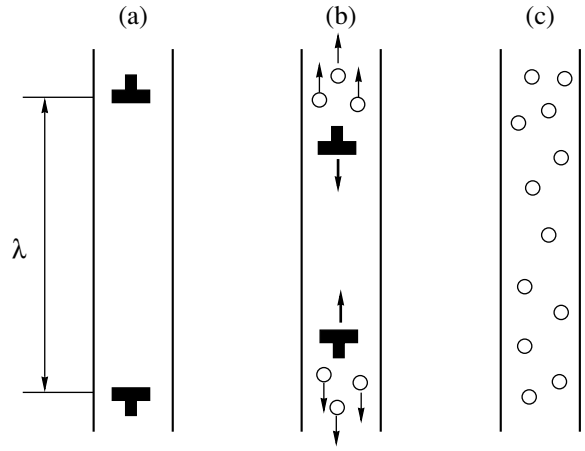

Fig. 3. Transformation of the grain-boundary dislocation dipole.

sary dislocations move to their "equilibrium" positions (Fig. 1b).

In our opinion, the grain-boundary dislocation transformations under study considerably affect the diffusion processes in nanocrystalline solids. Indeed, displacements of grain-boundary dislocations are accompanied by changes in their dilatation fields, which exert a noticeable effect on the migration of point defects, i.e., diffusion carriers, while the dislocation climb in grain boundaries is accompanied by the emission and absorption of point defects. The effect of the dilatation fields of grain-boundary dislocations on diffusion was studied in detail [14] for the case of transformation of such dislocations in the course of grain-boundary amorphization in nanocrystalline and polycrystalline solids. In the subsequent sections of this paper, we consider the effect of grain-boundary dislocation climb (as relaxation processes characteristic of grain-boundary structures) on vacancy emission and the corresponding diffusion enhancement in nanocrystalline solids.

2. VACANCY EMISSION IN THE CLIMB OF GRAIN-BOUNDARY DISLOCATIONS

The climb of grain-boundary dislocations is accompanied by the emission and absorption of vacancies and interstitials (Fig. 2). Note that because the mobility of vacancies is substantially higher than that of the interstitials [15], the emission of vacancies (the "detachment" of vacancies from the dislocation core and their subsequent migration into the adjacent grain-boundary phase, see Fig. 2a) is more intense than that of interstitial atoms (Fig. 2b). It should also be pointed out that the absorption of vacancies occurring in the course of the climb of a grain-boundary dislocation (Fig. 2c) requires a continuous vacancy supply from the surrounding material, whereas the emission of vacancies (Fig. 2a) is not impeded by such a restrictive requirement. Therefore, the emission of vacancies (Fig. 2a) proceeds at a higher rate than their absorption, Fig. 2c (the more so than that of the interstitials, Fig. 2d). In view of this, we restrict our subsequent analysis of the factors affecting diffusion to the grain-boundary dislocation climb processes that involve vacancy emission (Fig. 2a).

The major contribution to the energy of nonequilibrium defect structures in grain boundaries (Fig. 1a) usually results from the existence of excess grain-boundary dislocations. Therefore, the processes of climb and annihilation of such dislocations accompanied by vacancy emission are characteristic of the relaxation of grain-boundary structures in nanocrystalline solids. As an illustration, let us consider the climb and subsequent annihilation of two grain-boundary dislocations making up a vacancy-type dipole (Fig. 3).

Because the stress fields of the dislocations making up a dipole are screened efficiently with a screening radius λ (where λ is the dipole arm, see Fig. 3a), the energy W of this dislocation dipole is given in terms of the linear theory of dislocation elasticity [15, 16] by the approximate expression

$$W(\lambda) = 2W_d(\lambda) = \frac{Gb^2d}{2\pi(1-\nu)}\left[\ln\left(\frac{\lambda}{r_0}\right) + z\right]. \quad (1)$$

Here, $W_d(\lambda)$ is the energy of a dislocation characterized by the screening radius λ of its stress fields, d is the dislocation length, $\pm\mathbf{b}$ are the Burgers vectors of the dislocations, G is the shear modulus, ν is the Poisson ratio, r_0 is the dislocation core radius, and Z is a factor taking into account the contribution of the dislocation core to the dislocation energy. The climb of a grain-boundary dislocation to an average interatomic distance a in the grain boundary (Figs. 3a, 3b) reduces the dipole energy by an amount $\Delta W = W(\lambda) - W(\lambda - a)$ and is accompanied by the emission of d/a vacancies. Therefore, the energy of formation of one vacancy involved in the

climb of the dislocations making up the dipole (Figs. 3a, 3b) can be written as

$$\tilde{E}_v^f = E_v^f - W_v(\lambda), \quad (2)$$

where E_v^f is the energy of the vacancy formation in the dislocation-free grain-boundary phase and $W_v(\lambda)$ is the decrease in the dislocation dipole energy (Fig. 3a) caused by the emission of one vacancy:

$$W_v(\lambda) = \frac{a}{d}\Delta W(\lambda) \approx \frac{Gb^2 a}{2\pi(1-\nu)}\ln\left(\frac{\lambda}{\lambda - a}\right). \quad (3)$$

Equation (3) is valid for $\lambda > 2a$. For $\lambda \le 2a$, the stress fields of the dislocations making up the dipole are localized near the dislocation cores and the dislocation energy is determined by the factor Z. The climb of dislocations toward one another within the region of $\lambda \le 2a$ is essentially the process of dislocation annihilation, in which $2(d/a)$ vacancies are emitted and the dipole energy $W(\lambda = 2a) \approx \frac{Gb^2 dZ}{2\pi(1-\nu)}$ decreases to zero. As a consequence, for $\lambda \le 2a$, the energy of the dipole of annihilating dislocations decreases on the emission of one vacancy by an amount

$$W_v(\lambda) = \frac{a}{2d}W(\lambda = 2a) \approx \frac{Gb^2 aZ}{\pi(1-\nu)}. \quad (4)$$

The dependence of W_v on λ/a given by Eqs. (3) and (4) is plotted in Fig. 4 within the region of λ from 0 to $15a$ for the following characteristic values of the parameters: $G = 50$ GPa, $a \approx 0.3$ nm, $b \approx a/3$, $Z \approx 1$, and $\nu \approx 1/3$. The shape of this relation shows that the vacancy emission is facilitated when the dislocations making up the dipole approach each other.

3. EFFECT OF GRAIN-BOUNDARY DISLOCATION CLIMB ON THE DIFFUSION COEFFICIENT

The coefficient of diffusion occurring via the vacancy mechanism (which is usually the most efficient mechanism) is given by the relation (see, e.g., [15])

$$D = D_0\exp(-E_v^m/kT)\exp(-E_v^f/kT), \quad (5)$$

where k is the Boltzmann constant, T is the absolute temperature, D_0 is a constant, and E_v^m is the activation energy for the vacancy migration. The factor $\exp(-E_v^f/kT)$ in Eq. (5) characterizes the equilibrium concentration of vacancies (as the main diffusion carriers) in a solid when the influence of defect transformations and dilatation fields on diffusion is ignored. In the vicinity of climbing dislocations (Fig. 3), the vacancy concentration exceeds the equilibrium concentration, because the vacancies are produced here in more favorable conditions. This effect is characterized quantitatively by the change in energy for the vacancy formation $E_v^f \longrightarrow \tilde{E}_v^f = E_v^f - W_v$ and by the corresponding local change in the diffusion coefficient $D \longrightarrow D^*$, where D^* in the vicinity of climbing grain-boundary dislocations (Fig. 3) can be written as

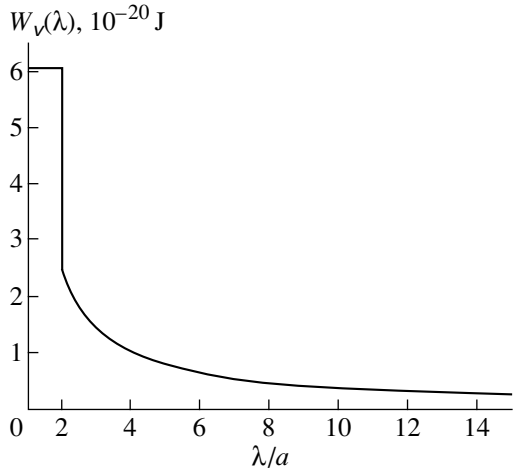

Fig. 4. W_v vs. λ/a relation.

$$D^* = D_0\exp(-E_v^m/kT)\exp(-(E_v^f - W_v)/kT) = D\exp(W_v/kT). \quad (6)$$

Using the $W_v(\lambda)$ relation (Fig. 4) and averaging the factor $\exp(W_v/kT)$ over λ within the λ interval from 0 to $15a$, we find that in the vicinity of climbing dislocations (Fig. 3), the diffusion coefficient is $D^* \approx 3\times 10^5 D$.

The average diffusion coefficient in a solid with climbing grain-boundary dislocations is $\tilde{D} \approx fD^*$, where f is the fraction of the regions with the climb. In nanocrystalline solids, during the relaxation period (after their preparation in strongly nonequilibrium conditions), practically all grain boundaries contain nonequilibrium defect structures, in particular, excess dislocations, whose climb enhances diffusion. In this case, the coefficient f is approximately equal to the volume fraction of the grain-boundary phase; i.e., $f \approx 0.1$–0.5, depending on the average grain size in the nanocrystalline solid. Therefore, we have $\tilde{D} \approx fD^* \approx (3$–$15)\times 10^4 D$. Thus, during the relaxation of grain-boundary structures, the climb of grain-boundary dislocations (Fig. 3) substantially enhances the diffusion processes, which is manifest in the average diffusion coefficient changing by four to five orders of magnitude.

To sum up, the macroscopic properties of nanocrystalline solids depend noticeably on the properties of grain boundaries. In particular, grain-boundary dislocation transformations are capable of appreciably affecting the diffusion characteristics of nanocrystalline solids. The theoretical analysis carried out in this work suggests that the climb of grain-boundary dislocations

making up dipoles (Fig. 3) is accompanied by intense emission of vacancies, which enhances the diffusion in nanocrystalline solids by several orders of magnitude. The theoretical estimates obtained are in satisfactory agreement with experimental data on the diffusion properties of fcc nanocrystalline materials [2, 9, 10].

ACKNOWLEDGMENTS

This work was supported by the Russian Foundation for Basic Research (grant no. 98-02-16075), INTAS (grant no. 99-1216), and the Office of US Naval Research (grant no. 00014-99-1-0569).

REFERENCES

1. *Nanomaterials: Synthesis, Properties, and Applications*, Ed. by A. S. Edelstain and R. C. Cammarata (Institute of Physics Publ., Bristol, 1996).
2. H. Gleiter, Prog. Mater. Sci. **33**, 79 (1989).
3. *R & D Status and Trends in Nanoparticles. Nanostructured Materials and Nanodevices in the United*, Ed. by R. W. Siegel, E. Hu, and M. C. Roco (International Technology Research Inst., Baltimore, 1997).
4. *Nanostructured Films and Coatings: Proceedings of the NATO Advanced Research Workshop*, Ed. by G.-M. Chow, I. A. Ovid'ko, and T. Tsakalakos (Kluwer, Dordrecht, 2000).
5. A. I. Gusev, *Nanocrystalline Materials: Methods of Preparation and Properties* (Ural. Otd. Ross. Akad. Nauk, Yekaterinburg, 1998).
6. H. Hahn and K. A. Padmanabhan, Nanostruct. Mater. **6**, 191 (1995).
7. R. W. Siegel and G. E. Fougere, Nanostruct. Mater. **6**, 205 (1995).
8. H.-E. Schaefer, R. Wurschum, T. Gessmann, *et al.*, Nanostruct. Mater. **6**, 869 (1995).
9. H. Gleiter, Phys. Status Solidi B **172**, 41 (1992).
10. J. Horvath, R. Birringer, and H. Gleiter, Solid State Commun. **62**, 391 (1987).
11. A. A. Nazarov, A. E. Romanov, and R. Z. Valiev, Nanostruct. Mater. **4**, 93 (1994).
12. V. G. Gryaznov and L. I. Trusov, Prog. Mater. Sci. **37**, 289 (1993).
13. A. A. Nazarov, A. E. Romanov, and R. Z. Valiev, Acta Metall. Mater. **41**, 1033 (1993).
14. R. A. Masumura and I. A. Ovid'ko, Mater. Phys. Mech. **1** (2000).
15. V. I. Vladimirov, *Physical Theory of Plasticity and Strength*, Part II: *Point Defects, Strengthening, and Recovery* (Leningrad. Pedagogich. Inst., Leningrad, 1975).
16. J. P. Hirth and J. Lothe, *Theory of Dislocations* (McGraw-Hill, New York, 1967; Atomizdat, Moscow, 1972).

Translated by G. Skrebtsov

Physics of the Solid State, Vol. 43, No. 1, 2001, pp. 39–41. Translated from Fizika Tverdogo Tela, Vol. 43, No. 1, 2001, pp. 39–41.

DEFECTS, DISLOCATIONS, AND PHYSICS OF STRENGTH

Magnetoplastic Effect in Twinning of Bismuth Crystals under a Concentrated Load

A. I. Pinchuk and S. D. Shavreĭ

Mozyr' State Pedagogical Institute, Mozyr', 247760 Belarus
e-mail: APinchook@usa.net

Received May 29, 2000

Abstract—Twinning of bismuth crystals under a concentrated load is found to be partly suppressed by a constant magnetic field. The main mechanisms of the influence of a constant homogeneous magnetic field on the twinning of bismuth single crystals subjected to long-term concentrated loading is studied. It is revealed that the length and the number of wedge twins at an indentation decrease in the magnetic field. This suggests a decrease in the mobility of partial twinning dislocations and in the intensity of the nucleation of wedge twin interlayers in a constant magnetic field. Application of the magnetic field increases the width of twins at the mouth. No anisotropy of the magnetoplastic effect is observed upon twinning. *© 2001 MAIK "Nauka/Interperiodica".*

1. INTRODUCTION

Over the last decade, the magnetoplastic effect in metals has been intensively investigated by several groups of researchers in Russia and other countries [1–4]. In spite of the significant achievements in this area, the effect of a magnetic field on twinning, an important kind of crystallographic form change, remains practically unexplored.

According to the modern concepts of the nature of the magnetoplastic effect, the external magnetic field brings about depinning of perfect dislocations from paramagnetic impurities (due to spin-dependent transitions in the system formed by a dislocation and an impurity center) and their subsequent motion in the elastic stress field. Since the cores of partial twinning dislocations contain no dangling interatomic bonds [5], they can have a smaller number of paramagnetic centers as compared to perfect dislocations. In this respect, experimental study of the magnetoplastic effect in metals in which plastic deformation proceeds through motion of both perfect and partial dislocations, i.e., through glide and twinning simultaneously, can provide better insight into the physical mechanisms of the magnetoplastic effect.

2. SPECIMENS AND EXPERIMENTAL TECHNIQUE

Bismuth single crystals grown by the Bridgman method from a 99.97% pure raw material (with a lead impurity) were used in the measurements. A smooth surface, suitable for investigations without additional processing, was prepared by cleaving a bismuth single crystal along the (111) cleavage plane. The specimens had the shape of a rectangular prism $10 \times 5 \times 5$ mm in size. As was shown earlier [6], the duration of the specimen exposure to air does not significantly affect the micromechanical characteristics of bismuth crystals. Measurements were carried out using a PME-3 microhardness tester with a diamond pyramid applying a concentrated load. A special device was used to place a specimen in the magnetic field in such a way as to eliminate instrumental effects, namely, distortion of the magnetic flux by ferromagnetic parts of the equipment and the Maxwell pressure forces. The components of the experimental equipment, the diamond-point chuck, and the loads on the indenter rod were prepared from nonferromagnetic materials (copper and brass). Special control tests showed that the action of the magnetic field on the elements of the measuring equipment did not cause instrumental effects. The dimensions of the diamond pyramid indentation in the absence of a load on the indenter rod neither increased nor decreased with an increase in the magnetic induction. The experimental setup was described in detail in [7].

In order to avoid magnetic flux distortion by the steel rotary table of the PMT-3 microhardness tester, the specimen was placed at a height of 10 cm from the rotary table, in the geometric center of the gap of the electromagnet limb. Measurements performed with a Hall probe showed that the relative change in the field along the specimen did not exceed 2–3%.

The indenter was pressed into the (111) cleavage plane of the bismuth crystals. The exposure of a specimen to a magnetic field was synchronous with the microindentation. We studied the wedge twins belonging to the $\{110\}\langle 001\rangle$ system. In this case, three twinning planes were symmetric about the load and settled at an angle of 120°. The magnetic induction B was constant in the gap of the electromagnet limb, where the specimen was enclosed, and amounted to 0.2 T. The times t of the specimen exposure to the magnetic field

1063-7834/01/4301-0039$21.00

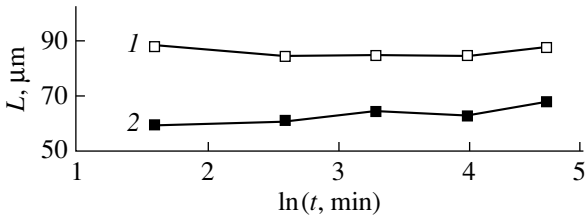

Fig. 1. Dependences of the mean length L of twins on the time t of concentrated loading (*1*) in the absence of a magnetic field and (*2*) in a magnetic field.

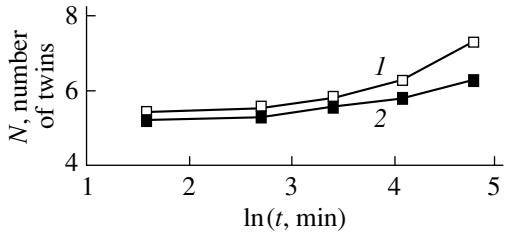

Fig. 2. The mean number of wedge twins N near the indentation as a function of the time t of concentrated loading (*1*) without a magnetic field and (*2*) in a magnetic field.

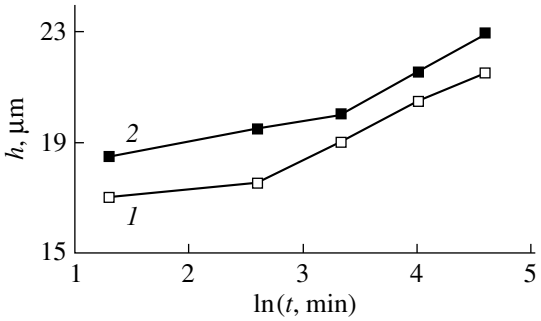

Fig. 3. Dependences of the mean width h of twins at the mouth as a function of the time t of concentrated loading (*1*) without a magnetic field and (*2*) in a magnetic field.

were 5, 15, 30, 60, and 120 min. The gravitational force acting on the indenter rod was $P = 0.14$ N. The length L of wedge twins, the width h of twins at the mouth, and the number N of twin interlayers were directly measured with an eyepiece micrometer of the PMT-3 instrument. The results of the measurements were averaged over the twin interlayers wedged about 20 indentations. The measurement error did not exceed 3%.

3. RESULTS AND DISCUSSION

We found that turning the magnetic field on and off before applying a load did not change the plastic deformation pattern. The magnetoplastic effect was observed in bismuth crystals when the magnetic field and the concentrated load were simultaneously applied to the specimen. The reversal of the field sign did not affect the plastic deformation.

The experiments revealed that the length of the wedge twins in the magnetic field is considerably smaller than that without it (curves *2*, *1* in Fig. 1, respectively). This indicates that the twinning dislocation path is reduced when the magnetic field is applied to the specimen. As can be seen from Fig. 1, the concentrated loading for $t = 5$–120 min does not change the length L of the twins either in the magnetic field or without it. The experimental dependences are plotted in semilogarithmic coordinates (the logarithm of the loading time $\ln t$ is plotted along the horizontal axis in all the graphs). Open symbols in the experimental dependences correspond to measurements in the absence of the field, and the filled symbols represent the data obtained upon applying the magnetic field to bismuth crystals.

As is seen from Fig. 2, the mean number N of wedge twins increases with t, but this process is partly suppressed in the magnetic field. A possible reason for this is that the magnetic field impedes the translation of twinning dislocations in the twinning plane and, therefore, increases the backward locking stresses that act on the twinning dislocation sources in the twin mouth [8].

Application of the magnetic field to the specimen stimulates multiplication of twinning dislocations at the existing twin–matrix interfaces, because the twin width h at the mouth in the magnetic field (curve *2* in Fig. 3) is larger than that in the absence of the magnetic field (curve *1* in Fig. 3). The physical reason for this phenomenon is not yet clear, since the backward locking stresses, which act on the twinning dislocation sources in the twin mouth, should increase with a decrease in the twin length.

Al'shits *et al.* [9] reported that the magnetoplastic effect depends on the mutual orientation of the dislocation L, its Burgers vector **b**, and the magnetic induction **B**. The anisotropy of the magnetic field effect on twinning, if it occurs, can be found in the following way. The wedge mechanical twins observed at the indentation can be considered segments. Then, we can statistically calculate the sum of the absolute values of all the segments projected onto the positive L^+ and negative L^- directions of the axis. The axis was aligned parallel to the magnetic inductance vector in the former case and perpendicular to it in the latter case. The experiment revealed that, in both cases, the ratio L^+/L^- is independent of the time of concentrated loading. The quantity L^+/L^- behaves likewise in the absence of the magnetic field. The numerical values of L^+/L^- are the same in the magnetic field and without it, providing that t is the same. Thus, no anisotropy of the magnetoplastic effect is found in the case of the twinning of bismuth crystals. The difference between the numerical values of L^+/L^- for curves *1* and *2* in Fig. 4 is determined by the indenter orientation relative to the twinning planes. Each point in the graphs was obtained at the same ori-

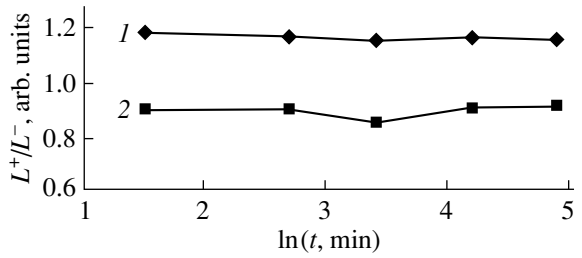

Fig. 4. Dependences of the ratio L^+/L^- on ln t: (*1*) the axis is parallel to the magnetic inductance vector and (*2*) the axis is perpendicular to the magnetic inductance vector.

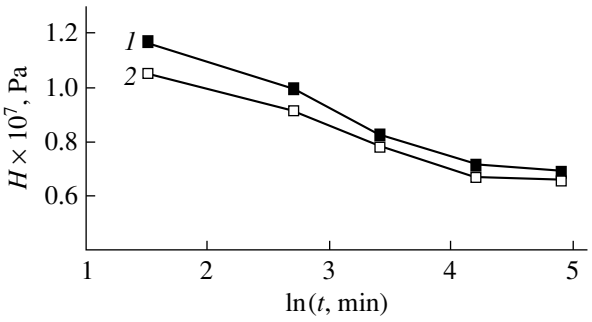

Fig. 5. Dependences of the microhardness H on the time of concentrated loading (*1*) in a magnetic field and (*2*) without a field.

entation of the diamond indenter with respect to the {110} planes.

The physical phenomena observed in this work can be interpreted in the following way. Twinning is an energy-consuming process. The work of gravity acting with the load on the indenter rod is spent for the nucleation and growth of twins. At the same time, twinning proceeds much faster than glide (hundreds of meters per second) [10, 11]. For this reason, twins rapidly drive the elastic energy away from the stress concentrators. Considerably smaller cleavage stresses are necessary for the glide to be realized through the motion of perfect dislocations in the $\{11\bar{1}\}$ planes [12], but this process is relatively slow. The force effect of the magnetic field on dislocations was excluded from our consideration due to the homogeneity of the magnetic field. Since the magnetic field was constant, the heating of the specimen by eddy currents and the pinching of the electron–hole plasma were also excluded. Earlier investigations [13–16] showed that the magnetic field enhances the mobility of perfect dislocations due to their depinning from paramagnetic obstacles or the decay of these obstacles into smaller ones. This can lead to a partial suppression of twinning. The experiments conducted by the authors revealed that the dimensions of dislocation rosettes, which consist of arrays of perfect dislocations, are considerably larger in the case when the magnetic field is applied to bismuth crystals. The effect of the magnetic field on the partial twinning dislocations is apparently less substantial, because their cores possess a smaller number of paramagnetic centers. Certainly, these interferences call for further experimental and theoretical investigations.

The microhardness H was found to be sensitive to the magnetic field (Fig. 5). At small t, the microhardness is larger in the magnetic field. This can be explained by a partial suppression of twinning by the magnetic field. As the glide evolves with time t, the microhardness H diminishes and becomes comparable to the microhardness obtained in the absence of the magnetic field.

ACKNOWLEDGMENTS

This work was supported by the Belarussian Foundation for Basic Research, project no. T97M-170.

REFERENCES

1. V. I. Al'shits, E. V. Darinskaya, and E. A. Petrzhik, Fiz. Tverd. Tela (Leningrad) **33** (10), 3001 (1991) [Sov. Phys. Solid State **33**, 1694 (1991)].
2. M. I. Molotskiĭ, Fiz. Tverd. Tela (Leningrad) **33** (10), 3112 (1991) [Sov. Phys. Solid State **33**, 1760 (1991)].
3. M. I. Molotskiĭ, R. E. Kris, and V. N. Flerov, Phys. Rev. B **51**, 1253 (1995).
4. Yu. I. Golovin and R. B. Morgunov, Chem. Rev. **23**, 23 (1998).
5. A. M. Kosevich and V. S. Boĭko, Usp. Fiz. Nauk **104** (2), 201 (1971) [Sov. Phys. Usp. **14**, 286 (1971)].
6. G. P. Upit, S. A. Varchenya, and I. P. Spalvin, Phys. Status Solidi **15**, 617 (1966).
7. A. I. Pinchook and V. S. Savenko, J. Appl. Phys. **86** (5), 2479 (1999).
8. M. V. Klassen-Neklyudova, *Mechanical Twinning of Crystals* (Akad. Nauk SSSR, Moscow, 1960; Consultants Bureau, New York, 1964).
9. V. I. Al'shits, E. V. Darinskaya, and E. A. Petrzhik, Fiz. Tverd. Tela (St. Petersburg) **35** (2), 320 (1993) [Phys. Solid State **35**, 162 (1993)].
10. V. I. Bashmakov, L. A. Skal'ko, and N. G. Yakovenko, Fiz. Met. Metalloved. **28** (5), 936 (1969).
11. V. I. Bashmakov and T. S. Chikova, Dokl. Akad. Nauk SSSR **259** (3), 582 (1981) [Sov. Phys. Dokl. **26**, 704 (1981)].
12. D. Z. Grabko, Yu. S. Boyarskaya, and N. P. Dyntu, *Mechanical Properties of Bismuth-type Semimetals* (Chishinau, Shtiintsa, 1982).
13. M. I. Molotskii and V. N. Flerov, Phys. Rev. B **52**, 15829 (1995).
14. Yu. I. Golovin, R. B. Morgunov, A. I. Tyurin, and V. I. Ivolgin, Dokl. Akad. Nauk **361**, 352 (1998).
15. Yu. I. Golovin and R. B. Morgunov, Zh. Éksp. Teor. Fiz. **115**, 605 (1999) [JETP **88**, 332 (1999)].
16. M. I. Molotskii and V. N. Flerov, Phys. Rev. Lett. **78**, 2779 (1997).

Translated by M. Lebedkin

Physics of the Solid State, Vol. 43, No. 1, 2001, pp. 42–46. Translated from Fizika Tverdogo Tela, Vol. 43, No. 1, 2001, pp. 42–46.

DEFECTS, DISLOCATIONS, AND PHYSICS OF STRENGTH

Generation and Evolution of Partial Misfit Dislocations and Stacking Faults in Thin-Film Heterostructures

M. Yu. Gutkin, K. N. Mikaelyan, and I. A. Ovid'ko

Institute of Problems in Machine Science, Russian Academy of Sciences, Vasil'evskiĭ ostrov, Bol'shoĭ pr. 61, St. Petersburg, 199178 Russia
e-mail: ovidko@def.ipme.ru

Received June 9, 2000

Abstract—An analysis is made of the specific features in the generation and evolution of partial misfit dislocations at the vertices of V-shaped configurations of stacking fault bands, which terminate in the bulk of the growing film at 90° partial Shockley dislocations. The critical thicknesses h_c of an epitaxial film, at which generation of such defect configurations becomes energetically favorable, are calculated. It is shown that at small misfits, the first to be generated are perfect misfit dislocations and at large misfits, partial ones, which are located at the vertices of V-shaped stacking-fault band configurations emerging onto the film surface. Possible further evolution of stacking-fault band configurations with increasing film thickness are studied. *© 2001 MAIK "Nauka/Interperiodica".*

The generation and evolution of various defect structures in the course of growth of thin-film heteroepitaxial systems has been for many years a subject of numerous experimental and theoretical studies (see, e.g., [1–16]). In particular, one is presently witness to intense development of the concept of misfit dislocations (MDs) whose formation at the interphase boundary between the substrate and the growing epitaxial film serves as an efficient channel of removing misfit stresses caused by differences in the crystalline structure and properties between the substrate and film materials [1–6]. The role of MDs may actually be played by both perfect lattice dislocations ("perfect misfit dislocations") and partial dislocations ("partial misfit dislocations"), which are associated with stacking faults. However, nearly all of the theoretical models proposed relate to the formation and behavior of perfect MDs, although a comparative consideration of the perfect and partial MDs suggests the existence of such parameters for a heterosystem at which the formation of partial MDs is found to be energetically preferable [7, 8]. In particular, as follows from the results of a theoretical analysis from [8], if the lattice misfit between the film and the substrate is large enough (>1%), the critical thickness for the formation of partial MDs connected with V-shaped stacking fault defects becomes less than that for the appearance of perfect MDs; i.e., such partial MDs form in a heterosystem before perfect MDs do. This conclusion is of considerable interest in view of the present demand in technology for the use of heterostructures with large misfits.

However, the case considered in [8] relates to fairly simple partial MD configurations, namely, to partial MDs located at the interphase boundary at the vertices of V-shaped stacking faults. The main objective of this work is to analyze theoretically the conditions favoring generation of experimentally observed [13] partial-MD configurations of a more complex type, more specifically, of configurations made up of three partial MDs located at the interphase boundary and in the bulk of the film and connected with V-shaped stacking faults.

1. GENERATION MECHANISMS OF PARTIAL MISFIT DISLOCATIONS

Consider the possible mechanisms of formation of partial MDs at the interphase boundary between an epitaxial film and a substrate. Formation of semiloops of split dislocations at the free surface of a growing epitaxial film, followed by their slide to the interphase boundary, is one of the major mechanisms of MD generation which appears to be best studied experimentally [9–13]. For instance, the splitting of sliding perfect 60° dislocations into partial 30° and 90° Shockley dislocations (Fig. 1a) with a subsequent slide of this already split configuration to the interphase boundary, brings about the formation of a partial MD, which is connected through a stacking fault to the second partial dislocation remaining in the bulk of the film [9, 10]. A reaction between two such partial MDs near the interphase boundary gives rise to the formation of sessile partial MDs located at the vertices of V-shaped stacking faults [12], at the ends of which Shockley partial dislocations are located (Fig. 1b). Such defect configurations are similar to the Lomer–Cottrell barriers in fcc metals [17], the only difference being that, here, a partial MD acts as the stair-rod sessile dislocation. If partial MDs form even at small film thicknesses (in systems with large misfits), the formation of the second Shockley partial dislocations becomes delayed and

stacking fault bands extend from the partial MD to the free film surface. As the film continues to grow, these partial dislocations will be generated on the surface and they will slide toward the vertex partial MD, after which this V-shaped defect configuration transforms (collapses) into a sessile Lomer perfect dislocation.

In [8], we considered the first case in detail, where stacking fault bands always reached the surface of the film as the film grew. When applied to the GaAs/Si(001) heterosystem, where such partial MDs were observed to exist at the vertices of V-shaped stacking faults [12], it is implied that each sessile 90° partial MD is formed of two partial 30° dislocations sliding toward each other to merge at the interphase boundary and that the 90° partial MDs, which should terminate the stacking fault bands, had no time to nucleate.

The present work considers the second, more general case, where partial 90° dislocations also slide from the film surface after the 30° partials, but stop at a certain distance from the surface (Fig. 1b). Thus, the V-shaped stacking fault is now bounded from below by a 90° partial MD at its vertex and from above by two 90° partial dislocations residing in the bulk of the film. Note that such defect configurations were observed experimentally [13], but have not been treated theoretically.

In the subsequent sections, we are going to calculate the critical parameters for the formation of partial MDs connected through V-shaped stacking faults with partial dislocations in the bulk of the growing film and analyze the further evolution of such defect configurations in the course of epitaxial growth. The analysis will be illustrated by GaAs/Si heteroepitaxial structures.

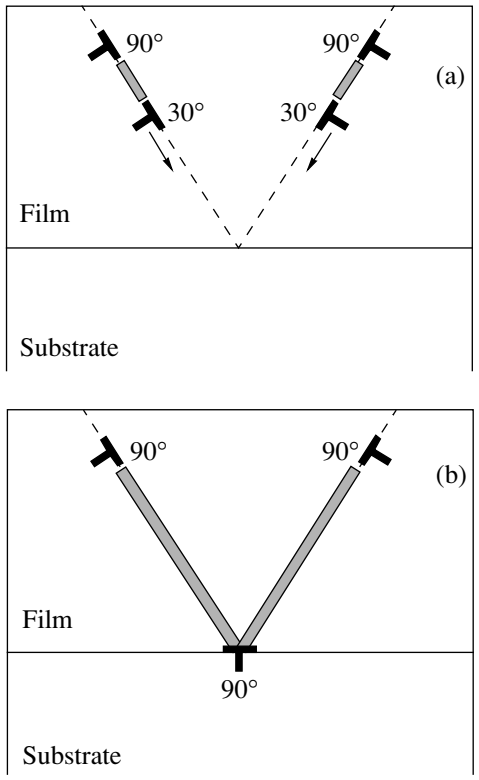

Fig. 1. Formation of partial misfit dislocations. (a) Slide of 60° dislocations split into Shockley partial 30° and 90° dislocations. (b) Formation of a sessile partial 90° MD connected through stacking fault bands with Shockley partial 90° dislocations in the bulk of the film.

2. CRITICAL PARAMETERS OF THIN-FILM HETEROSTRUCTURES WITH PARTIAL MISFIT DISLOCATIONS

One of the important parameters characterizing a heteroepitaxial system is the critical film thickness h_c, above which the formation of MDs becomes energetically favorable [1–6]. The appearance of the first MDs alone determines the magnitude of h_c; therefore, it is sufficient in itself for study of a system consisting of one partial MD connected through a V-shaped stacking fault with two partial 90° dislocations in the bulk of the film (Fig. 1b).

Consider a model heteroepitaxial system in the form of a thin elastically isotropic film of thickness h, which is grown epitaxially on a semi-infinite elastically isotropic substrate (Fig. 2). The elastic constants, the shear modulus G, and the Poisson ratio ν will be considered the same for the materials of the film and of the substrate. The original coherent state of the system is characterized by the elastic strain of the film $\varepsilon = -f$, where $f = (a_2 - a_1)/a_1 > 0$ is the original two-dimensional lattice misfit between the substrate and film whose lattice parameters are a_1 and a_2, respectively. We place a partial MD with the Burgers vector $\mathbf{b}$ at the point (h, 0) at the interface and partial 90° dislocations with Burgers vectors $\mathbf{b}_{p1} = -\mathbf{b}_x - \mathbf{b}_y$ and $\mathbf{b}_{p2} = \mathbf{b}_x - \mathbf{b}_y$ at points (d, $\pm s$) in the bulk of the film. The partial MD connects with these dislocations through the stacking fault bands making up a V-shaped configuration with an opening angle 2α. For convenience, we present each of these partial 90° dislocations as a superposition of two edge dislocations with Burgers vectors $\pm\mathbf{b}_x$ and $\mathbf{b}_y$ (Fig. 2).

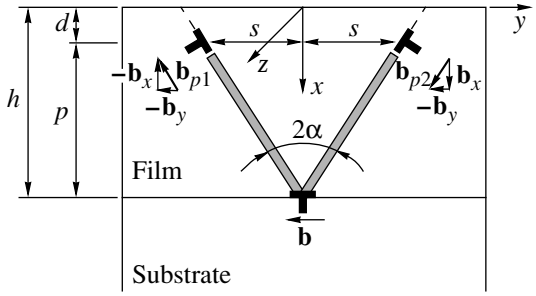

Fig. 2. Model of a V-shaped configuration of stacking fault bands with a partial 90° MD at the vertex and two Shockley partial 90° dislocations at the band ends.

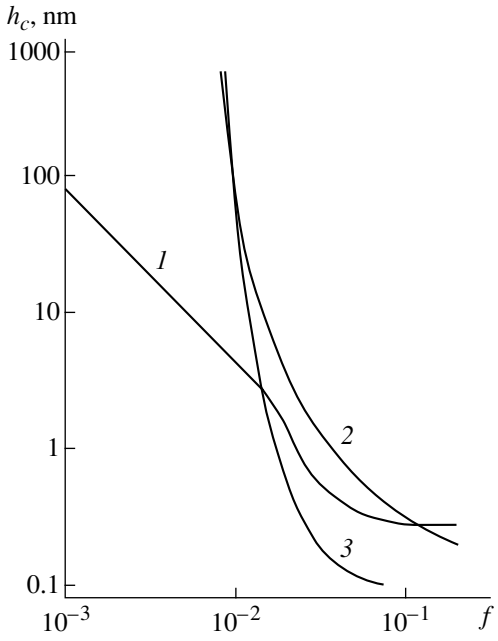

Fig. 3. *f*–*h* diagram (*1*) for a perfect MD, (*2*) for a partial MD with stacking fault bands and Shockley partial 90° dislocations at the band ends, and (*3*) for a partial MD with stacking fault bands reaching the surface of the growing film.

The total energy of the system per unit dislocation length, W^t, can be presented as

$$W^t = W^f + W^n + W^{fd} + W^\gamma + W^d, \tag{1}$$

where W^f is the elastic energy of the original misfit, $W^n = G(b^2 + 2b_p^2)/[4\pi(1-\nu)]$ is the total energy of the dislocation cores, $b_p^2 = b_{p1}^2 = b_{p2}^2$, $W^{fd} = -2Gf(bh + 2b_y d)(1+\nu)/(1-\nu)$ is the total interaction energy between dislocations and the elastic original-misfit stress field, $W^\gamma = 2\gamma(h-d)/\cos\alpha$ is the stacking-fault band energy, γ is the stacking fault energy, and W^d is the elastic energy of the dislocation subsystem including the interaction of dislocations with the free film surface and with one another. The last term is calculated using the relations for the stress fields of an edge dislocation located near a free surface [18], which finally yields (in units of $G/[4\pi(1-\nu)]$)

$$\begin{aligned}
W^d = {} & -b^2\left(\ln\frac{b}{2h-b} + \frac{2h(h-b)}{(2h-b)^2}\right) - \frac{4b_x b_y s d^3}{(d^2+s^2)^2} \\
& - 2bb_y\left(\ln\frac{(h-d)^2+s^2}{(h+d)^2+s^2} - \frac{2s^2}{(h-d)^2+s^2}\right. \\
& \left. + \frac{2(s^2+2dh)}{(h+d)^2+s^2} - \frac{8dhs^2}{[(h+d)^2+s^2]^2}\right) \\
& + 2bb_x s\left(\frac{2(h-d)}{(h-d)^2+s^2} - \frac{2(h-d)}{(h+d)^2+s^2} - \frac{8dh(h+d)}{[(h+d)^2+s^2]^2}\right) \\
& + b_y^2\left(\ln\frac{b_y^2 s^2}{(d^2+s^2)(2d-b_y)^2} + \frac{4d(d-b_y)}{(2d-b_y)^2} - \frac{d^2(d^2+3s^2)}{(d^2+s^2)^2}\right) \\
& - b_x^2\left(\ln\frac{b_x^2(d^2+s^2)}{s^2(2d-b_x)^2} + \frac{4d(d-b_x)}{(2d-b_x)^2} - \frac{d^2(3d^2+s^2)}{(d^2+s^2)^2}\right).
\end{aligned} \tag{2}$$

To find the critical film thickness h_c at which the formation of even the first partial MD alone becomes energetically favorable, we equate the change in energy that is associated with the formation of a partial MD connected through a V-shaped stacking fault with two partial 90° dislocations to zero,

$$\Delta W = W^t - W^f = 0, \tag{3}$$

and obtain a transcendental equation for h_c:

$$\begin{aligned}
& 2b_p^2 - 8\pi f(1+\nu)(bh + 2b_y d) + \frac{8\pi\gamma(1-\nu)(h-d)}{G\cos\alpha} \\
& + b^2\left(1 - \ln\frac{b}{2h-b} - \frac{2h(h-b)}{(2h-b)^2}\right) \\
& - 2bb_y\left(\ln\frac{(h-d)^2+s^2}{(h+d)^2+s^2} - \frac{2s^2}{(h-d)^2+s^2}\right. \\
& \left. + \frac{2(s^2+2dh)}{(h+d)^2+s^2} - \frac{8dhs^2}{[(h+d)^2+s^2]^2}\right) \\
& + 2bb_x s\left(\frac{2(h-d)}{(h-d)^2+s^2} - \frac{2(h-d)}{(h+d)^2+s^2}\right. \\
& \left. - \frac{8dh(h+d)}{[(h+d)^2+s^2]^2}\right) - \frac{4b_x b_y s d^3}{(d^2+s^2)^2} \\
& - b_y^2\left(\ln\frac{b_y^2 s^2}{(d^2+s^2)(2d-b_y)^2} + \frac{4d(d-b_y)}{(2d-b_y)^2}\right. \\
& \left. - \frac{d^2(d^2+3s^2)}{(d^2+s^2)^2}\right) - b_x^2\left(\ln\frac{b_x^2(d^2+s^2)}{s^2(2d-b_x)^2}\right. \\
& \left. + \frac{4d(d-b_x)}{(2d-b_x)^2} - \frac{d^2(3d^2+s^2)}{(d^2+s^2)^2}\right) = 0.
\end{aligned} \tag{4}$$

Using Eq. (4),we consider the dependence of h_c on the original misfit f for the case where the partial dislocations are located at a depth d. We use, as before [8], the parameters characteristic of the GaAs/Si(001) heterosystem [7, 19]: G = 32.5 GPa, ν = 0.31, b = 0.133 nm, b_p = 0.231 nm, b_x = 0.19 nm, b_y = 0.133 nm, $2\alpha \approx 70°$, and γ = 0.06 J m^{-2}.

Figure 3 presents the $h_c(f)$ dependences for a perfect MD (curve *1*, b = 0.398 nm, γ = 0), for a partial MD at the vertex of a V-shaped configuration of stacking-fault bands terminated by two partial 90° dislocations in the bulk of the film at a minimal depth $d = b_x$ = 0.19 nm (curve *2*), and for a partial MD at the vertex of the same configuration for the case where the stacking-fault bands reach the free surface (curve *3*, d = 0, b = 0.133 nm). As seen from the plots, perfect MDs can be generated at any misfits f (provided the film is thick enough), whereas for a partial MD, in both cases, there exists a limiting minimal misfit f_l below which their generation is energetically unfavorable. The values of f_l in the latter two cases are approximately equal, $f_l \approx 0.009$. It was also found that the formation of a partial MD with d = 0 is always more probable than that with $d = b_x$ (curve *3* passes below curve *2*). Consider now what happens as d increases. Figure 4 presents the dependence of h_c on d for a fixed misfit f = 0.02. As seen from the figure, for small d, the critical film thickness h_c increases with d to reach a maximum at $d \approx 4b_x \approx 0.76$ nm, after which it falls off while remaining substantially larger than the critical thicknesses for perfect MDs (≈0.14 nm) and partial MDs with d = 0 (≈0.12 nm). Thus, one can conclude that for small misfits ($f < 0.01$), the first to be generated are perfect MDs, whereas for large misfits ($f > 0.01$), partial MDs are generated first, with the stacking-fault bands reaching the surface of the growing film.

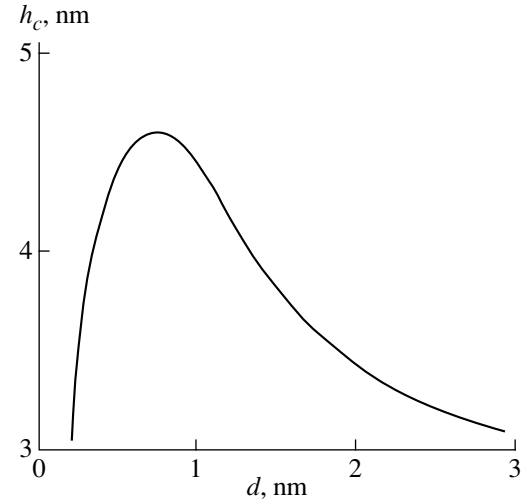

Fig. 4. Dependence of the critical thickness h_c on depth d of Shockley partial 90° dislocations, calculated for a misfit f = 0.02.

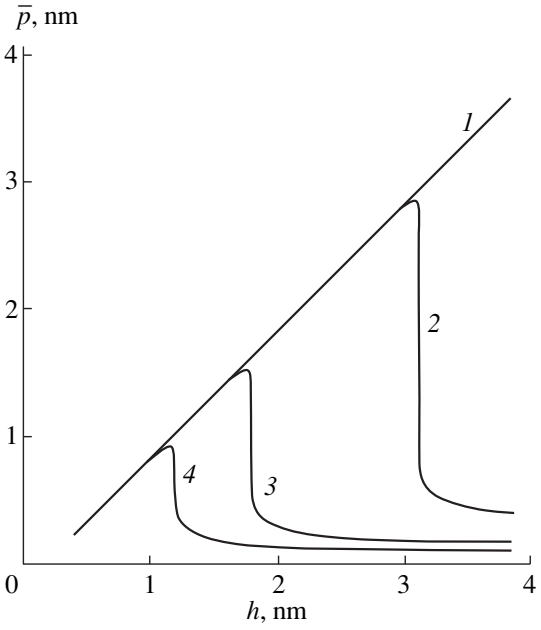

Fig. 5. Variation of the equilibrium distance $\bar{p}$ between Shockley partial 90° dislocations and the interphase boundary with increasing film thickness, calculated for the misfits f (*1*) 0.02, (*2*) 0.04, (*3*) 0.07, and (*4*) 0.10.

3. EVOLUTION OF PARTIAL MISFIT-DISLOCATION CONFIGURATIONS IN THE COURSE OF FILM GROWTH

Consider the development of the situation as the film continues to grow in the case of large misfits ($f >$ 0.01). We calculate the equilibrium position of the partial 90° dislocations terminating the stacking-fault bands in the bulk of the film (Fig. 2) using Eqs. (1) and (2). One can determine the change in the equilibrium distance $\bar{p}$ (i.e., corresponding to the maximum gain in energy ΔW) as the film thickness h increases with the misfit f kept fixed. The results of the calculation are plotted in Fig. 5 as $\bar{p}(h)$ functions for f = 0.02, 0.04, 0.07, and 0.10 (curves *1–4*, respectively). It is readily seen that, as long as the thickness h is small ($h < 1$ nm), we have $\bar{p}(h) = h - b_x$ for any of these misfits; i.e., the stacking-fault bands grow as the film grows to finally reach (to within b_x) the free surface. At the instant h reaches a critical value h_c', $\bar{p}$ exhibits a sharp drop, which can be treated as a fast displacement of 90° partial dislocations to the interface separating the film from the substrate; the drop is accompanied by a shortening of the stacking-fault bands until they disappear altogether and the V-shaped configuration collapses, with the partials transforming to perfect MDs. For instance, to the misfits f = 0.02, 0.04, 0.07, and 0.10 correspond now "new" critical thicknesses, $h_c' \approx 5.7$, 3.1, 1.9, and 1.3 nm, at which the partials become per-

fect MDs. The collapse of the V-shaped configurations of stacking-fault bands with partial MDs at their vertices, resulting in the formation of perfect MDs, confirms the conclusion [8] that a decrease in partial MD density and an increase in perfect MD density in the course of film growth inevitably occur and suggests that a natural mechanism is involved in the transformation of partial to perfect MDs. A decrease in the partial MD density and an increase in the perfect MD density with increasing thickness of the growing film were observed in the experiments in [13].

Thus, our theoretical consideration of partial MDs located at the vertices of V-shaped configurations of stacking-fault bands, which terminate at Shockley partial 90° dislocations in the bulk of the film, permits the following conclusions. At small misfits, the first to be generated are perfect MDs, while at large ones, partial MDs are generated at the vertices of the V-shaped configurations of stacking-fault bands emerging onto the film surface. In the latter case, as the film grows in thickness, the stacking-fault bands first grow longer and reach, as before, the film surface, but after the thickness has attained a critical value h_c', which decreases with increasing misfit, they shorten rapidly through the generation of Shockley partial 90° dislocations and their slide to the interphase boundary. As these dislocations approach the interface, the V-shaped configuration collapses and the partial MDs transform into perfect MDs. This mechanism of transformation of partial to perfect MDs accounts for the decrease in partial MD density and the increase in perfect MD density during the growth of nanolayer heterosystems, which is well known from experiments (see, for instance, [13]).

ACKNOWLEDGMENTS

This work was supported by the RF Scientific Council on R & D "Physics of Solid-State Nanostructures" (grant no. 97-3006), the Russian Foundation for Basic Research (grant no. 98-02-16075), the Office of US Naval Research (grant no. 00014-99-1-0569), and the INTAS program (grant no. 99-1216).

REFERENCES

1. Yu. A. Tkhorik and L. S. Khazan, *Plastic Deformation and Misfit Dislocations in Heteroepitaxial Systems* (Naukova Dumka, Kiev, 1983).
2. M. G. Mil'vidskiĭ and V. B. Osvenskiĭ, *Structural Defects in Epitaxial Layers of Semiconductors* (Metallurgiya, Moscow, 1985).
3. E. A. Fitzgerald, Mater. Sci. Rep. **7** (1), 87 (1991).
4. L. B. Freund, MRS Bull. **17** (1), 52 (1992).
5. R. Beanland, D. I. Dunstan, and P. I. Goodhew, Adv. Phys. **45** (1), 87 (1996).
6. S. C. Jain, A. H. Harker, and R. A. Cowley, Philos. Mag. A **75** (6), 1461 (1997).
7. A. K. Gutakovskiĭ, O. P. Pchelyakov, and S. I. Stenin, Kristallografiya **25** (4), 806 (1980) [Sov. Phys. Crystallogr. **25**, 461 (1980)].
8. M. Yu. Gutkin, K. N. Mikaelyan, and I. A. Ovid'ko, Fiz. Tverd. Tela (St. Petersburg) **40** (1), 2059 (1998) [Phys. Solid State **40**, 1864 (1998)].
9. B. C. De Cooman and C. B. Carter, Acta Metall. **37** (10), 2765 (1989).
10. B. C. De Cooman, C. B. Carter, Kam Toi Chan, and J. R. Shealy, Acta Metall. **37** (10), 2779 (1989).
11. J. Zou and D. J. H. Cockayne, Appl. Phys. Lett. **69** (8), 1083 (1996).
12. M. Loubradou, R. Bonnet, A. Vila, and P. Ruterana, Mater. Sci. Forum **207–209** (1), 285 (1996).
13. M. Tamura, Appl. Phys. A **A63** (2), 359 (1996).
14. A. F. Schwartzman and R. Sinclair, J. Electron. Mater. **20** (10), 805 (1991).
15. I. A. Ovid'ko, J. Phys: Condens. Matter **11** (34), 6521 (1999).
16. I. A. Ovid'ko, in *Nanostructured Films and Coatings: Proceedings of the NATO Advanced Research Workshop*, Ed. by G.-M. Chow, I. A. Ovid'ko, and T. Tsakalakos (Kluwer, Dordrecht, 2000), p. 231.
17. J. P. Hirth and J. Lothe, *Theory of Dislocations* (McGraw-Hill, New York, 1967; Atomizdat, Moscow, 1972).
18. T. Mura, in *Advances in Materials Research*, Ed. by H. Herman (Interscience, New York, 1968), Vol. 3, p. 1.
19. J. Zou, B. F. Usher, D. J. H. Cockayne, and R. Glaisher, J. Electron. Mater. **20** (10), 855 (1991).

Translated by G. Skrebtsov

Physics of the Solid State, Vol. 43, No. 1, 2001, pp. 47–50. Translated from Fizika Tverdogo Tela, Vol. 43, No. 1, 2001, pp. 47–50.

DEFECTS, DISLOCATIONS, AND PHYSICS OF STRENGTH

Dynamic Properties of Dislocations in Silicon Wafers Heat-Treated at Low Temperatures

M. V. Mezhennyĭ*, M. G. Mil'vidskiĭ, V. F. Pavlov*, and V. Ya. Reznik****

** Giredmet Federal State Unitary Enterprise, Moscow, 109017 Russia*

*** Institute for Chemical Problems of Microelectronics, B. Tolmachevskiĭ per. 5, Moscow, 109017 Russia*

e-mail: icpm@mail.girmet.ru

Received April 18, 2000

Abstract—The specific features of the dislocation motion in dislocation-free silicon wafers (single crystals are grown by the Czochralski method) heat-treated at 450 and 650°C have been investigated. It is found that the low-temperature treatment of silicon wafers with an oxygen content of $(7–8) \times 10^{17}$ cm^{-3} substantially affects the dynamic properties of dislocations generated into silicon wafers during their four-point bending and brings about an increase in the starting stresses of the onset of the dislocation motion. A characteristic spatial inhomogeneity is observed in the generation and propagation of dislocations from indentations upon the bending of heat-treated wafers. The reasons for the regularities revealed are discussed. © *2001 MAIK "Nauka/Interperiodica".*

1. INTRODUCTION

During the formation of active integrated-circuit elements, dislocation-free silicon wafers of large diameters are subjected to various mechanical and thermal actions, which can lead to undesirable generation of dislocations in these wafers. In this respect, the problem of the mechanical strength of silicon wafers, especially the problem concerning the nature of heterogeneous nucleation of dislocations and the factors responsible for their dynamic properties (see, for example, [1, 2]), is a prime consideration. The mechanical properties of Czochralski grown dislocation-free silicon single crystals, specifically their plasticity, are determined to a large extent by the content and the form of oxygen involved in these wafers. In the course of crystal growth, oxygen is incorporated into the crystal at sufficient concentrations to form supersaturated solid solutions over a wide range of temperatures. These solutions undergo decomposition both during postcrystallization cooling of an ingot (partially) and upon subsequent heat treatment of wafers cut from this ingot. Depending on their nature and size, the oxygen-containing precipitates formed during the crystal growth can play the role of heterogeneous nucleation sites of dislocations and act as stoppers against dislocation motion, thus hindering dislocation propagation and multiplication. The nature and size of the precipitates in a crystal matrix are governed by the oxygen content, thermal conditions of single-crystal growth, and heat treatment of silicon wafers. The purpose of this work was to investigate the dynamic properties of dislocations at different low-temperature treatments of silicon wafers during which the oxygen supersaturated solid solution undergoes decomposition with the formation of extremely small oxygen clusters [3].

2. SAMPLES AND EXPERIMENTAL TECHNIQUE

The experiments were carried out with wafers 150 mm in diameter (resistivity, 5 Ω cm; p-type conductivity; oxygen content, $\sim(7–8) \times 10^{17}$ cm^{-3}), which were cut from dislocation-free silicon single crystals grown by the Czochralski method in a "vacancy" mode [4] in the [001] direction. The wafers were heat-treated under the following conditions: 1000°C/15 min + 450°C/16 h (wafer *1*) and 1000°C/15 min + 650°C/16 h (wafer *2*). The high-temperature treatment was performed with the aim of dissolving oxygen-containing precipitates of the "growth" origin in the crystal matrix. The heat treatment of the samples at 450°C was accompanied by the vigorous formation of oxygen clusters with donor properties (thermodonors). The heat treatment at 650°C brought about the formation of wafers containing larger-sized (compared to the heat treatment at 450°C) oxygen clusters, the greater part of which possesses no electrical activity [3].

Samples for mechanical testing were cut from wafers in the form of parallelepipeds $25 \times 4 \times 0.7$ mm in size with the {100} large faces. The long side of the sample was oriented along the ⟨110⟩ direction. All samples were chemically polished in an acid mixture $HF : HNO_3 = 1 : 6$ for 5 min. In the process, a layer ~40 μm thick was removed from the surface. Then, several indentations were made on the sample surface with the use of a Knoopp indenter (the indenter loading was 0.25 N, and the loading time was 15 s). After the indentation, the sample was subjected to four-point bending in a special setup according to the procedure described in [5] at temperatures of 600 and 800°C. The sample side containing indentations was subjected to tensile deformation. The indentation of the sample sur-

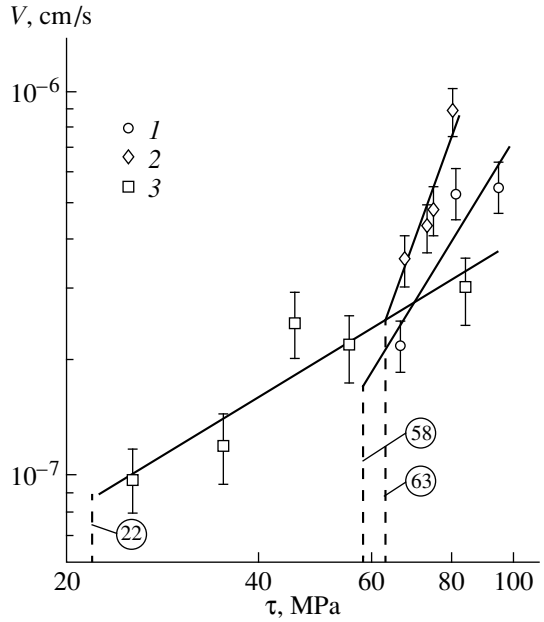

Fig. 1. Dependence of the velocity of dislocation motion in silicon wafers at 600°C on the applied stress (vertical dashed lines correspond to the starting stresses of the onset of dislocation motion in the samples under investigation).

face and the subsequent loading at a testing temperature gave rise to dislocation loops in the near-surface layer, which consisted of two 60° segments and one fragment of a screw dislocation aligned parallel to the sample surface. In the experiments performed, we examined the mobility of 60° dislocation-loop segments.

The structural transformations in the silicon wafers were controlled by x-ray topography and optical microscopy. For comparison, we studied the samples cut from a single-crystal wafer immediately after the growth (wafer *3*).

3. INVESTIGATION OF DISLOCATION DYNAMICS

Figure 1 displays the dependence of the velocity of dislocation motion in heat-treated silicon wafers at 600°C on the applied shear stress. For comparison, Fig. 1 also depicts similar dependences for samples cut from wafer *3* (the postgrowth state). As follows from comparison of the results obtained, the velocities of dislocation motion in samples after the low-temperature treatment are higher than those in the samples immediately after the growth. Noteworthy are the substantially larger values of the starting stresses of the onset of dislocation motion in heat-treated samples. For example, in samples cut from wafers *1* and *2*, the starting stresses were equal to 58 and 63 MPa, respectively (for samples of wafer *3*, the starting stress was 22 MPa). It should be mentioned that, at stresses of ~80–90 MPa, the bulk generation of dislocation slip bands from external sources was observed in all the samples, which brought about their macrodeformation and made the observation of indentation-induced dislocations difficult. At a testing temperature of 800°C, the starting stresses in samples of wafers *1* and *2* were equal to 25 and 43 MPa, respectively; the plastic bending in the samples was observed already at stresses of 45 and 50 MPa, respectively. The critical stress of the onset of dislocation motion in samples of wafer *3* at a temperature of 800°C was equal to 12 MPa, whereas the stress giving rise to plastic bending was 25 MPa. It is worth noting that, upon the four-point bending at 800°C, the samples are characterized by a large spread in the critical stresses of the onset of dislocation motion and the stresses responsible for the bulk generation of dislocation slip bands from external sources, which resulted in plastic bending of the samples. This inhomogeneity and the narrow stress range of observation of the motion of individual indentation-induced dislocations made correct determination of the dislocation motion velocity at 800°C impossible.

Thus, we can state that the velocities of dislocation motion in all the samples studied are close to each other. However, after the low-temperature annealings at 450 and 650°C, the starting stresses of the onset of dislocation motion considerably increase. The above regularities can be explained by the fact that the oxygen-containing clusters formed upon the low-temperature treatment are effective stoppers against the onset of dislocation motion, but they are not serious obstacles to moving dislocations.

4. INVESTIGATION OF SPATIAL INHOMOGENEITY IN GENERATION AND MOTION OF DISLOCATIONS

A characteristic feature of all the samples after the low-temperature treatment is a pronounced spatial inhomogeneity in the generation and propagation of dislocations from indentations at the same shear stresses. In the case when identical indentations are closely located at almost equal intervals (~50 μm) on the sample surface, the dislocation slip bands do not necessarily emanate from all indentations and the linear density of dislocations in the slip bands can considerably differ even for neighboring indentations. Such an unusual inhomogeneity most clearly manifests itself in the course of mechanical testing at 800°C. As an example, Fig. 2a shows typical patterns of the dislocation propagation from closely spaced indentations upon bending at 800°C. It can be seen that no dislocation slip bands are observed around certain indentations, but, where these bands are formed, the linear density of dislocations in them can differ by almost two orders of magnitude for individual closely located indentations. Figure 2b demonstrates the histogram of the linear density of dislocations in slip bands emanating from equally spaced indentations. As is clearly seen, there is a pronounced periodic inhomogeneity in the distribu-

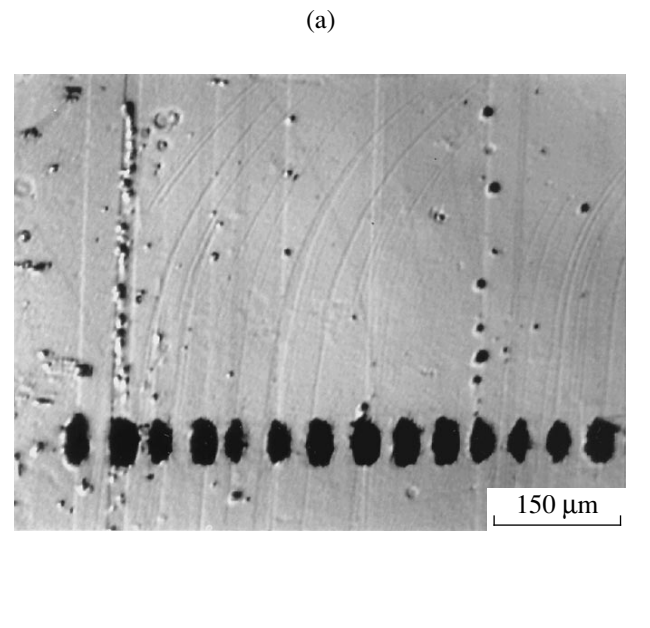

Fig. 2. A spatial inhomogeneity in the generation and propagation of dislocations from indentations: (a) the pattern of the selective etching of samples after their bending and (b) the histogram of the linear dislocation density in slip bands formed around individual indentations.

Fig. 3. A layered inhomogeneity revealed on the surface of wafer *1* by anodic etching.

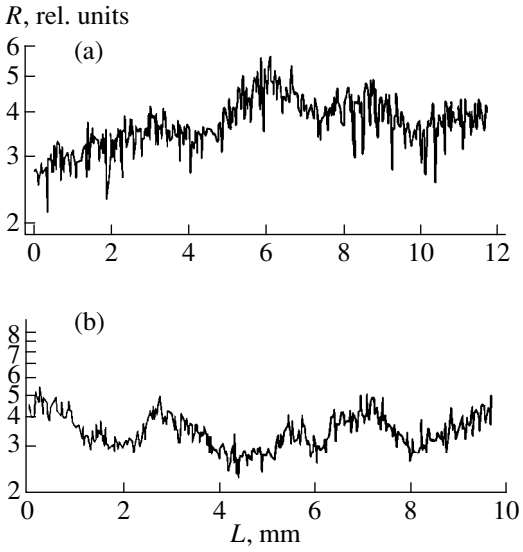

Fig. 4. Distribution of the spreading resistance along the radius of wafer *1* in (a) central and (b) middle regions.

tion of the linear dislocation density in the slip bands formed around individual indentations.

The heat-treated samples were subjected to anodic etching (electrolyte HF : CH_3COOH = 1 : 1; current density, 10 mA/cm^2; etching time, ~5 min [6]) with subsequent treatment in the solution HF : HNO_3 = 1 : 4 for 10–15 s. The anodic etching revealed a characteristic layered inhomogeneity (growth bands) in samples, which, most likely, stems from the inhomogeneous distribution of oxygen in the wafers under investigation. Figure 3 shows a typical pattern of the layered inhomogeneity, which was revealed by anodic etching in the samples heat-treated at 450°C.

The spreading resistance was measured in a wafer heat-treated at 450°C in order to confirm the inference that the layered inhomogeneity reflects the character of the oxygen distribution in the samples studied. As noted above, heat treatment of silicon single crystals at 450°C is accompanied by intensive generation of thermodonors—clusters consisting of several oxygen atoms. The concentration of thermodonors formed in the course of heat treatment at 450°C strongly depends

on the oxygen content in the sample under investigation. The spreading resistance is a unique characteristic of thermodonor concentration (and, correspondingly, the oxygen content).

The results of measurements of the spreading resistance in a silicon wafer after the heat treatment at 450°C are displayed in Fig. 4. These results convincingly indicate a periodic (layered) inhomogeneity in the oxygen distribution in the samples studied. This gives grounds to believe that the spatial inhomogeneity in the generation and propagation of dislocations from indentations in the heat-treated samples is primarily due to an inhomogeneous (layered) distribution of oxygen. During the low-temperature treatment of silicon wafers, the oxygen supersaturated solid solution undergoes decomposition with the formation of oxygen clusters. The volume density of the clusters thus formed is a very sensitive function of the oxygen concentration in the crystal. In the presence of a layered inhomogeneity in the oxygen distribution, the volume concentrations of oxygen clusters formed in adjacent regions upon heat treatment differ considerably. This can induce an elastic stress field modulated by a nonuniform distribution of clusters in which alternating regions experience elastic compressive and tensile deformation. In this case, the oxygen-rich regions with the maximum content of oxygen clusters should undergo compressive deformation and the generation and motion of dislocations in these regions should be hampered. The latter can be explained by the fact that the oxygen clusters, as was shown above, are effective stoppers against the onset of dislocation motion, because they bring about an increase in the starting stresses.

ACKNOWLEDGMENTS

We are grateful to I.M. Yur'eva and A.V. Kartavykh for measurements of the spreading resistance in the samples under investigation.

REFERENCES

1. K. Sumino, in *Proceedings of the 1st International Autumn School on Gettering and Defect Engineering in Semiconductor Technology, Garzau, 1985*, Ed. by H. Richter (Garzau, 1985) p. 41.
2. I. E. Bondarenko, V. G. Eremenko, V. I. Nikitenko, and E. B. Yakimov, Phys. Status Solidi A **60**, 341 (1980).
3. V. V. Voronkov, Semicond. Sci. Technol. **8**, 2037 (1993).
4. R. Falster and V. V. Voronkov, J. Cryst. Growth **194** (1), 76 (1998).
5. Yu. A. Kontsevoĭ, Yu. M. Litvinov, and É. A. Fattakhov, *Plasticity and Strength of Semiconducting Materials and Structures* (Radio i Svyaz', Moscow, 1982).
6. M. G. Mil'vidskiĭ and A. V. Berkova, Zavod. Lab. **27** (5), 557 (1961).

Translated by O. Borovik-Romanova

Physics of the Solid State, Vol. 43, No. 1, 2001, pp. 51–53. Translated from Fizika Tverdogo Tela, Vol. 43, No. 1, 2001, pp. 51–53.

DEFECTS, DISLOCATIONS, AND PHYSICS OF STRENGTH

Gauge-Invariant Self-organization of Strain Field Fluctuations

A. M. Avdeenko and E. I. Kuz'ko

Moscow Institute of Steel and Alloys, Leninskiĭ pr. 4, Moscow, 117936 Russia

Received May 23, 2000

Abstract—The method of laser range scanning profilometry is used to study the evolution of mesoscopic perturbations of strain fields in aluminum, copper, and iron polycrystals during loading. The fractal nature of mesoscopic perturbations of the flow fields with a power-flow increase of the correlation interval $\xi = \xi_0\theta^{-\nu}$ (θ is the dimensionless strain-hardening modulus) during loading is established. The fundamental structural scale ξ_0 and the index ν lie in the intervals ξ_0 = 30–150 μm and ν = 0.27–0.70. The dimensionality of the deformation relief increases in the course of loading from ~1.05–1.25 at the initial stage to ~1.35–1.65 for strains from ~0.30 to 0.35 for all the materials. The results indicate an essentially multilevel nature of plastic deformation and argue for the applicability of renormalization group methods for its description. *© 2001 MAIK "Nauka/Interperiodica".*

The self-organization of mesoscopic perturbations of plastic flow was discussed in several publications [1–3]. A theoretical description based on the renormalization group approach was proposed in [3, 4], and fluctuation-induced corrections for the synthesis of an effective diagram describing the deformation of heterogeneous media were taken into account in [5]. In this respect, complex experimental investigations into the dynamics of mesoscopic perturbations of strain fields during loading of plastic materials with the help of a specially developed technique of laser range scanning profilometry [6] is of special interest.

A light beam is used as the measuring instrument in this case. An optoelectronic detecting system determines the sign of deviation of the height of a specific point on the surface being measured from the focal plane of the objective, and then the point is brought to the focal plane by displacing the sample relative to the optical system. The measuring process is controlled entirely by a PC through an interface operating a specific program.

Since three-dimensional positioning systems normally use step motors, determining coordinates boils down to simply counting the number of steps within a known step. The displacement step along two horizontal directions has a length of 1.667 μm, while the step in the vertical direction (which is the quantity being measured) is 1.25 μm.

We experimentally studied the scaling of the relief of plastic flow during the evolution of instability under uniaxial extension. Planar samples made of annealed low-carbon steel (0.08% C) and of polycrystalline copper and aluminum were preliminarily polished. The tensile stress–strain diagram with a strain rate of 1×10^{-3} s^{-1} at 293 K in the real coordinates S vs. φ (Fig. 1) was approximated by the method of least squares using the expression

$$S = S_0\varphi^n, \quad (1)$$

where S is the stress normalized to Young's modulus E and φ is the strain.

The parameter S_0, the exponent n, and the homogeneous strain φ_{hom} measured away from the neck region after the fracture (i.e., in the region where the sample thickness does not change) are presented in Table 1. Formula (1) is also used to calculate the dimensionless strain-hardening modulus $\theta(\varphi) = dS/d\varphi$.

The inhomogeneity of elastic strain was measured from the surface profile of the deformed sample with the help of a laser range profilometer. The error in the measurement of the relief of a smooth surface can be

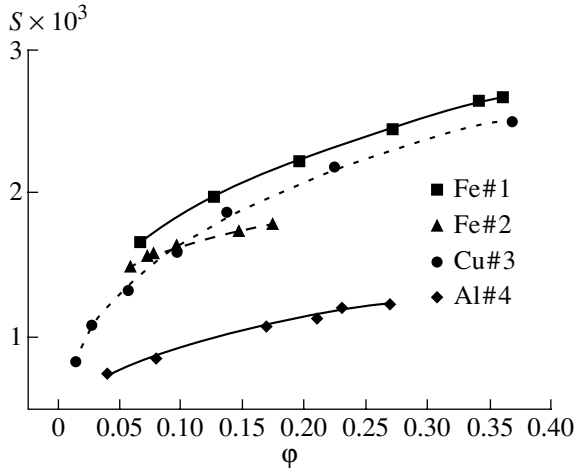

Fig. 1. Stress–strain diagram for the tested samples in real coordinates.

1063-7834/01/4301-0051$21.00

Table 1. Parameters of the stress–strain diagram

Sample	Young's modulus E, GPa	S_0	n	φ_{hom}
Fe#1	205	$(3.58 \pm 0.03) \times 10^{-3}$	0.28 ± 0.01	0.34
Fe#2	205	$(2.34 \pm 0.07) \times 10^{-3}$	0.16 ± 0.02	0.19
Cu#3	128	$(3.53 \pm 0.07) \times 10^{-3}$	0.33 ± 0.01	0.37
Al#4	71	$(1.76 \pm 0.03) \times 10^{-3}$	0.27 ± 0.01	0.29

reduced by using an objective with a shorter focal length; in our case, the error was $\delta = \pm 1.25$ μm. The scanning area was a square mesh with a step l, side $L = (N - 1)l$, and total number of counting points N^2. The same region of the sample was scanned in the initial state and after each of 5 to 8 deformation steps φ_i. Sample fracture occurred after the formation of a macroscopic neck, and control measurements were made after the fracture.

In order to compensate for the deviation from "horizontality" of the sample during the measurements, an experimentally determined relief was used to determine the macroscopic inclination of the area in the form $Z(x, y) = Ax + By + C$ by the least squares method; this value was subsequently subtracted. The parameters of the relief measurements are given in Table 2.

The modulus of the Fourier transform of the two-dimensional profile of the relief

$$C(\mathbf{k}) = (2\pi L)^{-2}\left|\int h(\mathbf{r})\exp^{ikr}d\mathbf{r}\right|, \qquad (2)$$

where $\mathbf{k} = 2\pi\mathbf{n}/L$ and $\mathbf{n} = (n_1, n_2)$ with $-N/2 < (n_1, n_2) \le N/2$, was calculated from the two-dimensional array of relative heights $h(\mathbf{r})$ in the wavelength range from $2l$ to L by using a traditional method.

Since $h(\mathbf{r})$ is a real-valued function and $C(n_1, n_2)$ is symmetric relative to the (0, 0) point, the subsequent spectral analysis was carried out for $0 \le n_1 \le N/2$ and $-N/2 \le n_2 \le N/2$, except for $C(0, 0)$, since this is the average value of the height and carries no information about the relief. Our subsequent calculations were based on an analog for the spectral function of the one-dimensional profile, namely, the power function

$$C^2(|\mathbf{k}|) = (2\pi|\mathbf{k}|)^{-1}\int\limits_{|\nu| = |k|}|C(\mathbf{v})|^2 d\mathbf{v}, \qquad 0 < |\mathbf{k}| \le \pi\sqrt{2}/l = k_{max} \qquad (3)$$

averaged over directions, and the radial correlation interval

$$\xi = \frac{1}{2\pi}\left(\frac{\int|\mathbf{k}|^{-2}C_m^2(|\mathbf{k}|)d|\mathbf{k}|}{\int C_m^2(|\mathbf{k}|)d|\mathbf{k}|}\right)^{1/2}. \qquad (4)$$

An increase in strain is accompanied by a decrease in the dimensionless strain-hardening modulus $\theta(\varphi) = dS/d\varphi$. The radial correlation interval for the relief is connected with this modulus through the relation

$$\xi = \xi_0\theta^{-\nu}. \qquad (5)$$

The linear regression of the dependence $\log\xi(\log\theta)$ led to the values $\nu = 0.27$–0.7 for the samples of Fe#1, Fe#2, Cu, and Al. The peak of the entropy of fluctuations corresponds to $\nu = 0.5$. The fundamental structural scale ξ_0 was $\xi_0 = 30$–80 μm in all cases.

The approximation of the integral (cumulative) spectrum in the logarithmic coordinates

$$Q(\mathbf{k}) = \int\limits_{v \ge k} C^2(\mathbf{v})d\mathbf{v} \sim |\mathbf{k}|^{-p} \qquad (6)$$

makes it possible, according to [7, 8], to calculate the fractal dimensionality of the surface $D = 3 - p/2$, which is a characteristic of the self-similar behavior of plastic flow fluctuations. Such an approximation was carried out by using the least squares method in the interval $[k_1, k_2]$ on which the measured dependence $\log Q(\log|\mathbf{k}|)$ is linear (Fig. 2). The lower boundary corresponds to the wavelength $\lambda_1 = (2\pi k_1)^{-1} = 3$ mm, while the upper boundary corresponds to the wavelength $\lambda_2 = 0.3$ mm. The variation of the spectrum $Q(|\mathbf{k}|)$ and of the fractal dimensionality in the course of deformation is illustrated in Figs. 2 and 3. The sharp decrease in the cumulative spectrum for wavelengths $\lambda < \lambda_2$ is a consequence of the finite sensitivity δ of the profilograph, because the amplitude of short waves is small, $|C(\lambda < \lambda_2)| < \delta$.

Table 2. Parameters of relief measurements

Sample	Mesh size l, μm	Area L^2, mm^2	Total number of points, N^2	Strains φ_i	Height span, h_{max}–h_{min}, μm	
					$\varphi = 0$	φ_{max}
Fe#1	150	89.3	4096	0.06; 0.12; 0.20; 0.26; 0.32	80	105
Fe#2	100	41.0	4225	0.058; 0.071; 0.078; 0.095; 0.147; 0.175	35	67
Cu#3	150	92.2	4225	0.01; 0.03; 0.06; 0.10; 0.14; 0.22; 0.37	42	80
Al#4	75	92.2	16641	0.04; 0.08; 0.17; 0.21; 0.23; 0.27	22	78

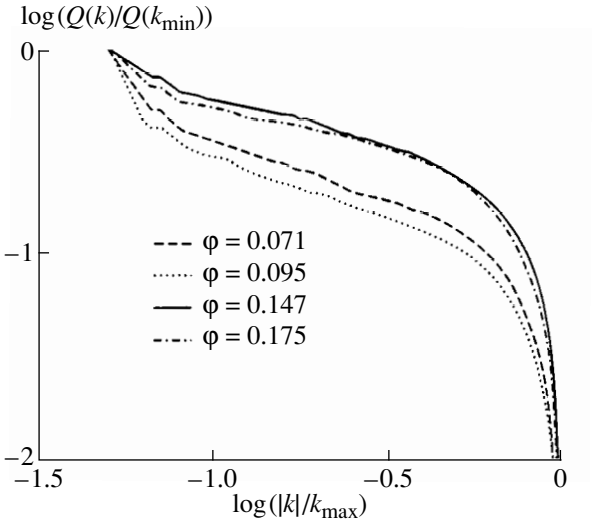

Fig. 2. Cumulative spectrum for the Fe#2 sample for various strains.

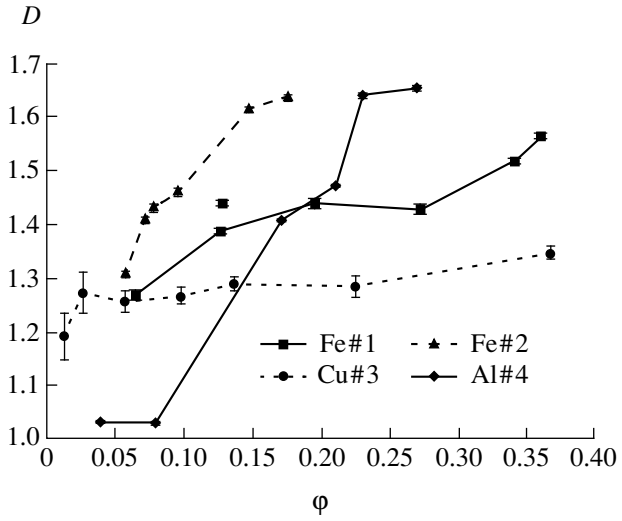

Fig. 3. Dependence of the fractal dimensionality on the real strain.

An increase in the strain in all materials is accompanied by a statistically significant increase in the dimensionality of the relief from ~1.05 (Al), 1.18 (Cu), and 1.25–1.30 (Fe) in the initial state (s = 0.02–0.06) to ~1.65 (Al), ~1.32 (Cu), and ~1.60–1.62 (Fe) in the region of the formation of a macroscopic neck.

Thus, measurements of the surface relief reveal early stages of the evolution of instability in plastic flow. A transition from random inhomogeneities upon an increase in their correlation radius culminates in the formation of a macroscopic neck when the neck radius becomes comparable to half the sample thickness [1]. The deformation relief, and hence mesoscopic perturbations of the flow in a wide interval, are self-similar and have a dimensionality increasing in the course of loading. The results speak in favor of the hypothesis of a multilevel deformation (see, e.g., [9]) wherein a nonuniform rotation of the scale level $(n - 1)$ generates flow distortion of the nth level, which in turn determines the nonuniform rotation of the $(n + 1)$th level, and so on [1–3].

The obtained results indicate that renormalization group methods can be used for describing the self-organization of mesoscopically induced deformation [4, 6]. The current scale of the deforming process, viz., the fluctuation correlation interval for flow fields, can be parametrized during loading by the strain-hardening modulus θ (for a known $\sigma(s)$–average-strain-s diagram) and can therefore be used as a universal variable in the construction of a system of equations relating the running dynamic parameters of the system (e.g., correlation functions of various orders for mesoscopic perturbations of the flow) to the process of loading.

REFERENCES

1. A. M. Avdeenko, Metallofizika **12** (1), 7 (1990).
2. V. E. Panin, E. E. Deryugin, L. S. Derevyagin, *et al.*, Fiz. Met. Metalloved. **84** (1), 35 (1997).
3. V. E. Panin, P. V. Kuznetsov, E. E. Deryugin, *et al.*, Fiz. Met. Metalloved. **84** (2), 138 (1997).
4. E. I. Kuz'ko, A. V. Kudrya, and S. V. Starikov, Zavod. Lab. **58** (9), 63 (1992).
5. A. M. Avdeenko, Izv. Akad. Nauk SSSR, Met., No. 1, 64 (1991).
6. A. M. Avdeenko and Yu. A. Krupin, Mekh. Kompoz. Mater. Konstr., No. 4, 134 (1999).
7. A. M. Avdeenko, E. I. Kuz'ko, and M. A. Shtremel', Fiz. Tverd. Tela (St. Petersburg) **36** (10), 3158 (1994) [Phys. Solid State **36**, 1677 (1994)].
8. B. B. Mandelbrot, D. E. Passoja, and A. J. Paullay, Nature **308**, 721 (1984).
9. V. A. Likhachev and V.G. Malinin, *Structural-Analytical Theory of Strength* (Nauka, St. Petersburg, 1993).

Translated by N. Wadhwa

Physics of the Solid State, Vol. 43, No. 1, 2001, pp. 54–60. Translated from Fizika Tverdogo Tela, Vol. 43, No. 1, 2001, pp. 54–60.

MAGNETISM AND FERROELECTRICITY

Localized Ferrons and the Mott Transition via the Ferromagnetic Phase in Doped Antiferromagnetic Semiconductors

É. L. Nagaev

Vereshchagin Institute of High-Pressure Physics, Russian Academy of Sciences, Troitsk, Moscow oblast, 142092 Russia

Received March 28, 2000

Abstract—The states of single- and double-charge donors in an antiferromagnetic crystal are investigated taking into account the formation of magnetized regions (localized ferrons) around them. Double-charge donors should be in a state of the $(1s)(2s)$ type, which is energetically favored over the $(1s)^2$ state. In doped antiferromagnetic semiconductors, the usual Mott transition is impossible because the single-charge donors in them are ferrons. Instead, the donor electrons are delocalized through the transition of the crystal to the single-electron state. It is unlikely that a ferromagnetic–antiferromagnetic (FM–AFM) mixed state will occur in this case. In the case of double-charge donors, transition to an FM–AFM mixed state should occur. © *2001 MAIK "Nauka/Interperiodica".*

INTRODUCTION

In this paper, we investigate antiferromagnetic (AFM) semiconductors moderately doped with donors or acceptors. It is well known that in nonmagnetic semiconductors, the Mott delocalization of electrons (or holes) occurs and the crystal passes from the insulating state to a highly conducting state as the concentration of donors (acceptors) increases. It will be shown in this paper that the usual Mott delocalization does not occur in AFM semiconductors if the *s–d* exchange is fairly strong. In this case, when the donor concentration n becomes equal to a certain critical value, the crystal passes from the state in which there is no ionized donors to a ferromagnetic (FM) state with delocalized electrons or to an AFM–FM mixed state in which all delocalized electrons are within the FM region of the crystal. The former alternative is most likely to occur in the case of single-charge donors, while the latter occurs in the case of double-charge donors. It is unlikely that a mixed AFM–FM state will arise in the case where the single donors are fixed in their positions.

The reason for this unusual behavior is that each single-charge donor is in fact a localized ferron (magnetic polaron) and, hence, there is an FM microregion around each donor. (The concept of a ferron was first introduced in [1, 2].) This region acts on the donor electron as a potential well, which is added to the Coulomb potential. For this reason, the radius of the electron orbit becomes much smaller than the effective Bohr radius corresponding to the Coulomb potential alone. This prevents the donor electrons from being delocalized, and the crystal remains in the AFM state. In the FM state, by contrast, the electron orbit radius equals the Bohr radius, which is favorable to electron delocalization. Therefore, the concentration phase transition can occur from the insulating AFM state with localized electrons to a highly conducting FM state with delocalized electrons. This transition can be thought of as going via a virtual insulating FM state.

The behavior of double donors, e.g., Se vacancies in EuSe (as well as acceptors, e.g., excess oxygen in $LaMnO_{3+y}$), is essentially different. If the AFM ordering in a crystal were not perturbed, such a donor in it would be in the $(1s)^2$ state with antiparallel electron spins and the total exchange energy between these spins and magnetic atoms would be close to zero. However, if the donor transfers to the $(1s)(2s)$ state with parallel spins and an FM region arises in the vicinity of it, this state will be energetically favored over the nonmagnetic $(1s)^2$ state, because the exchange energy between the donor electrons and magnetic atoms will be large in magnitude. Such localized ferrons have not yet been considered in the literature; their theory is, thus, first presented here.

Since the ionization energy of the $2s$ electrons is small, their delocalization can occur via the mixed FM–AFM state first considered in [2, 3]. Two scenarios are possible. In the first, FM droplets containing several electrons are formed in the AFM matrix when the donor concentration is close to the critical value for phase transition. This partial delocalization, where electrons are locked in a droplet, occurs instead of the complete Mott delocalization, and the state of the crystal as a whole is insulating. Further increase in the donor concentration causes the FM droplets to increase in size, and, at a certain concentration, they come in contact with one another, which means that percolation for FM ordering and for the electron liquid occurs. When the donor concentration is higher than its threshold value for percolation, the bulk of the crystal will be in an FM and highly conducting state and only AFM droplets will remain in the crystal. Therefore, the Mott transition

1063-7834/01/4301-0054$21.00

comes to an end and the delocalized electrons cause the crystal as a whole to be highly conducting only above this percolation threshold.

In the other possible scenario, the crystal immediately undergoes a crossover from the state with localized donor electrons to a highly conducting FM–AFM state. In general, the transition to a mixed FM–AFM state can also occur in the case of single donors and the transition to a FM state can take place in the case of double donors. However, these transitions are unlikely to occur for realistic values of the parameters. It is interesting to note that both the insulating and highly conducting FM–AFM states have been observed in EuSe with double donors [4].

1. IMPOSSIBILITY OF THE CONVENTIONAL MOTT TRANSITION IN ANTIFERROMAGNETS

First, we prove that the Mott transition is impossible in AFM semiconductors if the *s–d* exchange is not very weak. For this purpose, the well-known Mott calculation is generalized to the case of electrons strongly interacting with another subsystem (magnetic in the case under study). As is usually done, we consider the conditions for the existence of a discrete energy level in the potential well produced by the donor Coulomb potential screened by conduction electrons. The AFM ordering is caused by the direct *d–d* exchange between magnetic atoms, which models the superexchange between them. This interaction involves conduction electrons and thereby competes with the indirect exchange that favors the FM ordering. There is a critical donor concentration below which the AFM ordering is relatively stable [2]. For the sake of simplicity, the indirect exchange via charge carriers is assumed to be weak when compared to the direct *d–d* exchange. We show that the indirect exchange does nothing but enhance the effect under study.

The corresponding calculation is conducted including the local magnetization produced by an electron that occupies a discrete level and has its spin unpaired. For the sake of definiteness, the AFM ordering is assumed to be in staggered rows. The *s–d* model is used. The Hamiltonian of the system in the coordinate representation is given by

$$\begin{aligned} H &= H_s(\mathbf{r}) + H_{sd}(\mathbf{r}) + H_{dd}, \\ H_{sd} &= -\frac{\Delta}{2m} - \frac{e^2}{\varepsilon r}\exp\left(\frac{r}{r_s}\right), \\ H_{sd} &= -A\sum_g (\mathbf{S_g s}) D(\mathbf{r}-\mathbf{g}), \\ H_{dd} &= -\frac{1}{2}\sum_{\mathbf{g},\,\Delta} (\mathbf{S_g S_{g+\Delta}}), \end{aligned} \tag{1}$$

where $\mathbf{S_g}$ is the *d* spin of atom **g**, **s** is the spin of a conduction electron, $D(\mathbf{r} - \mathbf{g})$ equals unity within the unit cell **g** and zero outside it, **Δ** is the vector connecting two nearest neighbors, *m* is the effective electron mass, ε is the permittivity, and $\hbar = 1$. The screening radius r_s can be written as

$$r_s = \sqrt{\frac{\varepsilon\mu}{6\pi e^2 n}} \cong \frac{1}{2}\sqrt{a_B n^{-1/3}}, \tag{2}$$

$$a_B = \frac{\varepsilon}{me^2}, \tag{3}$$

$$\mu = \frac{(3\pi^2 n)^{2/3}}{2m}. \tag{4}$$

(In the case of double exchange, the band width for a "dressed" electron due to the *s–d* exchange interaction is $(2S + 1)^{1/2}$ times smaller and its effective mass is $(2S + 1)^{1/2}$ larger than the respective values for a "bare" electron [5].)

We use a variational procedure in which the variational parameters are the angles $\theta_\mathbf{g}$ between the spin of atom **g** and the local magnetization induced in the AFM crystal by the localized electron and the parameter *x* that defines the orbital radius of a localized electron a_B/x. The latter parameter is involved in the trial electron wave function

$$\psi(\mathbf{r}) = \left(\frac{x^3}{\pi a_B^3}\right)^{1/2} \exp\left(-\frac{xr}{a_B}\right). \tag{5}$$

We consider the limiting case of $AS/W \ll 1$ and the opposite limit (double exchange), where *S* is the *d*-spin magnitude and *W* is the conduction band width for a bare *s* electron. Assuming that the angles $\theta_\mathbf{g}$ vary smoothly, one can write

$$\begin{aligned} E &= \left[x^2 - \frac{8x^3}{(p+2x)^2}\right] \\ &- ua^3\sum_\mathbf{g} \psi(\mathbf{g})^2 \cos\theta_\mathbf{g} + \frac{\nu}{2}\sum_\mathbf{g} \cos 2\theta_\mathbf{g}, \end{aligned} \tag{6}$$

where *a* is the lattice parameter, the energy is measured in units of

$$E_B = \frac{e^2}{2\varepsilon a_B},$$

and the following notation is also used:

$$u = \frac{U}{E_B}, \quad \nu = \frac{z|I|S^2}{E_B}, \quad p = \frac{a_B}{r_s},$$

$$U = \frac{AS}{2} \quad (AS \ll W),$$

$$U = \frac{W}{2}\left(1 - \frac{1}{\sqrt{2S+1}}\right) \quad (AS \gg W).$$

In deriving Eq. (6), the FM ordering is assumed to be unsaturated in the region of the electron localization. Strictly speaking, the expression for U presented above is an approximation in the double-exchange limit (it is exact only in the case of large spins [2]). Minimizing the energy in Eq. (6) with respect to $\theta_{\mathbf{g}}$, we find that the value of $\theta_{\mathbf{g}}$ corresponding to an energy minimum is given by

$$\cos\theta_{\mathbf{g}} = \frac{ua^3\psi^2(\mathbf{g})}{2\nu}. \tag{7}$$

Using this expression, one can find the energy as a function of the single parameter x (in units of E_B):

$$E = \left[x^2 - \frac{8x^3}{(p+2x)^2}\right] - kx^3,$$
$$k = \left[\frac{u^2}{32\pi\nu b^2}\right], \quad b = \frac{a_B}{a}. \tag{8}$$

A discrete level appears when $E(x) = 0$ and $dE(x)/dx = 0$, which, in combination with Eq. (7), reduces to

$$x(1-kx)^3 = 0. \tag{9}$$

Solving Eq. (9) yields the critical value of parameter x for the appearance of a discrete level and, hence, the critical concentration (involved in the expression for the screening radius):

$$p = \frac{a_B}{r_s} = \sqrt{\frac{8x}{1-kx}} - 2x. \tag{10}$$

As follows from Eqs. (5), (7), and (8), this approach is adequate if

$$\frac{16x^3k}{u} < 1. \tag{11}$$

For inequality (11) to be fulfilled, the coupling between electrons and the magnetic subsystem should not be strong because $k \propto u^2$. On the other hand, Eq. (11) gives the upper limit for the values of x for which Eq. (9) is valid (formally, the absolute minimum of the energy E is attained as $x \longrightarrow \infty$, but this is an artifact).

Equation (9) has two positive roots up to $k_c = 0.210937$ (the other two roots are imaginary and, hence, physically meaningless). However, the largest of the positive roots, x_g, corresponds to negative values of p in Eq. (10) for $k < 0.12$. Clearly, negative p and the corresponding values of x have no physical meaning. Furthermore, the larger root is also physically meaningless for $p > 0$, because the value of p corresponding to it is smaller than that corresponding to the other positive root x_l (e.g., for $k = 0.13$, we have $x_g = 1.083$, $x_l = 0.652$, $p_g = 0.151$, and $p_l = 1.083$). Indeed, according to Eq. (4), p is proportional to $n^{1/6}$. Since we are considering the metal–insulator transition, which occurs as the concentration n decreases, only the transition corresponding to the larger value of n has physical meaning.

As for the smaller root, the value of p corresponding to it increases with k and, at $k_c = 0.21$, the constant $C = (p/2)^2$ in Mott's expression $n^{1/3}a_B = C$ is as large as 0.348 instead of the value 0.25 obtained by Mott (the corresponding x is 1.185). Therefore, as the s–d exchange energy AS increases, the Mott value of the concentration increases; that is, the AFM ordering hinders the metallization of the system.

At $k = k_c$, the two positive roots become equal and, as x increases still further, all the four roots of Eq. (9) become imaginary. This means that the potential well has no discrete level near the bottom of the conduction band and Mott's scenario for the insulator–metal transition is impossible. In order to understand the physics of this phenomenon, let us consider the insulating state of the system. In this state, the nonionized donors are localized ferrons; that is, the electron of each donor produces the FM order in the vicinity of the donor. The stronger the s–d exchange, the lower the energy of a localized ferron. If $u \gg 1 \gg \nu$, this energy is close to $(-u)$ irrespective of the screening radius, because the s–d exchange is not screened by free carriers. Therefore, the discrete level exists for any concentration of carriers and, if u is large enough, the metal–insulator transition is impossible.

This is especially true where the coupling between the electrons and the magnetic subsystem is so strong that inequality (11) is not valid. Therefore, this inequality is not a necessary condition for the Mott transition to not occur in AFM semiconductors. This is supported by a direct calculation based on Eq. (14), in which the first parenthetical term is replaced by the term in square brackets in Eq. (8).

Now, let us return to the problem of indirect exchange. Its rigorous consideration is made difficult by the fact that at $AS \ll W$, the RKKY exchange is long-range, in contrast to the d–d exchange. In the case of $AS \gg W$, only the ground state of an AFM system has been investigated [2]. However, for qualitative treatment, it will suffice to note that the indirect exchange is opposite in sign to the d–d exchange and, hence, it decreases the effective value of the parameter ν, thereby increasing the parameter k in Eq. (8). For this reason, Mott's scenario for the insulator–metal transition becomes impossible for an s–d coupling weaker than that in the case where there is no indirect exchange.

2. SINGLE-ELECTRON FERRONS

Even when the Mott transition is impossible in an AFM semiconductor, some other cooperative phenomena can occur in the system of donors (or acceptors) with increasing donor concentration. In order to investigate them, we first consider the state of an individual single-electron donor (localized ferron). Earlier, this problem was investigated only in the case of $AS \ll E_B$ and of very small $D = |zIS^2|$ [1] and it was assumed that a region of the saturated FM ordering occurs around the donor atom. More realistic is the case where only a partially magnetized noncollinear-AFM region arises and there is, perhaps, a saturated FM core in it. This model is investigated in what follows.

First we consider the case of a region with nonsaturated magnetization and with no FM core in it, where we can use Eq. (8). Putting $p = 0$ (no screening) and minimizing the energy in Eq. (8) with respect to x, we obtain for the optimal value of x the expression

$$x = \frac{1}{3k}(1 - \sqrt{1 - 6k}). \qquad (12)$$

It follows from Eq. (12) that the ferron with a noncollinear AFM ordering is stable only for $k \le 1/6$. At $k = 1/6$, the energy in Eq. (8) equals (–4/3), which is much lower than in the case where the magnetic moments of the sublattices are not canted.

Now, we consider the case where there is a region of saturated FM ordering. Taking again a trial function in the form of Eq. (5), the radius R of this region can be determined from Eq. (7) by putting $\cos\theta_R = 1$. The result is

$$r = \frac{R}{a_B} = \frac{1}{2x}\ln\left(\frac{2ux^3}{c}\right), \quad c = 4\pi\nu b. \qquad (13)$$

Using Eqs. (1), (5), and (13), the energy of the system can be found to be

$$E = (x^2 - 2x) + \frac{cr^3}{3} + \frac{c}{4x^3}\left(3r^2x^2 + \frac{7rx}{2} + \frac{15}{8}\right) - u. \qquad (14)$$

With Eqs. (5) and (7), we calculate the total moment of the localized ferron:

$$M = 4\pi S\left(\frac{r^3b^3}{3} + \frac{r^2}{2x} + \frac{r}{2x^2} + \frac{1}{4x^3}\right). \qquad (15)$$

Minimization of the energy in Eq. (14) with respect to x can be performed numerically.

In order to get insight into the properties of the localized ferron, we present some results of the numerical minimization. If $u = 5$ and $b = 1$, then E and M/S are found to be, respectively, –3.81 and 12.453 for $\nu = 0.1$, –5.164 and 52.748 for $\nu = 0.01$, and –5.748 and 181.483 for $\nu = 0.001$. For the same value of u and $b = 2$, the quantities E and M/S are, respectively, –1.837 and 6.23 for $\nu = 0.1$, –3.983 and 58.709 for $\nu = 0.01$, and –5.248 and 298.543 for $\nu = 0.001$. It is seen that the ferron moment M is gigantic even for a sufficiently large ν. For small values of ν, the moment increases with the Bohr orbit radius b (for a fixed value of a), but the situation is reversed for large ν. This is because a large localized ferron with $b = 2$ is more similar to a free ferron (first considered in [1]), which can exist only when the d–d exchange is sufficiently weak.

3. LOCALIZED DOUBLE-ELECTRON FERRONS

Now, we investigate localized double-electron ferrons, corresponding, for example, to Se vacancies or excess Se atoms in EuSe, which are donors and acceptors, respectively, with a charge of $2e$. The Hamiltonian of the system is

$$H = H_s(\mathbf{r}_1) + H_{sd}(\mathbf{r}_1) + H_s(\mathbf{r}_1)$$

$$+ H_{sd}(\mathbf{r}_1) + \frac{e^2}{\varepsilon|\mathbf{r}_1 - \mathbf{r}_2|} + H_{dd}, \qquad (16)$$

$$H_s = -\frac{\Delta}{2m} - \frac{2e^2}{\varepsilon r},$$

where H_{sd} and H_{dd} are given by Eq. (1). If the s–d exchange is weak, the system is analogous to the He atom: its electronic configuration corresponds to the $(1s)^2$ state when the spins of the electrons are antiparallel and the electrons do not induce local magnetization. In this case, the donor energy is equal to $E_{11} = -5.695$ (in units of E_B) [6]. However, when the s–d exchange is fairly strong, the $(1s)(2s)$ state with parallel electron spins is energetically favorable. For a crystal with FM ordering and favorable orientation of the electron spins, the corresponding energy is $E_{12} = -4.29 - 2u$ (the factor 2 in the last term occurs because there is a gain in the s–d-exchange energy for both electrons). Therefore, for $u > 0.7$, the $(1s)(2s)$ state is energetically favored over the $(1s)^2$ state. In a crystal with AFM ordering, the $(1s)(2s)$ state is energetically favorable if there is an FM order in the vicinity of the donor, which requires a certain expense of the d–d-exchange energy. Therefore, the donor energy in this state is higher than that in an FM crystal.

In order to calculate this energy, we again make use of the variational procedure. The orbital part of the trial

double-electron function is taken to be

$$\psi(\mathbf{r}_1, \mathbf{r}_2) = \frac{1}{\sqrt{2}}[\psi_{1s}(\mathbf{r}_1)\psi_{2s}(\mathbf{r}_2) - \psi_{1s}(\mathbf{r}_2)\psi_{2s}(\mathbf{r}_1)], \quad (17)$$

$$\psi_{1s} = \left(\frac{8}{\pi}\right)^{1/2}\exp(-2r), \quad (18)$$

$$\psi_{2s}(r) = K(1-yr)\exp(-xr),$$

$$y = \frac{2+x}{3}, \quad K^2 = \frac{3x^5}{\pi(x^2-2x+4)}, \quad (19)$$

where r is measured in units of a_B. The function ψ_{2s} is orthogonal to ψ_{1s}. The magnetic ordering is completely FM for $r < R$ and noncollinear AFM for $r > R$. It is assumed that the radius of the 1*s* state (equal to 1/2) is much smaller than the radius of the completely FM region R. For this reason, ψ_{1s} is taken in the form corresponding to the FM ordering and involves no variational parameter. However, the function ψ_{2s} depends on the radius of the FM region through the variational parameter x.

With Eqs. (16)–(19), the ferron energy can be found to be

$$E = E_{1s}^t + E_{2s}^k + E_{2s}^C + E_{2s}^F + E_{dd}^F + E_{2s}^{\mathrm{CAF}}, \quad (20)$$

where $E_{1s}^t = -4 - u$ is the total energy of the 1*s* electron; E_{2s}^k is the kinetic energy of the 2*s* electron,

$$E_{2s}^k = \frac{x^2(7x^2-2x+4)}{3(x^2-2x+4)}; \quad (21)$$

E_{2s}^C is the Coulomb interaction energy of the 2*s* electron with the ionized donor and with the 1*s* electron,

$$E_{2s}^C = -\frac{x(3x^2-4x+4)}{x^2-2x+4} - \frac{x^5(10+3x)}{(x^2-2x+4)(x^3+6x^2+12x+8)}; \quad (22)$$

E_{2s}^F is the energy of the 2*s* electron within the FM region and E_{dd}^F is the energy for the formation of this region,

$$E_{2s}^F = -4\pi K^2 u\int_0^R r^2(1-yr)^2\exp(-2xr)dr, \quad (23)$$

$$E_{dd}^F = \frac{4\pi R^3 b^3 \nu}{3}; \quad (24)$$

and E_{2s}^{CAF} consists of the 2*s*-electron energy and the *d*–*d*-exchange energy in the noncollinear (canted) AFM phase, which are calculated by minimizing the energy with respect to the angles of the *d* spins in the same way as in the case of Eqs. (6)–(8). The result is

$$E_{2s}^{\mathrm{CAF}} = -\frac{\pi u^2 K^4}{\nu b^3}\int_R^\infty r^2(1-yr)^4\exp(-4xr). \quad (25)$$

Although the integrals in Eqs. (23) and (25) are easily calculated analytically, the final expressions are too cumbersome to be written out here.

The radius of the FM region is determined from an equation that includes the effective field exerted on the *d* spins by the 1*s* electron:

$$R = \frac{1}{2x}\ln\left\{\frac{K^2(1-yR)^2 u}{2\nu b^3[1-4u\exp(-4R)/(\pi\nu b)^3]}\right\}. \quad (26)$$

When calculating numerically, we first find the radius R as a function of x from Eq. (26) and then minimize the energy in Eqs. (20)–(25) with respect to x. For example, for $u = 5$, $\nu = 0.02$, and $b = 1$, we thus obtain $R(x) \cong 1.75 - 0.3x$ and the optimal energy –10.908 for $x = 1.52$ and $R = 1.254$. In the case of the FM ordering, the energy is significantly lower. Using the expression for the energy of the He atom in the (1*s*)(2*s*) state presented in [6], the energy of the (1*s*)(2*s*) state is found to be –14.35. Thus, the energy of the double-electron donor in an FM crystal is lower by $3.442E_B$ than that in an AFM crystal.

4. THE ENERGY OF THE FERROMAGNETIC METAL OF IMPURITIES

For further investigation of donor-electron delocalization, we compare the energies of individual nonionized donors and of the FM metal composed of ionized donors. In general, the energy of the FM–AFM mixed state may be lower than the energy of the pure FM state for some donor concentrations. In both cases, one should calculate the energy of the FM metal of the impurities. To do this, one has to go beyond the jelly model and to calculate the energy of this FM–AFM state by treating the ionized donors as an array of point charges.

First we derive an expression for the energy of the metal of donors in an FM crystal with completely spin-polarized conduction electrons. According to [6], the energy per electron is given by the expression

$$E_{dm} = E_0 + \frac{3(6\pi^2 n)^{2/3}}{10m} + E_{\mathrm{ex}}(n), \quad (27)$$

where E_0 is the bottom of the conduction band and E_{ex} is the exchange energy between the conduction electrons. For completely spin-polarized electrons, this energy can readily be obtained by generalizing the cor-

responding Bloch expression for a completely depolarized electron gas (presented, e.g., in [6]) and has the form

$$E_{\rm ex}(n) = -\frac{3}{4}\left(\frac{6n}{\pi}\right)^{1/3}. \quad (28)$$

For calculating the energy E_0, we use the Wigner–Seitz procedure (see, e.g., [7]). Namely, a sphere of radius

$$L = \left(\frac{3}{4\pi n}\right)^{1/3}$$

is constructed around each ionized donor and it is assumed that within this Wigner–Seitz sphere the electron wave function ϕ with $k = 0$ satisfies the equation

$$\left(-\frac{\Delta}{2m} - \frac{e^2}{\varepsilon r} - E_0\right)\phi(r) = 0 \quad (29)$$

with boundary condition

$$\frac{d\phi}{dr}(L) = 0. \quad (30)$$

According to the theory of cohesive forces in metals, the wave function ϕ is roughly constant under the boundary condition given by Eq. (30). The problem is solved by a variational method. Within the cell, the trial wave function is taken to be

$$\phi(r) = K\left[1 + y\left(\frac{r^2}{2L^2} - \frac{r}{L}\right)\right], \quad (31)$$

where K is the normalization factor and y is a variational parameter. Calculations show that the energy differs from that corresponding to the function ϕ = const by less than 1% for the relative donor concentration ranging from 0.001 to 0.01. Therefore, we have

$$E_{\rm ex} = -3\left(\frac{4\pi n}{3}\right)^{1/3} E_B. \quad (32)$$

Equations (27), (28), and (32) can be generalized to the case of an FM–AFM state where the number of electrons n_e in the FM part of the crystal does not exceed the number of electrons n_d. Without the Coulomb energy, according to Eqs. (28) and (32), the energy in Eq. (27) takes the following form in this case (in units of E_B):

$$E_{\rm coh} = \frac{3}{5}(6\pi^2\zeta_e)^{2/3}b^2 - (36\pi\zeta_d)^{1/3}b - \frac{3}{2}\left(\frac{6\zeta_e}{\pi}\right)^{1/3} b, \quad (33)$$

where $\zeta_e = n_e a^3$, $\zeta_d = n_d a^3$, $b = a_B/a$, and a is the lattice parameter.

5. THE ENERGY OF THE FM–AFM STATE

The existence of the FM–AFM state was first indicated and investigated in [3], where the jelly model was employed, which allows one to determine the geometry of the mixed FM–AFM state. However, this model overestimates the energy. In this paper, we consider this state more accurately on the basis of the results obtained in the preceding section. First we discuss the case of single donors.

As in [2, 3], the variational method is used. As a variational parameter, we take the ratio $x = V_A/V_F$ between the volumes of the AFM and FM phases in the crystal. If the AFM phase is dominant ($x < 1$), the FM phase consists of geometrically identical droplets. In addition to Eq. (33), we also take into account the *s–d*-exchange energy, Coulomb energy, and electronic surface energy in the same way as in [2, 3] and find the total energy of the mixed FM–AFM state to be

$$E_{m1} = \frac{3[6\pi^2\zeta(1+x)]^{2/3}b^2}{5} + \frac{9\beta}{16}\left(\frac{\pi}{6}\right)^{1/3}(6\pi^2)^{2/3} \times \frac{[\zeta(1+x)]^{1/3}b^2}{R} + \frac{4\pi\zeta b R^2 f}{5} + \frac{\nu}{(1+x)\zeta} - \frac{4.836\zeta^{1/3}b}{1+x} - \frac{1.477\zeta^{1/3}b}{(1+x)^{2/3}} - u, \quad (34)$$

$$R(x) = \left[\frac{45\beta[6\pi^2(1+x)]^{1/3}b}{128 f\zeta^{2/3}}\right],$$

where $\beta = 1$ for $x > 1$ and $\beta = x$ for $x < 1$:

$$f(x) = 2x + 3 - 3(1+x)^{2/3}, \quad (x > 1),$$
$$f(x) = 2 + 3x - 3x^{1/3}(1+x)^{2/3}, \quad (x < 1).$$

Here, we have used the same notation as in Eq. (6) and the fact that the FM phase makes up the $1/(1 + x)$ volume fraction of the crystal. In other words, the relative donor concentration in the FM phase ζ_e is $(1 + x)$ times higher than the average concentration $\zeta = na^3$.

Minimizing the total energy in Eq. (34) with respect to x, one finds the optimal energy and the conditions for the existence of the mixed FM–AFM state. The equality of the optimized energy in Eq. (34) to the energy of an individual localized ferron in Eq. (14) or in Eq. (20) can be considered as the condition for the transition from the insulating state to a partially or totally highly conducting state. The partially highly conducting state is a state with $x > 1$, in which the crystal consists predominantly of the insulating AFM phase, with highly conducting FM droplets embedded in it. Since the electrons are locked in these droplets, the crystal as a whole is an insulator, even though there are local highly conducting regions in it. The totally highly conducting state corresponds either to a mixed FM–AFM state with $x < 1$, in which the bulk of the crystal is highly conducting, or to the totally FM state.

Now, we present some numerical results for single-electron donors. Calculations show that, for realistic values of the parameters ($U \propto 0.1$–0.5, $E_B \propto 0.05$–0.1 eV, $z|I|S^2 \propto 0.0001$–0.1 eV), only transitions to the FM

state are possible. For example, at $u = 5$ and $b = 1$, the energies of the localized ferrons and the metal become equal in the totally FM state for ν in the range from 0.001 to 0.1. When $\nu = 0.001$, the crystal becomes FM for $\zeta_F = 0.0012$ ($E_{m1} = -4.735$) and the energies are equal for $\zeta_T = 0.007$ ($E_{m1} = -5.731$), which corresponds to $n_T^{1/3} a_B = 0.199$. If $\nu = 0.01$, the crystal becomes FM for $\zeta_F = 0.006$ ($E_{m1} = -4.179$) and the energies are equal for $\zeta_T = 0.013$ ($E_{m1} = -5.211$), which corresponds to $n_T^{1/3} a_B = 0.229$. At $\nu = 0.1$, the crystal becomes FM when $\zeta_F = 0.03$ ($E_{m1} = -2.748$) and the energies are equal for $\zeta_T = 0.045$ ($E_{m1} = -3.87$), which corresponds to $n_T^{1/3} a_B = 0.359$.

It should be noted that, if the number of nonionized donors is fairly large, the crystal cannot be considered antiferromagnetic, because the bulk of the crystal exhibits a short-range FM order (in the regions around the donors). The transition to the FM state implies the change over from the short-range FM to the long-range FM order. In weak magnetic fields causing the local magnetic moments of all nonionized donors to be parallel to one another, the transition to the highly conducting state is accompanied by a sharp increase in the magnetization of the crystal. For example, the magnetization is doubled for $\nu = 0.1$ and is half as large for $\nu = 10.01$.

In general, there exist such values of the parameters for which, according to the criterion used in this paper, the system immediately passes to the mixed FM–AFM state (e.g., for $u = 15$, $b = 3.5$ and $\nu = 0.01$ and for $u = 20$, $b = 1$ and $\nu = 1$). In the latter case, the transition occurs to the state with $x = 0$ and $\zeta_T = 0.13$. However, these parameter values are not typical of the systems with single-electron donors.

Now, we consider the mixed FM–AFM state of a crystal with double donors. Only 2*s* electrons are assumed to be delocalized, because their orbital radius is far larger than that of the 1*s* orbital. In the AFM phase, the ionized donors of the He^+ type create FM regions in their neighborhood, which are surrounded by the canted AFM phase. Using 1*s* wave functions in the form of Eq. (5) and Hamiltonian (1), one can find the energy E_{1s}:

$$E_{1s} = 2\left(\frac{x^2}{2} - 2x\right) + \frac{cr^3}{3} + \frac{c}{4x^3}\left(3r^2x^2 + \frac{7rx}{2} + \frac{15}{8}\right) - u, \quad (35)$$

where the radius r of the FM region is given by Eq. (13) and the ferron moment is given by Eq. (15). For $u = 5$ and $b = 1$, we obtain from Eq. (35) $E_{1s} = -8.46$, $x = 2.193$, and $M/S = 18.46$.

The energy E_{1s} is higher than the energy of the ionized donor in the FM phase (equal to –9) by a value of $L = 0.54$. This can easily be taken into account by adding the term $L(1 + x)$ to the energy of the FM–AFM state in Eq. (34). As a result, we find that the energies of the localized ferrons and of the FM–AFM state become equal when the relative carrier concentration is $\zeta = 0.0045$. The corresponding value of x is 2.12, which corresponds to the FM–AFM state with FM droplets within the AFM matrix. At the critical concentration for the transition, each droplet contains five electrons, which justifies the multielectron approach employed in this paper. The conditions for the validity of this approach are even better fulfilled for the percolation concentration equal to 0.006, where each droplet contains eleven electrons.

There are sets of parameters for which the transition immediately occurs to the highly conducting mixed state or even to the FM state. However, in this case, the parameter values are not typical of the systems at hand. Therefore, for typical parameter values, the insulator–metal transition occurs to the FM state in the system of single-electron donors and to the mixed FM–AFM state in the system of double-electron donors.

ACKNOWLEDGMENTS

This work was supported in part by the Russian Foundation for Basic Research, grant no. 98-02-16148, NATO, grant no. HTECHLG972942, and INTAS, grant no. 97-open-30253.

REFERENCES

1. É. L. Nagaev, Pis'ma Zh. Éksp. Teor. Fiz. **6**, 484 (1967) [JETP Lett. **6**, 18 (1967)]; Zh. Éksp. Teor. Fiz. **54**, 228 (1968) [Sov. Phys. JETP **27**, 122 (1968)].
2. É. L. Nagaev, *Physics of Magnetic Semiconductors* (Nauka, Moscow, 1979).
3. É. L. Nagaev, Pis'ma Zh. Éksp. Teor. Fiz. **16**, 558 (1972) [JETP Lett. **16**, 394 (1972)]; V. A. Kashin and É. L. Nagaev, Zh. Éksp. Teor. Fiz. **66**, 2105 (1974) [Sov. Phys. JETP **39**, 1036 (1974)].
4. Y. Shapira, S. Foner, and N. Oliveira, Jr., Phys. Rev. B **10**, 4765 (1974).
5. É. L. Nagaev, Zh. Éksp. Teor. Fiz. **57**, 1274 (1969) [Sov. Phys. JETP **30**, 693 (1970)]; Fiz. Tverd. Tela (Leningrad) **14**, 773 (1974) [Sov. Phys. Solid State **14**, 658 (1974)].
6. P. Gombás, *Theorie und Lösungsmethoden des Mehrteilchenproblems der Wellenmechanik* (Birkhäuser, Basel, 1950; Inostrannaya Literatura, Moscow, 1953).
7. C. Kittel, *Quantum Theory of Solids* (Wiley, New York, 1963; Nauka, Moscow, 1967).

Translated by Yu. Epifanov

Physics of the Solid State, Vol. 43, No. 1, 2001, pp. 61–64. Translated from Fizika Tverdogo Tela, Vol. 43, No. 1, 2001, pp. 61–64.

MAGNETISM AND FERROELECTRICITY

On the Shape of Iron *K* Absorption Edges for Monoferrites with a *Me*(Mg, Mn, Ni, Zn)Fe_2O_4 Spinel Structure

N. Yu. Safontseva and I. Ya. Nikiforov

Don State Technical University, Rostov-on-Don, 334010 Russia
e-mail: root@sintez.rnd.su

Received February 28, 2000; in final form, May 18, 2000

Abstract—Calculations of the *K*-edge x-ray absorption near-edge structure (XANES) in a pure metal and in monoferrites of stoichiometric compositions $MgFe_2O_4$, $MnFe_2O_4$, $NiFe_2O_4$, and $ZnFe_2O_4$ are carried out using a FEFF8 program. It was confirmed that the Fe *K*-edge energy shift found experimentally occurs upon the transition from pure iron to monoferrites. It is demonstrated that this shift is identically directed for ferrites with a structure of normal ($MnFe_2O_4$, $ZnFe_2O_4$) and inverted ($MgFe_2O_4$, $NiFe_2O_4$) spinels, but numerical values of theoretical Fe *K*-edge shifts agree well with experimental data only for normal spinels. © *2001 MAIK "Nauka/Interperiodica".*

1. INTRODUCTION

This paper is devoted to the investigation of the influence of a metal ion type and the arrangement in tetrahedral and octahedral lattice sites of the *Me*(Mg, Mn, Ni, Zn)Fe_2O_4 spinels on the shape and energy of the iron *K* absorption edge. Specific features of the x-ray absorption near-edge structure (XANES) spectra were calculated using the FEFF8 program [1, 2]. Compared to previous versions, the application of this program opens up new opportunities for band-structure calculations: (1) simulation of the self-consistent crystal potentials for all atoms involved in each compound, (2) inclusion of the full multiple-scattering paths within a cluster of the chosen size, and (3) calculation of *K* absorption edges with various spin orientations for the absorbing iron atom. Additional applications of the FEFF8 program lead to a manifold increase in the time required for calculations even on modern workstations. For this reason, the cluster size was limited by the number of atoms which provided satisfactory agreement with the experimental results.

2. CALCULATION PROCEDURE

The crystal structure of spinels with the space group O_h^7-F3dm represents a closely packed face-centered cubic lattice of anions with tetrahedral and octahedral holes partially occupied by cations [3, 4].

The $MnFe_2O_4$ and $ZnFe_2O_4$ ferrites belong to the structure type of normal spinels in which manganese and zinc cations occupy tetrahedral sites and iron cations occupy octahedral sites. Thus, the AB_2O_4 formula unit should involve one *Me*(Mn, Zn) cation occupying the *A* tetrahedral site and two iron cations located in the *B* octahedral site. However, in the $MnFe_2O_4$ ferrite, eight tetrahedral sites are occupied by both Mn^{2+} and Fe^{3+} cations in the ratio $0.8Mn^{2+} + 0.2Fe^{3+}$ per *A* site [5]. Similarly, 16 octahedral sites are occupied by both Fe^{3+} and Mn^{2+} ions in the ratio $0.2Mn^{2+} + 1.8Fe^{3+}$ per two *B* sites. Hence, in our calculations, instead of the formula $MnFe_2O_4$, we used the formula $Fe_xMn_{1-x}[Fe_yMn_{2-y}]O_4$, where *x* and *y* are the concentrations of cations in the *A* and *B* sites, respectively.

The $MgFe_2O_4$ and $NiFe_2O_4$ ferrites belong to the structure type of inverted spinels in which one-half the iron ions occupy tetrahedral sites and the other half of the iron ions and all the *Me*(Mg, Ni) ions are located in octahedral sites. Since the *Me*(Mn, Mg, Ni)Fe_2O_4 ferrites are antiferromagnets, the magnetic moments of metal ions located in the *A* sites were assumed to be parallel to one another and antiparallel to the magnetic moments of atoms occupying the *B* sites. The exception was the $ZnFe_2O_4$ spinel. This compound exhibits no magnetic properties due to the presence of a nonmagnetic zinc ion, which favors antiparallel spin orientations of iron ions located in the same octahedral sublattice. The lattice parameters *a* and the anionic parameters *u*, which account for the displacement of oxygen atoms from ideal sites toward the [111] direction, are given in the table. Thus, when calculating the iron *K* absorption edges for *Me*(Mn, Ni)Fe_2O_4, we used the clusters containing atoms of six types: (1) the central absorbing iron atom with a certain orientation of the spin magnetic moment; (2, 3) the iron ions with two antiparallel spin orientations, which were located in the corresponding coordination spheres; (4, 5) *Me*(Mn, Ni) ions with allowance made for the orientation of the magnetic moments; and (6) oxygen ions. In the *Me*(Mg, Zn)Fe_2O_4 spinels, the cluster involved atoms of only five types, because magnesium and zinc are not magnets.

1063-7834/01/4301-0061$21.00 © 2001 MAIK "Nauka/Interperiodica"

Unit cell parameters (a), anionic parameters (u), Fe K-edge shifts (ΔE), charges of Fe ions (q_{Fe}/e), and parameters of the computation model for pure iron and Me(Mn, Zn, Mg, Ni)Fe_2O_4 ferrites

Material		α-Fe	$MnFe_2O_4$	$ZnFe_2O_4$	$MgFe_2O_4$	$NiFe_2O_4$
	a, Å [5]	2.86	8.512	8.442	8.364	8.340
	u [4]	–	0.385	0.385	0.381	0.381
	[5]	0	8.3 ± 0.5	7.3 ± 0.6	6.3 ± 0.3	6.0 ± 0.4
ΔE, eV	This work	0	~8	~7	~9	~9
$q_{Fe}/e \equiv n$	$n\uparrow$	0.009	0.203	0.231	0.234	0.263
	$n\downarrow$*	0.004	0.042	0.009	0.034	0.04
N_{max}	Fe_t	–	–	–	984	984
	Fe_o	–	981	981	974	974
	α-Fe	965				
RPATH, Å	Fe_t	–	–	–	13.62	13.58
	Fe_o	–	13.78	13.66	13.48	13.44
	α-Fe	14.02				
N_{FMS}	Fe_t	–	–	–	29	29
	Fe_o	–	27	27	27	27
	α-Fe	27				
R_{FMS}, Å	Fe_t	–	–	–	3.49	3.48
	Fe_o	–	3.74	3.71	3.66	3.65
	α-Fe	4.01				
$L_{Fe_t–O}$, Å		–	–	–	1.90	1.89
$L_{Fe_o–O}$, Å		–	2.05	2.03	2.04	2.04
Coordination number	Fe_o	–	6–O 6–Fe 6–Mn	6–O 6–Fe 6–Zn	6–O 2–Fe, 4–Mg 6–Fe 4–O	6–O 2–Fe, 4–Ni 6–Fe 4–O
Coordination number	Fe_t	–	–	–	6–Fe 6–Mg	6–Fe 6–Ni
	[5]	23.5	12.1	17.5	15.2	16.5
a–b, eV	This work	24.1	11.8	18.8	16.8	16.0

* The "up" spin is marked with the arrow ↑, and the "down" spin is marked with the arrow ↓.

The XANES calculations of the Fe K spectra for all the ferrites under investigation were carried out within a unified calculation model:

(1) The largest cluster size (N_{max}) was no more than 1000 atoms.

(2) The procedure of full multiple scattering was carried out for a fairly small cluster containing up to 30 atoms (N_{FMS}).

(3) Within the longest scattering path (RPATH), whose length was limited by the largest cluster size, only the meaningful scattering paths with a multiplicity of eight were taken into account.

(4) The Hedin–Lundqvist exchange potential was included in our computations: the self-consistent-field (SCF) potential was calculated for a fairly small cluster containing up to 30 atoms and the number of iterations (loops) was as much as ten.

The longest scattering paths, the interatomic distances ($L_{Fe–O}$ and $L_{Me–O}$), the cluster sizes (N_{max} and N_{FMS}), the coordination numbers, and the types of nearest-neighbor atoms are given in the table.

3. RESULTS AND DISCUSSION

Figure 1 shows the Fe K absorption edges for pure iron and Me(Mn, Mg, Zn, Ni)Fe_2O_4 ferrites, which were calculated using the FEFF8 code. The absorption edge for pure iron on the relative energy scale in Fig. 1a is taken as zero (E_0). The choice of this scale was caused by the necessity of comparing the theoretical Fe

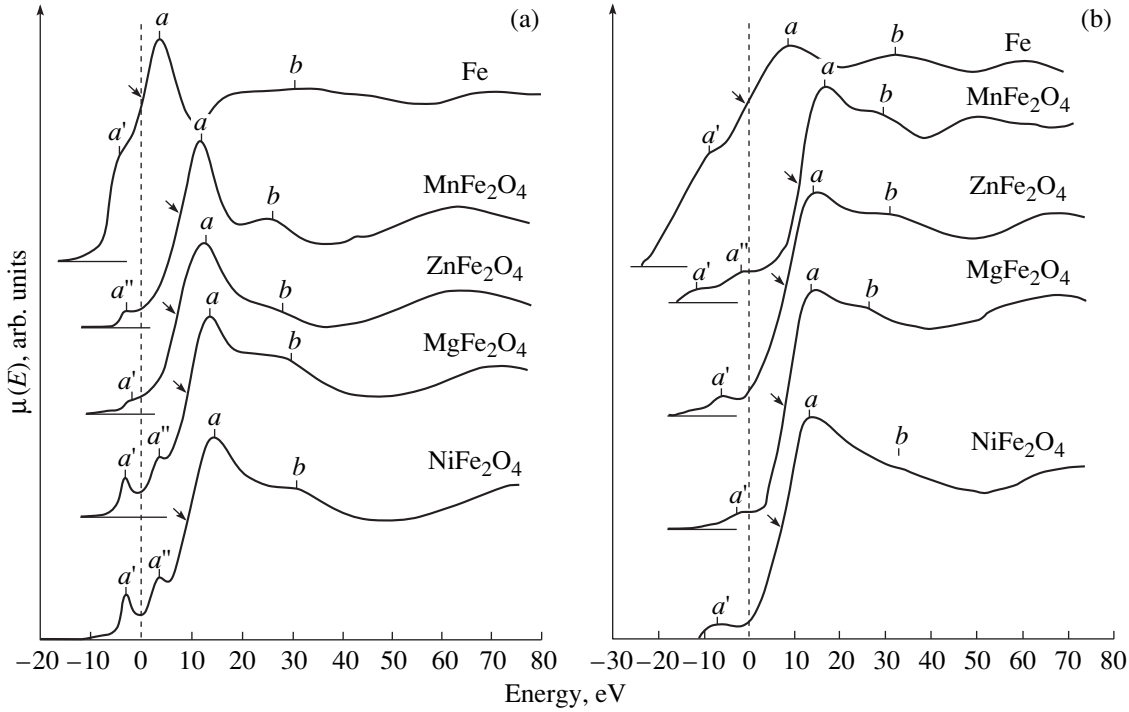

Fig. 1. Iron *K* absorption edges for monoferrites with a spinel structure: (a) theoretical *K* edges computed using the FEFF8 code and (b) experimental *K* edges [5]. The energy locations of the absorption edges are marked with arrows.

K spectra with the experimental curves shown in Fig. 1b, in which the shifts of the iron *K* edges upon the transition to ferrites are given with respect to pure iron. The experimental Fe *K* edges were taken from [5]. The energy location of the theoretical *K* edges (E_0) was defined as the inflection point of the arc tangent curve, which was used to approximate the theoretical Fe *K* edges for all the ferrites under investigation. In order to compare the theoretical *K* edges with the experiment, it is necessary to take into account that spinels contain two different iron ions with different charges and spin orientations. The experimental Fe *K* edges [5], which are displayed in Fig. 1b, represent the averaged absorption spectra for iron ions. For this reason, the theoretical Fe *K* edges shown in Fig. 1a also represent a superposition of Fe *K* edges for iron ions of different types.

Analysis of the Fe *K* spectra upon transition from pure iron to monoferrites revealed that the absorption edge shift to the high-energy range did not exceed ~9 eV. This trend exists for all the aforementioned compounds and is independent of the cation distribution in the unit cell, which is in good agreement with the experiment [5]. However, the analysis of the experimental and calculated numerical values of iron *K* edge shifts (see table) demonstrated that a reasonable agreement with the experiment was achieved only for the normal spinels $MnFe_2O_4$ and $ZnFe_2O_4$. The largest difference in the numerical value of the Fe *K* edge shift relative to pure metal (~3 eV) is observed in the theoretical curves for $MgFe_2O_4$ and $NiFe_2O_4$, which belong to inverted spinels. For these compounds, the intense shoulders in the pre-edge region were not revealed experimentally (*a*").

The pre-edge region can be interpreted as transitions of 1*s* electrons to unoccupied 3*d* states by analogy with the assignment of the main peak to the transition of 1*s* electrons to 4*p* states [5]. This conclusion is confirmed by our calculations, in which the local density of states for iron 3*d* electrons with the main peak located in the same energy range as the *a*' shoulders for all the aforementioned ferrites *Me*(Mg, Mn, Ni, Zn)Fe_2O_4 was computed using the LDOS code of the FEFF8 program. Since the main features of XANES, including the pre-edge region, are associated with the photoelectron wave scattering in a complex potential relief of the nearest-neighbor atoms, the *a*" shoulders in the pre-edge region of the Fe *K* spectra for $MgFe_2O_4$ and $NiFe_2O_4$ can be due to the existence of two types of iron atoms occupying tetrahedral (Fe_t) and octahedral (Fe_o) holes in inverted spinels. By contrast, iron atoms in the $MnFe_2O_4$ and $ZnFe_2O_4$ normal spinels are located only in the octahedral sites. As was mentioned above, the theoretical Fe *K* spectra represent a superposition of the Fe *K* spectra for iron ions, which have different spin orientations and occupy nonequivalent crystallographic sites. Because of this, the appearance of *a*" shoulders can be due to the different interatomic distances Fe_tO and Fe_oO and the variation in the nearest-neighbor

relief of the absorbing atom (see table). The absence of a similar complicated pattern in the pre-edge region of the Fe *K* spectrum of $Mn_{0.8}Fe_{0.2}[Fe_{1.8}Mn_{0.2}]O_4$ can be explained by the small number of Fe_t atoms compared to Fe_o atoms. Actually, $Fe_t = 0$ and $Fe_o = 2$ per formula unit AB_2C_4 for normal spinels and $Fe_t = 1$ and $Fe_o = 1$ for inverted spinels. Thus, the appearance of additional features *a*" should be associated with the atomic arrangement in the crystal lattice rather than with the type of atoms (other than iron) involved in ferrites.

An additional complication of the pre-edge region of the Fe *K* edge brings about ambiguity in determining the edge location, since the approximating arc tangent curve transforms into a multimodal curve. This can partly explain the discrepancy between the experiment and theory. However, the difference between the experimental and theoretical shifts for inverted spinels cannot be explained by problems in the determination of the edge location (its midpoint). As was noted in [5], the Fe *K*-edge shift should increase with an increase in the iron valence. An increase in the iron ion charge (q_{Fe}/e, where e is the electron charge) upon the transition from normal to inverted spinels, which was calculated using the FEFF8 program, correlates well with the increasing Fe *K*-edge shift (see table). Further calculations for other inverted spinels should show whether or not the result obtained is a generality in the trends of the absorption edge shift in normal and inverted spinels. As for now, we can state that the calculated Fe *K*-edge shape and the energy gap (*a–b*) from the main absorption edge *a* to the clearly defined features *b*, which are observed in a fine structure of the spectra, agree well with the experiment (see table). This fact and the exhibition of the general trend of the Fe *K*-edge shift to a high-energy range for both normal and inverted spinels demonstrate the adequate efficiency of the FEFF8 code for computations of absorption spectra.

ACKNOWLEDGMENTS

We thank A.L. Ankudinov (Los Alamos National Laboratory, Los Alamos, United States) for providing the FEFF8 program and attendant consultations.

REFERENCES

1. A. L. Ankudinov, B. Ravel, J. J. Rehr, and S. D. Conradson, Phys. Rev. B **58** (2), 7565 (1998).
2. J. J. Rehr and R. C. Albers, Phys. Rev. B **41** (12), 8139 (1990).
3. E. V. Gorter, Usp. Fiz. Nauk **57** (2), 279 (1955).
4. V. M. Talanov, *Energy Crystal Chemistry of Many-Sublattice Crystals* (Rostov. Univ., Rostov, 1986).
5. E. A. Zhurakovskiĭ and P. P. Kirichok, *Electronic States in Ferrimagnets* (Naukova Dumka, Kiev, 1985).

Translated by N. Korovin

Physics of the Solid State, Vol. 43, No. 1, 2001, pp. 65–72. Translated from Fizika Tverdogo Tela, Vol. 43, No. 1, 2001, pp. 65–71.

MAGNETISM AND FERROELECTRICITY

On a Mechanism of Nucleation in Crystals with Combined Anisotropy

R. M. Vakhitov* and A. R. Yumaguzin**

**Bashkortostan State University, ul. Frunze 32, Ufa, Bashkortostan, 450074 Russia*
***Institute of Molecular and Crystal Physics, Russian Academy of Sciences, Ufa, Bashkortostan, 450075 Russia*
e-mail: YumaguzinAR@ic.bashedu.ru

Received May 18, 2000

Abstract—The stable states of magnetic inhomogeneities of the "static"-soliton type in a (111) plate of a garnet ferrite with combined anisotropy are investigated theoretically, and the conditions for their occurrence are established. A model of static solitons is considered, and its fundamental properties are determined by solving the corresponding variational problem numerically. It is shown that these inhomogeneities originate at crystal defects and can significantly affect the kinetics of a phase transition of the spin-reorientational type. © *2001 MAIK "Nauka/Interperiodica".*

INTRODUCTION

The properties of magnetic materials are known to depend heavily on the presence of a domain structure in them. The magnetization distribution in the crystal and in domain walls (DWs) is determined by the geometry of the crystal, the symmetry of the crystal lattice, the higher order anisotropies, etc. [1–3]. However, even in the simplest cases, e.g., in a uniaxial ferromagnet, one-dimensional magnetic inhomogeneities with a nontrivial topology can exist. Investigations of the phase trajectories of the magnetization vector **M** in these crystals show that, in addition to 180° DWs that separate two domains with opposite directions of the vector **M**, there occur magnetic inhomogeneities of the 0°-DW type, static solitons (SSs) [4]. These inhomogeneities are sandwiched between two domains with the same **M** direction and have a bell-shaped magnetization distribution.

On the other hand, a number of magnetic materials, such as epitaxial garnet ferrite films [5], possess a combined anisotropy consisting of two components of different natures: induced uniaxial (IUA) and intrinsic cubic anisotropy (CA). Calculations show [6] that such a combined anisotropy is also favorable to the occurrence of SSs in magnets under certain conditions. It should be noted that localized solutions of this type have already been discussed in the literature (see, e.g., [7]), but they did not attracted considerable interest because of their topological instability. At the same time, DWs with such a structure were observed experimentally [2, 8, 9]; they occur in different materials, including garnet ferrites. Therefore, there is considerable current interest in studying the properties of these inhomogeneities and the conditions for their occurrence in plates with combined anisotropy.

1. STATIC SOLITONS IN AN IDEALIZED MODEL

Let us consider a ferromagnetic crystal in the form of an infinite plane-parallel plate of thickness D with combined IUA and CA. For the sake of definiteness, the plate is taken to be of the (111) type and the IUA easy axis is assumed to be parallel to the normal n to the plate, $\mathbf{n} \parallel z \parallel [111]$. The magnetization varies along the y axis, which lies in the (111) plane and makes an angle φ_0 with the $[\bar{1}10]$ axis. With allowance made for the exchange interaction, the CA and IUA energies, and the demagnetizing field of space charges in the Winter approximation [10], the energy of magnetic inhomogeneities in the (111) plate has the form

$$E = \int dV \left\{ A\left[\left(\frac{\partial\Theta}{\partial y}\right)^2 + \sin^2\Theta\left(\frac{\partial\varphi}{\partial y}\right)^2\right] + K_u\sin^2\Theta + K_1\left[\frac{\sin^2\Theta}{4} + \frac{\cos^4\Theta}{3} + \frac{\sqrt{2}}{3}\sin^3\Theta\cos\Theta\cos 3(\varphi-\varphi_0)\right] + 2\pi M_s^2(\sin\Theta\sin\varphi - \sin\Theta_\infty\sin\varphi_\infty)^2\right\}, \quad (1)$$

where A is the exchange parameter; K_u and K_1 are the IUA and CA constants, respectively; M_s is the saturation magnetization; Θ and φ are the polar and azimuth angles of the vector **M**, respectively; Θ_∞ and φ_∞ characterize the **M** direction in the domains; and V is the volume of the plate. The plate is assumed to be thick enough for the contribution from the demagnetizing

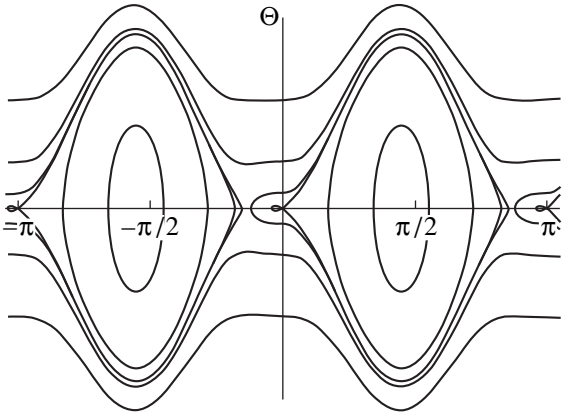

Fig. 1. Phase portrait of Eqs. (2) for $\varphi = 0$ and π; $\varphi_0 = 0$; and $\kappa = 1.4$.

field of surface charges to the energy in Eq. (1) to be negligible (idealized model).

The Euler equations minimizing the energy in Eq. (1) have the form

$$\frac{\delta E}{\delta \Theta} = 0, \quad \frac{\delta E}{\delta \varphi} = 0, \quad \frac{\delta E}{\delta \varphi_0} = 0 \tag{2}$$

with the proviso that

$$\delta^2 E > 0. \tag{3}$$

Solving these equations, one can find both the possible magnetic phases and the structure of the magnetic inhomogeneities in the (111) plate. Analysis shows that Bloch 180° DWs ($\varphi = 0, \pi$) exist for domains with **M** ∥ [111] and $\varphi_0 = \pi k/3$ ($k \in Z$) if $K_u > 0$ and $\kappa < 4/3$ ($\kappa = K_1/K_u$). When $1.314 < \kappa < 4/3$, the structure of a 180° DW exhibits cross ties (with additional inflection points in the **M** distribution), which are due to the emergence of metastable axes in the DW plane, causing the spin rotation to be slower near them. In the phase diagram for the (111) plate [6], these **M** directions correspond to a canted phase of the [*uuw*] type, which is metastable in this κ range, in contrast to the symmetric phase with **M** ∥ [111], which is stable. At $\kappa = 4/3$, a spin-reorientational ([*uuw*] ⟷ [111]) phase transition of the first order occurs. In the region $4/3 < \kappa < 3/2$, the [111] magnetic phase is metastable, whereas the [*uuw*] phase is stable. Accordingly, the domain structure of the plate is rearranged at $\kappa = 4/3$ and the 180° DW between **M** ∥ [111] domains transforms into a 180° DW between **M** ∥ [*uuw*] domains. The latter DW also has cross ties due to the metastable [111] easy axis lying in the DW plane. It is well known [11] that cross ties arising in the vicinity of a first-order spin-reorientational phase transition are nucleation centers for the new phase and are also favorable to domain structure rearrangement. In this case, the original 180° DW deforms and finally splits into two DWs; these are 70.5° and 109.5° DWs in the particular case of $\kappa \longrightarrow \infty$ ($K_u \longrightarrow 0$) [6]. At the same time, analysis of the phase portrait of the set of equations (2) shows that in the region $4/3 < \kappa < 3/2$, some trajectories of the vector **M** have the shape of closed loops (Fig. 1), which correspond to the solutions

$$\tan\Theta(y) = \frac{1}{a\cosh(by/\Delta_0) - c};$$

$$\varphi = 0, \pi; \quad \varphi_0 = \pi k/3, \quad k \in Z,$$

$$a = \frac{\sqrt{3\kappa - 4}}{2(1 - 2\kappa/3)}; \quad b = \sqrt{1 - 2\kappa/3}; \tag{4}$$

$$c = \frac{\sqrt{2}\kappa\cos 3(\varphi - \varphi_0)}{6(1 - 2\kappa/3)},$$

where $\Delta_0 = \sqrt{A/K_u}$. These solutions describe magnetic inhomogeneities of the SS type, for which **M** ∥ [111] in the domains. As follows from Eq. (4), the SS in the (111) plate can be of two types: large-angle (LAS) and small-angle soliton (SAS), which differ in energy E, width Δ_s, and the maximum angle Θ_s (amplitude) of the deflection of the magnetization vector **M** from its direction in the homogeneous state. The width and amplitude of the SS, which characterize its dimensions, are given by

$$\tan\Theta_s = 1/(a - c); \quad \Delta_s = 2(\delta/b - \Theta(\delta)/\Theta'(\delta)), \tag{5}$$

where $\delta = \ln(k + \sqrt{k^2 - 1})$ and k ($k > 1$) is the maximum root of the cubic equation

$$k^3 + pk + q = 0, \quad p = -\left(2 + \frac{1 + c^2}{a^2}\right);$$

$$q = 2\frac{c}{a}. \tag{6}$$

For the LAS, we have $E/E_0 \approx 1.4$, where $E_0 = 3\sqrt{AK_u}$, and $\Theta_s \approx 140°$–$160°$, while for the SAS, $E/E_0 \leq 10^{-2}$ and $\Theta_s \leq 20°$; as $\kappa \longrightarrow 3/2$, the SAS width increases indefinitely and $\Theta_s \longrightarrow 0$, which leads to spreading of the soliton; for the LAS in this limit, we have $\Delta_s \longrightarrow 8.54\Delta_0$ and $\Theta_s \longrightarrow 141.6°$ [6]. Analysis of inequality (3) for the solution given by Eq. (4) reveals that the SS is not stable, because it is a one-dimensional solution of the idealized model [12]. The point is that this model allows for no factors (e.g., the finiteness of the sample) that are responsible for the formation of a domain structure. In this case, account must be taken of the demagnetizing

fields of the plate, the contribution of which to the energy in Eq. (1) for the Bloch DWs can be written as

$$E_{ms} = M_s^2 L_x \int_{-\infty}^{\infty}\int_{-\infty}^{\infty} (\cos\Theta(y)\cos\Theta(y') - 1) \times \ln\left(1 + \frac{D^2}{(y-y')^2}\right) dy\,dy', \quad (7)$$

where L_x is the dimension of the plate along the x axis. We note that the energy E_{ms} (minus the energy of the homogeneous state) makes a negative contribution to the total energy in Eq. (1). At the same time, analysis of Eq. (7) shows that the larger the SS dimensions, the larger $|E_{ms}|$. Nonetheless, with the magnetostatic energy included, the SS state does not become stable, as will be shown later.

2. MODEL OF NUCLEATION IN REAL CRYSTALS

In order to investigate the stability of the SS, we consider the thermodynamics of its formation. The point is that the structure of these inhomogeneities and the conditions for their existence suggest that these magnetization inhomogeneities arise in the process of nucleation of the new phase. Owing to fluctuations, the nuclei always appear in the original phase in the vicinity of the first-order phase transition (in the region of coexistence of the phases). When the new phase is metastable and the original phase is stable (energetically favorable), the nuclei of the former phase are unstable and quickly decay [13]. However, they become stable if there are so-called condensation centers in the thermodynamic system. In magnetic materials, such centers are various defects: structural, chemical, thermic, etc. [14]. Their presence breaks the translational symmetry of crystals and leads to nonuniformities of the material parameters of the sample [15, 16].

As an example of a defect that stabilizes the SS, we consider a magnetic inclusion in the form of a platelet [17] in which the parameters A, K_u, and K_1 are different from their values in the host crystal; that is, the y dependence of these parameters is taken to be

$$K_u(y) = \begin{cases} K_u + \Delta K_u, & |y| \le L/2 \\ K_u, & |y| > L/2; \end{cases}$$

$$K_1(y) = \begin{cases} K_1 + \Delta K_1, & |y| \le L \\ K_1, & |y| > L/2; \end{cases} \quad (8)$$

$$A(y) = \begin{cases} A + \Delta A, & |y| \le L/2 \\ A, & |y| > L/2; \end{cases}$$

where L is the thickness of the defect.

To describe the process of nucleation at the defect quantitatively, we apply the variational method and take the SS magnetization variation in Eq. (4) as a trial function, with a, b, and c being variational parameters. Their values are determined by minimizing the energy in Eq. (1) with allowance made for Eqs. (7) and (8); that is, the energy of the static soliton E_s is taken to be

$$E_s = E + E_d + E_{ms}, \quad (9)$$

where E_d is given by

$$E_d = L_x D \int_{-L/2}^{L/2} \left\{ \Delta A \left(\frac{\partial\Theta}{\partial y}\right)^2 + \Delta K_u \sin^2\Theta + \Delta K_1 \left[\frac{\sin^4\Theta}{4} + \frac{\cos^4\Theta}{3} + \frac{\sqrt{2}}{3}\sin^3\Theta\cos\Theta \right] \right\} dy. \quad (10)$$

This approach is based on the assumption that the defect virtually does not affect the structure of the magnetic solitonlike inhomogeneities, but merely changes the structure parameters. Indeed, the magnetostatic field can significantly affect the structure of the DW (for example, the Bloch wall can be transformed into a Néel wall) only in the case of a fairly thin plate (with a thickness comparable to Δ_0) and of the quality factor of plate $Q = K_u/2\pi M_s^2$ satisfying the condition $Q \le 1$. In this paper, however, we assume that $D \gg \Delta_0$ and $Q > 1$. On the other hand, a numerical study of the topology of the magnetic inhomogeneities (without regard for the magnetostatic field) that arise near defects [16, 18] reveals that the SS with a structure similar to that given by Eq. (4) can form in crystals with a combined anisotropy. Therefore, the approximation used in this paper is justified.

3. STATIC PROPERTIES OF STATIC SOLITONS

In order to find the stable states of the SS in a crystal with the defects described by Eq. (8), one should solve the corresponding variational problem. Because the equations obtained by minimizing the energy E_s with respect to the parameters a, b, and c are cumbersome and their solution cannot be expressed in terms of known functions, we solve the variational problem by minimizing the reduced energy $\varepsilon_s = E_s/M_s^2 L_x D\Delta_0$ numerically. It is taken into account that the centers of the SS and the defect can differ in position and be separated by a distance ξ.

The results obtained are presented in Figs. 2–6, where all quantities with dimensions of length are measured in units of Δ_0. It is seen from Fig. 2 that the dependences of the SS parameters on the shift ξ have some specific features which are associated with the corresponding dependence of the interaction forces between the SS and the defect. The first feature to note is that the equilibrium position of the SS is determined by the

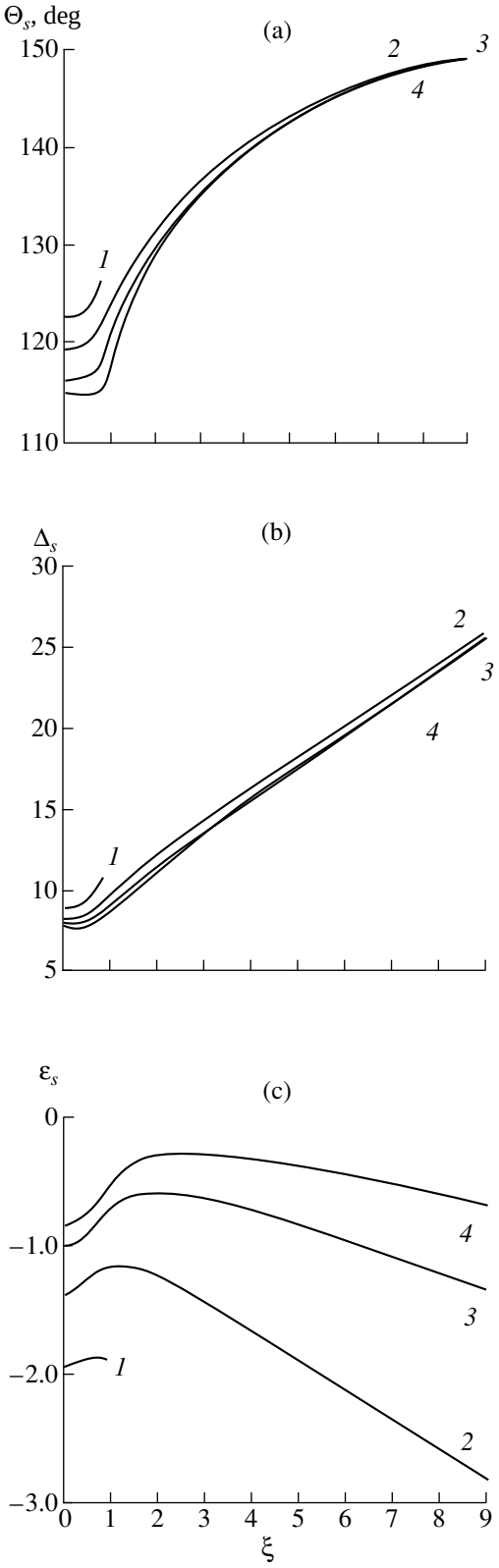

Fig. 2. Dependences of the SS parameters (a) Θ_s, (b) Δ_s, and (c) ε_s on the shift ξ for $\kappa = 1.42$, $\Delta A = 0$, $\Delta K_1 = 0.5$, $\Delta K_u = -1.5$, $L = 5$, $D = 35$, and various values of Q: (*1*) 5, (*2*) 8, (*3*) 15, and (*4*) 25.

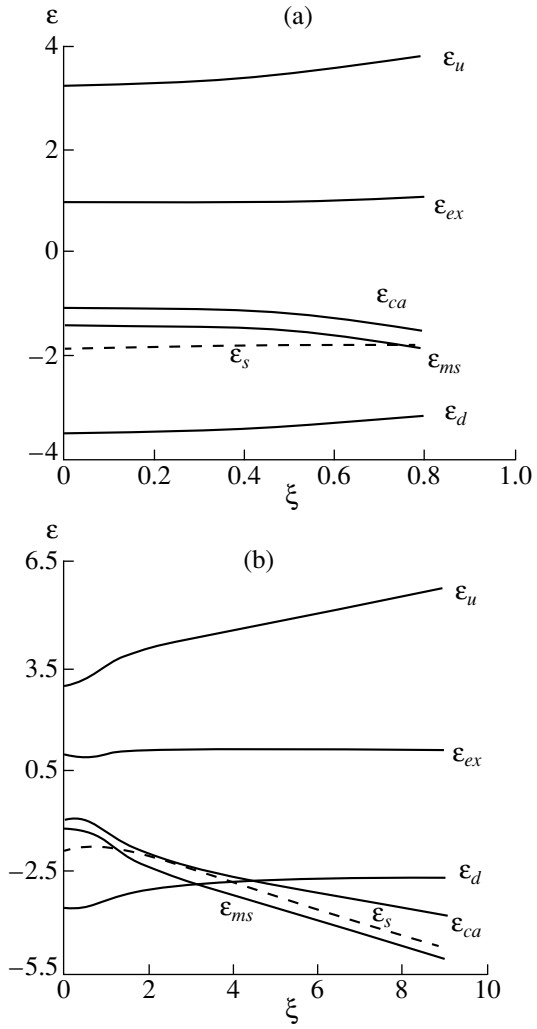

Fig. 3. Dependences of the different components of the total SS energy on the shift ξ for Q equal to (a) 5 and (b) 8. The other material parameters are the same as in Fig. 2.

defect center. A shift of the SS relative to the center gives rise to a quasi-elastic force, which obeys Hooke's law for small ξ. This SS–defect interaction force is determined fundamentally by the contribution described by Eq. (10) (curve ε_d in Fig. 3). As ξ increases, part of the spins in the SS find themselves outside the defect, which causes E_d to increase. However, this effect is reduced by the SS portions that displace and find themselves inside the defect, thereby being involved in the interaction with the defect (because of the short-range character of this interaction). As a result, the SS width and amplitude (dictated by the exchange forces) are increased and in turn cause a decrease in E_{ms}. At $K_1 > 0$, the CA easy axes are directed along $\langle 100 \rangle$, while the CA hard axes are parallel to the $\langle 111 \rangle$ axes. Therefore, any deflection of the spins from the [111] direction causes the CA energy E_{ca} to decrease, as can be seen from Fig. 3. The increase in

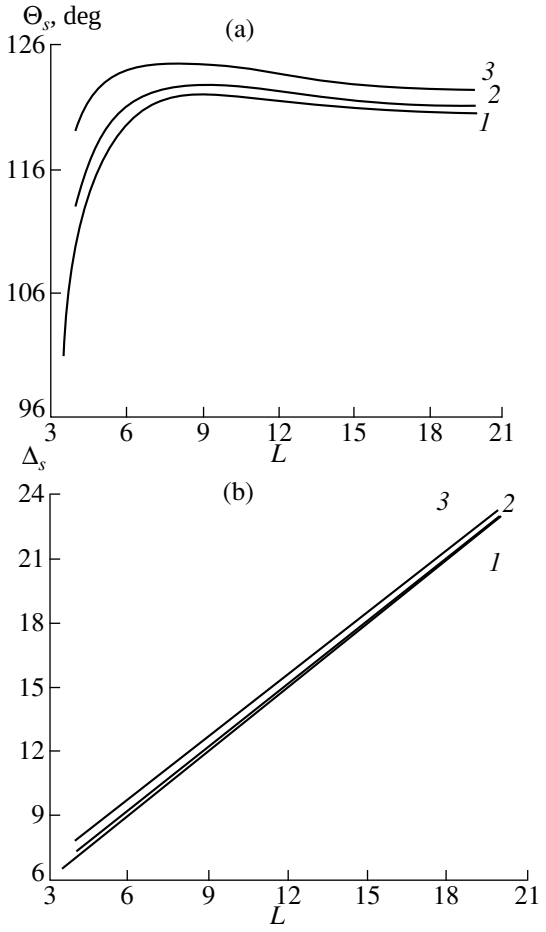

Fig. 4. Dependences of the SS parameters (a) Θ_s and (b) Δ_s on the defect width L for $Q = 5$, $\xi = 0$, and various values of κ: (*1*) 0.83, (*2*) 1.0, and (*3*) 1.42. The other material parameters are the same as in Fig. 2.

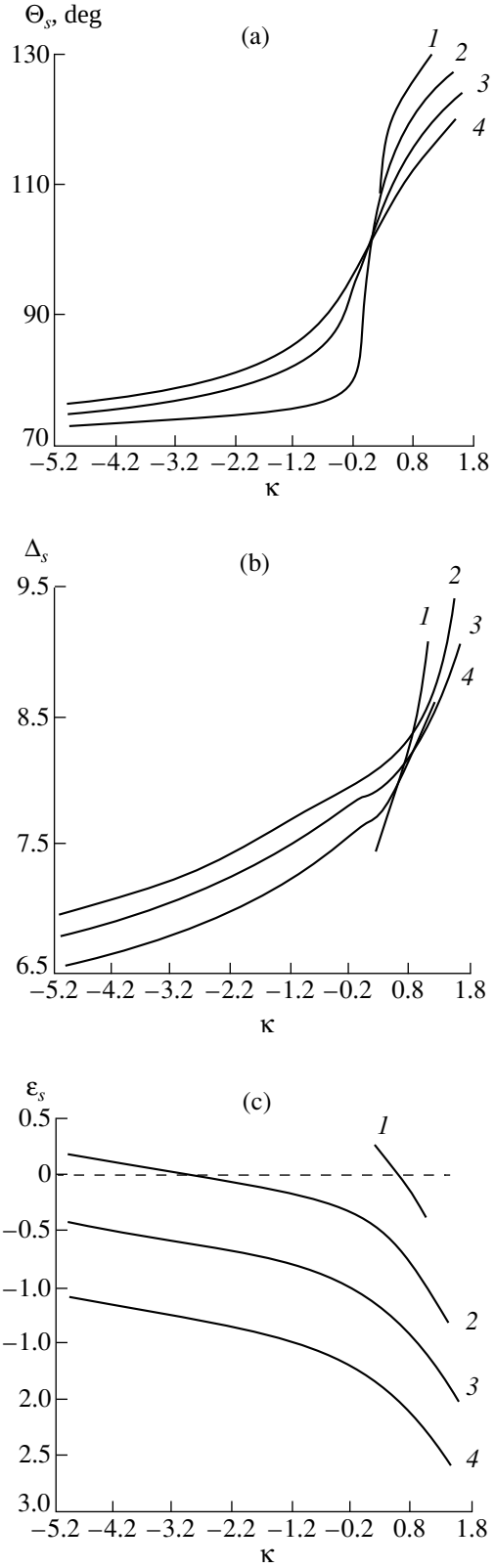

Fig. 5. Dependences of the SS parameters (a) Θ_s, (b) Δ_s, and (c) ξ_s on κ for $L = 5$ and different values of ΔK_u: (*1*) –0.9, (*2*) –1.2, (*3*) –1.5, and (*4*) –1.8. The other material parameters are the same as in Fig. 4.

the IUA energy E_a with an increase in the SS dimensions is explained in the same way.

As ξ is increased further, the ξ dependence of the resultant force becomes nonlinear (Fig. 2) and its magnitude reaches a maximum at $\xi = \xi_P$ corresponding to the inflection point of the function $\varepsilon_s = \varepsilon_s(\xi)$. Then, as the shift increases still further, the force decreases in magnitude and becomes equal to zero. At this point (ξ_m), the energy $\varepsilon_s(\xi)$ is maximal and the interaction changes sign; at $\xi > \xi_m$, the SS is repelled from the defect. Analysis of this process in the quasi-static approximation shows that the plate becomes uniformly magnetized with $\mathbf{M} \parallel [uuw]$, because, for the parameter ξ tending to infinity, we have $\varepsilon_s \longrightarrow -\infty$, $\Delta_s \longrightarrow \infty$, and $\Theta_s \longrightarrow \Theta_m$.

Thus, the stabilization of the SS structure, which is determined by the balance of the forces taken into account, is established in a certain range of the material parameters bounded by their limiting values. For example, if Q is decreased, i.e., the contribution E_{ms} to the

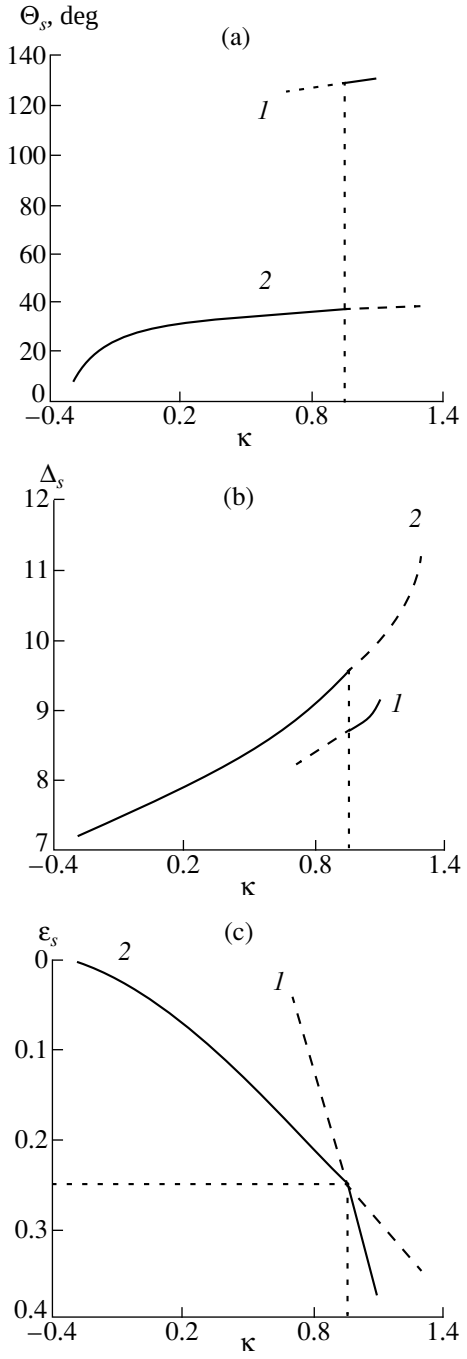

Fig. 6. Dependences of (*1*) the LAS and (*2*) the SAS parameters on κ for $\Delta K_u = -0.9$ and $\Delta K_1 = 0.5$. The other parameters are the same as in Fig. 5.

energy in Eq. (9) is increased, there is a critical value of ξ at which the magnetostatic field, which is favorable to the spin tilt to the plane of the plate, breaks the balance of the forces and the SS spreads out (curve *1* in Fig. 2): $\varepsilon_s \longrightarrow -\infty$, $\Delta_s \longrightarrow \infty$, and $\Theta_s \longrightarrow \pi$. It should be noted that the ranges of the material parameters in which the SS is stable are considerably wider in the absence of the stray demagnetizing fields ($Q \longrightarrow \infty$) than in the presence of them. There is always a (lower) critical value of Q at which the SS becomes unstable.

The stable SS states, as was shown above (Fig. 3), are determined fundamentally by the presence of the defect in the crystal structure. For example, it is seen from Fig. 4 that the SS width increases in proportion to the width of the defect, so that the SS spreads out in the limit as $L \longrightarrow \infty$. In this limit, the plate is homogeneous (but its material parameters are changed) and the factors that can stabilize the SS disappear. It is worth noting that the limiting values of Θ_s coincide with the values of the polar angle of **M** in the uniformly magnetized plate [6]. We also note that the SS has a growing tendency to adapt to the profile of the defect with increasing L. At the same time, it follows from Fig. 4 that the process of nucleation on the defect has a threshold character; namely, there is a minimal defect size at which the SS becomes unstable and collapses. This agrees with the corresponding general result of the thermodynamic theory of the "condensation" of a new phase [13] and correlates with the analogous dependences of the SS parameters on ΔA, ΔK_1, and ΔK_u (Figs. 5, 6). It follows from these dependences that there is a minimum defect energy at which the SS has a stable structure. This energy depends on the size and other parameters of the defect (ΔA, ΔK_1, ΔK_u). Calculations show that the SS width increases, but its amplitude decreases with increasing ΔA. This is due to the fact that the magnetization distribution in the SS becomes smoother when the exchange interaction in the defect is stronger. The dependence of the SS dimensions on ΔK_1, characterizing the jump in CA due to the defect, is more complicated; as ΔK_1 increases, the value of Θ_s increases significantly for $\kappa > 0$ and decreases moderately for $\kappa < 0$. This behavior is due to the nature of CA. Indeed, the ⟨001⟩ axes increase in importance with increasing K_1: the plane of spin rotation in the 0° DW contains the [001] axis, which makes the angle $\Theta \approx 35°$ with the [111] axis. At $K_1 > 0$, the greater part of spins tend to tilt to this axis, so that Δ_s and hence Θ_s (by virtue of the exchange interaction) increase. At $K_1 < 0$, in contrast, the spins in the 0° DW tend to tilt to the [111] axis. This explains the dependence of the 0°-DW dimensions on ΔK_1 mentioned above.

Calculations (some of which are presented in Figs. 5, 6) show that the SS dimensions increase with κ, which agrees with Eq. (5) derived in the idealized model. There is a κ range ($\Delta\kappa$) over which the SS dimensions increase so significantly that it can be said that the changeover from the SAS state to an LAS state occurs. This changeover proceeds continuously in the range $\Delta\kappa$, whose position shifts to higher or lower κ values depending on the defect parameters ΔA and ΔK_1 (but not on ΔK_u). The opposite situation occurs with the value of $\Delta\kappa$, which is determined fundamentally by the parameter ΔK_u, but virtually does not depend on ΔA and ΔK_1. At a certain, critical value of ΔK_u, $\Delta\kappa$ vanishes

($\Delta\kappa = 0$); that is, the changeover from the SAS to an LAS (and vice versa) occurs suddenly (Fig. 6), which is indicative of the possible rearrangement of the domain structure associated with the defect. With a further decrease in κ, the SAS decreases in size and collapses finally at a certain value of κ after the SS collapse, the plate becomes uniformly magnetized with $\mathbf{M} \parallel [111]$. It should be noted that this state can also appear at a larger value of κ, because $\varepsilon_s > 0$ in this case and the SS state is metastable. At the other, upper, bound of the κ range over which the SS is stable, the SS spreads out, because $\Delta_s \longrightarrow \infty$ and $\Theta \longrightarrow \Theta_m$. In this case, the plate is also uniformly magnetized with $\mathbf{M} \parallel [uuw]$. Therefore, the plate is remagnetized; that is, it undergoes the $[111] \longleftrightarrow [uuw]$ phase transition. The point of this spin-reorientational phase transition corresponds to the upper κ limit of the SS stability at which the SS spreads out.

It is seen from the results presented above that the κ range over which the SS is stable is fairly wide; it is wider than that predicted by the idealized model. The SS exists even at $\kappa = 0$, i.e., in the absence of CA. This is a nontrivial result, because it is the presence of the combined anisotropy that is the condition for SS-like solutions in the idealized model. We note, however, that the effect of defects on the DW structure was shown [16, 19] to be similar to the effect produced by higher order anisotropies. This is the reason why the combined-anisotropy effect is observed.

4. DISCUSSION OF RESULTS

The results obtained in this paper allow one to model the magnetization reversal in a crystal as follows: Let a magnet be in a uniformly magnetized state with $\mathbf{M} \parallel [111]$ under given external conditions defined by the temperature, external stresses, etc. As the parameter κ is increased, an SS will nucleate on the defect at a certain value of κ, which can be different from the critical value κ_{c1} for the SS collapse (because of possible hysteresis). With a further increase in κ, the SS dimensions increase and the SS spreads out finally at another critical value κ_{c2}; the magnet again becomes uniformly magnetized but with $\mathbf{M} \parallel [uuw]$; that is, a spin-reorientational phase transition occurs. A similar magnetization reversal of a crystal was reported in [3, 20], where it was of fundamental importance that, in the process of the spin-reorientational phase transition, a new phase (canted phase with $\mathbf{M}$ roughly parallel to the $[1\bar{1}1]$ axis) nucleated on a dislocation, grew, and, finally, occupied the bulk of the crystal, so that the remainder of the original phase with $\mathbf{M} \parallel [111]$ was located in a microregion around the dislocation. This microregion can be considered as an SS characterized by the canted phase with $\mathbf{M} \parallel [uuw]$. Clearly, this interpretation of the data presented in [3, 20] is qualitative, because the model of the crystal with a defect we consider here is one-dimensional, whereas the dislocations and magnetic inhomogeneities observed in [3, 20] are at least two-dimensional. (The explanation proposed in this paper is not the only one possible. In [21], the $\mathbf{M}$ distribution around a dislocation was calculated numerically and the results are in qualitative agreement with [20]. However, only the case of an infinite crystal was considered in [21] and the kinetics of the process was not investigated.) However, our interpretation is supported by the fact that the dimensions of the defect and the SS are comparable and $\Delta_s > L$, which was observed in the experiment [20]. Furthermore, the κ dependence of the SS dimensions correlates with the temperature dependence of the dimensions of the magnetized microregion localized on a dislocation, especially in the vicinity of the spin-reorientational phase transition. As the temperature is increased by $\Delta T \approx 1^\circ$K, the microregion expands rapidly and occupies the entire crystal; the SS also increases infinitely in size as κ is increased by $\Delta\kappa \approx 0.1$ in the vicinity of $\kappa \approx \kappa_{c2}$. Finally, as follows from the analysis given above, the SS tends to adapt to the defect profile; therefore, our model qualitatively explains the shape of magnetic inhomogeneities localized on dislocations.

5. CONCLUSION

Thus, the static soliton is shown to be stable in a certain range of the parameters of the crystal and of defects of a certain type. It has a number of interesting features, which allows one to consider the SS as a nucleus of a new phase localized on a defect and arises in a spin-reorientational phase transition. In this case, the SSs are an intermediate structure through which magnetization reversal of the crystal occurs. The analysis of these magnetic inhomogeneities can be used in interpreting the experimental data, in particular, the data on the processes of the magnetization reversal in a magnetic field, where various defects are of considerable importance. These inhomogeneities also have potential for device applications.

REFERENCES

1. S. V. Vonsovskiĭ, *Magnetism* (Nauka, Moscow, 1971; Wiley, New York, 1974).
2. G. S. Kandaurova and L. A. Pamyatnykh, Fiz. Tverd. Tela (Leningrad) **31** (8), 132 (1989).
3. V. K. Vlasko-Vlasov, L. M. Dedukh, M. V. Indenbom, and V. I. Nikitenko, Zh. Éksp. Teor. Fiz. **84** (1), 277 (1983) [Sov. Phys. JETP **57**, 159 (1983)].
4. P. P. Shatskiĭ, Zh. Éksp. Teor. Fiz. **107** (2), 568 (1995) [JETP **80**, 308 (1995)].
5. S. Chikasumi, *Physics of Ferromagnetism: Magnetic Characteristics and Engineering Applications* (Syokabo, Tokyo, 1984; Mir, Moscow, 1987).
6. R. M. Vakhitov, R. M. Sabitov, and M. M. Farztdinov, Fiz. Tverd. Tela (Leningrad) **27** (6), 1852 (1985) [Sov. Phys. Solid State **27**, 1111 (1985)].

7. A. M. Kosevich, Fiz. Met. Metalloved. **53** (3), 420 (1982).
8. A. M. Balbashov, A. V. Zalesskiĭ, V. G. Krivenko, and E. V. Sinitsyn, Pis'ma Zh. Tekh. Fiz. **14** (4), 293 (1988) [Sov. Tech. Phys. Lett. **14**, 129 (1988)].
9. L. J. Heyderman, H. Hiedoba, H. O. Gupta, and I. B. Puchalska, J. Magn. Magn. Mater. **96**, 125 (1991).
10. A. Hubert, *Theorie der Domanenwande in Geordneten Medien* (Springer-Verlag, Berlin, 1974; Mir, Moscow, 1977).
11. K. P. Belov, A. K. Zvezdin, A. M. Kadomtseva, and R. Z. Levitin, *Orientation Transition in Rare-Earth Magnetic* (Nauka, Moscow, 1979).
12. W. F. Brown, *Micromagnetics* (Interscience, New York, 1963; Nauka, Moscow, 1979).
13. L. D. Landau and E. M. Lifshitz, *Statistical Physics* (Nauka, Moscow, 1976; Pergamon, Oxford, 1980), Part 1.
14. V. V. Randoshkin and A. Ya. Chervonenkis, *Applied Magnetooptics* (Énergoatomizdat, Moscow, 1990).
15. A. I. Mitsek and S. S. Semyannikova, Fiz. Tverd. Tela (Leningrad) **11** (5), 1103 (1969) [Sov. Phys. Solid State **11**, 899 (1969)].
16. M. A. Shamsutdinov, V. G. Veselago, M. M. Farztdinov, and E. G. Ekomasov, Fiz. Tverd. Tela (Leningrad) **32** (2), 497 (1990) [Sov. Phys. Solid State **32**, 288 (1990)].
17. A. Sakuma, S. Tanigawa, and M. Tokunaga, J. Magn. Magn. Mater. **84**, 52 (1990).
18. V. G. Veselago, I. V. Vladimirov, R. A. Doroshenko, and V. D. Plavskiĭ, Preprint No. 53 (Moscow, 1989).
19. E. V. Sinitsyn and I. G. Bostrem, Zh. Éksp. Teor. Fiz. **85** (2), 661 (1983) [Sov. Phys. JETP **58**, 385 (1983)].
20. V. K. Vlasko-Vlasov and M. V. Indenbom, Zh. Éksp. Teor. Fiz. **86** (3), 1084 (1984) [Sov. Phys. JETP **59**, 633 (1984)].
21. A. B. Dichenko and V. V. Nikolaev, J. Magn. Magn. Mater. **53**, 71 (1985).

Translated by Yu. Epifanov

Physics of the Solid State, Vol. 43, No. 1, 2001, pp. 73–75. Translated from Fizika Tverdogo Tela, Vol. 43, No. 1, 2001, pp. 72–74.

MAGNETISM AND FERROELECTRICITY

On the Heat Capacity Discontinuity for a Gas of Nuclear Spin Waves in Ferromagnets

S. O. Gladkov

Semenov Institute of Chemical Physics, Russian Academy of Sciences, ul. Kosygina 4, Moscow, 117977 Russia

Received May 18, 2000

Abstract—It is demonstrated that the heat capacity discontinuity for a gas of nuclear spin waves occurs in ferromagnetic materials. The heat capacity discontinuity manifests itself at ultralow temperatures and stems from the specific spectrum of these quasiparticles. The effect is observed at the temperature $T_K \cong 2.37\hbar\omega_n$. The heat capacity discontinuity is found at this temperature. © *2001 MAIK "Nauka/Interperiodica".*

Investigations into the properties of magnetic structures in which the so-called hyperfine interaction plays an important role [1] are not a novel trend. They were started 30–35 years ago with investigations of the collective dynamics of novel quasiparticles, which were called nuclear spin waves (NSWs) and were originally predicted by de Gennes *et al.* [2] in 1963. Beginning with that time, a large number of papers have been concerned, in one way or another, with analysis of the properties exhibited by these quasiparticles [3–8] at temperatures sufficiently below the liquid-helium temperature.

In studies of the dynamic properties of magnetic materials in this temperature range, it is important to take into account the hyperfine interaction, which results in the formation of the NSW spectrum in the **k** space due to an indirect exchange interaction of neighboring nuclear spins (through the electron spins). This spectrum is very simple for ferromagnets and is almost indistinguishable from the frequency of the nuclear magnetic resonance (NMR). The NMR frequency is known as $\omega_n = AS/\hbar$, where A is the hyperfine interaction constant and S is the electron spin of the atomic outer shell. Actually, the NSW spectrum is as follows: $\omega_n(K) = \omega_n - \Delta\omega_n(k)$. Here, the dispersion, or the dynamic frequency shift, is $\Delta\omega_n(k) = A^2SI/\hbar^2\omega_e(k)$, where I is the nuclear spin and $\omega_e(k)$ is the magnon dispersion. The explicit form of the magnon dispersion is $\omega_e(k) = \omega_e + \omega_E(ak)^2$, where $\omega_e = \gamma_e(H + H_a)$ is the ferromagnetic resonance frequency, γ_e is the gyromagnetic ratio, H is the external magnetic field, H_a is the anisotropy field, ω_E is the exchange frequency ($\omega_E = J_{ex}/\hbar$, where J_{ex} is the Dirac exchange integral), and a is the interatomic distance.

By virtue of the specific character of the NSW spectrum in ferromagnets, only the processes occurring with conservation of the number of quasiparticles (the case in point is the interaction within the NSW system; the interaction with phonons and magnons is considered negligibly weak) are allowed by the laws of conservation of energy and momentum. Actually, for three NSWs, the energy conservation law is as follows: $\omega_n(k_1) = \omega_n(k_2) + \omega_n(k_3)$. It is clear that this law breaks down for the NSW spectrum at any wavevector due to small dispersion $\Delta\omega_n(k)$, which is considerably less than the NMR frequency. By contrast, the four-particle interaction, whose Hamiltonian commutes with the operator for the number of quasiparticles $N = a_k^+ a_k$, is allowed by the conservation laws. Hence, for this interaction, the equilibrium function takes the form of a Bose distribution with the nonzero chemical potential μ: $n(k) = [\exp(\hbar\omega_n(k) - \mu)/T - 1]^{-1}$ (the Boltzmann constant is taken to be unity). However, since the dispersion is small, we can assume that $\hbar\omega_n(k) = \hbar\omega_n$.

Thus, we come now to the solution of the problem of calculating the heat capacity discontinuity, which should manifest itself from the above reasoning on the NSW spectra. This can be proved by rigorous mathematical treatment.

It is known that the complete number of nuclear spin waves is determined by the following integral: $N = (V/(2\pi)^3)\int d^3k n(k) = (\pi V/6a^3)n(\hbar\omega_n - \mu)$. Since $V/a^3 = N_a$ (where N_a is the number of atoms in a substance), from the equation $n(\hbar\omega_n - \mu) = (6/\pi)(N/N_a)$ for $\mu = 0$, we determine the required temperature at which this condition is met:

$$T_K = \hbar\omega_n/\ln[(\pi/6)(N_0/N_a) + 1], \quad (1)$$

where N_0 is the number of quasiparticles for $\mu = 0$ (T_K should not to be confused with the Bose condensation temperature [9]).

The order of magnitude of the T_K temperature is about 10^{-2} K. Let us calculate the heat capacity of the

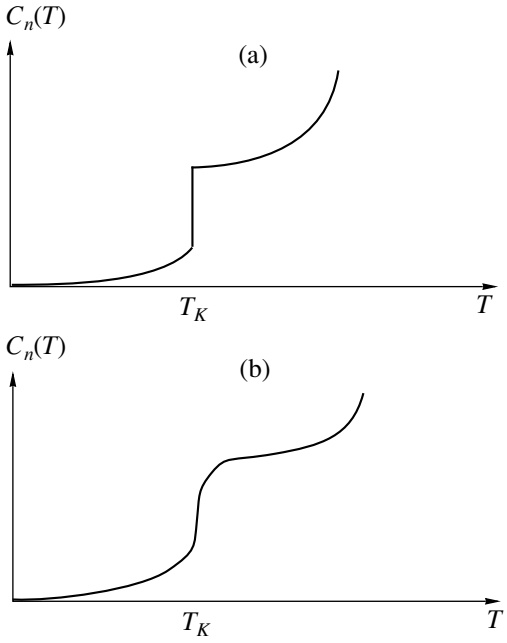

Fig. 1. Schematic representation of the heat capacity discontinuity in ferromagnets due to nuclear spin waves (a) without the interaction and (b) with inclusion of the interaction.

nuclear spin waves at the temperature found from Eq. (1). Since

$$N = N_0 + (V/(2\pi^2))\int_0^{\pi/a} k^2 dk[n(\hbar\omega_n - \mu) - n(\hbar\omega_n)]$$

and the chemical potential is small at temperatures close to T_K, after the decomposition of the integrand, we obtain

$$N = N_0 - N_a(\pi/6\hbar)(\partial n_0/\partial\omega_n)\mu,$$

where $n_0 = n$ ($\mu = 0$).

As a consequence,

$$\mu = (6\hbar/\pi)[(N_0 - N)/N_a]1/(\partial n_0/\partial\omega_n). \quad (2)$$

By virtue of the fact that the derivative $\partial E/\partial\mu = N \cong N_0$, we have $E = E_0 + \mu N_0$. Taking into account Eq. (2), we obtain

$$E = E_0 + (6\hbar/\pi)[(N_0 - N)/N_a]1/(\partial n_0/\partial\omega_n)N_0.$$

Double differentiation of the obtained equation with respect to temperature gives

$$\Delta C_n = T\partial^2 E/\partial T^2 = \hbar T\left\{\partial^2 N_0/\partial T^2[\partial \ln n_0/\partial\omega_n]^{-1} - \frac{2(N_0/\partial T)\partial[\partial \ln n_0/\partial\omega_n]/\partial T}{[\partial \ln n_0/\partial\omega_n]^2}\right\}.$$

By calculating the derivatives and substituting Eq. (1), we find

$$\Delta C_n = -(\pi/6)N_n n_0(\hbar\omega_n/T)^2\big|_{T=T_K} = -N_0/\ln^2[(\pi/6)(N_0/N_a) + 1]. \quad (3)$$

On the other hand, at $T < T_K$, the energy of the NSW gas is determined by the equation

$$E = (V/(2\pi^2))\int_0^{\pi/a} \hbar\omega_n(k)n(\hbar\omega_n)k^2 dk = (\pi/6)N_0 n_0\hbar\omega_n. \quad (4)$$

Then, the heat capacity to the left of the T_K point is

$$C_n^- = \lim_{T\to T_K - 0} T\partial^2 E/\partial T^2 = (\pi/6)\hbar\omega_n N_a T_K \partial^2 n_0/\partial T_K^2 = \{N_0/\ln^2[(\pi/6)(N_0/N_a) + 1]\} \times \{[(1 + 6N_a/\pi N_0)(1 + 12N_a/\pi N_0)/\ln[(\pi/6) \times (N_0/N_a) + 1] - 2]\}. \quad (5)$$

From Eqs. (3) and (5), we derive the heat capacity at $T > T_K$:

$$C_n^+ = C_n^- + \Delta C_n = \{N_0/\ln^2[(\pi/6)(N_0/N_a) + 1]\}\{(1 + 6N_a/\pi N_0) \times (1 + 12N_a/\pi N_0)/\ln[(\pi/6)(N_0/N_a) + 1] - 2\}. \quad (6)$$

Let us dwell briefly on the justification of the above situation. The condition of the nonzero NSW chemical potential, which is necessary to realize the case under consideration, requires estimation of the ratio between concrete relaxation times. Indeed, a similar situation occurs only if the relaxation time $\tau_{n-n-ph-e}$ of the NSW temperature is substantially less than the relaxation time τ_{n-n-ph} of the chemical potential. The time $\tau_{n-n-ph-e}$ is governed by the mechanism of the annihilation interaction of nuclear spin waves with phonons and magnons (see, for example, [10]) and is determined by multiplying the operators $\alpha_{nk}^+\alpha_{nk'}b_q\alpha_{ek''}^+$, where $\alpha_{nk}^+(\alpha_{nk})$ is the production (annihilation) operator for nuclear spin waves with wavevector k, α_{ek}^+ is the production operator for a magnon with wavevector k, and $b_q^+(b_q)$ is the production (annihilation) operator for a phonon with wavevector q. The estimation of the relaxation time for this mechanism gives $[\tau_{n-n-ph-e}]^{-1} \cong B_1\omega_n(\omega_n/\omega_E)^3(\omega_T/\omega_e)^2$, where B_1 is a constant. As regards the time τ_{n-n-ph}, it is determined by the mechanism of the interaction of the type $\alpha_{nk}^+\alpha_{nk'}^+ b_q$. In this case, a simple estimation demonstrates that $[\tau_{n-n-ph}]^{-1} = B_2\omega_n(\hbar\omega_n/\theta_D)^3$ in order of magnitude. It follows

from comparison of these times that the scheme of relaxation required to realize this situation, which is represented as $\alpha^+_{nk}\alpha_{nk}b_q\alpha^+_{ek''} \longrightarrow \mu \neq 0$, $T_n \longrightarrow T$ and $\alpha^+_{nk}\alpha^+_{nk'}b_q \longrightarrow \mu \longrightarrow 0$ can be realized if, for example, $\omega_T \gg \omega_e$, where ω_e is the ferromagnetic resonance frequency and $\omega_T = 2A\omega_E IS/\hbar$.

Thus, the inclusion of the adiabatic interaction between nuclear spin waves and a thermostat leads to a decrease in the chemical potential μ, which becomes zero after a very long, but finite amount of time. In this case, the knee shown in Figs. 1a and 1b gradually disappears. By virtue of the specific interaction, this time should be very long; namely, its characteristic values fall in the range from several months to centuries. The reason for this is that the phonon region of the phase space is very small for this type of interaction and is of the order of $(\hbar\omega_n/\theta_D)^3$. It should be noted that the instant of time at which all the subsystems attain thermodynamic equilibration can be determined rather exactly from the time of the disappearance of this knee.

For antiferromagnets, the situation is somewhat complicated and the above effect does not necessarily manifest itself. In fact, owing to the large dynamic frequency shift in the NSW spectrum, which is caused by the exchange interaction, the effect can manifest itself only in antiferromagnets with a low Néel temperature and, correspondingly, a small dynamic frequency shift. This is known as the necessary condition for the prohibition of three-particle scattering with the proviso that introducing the chemical potential is meaningful.

In conclusion, it should be emphasized once again that the above-predicted heat capacity discontinuity, which is due to the presence of the nuclear spin subsystem, occurs only at the so-called ultralow temperatures. The specific effects and the results of calculations for temperatures $T \leq \hbar\omega_n$ were considered in detail, for example, in [10]. Note that the nonstandard NSW spectrum, which is characteristic of the ferromagnets with a small dynamic frequency shift, is the most important feature in our consideration. The temperature of the heat capacity discontinuity can easily be estimated from Eq. (1). If $N_a = N_0$, we obtain $T_K \cong 0.071$ K for $AS = 0.03$ K.

REFERENCES

1. E. A. Turov and M. P. Petrov, *Nuclear Magnetic Resonance in Ferro- and Antiferromagnets* (Nauka, Moscow, 1969; Wiley, New York, 1972).
2. P. G. de Gennes, P. A. Pincus, F. Hartman-Boutron, and M. Winter, Phys. Rev. **129**, 1105 (1963).
3. S. O. Gladkov, Fiz. Tverd. Tela (Leningrad) **20** (7), 1969 (1978) [Sov. Phys. Solid State **20**, 1137 (1978)].
4. N. I. Evtikhiev, V. S. Lutovinov, M. A. Savchenko, and V. L. Safonov, Pis'ma Zh. Tekh. Fiz. **6** (24), 1527 (1980) [Sov. Tech. Phys. Lett. **6**, 659 (1980)].
5. S. O. Gladkov, Fiz. Tverd. Tela (Leningrad) **23** (9), 2686 (1981) [Sov. Phys. Solid State **23**, 1575 (1981)].
6. S. O. Gladkov and M. I. Kaganov, Zh. Éksp. Teor. Fiz. **80** (4), 1577 (1981) [Sov. Phys. JETP **53**, 811 (1981)].
7. V. L. Sobolev, Fiz. Met. Metalloved. **56** (5), 837 (1983).
8. V. L. Safonov, Zh. Éksp. Teor. Fiz. **94** (11), 263 (1988) [Sov. Phys. JETP **67**, 2324 (1988)].
9. L. D. Landau and E. M. Lifshitz, *Statistical Physics* (Nauka, Moscow, 1976; Pergamon, Oxford, 1980).
10. S. O. Gladkov, Phys. Rep. **182** (4–5), 211 (1989).

Translated by N. Korovin

Physics of the Solid State, Vol. 43, No. 1, 2001, pp. 76–81. Translated from Fizika Tverdogo Tela, Vol. 43, No. 1, 2001, pp. 75–79.

MAGNETISM AND FERROELECTRICITY

Nonreciprocal Light Birefringence in the $R_3B_7O_{13}X$ Boracites (R = Co, Cu, Ni; X = I, Br)

B. B. Krichevtsov

Ioffe Physicotechnical Institute, Russian Academy of Sciences, Politekhnicheskaya ul. 26, St. Petersburg, 194021 Russia

Received May 26, 2000

Abstract—The field and angular dependences of nonreciprocal birefringence (NB), which is linear in magnetic field **B** and is due to magnetic-field-induced spatial dispersion, have been studied in the cubic (symmetry class T_d) paraelectric phase of the $R_3B_7O_{13}X$ boracites (R = Co, Cu, Ni; X = I, Br) at a wavelength λ = 633 nm. It is shown that the NB in crystals with different 3*d* and halogen ions exhibits the same anisotropy. The relation between the A and g parameters, $A = 2g$, which determine the NB anisotropy, suggests that the microscopic mechanism of the NB is the manifestation of second-order magnetoelectric susceptibility at optical frequencies.

The optical-frequency permittivity tensor $\varepsilon_{ij}(\omega, \mathbf{B}, \mathbf{k})$ of noncentrosymmetric diamagnets and paramagnets can have a Hermitian symmetric component bilinear in the external magnetic field **B** and the wave vector of light **k**: $\delta\varepsilon_{ij} = \gamma_{ijkl}B_k k_1$ [1, 2]. This component describes the phenomena of magnetic-field-induced spatial dispersion, one of which is the nonreciprocal (gyrotropic) birefringence of light. Nonreciprocal birefringence (NB) has been observed to date in the β-$LiIO_3$ diamagnet (symmetry class C_6) [3]; $Cd_{1-x}Mn_xTe$ and $Zn_{1-x}Mn_xTe$ magnetic semiconductors [4, 5]; and CdS, CdSe (class C_{6v}) [6, 7], CdTe, ZnTe, and GaAs (class T_d) [8, 9] semiconductors. The microscopic mechanisms responsible for NB in conventional and magnetic semiconductors were considered in [4–10]. It was shown that the large NB observed near the band edge of the semiconductor crystals is primarily due to the contributions, linear and bilinear in **B** and **k**, to the dispersion of the conduction band and the valence bands between which virtual optical transitions take place (the interband mechanism) or to the exciton-branch dispersion (the exciton mechanism). Obviously enough, these mechanisms do not operate in the cases where the NB originates from local optical rather than interband or exciton transitions, i.e., where the excitation is localized on an ion and cannot propagate over the crystal. This may be expected to occur, for instance, with the optical *d–d* transitions in transition-metal ions or the *f–f* transitions in rare-earth ions. NB has recently been observed [11] in the $Co_3B_7O_{13}I$ boracite (class T_d) in the energy region $E \sim$ 2.1 eV (E is the photon energy) corresponding to the optical transition $^4A_2(^4F) \longrightarrow {}^4E(^4P)$ within the 3*d* shell of the Co^{2+} ion. In this spectral region, the NB has a resonant character with an S-shaped dispersion. In the case of local optical transitions, the NB microscopic mechanisms can be associated with (i) the second-order magnetoelectric susceptibility at optical frequencies (the magnetoelectric mechanism) and (ii) the quadrupole moment induced by the electric field of light in the presence of a magnetic field **B** (the quadrupole mechanism) [11]. The second-order magnetoelectric susceptibility describes the magnetic moment $\delta\mathbf{M}^\omega$ and the electrical polarization $\delta\mathbf{P}^\omega$ that are induced by the electric $\mathbf{E}^\omega$ and magnetic $\mathbf{H}^\omega$ fields of the light wave, respectively, and oscillate at the light frequency ω in phase with the respective $\mathbf{E}^\omega$ and $\mathbf{H}^\omega$ fields. The induced magnetic moment can occur in noncentrosymmetric crystals placed in an external magnetic field **B** and is described by a third-rank polar i-tensor $G_{ijk}(\omega)$: $\delta M_i^\omega = G_{ijk}(\omega)E_j^\omega B_k$. Because the magnetic moment is an axial c vector, it cannot be induced by an electric field in centrosymmetric crystals in the absence of a magnetic field. The quadrupole moment Q_{ij}^ω that is induced by a field $\mathbf{E}^\omega$ in the presence of an external magnetic field **B** and is responsible for the NB oscillates with a 90°-phase shift relative to the $\mathbf{E}^\omega$ field and is described by a fourth-rank tensor $a'_{ijkl}(\omega)$: $Q_{ij}^\omega = (1/\omega)a'_{ijkl}(\omega)\dot{E}_k^\omega B_1$. Both mechanisms can contribute to the γ_{ijkl} tensor and determine the magnitude and relation between the A and g parameters of this tensor in the symmetry class T_d. As is shown in [11], in this class, the magnetoelectric mechanism results in an exact relation $A = 2g$ between the parameters, while the quadrupole mechanism, which is described by a higher rank tensor, does not relate these parameters. The experimental value $A/g = 1.9$ obtained for $Co_3B_7O_{13}I$ suggests that the NB in this crystal is due primarily to the magnetoelectric mechanism [11]. Nevertheless, direct evidence for the operation of this mechanism was lacking, because, in principle, the $A/g = 2$ relation, as well as any other relation of this kind, is not forbidden for the quadrupole

Table 1. Ferroelectric phase transition temperature T_C, the temperature of the transition to the magnetically ordered state T_N, and the Curie temperature T_C^m for the boracites studied [14]

	CoI	CuBr	NiBr
T_C, K	200	224	398
T_N, K	38	24	40
T_C^m, K	–80	–47	–31

mechanism. A rigorous proof of the magnetoelectric mechanism being dominant can be based on the fact that the $A = 2g$ relation (in the T_d class) for this mechanism follows from symmetry considerations alone and, therefore, must hold for any 3*d* ion and any optical transition in these ions. The objective of this work was an experimental investigation of the field and angular dependences of the NB in boracites with different 3*d* ions and the determination of the relation between *A* and *g*.

1. EXPERIMENT

The method used to determine the *A* and *g* parameters for class-T_d crystals is described in [4, 5]. The *A* and *g* parameters were found by analyzing the angular dependences of NB with light propagating along the [110]-type crystallographic direction and magnetic field **B** lying in a (110)-type plane perpendicular to this direction. We measured the field dependences of the angle of turn α of the plane of the polarization for light which has passed through a crystal placed in a magnetic field and a $\lambda/4$ plate for different angles θ between the magnetic field and the [001]-type crystallographic direction. The NB accounts for the $\alpha(B)$ dependences linear in the magnetic field, with the magnitude and sign of $d\alpha/dB$ depending on the θ angle. The experiments were carried out in the **E** || **B** geometry (the magnetic field **B** is oriented parallel to the incident-light polarization **E**) and for **E**45**B**, a geometry in which the angle between **E** and **B** was 45°. In both cases, the principal direction of the $\lambda/4$ plate was parallel to **E**. As is shown in [4, 5], in the first case the $d\alpha/dB(\theta)$ relations have the form $a\cos\theta + b\cos 3\theta$ and, in the second, $a'\sin\theta + b'\sin 3\theta$. The *A* and *g* parameters could be derived from the $d\alpha/dB(\theta)$ angular relations to within ~10%. In this work, we studied NB in the boracites $Co_3B_7O_{13}I$, $Cu_3B_7O_{13}Br$, and $Ni_3B_7O_{13}Br$ at a wavelength $\lambda = 633$ nm. The sensitivity to the angle of turn of the polarization plane was $\delta\alpha \approx 10''$. The measurements were carried out in fields of up to ±1.5 T within the temperature range of 294–470 K.

The boracite family includes crystals with a general formula $R_3B_7O_{13}X$, where *R* stands for the ion of a divalent metal and *X* stands for the halogen ion. For $T > T_C$ (T_C is the Curie temperature), in the paraelectric state, their structure is described by the space group T_d^5 and the point-symmetry class T_d [12, 13]. The metal ions occupy 24 *c*-positions of point symmetry S_4 in the unit cell. The nearest neighbor environment of R^{2+} is a distorted octahedron formed by two halogen ions X^- and four oxygen ions O^{2-}. The oxygen ions on the square diagonals are displaced from the basal plane along the *z* axis by $\pm\delta$, so that the point symmetry of the complex is D_{2d}. At $T < T_C$, a first-order phase transition to the ferroelectric state occurs in the boracites. The crystal symmetry lowers to C_{2v}^5 [12, 13]. At $T < T_N$, the boracites undergo a transition to an antiferromagnetic state with weak ferromagnetism [14]. The Curie temperature T_C of the ferroelectric transition, the point of transition to the magnetically ordered state T_N, and the corresponding Curie magnetic temperature T_C^m are given in Table 1 for the crystals studied in this work. The magnetic and magnetoelectric properties of the boracites were investigated in [14, 15]. Their absorption spectra were studied in [16, 17]. In the 0.3–3-eV region, these spectra consist of several bands of different intensities, which are due to transitions within the 3*d* shell of the metal ions. The positions of the strongest absorption bands lying near $E = 1.96$ eV ($\lambda = 633$ nm), the absorption coefficient at the maximum, α^m, and the transition assignments for the boracites under study are listed in Table 2.

Table 2. Position of some absorption bands E_0, the maximum absorption coefficient α^m, and the type of transition in the boracites studied [16, 17]

Boracite	CoI	CuBr	NiBr
Transition	$^4A_2(^4F) \longrightarrow {}^4E(^4P)$	$^2B_1(^2D) \longrightarrow {}^2E(^2D)$	$^3A_2(^3F) \longrightarrow {}^3E^b(^3P)$
E_0, eV	2.1	1.5	2.9
α^m, cm^{-1}	1400	3000	2500
Transition	$^4A_2(^4F) \longrightarrow {}^4A_2(^4P)$	$^2B_1(^2D) \longrightarrow {}^2B_2(^2D)$	$^3A_2(^3F) \longrightarrow {}^3E^a(^3F)$
E_0, eV	2.7	1.2	1.5
α^m, cm^{-1}	1300	2500	600

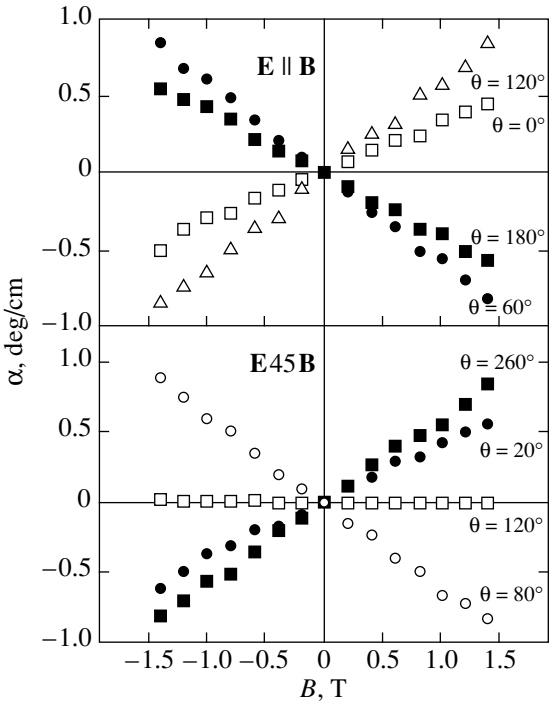

Fig. 1. Field dependences $\alpha(B)$ obtained for $Cu_3B_7O_{13}Br$ in (a) the **E** ∥ **B** and (b) the **E**45**B** geometries at different θ angles.

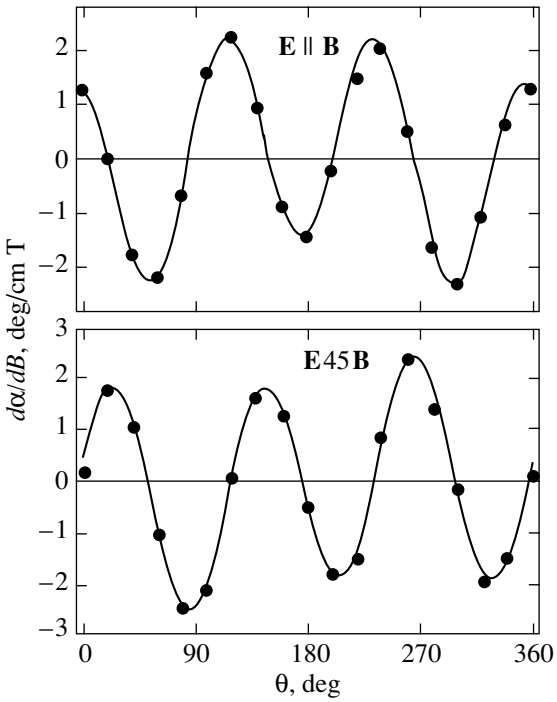

Fig. 2. Angular dependences of $d\alpha/dB$ in the CoI boracite obtained in the **E** ∥ **B** and **E**45**B** geometries.

The boracite platelet samples measuring 2 × 2 mm were cut of boules grown by the method described in [18]. The platelet thickness was $d \approx 90$ μm for the CoI boracite, ≈800 μm for the CuBr boracite, and ≈900 μm for the NiBr boracite. The samples were ground and polished with a diamond abrasive. The samples were oriented using x-ray diffraction patterns and boule faceting. The spontaneous birefringence associated with the growth-induced strains and defects was $\Delta n = 6.7 \times 10^{-6}$, 7.0×10^{-6}, and 1.2×10^{-5} for the CoI, CuBr, and NiBr boracites, respectively, and did not affect the $\alpha(B)$ relations. For comparison, the Faraday effect was measured on all samples. The Faraday effect measurements were conducted in a longitudinal magnetic field of ±0.05 T.

2. RESULTS OF THE EXPERIMENT

All the boracites studied exhibited linear $\alpha(B)$ dependences in the **E** ∥ **B** and **E**45**B** geometries. The nonreciprocity of the induced birefringence was verified by turning the crystal around an axis parallel to **B** and an axis perpendicular to **B** and **k**. Figure 1 presents field dependences $\alpha(B)$ obtained in both geometries for the CuBr boracite. Figures 2 and 3 display angular dependences $d\alpha/dB(\theta)$ for the CoI and CuBr boracites obtained in the (110)-type plane in the **E** ∥ **B** and **E**45**B** geometries. In accordance with theory, the angular dependences are described by first- and third-order harmonics. The $d\alpha/dB$ function exhibits extrema at $\theta = N \times 60°$ ($N = 0, \ldots, 5$) in the **E** ∥ **B** geometry and at $\theta = 30° + N \times 60°$ in the **E**45**B** geometry. We may recall that the $d\alpha/dB$ function obtained in the **E** ∥ **B** geometry at θ = 0° is determined by the g parameter alone and, for **E**45**B** at θ = 90°, by the combination $3A + 2g$ [4, 5].

In all the CoI boracite samples studied in this work, the NB was found to be in agreement with the results of [11] both in magnitude and in the character of anisotropy. As is seen from Figs. 2 and 3, the value of the NB in CuBr is smaller than that in the CoI boracite. In the CoI boracite, the extremum values are $d\alpha/dB \approx 2°$/cm T, while in the CuBr boracite, they are $d\alpha/dB \approx 0.6°$/cm T. Nevertheless, the character of anisotropy, i.e., the relation between the values of $d\alpha/dB$ at the angles θ = 0°, 180° and θ = 60°, 120° in the **E** ∥ **B** geometry, as well as at θ = 90°, 270° and θ = 30°, 150° in the **E**45**B** geometry, is the same for the two boracites.

Figure 4 presents the angular dependences of $d\alpha/dB$ obtained for the NiBr boracite at $T = 450$ K. The NB found for this boracite, $d\alpha/dB \approx 0.2°$/cm T, is substantially smaller than that for the CoI and CuBr boracites. Nevertheless, as can be seen from Fig. 4, the anisotropy of NB in the NiBr boracite has the same character. Thus, the relations shown in Figs. 2–4 indicate that while the magnitude of the NB depends substantially on the type of the 3d ion in the boracite structure, the NB anisotropy in crystals with different metal and halogen ions is the same.

Note that the $\alpha(B)$ dependences measured in the **E**45**B** geometry are linear in all the crystals studied. This implies that the NB at the wavelength used is sub-

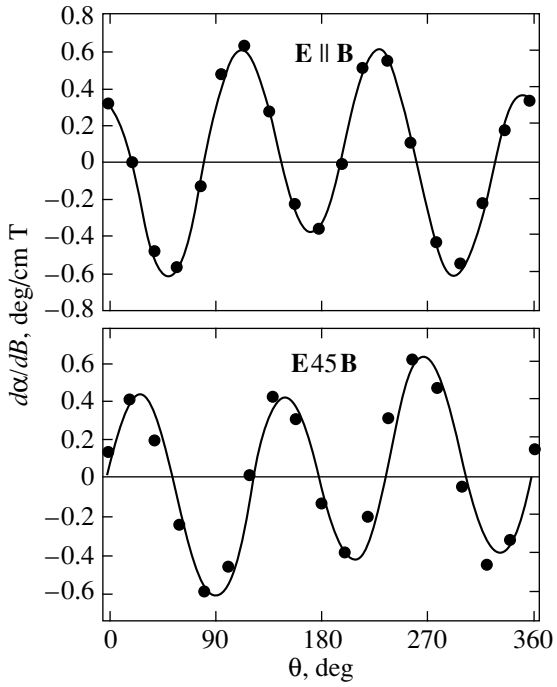

Fig. 3. Angular dependences of $d\alpha/dB$ in the CuBr boracite obtained in the **E** ∥ **B** and **E**45**B** geometries.

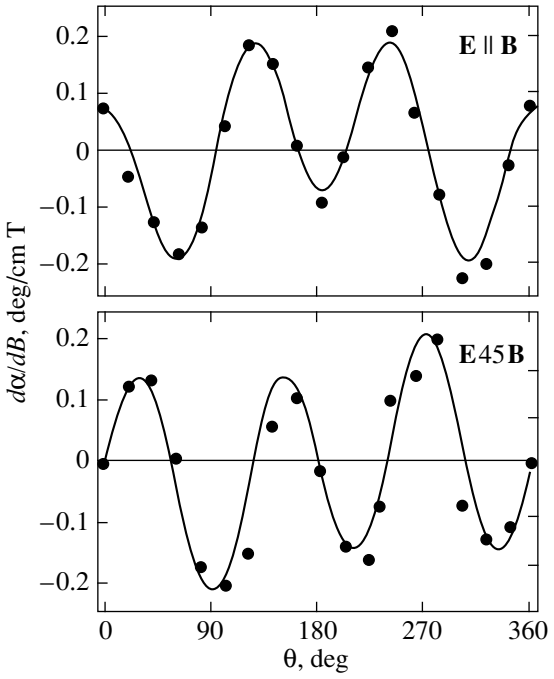

Fig. 4. Angular dependences of $d\alpha/dB$ in the NiBr boracite obtained in the **E** ∥ **B** and **E**45**B** geometries at T = 450 K.

stantially larger than the birefringence associated with the Cotton–Mouton effect, which is quadratic in a magnetic field. Thus, the magnetooptic properties of boracites in their transparency region are determined by two nonreciprocal phenomena, namely, the Faraday effect and the nonreciprocal birefringence.

3. DISCUSSION OF RESULTS

The NB angular dependences were analyzed to determine the A and g parameters of the γ_{ijkl} tensor. The refractive index used in the calculations was n = 1.9. Table 3 lists the maximum values of the NB (obtained at θ = 90° in the **E**45**B** geometry), the A and g parameters, their ratio, and the Verdet constant for the crystals studied. As can be seen from Table 3, the values of the NB and of the Faraday effect do not correlate. Indeed, the magnitude of NB in the CoI boracite is an order of magnitude larger than that for the NiBr boracite, whereas the magnitude of the Faraday effect in these crystals differs by about a factor three. The magnitude of the Faraday effect in the CuBr boracite is nearly 40 times smaller than that for the CoI boracite and an order of magnitude smaller than that in the NiBr boracite. By contrast, the NB in the CuBr boracite is only four times smaller than that in the CoI boracite and three times that in the NiBr boracite. The absence of a correlation is evidence that the microscopic mechanisms of these phenomena are different. The Faraday effect is known to be due to the magnetic-field-induced splitting of energy levels and to be associated with optical-transition matrix elements of the $\mathrm{Im}(d^i_{ab}\, d^j_{ba})$ type, where **d** is the transition dipole-moment operator and $|a\rangle$ and $|b\rangle$ are the wave functions of the ground and excited states [19, 20]. While the NB is also connected with the level splitting induced by a magnetic field, the matrix elements involved are of another kind, namely, $\mathrm{Re}(d^i_{ab}\, m^j_{ba})$ in the case of the magnetoelectric mechanism and $\mathrm{Im}(d^i_{ab}\, Q^{jk}_{ba})$ for the quadrupole mechanism [11], where **m** is the magnetic-moment operator and Q^{ik} is the quadrupole moment operator. Because the parameter ratio A/g = 2 (Table 3) holds for different 3d ions having different electronic configurations, namely, $Co^{2+}(3d^7)$, $Ni^{2+}(3d^8)$, and $Cu^{2+}(3d^9)$, it is the magnetoelectric mechanism that accounts primarily for the NB.

Table 3. Maximum value of $d\alpha/dB$, the A and g parameters, the A/g ratio, and the Verdet constant V at the wavelength λ = 633 nm in the boracites studied

Boracite	CoI	CuBr	NiBr
$d\alpha/dB$, deg/cm T	2.5	0.62	0.2
A, 10^{-8} μm/T	16.6	4.2	1.35
g, 10^{-8} μm/T	8.7	2.2	0.67
A/g	1.9	1.9	2.0
V, deg/cm T	8.1	–2.3	27.4

As is shown in [11], the NB due to the second-order magnetoelectric susceptibility at optical frequencies can be written as

$$\partial\alpha/\partial B = N\sum_{b,\,ijt}\mathrm{Re}(d^i_{a_t b_t} m^j_{b_t a_y}) \times Z_{ab}\omega_{ab}\mu_B g_t/k(T - T^m_C), \quad (1)$$

where N is a parameter depending on the number of 3d ions per unit volume and on the angle f between the X, Y, and Z crystallographic axes and the local axes x, y, and z of the oxygen–halogen octahedron, respectively ($f \sim 24°$); $Z_{ab} = (\omega^2_{ab} - \omega^2)/[(\omega^2_{ab} - \omega^2)^2 + \Gamma^2_{ab}\omega^2]$, ω_{ab} is the resonant frequency of the optical transition, Γ_{ab} is the damping parameter, and g_t is the ground-state g factor for the magnetic field **B** aligned with the octahedron local axis **t**(x, y, z); $|a_t\rangle$ and $|b_t\rangle$ are the ground- and excited-state wave functions for **B** || **t**; μ_B is the Bohr magneton; and k is the Boltzmann constant. Because the local environment of the 3d ions in boracites has D_{2d} symmetry, the magnetoelectric tensor $G_{ijk}(\omega)$ has three independent components and the indices ijk take on the values yzx, zxy, and xyz. Let us use Eq. (1) to compare the matrix elements $\mathrm{Re}(d^i_{ab}\, m^j_{ba})$ for different optical transitions as calculated in the single-oscillator model. To do this, we assume that the ND at the wavelength λ = 633 nm is determined by the strong absorption band closest to this wavelength. In the case of the CoI boracite, this is the $^4A_2(^4F) \longrightarrow {}^4E(^4P)$ transition at E_0 = 2.1 eV, while for the CuBr boracite, it is $^2B_1(^2D) \longrightarrow {}^2E(^2D)$ at E_0 = 1.5 eV, and for the NiBr boracite, it is $^3A_2(^3F) \longrightarrow {}^3E^b(^3P)$ at E_0 = 2.9 eV (Table 2). The Γ_{ab} parameter can be estimated from the absorption spectra [16, 17] to be ~0.1 eV. We also neglect the g-factor anisotropy, i.e., replace g_t in Eq. (1) by $g = (g_\perp + g_\parallel)/2$, and introduce the notation $\mathrm{Re}(d_{ab}m_{ba}) \equiv \mathrm{Re}(d^y_{a_x b_x} m^z_{b_x a_x} + d^z_{a_y b_y} m^x_{b_y a_y} + d^x_{a_z b_z} m^y_{b_z a_z})$. The ground-state g factor of the Co^{2+} ion is g = 4.2 and that of the Cu^{2+} and Ni^{2+} ions is g = 2.2 [21, 22]. Substituting these figures, as well as the values of $d\alpha/dB$ (Table 3) and of T^m_C (Table 1), in Eq. (1) shows that the value of $\mathrm{Re}(d^i_{ab}m^j_{ba})$ for the transition responsible for the NB in the CuBr boracite is 1.8 times larger than that for the CoI boracite, while in the NiI boracite it is 0.8 of this value. The above rough estimation suggests that while the matrix elements $\mathrm{Re}(d^i_{ab}m^j_{ba})$ for different optical transitions may differ by a few times, they are nevertheless of the same order of magnitude. More precise information on the magnitude and sign of the $\mathrm{Re}(d^i_{ab}m^j_{ba})$ matrix elements can be derived from spectral measurements of the NB or of the nonreciprocal linear dichroism.

Thus, the main mechanism accounting for the NB magnitude and its anisotropy in the boracites is the manifestation of the second-order magnetoelectric susceptibility at optical frequencies. The magnitude and sign of the magnetoelectric susceptibility is determined by the optical-transition matrix elements $\mathrm{Re}(d^i_{ab}m^j_{ba})$, which can be derived from spectral measurements of the NB or the nonreciprocal linear dichroism. The magnitude of the NB in the boracites, ~2°/cm T, is comparable to that observed in conventional and magnetic semiconductors near the band edge [4, 5, 9] and can readily be measured by present-day polarimetric techniques. Note that the value of NB obtained in this work for the CuBr boracite, $d\alpha/dB$ = 0.6°/cm T, is only four times smaller than the magnitude of the Faraday effect (V = 2.4°/cm T). The absence of a correlation between the values of the NB and of the Faraday effect in different boracites indicates that these phenomena have radically different dispersions. This implies, in turn, a different relation (both in magnitude and sign) between the $\mathrm{Im}(d^i_{ab}d^j_{ba})$ and $\mathrm{Re}(d^i_{ab}m^j_{ba})$-type matrix elements for different optical transitions that occur in the 3d shell of the metal ions.

ACKNOWLEDGMENTS

The author is indebted to V.N. Gridnev for fruitful discussions, to G.T. Andreeva for providing the boracite single crystals, and to N.F. Kartenko for x-ray diffraction measurements.

This work was supported by the Russian Foundation for Basic Research (grant no. 99-02-18028) and the "Fundamental Spectroscopy" program.

REFERENCES

1. D. L. Portigal and E. J. Burstein, Phys. Chem. Solids **32** (3), 603 (1968).
2. V. M. Agranovich and V. L. Ginzburg, *Crystal Optics with Spatial Dispersion and Excitons* (Nauka, Moscow, 1979; Springer-Verlag, New York, 1984).
3. V. A. Markelov, M. A. Novikov, and A. A. Turkin, Pis'ma Zh. Éksp. Teor. Fiz. **25** (6), 406 (1977) [JETP Lett. **25**, 378 (1977)].
4. B. B. Krichevtsov, R. V. Pisarev, A. A. Rzhevsky, *et al.*, Phys. Rev. B **57** (3), 14611 (1998).
5. B. B. Krichevtsov, R. V. Pisarev, A. A. Rzhevskiĭ, *et al.*, Zh. Éksp. Teor. Fiz. **114** (3), 1018 (1998) [JETP **87**, 553 (1998)].
6. E. L. Ivchenko, V. P. Kochereshko, G. V. Mikhaĭlov, and I. N. Ural'tsev, Pis'ma Zh. Éksp. Teor. Fiz. **37**, 164 (1983) [JETP Lett. **37**, 164 (1983)]; Phys. Status Solidi B **121**, 221 (1984).
7. V. P. Kochereshko, G. V. Mikhaĭlov, and I. N. Ural'tsev, Fiz. Tverd. Tela (Leningrad) **25**, 769 (1983) [Sov. Phys. Solid State **25**, 439 (1983)].

8. O. V. Gogolin, V. A. Tsvetkov, and E. G. Tsitsishvili, Zh. Éksp. Teor. Fiz. **87** (3), 1038 (1984) [Sov. Phys. JETP **60**, 593 (1984)].
9. B. B. Krichevtsov, R. V. Pisarev, A. A. Rzhevskiĭ, and H.-J. Weber, Pis'ma Zh. Éksp. Teor. Fiz. **69** (7), 514 (1999) [JETP Lett. **69**, 551 (1999)].
10. E. G. Tsitsishvili, Fiz. Tekh. Poluprovodn. (Leningrad) **20** (4), 650 (1986) [Sov. Phys. Semicond. **20**, 412 (1986)].
11. B. B. Krichevtsov, A. A. Rzhevsky, and H.-J. Weber, Phys. Rev. B **61** (15), 10084 (2000).
12. R. J. Nelmes, J. Phys. C **7** (9), 3840 (1974).
13. R. J. Nelmes and F. R. Thornley, J. Phys. C **7** (9), 3855 (1974).
14. G. Quezel and H. Schmid, Solid State Commun. **6** (7), 447 (1968).
15. M. Clin, J.-P. Rivera, and H. Schmid, Ferroelectrics **108**, 213 (1990).
16. R. V. Pisarev, V. V. Druzhinin, S. D. Prochorova, *et al.*, Phys. Status Solidi **35** (1), 145 (1969).
17. N. N. Nesterova, Candidate's Dissertation (Leningrad, 1974).
18. H. Schmid and H. Tippman, J. Cryst. Growth **46**, 723 (1979).
19. L. D. Barron, *Molecular Light Scattering and Optical Activity* (Cambridge Univ. Press, Cambridge, 1980).
20. A. K. Zvezdin and V. A. Kotov, *Modern Magnetooptics and Magnetooptical Materials* (Inst. of Physics Publ., Bristol, 1997).
21. W. Low, *Paramagnetic Resonance in Solids* (Academic, New York, 1960; Inostrannaya Literatura, Moscow, 1961).
22. M. P. Petrov, S. A. Kizhaev, G. T. Andreeva, and G. A. Smolensky, J. Phys. Soc. Jpn. **28**, S128 (1970).

Translated by G. Skrebtsov

Physics of the Solid State, Vol. 43, No. 1, 2001, pp. 82–89. Translated from Fizika Tverdogo Tela, Vol. 43, No. 1, 2001, pp. 80–87.

MAGNETISM AND FERROELECTRICITY

Thermodynamics and Kinetics of the Initial Stages of Polarization Switching in Ferroelectrics

S. A. Kukushkin and A. V. Osipov

Institute of Problems in Mechanical Engineering, Russian Academy of Sciences, Vasil'evskiĭ ostrov, Bol'shoĭ pr. 61, St. Petersburg, 199178 Russia
e-mail: ksa@math.ipme.ru

Received March 28, 2000; in final form, May 25, 2000

Abstract—The thermodynamics and kinetics of polarization switching in ferroelectrics are studied in the specific case of switching in intrinsic ferroelectrics with 180° domains. The initial stage of the switching in the region of weak metastability is analyzed. An expression relating the critical domain size to the switching field is derived. An equation describing the evolution of the size distribution function of the switched domains is obtained. Expressions for calculating the number of polarization switching nuclei as a function of the switching field are derived. *© 2001 MAIK "Nauka/Interperiodica".*

1. INTRODUCTION

Ferroelectric crystals and films are widely employed as storage cells in integrated electronic devices and other areas of technology [1]. The most essential property of these structures is their ability to reverse the direction of polarization. As a result, a switching current appears. Multiple switchings caused by alternating pulses bring about a decrease in the switched charge in these systems and, as a consequence, a decrease in the switching current [1–6]. The switching phenomenon in ferroelectrics is intensively investigated, both theoretically [6–9] and experimentally [2–5]. For instance, the review by Scott [1] contains a generalized analysis of these studies and a review of microscopic studies of the structural evolution of domains formed in the course of switching is given in [5].

There are presently two main approaches to the description of switching kinetics. Both approaches are based on the idea that the switching processes are first-order phase transitions, which result in the nucleation of regions (domains) with the polarization opposite to the previous one in the bulk of the ferroelectric. Within the first approach [1], the parameters determining the time dependence of the current represent a set of empirical fitting quantities. In the second approach [2–4, 6], the corresponding parameters are expressed in terms of the parameters of the Kolmogorov–Avrami model [10, 11], which is widely used in describing the degree of volume filling by growing crystals. Attempts are presently being made to improve the second approach. In particular, allowances are made for the effects associated with the ferroelectric samples being of a finite size [4], etc.

However, despite all the efforts of the researchers, progress in understanding the switching process is presently lacking. In our opinion, this is associated with the fact that the Kolmogorov–Avrami model is a purely geometric model. The equations used in this model contain parameters such as the nucleation rate of the domains and the rate of their growth. These quantities are not defined within the Kolmogorov–Avrami model and should be found from thermodynamics and kinetic theory. The researchers engaged in the growth of crystals and films from vapor, solutions, or melts were faced with the same problems [12–14], and the Kolmogorov–Avrami model was the first to be used in describing the growth of crystals and films.

Presently, the rigorous kinetic theory of first-order phase transitions is available and its results are summed up in [12, 14]. It was shown [12, 14] that the first-order phase transitions are complex multistage processes accompanied by various nonlinear phenomena. The theory developed in [12–14] permits one to treat the rich diversity of the processes involved within a unified approach and to calculate all the most important characteristics of a phase transition (the rate of nucleation of the new phase, the nucleus growth rate, the evolution of the nucleus size distribution function, the degree of filling the sample volume with nuclei, the interface structure, etc.). It is the latter approach that we will use to describe the switching processes in ferroelectrics in an electric field. The consideration will be exemplified by an intrinsic ferroelectric crystal with 180° domains.

2. THERMODYNAMICS OF SWITCHING

Let us consider a ferroelectric crystal residing in a completely ordered state at a temperature below the Curie point and representing a plate of thickness L placed between the plates of a capacitor. The polarization axis is directed along the z axis. We assume that the dielectric properties of the crystal along the x and y axes

have no anomalies. This means that when considering the thermodynamic properties of such a ferroelectric, it is sufficient to include only the z component of the polarization vector P_z in the thermodynamic potential. We impose an external electric field on the ferroelectric. According to [15, 16], the thermodynamic potential of a ferroelectric in an electric field at a temperature near the Curie point can be represented as

$$\tilde{\Phi} = \Phi_0(p, T) + a(T - T_C)P_z^2 + bP_z^4 - E_zP_z - \frac{\varepsilon_0 E_z^2}{2}, \quad (1)$$

where Φ_0 is the part of the thermodynamic potential which does not depend on the degree of polarization, p and T are the pressure and temperature of the medium in which the crystal resides, E_z is the z component of the electric field, T_C is the Curie temperature, a and b are the coefficients of the thermodynamic potential expansion in powers of P_z, and ε_0 is the permittivity of free space.

We are not interested in the behavior of crystals at temperatures $T > T_C$. Consider the temperature region $T < T_C$. Differentiating Eq. (1) at the constant E_z yields the following equation:

$$2a(T - T_C)P_z + 4bP_z^3 = E_z, \quad (2)$$

which relates the field strength to the polarization of the ferroelectric [15, 16]. The form of the function $E_z(P_z)$ described by Eq. (2) is shown in Fig. 1.

If $T < T_C$, the value $P_z = 0$ cannot correspond to the stationary state of the ferroelectric. For $E_z = 0$, spontaneous polarization of the pyroelectric phase sets in. Then,

$$P_{z1,\,20} = \pm\sqrt{\frac{2a(T_C - T)}{2b}}, \quad (3)$$

where P_{z10} and P_{z20} are the equilibrium values of the polarization.

Expression (3) allows one to draw a curve describing equilibrium states in a ferroelectric with the polarization oriented along and opposite to the z axis direction. The curve describing the equilibrium state of phases is called the binodal. Figure 2 shows a binodal bounding the region of the two-phase state of a ferroelectric with up and down polarizations. To determine the boundaries of the metastability region, we have to find the derivative $(\partial E_z/\partial P_z)_T$ and equate it to zero:

$$P_{1,\,2s} = \pm\sqrt{\frac{a(T_C - T)}{6b}}. \quad (4)$$

The curve bounding the metastability region is called the spinodal; it is shown in Fig. 2.

The most important characteristic of the first-order phase transitions is the quantity called the supersaturation [12–14]. In describing the switching processes, we can introduce a similar quantity

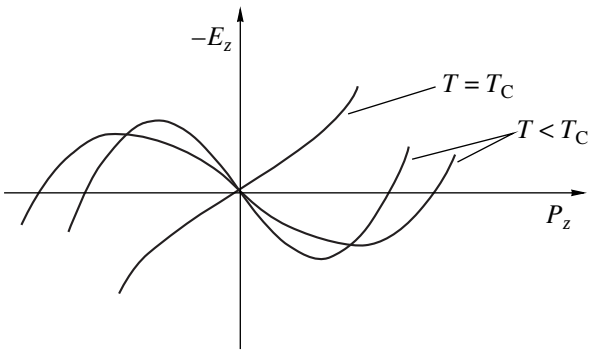

Fig. 1. The $E_z(P_z)$ function [a plot of Eq. (2)].

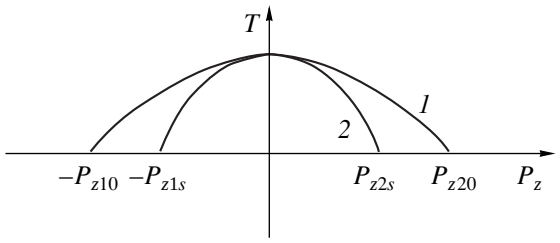

Fig. 2. (*1*) The phase equilibrium curve of a ferroelectric with states at the "up" polarization (P_z) and "down" polarization ($-P_z$); $P_{z1,\,20}$ are the equilibrium values of the polarization. (*2*) The curve (spinodal) bounding the regions within which the polarization of a ferroelectric cannot be uniform in any conditions; $P_{z1,\,2s}$ are the boundaries of the metastability region.

$$\xi = \frac{|P_z|}{|P_{z10}|} - 1 = \frac{|P_z| - |P_{z10}|}{|P_{z10}|}. \quad (5)$$

We will call it the relative repolarization and $\Delta = P_z - P_{z10}$, the repolarization. In rather weak fields, the polarization $P_z = P_{z10} + \chi\varepsilon_0 E_z$ [15, 16], where χ is the permittivity. Substituting the last expression in Eq. (5) and then in the relationship for ΔP yields

$$\xi = \frac{\chi\varepsilon_0 E_z}{P_{z10}}, \quad (6)$$

$$\Delta P = \chi\varepsilon_0 E_z. \quad (7)$$

Recasting formula (7) as $\Delta P/\chi\varepsilon_0 = E_z$, we obtain the relationship for the repolarization as a function of an electric field. Thus, the electric field strength in ferroelectrics in the switching processes is an analog of the supersaturation or supercooling in conventional phase transitions. Because, according to [15, 16], $\chi = 4a(T_C - T)^{-1}$ at $T < T_C$, from Eq. (7), it follows that at $T \longrightarrow T_C$, the increase in χ is accompanied by an increase in repolarization.

The quantity $\xi_{max} = |P_{z1s}|/|P_{z10}| - 1$ has the meaning of the maximum possible repolarization. For $\xi > \xi_{max}$,

the initial orientation of the ferroelectric phase becomes completely unstable and spontaneous polarization switching of the ferroelectric starts.

3. SWITCHING KINETICS AND NUCLEATION OF SWITCHED REGIONS

The most general method for studying phase transitions is the field theory [12, 17], which allows one to describe first-order phase transitions within a unified approach. In this approach, it is inessential whether the system undergoing the transition is in the region of strong or weak metastability. Nevertheless, using this method requires knowledge of the equation of state of the system. If the equation of state is unknown, it can be found in an approximate way by using the Landau expansion for the thermodynamic potential. This expansion (and the equation of state) is valid, as is well known, only in the vicinity of the second-order phase transition, which narrows substantially the region of its applicability. The classical theory makes use of such a phenomenological parameter as surface tension, but it does not permit calculation of the interface structure. At the same time, the structure of the interface can be calculated in terms of the field theory. In our study of first-order phase transitions in ferroelectrics, we will use both the field approach and the classical theory of nucleation, because the equation of state (2) is known only in the vicinity of the Curie point. At the same time, we are interested in a description of phase transitions throughout the region of variations in the thermodynamic parameters. We consider first the switching processes in the region of weak metastability.

4. KINETICS OF THE INITIAL STAGE OF SWITCHING IN THE REGION OF WEAK METASTABILITY

Recall that the polarization P_z used above is defined in the following way [16]:

$$P_z = \frac{1}{\omega}\sum_i e_i r_{zi},$$

where ω is the unit cell volume of the crystal, $p_{zi} = \sum_i e_i r_{zi}$ is the dipole moment of the unit cell in the point-charge approximation, e_i is the charge of the ith ion, and r_{zi} is the z component of the ith charge position vector. From this,

$$p_{zi} = P_z\omega. \tag{8}$$

We assume the elementary structural units of domains to be crystal unit cells with the dipole moment p_{iz}. The number of unit cells in a domain of volume V_d is

$$n = \frac{V_d}{\omega},$$

and for the polarization of this domain, we have

$$P_{zn} = p_{zi}n. \tag{9}$$

We introduce the distribution function $f(n, t)$ of domains in the number of unit cells they contain, which is normalized against the number of domains $N(t)$ per unit volume of the crystal; that is,

$$N(t) = \int_0^\infty f(n, t)dt.$$

We can change over from $f(n, t)$ to the distribution function of domains in the degree of polarization $f(P_{zn}, t)$ by using the relationship $f(n, t)dn = f(P_{zn}, t)dP_{zn}$ and Eq. (9).

According to the classical theory of nucleation [12–14, 18], the kinetic equation describing the process of new phase nucleation can be cast in the form

$$\frac{\partial f}{\partial t} = I_{n-1} - I_n, \tag{10}$$

where $f(n, t)$ is the distribution function of the switched domains in the number of unit cells they contain, I_{n-1} is the flux of new phase nuclei transferring from size $n-1$ to size n, and I_n is the flux of the new phase nuclei transferring from size n to size $n-1$. Hence, it follows that

$$I_{n-1} = W_{n-1,n}f(n-1, t) - W_{n,n-1}f(n, t),$$
$$I_n = W_{n,n+1}f(n, t) - W_{n+1,n}f(n+1, t).$$

Here, $W_{n-1,n}$, $W_{n,n-1}$, and $W_{n,n+1}$ are the transition probabilities of the nuclei moving from the state with a particular number of unit cells to another. Depending on the actual size of the switching nuclei, they can be divided in two classes: nuclei with $n < n_c$ and those with $n > n_c$, where n_c characterizes the nucleus of a critical size which is in equilibrium with the medium. The nuclei with $n < n_c$ decay, because the medium is "underswitched" for them, and those with $n > n_c$ grow, because the medium is "overswitched." Such a size distribution of the nuclei is due to the existence of the interface energy between a nucleus with the polarization vector along the field and the medium with the oppositely directed polarization vector. In the region between the nucleus and the medium, the polarization vector turns, which accounts for the creation of additional energy.

For $n \gg 1$, we can change over from the difference equation (10) to a differential one. In this case, we obtain

$$\frac{\partial f}{\partial t} = \frac{\partial}{\partial n}W_{n,n+1}\left[\frac{1}{k_B T}\frac{\partial R_{\min}}{\partial n}f(n, t) + \frac{\partial f}{\partial n}\right], \tag{11}$$

where $W_{n,n+1}$ is the diffusion coefficient of the switching nuclei in the size space, $R_{\min}(n)$ is the minimum work done by the system to create the nuclei, and $\partial R_{\min}/\partial n$ is the change in the minimum work due to a

change in the number of structural units in a domain at $n < n_c$.

The quantity $(W_{n,n+1}/k_BT)(\partial R_{min}/\partial n)$ is the growth rate of nuclei of size n, that is,

$$\frac{dn}{dt} = -W_{n,n+1}\frac{1}{k_BT}\frac{\partial R_{min}}{\partial n}, \quad (12)$$

and the quantity $W_{n,n+1}(\partial f/\partial n)$ describes a random walk of a nucleus in the size space.

By solving Eq. (11), we can determine the main characteristic of the switching process, namely, the distribution function $f(n, t)$, as well as the dependence of the number of domains created in the course of the switching, the variation in the domain mean size, and many other parameters of this process.

Any first-order phase transformation can be conventionally divided into a number of characteristic time stages [12, 13] to facilitate their analysis. In the initial stage, the system undergoing a phase transition does not feel that a new phase has already been formed and its thermodynamic parameters do not change. In the subsequent stages of the phase transformation, the thermodynamic parameters of the system vary and this becomes reflected in the nucleation.

In the initial stage of nucleation, it is sufficient to consider the steady-state equation (11) and to determine the stationary flux of the polarization switching nuclei. To find it, we should determine the coefficient $W_{n,n+1}$, the minimum work to be done to produce a nucleus $R_{min}(n_c)$, and the critical size of the polarization switching nucleus n_c. These quantities can be found in two equivalent approaches. The first of them is the classical approach [18], which requires knowledge of the equilibrium distribution function for the determination of the nucleus flux. The second approach, which was developed in [19], makes use of certain relationships between the coefficients of absorption, $W_{n,n+1}$, and those of emission, $W_{n+1,n}$. They allow one to derive the expression for the stationary flux of nuclei without recourse to the equilibrium distribution functions. Both approaches yield the same result. We will employ the latter technique to calculate the polarization switching nucleus flux.

Thus, for nuclei with $n < n_c$, the distribution function $f(n) \sim \exp(-R(n)/k_BT)$ $(T < T_C)$ makes the left-hand side of Eq. (11) vanish; i.e., $\partial f/\partial t = 0$. This means that the transition probabilities $W_{n,n+1}$ and $W_{n+1,n}$, which change the nucleus size by one structural unit, are exactly the same as for heterophase fluctuations at equilibrium.

Using the approach developed in [19], we can obtain relationships between the absorption and emission coefficients which would be valid for all values of n. We consider an auxiliary ferroelectric crystal with a polarization at which a nucleus of size $n > n_c$ will be in equilibrium with the crystal. The auxiliary-ferroelectric–true ferroelectric system resides in a local thermodynamic equilibrium. Introduction of such an auxiliary system permits one to obtain the relationship

$$\frac{W_{n,n+1}}{W_{n+1,n}} = \begin{cases} \exp\left(\frac{-\tilde{R}_{min}}{k_BT}\right), & n < n_c \\ \exp\left(\frac{-\tilde{R}_{min}}{k_BT}\right), & n > n_c, \end{cases} \quad (13)$$

which is valid for all values of n.

Let us calculate the minimum work done to create a nucleus of the switched phase with polarization P_{zn} in a ferroelectric crystal. According to [20], the minimum work required to form a nucleus in a medium is $R_{min} = \Delta W + \Delta_0 W$, where ΔW is the total change in the nucleus energy and $\Delta_0 W$ is the change in the energy of the medium as a result of the nucleus formation. The quantities with the subscript zero refer to the medium, and those without a subscript, to the nucleus. We consider the quantity $\Delta_0 W$. As follows from thermodynamics, the change in the energy upon the reverse transition from one state to another can be represented in the form

$$\Delta_0 W' = -p_0\Delta_0 V + T_0\Delta_0 S + \mu_0\Delta_0 n. \quad (14)$$

In the case of a ferroelectric in an electric field, the work done by the electric forces should also be taken into account; that is,

$$\Delta_0 W = \Delta_0 W' + E_{z0}\Delta_0 D_{z0} = \Delta_0 W' + E_{z0}\Delta_0 P_{z0} + \Delta_0\left(\frac{\varepsilon_0 E_z^2}{2}\right). \quad (15)$$

In expression (14), p_0, T_0, and μ_0 are the pressure, temperature, and chemical potential of the medium, respectively; $\Delta_0 V$ and $\Delta_0 S$ are the corresponding changes in the volume and entropy of the medium; E_{z0} is the electric field strength in the medium; D_0 is the electric induction of the medium; and P_{z0} is the polarization of the medium. The quantity $\varepsilon_0 E_z^2/2$ is the work associated with electric-field generation between the capacitor plates. Because we investigate the internal field of a ferroelectric, this quantity will be disregarded and all parameters will be expressed in terms of the polarization rather than through induction. The minus sign before the work of the electric forces in Eq. (14) appears because the medium does the work required for a nucleus to form.

The pressure, volume, and temperature in the system remain fixed, and hence, $p_0 = p$, $T_0 = T$, $n_0 = n$, and $\Delta_0 V = -\Delta V$. For the change in entropy, we can write $\Delta S + \Delta_0 S = 0$. The polarization and field components in the medium and the nucleus are oppositely directed; i.e., $\Delta_0 P_{z0} = -\Delta P_z$ and $E_{z0} = -E_z$. Then, for $R_{min}(n)$, we obtain

$$R_{min}(n) = \Delta(W + p_0 V - T_0 S - E_{z0}P_z) - \mu_0 n. \quad (16)$$

Because the electric field in a nucleus of size n is E_{zn}, we can recast Eq. (16) in a more convenient form. In view of Eq. (15), we come to the relationship

$$R_{\min}(n) = \Delta(W + p_0V - T_0S - E_{zn}P_z) + (E_{zn} - E_{z0})P_z - \mu_0 n. \quad (17)$$

Now, we consider the nucleus energy W entering into Eq. (16). It consists of a volume part of the nucleus energy W_v and a surface part W_s. To calculate them, we have to know the nucleus shape. Unlike the nuclei forming in conventional phase transitions, the shape of the polarization switching nuclei cannot be arbitrary. This follows from the solution of Maxwell's equations for a dielectric [15, 16]. Indeed, as follows from the solution of Maxwell's equations, at the domain interface, the normal component of the electric induction vector is continuous, as is also the tangential component of the electric field **E**. This means that the interfaces separating the domains of the old and new phases should be parallel to the z axis. Therefore, the polarization switching in a ferroelectric crystal will give rise to domains shaped as planar plates or cylinders, which with such a shape should extend throughout the crystal thickness L. However, as will be shown later, the probability of domain formation for a large thickness L will tend to zero. This is associated with the energy expended by the system to create the interface. This problem does not arise when analyzing conventional first-order phase transitions [12], because the nuclei either have a close-to-spherical shape or represent two-dimensional cylindrical formations whose height H is of the order of interatomic distances. In the general case, the domain shape is not retained upon switching. In some cases, the radius of a domain can decrease as it grows into the crystal, while in others, the domain will become faceted. For simplicity of the calculations, we assume that domains of height H, which is equal in order of magnitude to the size of the crystal unit cell $H \sim \omega^{1/3}$, are formed throughout the crystal thickness. After the growth, they merge instantly to produce one long bubble domain. The width (or radius) of such domains will change in the course of their nucleation and subsequent evolution. In this case, $W_s = 2(\pi H\omega)^{1/2}\sigma n^{1/2}$, where σ is the surface tension of the domain wall.

Note that the expression under the Δ sign in Eq. (17) is the thermodynamic potential of the nucleus with an internal field E_{zn}; that is,

$$\phi(P_{zn}) = \Delta(W + p_0V - T_0S - E_{zn}P_z) = \tilde{\mu}n. \quad (18)$$

Here, $\tilde{\mu}$ is the chemical potential of the new-phase nucleus of size n with inclusion of the surface tension; that is,

$$\left.\frac{\partial\phi(P_{zn})}{\partial n}\right|_{E_z, p, T} = \tilde{\mu}(E_{zn}, p, T) = \mu(E_{zn}, p, T) + \frac{(\pi H\omega)^{1/2}\sigma}{n^{1/2}}. \quad (19)$$

Now, we can find the quantity $\tilde{R}_{\min}$ entering into formula (13):

$$\tilde{R}_{\min} = \left.\frac{\partial R_{\min}}{\partial n}\right|_{E_z, p, T} = (\tilde{\mu} - \mu_0) + (E_{zn} - E_{z0})\frac{\partial}{\partial n}P_z, \quad (20)$$

where $\partial P_z/\partial n$ is the polarization per structural unit in a nucleus, i.e., the quantity p_{zi} introduced earlier [see Eq. (9)].

Let us write $\tilde{\mu}(E_{zn}, p, T) - \mu_0(E_{zn}, p, T)$ in an explicit form, taking into account that the equilibrium magnitude of the nucleus–medium polarization is given by the expression

$$\tilde{\mu}(E_{zn}, p, T) = \mu(E_{zn}, p, T) + \frac{(\pi H\omega)^{1/2}\sigma}{n^{1/2}} = \mu_0(E_{zn}, p, T). \quad (21)$$

The equilibrium value of the nucleus–medium field $\tilde{E}_z$ (the nucleus of an infinite size $n \longrightarrow \infty$) can be found from the condition

$$\mu(\tilde{E}_z) = \mu_0(\tilde{E}_z). \quad (22)$$

By subtracting Eq. (22) from Eq. (21) and expanding the left- and right-hand sides of the relationship thus obtained in the vicinity of the $\tilde{E}_z$ point in the small deviation $(E_{zn} - \tilde{E}_z)/\tilde{E}_z$, we obtain for the main part of the nucleus distribution spectrum

$$\frac{\partial\mu}{\partial E_z|\tilde{E}_z}(E_{zn} - \tilde{E}_z) + \frac{(\pi H\omega)^{1/2}\sigma}{n^{1/2}} = \frac{\partial\mu_0}{\partial E_z|\tilde{E}_z}(E_{zn} - \tilde{E}_z). \quad (23)$$

Since the deviation of E_{zn} from $\tilde{E}_z$ is small, we have retained only the first term in the last expansion.

Because $-\partial\mu/\partial E_z|\tilde{E}_z = p_{zi2}$ and $-\partial\mu_0/\partial E_z|\tilde{E}_z = p_{zi1}$ (where p_{zi1} is the elementary polarization of the medium and p_{zi2} is the elementary polarization of the nucleus), these quantities are equal in absolute magni-

tude and have opposite directions. Denote $p_{zi1} = p_{zi}$, then $p_{zi2} = -p_{zi}$, and from Eq. (23), we obtain

$$2(E_{zn} - \tilde{E}_z)p_{zi} = \frac{(\pi H\omega)^{1/2}\sigma}{n^{1/2}},$$
$$n^{1/2} = \frac{(\pi H\omega)^{1/2}\sigma}{2p_{zi}(E_{zn} - \tilde{E}_z)}. \quad (24)$$

As is seen from Fig. 2, the equilibrium state of the ferroelectric corresponds to the field $\tilde{E}_z = 0$. On the other hand, the critical size of the polarization switching nucleus, which is in equilibrium with the ferroelectric in the switching field, is determined by the relationship $E_{znc} = E_{z0}$.

Taking into account this relationship and $\tilde{E}_z = 0$, from formula (24), we obtain

$$n_c^{1/2} = \frac{(\pi H\omega)^{1/2}\sigma}{2p_{zi}E_{z0}}. \quad (25)$$

Dropping the index 0, which identifies the field with the medium (i.e., with the part of the ferroelectric that has not yet switched), we have

$$n_c^{1/2} = \frac{(\pi H\omega)^{1/2}\sigma}{2p_{zi}E_z}. \quad (26)$$

This relationship determines the number of structural units in the critical switching nucleus. It is similar to the expressions describing the number of structural units in the critical nuclei formed in solutions and melts [12–14, 19]. The electric field plays the part of supersaturation or supercooling.

We rewrite expression (26) in terms of the radius of the critical domain R_c rather than through the number of unit cells n_c; that is,

$$R_c = \frac{\sigma\omega}{2p_{zi}E_z}. \quad (27)$$

Now, we can obtain an expression for the work to be done to create a nucleus of the critical size. As follows from Eqs. (17)–(24), it can be written as

$$R_{\min}(n_c) = (\pi H\omega)^{1/2}\sigma n_c^{1/2}. \quad (28)$$

Using the relationships derived above and Eq. (21), we recast expression (20) in the form

$$\tilde{R}_{\min} = \frac{\partial R_{\min}}{\partial n} = \mu_0(E_{zn}, p, T) - \mu_0(E_{z0}, p, T)$$
$$-(E_{zn} - E_{z0})p_{zi} = \frac{\partial\mu_0}{\partial E_z\big|E_{z0} \approx E_{zn}}(E_{zn} - E_{z0}) \quad (29)$$
$$-(E_{zn} - E_{z0})p_{zi} = -2(E_{zn} - E_{z0})p_{zi}.$$

Note that by introducing an auxiliary ferroelectric and deriving relationships (13), we obtained an expression for $\tilde{R}_{\min}$ which is valid throughout the range of n values near the critical size. As follows from Eq. (29), if $E_{zn} = E_{znc} = E_{z0}$, the derivative $\partial R_{\min}/\partial n$ for a nucleus of critical size is zero.

We are turning now to calculating the polarization switching nucleus flux in the size space.

5. DETERMINATION OF THE DIFFUSION COEFFICIENT $W_{n, n+1}$ IN THE SIZE SPACE

In order to calculate the diffusion coefficient $W_{n, n+1}$ in the size space, we revert to Eq. (12). It follows from this equation that the growth rate $\partial n/\partial t$ of domains of size n depends both on $W_{n, n+1}$ and on $\partial R_{\min}/\partial n$ [see Eq. (29)]. To find $W_{n, n+1}$, we define the growth rate in a different manner, namely, as

$$\frac{dn}{dt} = [\beta(E_{zn}) - \beta(E_{z0})]S, \quad (30)$$

where $\beta(E_{zn})$ is the flux of the switched elementary regions (cells) attaching to the side surface of a domain, $\beta(E_{z0})$ is the reverse cell flux bringing about "domain dissolution", E_{zn} is the field in the auxiliary medium which is in equilibrium with a domain of size n, E_{z0} is the field in the medium of the ferroelectric under study, and $S = 2(\pi H\omega)^{1/2}n^{1/2}$ is the side surface of a bubble domain. Note that we are considering a domain of size $n > n_c$, which is in equilibrium with the auxiliary ferroelectric. We assume that the domain grows through the transfer of atoms in the cells from one state to another directly at the interface separating the domains. In this case, we can determine the $\beta(E_{zn})$ and $\beta(E_{z0})$ fluxes in the following way. If the ferroelectric is in an equilibrium state (there is no external electric field and its total polarization is zero), the unit cell fluxes induced by thermal fluctuations from domains with polarizations in the directions along and opposite to the z axis are equal. In a nonequilibrium state, the polarization of the system will vary. Consider the quantity

$$\beta_0' = \nu\exp(-V_0/k_BT),$$

where ν is the vibrational frequency of atoms in the unit cells on the domain surface and V_0 is the height of the energy barrier separating the domains located in two symmetric positions with oppositely directed polarizations in the absence of the field. By multiplying β_0' by the number of unit cells N_s on the surface of domains, we can obtain the equilibrium unit cell flux

$$\beta_0 = N_s\nu\exp(-V_0/k_BT).$$

The magnitude of N_s can be estimated as $N_s \sim 1/\omega^{2/3}$, where $\omega^{2/3}$ is the area occupied by a cell on the domain surface.

If the ferroelectric is in an external field, the height of the energy barrier V_0 changes. For each cell in a

domain with the polarization aligned along the field, the barrier height decreases to $V_0 - p_{zi}E_z$, and for the cells residing in domains with the oppositely directed polarization, it increases to $V_0 + p_{zi}E_z$. In the presence of a field, the fluxes of cells from the surface of one domain to another are no longer equal. The cell flux from the medium is $\beta(E_{zn}) = \beta_0\exp(p_{zi}E_{zn}/k_BT)$, and the cell flux from a nucleus of the critical size is $\beta(E_{z0}) = \beta_0\exp(p_{zi}E_{z0}/k_BT)$. If $p_{zi}E_z \ll k_BT$, the exponentials in the expressions for these fluxes can be expanded in a series. Limiting ourselves to linear terms of the expansion in formula (30), we obtain the growth rate for the side surface of a domain of size $n > n_c$:

$$\frac{dn}{dt} = 2(\pi H\omega)^{1/2}\beta_0\frac{p_{zi}(E_{zn} - E_{z0})}{k_BT}n^{1/2}. \quad (31)$$

Now, we can determine the diffusion coefficient W_n in the size space. To do this, we compare Eq. (31) with Eq. (12) and recall expression (29) to obtain

$$W_n = (\pi H\omega)^{1/2}\beta_0 n^{1/2}. \quad (32)$$

Then, for a nucleus of the critical size, we have

$$W_{n_c} = (\pi H\omega)^{1/2}\beta_0 n_c^{1/2}. \quad (33)$$

6. THE FLUX OF POLARIZATION SWITCHING NUCLEI

Knowing the work needed to create a nucleus of the critical size and the expression for the diffusion coefficient in the size space and using the standard technique, we can calculate the stationary flux of the polarization switching nuclei passing through the critical barrier. According to [12, 13, 18, 19], this flux can be written as

$$I = N_v W_{n_c}\frac{1}{\sqrt{\pi}} \times\sqrt{-\frac{1}{2k_BT}\frac{\partial^2 R_{\min}}{\partial n^2}\Big|n = n_c}\exp\left[-\frac{R_{\min}(n_c)}{k_BT}\right], \quad (34)$$

where N_v is the number of unit cells per unit volume of the crystal, which can be estimated as $N_v \approx 1/\omega$.

Substituting the values of W_{n_c} from Eq. (33), $R_{\min}(n_c)$ from Eq. (28), and

$$\left.\frac{\partial^2 R_{\min}}{\partial n^2}\right|_{n_c} = \frac{(\pi H\omega)^{1/2}\sigma}{4n_c^{3/2}}$$

in formula (34), we finally come to

$$I = \frac{N_v\pi^{1/4}\beta_0(H\omega)^{3/4}\sigma^{1/2}}{2\sqrt{2}n_c^{1/4}\sqrt{k_BT}}\exp\left(-\frac{(\pi H\omega)^{1/2}\sigma n_c^{1/2}}{k_BT}\right). \quad (35)$$

We now express the critical radius n_c in Eq. (35) in terms of the field strength according to Eq. (26); that is,

$$I = \frac{N_v\beta_0(H\omega)^{1/2}(p_{zi}E_z)^{1/2}}{2\sqrt{k_BT}}\exp\left(-\frac{\pi H\omega\sigma^2}{2k_BTp_{zi}E_z}\right). \quad (36)$$

Relationship (36) describes the flux of switched domains as a function of the applied field. Next we take the logarithm of expression (36) to obtain

$$\ln I = \ln K - \frac{1}{2}\ln E_z - \frac{\pi H\omega\sigma^2}{2k_BTp_{zi}E_z}, \quad (37)$$

where

$$K = \frac{\beta_0(H\omega p_{zi})^{1/2}}{2\sqrt{k_BT}}.$$

Because the logarithm is a slowly varying function, as a first approximation, we assume the second term in expression (37) to be field independent. In this case, we obtain a convenient expression for the estimation of experimental data

$$\ln I \approx \text{const} - \frac{\pi H\omega\sigma^2}{2k_BTp_{zi}E_z}, \quad (38)$$

where const stands for the first two terms in Eq. (37).

We now estimate the time of the establishment and existence of a stationary flux of the switching nuclei. The region with $n < n_c$ is determined primarily by heterophase fluctuations of polarization switching. Hence, the existing flux sets in during the time it passes the region δn_0 in the vicinity of the critical point at which the hydrodynamic growth rate of the switching nuclei is zero, i.e., where $dn/dt = 0$ and $\partial R_{\min}(n)/\partial n|n = n_c = 0$. The width of this region is

$$\delta n_0 = \left(-\frac{1}{2k_BT}\frac{\partial^2 R_{\min}(n)}{\partial^2 n}\right)^{1/2}. \quad (39)$$

Hence, it follows that the time required for the stationary flux to set in can be estimated as

$$t \sim \frac{(\delta n_0)^2}{W_{n, n+1}}. \quad (40)$$

The time of the persistence of the stationary flux is determined by the condition that the time required for a nucleus to cross the region δn_0 in the size space should be substantially shorter than that taken for a nucleus of the critical size to emerge from the vicinity of the critical point (δn_0):

$$\frac{(\delta n_0)^2}{W_{n, n+1}} \le \frac{\delta n_0}{dn_c/dt}. \quad (41)$$

Substitution of the corresponding values of δn_0 and $W_{n,n+1}$ in relationship (40) yields

$$t \sim \frac{8k_B T n_c}{\pi H \omega \beta_0 \sigma},$$

and, taking into account expression (26) for n_c, we obtain

$$t \sim \frac{2k_B T \sigma}{\beta_0 (p_{zi} E_z)^2}. \quad (42)$$

Thus, the time for the stationary flux to set in, or the time for the first nucleus to appear (the incubation period), is inversely proportional to the squared electric field.

Note that we have found relationship (35) [or (36)] for the stationary flux of the nucleating domains. There are presently methods permitting one to solve the Fokker–Planck nonstationary equation (11) and to find the nonstationary flux of polarization switching domains [12, 13]. However, the main process of the formation of the new phase starts in the next stage when the system contains so many nuclei that they change the supersaturation in the system (in our case, the field in the ferroelectric), which results in the nucleus flux becoming dependent on time. This stage will be studied in the future.

ACKNOWLEDGMENTS

This work was supported in part by the Russian Foundation for Basic Research (project nos. 98-03-32791 and 99-03-32768), the Russian Center "Integration" (project no. A0151), the NATO Grant "Science for Peace" (grant Stp 973252), and the CONACYT Grant (project no. 32208).

REFERENCES

1. J. F. Scott, Ferroelectr. Rev. **1**, 1 (1998).
2. V. Ya. Shur, E. L. Rumyantsev, and S. D. Makarov, Fiz. Tverd. Tela (St. Petersburg) **37** (6), 1687 (1995) [Phys. Solid State **37**, 917 (1995)].
3. V. Ya. Shur, E. L. Rumyantsev, and S. D. Makarov, Ferroelectrics **172**, 361 (1995).
4. V. Ya. Shur, N. Yu. Ponomarev, and N. A. Tonkacheva, Fiz. Tverd. Tela (St. Petersburg) **38** (6), 1889 (1996) [Phys. Solid State **38**, 1044 (1996)].
5. L. I. Dontzowa, N. A. Tikhomirova, and L. A. Shuvalov, Ferroelectrics **97**, 87 (1989).
6. Y. Ishibashi and Y. Takagi, J. Phys. Soc. Jpn. **31**, 506 (1971).
7. W. Yang and T. Zhu, J. Mech. Phys. Solids **46** (2), 291 (1998).
8. C. L. Wang, L. Zhang, W. L. Zhong, and P. L. Zhang, Phys. Lett. A **254**, 297 (1999).
9. J. M. Liu and Z. G. Liu, Mater. Lett. **36**, 17 (1998).
10. A. N. Kolmogorov, Izv. Akad. Nauk SSSR, Otd. Mat. Estestv. Nauk, Ser. Mat. **3**, 355 (1937).
11. M. Avrami, J. Chem. Phys. **7**, 1103 (1939); **9**, 17 (1941).
12. S. A. Kukushkin and A. V. Osipov, Usp. Fiz. Nauk **168** (10), 1083 (1998) [Phys. Usp. **41**, 983 (1998)].
13. S. A. Kukushkin and A. V. Osipov, Prog. Surf. Sci. **56** (1), 1 (1996).
14. S. A. Kukushkin and V. V. Slezov, *Dispersive Systems on Solid Surfaces (Evolution Approach): Mechanisms of the Formation of Thin Films* (Nauka, St. Petersburg, 1996).
15. L. D. Landau and E. M. Lifshitz, *Course of Theoretical Physics*, Vol. 8: *Electrodynamics of Continuous Media* (Nauka, Moscow, 1982; Pergamon, New York, 1984).
16. B. A. Strukov and A. P. Levanyuk, *Physical Principles of Ferroelectric Phenomena in Crystals* (Nauka, Moscow, 1995).
17. A. Z. Pokrovskiĭ and B. I. Shumilo, Zh. Éksp. Teor. Fiz. **77** (4), 1417 (1979) [Sov. Phys. JETP **50**, 712 (1979)].
18. Ya. B. Zel'dovich, Zh. Éksp. Teor. Fiz. **12** (4), 525 (1942).
19. V. V. Slezov and S. A. Kukushkin, Fiz. Tverd. Tela (St. Petersburg) **38** (2), 433 (1996) [Phys. Solid State **38**, 239 (1996)].
20. L. D. Landau and E. M. Lifshitz, *Course of Theoretical Physics*, Vol. 5: *Statistical Physics* (Nauka, Moscow, 1995; Pergamon, Oxford, 1980), Part 1.

Translated by G. Skrebtsov

Physics of the Solid State, Vol. 43, No. 1, 2001, pp. 9–16. Translated from Fizika Tverdogo Tela, Vol. 43, No. 1, 2001, pp. 11–18.

METALS AND SUPERCONDUCTORS

The Large-N Limit in Statistical Physics and the One-Particle Schrödinger Equation

B. N. Shalaev

Ioffe Physicotechnical Institute, Russian Academy of Sciences, Politekhnicheskaya ul. 26, St. Petersburg, 194021 Russia
University of Essen, Essen, D-45117 Germany
e-mail: shalaev@izing.ioffe.rssi.ru

Received May 12, 2000

Abstract—Nonlinear d-dimensional vector σ models, such as $O(N)$, $SU(N)$, and CP^N, are considered in the limit of an infinite number of components N. It is shown that the equation for the two-point correlation function in these models is similar to the Schrödinger equation for a quantum particle moving in a δ-function potential well $(-T)\delta(\mathbf{x})$, where T is the temperature. This equation adequately describes the systems under study both above and below the Curie point. Within this approach, the critical behavior of the $SU(N)$-invariant Ginzburg–Landau model in an external uniform magnetic field is determined in the vicinity of the upper critical magnetic field. The critical indices in this case are the same as in the spherical model in a random magnetic field. An exact equation describing the $H_{c2}(T)$ curve of continuous phase transitions is derived, which allows one to determine the asymptotes of this curve in strong and weak fields. The relation between the one-particle Schrödinger equation and critical phenomena is analyzed, and applications of this method to various models in solid state physics and statistical mechanics are discussed. © *2001 MAIK "Nauka/Interperiodica".*

INTRODUCTION

The approach based on an expansion in powers of the small parameter $1/N$, where N is the number of the components of an order parameter, is extensively used in modern statistical mechanics and quantum field theory. It is well known that statistical models in the limit of an infinite N are ideal theoretical objects, which allow investigators to elucidate the essential features of systems belonging to a continuous symmetry group [1–8].

The standard method for investigating field-theoretical models and many-particle systems consists in solving an infinite set of the nonlinear Schwinger–Dyson equations [1–3, 6]. It can easily be shown that the limit of $N \longrightarrow \infty$ is equivalent to the Hartree–Fock approximation, and, therefore, solving the corresponding equations presents no problems. In this paper, the two-point correlation functions $\langle S_a^*(\mathbf{x})S_b(0)\rangle$ in the nonlinear σ models in this limit are shown to be a solution to the one-particle Schrödinger equation (SE) for a particle moving in the potential $(-T)\delta(\mathbf{x})$, where T is the temperature. It should be remarked that this result is true for a variety of nonlinear vector σ models, such as CP^N, $O(N)$, and $SU(N)$.

It is of interest that this SE was proposed in the context of quantum field theory many years ago as a nonrelativistic "toy" model for field effects such as dimensional transmutation and dynamical generation of mass [9]. It is worth noting that some aspects of this problem were recently discussed in [10], where the behavior of the energy and radius of a bound state of a quantum particle was analyzed near the threshold value of the potential-well depth. It was found that the critical behavior of these quantities is characterized by the same critical indices as in the spherical model, that is, by those for an N-component Heisenberg ferromagnet in the limit of $N \longrightarrow \infty$ [10].

Analogous renormalization group (RG) equations arise in studying the properties of a low-density Bose gas with short-range interaction [11, 12] and in considering phase transitions in systems that contain extended linear components (strings), such as Abrikosov vortex lines, polymers, dislocations, domain walls (in the two-dimensional case), etc. [13], which could be considered to have nothing to do with nonlinear σ models with a large N.

In this paper, we will show that these facts are manifestations of the universal critical behavior of nonlinear vector σ models in the large-N limit. All these models turn out to be equivalent to the conventional SE with a δ-function potential. Therefore, the critical phenomena in statistical physics possess a very simple and, perhaps, useful interpretation in terms of one-particle quantum mechanics.

A basic and very efficient method for investigating critical phenomena is the RG method [2, 3]. Among investigators, there is a widespread opinion that this method works well only in the case of systems with an infinite number of degrees of freedom, where ultraviolet divergences take place in perturbation-theory diagrams. In quantum mechanics, these divergences are absent and, therefore, the RG method is inappropriate. However, it should be remembered that this reasoning fails in the case of singular quantum mechanical poten-

tials, for example, those of the δ-function type, which require ultraviolet regularization. The RG transformation in quantum mechanics is a so-called isospectral deformation, i.e., a transformation of the potential energy that leaves the spectrum unchanged. The theory of these transformations is closely related to the theory of solitons and is now a well-developed field of mathematical physics, to which a great number of books, reviews, and articles are devoted (see, e.g., [14, 15]).

The SE method is also used in this paper for investigating the $SU(N)$-invariant Ginzburg–Landau (GL) model in an external uniform magnetic field. This model describes type-II superconductors in the vicinity of the upper critical field $H_{c2}(T)$ and is of great importance for solid state physics and applications. The model was proposed in the early 1950s, and its history is described in detail in the literature (see reviews [16, 17]).

For the infinite-N case, the GL model in the vicinity of $H_{c2}(T)$ was first calculated by Affleck and Brézin [18] in 1985 and has been considered repeatedly in the literature since then (unfortunately, without reference to [18] in some cases, see [19–21] and the discussion in [22, 23]). In contrast to the conventional spherical model, solution of the GL model in this limit is not trivial and the results obtained by different groups of investigators were contradictory to each other. The correct result, first obtained in [24], was unexpected. It was found that the true ground state of this model at $N = \infty$ differs essentially from the Abrikosov ground state, which is unstable (see below), and the previously derived solutions are erroneous [24]. In this paper, we show that the SE method gives results that are similar to those obtained in [24].

This paper is organized as follows: In Section 1, we derive the SE for the two-point correlation function in a d-dimensional $SU(N)$-symmetrical nonlinear σ model in the infinite-N limit. In Section 2, the RG method is used to investigate the equation derived and interesting parallels between quantum mechanics and the theory of phase transitions are discussed. The critical properties of the GL model in the vicinity of the upper critical magnetic field are investigated in Section 3. Finally, the method developed here is applied to other statistical models and the results are discussed in the concluding section.

Some results obtained by the author in [25] are used in this paper.

1. SCHRÖDINGER EQUATION FOR THE TWO-POINT CORRELATION FUNCTION

Let us consider an $SU(N)$-symmetric spin model constructed on a d-dimensional hypercubic lattice. Its Hamiltonian has the usual form

$$H = -J\sum_{\langle i,j\rangle}(\mathbf{S}_i\mathbf{S}_j^* + \text{H.c.}), \tag{1}$$

where the variable $\mathbf{S} = (S_1, \ldots, S_N)$ is an N-component (complex) unit vector

$$S_a(\mathbf{x})S_a^*(\mathbf{x}) = 1. \tag{2}$$

The angular brackets in $\langle i, j\rangle$ signify the summation over the nearest neighbors, and J is the exchange integral.

The nonlinear σ model is the continuum limit of the lattice model in Eq. (1):

$$H = \frac{J}{2}\int d^dx|\partial_\mu S_a|^2. \tag{3}$$

Here, a summation convention over repeated indices $\mu = 1, \ldots, d$ and $a = 1, \ldots, N$ is adopted. The partition function for the system with the Hamiltonian (3) is written in the form

$$Z = \int\prod_{a=1}^{N} DS_aDS_a^*\exp\left(-\frac{H}{T}\right)\delta(|\mathbf{S}|^2 - 1), \tag{4}$$

where the spin coupling constant J is conveniently included in the temperature T.

Let us now derive an equation for the two-point correlator in the disordered phase (at $T > T_c$) in which the $SU(N)$ symmetry is not broken:

$$G_{ab}(\mathbf{x}) = \langle S_a(\mathbf{x})S_b(0)\rangle. \tag{5}$$

Following [5], we represent the correlator in Eq. (5) in the form of a continual integral:

$$\begin{aligned} G_{ab}(\mathbf{x}) &= \frac{1}{Z}\int\prod_{a=1}^{N} DS_aDS_a^*D\lambda S_a(\mathbf{x})S_b^*(0) \\ &\quad\times\exp[-A_1(\mathbf{S}(\mathbf{x}), \lambda(\mathbf{x}))], \\ Z &= \int\prod_{a=1}^{N} DS_aDS_a^*D\lambda\exp[-A_1(\mathbf{S}(\mathbf{x}), \lambda(\mathbf{x}))], \\ A_1(\mathbf{S}(\mathbf{x}), \lambda(\mathbf{x})) &\equiv \frac{1}{2T}\int d^dx[|\partial_\mu S_a|^2 + \lambda(|\mathbf{S}|^2 - 1)], \end{aligned} \tag{6}$$

in which $A_1(\boldsymbol{S}(\mathbf{x}), \lambda(\mathbf{x}))$ is the effective action and $\lambda(\mathbf{x})$ is the Lagrange multiplier that ensures the fulfillment of the condition given by Eq. (2). Integrating with respect to the fields $S_a(\mathbf{x})$ yields [5]

$$\begin{aligned} G_{ab}(\mathbf{x}) &= \frac{1}{Z}\int D\lambda G(\mathbf{x}, \mathbf{y}; \lambda)\exp[-A_2(\lambda(\mathbf{x}))], \\ Z &= \int D\lambda\exp[-A_2(\lambda(\mathbf{x}))], \\ A_2(\lambda(\mathbf{x})) &= \frac{1}{2T}\int d^dx\left[\lambda(\mathbf{x}) - \frac{N}{2}\text{Trlog}(-\Delta + \lambda(\mathbf{x}))\right], \end{aligned} \tag{7}$$

where Δ is the Laplace operator and

$$G(\mathbf{x}, \mathbf{y}; \lambda) = \left\langle \mathbf{y}\left|\frac{1}{-\Delta + \lambda}\right|\mathbf{x}\right\rangle. \tag{8}$$

It should be emphasized that the quantity TN remains constant as $N \longrightarrow \infty$, and, therefore, the continual integral in Eq. (7) can be calculated by the saddle-point method [2, 3, 5]:

$$\langle S_a(\mathbf{x}) S_b^*(0)\rangle = T\delta_{ab} G(\mathbf{x}, \mathbf{y}; \lambda_0), \tag{9}$$

where λ_0 is the saddle-point value. An equation for the desired Green's function has a simple form [2–5]

$$[-\Delta + m^2] G_{ab}(\mathbf{x}) = T\delta_{ab}\delta(\mathbf{x}), \tag{10}$$

where $m^2 \equiv \lambda_0$. Using Eq. (2), which can be considered as the boundary condition at the equal arguments, $G_{cc}(0) = 1$, the inhomogeneous equation (10) can be transformed into a homogeneous one. Indeed, inserting unity into the right-hand side of Eq. (10), namely, $T\delta_{ab}\delta(\mathbf{x}) = T\delta_{ab}\delta(\mathbf{x})G_{cc}(\mathbf{x})$, we obtain

$$[-\Delta + m^2] G_{ab}(\mathbf{x}) = T\delta_{ab}\delta(\mathbf{x}) G_{cc}(\mathbf{x}). \tag{11}$$

In the symmetrical phase (at $T > T_c$), we conveniently introduce the "wave function" $G_{ab}(\mathbf{x}) \equiv \delta_{ab}\Psi(\mathbf{x})$. Substituting it into Eq. (11), we obtain an equation for the eigenfunctions and eigenvalues:

$$\hat{H}\Psi(\mathbf{x}) = -|E|\Psi(\mathbf{x}), \tag{12}$$

where the Hamiltonian $\hat{H}$ is

$$\hat{H} = -\Delta - TN\delta(\mathbf{x}), \quad |E| = m^2. \tag{13}$$

Equation (12) is the time-independent Schrödinger equation for a quantum particle moving in a δ-function potential, and the one-particle Green's function corresponds to the lowest eigenvalue in the spectrum of Hamiltonian (13). We note that this equation is obtained as the result of two limiting processes (continual and $N \longrightarrow \infty$) in the lattice model described by Eq. (1). The sign of the coupling constant T corresponds to attraction; that is, the particle moves in a potential well that has a single discrete energy level. Geometrically, this result is due to the fact that the spin variable belongs to a compact manifold, namely, the S^{2N-1} sphere.

As was already noted, the boundary condition for the wave function is Eq. (2). Since we deal with the one-particle Schrödinger equation, the energy of the discrete level is not the energy of a bound state of two particles belonging to the multiplet with N components of the model at hand.

2. QUANTUM MECHANICS OF ONE PARTICLE AND CRITICAL PHENOMENA

In this section, the RG method is applied to the SE with a δ-function potential and the analogies between phase transitions and threshold phenomena in quantum mechanics are discussed in detail in the spirit of [9, 10].

Let us find the eigenfunctions and eigenvalues of the discrete spectrum of the d-dimensional Schrödinger equation (12). This can readily be done using the Fourier transform

$$(k^2 + m^2)\psi(\mathbf{k}) = TN\Psi(0), \tag{14}$$

where

$$\psi(\mathbf{k}) = \int d^d x \Psi(\mathbf{x}) \exp(-i\mathbf{k}\mathbf{x}),$$
$$\Psi(\mathbf{x}) = \int \frac{d^d x}{(2\pi)^d} \psi(\mathbf{k}) \exp(i\mathbf{k}\mathbf{x}). \tag{15}$$

It follows from Eq. (14) that

$$\Psi(0) = TN\Psi(0)\int \frac{d^d k}{(2\pi)^d (k^2 + m^2)},$$
$$1 = TN\int \frac{d^d k}{(2\pi)^d (k^2 + m^2)}. \tag{16}$$

The last equation relates the bound-state energy and the coupling constant (temperature) T [9]. The integral in the right-hand side of Eq. (16) diverges, because $\delta(\mathbf{x})$ is a singular potential in $d \geq 2$ dimensions and a cutoff $\Lambda = a^{-1}$ has to be introduced at short distances (a is the width of the well).

The bound-state energy is an observable physical quantity which does not depend on the choice of cutoff. Therefore, the dependence of the coupling constant $T(\Lambda)$ on Λ must be such that E is independent of Λ. In fact, this is the simplest case of an isospectral deformation, i.e., a transformation of the potential energy that leaves the spectrum unchanged. It is well known that in the one-dimensional case there is an infinite group of such deformations which is isomorphic to the symmetry group of the Korteweg–de Vries (KdV) equation [14, 15]. However, in the case at hand, we deal with the d-dimensional Schrödinger equation (12), rather than with the KdV equation.

After an elementary calculation of the integral, Eq. (16) becomes

$$1 = TN\left(\frac{S_d \Lambda^{d-2}}{(2\pi)^d d - 2} - K_d m^{d-2}\right),$$
$$S_d = \frac{2\pi^{d/2}}{\Gamma(d/2)}, \quad K_d = \frac{1}{2^d \sin(\pi d/2)\Gamma(d/2)\pi^{(d-2)/2}}, \tag{17}$$

where S_d is the area of a unit d-dimensional sphere. In the spirit of the theory of critical phenomena, it is convenient to introduce a dimensionless coupling constant $t = T\Lambda^{2-d}$, which obeys the equation

$$\Lambda\frac{dt}{d\Lambda} = (d-2)t - t^2. \tag{18}$$

From this equation, it follows that there is a critical value of the coupling constant or the Curie temperature

Table 1. Correspondence between quantum mechanics and statistical physics

Quantum mechanics	Statistical physics
Wave function $\psi(\mathbf{x})$	Correlator $G(\mathbf{x}) = \langle \mathbf{S}(\mathbf{x})\mathbf{S}^*(0)\rangle$
Quantum well $-T[\delta(\mathbf{x})]$	Coupling constant T
Bound state	Dynamical mass generation
Energy gap E_{bs}	Inverse correlation radius ξ^{-1}
Generator of isospectral deformations	Beta function $\beta(T)$
Threshold T_c	Curie temperature T_c
$E_{bs} \sim (T - T_c)^{\nu}$;	$\xi \sim (T - T_c)^{-\nu}$;
$\nu = 1/(d-2)$	$\nu = 1/(d-2)$
$T > T_c$;	$T > T_c$;
$\psi(\mathbf{x}) \sim x^{(1-d)/2}\exp(-x/\xi)$	$G(\mathbf{x}) \sim x^{(1-d)/2}\exp(-x/\xi)$
$T \le T_c$; $\psi(\mathbf{x}) \sim x^{2-d}$	$T \le T_c$; spin waves
	$G(\mathbf{x}) \sim x^{2-d}$
No analog	Local order parameter $\langle \mathbf{S}(\mathbf{x})\rangle$

(a fixed point)

$$T_c = \frac{(d-2)(2\pi)^d}{NS_d}\Lambda^{2-d}. \quad (19)$$

The equations derived above can be discussed either in terms of elementary quantum mechanics or in terms of the modern theory of phase transitions and critical phenomena.

Let us first consider the motion of a quantum particle in a singular potential well.

In the two-dimensional case, the Hamiltonian involves only dimensionless parameters and is scale-invariant. Nonetheless, there is a single discrete energy level in the spectrum, $|E_{bs}| \equiv m^2$, whose emergence implies dynamic mass generation. A bound state always exists in such a well, no matter how deep it is. If the space dimension is higher than two, there is a threshold depth of the well above which there is a single discrete energy level. In a shallow well, i.e., below the threshold, there is no gap in the spectrum and only a continuous spectrum exists, which starts from zero. It is the presence of the threshold that essentially distinguishes the two-dimensional case from a higher dimensional case.

The bound-state energy E_{bs} is a continuous function of the coupling constant and decreases according to the law $|E_{bs}| \sim |T - T_c|^{1/(d-2)}$ as the threshold is approached from above. At the same time, the characteristic size (extension in space) of the wave function of the bound state $\xi \sim E_{bs}^{1}$ increases as $\xi \sim \tau^{-\nu}$, where $\tau = (T - T_c)/T_c$.

The asymptotic form of the wave function of the discrete spectrum for large distances $x \gg \xi$ is

$$\Psi(x) \sim \frac{\exp(-x/\xi)}{x^{(d-1)/2}}. \quad (20)$$

Below the threshold, $T \le T_c$, the energy gap disappears, $E_{bs} = 0$, and the wave function follows the power law

$$\Psi(x) \sim x^{2-d}. \quad (21)$$

Now, we discuss the spin model at hand in terms of statistical mechanics. For simplicity, let us consider a d-dimensional Heisenberg ferromagnet with $N \longrightarrow \infty$, in which a second-order phase transition occurs at the Curie point, defined by Eq. (19), at $d \ge 2$. In the symmetrical phase, the pair spin Green's function is given by Eq. (20). In the ordered phase, the gap in the spectrum disappears and massless Goldstone excitations (spin waves) arise in the system, with their correlator being the power function given by Eq. (21). The beta function in Eq. (18) is the well-known Gell-Mann–Low function in the spherical model, whose critical indices are given by formulas of quantum mechanics:

$$\nu = \frac{1}{d-2}, \quad \eta = 0.$$

In the two-dimensional case, the continuous symmetry cannot be broken spontaneously (Mermin–Wagner theorem). For this reason, the Curie temperature [nontrivial fixed point given by Eq. (19)] vanishes and the critical index for the correlation radius ν becomes infinite. Dynamical mass generation (asymptotic freedom) takes place in the system; that is, all excitations have nonzero masses. In terms of quantum mechanics, this theorem means that there is no threshold depth for a two-dimensional potential well.

Clearly, the analogy between quantum mechanics and critical phenomena is not perfect, because spontaneous breaking of symmetry does not occur in quantum mechanics of a finite number of particles. In other words, the wave function of the ground state always exhibits the full symmetry of the Hamiltonian. This means that in quantum mechanics there is no analog for the order parameter. In quantum mechanics, the phase transition is associated with the energy gap vanishing according to the power law in the spectrum near the threshold and with the different behavior of the correlation function above and below the threshold; more specifically, the asymptotic form of Green's function changes over from an exponential to a power law (as in the case of the Berezinskiĭ–Kosterlitz–Thouless transition [2, 4, 8]).

The results of this section are summarized in Table 1.

In concluding this section, we make a remark with reference to the critical indices in the spherical model. In the three-dimensional case, these indices and their certain combinations coincide with their respective counterparts for the two-dimensional Ising model on a

dynamical planar lattice (DPL) [1, 26]. Furthermore, in $d = 8/3$ dimensions, we obtain critical indices that are identical to those of the three-component Potts model on the DPL. These critical indices are listed in Table 2. To avoid misunderstanding, it should be stressed that we do not assert that all critical indices coincide, which is impossible for systems with different space dimensions d. Indeed, some scaling relations involve d explicitly, for example, $d\nu - 2 = -\alpha$ and $\delta = (d + 2 - \eta)(d - 2 + \eta)$. In particular, the spherical model and the models on a DPL mentioned above have different indices ν and η. Thus, there is an interesting, but incompletely understood, relation between the conventional Schrödinger equation and statistical models on dynamical planar lattices.

3. $SU(N)$-INVARIANT GINZBURG–LANDAU MODEL IN AN EXTERNAL UNIFORM MAGNETIC FIELD

In this section, the critical behavior of the $SU(N)$-symmetric nonlinear GL vector σ model in an external magnetic field is investigated in terms of the Schrödinger equation. This model describes the properties of type-II superconductors in the vicinity of the $H_{c2}(T)$ curve of phase transitions. We consider the case of large N values. As a preliminary, we make some general remarks.

It is well known that an external magnetic field radically alters the critical properties of superconductors [16, 17]. It primarily hinders the growth of critical fluctuations in the plane perpendicular to **H**. The characteristic scale in this plane is the magnetic length $l_H = \sqrt{hc/eH}$, which is much less than the correlation radius ξ in the region of strong fields. Therefore, the critical fluctuations in this plane are frozen and are of little importance; the effective space dimension decreases by 2: $d_{\text{eff}} = d - 2$ (dimensionality reduction). In particular, the lower critical dimensionality becomes equal to 4.

A critical question is the kind of phase transition. If critical fluctuations are ignored and the phase transition is treated in the mean-field approximation, one will arrive at a continuous phase transition to a mixed state, which consists of a lattice of Abrikosov vortices. Unfortunately, a straightforward application of the RG method fails in this case for at least two reasons.

First, the RG equations are written for the $(6-\varepsilon)$-dimensional space (near the upper critical dimensionality) [27, 28] and the applicability of their (one-loop) solutions for $d = 3$, i.e., below the lower critical dimensionality, is highly questionable.

Second, the application of the RG method to the standard ψ^4 model in an external magnetic field leads to RG equations with an infinite number of invariant charges; that is, in effect, the theory is unrenormalizable, which involves severe problems [27, 28].

Table 2. Critical indices of the d-dimensional spherical model (SM) for $d = 3$ and 8/3, as well as of the Ising model (IM) and three-component Potts model (PM) on dynamical planar lattices (DPLs)

Critical index	SM in d dimensions	SM ($d = 3$) and IM on DPL	SM ($d = 8/3$) and PM on DPL
α	$(d-4)/(d-2)$	–1	–2
β	1/2	1/2	1/2
γ	$2/(d-2)$	2	3
δ	$(d+2)/(d-2)$	5	7
$d\nu$	$d/(d-2)$	3	4

The unrenormalizability can be overcome, for example, by the $1/N$-expansion method [2, 3]. The characteristic feature of this approximation is the absence of symmetry between the particle–hole and particle–particle channels, because the latter channel is suppressed in the $1/N$ expansion. For this reason, the Abrikosov solution is unstable and the lower critical dimensionality is equal to 4 [29].

An ingenious method was proposed in [29], where this difficulty was resolved by modification of the quadric interaction. The $SU(N)$-symmetric term $(\phi_a^* \phi_a)^2$ was replaced by $2(\phi_a^* \phi_a)^2 - \phi_a^* \phi_b \phi_a^* \phi_b$, which possesses the $O(N) \times U(1)$ symmetry. This change in the symmetry of the original system restores the stability of the vortex lattice arising as the result of the first-order phase transition.

In paper [18], as was mentioned in the Introduction, the $1/N$ expansion was used and it was found that the first-order phase transition occurs in the $SU(N)$-symmetric GL model when $d \geq 4$. In later publications [19–21], however, it was advocated that a continuous phase transition takes place in the system. Although this question is of academic interest, because the dimension $d \geq 4$ is unphysical, the correct result obtained recently in [24] is very interesting.

In [2, 4], a convenient technique was proposed, which is commonly combined with the $1/N$ expansion. It is assumed that below T_c only one of the N components of the order parameter condenses. This component can be any component, because the model possesses continuous symmetry, say, $SU(N)$. Integrating over the other $N - 1$ Goldstone modes, one obtains the effective action for the remaining component and for the auxiliary field $\lambda(\mathbf{x})$ (the Lagrange multiplier). This method is commonly used and it works well, e.g., in the case of a Heisenberg ferromagnet. In this method, however, the ordered phase is implicitly assumed to be spatially homogeneous. The homogeneity of the condensate allows one to perform rotations in spin space. However, the order parameter is not spatially homogeneous in the Abrikosov phase. It can be shown that a true minimum of the free energy is attained when all N components of the order parameter condense and

form a complicated structure, which consists of the interlocked Abrikosov vortex lattices [24]. It is significant that the resultant density of the condensate remains constant in the limit as $N \longrightarrow \infty$.

Let us now consider the nonlinear GL σ model, whose Hamiltonian has the well-known form

$$H = \frac{1}{2}\int d^d x \left|\left(\partial_\mu + i\frac{2\pi}{\Phi_0}A_\mu\right)S_a\right|^2, \quad (22)$$

where $\Phi_0 = hc/2e$ is the magnetic flux quantum. The vector potential A_μ is conveniently taken in the symmetrical gauge

$$\mathbf{A} = \frac{1}{2}\mathbf{B}\times\mathbf{r}, \quad (23)$$

and the magnetic field **B** is applied along the z axis. The partition function is

$$Z = \int\prod_{a=1}^{N} DS_a DS_a^* \exp\left(-\frac{H}{T}\right)\delta(|S|^2 - 1). \quad (24)$$

Our prime interest is in the gauge-noninvariant correlation function

$$G_{ab}(\mathbf{r}, \mathbf{r}') = \langle S_a(\mathbf{r})S_b^*(\mathbf{r}')\rangle, \quad (25)$$

where $G_{ab}(\mathbf{r}, \mathbf{r}')$ is Green's function for the d-dimensional Hamiltonian operator

$$\left[\left(-i\partial_\mu - \frac{2\pi}{\Phi_0}A_\mu\right)^2 + m_0^2\right]G_{ab}(\mathbf{r}, \mathbf{r}') = T\delta_{ab}\delta(\mathbf{r} - \mathbf{r}'). \quad (26)$$

This function can be written explicitly in an auxiliary gauge [30]:

$$G_{ab}(\mathbf{r}, \mathbf{r}') = T\delta_{ab}\exp\left(-i\frac{2\pi}{\Phi_0}\int_{\mathbf{r}}^{\mathbf{r}'} dx_\mu A_\mu\right)(4\pi)^{(2-d)/2}$$

$$\times\int_0^\infty du\frac{\omega u^{(2-d)/2}}{2\sinh(u\omega/2)}\exp\left\{-m_0^2 u - \frac{(z-z')^2}{4u}\right. \quad (27)$$

$$\left. - \frac{\omega}{8}\coth\left(\frac{1}{2}u\omega\right)[(x-x')^2 + (y-y')^2]\right\},$$

where $\omega = 2eB/c$ is the cyclotron frequency (we use the system of units in which $\hbar = 1$, $2m = 1$) and z and z' are the $(d-2)$-dimensional longitudinal coordinates. The integral in Eq. (27) is taken along the straight line connecting the points **r** and **r**'.

Taking into account the restriction imposed by Eq. (2) on the complex fields, we obtain the SE for the effective wave function,

$$\left[\left(-i\partial_\mu - \frac{2\pi}{\Phi_0}A_\mu\right)^2 + m_0^2\right]\Psi(\mathbf{r}, \mathbf{r}') = TN\delta(\mathbf{r} - \mathbf{r}')\Psi(\mathbf{r}, \mathbf{r}'), \quad (28)$$

which describes the motion of a quantum particle in a external uniform magnetic field and a δ-function potential well. Here, $\delta_{ab}\Psi(\mathbf{r}, \mathbf{r}') \equiv G_{ab}(\mathbf{r}, \mathbf{r}')$.

This simple SE is completely equivalent to the original $SU(N)$-symmetric nonlinear GL σ model. It should be stressed that the δ-function potential in this equation is of fundamental importance, because in the absence of this potential we have a trivial equation describing Gaussian fluctuations.

According to quantum mechanics, there is always a bound state for a particle moving in a three-dimensional potential well in a uniform magnetic field, no matter how deep the well is [31]. This means that, in our case, the phase transition does not occur if $d = 3$.

Equation (28) can be readily solved [25]. In what follows, we derive an exact formula for the upper critical field $H_{c2}(T)$. Using the boundary condition for the wave function at equal arguments, one can obtain an equation that relates the temperature and the "physical" mass m (the reciprocal of the correlation radius ξ):

$$\Psi(\mathbf{x}, \mathbf{x}) = \frac{TN\omega}{(4\pi)^{d/2}}\int_{a^2}^\infty du\frac{\exp(u\omega/2 - m^2 u)}{2u^{(d-2)/2}\sinh(u\omega/2)} = 1. \quad (29)$$

When deriving this relation, the mass renormalization $m_0^2 + \omega/2 = m^2$ was performed. Along the curve of the phase transition, we have $m = 0$. After simple algebra, we obtain from Eq. (29)

$$\frac{T(0)}{T(H)} = \frac{d-2}{2}\left(\frac{H}{H_0}\right)^{(d-2)/2}\int_{H/H_0}^\infty dt\frac{t^{(2-d)/2}\exp t}{\sinh t}, \quad (30)$$

where

$$T(0) = \frac{2(4\pi)^{d/2}a^{d-2}}{N}, \quad H_0 = \frac{\Phi_0}{a^2}. \quad (31)$$

Here, $T(0)$ is the superconducting transition temperature in a zero magnetic field and $H_0 \sim 10^5$ T is the magnetic field scale in the model at hand. The right-hand side integral of Eq. (30) is convergent for $d > 4$ and divergent for $d \le 4$; that is, if the dimensionality is less than four, the phase transition does not occur at all (because of the dimensionality reduction). It is significant that, when deriving the exact equation (30), we did not employ the lowest Landau level (LLL) approximation [18, 27].

This approximation, sometimes referred to as the ultraquantum limit, is valid in the range of extremely strong fields, where $l_H \ll a \ll \xi$.

Using the exact solution, we will investigate its asymptotic behavior in the range of weak fields, where the LLL approximation fails, and in the range of strong fields, where we will calculate corrections to the LLL approximation.

In the case of weak fields, $s \equiv H/H_0 \ll 1$, we obtain

$$\frac{T(0)}{T(H)} = 1 + \frac{d-2}{d-4}s + A_d s^{(d-2)/2} - \frac{d-2}{3(d-6)}s^2 + \frac{d-2}{45(d-10)}s^4 + O(s^6), \quad (32)$$

where A_d is a constant equal to

$$A_d = -2\frac{d-3}{(d-4)} + \frac{d-2}{2}\int_1^\infty dt\, t^{(d-2)/2}\frac{e^t}{\sinh t} + \frac{d-2}{2}\int_0^1 dt\, t^{(d-2)/2}\frac{t\exp t - \sinh t - t\sinh t}{t\sinh t}. \quad (33)$$

Equation (32) describes the vicinity of the critical end point $T = T_c$, $H = 0$, in which several phases exist. A characteristic feature of this point is the divergence of the second derivative of $T(H)$ with respect to H, $T''(H) \sim H^{(d-6)/2}$, as $H \longrightarrow 0$.

In the range of strong fields $s \gg 1$, we have

$$\frac{T(0)}{T(H)} = 2\frac{d-2}{d-4}s + \frac{d-2}{2}\exp(-2s) - \frac{(d-2)^2}{8s}\exp(-2s) + O(s^{-2}\exp(-2s)). \quad (34)$$

The corrections to the LLL approximation are exponentially small, which is not surprising because there is a gap between the lowest Landau level and higher levels. In the limit as $T \longrightarrow 0$, the $H_{c2}(T)$ curve goes to infinity.

Thus, the second-order phase transition occurs in the model at hand only in the case of the dimensionality $d \geq 4$; the critical indices are $\nu = 1/(d-4)$ and $\eta = 0$ [21, 24, 25]. If the dimensionality is less than four, the phase transition does not occur because of the dimensionality reduction effect.

The critical indices calculated above coincide with those of the spherical model in a random magnetic field. In both models, the dimensionality reduction effect takes place and both belong to the same universality class. The reason for the latter is still unclear. This may be an accidental coincidence, because the GL model differs significantly from the spherical model: there is no frozen disorder and no hidden supersymmetry in it [2, 32].

4. CONCLUSION

In this paper, we showed that, in the large-N limit, all d-dimensional nonlinear vector σ models, such as $O(N)$, $SU(N)$, and CP^N, are equivalent to the Schrödinger equation for a particle moving in a δ-function potential well. This equation, as well as the beta function, has the same, universal form for all models, because, as is well known, all systems that possess continuous global symmetry are almost identical when N is large [5]. Mathematically, however, this seems somewhat strange, because $SU(\infty) \neq SO(\infty)$.

More complicated gauge and matrix theories are not equivalent to the Schrödinger equation. This is because, in contrast to these, the vector models in the spherical limit are systems of free massless Goldstone particles [2, 5].

In itself, solution of the canonical $SU(N)$-symmetric GL model in an external magnetic field in the limit of $N \longrightarrow \infty$ is undoubtedly of interest. However, this model, unfortunately, possesses a number of nonphysical features which are not observed in real type-II superconductors. Among these features are primarily the absence of a vortex lattice below the $H_{c2}(T)$ curve of phase transitions; the continuous transition to the homogeneous condensate state [20], which occurs in dimensions higher than four; the astronomical values of the upper critical field $H_0 \sim 10^5$ T; the low-temperature asymptotic behavior of the upper critical field [$H_{c2}(T) \longrightarrow \infty$ as $T \longrightarrow 0$] inconsistent with the experiment; etc.

Thus, the GL model, while exactly solvable in the limit under consideration, is obviously nonrealistic and needs modification.

At present, there is no one physically reasonable way of clearing all troubles (see, e.g., [33]). An interesting procedure in which the symmetry of the initial action is modified was proposed in [29] and discussed in this paper. It is also well known how to construct the GL model in physical dimensions $d \geq 2$ in such a way that a phase transition occurs in it. An example of such a model is a model of a superconductor on the lattice in a magnetic field [25, 34–36].

The method developed in this paper leads to a somewhat surprising interpretation of the $SU(N)$-symmetric GL model on the lattice. In this model, the two-point correlator obeys the discrete Schrödinger equation on the lattice in an external magnetic field. In terms of solid state physics, this equation describes a Bloch electron moving via sites of a d-dimensional lattice placed in an external uniform magnetic field; furthermore, the lattice has a δ-function potential well, produced by an impurity atom. This is the famous Azbel–Harper–Hofstadter problem [37–39]. The electron can be captured by the impurity and form a bound state. The threshold depth of the potential well for the formation of the bound state depends on the magnetic field, and it is this dependence that describes the $T_c(H)$ curve in a superconductor. For the magnetic flux Φ through a plaquette whose magnitude is given by the relation $\Phi/\Phi_0 = 2\pi p/q$, where p and q are relatively prime integers, the $T_c(q)$ dependence can be calculated numerically.

The SE method can also be applied to other models in statistical physics and quantum field theory, e.g., to the supersymmetric $O(N)$-symmetric nonlinear Witten

σ model [40, 41]. The universal beta function in Eq. (18) was also arrived at in the two-particle sector of the Kadar–Parisi–Zhang model [42]. Applications of the SE method to lattice systems and to models with disorder will be considered elsewhere.

ACKNOWLEDGMENTS

The greater part of this work was done at the University of Essen, Germany. I am grateful to the members of the staff of the University H.W. Diehl and K. Wiese for their warm hospitality and encouragement and many helpful discussions. It is a pleasure to thank Yu.M. Pis'mak, A.I. Sokolov, S.A. Ktitorov, and A.V. Gol'tsev for interesting discussions. Special thanks are due to M.V. Sadovskiĭ, who called my attention to paper [10], and T. Newman, E.B. Kolomeisky, and Z. Tečanovich, who sent me their interesting notes and several key references, among them [24], by e-mail. Finally, I am grateful to J. Zinn-Justin for a useful discussion.

This work was supported in part by the Russian Foundation for Basic Research, grant no. 98-02-18299.

REFERENCES

1. *The Large N Expansion in Quantum Field Theory and Statistical Physics*, Ed. by E. Brézin and S. R. Wadia (World Scientific, Singapore, 1993).
2. J. Zinn-Justin, *Quantum Field Theory and Critical Phenomena* (Clarendon Press, Oxford, 1999).
3. A. N. Vasil'ev, *Quantum Field Renormalization Group in the Theory of Critical Behavior and Stochastic Dynamics* (Peterburg. Inst. Yad. Fiz., St. Petersburg, 1998).
4. E. Brézin and J. Zinn-Justin, Phys. Rev. B **14** (7), 3110 (1976).
5. A. M. Polyakov, *Gauge Fields and Strings* (Inst. Teor. Fiz. im. L. D. Landau, Chernogolovka, 1995).
6. S. R. Wadia, Phys. Rev. D **24** (3), 970 (1981).
7. A. M. Polyakov, Phys. Lett. B **59B** (1), 79 (1975).
8. J. B. Kogut, Rev. Mod. Phys. **51** (3), 659 (1979).
9. K. Huang, *Quarks, Leptons, and Gauge Fields* (World Scientific, Singapore, 1982; Mir, Moscow, 1985); C. Thorn, Phys. Rev. D **6** (1), 39 (1972).
10. S. M. Apenko, J. Phys. A **31** (7), 1553 (1998).
11. E. B. Kolomeisky, Phys. Rev. B **46** (21), 13956 (1992).
12. E. B. Kolomeisky and J. P. Straley, Phys. Rev. B **46** (18), 11749 (1992); Phys. Rev. B **46** (21), 13942 (1992).
13. E. B. Kolomeisky and J. P. Straley, Phys. Rev. B **51** (13), 8030 (1995); T. Hwa and T. Natterman, Phys. Rev. B **51** (1), 455 (1995).
14. S. V. Novikov, S. V. Manakov, L. P. Pitaevskii, and V. E. Zakharov, *Theory of Solitons: The Inverse Scattering Method* (Nauka, Moscow, 1980; Consultants Bureau, New York, 1984).
15. M. J. Ablowitz and H. Segur, *Solitons and the Inverse Scattering Transform* (SIAM, Philadelphia, 1981; Mir, Moscow, 1987).
16. M. Rasolt and Z. Tesanovich, Rev. Mod. Phys. **64** (3), 709 (1992).
17. G. Blatter, M. V. Feigel'man, V. B. Geshkenbein, *et al.*, Rev. Mod. Phys. **66** (4), 1125 (1994).
18. I. A. Affleck and E. Brézin, Nucl. Phys. B **257** (3), 451 (1985).
19. S. A. Ktitorov, B. N. Shalaev, and L. Jastrabik, Phys. Rev. B **49** (21), 15248 (1994).
20. L. Radzihovsky, Phys. Rev. Lett. **74** (23), 4722 (1995).
21. G. Jug and B. N. Shalaev, Phys. Rev. B**58** (18), 12404 (1998).
22. I. F. Herbut and Z. Tečanovich, Phys. Rev. Lett. **76** (23), 4450 (1996).
23. L. Radzihovsky, Phys. Rev. Lett. **76** (22), 4451 (1996).
24. M. A. Moore, T. J. Newman, A. J. Bray, and S.-K. Chin, Phys. Rev. B **58** (2), 936 (1998).
25. B. N. Shalaev, cond-mat/9912424.
26. V. A. Kazakov and A. A. Migdal, Nucl. Phys. B **311** (1), 171 (1988).
27. E. Brézin, D. R. Nelson, and A. Thiaville, Phys. Rev. B **31** (12), 7124 (1985).
28. T. J. Newman and M. A. Moore, Phys. Rev. B **54** (9), 6661 (1996).
29. A. Lopatin and G. Kotliar, Phys. Rev. B **59** (5), 3879 (1999).
30. R. P. Feynman and A. R. Hibbs, *Quantum Mechanics and Path Integrals* (McGraw-Hill, New York, 1965; Mir, Moscow, 1968).
31. Yu. N. Demkov and G. F. Drukarev, Zh. Éksp. Teor. Fiz. **49** (1), 257 (1965) [Sov. Phys. JETP **22**, 182 (1965)].
32. G. Parisi and N. Sourlas, Phys. Rev. Lett. **43** (3), 744 (1979).
33. Z. Tečanovich, Phys. Rev. B **59** (12), 6449 (1999).
34. J. Toner, Phys. Rev. Lett. **66** (19), 2523 (1991).
35. S. A. Ktitorov, Yu. V. Petrov, B. N. Shalaev, and V. S. Sherstinov, Int. J. Mod. Phys. B **6** (3), 1209 (1992).
36. M. Y. Choi and S. Doniach, Phys. Rev. B **31** (10), 4516 (1985).
37. P. G. Harper, Proc. Phys. Soc. London, Sect. A **68** (3), 874 (1955).
38. M. Ya. Azbel, Zh. Éksp. Teor. Fiz. **46**, 929 (1964) [Sov. Phys. JETP **19** (2), 634 (1964)].
39. D. R. Hofstadter, Phys. Rev. B **14** (5), 2239 (1976).
40. E. Witten, Phys. Rev. D **16** (7), 2991 (1977).
41. A. I. Vaĭnshteĭn, V. I. Zakharov, V. A. Novikov, and M. A. Shifman, Fiz. Élem. Chastitsy At. Yadra **17** (3), 472 (1986) [Sov. J. Part. Nucl. **17**, 204 (1986)]; V. A. Novikov, M. A. Shifman, and V. I. Zakharov, Phys. Rev. **116** (3), 103 (1984).
42. K. J. Wiese, J. Stat. Phys. **93** (2), 143 (1998).

Translated by Yu. Epifanov

Physics of the Solid State, Vol. 43, No. 1, 2001, pp. 90–97. Translated from Fizika Tverdogo Tela, Vol. 43, No. 1, 2001, pp. 88–95.

MAGNETISM AND FERROELECTRICITY

Polarization Switching Kinetics in Ferroelectrics

S. A. Kukushkin and A. V. Osipov

Institute of Problems in Mechanical Engineering, Russian Academy of Sciences, Vasil'evskiĭ ostrov, Bol'shoĭ pr. 61, St. Petersburg, 199178 Russia
e-mail: ksa@math.ipme.ru

Received March 28, 2000

Abstract—The switching kinetics in ferroelectrics in the bulk polarization switching stage and in the final stage of the process are studied. Consideration is given to the specific case of switching of intrinsic ferroelectrics with 180° domains. A complete system of equations describing the switching processes and taking into account the change in repolarization in the course of a phase transformation is derived. The solution of this system is found. All the main characteristics of the switching process are calculated; namely, the evolution of the domain size distribution function is revealed and the time dependences of the domain density and flux are determined. An expression describing the variation in repolarization with time is obtained. The mechanisms of domain growth are studied. An equation for calculating the switching current and its variation with time is derived. A method is proposed for determining a number of constants for ferroelectric crystals by studying the switching current evolution. *© 2001 MAIK "Nauka/Interperiodica".*

1. INTRODUCTION

This study is a continuation of the investigation in [1] into the switching processes in ferroelectric crystals in an electric field. In the present work, we will consider the main and final stages in the switching process and derive analytic expressions for the switching current. Earlier [1], we noted that any first-order phase transition can be conventionally divided into three stages. In the first stage, the system does not yet "feel" the formation of a new phase and its thermodynamic parameters remain almost unchanged. In the subsequent stages of the phase transformation, the thermodynamic parameters vary and their variations affect the nucleation process. It turns out [1] that in the first stage of the phase transformation, it will suffice to determine the stationary flux of the nuclei, which specifies a boundary condition to the coupled equations describing the next stage of the phase transition. We turn now to its study.

2. KINETICS OF BULK POLARIZATION SWITCHING IN A FERROELECTRIC CRYSTAL

According to the general theory of phase transitions [2–4], after the maximum in the size spectrum of nuclei has reached the critical size in its evolution, fluctuations no longer affect the growth of nuclei of the new phase significantly. Therefore, the master kinetic equation for first-order phase transitions (see Eq. (11) in [1]) can be recast in the form

$$\frac{\partial f}{\partial t} + \frac{\partial}{\partial n}[V_n f(n, t)] = 0, \qquad (1)$$

where V_n is the growth rate of a nucleus and $f(n, t)$ is the size distribution function of the switched domains. Thus, the term describing the fluctuations is disregarded in this stage. In this stage of the phase transition, the repolarization in the system is not a constant quantity: it varies in the course of the phase transformation, because the formation of polarization switching nuclei changes the overall polarization of the crystal. Hence, Eq. (1) for the distribution function should be complemented by an equation describing the conservation of the total dipole moment in the crystal.

We write this equation in the differential form

$$J(E_z^0)\frac{p_i}{P_{z10}} = \frac{d\xi}{dt} + \frac{p_i}{p_{z10}}\int_0^\infty V_n f(n, t)dn. \qquad (2)$$

Here, ξ is the relative repolarization (the notion of repolarization was introduced in Section 2 of [1]), P_{z10} is the equilibrium value of the polarization, p_{zi} is the dipole moment of the unit cell volume ω, $J(E_z^0)p_{zi}/P_{z10}$ is the polarization switching source generated by the external field, and p_i/P_{z10}, $\int_0^\infty V_n f(n, t)dn$ is the rate of "polarization consumption" by the new-phase domains. Now, we determine the source $J(E_z^0)$. The field applied to a ferroelectric will change the direction of polarization in its unit cells. In order to find the number of elementary polarization vectors formed per unit volume of the crystal in a unit time, we will proceed as we did when calculating the domain growth rate in [1]. Let $J(E_z^0)$ be the number of elementary polarization vectors induced by the field. Using the results obtained in [1], we can

immediately write an expression for the number of switched cells appearing in a unit volume of the crystal per unit time; that is,

$$J(E_z^0) = \beta_0'' \frac{p_{zi}(E_z^0 - \bar{E}_z)}{k_B T},$$

where $\beta_0'' = N_v \nu \exp(-V_0'/k_B T)$, V_0' is the energy barrier height required for an elementary dipole in a cell to turn from a state with one direction of polarization to another in the absence of an external field, $N_v = 1/\omega$ is the number of unit cells per unit volume of the crystal, ω is the volume per unit cell, ν is the frequency of atomic vibrations in the cell, E_z^0 is the external field of the source at the instant of the onset of bulk polarization switching, and $\bar{E}_z$ is the field that acted on the system before actuation of the source. Recalling that $P_z^0 = P_{z10} + \chi\varepsilon_0 E_z^0$ [1], where χ is the permittivity and ε_0 is the permittivity of free space, we obtain

$$\xi^0 = \frac{J(E_z^0) p_{zi} \tau}{P_{z10}} = \frac{(P_z^0 - \bar{P}_z)}{P_{z10}}, \quad (3)$$

where $\tau = k_B T \chi \varepsilon_0 / \beta_0'' p_{zi}^2$. In a general case, the source $(J(E_z^0) p_{zi})/P_{z10}$ can be time dependent. By analogy with [2–4], the coupled equations (1) and (2) can be solved numerically for sources of any kind, specifically of pulsed action. We rewrite Eq. (2) in the form

$$\frac{\xi^0}{\tau} = \xi'(t) + \frac{p_i}{p_{z10}} \int_0^\infty V_n f(n, t) dn. \quad (4)$$

If the time τ is short enough to allow neglection of derivative $\xi'(t)$ due to the smallness of its change in this stage, the system of Eqs. (1) and (2) has an analytical solution. A method of solving such systems was developed in [2, 4]. Equation (4) can be recast now as

$$\xi^0 = \tau \frac{p_i}{p_{z10}} \int_0^\infty V_n f(n, t) dn. \quad (5)$$

Equations (1) and (5) describe the switching kinetics in ferroelectric crystals. In order to solve them, we need to know the expression for the domain growth rate V_n. It was obtained in [1] in the form

$$V_n = 2(\pi H \omega)^{1/2} \beta_0 \frac{p_{zi}(E_z - E_{zn})}{k_B T} n^{1/2}, \quad (6)$$

where H is the height of the nucleus, which we accepted approximately equal to $\omega^{1/3}$, and β_0 is the equilibrium flux of the unit cells.

As was shown in [2, 3], in this stage of the phase transition, the supersaturation (in our case, repolarization) changes insignificantly and is still sufficiently large, so that the size n of the forming and growing nuclei is considerably exceeds the critical value; i.e., $n \gg n_c$. In this connection, we recast expression (6) as

$$V_n = 2 \text{const} E_z(t) n^{1/2}, \quad (7)$$

where const $= \beta_0 (\pi H \omega)^{1/2} p_{zi}/k_B T$.

The system of equations is now complete, and we can find its solutions. To accomplish this, we rewrite Eq. (7) in the form

$$V_n = \frac{dn}{dt} = 2 \frac{\xi(t)}{t_0} n^{1/2}, \quad (8)$$

where t_0 is the characteristic time of the growth

$$t_0 = \left(\frac{\beta_0 (\pi H \omega)^{1/2} p_{zi} P_{z10}}{k_B T \chi \varepsilon_0} \right)^{-1}.$$

Next we introduce the dimensionless radius ρ of the nuclei in order to make the growth rate independent of n; i.e., we transform the variable to $\rho = n^{1/2}$.

Because $f(n, t) dn = g(\rho, t) dp$, Eqs. (1) and (2) can be rewritten as

$$\frac{\partial g(\rho, t)}{\partial t} + \frac{\xi(t)}{t_0} \frac{\partial}{\partial \rho} [g(\rho, t)] = 0, \quad (9)$$

$$\frac{\xi_0}{\xi(t)} - 1 = \lambda \int_0^\infty \rho g(\rho, t) d\rho \quad (10)$$

with boundary and initial conditions of the form $g(0, t) = I(\xi(t)) t_0/\xi(t)$, $g(\rho, 0) = 0$ $(\rho > \rho_c)$, $\lambda = 2 k_B T \chi \varepsilon_0 / (t_0 \beta_0'' p_{zi} P_{z10})$, and $\xi_0 = (P_z^0 - P_{z10})/P_{z10}$. When deriving the last equation, we transformed the variable from ξ^0 to ξ_0.

The coupled equations (8)–(10) fully describe the switching kinetics in ferroelectrics in the stage when the maximum in the nucleus size distribution has not yet reached critical size [2–4] and the rate of change of supersaturation is small compared to the flux of switched nuclei entering the system. This system can be solved by the method developed in [4]. The solution has the following form:

$$I(t) = \frac{I(\xi_0) \exp[-T^k(t) \varphi_k(T(t))]}{1 + (1/\Gamma) T^k(t) \varphi_k(T(t))}, \quad (11)$$

$$N(t) = I(\xi_0) t_k \varphi_k(T(t)), \quad (12)$$

$$\xi(t) = \frac{\xi_0}{1 + (1/\Gamma) T^k(t) \varphi_k(T(t))}, \quad (13)$$

where $I(t)$ is the flux of the switched domains at the instant of time t; $N(t)$ is the density of the newly formed, switched domains at the instant t; and $\xi(t)$ is

the relative repolarization at the instant t. Here, Γ is a parameter [4] defined as

$$\Gamma = -\xi_0 \frac{dR_{\min}}{d\xi}\bigg|_{\xi=\xi_0},$$

where $R_{\min}$ is the minimum work needed to form new-phase nuclei in a ferroelectric, the expression for which was obtained in [1]. In this case,

$$\Gamma = \frac{\pi H \sigma^2 \omega \chi \varepsilon_0}{2 k_B T p_{zi} P_{z10} \xi_0}.$$

The distribution function of the switched regions in the magnitude of polarization can be written in the form

$$f(\rho, t) = \begin{cases} \dfrac{I(\xi_0)t_0}{\xi_0}\exp\left[-T(t) - \left(\dfrac{t_0\rho}{t_k\xi_0}\right)^k\right]\varphi_k\left[T(t) - \dfrac{t_0\rho}{t_k\xi_0}\right] \\ \rho \le \dfrac{\xi_0 t_k}{t_0}T(t) \\ 0, \quad \rho > \dfrac{\xi_0 t_k}{t_0}T(t). \end{cases} \tag{14}$$

Here, $I(\xi_0)$ is the flux of nuclei, which is found from Eq. (36), derived in [1]:

$$T = \frac{t}{t_k} - \frac{1}{\Gamma}\int_0^T x^k \varphi_k(x)dx,$$

$$t_k = \frac{t_0}{\xi_0}\left[\frac{\xi_0}{(k+1)\omega\Gamma I(\xi_0)\tau}\right]^{1/(k+1)}, \tag{15}$$

where the auxiliary function $\varphi_k(x)$ is determined from the solution to the equation $d\varphi_k/dx = \exp(-x^k\varphi_k)$ subject to the condition $\varphi_k(0) = 0$ [2, 4], k is a coefficient depending on the mechanism of the nucleus growth [2–4], and $\tau = (k_B T\chi\varepsilon_0)/(\beta_0'' p_{zi}^2)$. In this case, $k = 1$.

The maximum size of the switched region can be determined from the relationship

$$\rho_{\max} = \frac{\xi_0 t_k T(t)}{t_0}.$$

Then,

$$T = \frac{t_0\rho_{\max}}{t_k\xi_0}.$$

This equality can be used as a definition of the renormalized time.

We note in conclusion that the solution (11)–(15) has a meaning only for $\Gamma \gg 1$. If the converse is true, the system should be solved numerically.

We turn now to the study of the later stage in the evolution of an ensemble of switched regions.

3. OSTWALD RIPENING OF AN ENSEMBLE OF SWITCHED DOMAINS

Ostwald ripening is the final stage of a phase transition where no new nuclei are formed and the repolarization tends to zero [2, 3]. In these conditions, a specific interaction sets in among the switched domains. The mean size of the polarization switching nuclei in the ensemble will grow as a result of "dissolution," i.e., the rotation of the polarization vector "against the field" and the growth of large nuclei due to aligning a part of the polarization vectors with the field.

In this process, the average magnitude of repolarization in the crystal will decrease. This is due to the decrease in the free energy of the system as a result of diminishing the interface and, accordingly, diminishing stresses at the domain walls. In a general case, large domains will absorb small ones. A specific interaction sets in between the polarization switching nuclei, because each domain feels the cooperative polarization field of the whole domain system. This should be connected with the law of conservation of the total polarization in the system [see Eq. (2)]. We rewrite Eqs. (1) and (2) with the variables R and t, where R is the radius of the switched regions. Since

$$f(n, t)dn = f(R, t)dR,$$

we have

$$\frac{\partial f}{\partial t} + \frac{\partial}{\partial R}[V_R f(R, t)] = 0. \tag{16}$$

In the stage of Ostwald ripening, domains of different sizes compete because of the growth of the critical nuclei in the system, which become comparable in radius to domains.

In the case when the domain dimensions become comparable with the critical size, we should take into account not only the flux of the cells attaching to a domain, but the reverse cell flux bringing about dissolution of a domain as well. Therefore, in order to describe the growth rate of domains, we turn to Eq. (6). Recall that E_n can be expressed through the number of particles according to expression (24) derived in [1]. After simple manipulations, we obtain the following equation for the domain growth:

$$V_n = \frac{\pi H \omega \beta_0 \sigma}{k_B T}\left(\frac{n^{1/2}}{n_c^{1/2}} - 1\right). \tag{17}$$

This equation was derived taking into account expression (26) from [1].

Note that expression (17) for domain growth rate was obtained under the assumption that the domain wall grows through equiprobable attachment of structural elements to any point on its surface. This mechanism of the growth corresponds to the growth of rough crystal surfaces [2, 3, 5] and is called the normal mechanism. As is well known from the theory of crystal growth [5], there are two more possible mechanisms of

crystal face growth, namely, the layer-by-layer process and the growth through two-dimensional formation of nuclei with their subsequent coalescence. In the stage of nucleation and bulk polarization switching, the domains are still small in size and their surfaces are not fully formed. For this reason, we considered only one mechanism of their growth, the most probable one. In the later stage of the evolution, the polarization switching approaches zero and the conditions are close to equilibrium. In this case, the domain wall surfaces can be smooth. As a result, the domains can increase in size, apart from their growth by the normal mechanism, through the layer-by-layer growth of their faces. In this connection, we now consider the other growth mechanisms in more detail.

4. MECHANISMS OF DOMAIN GROWTH

We will not study the domain growth by two-dimensional nucleation for two reasons. First, its description would require more comprehensive knowledge of the domain-wall surface structure. As a rule, the formation of two-dimensional nuclei is most probable on face defects which enhance the formation considerably. Second, after the formation of two-dimensional nuclei, the wall continues to grow by the layer-by-layer mechanism.

In order to calculate the rate of domain growth by the layer-by-layer mechanism, we reason as follows. Let a domain consist of N faces and two-dimensional nuclei are formed on each of the domain faces so that they completely fill its surface.[1] In a general case, these nuclei can be represented in the form of two-dimensional flat plates, for instance, squares with a linear dimension of face l. The area of each of these two-dimensional nuclei can be estimated as $S_c \approx \pi(l/2)^2$, or $S_c \approx \pi r_c^2$, where r_c is the radius of a disk-shaped two-dimensional nucleus inscribed into the square. The number of nuclei making up the domain face of height H is $N \approx H/2r_c$. The volume of the bubble domain thus faceted is the sum of the volumes of its identical rectangular parallelepipeds, whose base is the two-dimensional square. The thickness of these parallelepipeds is equal to the domain radius R.

The change in the thermodynamic potential of an N-faced domain can be written as

$$\Delta\Phi = -\Delta\bar{\mu}N\frac{H}{2r_c\omega}S_cR + \sigma N\frac{H}{2r_c}S_c, \qquad (18)$$

where $\Delta\mu(R)$ is the mean difference of chemical potentials between the medium and the switched domain. In a general case, r_c is a function of R. To a first approximation, the relation between $r_c(R)$ and R can be considered linear. The critical radius of a two-dimensional nucleus on the domain surface is determined by the mean value of $\Delta\mu(R)$ at this surface,

$$r_c(R) = \frac{\sigma_{st}\omega}{\Delta\mu(R)}, \qquad (19)$$

where σ_{st} is the surface tension of a step. The chemical potential difference between the medium and the switched domain $\Delta\mu(R)$ is found from expression (24) derived in [1], in which the number of particles n is expressed in terms of the domain radius R.

In order to determine the critical size of the domain thus faceted, we differentiate $\Delta\Phi$ with respect to R and equate the resulting expression to zero. As a result, we find (this can be readily shown, and we do not present here a detailed derivation) that the critical radius of this domain is determined by expression (26) obtained in [1]. This means that the critical radius of domains bounded in this way does not differ from that of unfaceted domains. Therefore, we can write an expression for the rate of layer-by-layer growth of domains. For this purpose, we invoke the analogy between the growth of bounded nuclei studied in [6, 7] and that of domains. This analogy implies that the growth rate of a domain along the normal to its surface should be proportional to the difference between the fluxes of the unit cells, which are attached to and detached from the unit area of the step. In addition, this rate is proportional to the fraction of the area of the domain side surface to which switched cells are attached. This area fraction S is equal to the number of two-dimensional nuclei forming the domain face of height H, i.e., $H/2r_c$. Denoting the flux of the unit cells which are attached to the unit area of the step by $\beta_{st}(E)$ and the flux of detaching cells by $\beta_{st}(E_n)$, we obtain for the domain growth rate

$$V_n = \frac{H}{2r_c}[\beta_{st}(E) - \beta_{st}(E_n)]S. \qquad (20)$$

Substituting $S = 2(\pi H\omega)^{1/2}n^{1/2}$ into Eq. (20) gives

$$V_n = \frac{\pi^{1/2}H^{3/2}}{r_c}(\omega)^{1/2}[\beta_{st}(E) - \beta_{st}(E_n)]n^{1/2}. \qquad (21)$$

The coefficients $\beta_{st}(E)$ and $\beta_{st}(E_n)$ depend on the external field E. To calculate them, we use the technique applied in [1] and write the expression for the domain wall growth rate:

$$V_n = \frac{\pi^{1/2}H^{3/2}}{n_c}(\omega)^{1/2}\beta_{st0}\frac{p_{zi}(E_z - E_{nz})}{k_BT}n^{1/2}. \qquad (22)$$

In this expression, $\beta_{st0} = N_{st}\nu_{st}\exp(-\nu_{st0}/k_BT)$, N_{st} is the number of unit cells at the step, ν_{st} is the frequency of atomic vibrations in cells at the step, $\nu \sim \nu_{st}$, and V_{st} is the energy expended on transferring an atom in the cell from one state to another as a result of polarization switching at the kink in an equilibrium state and with no field applied.

[1] If a face is filled incompletely, charges appear at the interface between the medium with one direction of polarization and the nucleus polarized in the opposite direction, which violates the continuity of the normal component of the electric field (see [1]).

Thus, we considered two domain growth mechanisms, which we believe to be the most probable ones. We now express Eqs. (17) and (22) not in terms of the number of particles n in a domain but through domain radius R. As a result, the rate of domain growth by the normal mechanism is represented in the form

$$\frac{dR}{dt} = \frac{\beta_0 \omega^2 \sigma}{2k_B TR}\left(\frac{R}{R_c} - 1\right). \quad (23)$$

A similar transformation of Eq. (22) yields the following relationship for the domains growing by the layer-by-layer mechanism:

$$\frac{dR}{dt} = \frac{H\omega^2 \beta_{st0} \sigma^2}{4k_B T \sigma_{st} R_c R}\left(\frac{R}{R_c} - 1\right). \quad (24)$$

We turn now to an analysis of the relationships derived. The balance equation (2) has the form

$$Q_0 + \int_0^t \xi_0(t')dt' = \frac{\bar{P}_z(t) - P_{z10}}{P_{z10}} + \frac{\pi H p_i}{P_{z10}\omega}\int_0^\infty f(R, t)R^2 dR, \quad (25)$$

where

$$Q_0 = \frac{P_{z0} - P_{z10}}{P_{z10}} + \frac{\pi H p_i}{P_{z10}\omega}\int_0^\infty f_0(R)R^2 dR.$$

As in [2, 8], we assume that the source $\int_0^t \xi_0(t)dt$ decays in time and can be approximated by the polynomials $\xi_0(t) = (\xi_0/\tau)t^{n-1}$, where $n \geq 0$ is the field growth index and ξ_0 and τ are from the calculations above. For simplicity, we assume that the source is uniformly distributed in the sample.

The coupled equations (16) and (25), together with Eq. (23) or Eq. (19), which describe the growth rate of nuclei, make up a complete system and formally coincide fully with the equations describing the late stage in a first-order phase transition [8] (the Ostwald ripening stage).

The solution to such a system was first obtained by Lifshitz and Slezov (see [2, 3, 8]). However, there also exists a different and more rigorous asymptotic treatment [9] (see also [2]), whose results will be used here. The Ostwald ripening stage can occur only in the case when the external field either is turned off after the formation of switched domains or varies with time so that the index n in Eq. (25) becomes smaller than $n < 2/p$, where p is the growth index, $p = 2$ for the growth of nuclei by the rough process, and $p = 3$ for the layer-by-layer growth of nuclei. Then, the mean size of nuclei will vary with time as a result of evolution [3, 9] as

$$R(t) \longrightarrow \text{const}' \cdot t^{1/p}, \quad (26)$$

where $p = 2$ if the growth of nuclei is rate-limited by the boundary kinetics and $p = 3$ for the layer-by-layer growth. The density of the nuclei varies with time as follows:

$$N(t) \longrightarrow \text{const}'' \cdot t^{(n-3/p)}. \quad (27)$$

The nucleus size distribution functions in dimensionless coordinates have the same form for the late stage of all phase transitions. Rather than write them out here, we refer the reader to [2, 3, 8, 9].

We note in conclusion that because both the mean and critical sizes in the Ostwald ripening stage vary with time by relationship (26), the repolarization change with time should be as follows:

$$\xi(t) \longrightarrow \text{const}''' \cdot t^{-1/p}. \quad (28)$$

In Eqs. (26)–(28), const', const", and const"' are constants depending on the actual domain growth mechanism. These constants are readily found in the Lifshitz–Slezov theory [2, 3, 8, 9]. According to [9], in a general case, these constants are not determined theoretically and can be found only from comparison of the theoretical expressions with experimental data.

The relaxation of repolarization to the equilibrium state was studied experimentally [10]. The experimental curves were fitted by damped exponentials. As follows from our theory, in the late stages, these exponentials should be functions of type (28). In an earlier stage, as follows from Eq. (13), repolarization decays exponentially in time.

5. SWITCHING CURRENT IN FERROELECTRICS

The dependence of the switching current density on time in a ferroelectric capacitor can be written as follows [11]:

$$J = -2P_{z10}\frac{dQ}{dt}, \quad (29)$$

where dQ/dt is the rate of change in the ferroelectric volume fraction Q which has not yet switched and P_{z10} is the starting value of the spontaneous polarization of the ferroelectric. In the earliest switching stage, i.e., in the first stage of the phase transition, which we studied in [1], the switching current should be zero. Indeed, the expression for the nucleus flux I derived in [1] describes the switching process only in the case when no noticeable volume fraction of the crystal has become involved in the phase transition and the rate of change in the crystal volume fraction is zero. The main switching current will start to flow when the system enters the stage of bulk polarization switching. The time of the onset and the duration of this stage can be estimated from formula (15). To calculate the switching current in this stage, we pursue the following reasoning. The volume fraction, or the degree of sample volume filling by the nuclei of the new phase, can be calculated using two approaches. One of them is based on the well-known Kolmogorov–Avrami method [12, 13]. This method

was employed in [11] to determine the switching current. However, it is known [2, 3] that quantities such as the nucleation rate and the growth rate of the nuclei, which enter into the Kolmogorov–Avrami expression, are not parameters of this theory. They are calculated from other considerations. It is these parameters that we have just found. Now, we can insert them into the Kolmogorov–Avrami expression and calculate the current.

However, the Kolmogorov–Avrami expression is valid only in the case when the growth rate of nuclei does not depend on their radius and the repolarization remains constant throughout the process. As is seen from Eqs. (11)–(13), this is not so. Therefore, application of this theory to the process of transformation is not justified from the physical standpoint. Note that attempts at correcting this drawback have recently appeared [14]. However, we will use another approach, which makes it possible to describe rigorously the process of filling the system volume by growing nuclei with due regard for the change in the repolarization and the dependence of the growth rate of nuclei on their size.

This approach is based on the system of kinetic equations derived above [Eqs. (1)–(10)]. In the general case, the switching domains, as nuclei of the new phase [2, 3, 15], can collide with one another and coalesce. If the system is sufficiently tenuous, we can assume the collisions to be primarily binary. To take them into account, we add the collision integral to the right-hand side of Eq. (1). This procedure was employed in [15] to take into account the collisions between nuclei in volume and surface systems. We can write the equation of evolution for the distribution function of polarization switching domains with inclusion of their possible collisions and coalescence; that is,

$$\frac{\partial f}{\partial t} + \frac{\partial [V_n f(n,t)]}{\partial n} = \frac{1}{2}\int_0^n \beta(n-n', n') f(n-n') f(n') dn' - f\int_0^\infty \beta(n, n') f(n') dn', \quad (30)$$

$$f(n_0 t) = I(t)[1 - Z(t)] V_n^{-1}\big|_{n=n_0}, \quad f(n, 0) = 0, \quad (31)$$

where $I(t)$ is the rate of nucleation, $Z = 1 - Q$ is the degree of filling of the ferroelectric volume by the polarization switching domains, and β is the coagulation kernel [15] [it is assumed that $f(n, t) = 0$ at $n < n_0$]. Because the functions V_n and $I(t)$ depend on the repolarization $\xi(t)$, Eq. (30) should be complemented by the law of polarization conservation. We rewrite Eq. (4) with due regard for the fact that part of the unit volume of the ferroelectric is already occupied by switched regions. The region filled by the polarization switching nuclei is given by

$$Z(t) = \omega\int_0^\infty n f(n, t) dn. \quad (32)$$

Then, the law of conservation (4), which was written taking into account that nucleation occurs only in empty sites, can be recast as

$$\frac{d\xi}{dt} = \frac{\xi_0}{\tau} - \frac{\xi}{\tau} - \frac{\left(\frac{P_z}{P_{z10}} - 1 - \xi\right)}{(1 - Z)}\frac{dZ}{dt}, \quad (33)$$

where the ratio P_z/P_{z10} accounts for the difference in the volume fraction occupied by switched cells in the equilibrium state and in the completely switched state in the presence of the field.

By solving the set of Eqs. (30)–(32) with the use of Eqs. (11)–(13), we can find all the main characteristics of the switching process. For some kinds of coagulation kernels, it is possible to obtain analytic expressions. Comprehensive analysis of the system requires knowledge of the mechanisms by which polarization switching domains interact with one another. These coupled equations were analyzed in the specific case of the growth of crystalline new-phase nuclei on the substrate surface [2, 3, 15]. For rigorous calculations of the switching current, we can use the analogy and invoke these results. We consider the application of this method in the simplest case, without inclusion of domain coalescence; i.e., the integral in the right-hand side of Eq. (30) is taken equal to zero. We write the expression for $Z(t)$ in the variables ρ and t bearing in mind that $\rho = n^{1/2}$ and $f(n, t)dn = q(\rho, t)d\rho$. Differentiating $Z(t)$ with respect to time and transforming it with the use of Eqs. (8), (9), and (37) under the condition that $q(\rho, t)|_{\rho\to\infty} = 0$, we obtain

$$\left(\frac{Z'}{\xi}\right)' = \frac{2\omega\xi}{t_0^2}N, \quad (34)$$

where t_0 is the characteristic growth time introduced earlier [see Eq. (8)] and N is the number of created nuclei. In the latter expression, the prime denotes the time derivative. Differentiating Eq. (34) once more with respect to time yields

$$\left[\frac{1}{\xi}\left(\frac{Z'}{\xi}\right)'\right]' = \frac{2\omega}{t_0^2} I(\xi(t)), \quad (35)$$

where $I(\xi(t))$ is the flux of the nuclei.

Since the equation for the switching current contains not Z' but $Q = (1 - Z)'$, the switching current takes

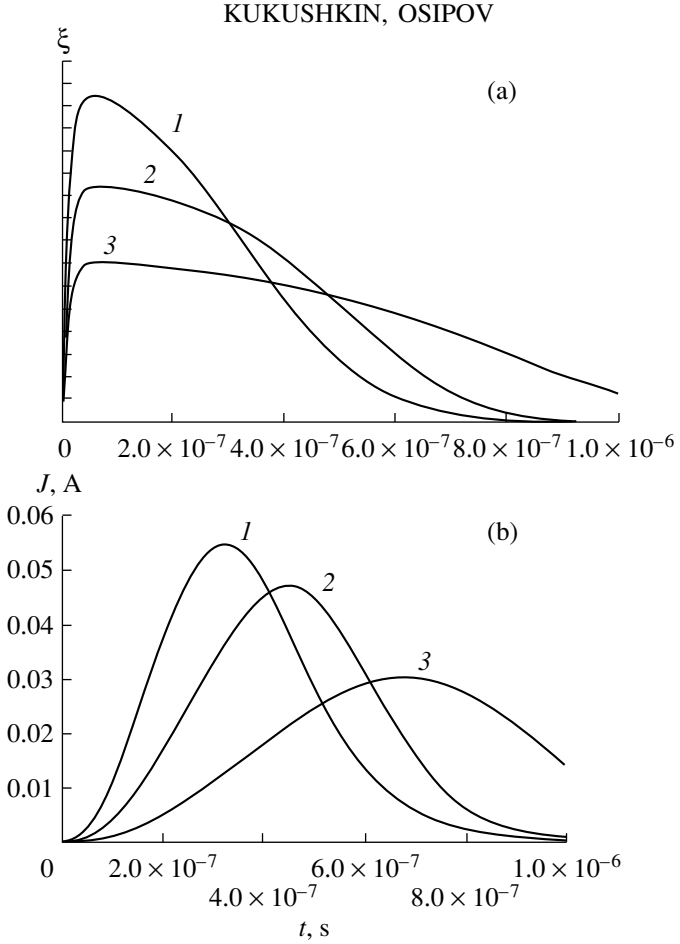

Fig. 1. Time dependences of (a) polarization switching and (b) switching current in different electric fields E_z at $I_0 \sim 10^{38}$, $\alpha \sim 10$, $t_0 \sim 10^{-13}$ s, $P_z/P_{z10} \sim 1.5$, and $S \sim 10^{-9}$ m^2. E_z (V m^{-1}): (*1*) 10^6, (*2*) 1.5×10^5, and (*3*) 10^5.

the form

$$\left[\frac{1}{\xi}\left(\frac{j}{\xi}\right)'\right]' = \frac{4\omega P_{z10}}{t_0^2} I(\xi). \quad (36)$$

Thus, Eq. (36) together with Eq. (33) make up coupled equations for calculating the dependence of the switching current on time and applied field. We transform Eq. (33) to the form

$$j = -\frac{2P_{z10}(\xi_0/\tau - \xi' - \xi/\tau)(1-Z)}{(P_z/P_{z10}) - 1 - \xi}. \quad (37)$$

Substituting Eq. (37) in Eq. (36) yields

$$\left[\frac{1}{\xi}\left(\frac{(\xi_0/\tau - \xi' - \xi/\tau)(1-Z)}{((P_z/P_{z10}) - 1 - \xi)\xi}\right)'\right]' = \frac{2\omega}{t_0^2} I(\xi). \quad (38)$$

This equation determines the dependence of the supersaturation on time. The initial conditions here are that the switching current, its derivatives with respect to time, and the supersaturation are zero.

The $I(\xi)$ dependence was found earlier in [1]; we recast it in the form

$$I(\xi) = I_0 \xi^{1/2} e^{-a/\xi}, \quad (39)$$

where

$$I_0 = \frac{N_v \beta_0 \sqrt{H\omega p_{zi} P_{z10}}}{2\sqrt{k_B T \chi \varepsilon_0}}; \quad \alpha = \frac{\pi H \omega \sigma^2 \chi \varepsilon_0}{2 k_B T p_{zi} P_{z10}}.$$

The constants I_0, t_0, and α entering into the expression for the flux of the nuclei $I(\xi)$ can be determined by comparing the theoretical dependences of the switching current with the experiment. These data can be used to obtain a number of the parameters for ferroelectrics (surface tension σ, the kinetic coefficients β_0, etc.). Moreover, the equations derived make it possible to determine the flux and the number of the switched domains formed in the course of polarization switching.

Thus, investigation of the polarization current in ferroelectrics opens up a unique possibility for studying some parameters of materials, which are difficult to determine otherwise.

Note that if the mechanisms of domain coalescence are known, solving the complete system (36)–(39) will provide more complete and accurate information on these constants. It should be remembered that in developing our theory, we assumed that the ferroelectric crystal was a perfect dielectric, the leakage current was

zero, and that there were no pinning centers impeding domain wall motion. Usually, ferroelectric crystals contain defects of various types. Nucleation is known to proceed more intensively at defects. In principle, this can be taken into account. Such a study was performed in the specific case of nucleation of a new phase on the surface of a substrate [2].

6. DISCUSSION OF THE RESULTS AND COMPARISON WITH THE EXPERIMENT

Now, we estimate some of the relationships obtained for TGS crystals with 180° domains. According to [16, 17], these crystals are characterized by the following parameters: the Curie temperature $T_c \sim 322$ K, surface tension $\sigma \sim 0.6 \times 10^{-3}$ J m^{-2} at $T \sim 302$ K, $P_{z10} \sim 3 \times 10^4$ μC m^{-2}, $\chi \sim 20$, $\varepsilon_0 = 8.85 \times 10^{-12}$ F m^{-1}, $\omega \sim 6.7 \times 10^{-28}$ m^3, and $N_v \sim 1/\omega$. Hence, it follows that in the field $E = 10^5$ V m^{-1}, the critical domain size calculated from Eq. (27) derived in [1] should be $R_c \sim 10^{-1}$ μm, which is in good agreement with the data obtained in [16]. Substituting the data in Eq. (42) of [1] and accepting the estimate $\beta_0 \sim 10^{31}$ m^{-2} s^{-1} yields, for the time of establishment of a stationary flux, $t \sim 10^{-10}$ s for fields $E \sim 10^5$ V m^{-1}. In a similar way, we can estimate the flux I of the nucleating domains from Eq. (38) derived in [1]. For instance, if the switching field is $V \sim 10^7$ V m^{-1}, then, for the same crystal at the same temperature, we have $I = 10^{44}\sqrt{H}\exp(-H10^8)$ m^{-3} s^{-1}.[2] For $H = 5 \times 10^{-10}$ m, $I \sim 10^{39}$ m^{-3} s^{-1}.

For $H \sim 10^{-8}$ m, the constants entering into formula (39) have the following approximate values: $I_0 \sim 10^{38}$, $\alpha \sim 10$, and $t_0 \sim 10^{-13}$ s. Figures 1a and 1b show the time dependences of the polarization switching and the switching current in different fields for the same values of the constants (TGS crystals), $P_z/P_{z10} \sim 1.5$, and the sample area $S \sim 10^{-9}$ m^2, which were calculated from Eqs. (32)–(39). We readily see that the switching current curves calculated follow qualitatively well the evolution of the switching current in ferroelectrics [18, 19].

In conclusion, we note that switching processes in ferroelectric crystals of a broader class [18–20] can be studied in a similar way to intrinsic ferroelectrics with 180° domains. To do this, one should introduce additional terms into the Gibbs thermodynamic potential and take into account the attendant elastic energy components. We are planning to further pursue this approach. Nevertheless, the equations derived in this work should retain their general form.

[2] The reader interested in the dependence of the nucleation rate on H should refer to [1]. We accepted therein that $H \sim 1/\omega^{1/3}$. In a general case, the nucleation rate depends, as this can be seen, on sample thickness. In thin films, which consist, as a rule, of small crystallites, the probability of nucleation of polarization switching domains should depend considerably on the crystallite size.

ACKNOWLEDGMENTS

We are grateful to A.G. Ambrok for his assistance in the numerical computation of Eqs. (30) and (39).

This work was supported in part by the Russian Foundation for Basic Research (project nos. 98-03-32791 and 99-03-32768), the Russian Center “Integration” (project no. A0151), the NATO Grant “Science of Peace” (grant Stp 973252), and the CONACYT Grant (project no. 32208).

REFERENCES

1. S. A. Kukushkin and A. V. Osipov, Fiz. Tverd. Tela (St. Petersburg) **43** (1), 80 (2001) [Phys. Solid State **43**, 82 (2001)].
2. S. A. Kukushkin and A. V. Osipov, Usp. Fiz. Nauk **168** (10), 1083 (1998) [Phys. Usp. **41**, 983 (1998)].
3. S. A. Kukushkin and A. V. Osipov, Prog. Surf. Sci. **56** (1), 1 (1996).
4. S. A. Kukushkin and A. V. Osipov, J. Chem. Phys. **107**, 3247 (1997).
5. A. A. Chernov, in *Modern Crystallography*, Vol. 3: *Crystal Growth* (Nauka, Moscow, 1980; Springer-Verlag, Berlin, 1984).
6. S. A. Kukushkin and T. V. Sakalo, Fiz. Tverd. Tela (St. Petersburg) **34** (4), 1102 (1992) [Sov. Phys. Solid State **34**, 587 (1992)].
7. S. A. Kukushkin and T. V. Sakalo, Acta Metall. Mater. **41** (4), 1237 (1993).
8. V. V. Slezov, Phys. Rev. **17**, 1 (1995).
9. S. A. Kukushkin and A. V. Osipov, Zh. Éksp. Teor. Fiz. **113**, 2193 (1998) [JETP **86**, 1201 (1998)].
10. V. V. Gladkiĭ, V. A. Kirikov, and E. S. Ivanova, Fiz. Tverd. Tela (St. Petersburg) **39** (2), 353 (1997) [Phys. Solid State **39**, 308 (1997)].
11. Y. Ishibashi and Y. Takagi, J. Phys. Soc. Jpn. **31**, 506 (1971).
12. A. N. Kolmogorov, Izv. Akad. Nauk SSSR, Otd. Mat. Estestv. Nauk, Ser. Mat. **3**, 355 (1937).
13. M. Avrami, J. Chem. Phys. **7**, 1103 (1939).
14. V. G. Dubrovskiy, Phys. Status Solidi B **171**, 345 (1992).
15. A. V. Osipov, Thin Solid Films **261**, 173 (1995).
16. L. I. Dontzova, N. A. Tikhomirova, and L. A. Shuvalov, Ferroelectrics **97**, 87 (1989).
17. *Ferroelectrics and Antiferroelectrics*, Ed. by G. A. Smolenskiĭ *et al.* (Nauka, Leningrad, 1974).
18. C. L. Wang, L. Zhang, W. L. Zhong, and P. L. Zhang, Phys. Lett. A **254**, 297 (1999).
19. N. N. Kraĭnik and L. S. Kamzina, Fiz. Tverd. Tela (St. Petersburg) **37** (4), 999 (1995) [Phys. Solid State **37**, 542 (1995)].
20. V. V. Lemanov, E. P. Smirnova, and E. A. Tarakanov, Fiz. Tverd. Tela (St. Petersburg) **39** (4), 714 (1997) [Phys. Solid State **39**, 628 (1997)].

Translated by G. Skrebtsov

Physics of the Solid State, Vol. 43, No. 1, 2001, pp. 98–109. Translated from Fizika Tverdogo Tela, Vol. 43, No. 1, 2001, pp. 96–107.

MAGNETISM AND FERROELECTRICITY

Magnetic Resonance of Exchange-Coupled Copper Complexes in Perovskite-Structure Crystals: The Potassium Tantalate and Cuprate Superconductors

P. G. Baranov, A. G. Badalyan, and D. V. Azamat

Ioffe Physicotechnical Institute, Russian Academy of Sciences
Politekhnicheskaya ul. 26, St. Petersburg, 194021 Russia

Received April 25, 2000

Abstract—This paper reports on parallel EPR studies of high-temperature superconductors based on the cuprate perovskites $R Ba_2Cu_3O_{6+x}$ (R = Y, Gd, Nd) and of $KTaO_3$: Cu, which also has a perovskite structure. EPR measurements performed on copper-doped $KTaO_3$ crystals revealed Cu^{2+}–Cu^{2+} copper pair centers. The copper ions making up pairs are assumed to occupy adjacent tantalum sites. The pair centers are chains consisting of two equivalent Cu^{2+} ions and three oxygen vacancies aligned in the ⟨100⟩ direction. The crucial point in the model proposed is the presence of an oxygen vacancy sandwiched between two Cu^{2+} ions, whereas the outer vacancies do not necessarily occupy neighboring sites. In this structure, complete charge compensation is achieved. Ferromagnetic exchange coupling takes place between the two copper ions. An investigation of the exchange and superhyperfine interactions of copper centers in crystalline potassium tantalate has permitted the estimation of the respective interactions in crystals of the cuprate superconductors which exhibit magnetic resonance signals due to exchange-coupled copper clusters in the case of oxygen deficiency. © *2001 MAIK "Nauka/Interperiodica".*

The discovery of high-temperature superconductors (HTSCs) based on cuprate perovskites [1] has stimulated an ever-increasing interest in the investigation of the copper–oxygen-vacancy complexes in these compounds. Electron paramagnetic resonance (EPR) is the main method used to study the structure of copper complexes in various materials; suffice it to mention that the first observation of EPR was made by Zavoĭsky on copper ions as far back as 1944 [2]. In a number of EPR studies of HTSC compounds of the $R Ba_2Cu_3O_{6+x}$ type (where R = Y, Gd, Nb; x varies from 0 to 1), there was success in observing broad unresolved magnetic resonance (MR) lines [3–5], which could be conventionally assigned to the copper ions. These MR spectra depend substantially on the concentration of oxygen (oxygen vacancies) in the HTSCs. It is of interest to find model objects that are structurally close to the cuprate perovskites and in which the copper–oxygen-vacancy complexes can form. The main objective underlying our studies is, on the one hand, to provide convincing arguments that the MR lines observed in the HTSCs [3–5] do belong to copper complexes and, on the other, to obtain quantitative information on the exchange, hyperfine (HF), and superhyperfine (SHF) interactions and g factors for the copper complexes in materials approaching the cuprate perovskites in their properties. These studies are assumed to culminate in providing information on the electronic structure of these complexes and the spatial distribution of the wave functions. It is also essential to understand which of the copper ions—in chains or in the planes—are responsible for the observed MR signals. For our studies, we chose copper-doped $KTaO_3$ crystals, in which the oxygen vacancies play a major part in the charge compensation of the copper impurity ions. In this paper, we report on an EPR observation of copper pair centers in these crystals. The preliminary results were published in [6].

1. EXPERIMENTAL TECHNIQUES

We used the ceramics and single crystals of the R–Ba–Cu–O cuprate superconductors (R = Y, Nd, Gd, Sm) prepared in various laboratories. The starting samples were, as a rule, pure single-phase superconductors with $T_C \simeq 90$ K, and they exhibited only microwave absorption in a zero magnetic field (low-field signal) and the strong microwave-absorption fluctuations characteristic of the superconducting phase. The quenching was done by heating the samples to various temperatures (up to 1050 K) in air and rapidly cooling them subsequently in water or liquid nitrogen. In the course of annealing, the samples were heated and maintained at various temperatures in air or in a vacuum, after which they were cooled slowly (over 1–5 min).

The Gd–Ba–Cu–O and Nd–Ba–Cu–O crystals were grown by direct RF melting in a cold crucible [3] and represented actually a sandwich made up of thin platelets about 1 μm thick. The total sample thickness was approximately 50–100 μm. The c axis was normal to the platelet plane.

The $KTaO_3$: Cu crystals were grown by spontaneous crystallization in a platinum crucible [6]. The copper concentration in the charge varied from 0.05 to 0.5 mol %. The angular dependences were measured by rotating the sample about the ⟨100⟩ or ⟨110⟩ axis.

We used the standard JEOL EPR spectrometer operating in the *X* and *Q* ranges at frequencies of 9.3 and 35 GHz, respectively. The sample temperature in the EPR studies could be varied smoothly within the 3.5- to 300-K range in a helium-flow cryostat. The MR measurements in the *Q* range at 1.6 K were carried out in a laboratory-designed instrument providing microwave power modulation in the cavity.

2. EXPERIMENTAL RESULTS

2.1. $YBa_2Cu_3O_{6+x}$

Consider first the results obtained in the MR studies of the $YBa_2Cu_3O_{6+x}$ compounds. $YBa_2Cu_3O_{6+x}$ crystals are believed to have ionic bonding, with the oxygen concentration (x) playing a specific part, because it radically affects the physical properties of this crystal. Depending on the actual oxygen concentration x, the $YBa_2Cu_3O_{6+x}$ compound crystallizes in two phases, orthorhombic and tetragonal. The orthorhombic phase, presented conventionally in Fig. 1a, is obtained at oxygen concentrations corresponding to the values of x lying within the 0.5–1 interval, while at lower oxygen concentrations the tetragonal phase sets in. Figure 1a shows the accepted numbering of the various inequivalent positions of copper and oxygen. The crystal has a layered perovskite-like structure, which consists of two $^{II}CuO_2$ planes in the unit cell (the figure shows four unit cells) separated by a Y ion layer. The Y ions are coupled with oxygen through the Ba and ^{I}Cu layers. For intermediate values of x, the structure of the crystal depends on the way in which the oxygen is removed. Theoretical calculations of the phase diagram in the x–T plane predict the formation of more complex phases with periodic filling of the chains, the appearance of chains of a finite length, etc. (see, e.g., [7]).

There are two inequivalent copper positions in these crystals, with the copper ions residing in the CuO_2 planes (^{II}Cu) and in the chains (^{I}Cu); it is assumed that the charge state of the copper depends on the x parameter. The stoichiometric oxygen composition x can be varied by annealing the crystal in an atmosphere with a preset partial pressure of oxygen, followed by quenching of the crystal.

At $x = 0$, $YBa_2Cu_3O_6$ is an antiferromagnetic insulator with the $^{II}Cu^{2+}$ ions magnetically ordered on the CuO_2 plane. It is assumed that the chain copper ions (^{I}Cu) are in the zero-spin state $^{I}Cu^{+}$. It is believed that when oxygen is added ($0 < x \le 1$), it becomes incorporated into the copper chains and acts as an acceptor by capturing electrons from the $^{II}CuO_2$ plane and creating holes in it. Thus, in the limiting case of $YBa_2Cu_3O_7$, we have an intrinsic p-type semiconductor. In these conditions, the hole concentration for $x = 1$ is 5×10^{21} cm^{-3} (one hole per unit cell).

The $x = 1$ structure has layers formed of apex-joined, square-based oxygen pyramids with the ^{II}Cu ions inside and chains of planar oxygen squares containing ^{I}Cu ions. The decrease in the oxygen content from O_7 to O_6 is associated with the breakdown of the chains up to their total disappearance, and the connec-

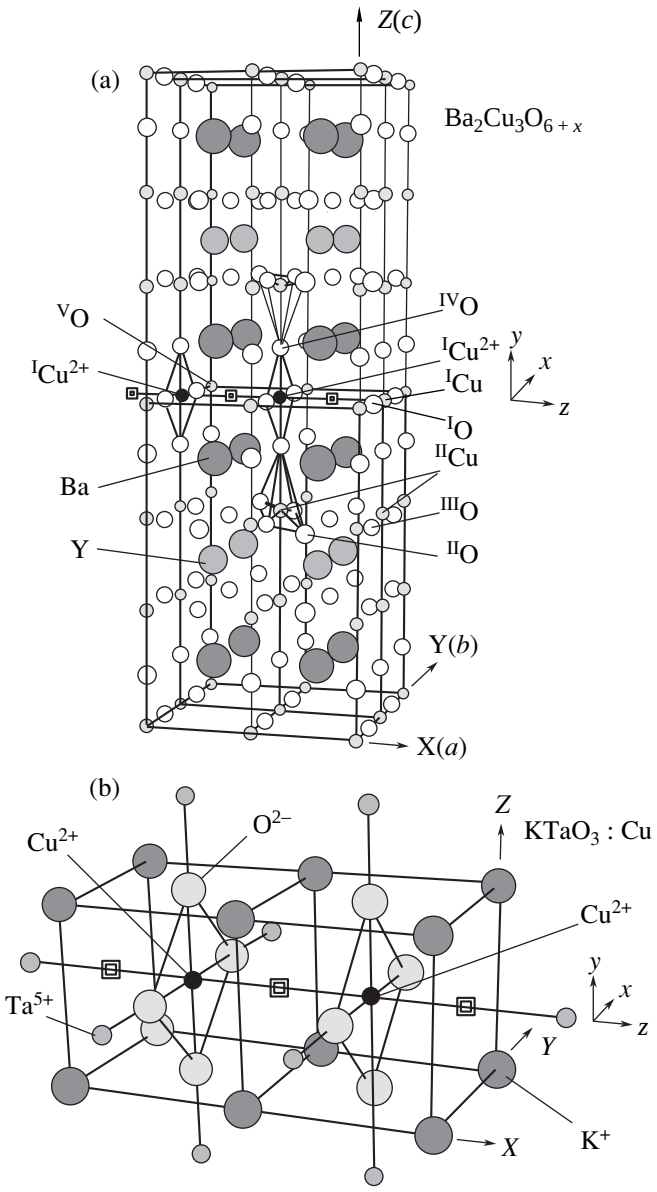

Fig. 1. Comparison of copper-pair center models in (a) the $YBa_2Cu_3O_{6+x}$ HTSC and (b) the $KTaO_3$: Cu crystals. The $YBa_2Cu_3O_{6+x}$ crystal is represented by four unit cells of the $x \sim 1$ structure; it is assumed that the fragment of the copper pair center highlighted in (a) is realized in the $x \sim 0.5$ structure. *X, Y, Z* are the axes corresponding to the principal crystallographic directions specified in parentheses; and *x, y, z* are the local axes of a Cu^{2+}–Cu^{2+} copper pair center.

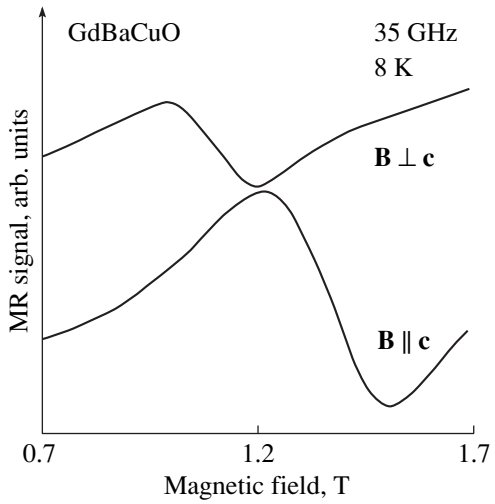

Fig. 2. MR signals (the absorption derivative), which were detected at 35 GHz at a temperature of 8 K in a Gd–Ba–Cu–O crystal quenched from 1020 K, for two crystal orientations in the magnetic field, **B** ∥ **c** and **B** ⊥ **c**. The EPR spectra were obtained by the conventional method, with a 5-G magnetic field modulated at a frequency of 100 kHz.

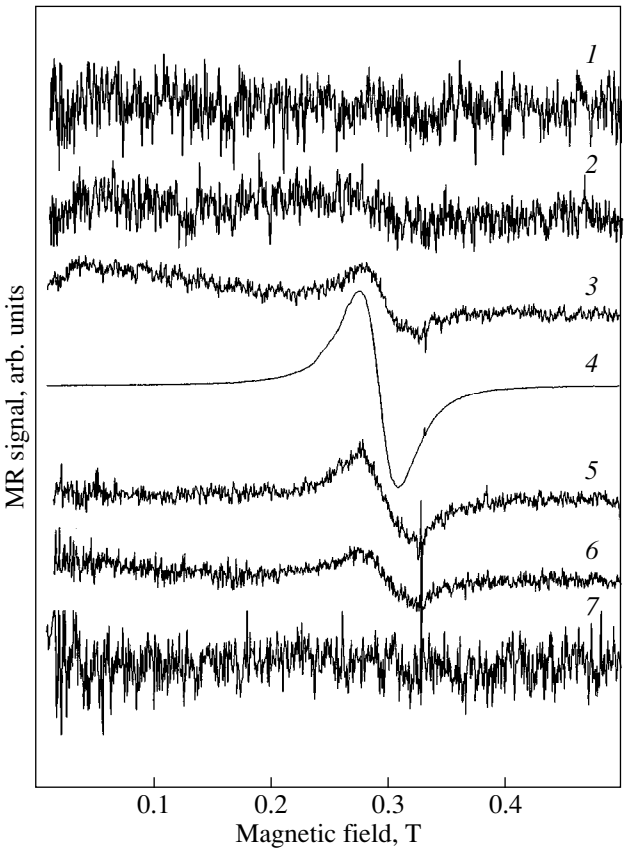

Fig. 3. MR spectra obtained in the Y–Ba–Cu–O ceramic at 5 K in the *X* range: (*1*) starting ceramic with T_C = 95 K; (*2–4*) after quenching in air at 950, 1030, and 1100 K, respectively; and (*5–7*) after a 5-min annealing at 500, 550, and 615 K, respectively. The observed fluctuations are due to the presence of the superconducting phase in the sample and are not background noise. The narrow line is due to the DPPH.

tion of this process with the loss of superconducting properties is usually interpreted to be due to a decrease in the hole concentration in the $^{II}CuO_2$ planes which are responsible for these properties. As is seen from Fig. 1a, the $YBa_2Cu_3O_7$ crystal is divided into planar two-dimensional conducting $^{II}CuO_2$ regions separated by yttrium ions and the latter can be readily replaced by practically any rare-earth ion without a substantial change in the electrophysical (including superconducting) properties of the crystal. It is believed that the copper in the ^{II}Cu layers resides in the +2 oxidation state for any value of *x*, whereas the state of the chain copper undergoes a change from $^{I}Cu^{3+}$ at $x = 1$ to $^{I}Cu^{+}$ at $x = 0$.

It is known that quenching an *R*–Ba–Cu–O cuprate superconductor from temperatures above 750 K [8] results in an oxygen deficiency (a decrease in the *x* parameter) and, accordingly, in a decrease in T_C. The plot relating the critical temperature T_C with the oxygen content *x* has two plateaus near 90 ($x \sim 6.9$) and 50 K ($x \sim 6.5$). When ceramics and crystals of the 1–2–3 type are quenched in air from temperatures above 1000 K, the superconducting phase in these samples practically disappears and strong MR signals are observed.

Figure 2 displays MR spectra measured at 35 GHz on a Gd–Ba–Cu–O crystal quenched in air from a temperature of 1020 K. The spectra are given for two crystal orientations in a magnetic field, **B** ∥ **c** and **B** ⊥ **c**. The measurements were performed at 8 K. The EPR spectra were obtained by the standard technique, with the magnetic field modulated at 100 kHz (the modulation amplitude 5 G), and, therefore, the signal has the shape of the derivative. The MR absorption signals obtained at a temperature of 1.6 K (with the microwave power modulated at a frequency of 200 Hz) were measured on quenched Gd–Ba–Cu–O and Nd–Ba–Cu–O crystals.

Similar MR signals were also observed on a Y–Ba–Cu–O ceramic after quenching in air from different temperatures (Fig. 3). Spectrum *1* was obtained on the starting ceramic with T_C = 95 K before the quenching. One readily sees microwave absorption fluctuations typical of the superconducting state. This sample also exhibited a strong low-field signal (not shown in the figure) characteristic of the superconducting state. Spectra *2*, *3*, and *4* were measured on the same ceramic after quenching in air from the temperatures of 950, 1030, and 1100 K, respectively. The microwave absorption fluctuations are seen to decrease strongly in amplitude because of the decreasing fraction of the superconducting phase in the ceramic, and an MR signal with a *g* factor of ~2.20 and a linewidth of about 400 G appears. The narrow line belongs to diphenyl β-picryl hydrazyl (DPPH). Thus, the MR signal intensity is in anticorrelation with the fraction of the superconducting phase in the material under study.

The superconducting properties lost in the quenching of the material can be partially recovered by annealing the material in air, after which the MR signal again

falls practically to zero. Spectra *5*, *6*, and *7* in Fig. 3 were measured on the same ceramic after annealing in air for five minutes at 450, 550, and 615 K, respectively. Annealing results in the recovery of the superconducting phase with $T_C \simeq 50$ K. To recover the superconducting phase completely, the annealing should be done in an oxygen environment. It should be pointed out that annealing brings about some changes in the MR signal and causes the *g* factor to decrease; i.e., the MR line shifts toward higher fields.

Both in crystals and ceramics, the MR signals appear at temperatures below ~40 K and their intensity increases strongly with decreasing temperature. Estimates show that the intensity of the MR signals corresponds to spin concentrations of the order of 10^{20} cm^{-3}, which implies that these signals cannot be due to impurities. The MR signals are anisotropic; in magnetic fields oriented parallel to the *c* axis of the crystal, the resonance is observed in higher magnetic fields; i.e., the lines correspond to smaller *g* factors. The magnitude of the *g* factor depends on the type of the 1–2–3 compound, because, in the Nd–Ba–Cu–O crystal, the anisotropy is smaller than in Gd–Cu–Ba–O, but in all the materials studied $g_{\perp \mathbf{c}} > g_{\parallel \mathbf{c}}$, where $g_{\parallel \mathbf{c}}$ and $g_{\perp \mathbf{c}}$ are the *g* factors for the MR signals measured in an external magnetic field parallel and perpendicular to the crystal *c* axis, respectively. In the case of the ceramic, naturally, we obtain an averaged *g* factor. As follows from studies performed in the *X* and *Q* ranges, the MR signal anisotropy increases and the lines broaden substantially with an increasing microwave frequency [4, 5].

The presence of the superconducting phase in a crystal appreciably affects the shape and position of the MR lines. Figure 4a presents the MR signal of a Gd–Cu–Ba–O crystal quenched from a temperature of 1020 K that contains a small fraction of the superconducting phase (curve *1*) and an MR signal of the starting crystal with $T_C \sim 60$ K (curve *2*). The spectra were obtained first in the $\mathbf{B} \perp \mathbf{c}$ orientation and then for $\mathbf{B} \parallel \mathbf{c}$, immediately after a rotation through 90° and five minutes after the rotation. In the first sample, the $\mathbf{B} \parallel \mathbf{c}$ spectrum did not change with time, while in the superconducting sample, we observed a substantial variation of the signal with time. Similar relaxation effects in MR signals were observed when the superconducting crystal was turned rapidly through 360°. Figure 5a displays an MR signal measured in the $\mathbf{B} \perp \mathbf{c}$ orientation on the same superconducting crystal as in Fig. 4 (*1*) immediately after the cooling (in this magnetic-field orientation, the crystal was cooled to the measurement temperature), (*2*) after a rapid turn of the crystal through 360°, and (*3*–*6*) at different instants of time after the start of the first rotation (between the instants corresponding to curves *4* and *5*, the crystal was again turned rapidly through 360°). Figure 5b shows the variation of the MR signal in time after two turns through 360° at 18 K (solid line) and after a 360° turn at 9.5 K (dashed line).

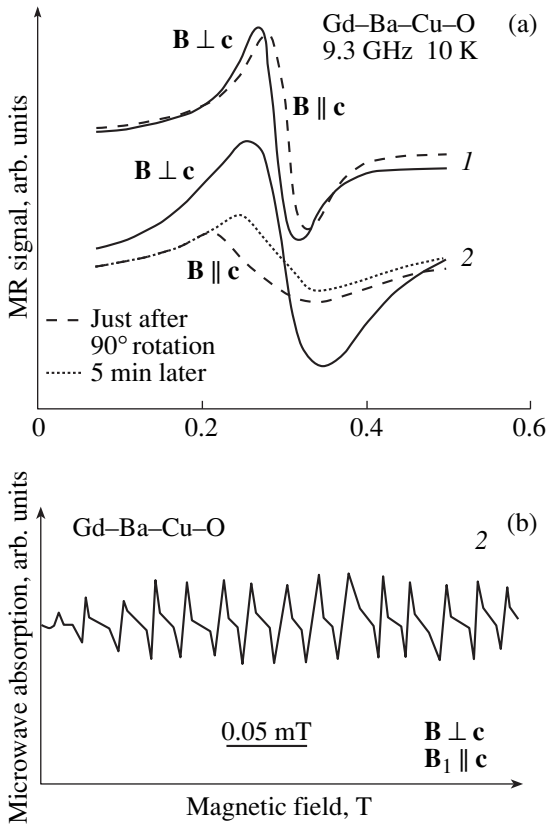

Fig. 4. (a) MR signals measured at 10 K for two magnetic-field orientations in a Gd–Ba–Cu–O crystal (*1*) quenched from 1020 K and (*2*) in the starting superconducting crystal with $T_C \approx 60$ K. The spectra were first measured in the $\mathbf{B} \perp \mathbf{c}$ orientation and, after this, in the $\mathbf{B} \parallel \mathbf{c}$ geometry immediately following a 90° rotation and 5 min thereafter. (b) Low-field signal measured in the superconducting crystal in which the MR signal (*2*) was observed. $\mathbf{B}_1$ is the microwave field.

The figures at the solid line specify the instants of time at which the MR measurements of Fig. 5a were made.

2.2. $KTaO_3$: Cu

The $KTaO_3$: Cu crystals were studied in two frequency ranges (*X* and *Q*) in the 4- to 300-K interval. Figure 6 presents the orientational dependences of the EPR spectra measured on the $KTaO_3$: Cu crystal at a frequency of 35 GHz and a temperature of 300 K. The crystal was rotated in a magnetic field in the {100} plane. While there is a large number of EPR lines, practically all of them belong to three types of copper centers, namely, to two single Cu^{2+} centers and one copper-pair type, Cu^{2+}–Cu^{2+}, with the spin $S = 1$. Studies in two frequency ranges were necessary for a final assignment of the EPR spectra, because in this case one can separate the EPR line shifts due to a change in the electronic *g* factor from those originating from the fine, hyperfine, and superhyperfine structures. The EPR spectra of copper are extremely informative, because they contain

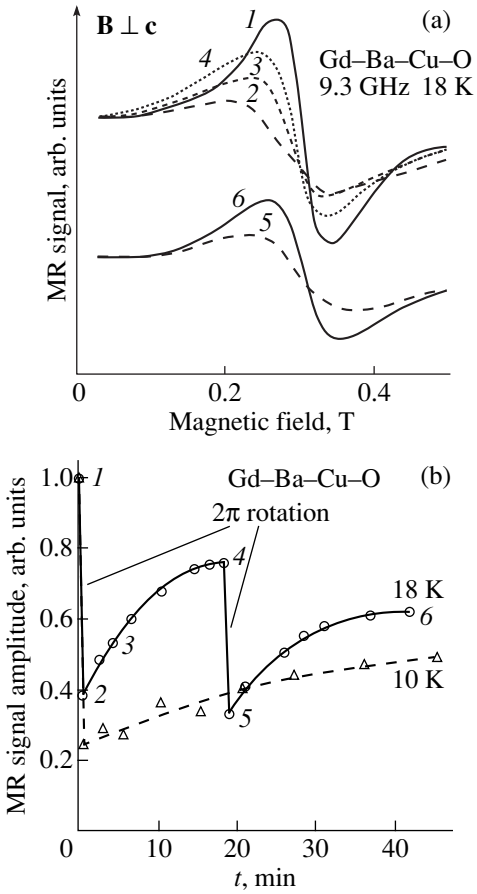

Fig. 5. (a) MR signals measured in the **B** ⊥ **c** orientation in the superconducting crystal referred to in Fig. 4: (*1*) immediately after the cooling (the sample was cooled in this magnetic-field orientation to the temperature of the measurement), (*2*) after a rapid 360° turn of the crystal, and (*3–6*) at different times after the beginning of the first rotation (between the measurements *4* and *5*, the sample was again turned rapidly through 360°). (b) Variation of the MR signal amplitude in time after two 360° turns at 18 K (solid line) and after a 360° turn at 10 K (dashed line). The figures adjoining the solid line refer to the corresponding MR spectra in Fig. 5a.

signatures of practically all the interactions detectable by the EPR technique; more specifically, the *g* factor shifts providing information on the character of the wave functions of the copper ions (single and paired), the fine structure in the copper pair, the HF interaction between the unpaired electron and the nuclear magnetic moment of the copper atom, and the SHF interaction between the unpaired electron and the ligands. The temperature dependences of the EPR intensity offered the possibility of deducing the character of the exchange interaction in copper pairs, which is very likely to be ferromagnetic; i.e., the state with the maximum spin ($S = 1$) has the lowest energy.

The spectrum in Fig. 6 obtained in the **B** ∥ [100] orientation contains the EPR lines (identified by vertical bars) corresponding to the two types of Cu^{2+} centers denoted by $Cu^{2+}(1)$ and $Cu^{2+}(2)$. Both centers were found (within experimental error) to have a tetragonal symmetry. Unlike the low-symmetry crystal $RBa_2Cu_3O_{6+x}$, in the $KTaO_3$ cubic crystal, the tetragonal axis of the Cu^{2+} centers may be aligned with any of the three equivalent ⟨100⟩ directions with equal probability and, therefore, the EPR spectrum taken in the **B** ∥ ⟨100⟩ geometry exhibits the EPR lines corresponding to the magnetically inequivalent centers with **B** ∥ *z* (where *z* is the tetragonal symmetry axis of the center) and **B** ⊥ *z* simultaneously. When the orientation deviates from **B** ∥ ⟨100⟩, the signal corresponding to **B** ⊥ *z* undergoes a further splitting. To simplify the general pattern and to make a comparison of the copper EPR spectra in $KTaO_3$: Cu with the MR results obtained in uniaxial crystals of the 1–2–3-type compounds, Fig. 6 presents the experimental (points) and theoretical (lines) dependences only for the copper centers oriented along the [001] axis. Additionally, for the **B** ∥ [001] and **B** ∥ [010] orientations, Fig. 6 contains only the parts of the EPR spectra that correspond to the angles $\Theta = 0°$ and $\Theta = 90°$ (one cannot naturally separate these spectra completely). The theoretical orientational dependences of EPR signals are shown for the copper pairs by solid lines and for the single copper centers [for $Cu^{2+}(2)$ only] by dashed lines.

The EPR spectra obtained for each type of the Cu^{2+} centers in the **B** ∥ *z* orientation consist of four relatively broad lines due to the HF interaction. Copper has two stable isotopes, Cu^{63} (69.2%) and Cu^{65} (30.8%); both isotopes have nuclear spins $I = 3/2$ and nuclear *g* factors close in magnitude, and, therefore, for the ratio of the individual linewidths to the line separations observed experimentally in the EPR spectra, it is difficult to detect the copper isotopic splitting. In some orientations, each copper HF component reveals an additional splitting caused by the SHF interaction with the ligands. This additional structure is not seen in Fig. 6 for $\Theta = 0°$ and only affects the width of individual lines, because the spectra are presented over a broad range of magnetic fields. In Fig. 6, the SHF interaction manifests itself partially in the **B** ⊥ *z* EPR component, which remains fixed in all magnetic-field orientations when rotated in the {100} plane.

The spin Hamiltonian describing the EPR spectra has the standard form

$$\hat{H} = \mu_B \mathbf{B} \cdot \overleftrightarrow{g} \cdot \mathbf{S} + \mathbf{S} \cdot \overleftrightarrow{A} \cdot \mathbf{I} + \sum_{i=1}^{N} \mathbf{S} \cdot \hat{a}_i \cdot \mathbf{I}_i, \qquad (1)$$

where $S = 1/2$ for the Cu^{2+} centers; the first term is the Zeeman interaction; the second and third terms correspond to the HF and SHF interactions, respectively; μ_B is the Bohr magneton; $\overleftrightarrow{g}$ is the *g* tensor; $\overleftrightarrow{A}$ is the HF interaction tensor; and $\hat{a}_i$ is the tensor describing SHF interaction with the nucleus of the *i*th ligand ion.

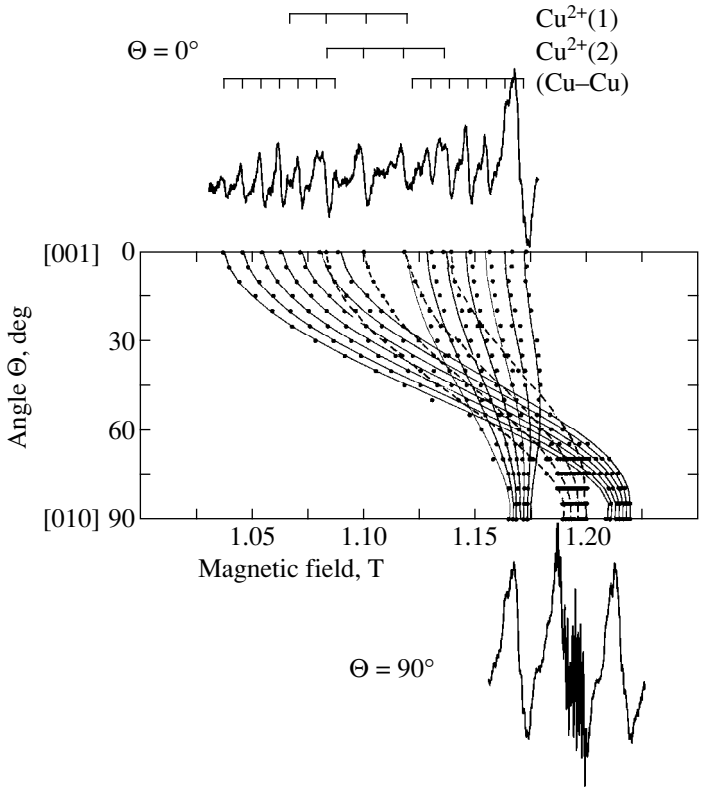

Fig. 6. Orientational dependences of the EPR spectra observed in $KTaO_3$: Cu crystals in the *Q* range at 300 K. The crystal was rotated so that the ⟨100⟩ axis was perpendicular to the dc magnetic field. Fragments of the measured EPR spectra are shown only for the **B** ∥ [001] and **B** ∥ [010] orientations. The points specify the experimental positions of the EPR lines for single and pair copper centers oriented only along one of the [001] crystal directions (one-third of all centers in the crystal). The solid (Cu^{2+}–Cu^{2+} pairs) and dashed [Cu^{2+}(2)] lines refer to theoretical calculations.

The parameters of the spin Hamiltonian (1) for the Cu^{2+}(1) and Cu^{2+}(2) centers at 300 K are as follows: for Cu^{2+}(1): $g_\parallel = 2.24$, $g_\perp \cong 2.04$, $A_\parallel = 173 \times 10^{-4}$ cm^{-1}, and $A_\perp \cong 30 \times 10^{-4}$ cm^{-1}; and for Cu^{2+}(2): $g_\parallel = 2.20$, $g_\perp \cong 2.04$, $A_\parallel = 193 \times 10^{-4}$ cm^{-1}, and $A_\perp \cong 30 \times 10^{-4}$ cm^{-1}; here, the ∥ and ⊥ symbols denote the parallel and perpendicular magnetic-field orientations with respect to the local *z* axis of the center, respectively. These data are close to the results reported in [9]. The EPR spectra observed have a resolved SHF structure, and we report the first observation of two different kinds of SHF interactions which differ in the magnitude and character of the orientational dependences. The SHF structure with a small splitting, of the order of 0.3 mT (we call it a weak SHF interaction), was modulated in the magnetic field by a structure with a splitting of about 1.5 mT (accordingly, we call it a strong SHF interaction). The strong SHF-interaction structure in Fig. 6 is partially resolved for Θ = 90°. For centers whose orientation was close to **B** ∥ *z*, an SHF structure with a splitting of 0.3 mT for Cu^{2+}(1) and of 0.37 mT for Cu^{2+}(2) was observed. When turned by more than 20° from this orientation, the lines broadened and the structure corresponding to the weak SHF interaction was practically unresolved; the structure due to the strong SHF interaction persisted and comprised at least seven lines with symmetrically distributed intensities. We believe that the total resolved SHF structure observed is due only to the interaction with the Ta^{5+} ions (the validity of this statement will be corroborated below). More specifically, the weak interaction is due to the Ta^{5+} ions on the tetragonal axis of the center (the local *z* axis), while the strong interaction is associated with the four equivalent Ta^{5+} ions located in the equatorial plane perpendicular to the local *z* axis of the center. The anomalous intensity ratios of the strong SHF interaction components are apparently due to the existence of a strong quadrupole interaction (the tantalum nuclei are characterized by one of the largest known quadrupole moments). The existence of a strong quadrupole SHF interaction with tantalum ions was proved by ENDOR for iron nuclei in $KTaO_3$ [9]. It appears only natural that the SHF interaction for the oxygen ions sandwiched between the copper and tantalum ions and participating in electron spin transfer from copper to tantalum could not be detected in the conditions of this experiment because of the low natural abundance of the ^{17}O isotope having a nuclear spin, although our estimates suggest that this interac-

tion should be fairly strong; therefore, the EPR spectra of a $KTaO_3$ crystal enriched in the ^{17}O isotope should be substantially different from the ones in Fig. 6. It should be pointed out that the relative concentrations of the $Cu^{2+}(1)$ and $Cu^{2+}(2)$ centers depend on the sample and vary over a broad range.

Besides the EPR spectra of single Cu^{2+} copper ions, EPR spectra belonging to copper pairs were observed in $KTaO_3$: Cu crystals with enhanced copper concentrations [6], which is apparently the first observation of copper pairs in perovskite crystals. Figure 6 shows several groups of lines of the Cu^{2+}–Cu^{2+} copper pair center denoted by (Cu–Cu) in the upper spectrum, which was measured in the $\mathbf{B} \parallel \langle 100 \rangle$ orientation. As in the case of the Cu^{2+} centers, there are lines with the $\mathbf{B} \parallel z$ ($\Theta = 0°$) and $\mathbf{B} \perp z$ ($\Theta = 90°$) orientations, with z aligned with $\langle 100 \rangle$ and also being the tetragonal axis of the center symmetry. In contrast to the Cu^{2+} centers, there are two groups of lines for the parallel and perpendicular orientations each, with the distance between the centers of these groups in a parallel magnetic-field orientation being about twice that for the perpendicular orientation, which implies that we have here the EPR spectra characteristic of the triplet states ($S = 1$) of axial symmetry, with the fine-structure splitting substantially smaller than the Zeeman splitting. The angular dependence of these groups of lines is also characteristic of a triplet center. For $\Theta = 0°$, each (Cu–Cu) group contains seven HF lines, with a width of ~2.5 mT and an intensity ratio of approximately 1 : 2 : 3 : 4 : 3 : 2 : 1, which is a signature of the interaction of an unpaired electron with two equivalent nuclei of the spin $I = 3/2$. The HF structure constant in the spectrum of the new center is approximately one-half the sum of the HF constants for the $Cu^{2+}(1)$ and $Cu^{2+}(2)$ centers. All this argues in favor of the new EPR spectrum (in Fig. 6) belonging to an exchange-coupled pair of equivalent Cu^{2+} ions sitting at neighboring tantalum sites, with the z axis of the center directed along the $\langle 100 \rangle$ axis of the crystal.

The Hamiltonian of an exchange-coupled pair that includes the isotropic exchange interaction of two identical magnetic centers with the spins $S_1 = S_2 = 1/2$ and the Zeeman interaction (but does not take into account the HF and SHF interactions) can be written as [10]

$$\hat{H} = J\mathbf{S}_1 \cdot \mathbf{S}_2 + \mu_B \mathbf{B} \cdot \overleftrightarrow{g} \cdot (\mathbf{S}_1 + \mathbf{S}_2), \qquad (2)$$

where J is the isotropic exchange constant; μ_B is the Bohr magneton; and $\overleftrightarrow{g}$ is the copper dimer g tensor, which was found to be equal, within experimental error, to the average magnitude of the g tensors of the two single copper centers, $Cu^{2+}(1)$ and $Cu^{2+}(2)$. In the case where the isotropic exchange constant $J \gg g\mu_B B$, the situation realized for the copper pairs in our experiment, the system can conveniently be recast in the representation of the total spin equal to zero or unity. Note that the exchange energy does not have a simple scalar form as the first term in Eq. (2) does but rather is characterized by an anisotropy (in our case, apparently, a weak enough one) which can be described by a more general expression of the type $\mathbf{S}_1 \cdot \overleftrightarrow{J} \cdot \mathbf{S}_2$. For an axial system with spin $S = 1$, this anisotropy can be taken into account by adding the fine-structure term to the spin Hamiltonian (1) which reduces to one-half the HF and SHF interaction constants:

$$\hat{H} = \mu_B \mathbf{B} \cdot \overleftrightarrow{g} \cdot \mathbf{S} + D\left[S_z^2 - \frac{1}{3}S(S+1)\right] + \mathbf{S} \cdot \frac{\overleftrightarrow{A}}{2} \cdot (\mathbf{I}_1 + \mathbf{I}_2) + \sum_{l=1}^{N} \mathbf{S} \cdot \frac{\hat{a}_i}{2} \cdot \mathbf{I}_i. \qquad (3)$$

The spin Hamiltonian parameters for the Cu^{2+}–Cu^{2+} center in the $KTaO_3$: Cu crystal for 300 K are as follows: $|D| = 420 \times 10^{-4}$ cm^{-1}, $g_\parallel = 2.22$, $g_\perp = 2.04$, $A_\parallel = 90 \times 10^{-4}$ cm^{-1}, and $A_\perp \cong 15 \times 10^{-4}$ cm^{-1}. It should be added that in the $K_{1-x}Li_xTaO_3$: Cu crystal $|D| = 455 \times 10^{-4}$ cm^{-1}, which is slightly larger than in $KTaO_3$: Cu, so that the D parameter is very sensitive to weak changes in the crystal structure. In the case of pairs, we detected only an SHF structure with a small splitting of ~1.5 G in the $\mathbf{B} \parallel z$ orientation.

A study of the temperature dependence of the EPR signal showed that the amplitude of the copper pair-center signal increases with the temperature decreasing to 3.5 K. This observation suggests that the isotropic exchange most likely has a ferromagnetic character; i.e., the triplet spin state has a lower energy than the singlet one.

Spectra of the Cu^{2+}–Cu^{2+} pair centers were detected in potassium tantalate crystals within a broad copper concentration range, and their relative intensity increases with the copper concentration. It was found that the observed spectrum is stronger in the samples in which the $Cu^{2+}(1)$- and $Cu^{2+}(2)$-center concentrations are roughly equal in value. The presence of one vacancy in the nearest environment of Cu^{2+} is not enough for complete charge compensation. On the other hand, single Cu^{2+} centers with two nearest neighbor vacancies along $\langle 100 \rangle$ can form and one cannot rule out the possibility that one of the oxygen vacancies is not in the nearest neighborhood on the $\langle 100 \rangle$ axis, because in this case an excess positive charge would appear. Two such centers, $Cu^{2+}(1)$ and $Cu^{2+}(2)$, fully satisfy the charge neutrality condition even if located at a considerable distance from each other. If two Cu^{2+} ions occupy adjacent tantalum sites, they form a pair center, whose model is shown in Fig. 1b and which has the form of a chain of two equivalent Cu^{2+} ions and three oxygen vacancies strung out along the $\langle 100 \rangle$ axis. The crucial point in this model is the presence of an oxygen vacancy between two Cu^{2+} ions (inner vacancy); the outer vacancies may be farther away from the copper. In this structure, complete charge compen-

sation obtains. This is apparently what accounts for the appearance in the crystals studied of copper pair concentrations exceeding by several orders of magnitude the values obtained from a statistical analysis of the pair formation. Because $g_{\parallel} > g_{\perp} \geq 2$, the wave functions of each of the Cu^{2+} ions in a pair have the form $3d(x^2 - y^2)$, where the local axis z is directed along the pair axis $\langle 100 \rangle$. Therefore, the exchange coupling in the pair can be mediated by the p_z orbital of the oxygen ion, which also argues for the model proposed, because the ferromagnetic exchange following from our experiments finds a natural explanation in this way.

This model of the Cu^{2+}–Cu^{2+} pair center can be logically extended to a model of two single copper centers, with each of them representing a copper ion with one or two nearest neighbor oxygen vacancies along the $\langle 100 \rangle$ direction. In other words, single centers are actually two constituents of the pair center. This conclusion gets additional support from the fact that only one type of pair center was observed, with its parameters (the g factor and the HF and SHF interaction constants) being equal in magnitude, with a high precision, to the average values of the corresponding parameters of the two single $Cu^{2+}(1)$ and $Cu^{2+}(2)$ centers. As was already mentioned, for the copper pairs there has been success in detecting only an SHF structure with a small splitting, ~1.5 G, in the **B** || z orientation. This observation easily finds an explanation in terms of the proposed model of the pair center; indeed, because the weak SHF interaction originates from two tantalum ions lying on the local z axis, this structure changes only insignificantly as one goes over from single Cu^{2+} ions to their pairs. The decrease in the splitting to one-half that for the single Cu^{2+} ions has the same nature as the corresponding decrease in the HF interaction constant [in accordance with expression (3)]. The structure due to the strong SHF interaction with the tantalum ions lying in the equatorial plane (equatorial Ta ions), which is perpendicular to the center z axis, is not resolved, because the situation for the pair differs radically from that for single copper ions; indeed, there are eight equatorial Ta ions located in the two planes that are perpendicular to the axis of the copper pair center and pass through each copper ion. Thus, the number of the Ta ions doubles, whereas the SHF splitting decreases by one half, and it is this that probably results in the unresolved SHF structure.

Consider the SHF interaction, which is essential for obtaining information on the spin-density spatial distribution in the Cu^{2+} centers and Cu^{2+}–Cu^{2+} pairs. As was already mentioned, the observed SHF structure suggests the existence of several types of interaction with inequivalent ligand ions. If we exclude the interaction with impurities, $KTaO_3$ has ligand ions of three types, namely O^{2-}, K^+, and Ta^{5+}. The SHF interaction with oxygen may be disregarded, because only a very small fraction of the natural oxygen (0.038% ^{17}O) has a nonzero nuclear spin. In contrast to oxygen, the potassium and tantalum nuclei have magnetic, I, and quadrupole, Q, moments: for ^{39}K (93.26%), $I = 3/2$ and $Q = 0.054$; and for ^{181}Ta (99.99%), $I = 7/2$ and $Q = 3.44$. The isotropic HF interaction constant for potassium atoms (for the 4s electron) is 228 MHz, whereas the corresponding constant for the tantalum ion (6s electron) is 15020 MHz and the anisotropic HF interaction constant (5d electron) is 445.4 MHz (without the angular coefficient) [11]. The isotropic and anisotropic HF interaction constants for the inner s and p electrons of the K^+ (3s, 3p) and Ta^{5+} (5s, 5p) ions were theoretically calculated with the use of the wave functions given in [12]; it is essential that the constants for tantalum exceed those for potassium by more than 50 times. Thus, even if the electron spin density is transferred equally to the potassium and tantalum nuclei (which, in actual fact, is not the case, because the spin-density transfer to the tantalum should be substantially larger due both to the covalency effects and to the wave-function overlap), the SHF interaction constant with potassium should be negligible compared to that with tantalum. Therefore, there are solid grounds for believing that the SHF structure observed in the experiments originates only from the interaction with the tantalum ions. There are at least two major mechanisms capable of contributing to the electron spin density at the tantalum nuclei. The first of them is due to the overlap of the wave functions related to the cluster under study, because the wave functions of different ions are, in general, not orthogonal to one another. This mechanism ensues from the Pauli principle, which brings about a spin-density redistribution resulting from the redistribution of the electron charge densities in filled shells having oppositely directed spins. This effect was first considered for the case of F centers in ionic crystals [13]. For the Pauli principle to be satisfied, the wave function of the cluster under study was presented in the form of a determinant. It should be stressed that in these conditions one observes the appearance of a spin density inside filled electronic shells of the originally diamagnetic ligand ions, for instance, in the case of $KTaO_3$, in the inner shells of K^+ (3s, 3p, etc.), Ta^{5+} (5s, 5p, etc.), and O^{2-} (2s, 3p, etc.). The covalency is a radically new effect in which an electron is transported between a magnetic ion and its diamagnetic environment. The most essential illustration is provided by the case of an electron with the appropriate spin being transferred from the filled shell of a ligand to the free energy level of a magnetic ion [for instance, in the case of the $Cu^{2+}(3d^9)$ ions, an electron with the appropriate spin is transferred from the O^{2-} ion to the only empty orbital in the copper 3d shell to make the shell filled]. It should be noted that, considered from the physical standpoint, both of the above effects provide the same contribution to the SHF interaction and, therefore, these contributions are practically indistinguishable (however, their contributions to the HF interaction for the magnetic ion are opposite in sign and in this case

there exists, at least in principle, the possibility of their separation). Because the tantalum ions are located in the second coordination shell with respect to the copper ions, the spin density transport takes place primarily via the oxygen; i.e., this is a two-step process and, hence, it is less efficient than the transfer to the oxygen. Nevertheless, the observed SHF interaction with the tantalum ions may provide indirect information on the spin density at the oxygen ions, which appears important when studying HTSC compounds.

Consider both possible mechanisms of cation–cation spin-density transport from the copper ion to the tantalum ions lying in the equatorial plane. Figure 1b suggests that the main contribution should be provided by the Cu–O–Ta 180° bond in the *xy* plane, i.e., the one perpendicular to the local copper-center *z* axis. The arrangement of the K^+ ions is apparently unfavorable for the spin density transfer from the copper to the tantalum. An analysis of the overlap and covalency effects yields the following expression to estimate the constants of the isotropic, a_s, and anisotropic, a_p, SHF interaction with the four equivalent tantalum ions in the equatorial plane:

$$a_s = C_1\frac{1}{4}(\sqrt{3}\langle 3d|2p_\sigma\rangle + \gamma)^2\langle 2p|5s\rangle^2\Psi_{5s}^2(0);$$
$$a_p = C_2\frac{1}{4}(\sqrt{3}\langle 3d|2p_\sigma\rangle + \gamma)^2\langle 2p|5p\rangle^2\langle r^{-3}\rangle_{5p}, \quad (4)$$

where $C_1 = (8\pi/3)g\mu_B g_I\mu_N$; $C_2 = (2/5)g\mu_B g_I\mu_N$; g_I and μ_N are the nuclear g factor and nuclear magneton, respectively; $\Psi_{5s}^2(0)$ is the density of the 5*s*-electron wave function of the Ta^{5+} ion; $\langle 3d|2p_\sigma\rangle$ is the two-center overlap integral of the 3*d* wave function of copper with the $2p_\sigma$ wave function of oxygen; the $\sqrt{3}$ coefficient takes into account the fact that one should use the group integral involving the $3d(x^2 - y^2)$ wave function of copper and the corresponding molecular orbital, which is composed of the $2p_\sigma$ orbitals of the equivalent equatorial oxygen ions; γ is a parameter taking into account the covalent transport between the oxygen and copper; and $\langle 2p|5s\rangle$ and $\langle 2p|5p\rangle$ are the overlap integrals of the 2*p* wave function of oxygen with the 5*s* and 5*p* wave functions of Ta^{5+}. The overlap integrals were calculated with the use of the wave functions presented in [12]. Our estimates show that, for a covalency coefficient chosen as 15%, $a_s \sim 1$ mT; i.e., it is in approximate agreement with the strong isotropic SHF interaction constants observed experimentally. Note that the experimentally measured anisotropic SHF interaction constant with the tantalum ions (about 0.5 mT) cannot be accounted for if one accepts relation (4). One has to invoke an additional mechanism of spin-density transfer to the tantalum nuclei. Such a mechanism could be a strong covalent transfer of oxygen electrons to the empty 6*s* and 5*d* shells of tantalum. In this case, the spin density at the oxygen, which is produced through covalent transfer of one of the oxygen electrons to the Cu^{2+} copper ion, is preserved in the covalent oxygen-electron transfer to the tantalum as well. The weak SHF interaction with the two tantalum ions at the tetragonal axis of the center may be due to an admixture of the $3d(z^2)$ excited orbital caused by the electron–lattice-vibration coupling.

3. DISCUSSION OF RESULTS

The main objective of this work was to establish the nature of the magnetic resonance, which is observed in the HTSCs based on the 1–2–3-type perovskite cuprates, from EPR studies of the copper complexes in $KTaO_3$: Cu. As was already mentioned, an estimation of the MR signal intensity yielded a center concentration above 10^{20} cm^{-3}, which implies that the signal could be due only to the matrix ions, i.e., the copper and oxygen ions. We believe that the signal is associated with copper, because it would be difficult to explain such a large MR linewidth of oxygen, which practically does not have nuclei with magnetic moments. The 123-type materials have copper ions of two types, which are located in the ^{I}Cu chains and ^{II}Cu planes, and the problem consists in correctly identifying the observed MR signal with the type of copper ion involved.

We introduce the following coordinate frames (Figs. 1a, 1b): *Z*, *X*, and *Y* are related to the crystallographic axes *c*, *a*, and *b* of $YBa_2Cu_3O_{6+x}$, respectively, while for the $KTaO_3$: Cu crystal the vertical axis [001] corresponds to the *Z* axis; the local axes of the copper pair center are denoted by *z*, *x*, and *y*, with *z* directed along the pair-center axis. Consider first the possibility of the formation of copper pairs (or of a larger number of copper ions) in the planes. In doing this, we shall look for a structure similar to the one in Fig. 1b, because such a structure has the *g* factors observed experimentally for the MR. The copper pair structure shown in Fig. 1b cannot be realized in a plane, because the copper is in the pyramids, which allows wave functions of the type $3d(X^2 - Y^2)$ or $3d(3Z^2 - R^2)$. One usually considers $3d(X^2 - Y^2)$ states at the copper sites and $2p_\sigma(X, Y)$ states at the oxygen sites in the $^{II}CuO_2$ plane, where the σ index refers to the σ bonding. However, in this case, the relation observed in our experiments between the *g* factors, $g_{\perp c} > g_{\parallel c}$, cannot be satisfied.

Our preceding papers [3–5] discussed the possibility of the MR signal being related to the in-plane copper and oxygen ions. It was assumed that the MR signals observed in [3–5] were due to individual magnetically ordered clusters containing a certain number of exchange-coupled Cu^{2+} ions. These magnetic clusters, forming in the course of quenching in HTSC samples, are in a metastable state; when annealed above room temperature, they begin to diffuse and overlap to produce fractal percolation networks, which give rise to

superconductivity [14]. The clusters have a quasi-one-dimensional structure with magnetic ordering in directions perpendicular to the *c* axis. Our new data obtained in EPR studies of copper complexes in the $KTaO_3$: Cu crystals apparently allow the assignment of the MR signals to the chain copper complexes. The short-range order in the chains substantially affects the electronic properties of the superconductor; therefore, an investigation of copper chains is of particular interest for the problem of the superconducting state and the role of the two types of copper in the onset of this state. The results obtained by us along these lines fit perfectly into the phase separation model, because the doping of the conducting $^{II}CuO_2$ plane achieved through charge transport from the chains to the plane is of a local nature and the hole concentration is qualitatively in anticorrelation with the appearance of the magnetic resonance signal.

In Fig. 1a, a fragment containing two $^{I}Cu^{2+}$ copper ions is highlighted, which is similar in shape to the vacancy–copper complex in the $KTaO_3$: Cu crystal presented in Fig. 1b. For the sake of convenience, Fig. 1a displays the structure of the $YBa_2Cu_3O_7$ crystal, in which there are ideal ^{I}Cu chains with the four nearest neighbor oxygen ions lying in the plane perpendicular to the *a* axis. As was already mentioned, the orientational dependences of MR signals in the 1–2–3-type materials imply that $g_{\perp c} > g_{\parallel c}$. A comparison of this relation with the results of the study of copper pairs in $KTaO_3$ crystals suggests that the axis of the copper pair (the *z* axis) should be directed perpendicular to the *c* axis of the HTSC crystal. Then the condition $g_{\parallel} > g_{\perp} \geq 2$ for the local axes of the copper pair will be met and the wave functions of each Cu^{2+} ion in the pair will have the form $3d(x^2 - y^2)$, where the *z* axis is aligned with the $\langle 100 \rangle$ pair axis. It should be pointed out that, because the $KTaO_3$ crystal is cubic, the copper-pair center axes (the *z* axes) in this crystal can be oriented along three equivalent $\langle 100 \rangle$ directions, whereas in the $YBa_2Cu_3O_{6+x}$ crystal there is only one such axis (taking into account the formation of twins, there can be two *z* axes in the *ab* plane).

We consider the two copper complexes in Figs. 1a and 1b in more detail taking into account the distances between the copper ions, as well as between the copper and the oxygen. The $YBa_2Cu_3O_7$ base structure can be derived from that of a standard, BaCuO-based perovskite by tripling the vertical extent of the unit cell, with substituting a Y atom in one of the cells for the Ba atom and changing the number of the oxygen atoms. The chains consisting of the ^{I}Cu, ^{I}O, and ^{IV}O atoms emerge from the planes because of the oxygen vacancies forming when the ^{V}O atoms are removed. The main structural parameters of $YBa_2Cu_3O_7$ in the orthorhombic phase at 300 K are as follows (in Å) [15]: $a = 3.828$, $b = 3.888$, $c = 11.65$; the bond lengths: $^{I}Cu–^{I}O \cong {}^{I}Cu–^{IV}O = 1.94$, $^{II}Cu–^{II}O = 1.92$, $^{II}Cu–^{III}O = 1.96$, $^{II}Cu–^{IV}O = 2.3$, and $^{I}Cu–^{V}O \cong a/2$. The bond lengths, both in the plane and in the chains, are approximately equal, except the $^{II}Cu–^{IV}O$ bond in the $^{II}CuO_5$ pyramid, and are in agreement with those in the other perovskite compounds. Because the $^{II}Cu–^{IV}O$ distance is larger than the distances from the copper atoms to the other nearest oxygen atoms, the copper–oxygen plane coupling with the copper–oxygen chains, which is mediated by the ^{IV}O atoms, is weak enough to permit considering the given structure as layered. When an oxygen atom is removed from the ^{I}O position (the $YBa_2Cu_3O_6$ phase) or the vacancy is filled by the ^{V}O oxygen atom (the $YBa_2Cu_3O_8$ phase), the crystal symmetry becomes higher (tetragonal). It is highly probable that at intermediate oxygen concentrations a statistical distribution of the oxygen vacancies between the ^{I}O and ^{V}O positions sets in.

Consider the general characteristics of the two copper pair complexes shown in Fig. 1 for the $YBa_2Cu_3O_7$ and $KTaO_3$ crystals:

(1) The lattice constant of $KTaO_3$ $a = 3.88$ Å; i.e., the bond length between the copper occupying the tantalum site and oxygen, Cu–O, is 1.91 Å, which is about equal to the bond length $^{I}Cu–^{V}O \cong a/2 = 1.92$ Å in $YBa_2Cu_3O_7$. Thus, the distance between two $^{I}Cu^{2+}$ ions in the $^{I}Cu^{2+}–^{I}Cu^{2+}$ pair practically coincides with that between the two Cu^{2+} ions in the $Cu^{2+}–Cu^{2+}$ pair in the $KTaO_3$ crystal.

(2) Between the two Cu^{2+} ions in a pair, there is an oxygen vacancy in both cases.

(3) In both cases, each copper ion is surrounded by four O^{2-} oxygen ions located in the plane perpendicular to the pair axis.

(4) As follows from an analysis of the *g* factors, the wave functions of the Cu^{2+} ions in each pair have the same form, namely, $3d(x^2 - y^2)$, where the *z* axis coincides with the bond axis in the pair. This electron configuration is a consequence of the Jahn–Teller effect and should bring about substantial lattice relaxation near the copper centers, in which the equatorial oxygen ions displace toward the axis of the center, whereas the axial ligand ions move apart.

This work assumes that, at some oxygen concentrations (near $x \approx 0.5$), clusters of pairs or of a larger number of ferromagnetically ordered copper ions exchange-coupled through oxygen vacancies and having a total electronic spin $S > 1/2$ are formed in the copper (^{I}Cu) chains. The formation of such magnetic clusters is associated with oxygen redistribution around the ^{I}Cu ions in chains. It is assumed that the copper in the ^{II}Cu layers is in the oxidation state of +2 for all values of *x*, whereas the state of the chain copper changes from $^{I}Cu^{3+}$ at $x = 1$ to $^{I}Cu^{+}$ at $x = 0$. Thus, at intermediate oxygen concentrations *x*, copper clusters of several $^{I}Cu^{2+}$ ions are very likely to form. Note that the neighboring copper ions surrounding the $^{I}Cu^{2+}$ clusters can be in the

diamagnetic $^{I}Cu^{+}$ state [similar to the Ta^{5+} diamagnetic ions around the copper complex in the $KTaO_3$ crystals (Fig. 1b)]. The bonding with the in-plane copper ions, which is mediated by the ^{IV}O oxygen, is too weak to exert a noticeable effect on the magnetic properties of the complex chain-copper centers.

Taking into account the general structural characteristics of the copper pair centers in $YBa_2Cu_3O_7$ and $KTaO_3$, we believe that one may justifiably use the EPR spectral parameters of the copper pair centers in $KTaO_3$ in interpreting the MR spectra observed in the 1–2–3-type compounds. An investigation of the copper pair centers in $KTaO_3$ produced the following results:

(1) The exchange interaction in a pair has a ferromagnetic nature; i.e., the triplet state has a lower energy, with the singlet state lying substantially above the former (apparently by more than 5 cm^{-1}, because we did not succeed in observing a manifestation of this splitting in our experimental conditions).

(2) The fine-structure splitting (the D parameter) is small. Thus, the exchange interaction between copper ions is predominantly isotropic and is due to the direct exchange interaction between two Cu^{2+} ions with the wave functions $3d(x^2 - y^2)$. The magnitude of the D parameter depends substantially on the structural nonuniformities of the crystal; for instance, the introduction of a Li impurity changes the value of D.

(3) The HF structure results in a width of the magnetic resonance line envelope of about 40 mT. Taking into account the fine structure, the linewidth increases about twofold.

The above models can readily be extended to clusters containing more copper ions, but in this case the total electronic spins $S > 1$. Such clusters were discussed in [16, 17]. Because clusters of different sizes in an HTSC crystal are apparently statistically distributed, this results in a distribution of the g factors and of the fine-structure parameter D; the HF structure due to the interaction with copper is not resolved. The interactions between clusters also probably result in a broadening of the MR lines. As for the total width of the unresolved MR line, it is apparently determined by the HF structure and the distributions of the fine-structure parameter D and of the g factor, because of the copper complexes being of different sizes. It should be stressed that our results on $KTaO_3$ indicate that the D parameter is small, which precludes its effect on such characteristics as the low-temperature dependence of the HTSC heat capacity, whereas the exchange splittings very likely lie within the ranges that would allow an explanation for this dependence. In addition, it should be noted that there is a ferromagnetic order and, therefore, the state with the maximum possible spin is energetically preferable.

The annealing-induced shift of the g factor of the magnetic clusters (Fig. 3) indicates that the cluster structure depends on the heat treatments. The size and shape of the clusters apparently change. One cannot rule out the possibility that the g factors (the internal magnetic fields) can be affected to a certain extent by vortex magnetic fields; the latter depend on the fraction of the superconducting phase in the sample, which increases with the anneal temperature. Thus, it may be conjectured that the magnetic resonance is represented by the total signal of many clusters differing in the g factor. This spread manifests itself particularly strongly in the MR linewidth in the Q range, where it is substantially larger than in the low-frequency X range.

We believe that the MR signals observed in the HTSCs are due to ferromagnetically ordered individual clusters containing a certain amount of the $^{I}Cu^{2+}$ ions, which are exchange-coupled through oxygen vacancies.

The temperature dependences of the resonance magnetic fields (and g factors) measured in the X and Q ranges for different HTSC crystal orientations in a magnetic field [4, 5] resemble in shape those observed in quasi-one-dimensional ferromagnets [18]. It was shown that the resonance magnetic fields for such quasi-one-dimensional systems with small spin-aligned regions should be strongly temperature dependent. The resonance field is lower in the direction of the easy magnetization axis; i.e., our experimental data suggest that the easy axis in magnetic clusters lies in a plane perpendicular to the c axis of the crystal, which corresponds to the z axis in our experiments.

As can be seen from the MR spectra in Figs. 4 and 5, the superconducting phase can coexist with the MR, as a result of which the MR lines are strongly broadened, and one observes relaxation effects which manifest themselves in the variation of the linewidth due to rotating the sample and in a subsequent partial recovery of the initial linewidth and shape in time. These experiments strongly suggest that magnetic clusters act as pinning centers for the magnetic flux vortices, thus permitting their use to probe vortex fields in HTSC materials.

ACKNOWLEDGMENTS

The authors are indebted to M.A. Borik and P.P. Syrnikov for providing some materials for the study and to I.V. Il'in for assistance in HTSC measurements.

This study was supported in part by the Russian Foundation for Basic Research, grant no. 00-02-16950.

REFERENCES

1. K. A. Müller, in *Phase Separation in Cuprate Superconductors*, Ed. by E. Sigmund and K. A. Müller (Springer-Verlag, Berlin, 1994), p. 1 and references therein.
2. E. K. Zavoisky, J. Phys. **9** (211), 245 (1945).
3. V. I. Aleksandrov, A. G. Badalyan, P. G. Baranov, *et al.*, Fiz. Tverd. Tela (Leningrad) **29**, 3710 (1987) [Sov. Phys. Solid State **29**, 2123 (1987)]; A. G. Badalyan, P. G. Bara-

nov, V. I. Aleksandrov, *et al.*, Pis'ma Zh. Éksp. Teor. Fiz. **49** (11), 606 (1989) [JETP Lett. **49**, 697 (1989)].

4. P. G. Baranov and A. G. Badalyan, Solid State Commun. **85**, 987 (1993); P. G. Baranov and A. G. Badalyan, in *Phase Separation in Cuprate Superconducrors*, Ed. by E. Sigmund and K. A. Müller (Springer-Verlag, Berlin, 1994), p. 118; P. G. Baranov and A. G. Badalyan, Physica C (Amsterdam) **235–240**, 267 (1994).
5. P. G. Baranov, A. G. Badalyan, and I. V. Il'in, Fiz. Tverd. Tela (St. Petersburg) **37**, 3296 (1995) [Phys. Solid State **37**, 1811 (1995)] and references therein.
6. D. V. Azamat, A. G. Badalyan, P. G. Baranov, *et al.*, Pis'ma Zh. Éksp. Teor. Fiz. **69**, 890 (1999) [JETP Lett. **69**, 943 (1999)].
7. V. E. Zubkus, S. Lapinskas, and E. E. Torneau, Physica C (Amsterdam) **166**, 472 (1990).
8. K. Nakahigashi, S. Nakanishi, M. Kogachi, *et al.*, Int. J. Mod. Phys. B **2**, 1431 (1988).
9. M. D. Glinchuk, Izv. Akad. Nauk SSSR, Ser. Fiz. **51**, 2124 (1987) and references therein; V. V. Laguta, A. A. Karmazin, I. P. Bykov, *et al.*, Izv. Akad. Nauk SSSR, Ser. Fiz. **51**, 2130 (1987).
10. J. Owen and E. A. Harris, in *Electron Paramagnetic Resonance*, Ed. by S. Geschwind (Plenum, New York, 1972), p. 427.
11. J. R. Morton and K. F. Preston, J. Magn. Reson. **30**, 577 (1978).
12. E. Clementi and C. Roetti, At. Data Nucl. Data Tables **14**, 177 (1974); A. D. McLean and R. S. McLean, At. Data Nucl. Data Tables **26**, 197 (1981).
13. B. S. Gourary and F. J. Adrian, Phys. Rev. **105**, 1180 (1957).
14. R. K. Kremer, E. Sigmund, V. Hizhnyakov, *et al.*, Z. Phys. B: Condens. Matter **86**, 319 (1992).
15. S. K. Filatov, V. V. Semin, V. B. Trofimov, and A. N. Nazarenko, *High-Temperature Superconductivity: Fundamental and Applied Investigations* (Mashinostroenie, Leningrad, 1990), Vol. 1.
16. M. V. Eremin and E. Sigmund, Solid State Commun. **91**, 367 (1994).
17. R. M. Eremina, Fiz. Tverd. Tela (St. Petersburg) **39**, 1320 (1997) [Phys. Solid State **39**, 1171 (1997)].
18. R. Hoogerbeet and A. J. van Duyneveldt, Physica B (Amsterdam) **121**, 233 (1983).

Translated by G. Skrebtsov